Corrosion Derived Iron Carbonate SLIPS for Calcium Carbonate Scale Mitigation

Alexander Saul

Submitted in accordance with the requirements for the degree of
Doctor of Philosophy

The University of Leeds
Institute of Functional Surfaces
School of Mechanical Engineering

April 2025

Intellectual Property and Publication Statements

The candidate confirms that the work submitted is his/her own, except where work which has formed part of jointly authored publications has been included. The contribution of the candidate and the other authors to this work has been explicitly indicated below. The candidate confirms that appropriate credit has been given within the thesis where reference has been made to the work of others.

In all papers listed below, the primary author completed all experimental studies, evaluation of data and preparation of publications. All authors contributed to proof reading of the articles prior to publication.

- Saul, A., Barker, R., Baraka-Lokmane, S., Le Beulze, A., Charpentier, T., Tangparitkul, S., … Neville, A. (2021). Corrosion derived lubricant infused surfaces on X65 carbon steel for improved inorganic scaling performance. Journal of Adhesion Science and Technology, 36(6), 632–653. https://doi.org/10.1080/01694243.2021.1932315
- Saul, Alexander, Neville, Anne, Baraka-Lokmane, Salima, Le Beulze, Aurelie, Charpentier, Thibaut, Tangparitkul, Suparit, and John-Richard Ordonez-Varela. "Iron Carbonate Based Slippery Liquid Infused Porous Surfaces (SLIPS) for Enhanced Mineral Fouling Resistance." Paper presented at the CORROSION 2021, Virtual, April 2021.

Acknowledgements

First and most importantly I would like to thank Prof Anne Neville for giving me the opportunity, for her supervision, continued support, enthusiasm and advice throughout the PhD. I am forever grateful for the time I was able to spend with her. RIP.

A thank you to my initial supervisor, Thibaut Charpentier. And a big thank you to my final supervisor, who was forced to pick up the pieces and continued to stick by me after a lengthy writing process. Although I am slightly upset he was not on board my attempts to break the 52 year long PhD record.

Many thanks to my financial sponsors Total, in particular Salima and John Richard for their technical support.

I would like to express my gratitude and appreciation to the Leeds admin, postgrad studies and lab staff. Mick, Ryan, Paul, Jordan, Joanne, Victoria and everyone else who was unfortunately associated with me.

Also a thank you to all the colleagues and friends made at Leeds during the course of the PhD and the pandemic. You know who you are.

And of course Mum and Dad for the constant badgering that got me over the finish line.

"Research is what I'm doing when I don't know what I'm doing."

Abstract

The focus of this research is to build on an emerging surface technology, known as Slippery Liquid Infused Porous Surfaces (SLIPS) or Lubricant Infused Surfaces (LIS). The newly designed surface is intended specifically to provide anti-fouling capabilities in an oilfield environment. This concept brings together a number of large research bodies including CO_2 corrosion, mineral scaling, surface engineering and SLIPS knowledge. The idea is to use the corrosion by-products, already occurring in oil pipelines to generate an anti-scale surface in the framework of temporary SLIPS design.

SLIPS is a concept idea that has yet to be fully commercialised in the industry but has shown great promise in a number of similar applications. This research is undertaken to confirm existing understanding of the SLIPS system and investigate a new SLIPS combination for oilfield scale applications, specifically calcium carbonate ($CaCO_3$) environments. The intended starting point for this research is the construction of a SLIPS with commercial relevance. Here carbon steel has been used initially due to its prevalence in the industry. The surface will be modified for lubricant infusion by incorporating a naturally occurring CO_2 corrosion process to form a corrosion by-product film. The corrosion product will be an initially, corrosion resistant, iron carbonate ($FeCO_3$) crystal layer. This layer has been fabricated based on optimum environmental conditions and characterised to provide further details on key surface properties. Next a predictive model has been applied to theoretically and experimentally validate the various components of the SLIPS system (i.e substrate, fabrication method, and lubricant). The end product is the formation of a repeatable and stable SLIPS base layer that has been successfully tested with four different lubricant options in preliminary conditions to stimulate flow assurance issues in the Oilfield. This work develops the body of knowledge in the SLIPS and Flow assurance field (including corrosion and scaling) and how they interact together.

Table of Contents

List of Tables

List of Figures

Nomenclature

a	ionic activity / geometric factor / unit cell parameter
aa, ac	transfer coefficients
AAS	Atomic Absorption Spectroscopy
B	Stern-Geary constant
BMIM TFSI	1-Butyl-3-methylimidazolium Bis(trifluoromethanesulfonyl)imide
c	unit cell parameter
CA	Contact Angle
$CaCO_3$	Calcium Carbonate
Ca^{2+}	Calcium ion
CE	Counter Electrode
CO_2	Carbon Dioxide
CO_3^{2-}	Carbonate
CR	Corrosion Rate
CS	Carbon Steel
C_{dl}	double layer capacitance
d	interplanar spacing / droplet
DI	Distilled Water
DLC	Diamond-Like Carbon
DVLO	Dejaguin, Landau, Verwey and Overbeck theory
E	Electrode Potential
e^-	electron
E_{corr}	Corrosion Potential
EDL	Electric Double Layer
EDX	Energy-Dispersive X-ray Spectroscopy
EEC	Equivalent Electrical Circuit
EIS	Electrochemical Impedance Spectroscopy
EOR	Enhanced Oil Recovery
F	Faraday's Constant

f	fractional area
Fe	Iron
Fe^{2+}	Ferrous ion
$FeCO_3$	Iron Carbonate
$Fe_2(OH)_2CO_3$	Chukanovite
Fe_3C	Iron Carbide (Cementite)
Fe_3O_4	Iron (II,III) Oxide (Magnetite)
$Fe_xCa_yCO_3$	Iron-calcium carbonate
FIB	Focused Ion Beam
FTIR	Fourier-Transform Infrared Spectroscopy
ΔG	Gibbs Free Energy Change
ΔG*	activation barrier for nucleation
ΔG_{crit}	critical free energy
ΔG_{het}	homogeneous nucleation free energy
ΔG_{hom}	heterogeneous nucleation free energy
ΔGN	Free energy of nucleation
ΔGS	Surface excess free energy
ΔGV	Volume free energy
h, k, l	Miller indices
H^+	Hydrogen ion
H_2	Hydrogen gas
H_2CO_3	Carbonic acid
HCO_3^-	Bicarbonate
I_{corr}	Corrosion Current
IL	Ionic Liquid
J	Nucleation Rate
K_{sp}	Solubility Product Constant
Krytox	Perfluoropolyether
l	lubricant

LB	Lower Boundary
LIS	Lubricant Infused Surfaces
LPR	Linear Polarization Resistance
LW	Lifshitz theory of van der Waals forces
M	Metal
M^{n+}	Metal ion
M_m	molar mass
m	wetting parameter
Micro CT	Micro-Computed Tomography
n	Moles of Electrons
N	density of nucleation sites
OCP	Open Circuit Potential
PFAE	Perfluoroalkyl ether
PFPE	Perfluoropolyether
QCM	Quartz Crystal Microbalance
R	Ideal Gas Constant / Roughness Ratio
r	radius
Ra	Arithmetic Average Roughness
rc	critical radius
R-$FeCO_3$	Roughness corrected Iron Carbonate
RE	Reference Electrode
R_p	Polarization Resistance
R_s	solution resistance
R_{sk}	Skewness
R_{ct}	charge transfer resistance
s	solid
S	Spreading coefficient
SCE	Saturated Calomel Electrode
S_{dr}	Developed Interfacial Area Ratio

SEM	Scanning Electron Microscopy
SFE	Surface Free Energy
SHE	Standard Hydrogen Electrode
SI	Saturation Index
SiC	Silicon Carbide
SLIPS	Slippery Liquid Infused Porous Surfaces
SLIPS BM	SLIPS with BMIM TFSI lubricant
SLIPS Kr	SLIPS with Krytox lubricant
SLIPS NW	SLIPS with Non-waxy Crude Oil lubricant
SLIPS W	SLIPS with Waxy Crude Oil lubricant
SS	Supersaturation Ratio
T	Absolute Temperature
t_{ind}	induction time
t_g	growth time
t_n	nucleation time
t_r	relaxation time
UB	Upper Boundary
v	crystal molecular volume
vOCG	van Oss-Chaudhury-Good
WCA	Water Contact Angle
WE	Working Electrode
wt.%	weight percent
XRD	X-Ray Diffraction
y	molar fraction
Z	Impedance / Zeldovich factor
Z'	real impedance
Z''	imaginary impedance
β	Boltzmann constant
β_a	Anodic Tafel constant

β_c	Cathodic Tafel constant
β^*	atomic attachment rate
γ, σ	Surface Energy / Surface Tension
γ^+/ γ^-	LW acid/base components of surface energy
γ_{sL}	solid-liquid interfacial tension
γ_{sv}	solid-vapor surface tension
ΔE	Change in Potential
ΔI	Change in Current
$\Delta\theta$	Contact angle hysteresis
θ	Contact Angle
θ_c	critical contact angle
θ_e	equilibrium contact angle
λ	wavelength
ρ	density
σ_{cs}	crystal-substrate interfacial energy
σ_{cw}	crystal-water interfacial energy
σ_{sw}	substrate-water interfacial energy
Φ, φ_s	solid/liquid contact area fraction
ω	angular frequency

Chapter 1
Introduction, Motivation of Study, Research Objectives and Thesis Structure

1.1 Introduction

The oil and gas sector plays a critical role in the global economy and energy framework, with far-reaching effects on industrial activities, energy consumption and geopolitical relations. Growth in oil demand is expected to rise by 3.2 mb/d between 2023 and 2030, supported by increased use of jet fuel and feedstocks from the petrochemical sector. The bulk of this demand being driven by non-OECD (Developing) countries as seen in Figure 1. To meet this growing demand, global upstream capital expenditures to boost capacity were USD 538 billion in 2023 alone [1]. Despite increasing investments in renewable energy and societal awareness, fossil fuels account for 82% of global primary energy consumption, a trend that is not expected to change [2].

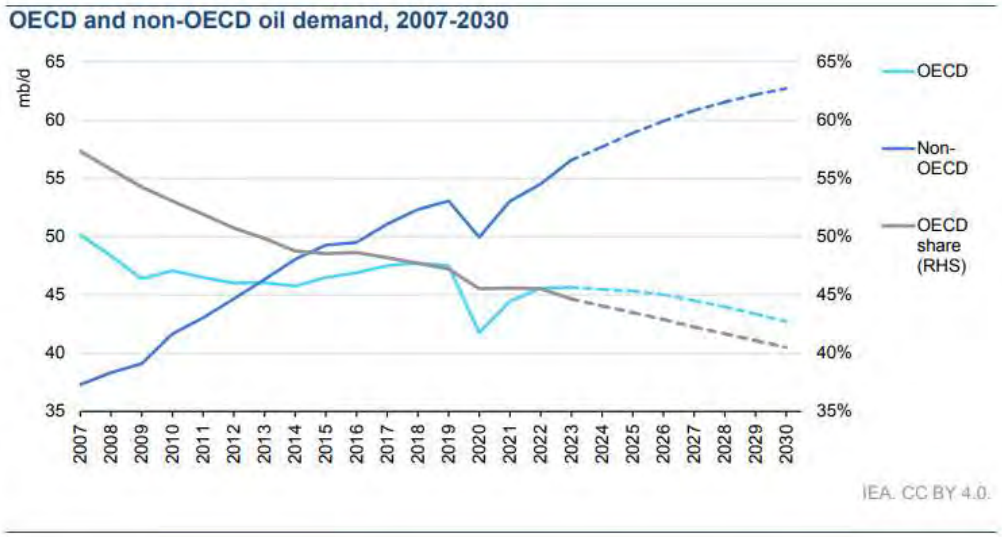

Figure 1 OECD vs non-OECD oil demand projections from 2007-2030

From a technological standpoint, the oil and gas industry has been a driving force behind significant advancements in exploration, extraction, and

processing technologies. Techniques such as hydraulic fracturing (fracking), deepwater drilling, and enhanced oil recovery (EOR) have enabled the development of previously untapped reserves, such as shale gas and deepwater fields (Figure 2). These innovations have not only augmented the global supply of oil and gas but have also enhanced the economic feasibility of extraction, making it possible to access reserves in increasingly challenging environments [3-6].

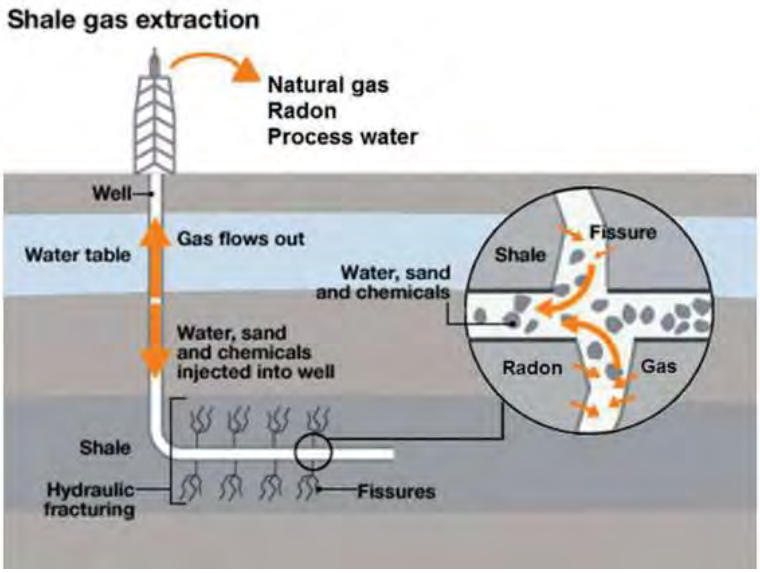

Figure 2 Schematic of unconventional reservoir: shale gas [7]

Flow assurance is essential in the oil and gas industry, ensuring the continuous and reliable transportation of hydrocarbons from reservoirs to processing facilities. The primary causes of flow assurance issues are attributed to corrosion and fouling, either external or internal. Failure to manage these issues can lead to significant financial losses, with unplanned downtime costing operators between $38 to over $88 million per year [8]. Annual scale removal costs from one well can be up to $2.5 million [9], while the global market for preventative maintenance solutions such as corrosion inhibitors is projected to reach $10.1 billion by 2026 [10]. In worst case scenarios, the environmental fallout from oil spills can lead to fines and cleanup costs up to $43 billion (Figure 3) [11]. Thus, effectively managing flow assurance is critical for minimising downtime, optimising costs, and ensuring safety and environmental protection.

Issue	Amount BP has spent/set aside, in 2010 US$
Litigation and settlement cots	$25.87 billion
Spill response costs	$14.30 billion
Clean Water Act penalties	$3.51 billion
Environmental costs	$3.03 billion
Other costs	$1.94 billion
Sub-total	$48.65 billion
Less recoveries	$5.68 billion
Total	$42.97 billion

Figure 3 Costs to BP associated with Deepwater Horizon oil spill [11]

Coatings and surface-based solutions have become integral to addressing flow assurance challenges in the oil and gas industry, where issues such as scaling formation and corrosion can disrupt operations. Coatings, including anti-fouling, anti-corrosion, and scale inhibitor coatings, as well as advanced surface modification techniques, offer innovative ways to enhance the performance and longevity of pipelines, risers, and other production infrastructure. Recent advancements in coatings, inspired by nature, have the potential to revolutionize flow assurance strategies in the oil and gas industry. Nature has long provided solutions for enhancing surface properties, such as the self-cleaning ability of lotus leaves or the slipperiness of fish scales (Figure 4). These natural phenomena have inspired the development of bio-inspired coatings, particularly slippery liquid-infused porous surfaces (SLIPS). SLIPS coatings mimic the low-friction properties of certain plants and animals, are designed to reduce the adhesion of fouling agents and the potential occurrence of flow assurance issues. These coatings work by creating a lubricated, non-stick surface that prevents the buildup of unwanted materials. By combining advanced materials science with principles drawn from nature, these bio-inspired coatings offer a promising solution to address critical flow assurance challenges in offshore and deepwater oil and gas operations.

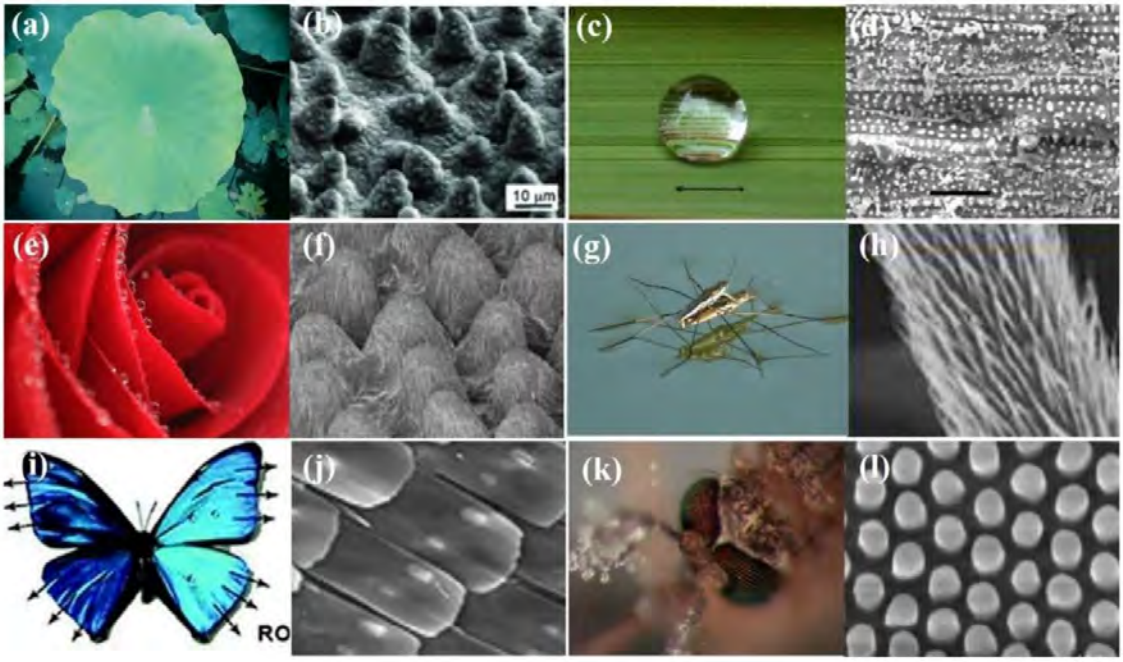

Figure 4 Natural organisms and SEM images of corresponding surface texture [12]

1.2 Motivation, Research Questions and Objectives

The growing complexity of flow assurance challenges in the oil and gas industry, necessitates the development of innovative solutions for existing challenges. Traditional methods to manage corrosion and scaling have limitations in terms of longevity, environmental impact, and cost-effectiveness. As such, research in the area of Slippery Liquid-Infused Porous Surfaces (SLIPS) presents a compelling avenue for advancing flow assurance technologies. SLIPS coatings, inspired by nature, offer a novel approach to preventing material buildup on critical infrastructure. This combines a number of superior capabilities over traditional surface coatings (such as self-healing, self-cleaning etc.) in improving operational and maintenance related outcomes. The area remains high in potential for further breakthroughs into optimizing their performance, scalability, and applicability in harsh, real-world oil and gas conditions. This research could pave the way for more sustainable, cost-effective, and reliable flow assurance solutions, ultimately benefiting the industry by improving operational efficiency and minimizing environmental harm.

Various SLIPS have been created using several substrates and fabrication methods in a range of applications. This project looks into the development of a new SLIPS system (Figure 5). This SLIPS will be a novel combination of substrates, fabrication methods and lubricant choice for a potential future application in the Petroleum industry. The fundamental research question is “Can a SLIPS system for an oilfield scale environment be fabricated?”. This research, in collaboration with Total UK, will investigate the feasibility of a SLIPS system for use in Oil and Gas scenarios. Bridging the gap between industrial and academic questions. This question has been broken down into a series of further objectives which have formed the basis of chapters in this thesis. These objectives revolve around 1) The fabrication and characterisation of the SLIPS system, 2) Scaling performance/evaluation in $CaCO_3$ conditions and 3) Electrochemical analysis

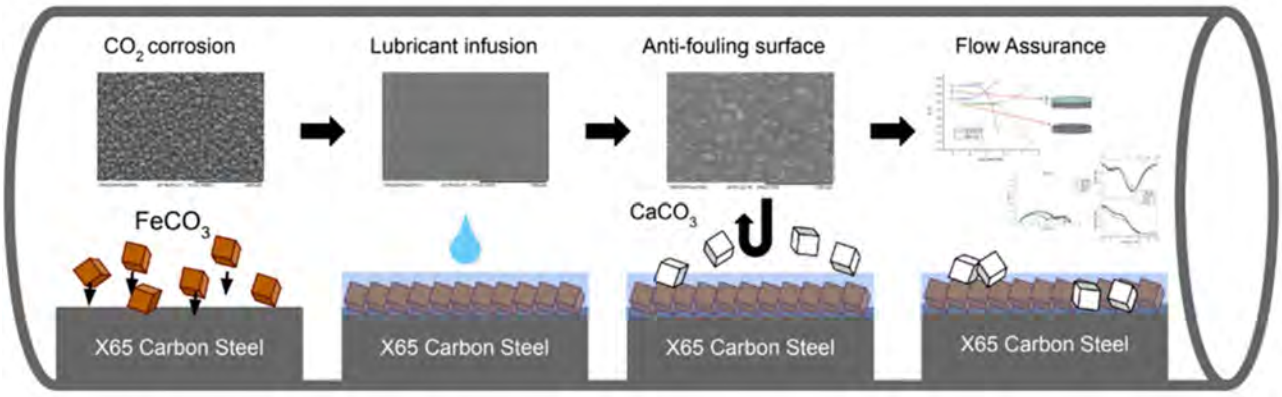

Figure 5 Graphical schematic of thesis structure

The SLIPS system contains several components which must be fabricated and characterised. Central to the idea of an industrially relevant SLIPS is the use of an applicable base material, which in this case is X65 carbon steel. It is well documented that the CO_2 corrosion process produces a $FeCO_3$ layer that will form the foundation of the SLIPS system in this case. The research objectives in this case are:

- Understanding the conditions for the formation of protective $FeCO_3$ layers. Including the influence of environmental parameters and surface roughness.
- Establishing a suitable $FeCO_3$ layer to be used as a SLIPS base layer. Evaluating surface characteristics of this layer including roughness and surface energy.
- Determining suitability of SLIPS components (i.e $FeCO_3$ and lubricant) based on prevailing design theory and experimental validation.

After fabrication of the complete SLIPS system, the research focus shifts to testing and performance evaluation. The testing conditions are related to a common scale encountered in oilfields, $CaCO_3$.

- Characterisation of the SLIPS with regards to surface energy (a parameter linked to scaling mitigation)
- A broad fundamental understanding of $CaCO_3$ scale deposition on SLIPS employing a framework of analytical methods for scale performance evaluation.
- Investigation of dual flow assurance (corrosion and scale) phenomena and in-situ analysis of SLIPS behaviour.

1.3 Thesis Structure

The thesis is divided into the following chapters to address the preceding research questions and topics.

Chapter 1. Contains the preamble information related to the thesis. Including a brief introduction of the work, research questions, objectives and the thesis structure.

Chapter 2. Consists of a comprehensive literature review compromising one of the three main fields of research involved. The first section includes general aqueous CO_2 corrosion and the formation of $FeCO_3$

Chapter 3. Continuation of literature review. The second section deals with theories of mineral scaling, $CaCO_3$ deposition and oilfield mitigation methods.

Chapter 4. Continuation of literature review. This final section explores literature related to SLIPS theories, capabilities and design.

Chapter 5. Experimental methodology that outlines the main materials, procedures, analytical techniques and calculation methods for all research work undertaken.

Chapter 6. The first results chapter, which explores the development of an $FeCO_3$ base layer from varying environmental conditions, surface roughness and the characterisation of this fabricated layer. The results also cover the compatibility of this layer with lubricant choices (4) in the context of prevailing SLIPS design theory.

Chapter 7. The second results chapter covers the testing of these 4 SLIPS systems in a $CaCO_3$ scaling environment. Analytical results from SEM, EDX, XRD and FTIR for two brine systems of different saturation index are covered. This chapter also includes characterisation of the bulk brine system and surface energy calculations of the fabricated SLIPS.

Chapter 8. The final results chapter looks at both flow assurance issues, corrosion and mineral scaling. Here Tafel and EIS experiments have been conducted to explore the corrosion and in-situ behaviour of the SLIPS samples.

Chapter 9. Provides concluding remarks and recommendations for future work.

Chapter 2
All things corrosion

2 CO_2 Corrosion Theory

2.1 Definition

Corrosion is an ancient phenomena that has existed since the times of Plato (427-347 BC) [13]. At its basic level it is commonly defined as:

"the destructive attack of a metal by chemical or electro chemical reaction with its environment" [14]

Corrosion has, and continues to be, a serious issue for a number of modern-day industries. The oil and gas industry is particularly susceptible to corrosion at all levels of the petroleum process, whether that be Upstream (Drilling), Midstream (Transportation) or Downstream (Refinement) operations. Corrosion in the oilfield begins at the reservoir where a complex solution containing dissolved gasses (typically Carbon Dioxide/CO_2 or Hydrogen Sulphide/H_2S) are extracted and brought to the surface. If left unchecked or poorly managed, oilfield corrosion has the potential to lead to disastrous consequences. Over 25% of failures in the Petroleum industry are the result of corrosion related issues [15] of which at least half are caused by CO_2 induced corrosion.

At its crux, the degradation of metal material that occurs during the corrosion process is an electron transfer reaction, as seen in Equation 1. Here a neutrally charged metal atom will lose electrons to become a charged metal ion and involves both an anodic and corresponding cathodic reaction. The anodic reaction, being oxidation with the loss of electrons from the metal while the cathodic reaction is the reduction of electrons in the local environment.

$$M \rightarrow M^{n+} + ne^{-}$$

Equation 1

For this research, an understanding of the nature of the CO_2 corrosion process is vital to the construction of the SLIPS system. It is through the process of corrosion that the original substrate-electrolyte interface is modified (through the formation of a rough, porous corrosion product) in order to provide a suitable surface for lubricant infusion. The literature review seeks to cover the driving forces behind corrosion and the corrosion product formation mechanisms, specifically in the context of CO_2 corrosion, in order to understand and better control the fabrication of its by-products.

The following section will outline some of the fundamental concepts associated with corrosion and its products, particularly relevant to this PhD and the oil and gas industry.

2.2 Thermodynamics of Corrosion

Basic corrosion mechanisms are best understood using the principles of the electrochemical cell, as shown in Figure 6. An electrochemical cell is made up of four components which include [16]:

- Anode- The target of the cell reaction (i.e. metal to be corroded). Generates electrons.
- Cathode- Another electrical conductor to receive electrons.
- Electrolyte- Aqueous solution that provides ionic pathway.
- Return path- A conductive bridge between the anode and cathode.

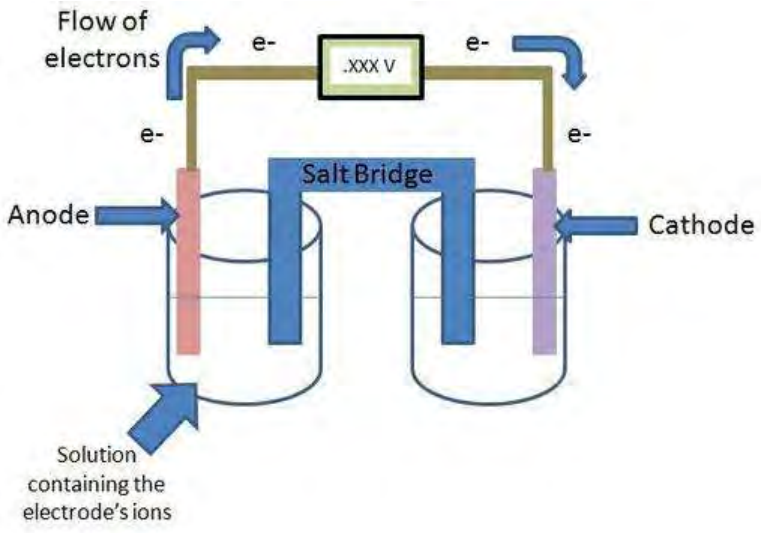

Figure 6 General electro-chemical cell set-up [17]

The anode is the negative pole that discharges ions/ generates electrons into the electrolyte solution in a process known as oxidation. The cathode is the positive pole that takes the electrons/ions during the reduction process. The electrolyte solution acts as a conduit for the ions to pass from the anode to cathode. Whilst the return path provides a bridge from which electrons can move [18]. In oilfield pipelines the electrochemical cell is simulated on the metal surface, with different areas of the pipe material acting as anode and cathode.

The susceptibility of metallic materials corroding can also be explained thermodynamically [19], as corrosion will only occur if the reaction is energetically favourable. Metals will attempt to revert to the lowest stable energy, which can lead to spontaneous reactions with the surrounding environment, creating solutions and compounds until a constant state is achieved. According to the 2nd law of thermodynamics this represents the total changes in enthalpy, entropy and temperature, also commonly defined as free energy. Pourbaix diagrams often summarise the stable thermodynamic states that exist for various metals through a plot consisting of potential vs pH [20, 21], as shown in Figure 7.

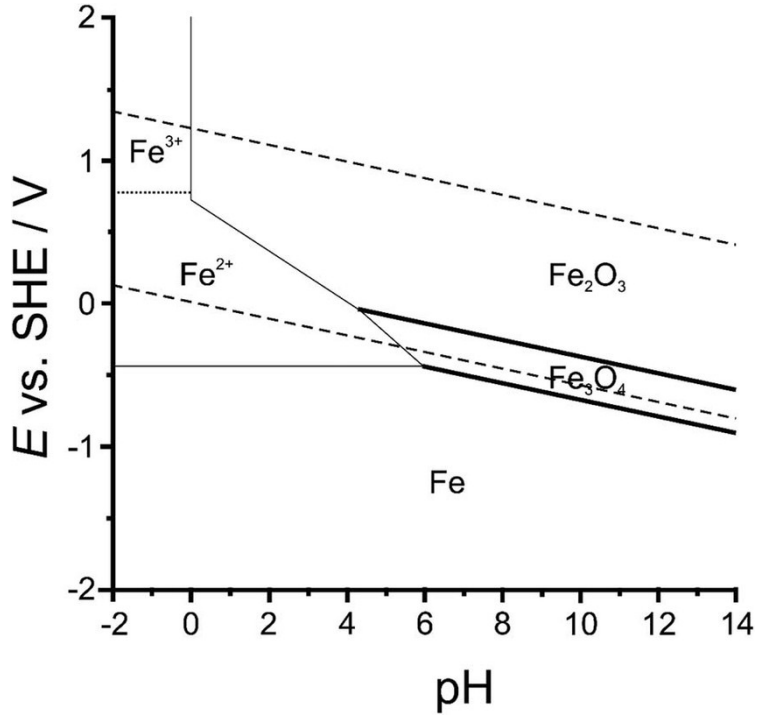

Figure 7 Pourbaix diagram for Iron-water system [22]

The change in free energy between metal and the environment is referred to as the change in Gibbs free energy (ΔG) [23, 24]. This is the driving force behind corrosion and a key component in understanding the probability of it occurring [14]. When ΔG = 0, the system remains in equilibrium. At ΔG < 0, corrosion occurs spontaneously and when ΔG > 0 the metal is in a stable state. The relation between ΔG, E (measured cell potential), n (number of electrons) is incorporated with Faraday's law in the general equation [25] below:

$$\Delta G = (-nF)E$$

Equation 2

Equation 2 is further refined for standard conditions [16] providing a standard redox potential for various metals that make up the electrochemical series, as seen in Table 1. The change in Gibbs free energy is a good indicator for

whether materials may corrode but will not provide information on the corrosion rate itself.

Table 1 Standard electrode potentials of various metals (vs SHE) [12]

Metal	Reaction	Electrode Potential (V)
Gold	$Au^{+} + e^{-} = Au$	+ 1.692
Silver	$Ag^{+} + e^{-} = Ag$	+0.7996
Copper	$Cu^{2+} + 2e^{-} = Cu$	+0.342
Iron	$Fe^{3+} + 3e^{-} = Fe$	-0.037
Lead	$Pb^{2+} + 2e^{-} = Pb$	-0.126
Nickel	$Ni^{2+} + 2e^{-} = Ni$	-0.257
Cadmium	$Cd^{2+} + 2e^{-} = Cd$	-0.403
Iron	$Fe^{2+} + 2e^{-} = Fe$	-0.447
Zinc	$Zn^{2+} + 2e^{-} = Zn$	-0.762
Aluminum	$Al^{3+} + 3e^{-} = Al$	-1.662

Another key thermodynamic relationship in corrosion is the Nernst equation [26, 27] (Equation 3) which is derived from the Gibbs Free energy. This relationship provides the potential of a metal in solution with given environmental concentrations and temperature. When the activity/concentration of products species increases relative to that of reactants, the electrode potential becomes more positive and vice versa.

$$E = E^{\circ} - \frac{RT}{nF} \ln \frac{[Products]}{[Reactants]}$$

Equation 3

Where R is the ideal gas constant in J/mol.K, T is the temperature in Kelvin and [Products] and [Reactants] are the molar concentrations/activities of the products and the reactants, respectively.

2.3 Corrosion Kinetics

Corrosion kinetics covers the rate of reactions taking place during the corrosion of a material, specifically the anodic and cathodic tendencies [28]. Before further discussion of electrochemical kinetics, an important concept that must first be defined is that of the Electric Double Layer (EDL) [29]. After the immersion of a metal in solution, a solid/liquid interface is generated with local anodic and cathodic sites differing in energy state. As the metal corrodes, the loss of these ions into the surrounding electrolyte, leads to a negatively charged surface. Subsequently those ions released into the adjacent electrolyte layer, provide an independent chemical composition to the surrounding bulk solution. Together, the negatively charge surface and adjacent electrolyte layer make up the EDL [30] as seen in Figure 8. The charge separation that occurs in this EDL allows for the creation of a measurable potential.

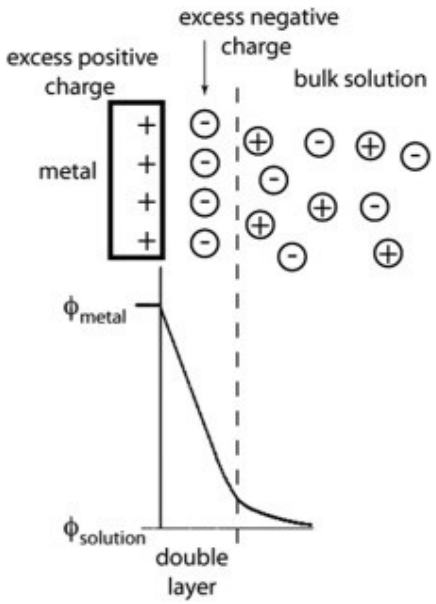

Figure 8 Simple structure of Electric Double Layer and potential distribution [31]

Mixed potential or Evans diagrams provide an indication of the link between the potential (E) and a corrosion current (I) [32, 33]. The graphical representation shows the existence of an equilibrium corrosion potential (E_{corr}) and corrosion current (I_{corr}) which occurs at the intersection of anodic and

cathodic reactions. These combined half-cell reactions appear as non-linear curves around the corrosion potential. The Evan's diagram (Figure 9) is crucial to understanding electrochemical reactions but does not allow the direct calculation of corrosion rates and is limited to qualitative estimations.

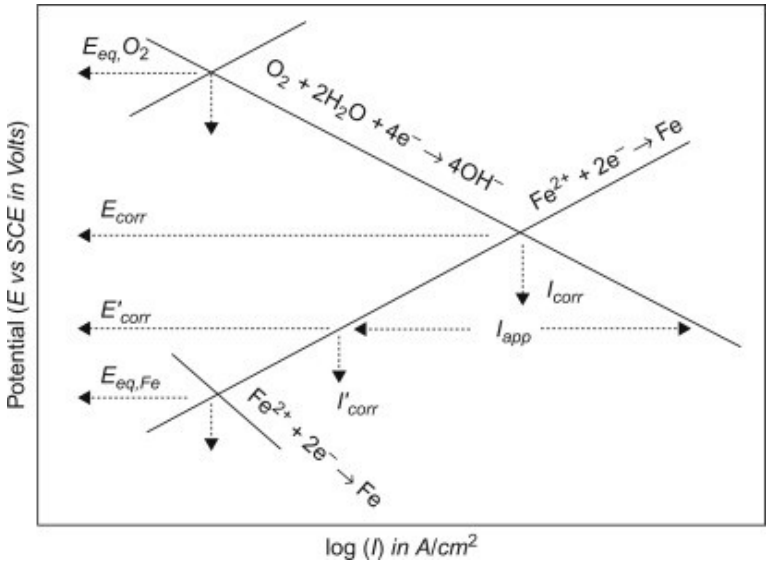

Figure 9 Evans diagram of the corrosion of Iron [34]

Generally for quantitative assessment of corrosion rates, the process of polarisation is used. The disturbance in the electrode or corrosion potential caused by changes in the current flow is known as polarisation. This resultant shift in potential is denoted as η or overpotential. Primarily it occurs in three forms:

1. Activation polarisation- This type revolves around overcoming activation energies or charge transfer which occur through slow material dissolution or deposition rates.
2. Concentration polarisation- Concentration refers to ion changes at the EDL and diffusion layer that exist close to the electrode.
3. Resistance polarisation (Ohmic)- Deals with potential drops caused by high resistivity or insulating effects.

The mathematical link that allows experimental measurement of corrosion current density from applied overpotential is the Butler Volmer equation (Equation 4). The Butler-Volmer equation can be monitored in-situ and

provides the foundation for converting electrochemical signals into corrosion rates. Although it must be noted that its applicability relies on the presence of single charge-transfer-controlled cathodic and anodic reaction.

$$i_o = i_{corr} \left[e^{\frac{(1-\alpha)nF(E-E_{corr})}{RT}} - e^{\frac{-\alpha nF(E-E_{corr})}{RT}} \right]$$

Equation 4

where E_{corr} is the free corrosion potential in Volts, i_o is the external current in Amps/cm^2 flowing to or from the electrode because of an applied potential, i_{corr} is the corrosion current density in Amps/cm2 that occurs when the electrode is at E_{corr}, E is the applied potential in Volts, α is a coefficient ranging from 0 to 1 and R, T, n and F have been defined previously. Corrosion kinetics are commonly calculated as penetration rates in millimetres per year (mmpy).

2.4 Corrosion Measurement Techniques

Three Electrode Cell

Corrosion measurement techniques encompass a wide range of direct current (DC) and alternate current (AC) electrochemical methods. Most use the same three electrode cell based on the electrochemical cell mentioned previously and displayed in Figure 10. The three-electrode cell is the foundation of laboratory experiments that allow for the measuring of potential and the calculation of corrosion rates. It includes 4 primary components:

1. Working electrode (WE)- The material of interest or test subject whose corrosion reactions will be studied.
2. Counter electrode (CE)- Completes the cell circuit and balances current in the system.
3. Reference electrode (RE)- Provides a reference control, measuring and controlling the WE potential without passing current.
4. Potentiostat- Electronic equipment/ analytical instrument that is connected to the electrodes and sits externally to the cell. Allowing for the measurement and generation of potentials and currents in the cell.

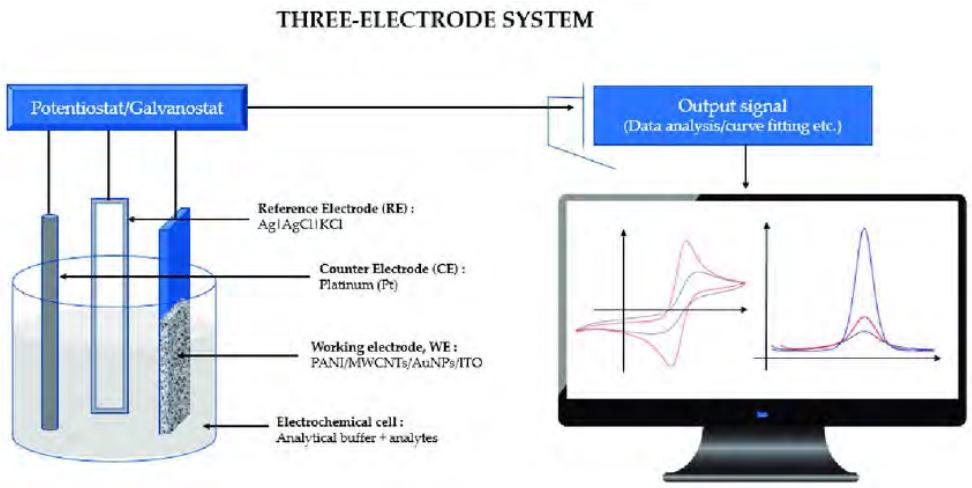

Figure 10 Typical set-up for generic 3 electrode corrosion cell [35]

Open Circuit Potential (OCP)

OCP represents the most basic electrochemical measurement technique. As the name suggests it represents the natural electrode potential difference between the two electrode half-cells in an open circuit. In essence this is the stable potential the test material exists in, with regards to its surrounding environment/electrolyte. This is the state that exists when there is no externally applied current or potential and is commonly referred to as the free corrosion potential. It provides an initial indication of the test materials susceptibility to corrosion, shows when the system is in equilibrium and provides numerical parameters for further corrosion testing.

Linear Polar Resistance (LPR)

LPR is a direct current method established by Stern and Geary to determine polarisation resistance (R_p). The method focuses on the polarisation relationship that exists between current (I) and potential (E) in close proximity to E_{corr}. The sample is polarised with small perturbations above and below the OCP to record R_p values in the linear region under activation control (as shown in the simplified Equation 5 and Figure 11).

$$R_p = \left(\frac{\Delta E}{\Delta I}\right)_{\lim_{E \to 0}}$$

Equation 5

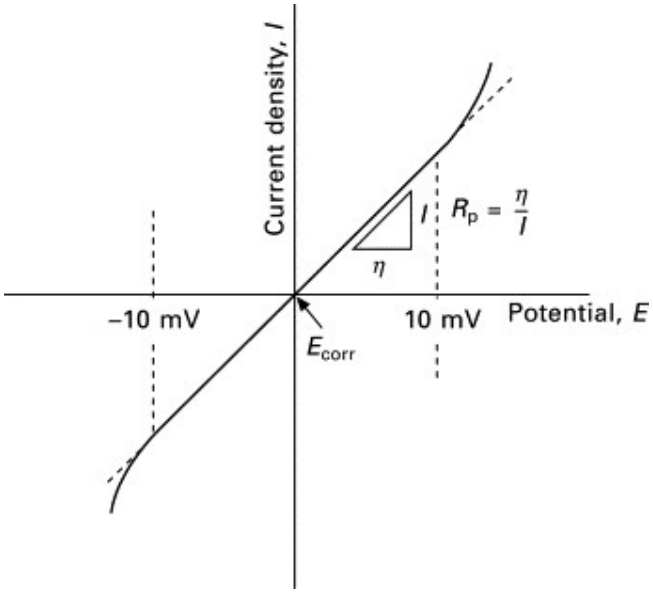

Figure 11 Relationship between current and potential used in LPR [36]

The Stern-Geary equation can be further refined with the incorporation of the proportionality constant, B (Equation 6). This constant is composed of both anodic (β_a) and cathodic (β_c) values determined from Tafel plots (to be discussed in next). Usually this constant is assumed (i.e 120mV for mild steel), with values taken from previous tests in literature. However direct measurements can also be calculated through Tafel extrapolation methodology to obtain real values for Tafel constants.

$$I_{corr} = \frac{B}{R_p} \; where \; B = \frac{\beta_a \beta_c}{2.303(\beta_a + \beta_c)}$$

Equation 6

This technique is non-destructive and allows for repeated measurements. The determination of corrosion rates is then made through Equation 7

$$CR = \frac{I_{corr} K\ M_m}{nF\rho}$$

Equation 7

Where K is the unit conversion factor, M_m is the molar mass, n are the equivalents per mole (2), F is the Faraday constant and ρ is the density.

Tafel Plot

The Tafel plot, is essentially the two curves that make up the Evans Diagram (mentioned previously). Tafel plots are a type of potentiodynamic polarisation and provide Tafel slopes of both the anodic and cathodic branches of the sample in question. A Tafel plot is drawn by measuring the current while applying an overpotential of some magnitude above (for anodic) or below (for cathodic) the corrosion potential. This potential is then plotted against the logarithmic current.

$$\beta_a = \frac{2.303\ RT}{\alpha_a nF}\ ,\ \beta_c = \frac{2.303\ RT}{\alpha_c nF}$$

Equation 8

The Tafel plot is significant as it allows the observation and measurement of several parameters. Firstly, using an extrapolation of the linear region towards the corrosion potential, the Tafel plot can be used to calculate corrosion rates directly. Extrapolation away from the corrosion potential can provide Tafel constants which can be incorporated into other techniques (i.e. LPR) to improve the accuracy of corrosion rate calculations. Visually the graphs also depict the separate anodic and cathodic behaviours of the sample in the surrounding environment (seen in Figure 12). Unfortunately, the test is a destructive technique as the potential sweep in the anodic direction will result in damage to the sample.

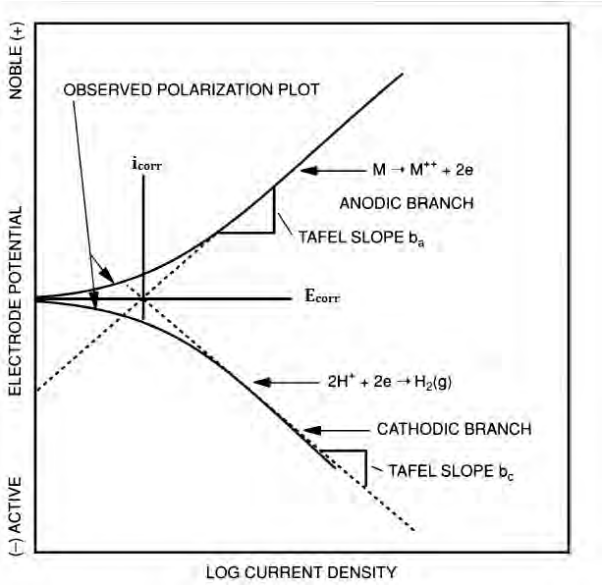

Figure 12 Combined anodic and cathodic Tafel plots [37]

Electrochemical Impedance Spectroscopy (EIS)

EIS is an alternate current method, as opposed to the DC methods mentioned above. It characterises the corrosion mechanisms at the surface interface and are useful in the study of different rate interactions occurring in thin films, oxides, coatings etc. Impedance (Z), in combination with Ohm's law, is usually defined as potential over current, as in Equation 9. Electrochemical impedance is the response of a corrosion system to an applied AC potential signal; this is usually done over several frequencies (ω). A small AC potential signal is applied to create a pseudo-linear current response. The resulting sinusoidal current response is recorded for each applied frequency. With each frequency producing values of resistance and capacitance, similar to that of an electrical circuit.

$$Z = \frac{E}{I}$$

Equation 9

The impedance information obtained shows potential interactions occurring at the EDL layer. Mathematically, the magnitude of this impedance can be resolved as vectors and calculated based on Equation 10. The vectors in the

simplified form refers to a real (Z') and imaginary (Z'') component. Graphically, impedance is shown in 3 distinct plots (Figure 13). The Nyquist plot being the primary display for the relationship between real (Z') and imaginary (Z'') impedance, often appearing as semi-circles. Bode plots provide further details by showing the dependency of either phase angle or impedance magnitude vs frequency.

$$Z(\omega) = Z' + jZ'' = R_s + \frac{R_p}{1 + (\omega R_p C_{dl})^2} + j\frac{-\omega {R_p}^2 C_{dl}}{1 + (\omega R_p C_{dl})^2}$$

Equation 10

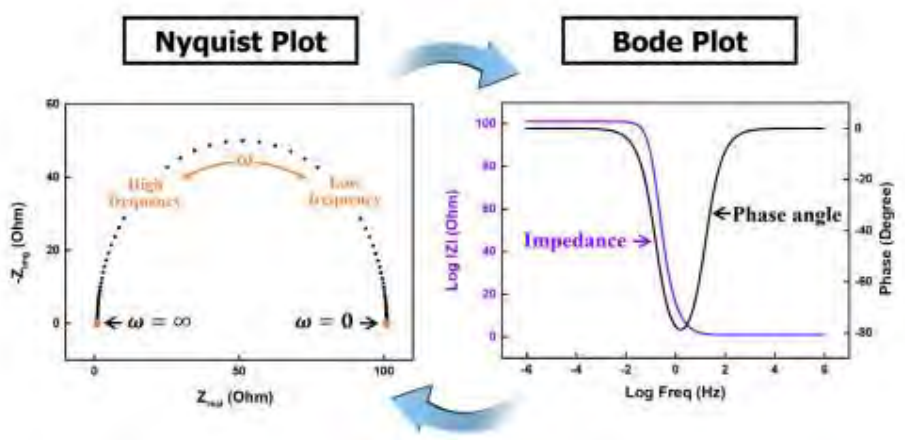

Figure 13 Examples of Nyquist and Bode plots used in EIS [38]

Equivalent electrical circuits accompanied with curve fitting are used to provide more quantitative data of the components within a corrosion impedance test. This is done by modelling the data according to specific and individual components of a common electronic system (i.e. capacitor, resistor etc.). The Randle's circuit (simplified version seen in Figure 14) is the simplest and most recognisable circuit to begin with. It consists of a resistor (representing solution resistance of the electrolyte) combined with a capacitor (representing the double layer) and resistor (charge transfer resistance) in parallel.

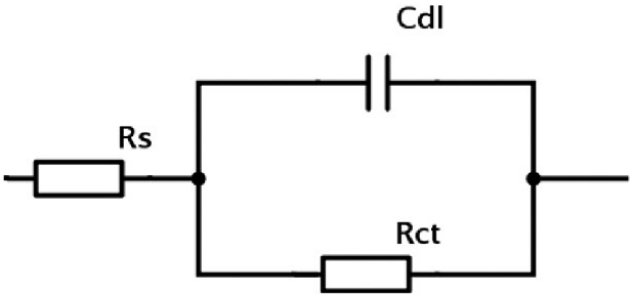

Figure 14 Simplified Randle's circuit [39]

2.5 CO_2 Corrosion Reactions

CO_2 corrosion, otherwise known as "sweet" corrosion [40], is the most common form encountered within the oil industry. Pipeline corrosion is a highly complex process [41], but in essence follows similar principles to that of an electrochemical cell, consisting of a set of anodic and cathodic reactions [42]. These reactions are well documented in literature [43-45] and follow the general development outlined below.

Preliminary bulk chemistry reactions:

Carbon dioxide dissolves in water to produce a generally weak carbonic acid [46-48].

$$CO_{2\,(g)} \rightleftharpoons CO_{2\,(aq)}$$

$$CO_{2\,(aq)} + H_2O \rightleftharpoons H_2CO_{3\,(aq)}$$

The carbonic acid only partially dissociates to form both bicarbonate and carbonate whilst providing H^+ ions [46, 48].

$$H_2CO_{3\,(aq)} \rightleftharpoons H^+_{(aq)} + HCO_3^-{}_{(aq)}$$

$$HCO_3^- \rightleftharpoons H^+_{(aq)} + CO_3^{2-}{}_{(aq)}$$

Cathodic Reactions

The primary reactions occurring at the cathode are often separated into half reactions. These can be primarily hydrogen evolution or occasionally the reduction of H_2CO_3 [44, 46, 49, 50].

$$2H^+ + 2e^- \rightleftharpoons H_2$$

$$2\mathrm{H}_2CO_3 + 2e^- \rightleftharpoons H_2 + 2HCO_3^-$$

Anodic Reactions

The key anodic reaction in the corrosion of carbon steel is the dissolution of the iron component to form ferrous ions. This is generically described through iron oxidation [50-52].

$$Fe \rightleftharpoons Fe^{2+} + 2e^-$$

Iron carbonate can then form and precipitate on the metal surface [50, 52, 53]. This summary of the system of reactions for CO_2 corrosion is by no means exhaustive and is subject to change depending on interpretation, environmental conditions and solution composition/concentration [46, 53-57].

2.6 Factors Affecting CO_2 Corrosion

Due to the highly complex nature of CO_2 corrosion, a definitive list of all the parameters affecting the process is difficult to find in literature [58]. Barker et al [59] provides a comprehensive review of factors affecting CO_2 corrosion with respect to iron carbonate. These factors are usually a combination of both environmental (i.e. Temperature, partial pressure, pH) and physical properties (i.e. fluid regime, velocity, surface properties) which are usually interdependent [60] . An understanding of the influence of key properties and the general trends on the corrosion process is outlined below.

pH

pH has an impact on the corrosion process through its effect on scale kinetics [61], iron carbonate morphology [62] and species solubility [49]. Generally speaking an increase in pH corresponds with a lower corrosion rate for a number of reasons (Figure 15). Firstly higher pH tends to accelerate the formation of protective iron carbonate films, by reducing iron carbonate solubility and increasing super saturation [56]. Studies show moving from a pH of 5 to 6 can reduce solubility of Fe^{2+} by a factor of 100 [41]. Iron carbonate acts as a barrier to corrosion and thus the rate is lower. At higher pH levels there is a retarding of the cathodic reduction of hydrogen and correspondingly,

a decrease in the dissolution of iron [60]. Morphology of the iron carbonate layer tends to be dense and well compacted, hence more protective at higher pH levels (>7.5) [62].

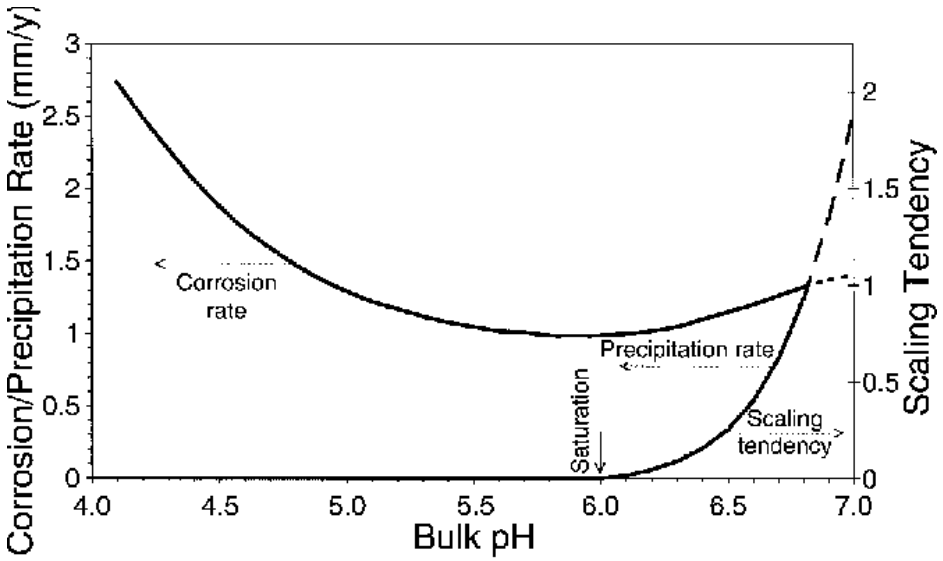

Figure 15 Relation between iron carbonate precipitation and pH [63]

Temperature

There exists a synergy between the effects of temperature and pH on iron carbonate formation [59]. Higher temperatures are generally associated with a more aggressive corrosive environment at low pH (Figure 16), however conditions at higher pH are conducive to accelerated accumulation of $FeCO_3$ protective films [56, 60, 63]. In the right pH conditions [64], temperatures between 60-80°C accelerate the kinetics of precipitation leading to a more protective film and reduced corrosion rate [60]. At lower temperatures, iron carbonate films suffer from a lack of adhesion to the surface and are usually porous and non-protective in nature [64]. Morphology of the layer is impacted by high temperatures with a thin, tight surface film being the result [65]. Work continues in the search for a critical temperature at which $FeCO_3$ formation occurs [59], whilst experimentally it is generally seen that higher temperatures benefit a more protective layer in much shorter timeframes, under the right conditions lower temperatures can also produce the same results with a high enough pH [66].

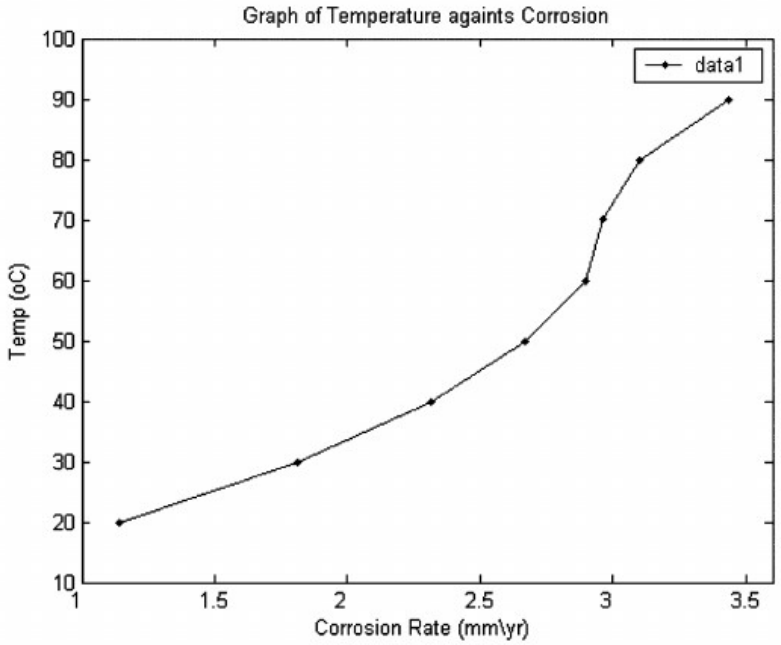

Figure 16 Impact of temperature on the corrosion rate of a gas pipeline [67]

Partial Pressure

The effect of partial pressure is complex and can influence corrosion rate both positively and negatively depending on conditions [41]. Increase in CO_2 partial pressure in the absence of protective films, tends to lead to an increase in the corrosion rate, as H_2CO_3 concentration increases and pH lowers, accelerating the electrochemical cathodic reaction [56] as seen in Figure 17. In this case the anodic reaction is relatively unaffected by increased partial pressures [68]. However the impact of partial pressure is closely tied to environmental conditions [60]. In the case of higher pH levels, higher partial pressures will increase bicarbonate/ carbonate ion concentrations thus accelerating $FeCO_3$ formation and reducing the corrosion rate [46, 49] through a protective film. The reduction in $FeCO_3$ solubility caused by higher partial pressure has been shown to easily form protective $FeCO_3$ films even from low Fe^{2+} concentrations [69]. $FeCO_3$ morphology shows a reduction in grain size and increased layer thickness when partial pressure is elevated, with high local super saturation favouring nucleation over growth. [70].

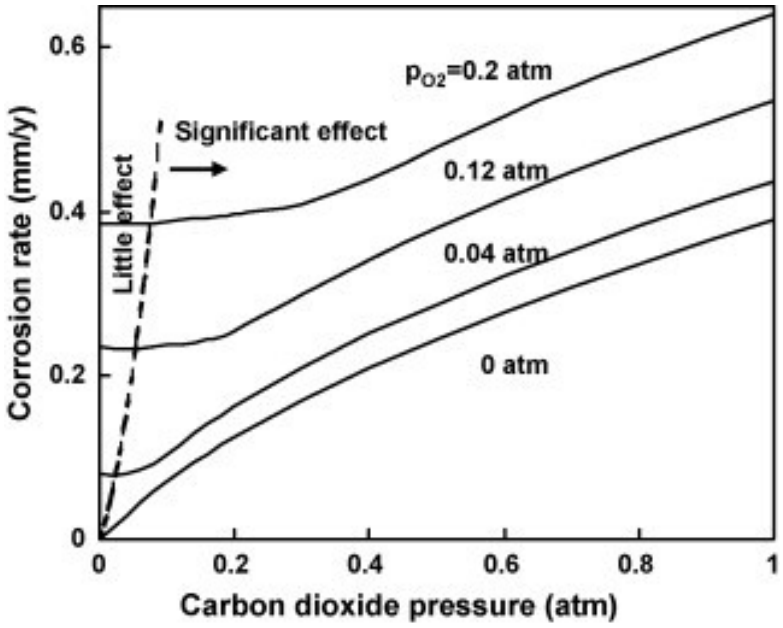

Figure 17 Influence of CO_2 pressure on corrosion rate [71]

Hydrodynamics

The effect of flow on corrosion kinetics is still a debated topic with a degree of uncertainty [56]. This impact appears to be generally negative depending on the presence of corrosion product layers. In a situation without a layer, increased flow velocity accelerates the mass transfer process by transporting Fe^{2+} away and bringing H^+ to the metal surface, thus increasing the corrosion rate when samples are under mass transfer control. [50, 72] shown in Figure 18. Even in the presence of a protective layer, corrosion rates can remain high. The impact of flow also effects the formation of the iron carbonate layer itself. Highly turbulent conditions, especially in combination with multi-phase flow can even damage stable, protective $FeCO_3$ layers resulting in higher corrosion rates [56, 60]. This damage can be both mechanical [73] or a result of chemical dissolution due to the mass transport of cathodic species [74].

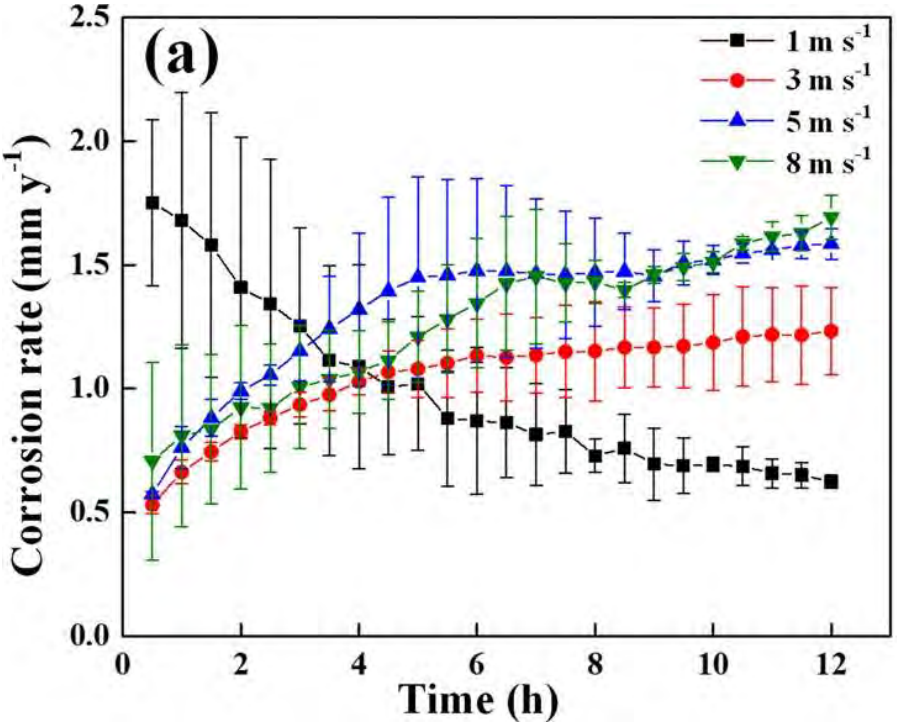

Figure 18 Corrosion rates over time at different flow velocities [75]

Material Properties

The type of steel, its composition and microstructure also influence the CO_2 corrosion process [49]. Due to the non-homogeneous nature of various alloys used in pipelines, there is a tendency for them to behave differently in corrosive environments [76]. In the case of carbon steel, this usually manifests itself in the difference between ferrite, cementite and pearlite, with ferrite preferentially corroding relative to cementite (iron carbide) [77, 78]. The iron carbide network left behind can have a large impact on the corrosion behaviour of the material. The iron carbide structure is usually porous and accentuates galvanic corrosion at the surface, increasing the corrosion rate [79]. However it can also prevent diffusion of Fe^{2+} ions away from the surface, which favours the local precipitation of $FeCO_3$ thereby lowering the corrosion rate [80, 81]. The carbide structure also imbues the surface with an extra roughness, providing numerous points for nucleation and adhesion for the iron carbonate film [77, 82] increasing its protective nature. Initial surface morphology can be influenced by the final finish of samples. This can impact

the corrosion rate, with rough topography increasing the surface contact area with the surrounding solution whilst smoother finishes provide better corrosion resistance (shown in Figure 19).

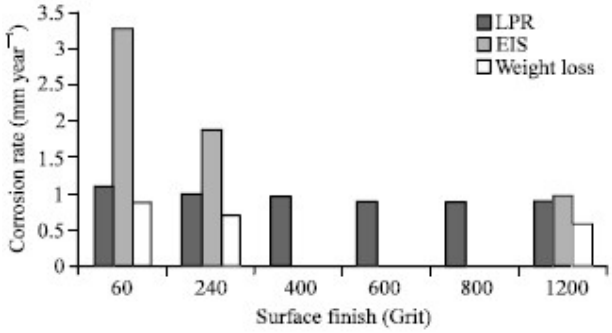

Figure 19 Corrosion rates from LPR/EIS for different surface finishes [83]

Solution Chemistry

Due to the numerous and often complex aqueous compositions encountered in the Petroleum industry, an understanding of the basic trends of several key species is important [56, 84]. Generally brine chemistry influences the corrosion process by either changing the solutions ionic strength (effecting $FeCO_3$ solubility), accelerating the corrosion rate or increasing competition with non-$FeCO_3$ scales [59]. Sodium chloride is the major component of seawater, often used in offshore installations and tends to increase the corrosion rate with increasing concentration [85, 86] as shown in Figure 20. There is evidence that this tends to have an upper limit of 3% NaCl, concentrations above which we see a decrease in corrosion rate [84]. However this may also be the result of artefacts associated with reduced H_2CO_3 due to reduced CO_2 solubility [87]. Experimentally, the addition of Mg^{2+} and Cr^{3+} have been shown to improve the protectiveness and adhesion of the iron carbonate layers, although some tests have been undertaken in unrealistic conditions not found within a pipeline system (i.e. Potentiostatic method) [88, 89]. A system mixed with Ca^{2+} ions (specifically higher concentrations) has been shown to reduce and delay the precipitation of $FeCO_3$ as the two cations compete with one another, $CaCO_3$ scale tends to precipitate more favourably [61, 90-92].

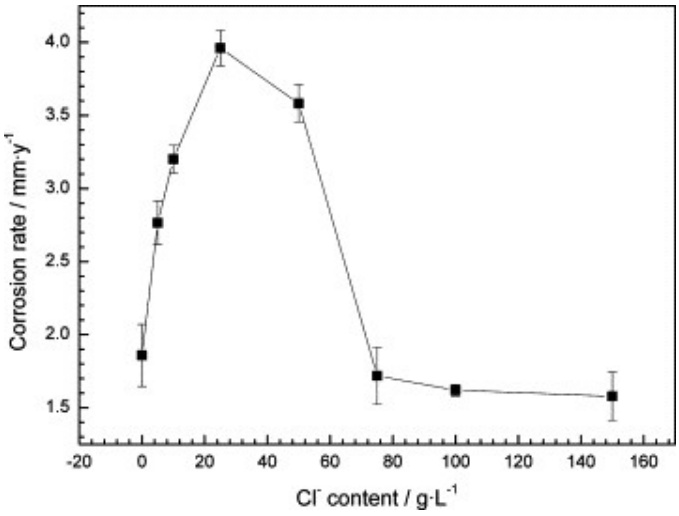

Figure 20 Influence of chloride concentration on corrosion rate [86]

2.7 Corrosion Products

The CO_2 corrosion process and subsequent corrosion rate is strongly dependent on the type of surface film formed, especially in the case of carbon steel. $FeCO_3$ (Iron carbonate) is more often discussed and the prevalent corrosion product encountered. However there exists several other corrosion products from the sweet (CO_2) corrosion process. Including Fe_3C (Cementite/Iron carbide), Fe_3O_4 (Magnetite) and combination scales such as $Fe_2(OH)_2CO_3$ (Chukanovite) and $Fe_xCa_yCO_3$ (Iron-calcium carbonate) that will be discussed first.

Cementite/ Iron Carbide

Iron carbide (Fe_3C) is not technically a corrosion product, but part of the original steel microstructure left behind following dissolution/corrosion [93] seen in Figure 21. This residual network is usually porous in nature and can be fragile [49, 93] . Iron carbide tends to negatively affect corrosion rates by two mechanisms. Firstly by inducing a galvanic effect on the metal surface, the system favours the cathodic reaction of hydrogen evolution [81]. Secondly, the layer becomes susceptible to internal acidification, particularly around the anodic regions increasing the corrosion rate and/or undermining the $FeCO_3$ layer [81, 94]. Conversely it has also been observed experimentally

to produce positive effects on the $FeCO_3$ layer by providing strong/protective anchor points [95] and near surface Fe^{2+} enrichment [49].

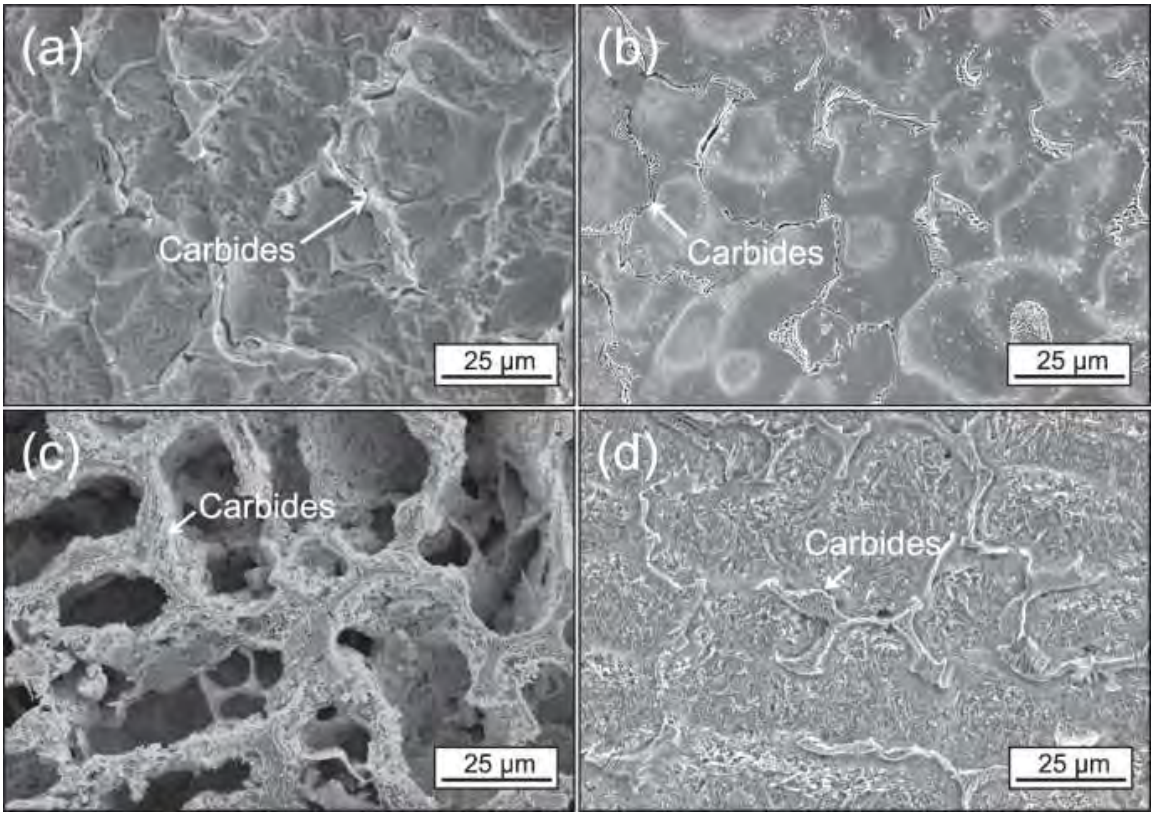

Figure 21 SEM image for a), b) as-cast and c), d) quenched specimens of a), c) Cu-free and b), d) Cu-added alloys after 7 h of corrosion in 1 N H2SO4 at room temperature [96]

Magnetite/ Iron Oxide

Fe_3O_4 is a corrosion product that occurs in the presence of oxygen contamination (Figure 22). It is an iron oxide with an octahedral crystal morphology and a density of ~5.2g/cm^3 [97]. Formation occurs according to the Schikorr reaction [98]:

$$3Fe_{(s)} + 4H_2O_{(aq)} \rightleftharpoons Fe_3O_{4\,(s)} + 4H_{2\,(g)}$$

Magnetite is known to form on carbon steel as passivating layers offering a degree of corrosion resistance [58, 99, 100]. The formation of the pseudo-passivation layer offered by Fe_3O_4 is however dependent on a critical pH [69, 101].

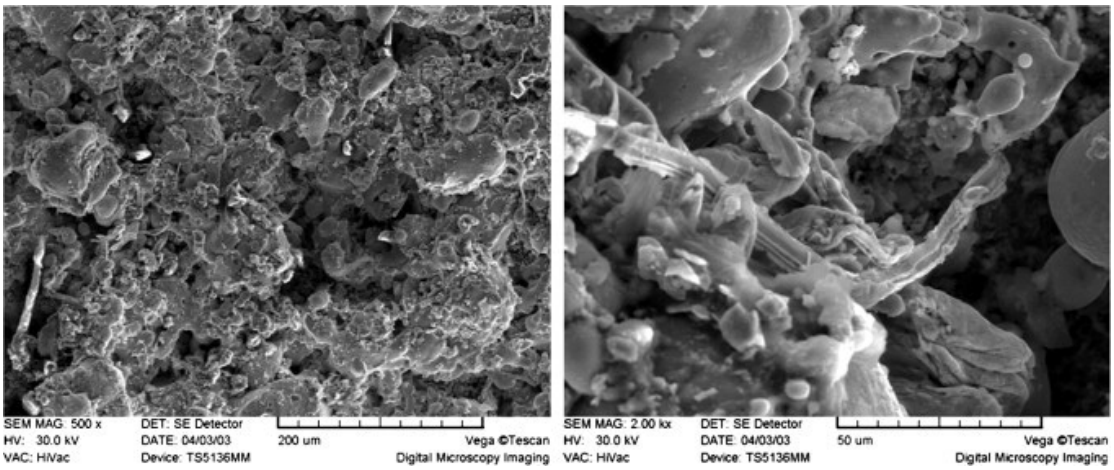

Figure 22 SEM image of magnetite scale layer at two different magnifications [102]

Mixed Corrosion Products

Chukanovite is a plate like or needle like crystal found in anaerobic and high pH CO_2 environments [103]. Although this mixed hydroxide carbonate is detected in laboratory experiments, this corrosion product is rarely found in actual field corrosion samples or failure analysis. Its uncommon occurrence has led some to conclude the crystal is metastable and is generally non-protective as a corrosion product [104].

Iron calcium carbonate, on the other hand, is a mixed corrosion product regularly encountered in CO_2 corrosion samples. $Fe_xCa_yCO_3$ is a scale that usually occurs in the presence of brines containing Ca^{2+} cations, which substitute into the $FeCO_3$ lattice [105]. This coexistence with Fe^{2+} produces morphological (Figure 23) and solubility differences which influence CO_2 corrosion mechanisms. The increase in calcium incorporation or concentration is strongly linked with poorer protective capabilities [106, 107]. This is a result of the tendency of $Fe_xCa_yCO_3$ to act like $CaCO_3$ rather than $FeCO_3$, where increases in solubility allow for easier film removal (via leaching) and curved crystal morphology create less dense layers (via erratic packing) [108]. Sometimes low corrosion rates are achieved in the presence of these $Fe_xCa_yCO_3$ layers, this is often created by a local

environment/diffusion barrier which allows the precipitation of more protective $FeCO_3$ crystals/films [109].

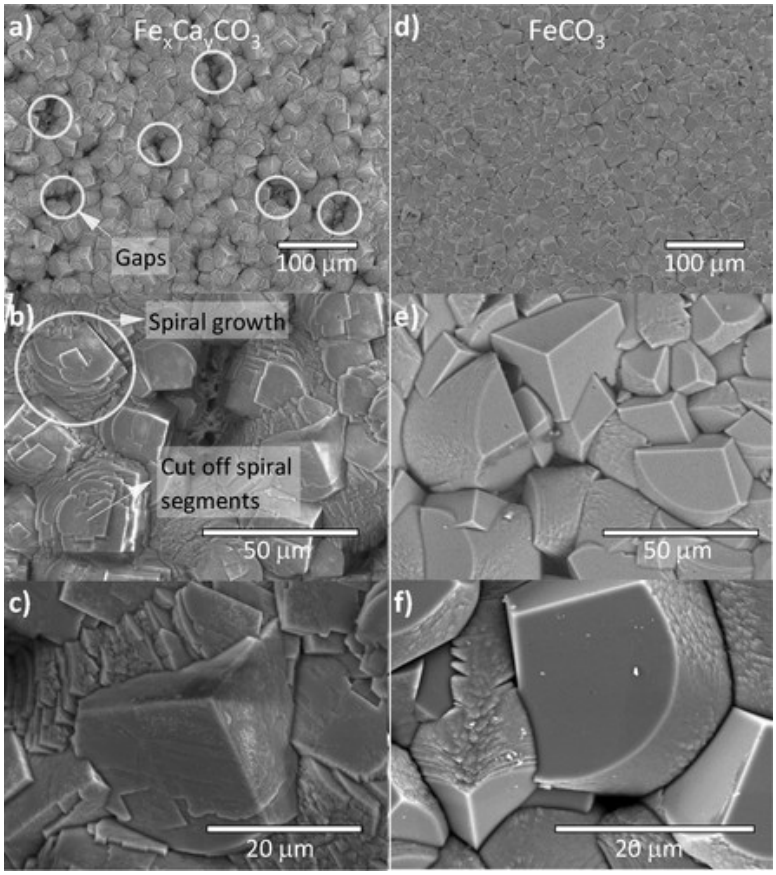

Figure 23 . (a−c) SEM images of $Fe_xCa_yCO_3$ at various magnifications. (a) $Fe_xCa_yCO_3$ rounded crystals showing gaps between them; (b) details of spiral crystal growth of $Fe_xCa_yCO_3$ in kink sites along steps and showing the development of a new spiral segment.20 (c) Details of $Fe_xCa_yCO_3$ crystals showing rough and smooth surfaces, and large anisotropy; (d−f) SEM images of $FeCO_3$ grown under identical conditions in the absence of Ca^{2+} [105]

Iron Carbonate

Iron carbonate, commonly known as Siderite, is an inorganic salt with a rhombohedral/cubic crystal morphology and a density of ~3.96g/cm^3 [110]. The main formation reactions are outlined below:

$$Fe^{2+} + CO_3^{2-} \rightleftharpoons FeCO_{3\,(s)}$$

$$Fe^{2+}{}_{(aq)} + 2HCO_{3\,(aq)}^{-} \rightleftharpoons FeCO_{3\,(s)} + CO_{2\,(aq)} + H_2O$$

The driving force for iron carbonate precipitation is saturation ratio. However this is not a kinetic parameter and the actual mechanism by which the $FeCO_3$ crystal precipitates is nucleation and crystal growth [111-113]. As $FeCO_3$ is essentially a scale, these two concepts are explored in more detail in the scale theory section.

Super saturation is a key influence on $FeCO_3$ formation as it results in homogenous nucleation/growth (Figure 24) and is defined in the following equation [114, 115]:

$$SS_{FeCO_3} = \frac{[\,Fe^{2+}\,][\,CO_3^{2-}\,]}{K_{sp\,FeCO_3}} > 1$$

Equation 11

K_{sp} is the solubility product of $FeCO_3$ and $[Fe^{2+}]$ $[CO_3^{2-}]$, the concentrations of ferrous and carbonate ions respectively. $FeCO_3$ nucleation begins when SS_{FeCO_3}>1 and these conditions provide the most advantageous conditions for a dense and homogenous layer on the surface. When super saturation is less than 0 in the bulk solution, $FeCO_3$ will not form uniformly. However in limited features (e.g., pits or porosity) localised pH may be different and iron carbonate will precipitate but its effectiveness as a barrier to corrosion is less [50, 116].

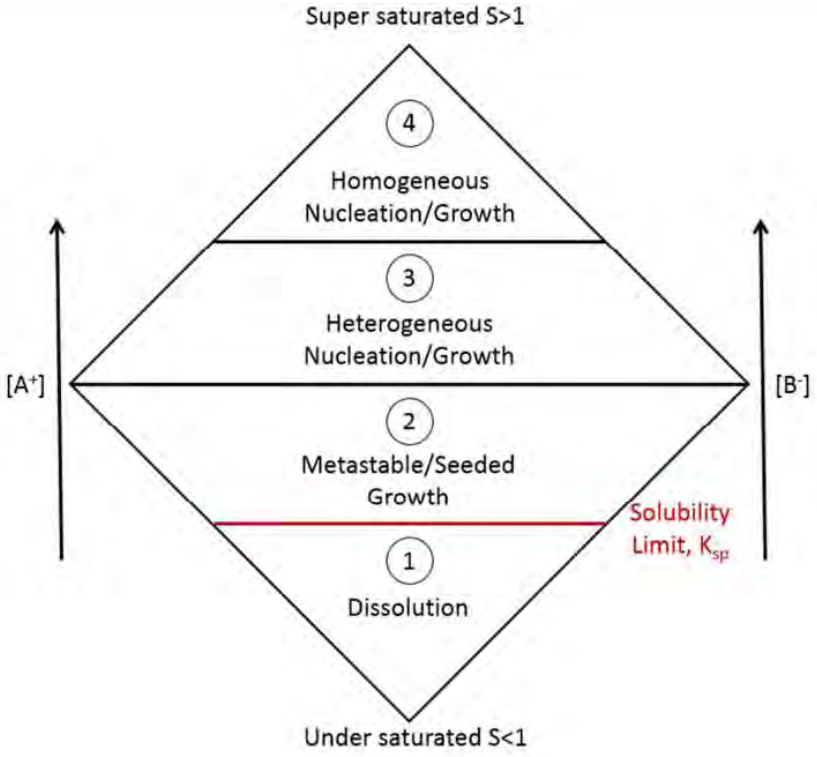

Figure 24 Regions of crystal growth [59]

$FeCO_3$ provides the greatest corrosion resistance of the corrosion products formed, particularly in oilfield applications. This occurs as the $FeCO_3$ layer forms a physical barrier to electrochemically active species and prevents electrolyte contact with the metal surface [49, 77, 117]. The protective capability of this layer is strongly influenced by its local environment in particular the precipitation and growth kinetics that favour a dense, well packed film [41]. In terms of film thickness, with the right conditions $FeCO_3$ layers can be protective at both nano and micro crystalline levels [118, 119]. With fully protective films offering both low uniform and localised corrosion damage and subsequently lower corrosion rates, shown in Figure 25.

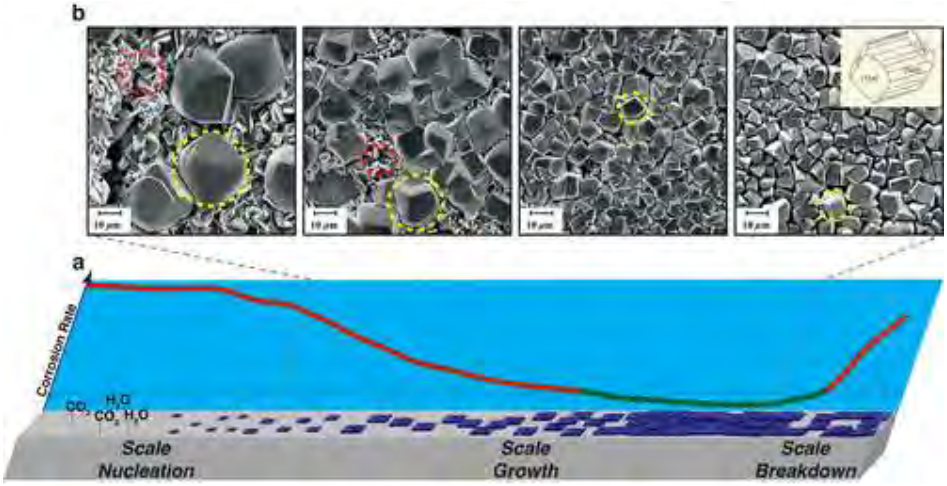

Figure 25 Evolution of a CO_2 corrosion product film. (a) Illustration of the lifecycle of a CO_2 corrosion product film, and the accompanying corrosion rate. For long-term structural integrity, the corrosion rate should be maintained in the green zone, that is, a protective film is required to form and remain. (b) Scanning electron microscopy (SEM) images showing the growth of a densely packed, protective corrosion product film on iron in CO_2-saturated water at 80 °C and pH 6.8. Primarily, the film consists of siderite crystallites (highlighted by broken yellow circles), which are micro faceted cylinders with trigonal-pyramidal caps; the inset in the right-hand SEM image shows a schematic of the habit, including orientation of exposed facets, as indicated previously. (12) Plate-like crystallites (highlighted by broken red circles), observed during the earlier stages of film growth, have been identified as Chukanovite ($Fe_2(OH)_2CO_3$) [120]

Changes in environmental conditions can influence the protective capability of $FeCO_3$ films by creating various interspersed non- $FeCO_3$ corrosion products [81, 121]. This impact often results in increasing corrosion rates, where the top-most layer appears complete and uniform but masks corrosion occurring beneath it, as in Figure 26. Conversely seemingly porous, unprotective layers (seen as Fe_3C) may be protective as the empty layers found deeper in the lattice fill with $FeCO_3$ (due to localised conditions more

conducive to $FeCO_3$ formation) [94]. Changes in these layers may also be a result of various removal mechanisms that occur after the formation of a protective layer. This layer can be compromised through mechanical removal from hydrodynamic forces, chemical film dissolution or a combination of the two [122-124].

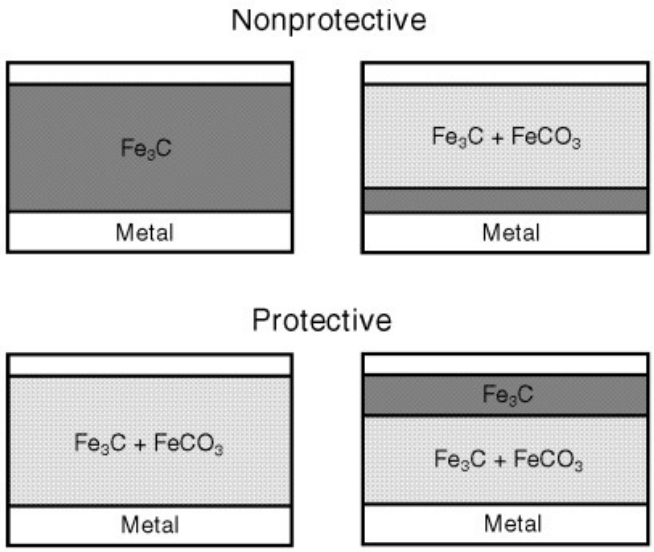

Figure 26 Layering of corrosion products for protective and non-protective films [81]

In summary, this literature chapter establishes a foundational understanding of the creation of iron carbonate layers during the CO_2 corrosion process. In the context of the SLIPS system, this is an important insight into how the base layer will be created. This includes what conditions are needed to fabricate it and how these conditions might influence the layer during operation. The formation of a dense, uniform and protective $FeCO_3$ layer has already been achieved, in a reliable and repeatable manner, within the existing literature. The formation of said layer depends on a number of key parameters which influence the nucleation and growth kinetics of iron carbonate. Three parameters have been chosen as a focus going forward, for the following reasons:

- Ease of control and replication within a laboratory environment.

- Strong consensus in the literature with regards to interactions.

Regarding environmental conditions, the influence of temperature (1) and pH (2) on the creation of protective iron carbonate films is well established. Whilst the impact of surface finish (3) is also relatively certain, but with some more limitations. These parameters have been taken into consideration when defining the formation parameters for a suitable SLIPS base layer in the experimental section. A layer that from its inception as a SLIPS surface is already corrosion resistant. The simplified relationships in relation to the 3 parameters and their impact on iron carbonate films are outlined in Table 2:

Table 2 Key relations for iron carbonate nucleation/growth

Environmental Conditions			
	Non-Protective	→	Protective
pH	<5	→	>6
Temperature	<50	→	>60
Surface Finish	>1200P	→	<600P
Layer characteristics			
Surface Coverage	0%	→	100%
Corrosion Rate	>10mmpy	→	<0.1mmpy

Chapter 3
All things Scale

3 Mineral Scaling and Mitigation

3.1 Background

Fouling or scaling is a key integrity issue that impacts a wide variety of industries and processes. The term ‘fouling’ being used in the general sense, with the word ‘scaling’ being reserved for mineral and industrial references. At its essence, fouling is a complex phenomenon that refers to the accumulation or deposition of material onto surfaces. These deposits can take many forms (as seen in Figure 27), at both the macro and micro level, including inorganic matter (scaling) such as the mineral precipitation of crystals in a pipeline (the major theme of this chapter) [125]. However, fouling also encompasses organic material, which can include both biofouling (the collection of living organisms) and carbon-hydrogen compounds such as paraffin. Indeed the first historical mention of fouling, dates back to the first century where Plutarch addresses the biological build-up (i.e. algae, barnacles) on ships hulls as a cause for increased drag [126].

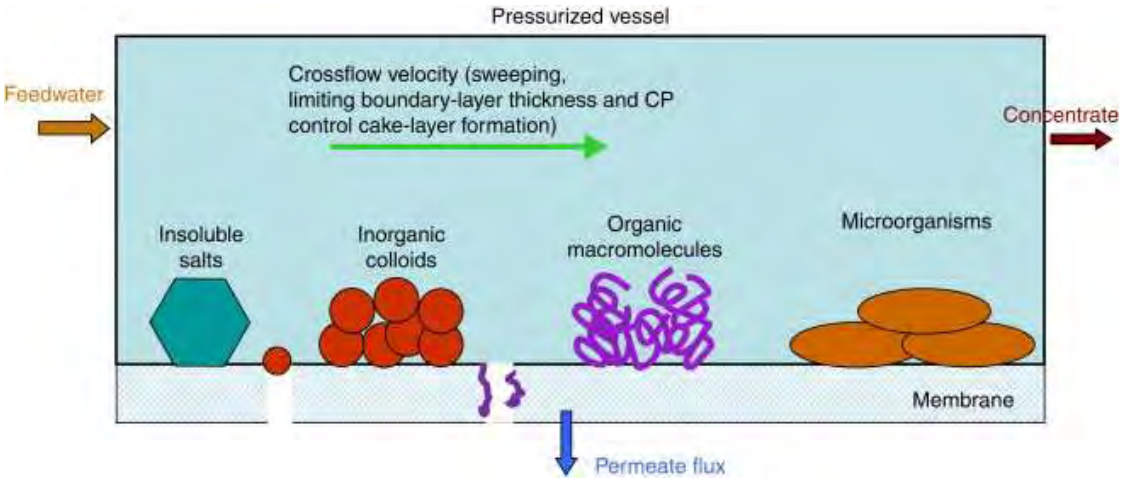

Figure 27 Various fouling types on a membrane [127]

Within the scope of this thesis, inorganic mineral scaling is the issue being addressed. Specifically the prevention of scaling as a tool for pipeline integrity

management. The scale problem has and continues to be one of the major issues facing the petroleum industry (Figure 28). Whether it is seawater being injected into the reservoir, or formation water returning, scale deposition results from the diverse range of elements and ionic components present in these liquids. Changes in environmental conditions (whether that be pressure or temperature etc.) cause solids to precipitate out of solution where they then deposit and grow on surfaces [128].

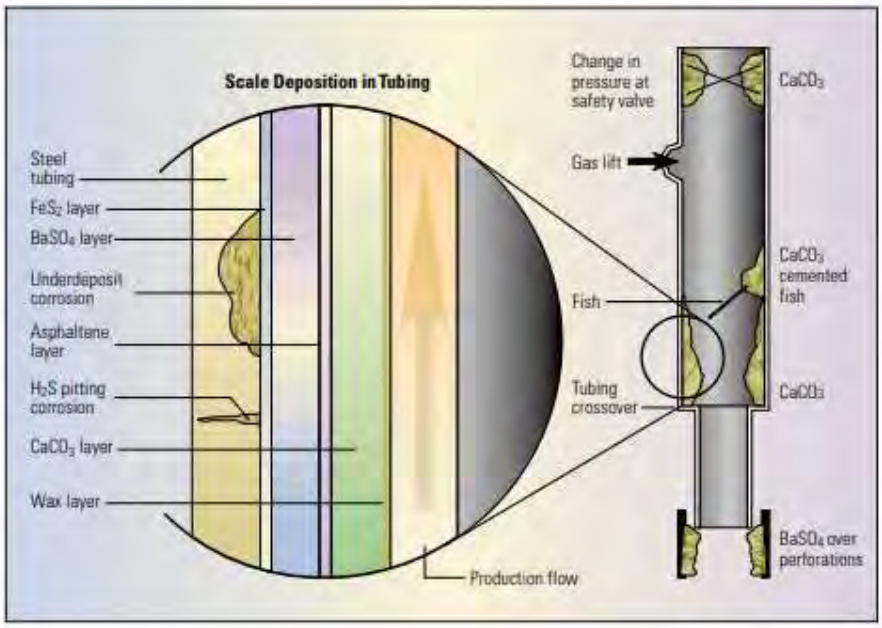

Figure 28 Depiction of various scale deposits in oilfield tubing [9]

This phenomenon is not limited to certain areas of the petroleum extraction process but plague all surfaces that come into contact with these aqueous solutions. Scale deposition can be found in upstream production tubing (seen in Figure 29), sub surface safety valves, water injection lines to top side refining equipment such as heat exchangers and transport lines. The first industrial reference to scaling occurs in the 17th century, with Perking observing the fouling on heat-transfer surfaces in a boiler [129]. Scale interference is not solely limited to equipment but can have a dramatic impact on reservoir characteristics through formation damage as well [130].

In industry, scale management is a critical production and flow assurance issue, especially in certain high-risk fields (i.e. North Sea). The severe impact of scale to operations is twofold (Figure 29) and represented in the following: 1. Financial costs, associated with lost production and treatment. 2. Safety and environmental factors, associated with failure of safety/ production equipment [9]. Although the mechanism of scale formation will be explored in more theoretical detail in this chapter, they primarily occur in the field under three mechanisms [131, 132]:

- Reduction of salt solubility in aqueous solution, caused by increase in temperature and/or pressure drop of brine.
- Mingling of two incompatible brines (i.e. formation water and injection water)
- Evaporation of brine causing increased salt concentration above the solubility limit.

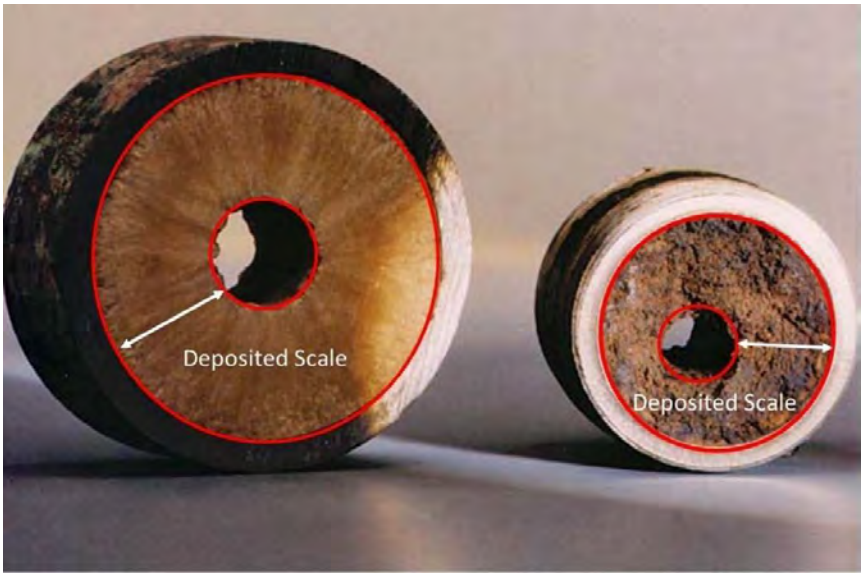

Figure 29 Restriction in tubing flow caused by scale deposit [133]

Depending on the environment, there exists many types of inorganic and organic scales, which will briefly be described in the following literature review [134]. However the focus of this research is Calcium carbonate ($CaCO_3$), one of the more common and predominant scales encountered. In this research, scaling is the issue for which a solution is being targeted. Therefore, an understanding of the mechanisms through which scale forms, particularly in

an oil and gas setting are key concepts to explore. As are the existing methods used for the prevention and control of scaling issues in the industry.

3.2 Fundamental Theories of Crystallisation

Aspects of corrosion, particularly the deposition of $FeCO_3$ or other crystal layers are essentially examples of fouling or mineral scaling. There exist many similarities with regards to their mechanisms and theory. Crystallisation refers to the process from which solid crystals form, of which there are two primary components, nucleation and crystal growth (as seen in Figure 30). In addition to this, there exists several core concepts related to crystallisation including supersaturation and induction time which will be explored in the next section.

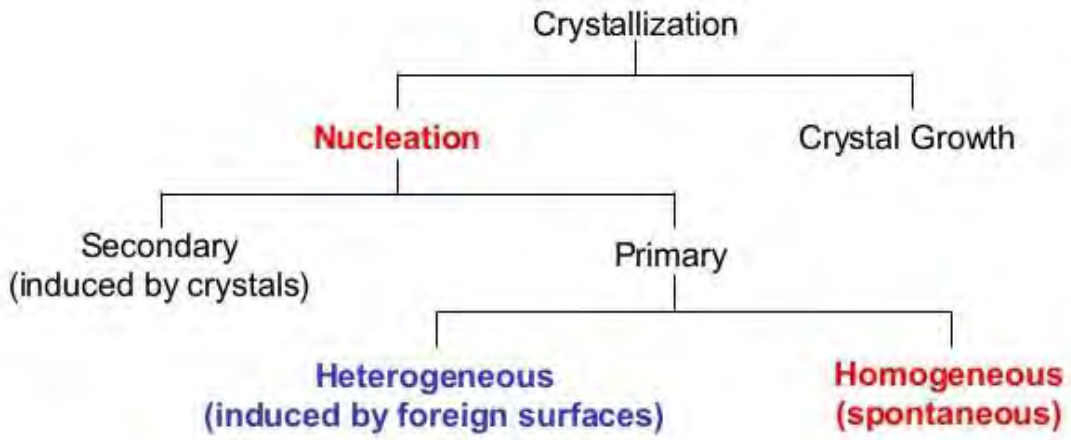

Figure 30 Summary of Crystallization pathways [135]

3.2.1 Solubility and Saturation

Before the process of crystallisation can begin there are two thermodynamic concepts that must be considered: solubility and supersaturation. Solubility addresses the amount of substance required to saturate a given solution, generally as a function of temperature [135]. A solubility equilibrium can exist dependent on temperature when a compound in its solid state is in equilibrium with a solution containing the same compound. Solubility product (K_{sp}) is a

common expression used to determine maximum solution concentrations for ionic compounds

$$K_{sp} = [A]^x[B]^y (\text{where [A], [B] are the concentrations of the compound } \mathrm{A}_x\mathrm{B}_y)$$

Within these solutions, they can exist in states of saturation, undersaturation or oversaturation. Crystallisation begins with the mixing of two solutions, to form a product (precipitate) with low solubility.

Super saturation is another important concept that drives the crystallisation and precipitation process. The process is largely temperature and pH dependent. As described previously with iron carbonate (where Ca substitutes for Fe), Super saturation ratio (SS) is calculated as [135, 136]:

$$SS_{CaCO_3} = \frac{(\alpha Ca^{2+})(\alpha CO_3^{2-})}{K_{sp,\ CaCO_3}} > 1$$

Equation 12

Here solution concentration is commonly represented as ionic activity product (α) of the anion/cation respectively. The formation of scale can be expressed in terms of saturation ratio in four primary scenarios[135, 137]:

1. SR<1: Solution is under saturated and scale formation is not feasible.
2. SR=1. Solution is in equilibrium with both formation and dissolution of scale occurring at the same rate.
3. SR>1. Solution is super saturated and scale formation is feasible.
4. SR>40. Spontaneous precipitation of calcium carbonate.

The impact of saturation on crystallisation is divided into three zones corresponding to the states mentioned above and modelled along the solubility line, these zones are Under saturated, saturated and super saturated [138, 139]. The final super saturation zone is further divided into 3 separate areas: Metastable, labile super saturation and precipitation area (Figure 31). When the solution is metastable, homogenous nucleation does not occur and crystals will not grow. Spontaneous homogenous nucleation will occur in the

labile zone and added crystals will grow. Finally in the precipitation zone, amorphous precipitation and aggregation occur.

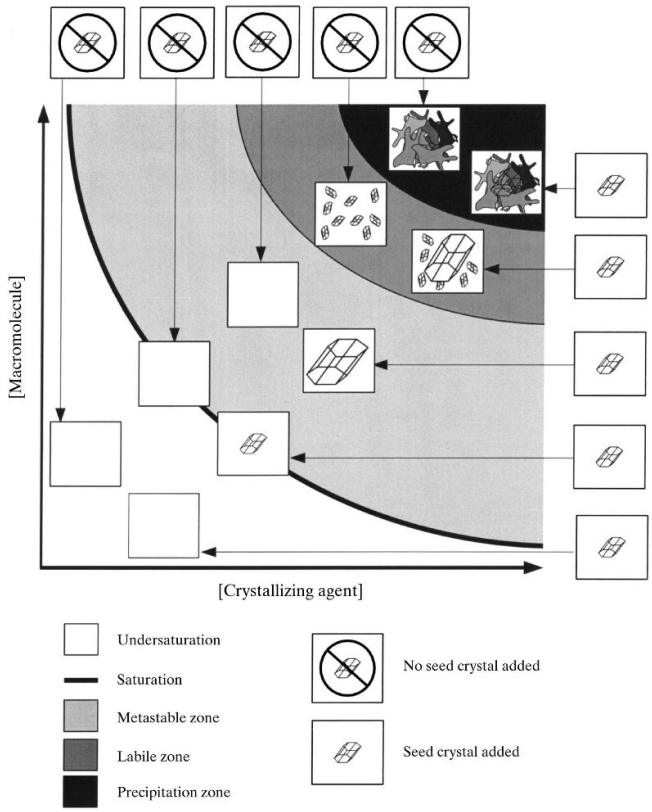

Figure 31 Crystallisation zones in respect to saturation and seed presence [139]

3.2.2 Induction Time

Induction time is referred to as the time between reaching of super saturation in solution, to the first observable change in physical properties of that system (i.e. appearance of crystals/ turbidity etc.) [135, 140, 141]. This is the time that elapses from the metastable state to an unstable state, where nucleation can occur (Figure 32). As such induction time is inversely related to the nucleation rate [135, 142] and supersaturation.

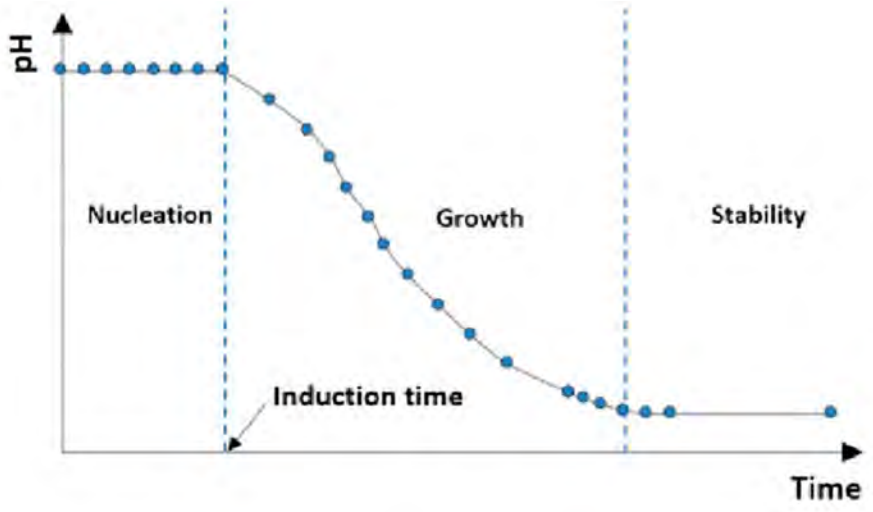

Figure 32 Induction time and the stages of crystallisation

Issues in visual detection mean that the induction time is difficult to experimentally measure [143] and is often predicted as a combination of different periods in the following relation [144]:

$$t_{ind} = t_r + t_n + t_g$$

Equation 13

Where:

- t_r, (relaxation) is the time needed for molecular clusters to reach a quasi-steady state.
- t_n (nucleation) is the time needed to form stable nuclei.
- t_g (growth) is the time needed for the crystal to grow to a visible size.

3.2.3 Nucleation

Nucleation is the complex process of forming a stable nuclei after a solution has reached super saturation. It is the interaction between ions that produce clusters in turn forming a stable nucleus from which crystallisation occurs. The process of nucleation is divided into 4 typical categories (Figure 33)

depending on environmental conditions, Primary, Heterogeneous, Homogenous and Secondary nucleation [135, 140, 145].

.

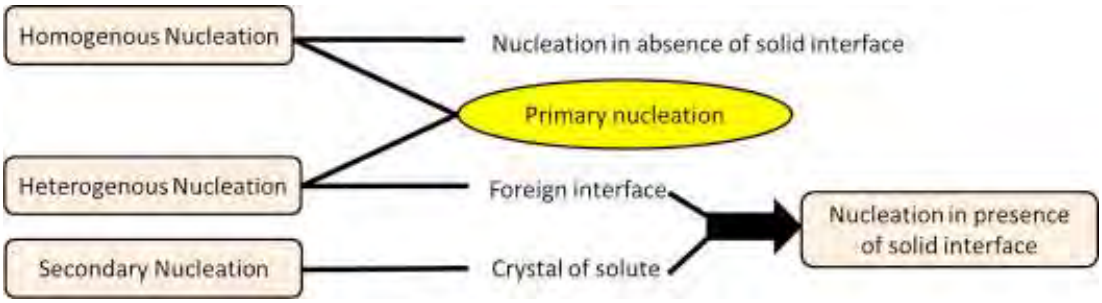

Figure 33 Types of nucleation pathways [146]

Primary nucleation is when the solution is supersaturated but where there is no crystalline matter in the system to begin with [135]. This type of nucleation is then further divided into homogenous and heterogeneous nucleation (Figure 34). Homogenous nucleation will occur in the bulk solution where external changes permit (i.e. solution is agitated). Changes in internal conditions such as high super saturation (i.e. >40) will result in spontaneous nucleation [147]. Nucleation is initiated when an excess of free energy is encountered in the system. This change in free energy (ΔG), known as free enthalpy is a combination of surface excess free energy (ΔG_s) and volume free energy (ΔG_v) and is needed for nuclei formation [144].

$$\Delta G_N = \Delta G_S + \Delta G_V = 4\pi r^2\sigma + \frac{4}{3}\pi r^3 \Delta G_V$$

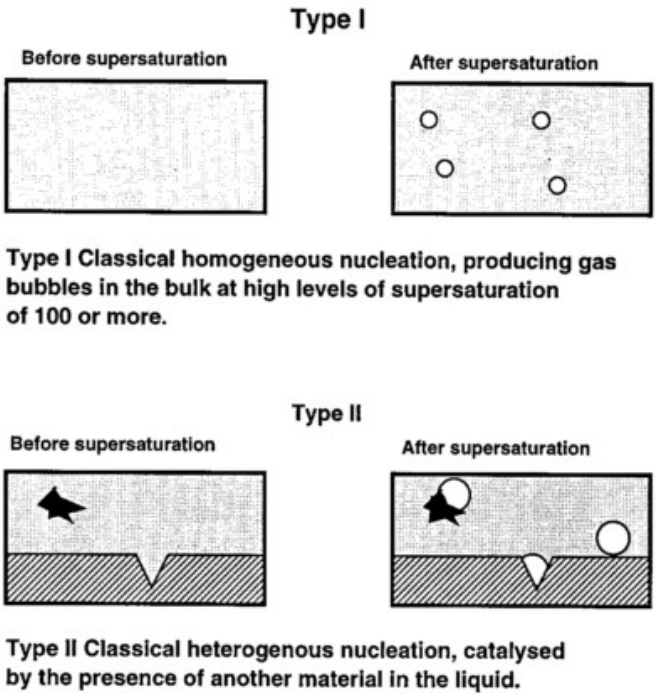

Figure 34 The 2 types of primary nucleation, homogeneous and heterogeneous.

Nucleation occurs when ΔG_N reaches a maximum value or critical free energy. This critical free energy is based on a critical radius (r_c), the minimum size for a stable nucleus, in the following relations[135]:

$$\Delta G_{crit} = \frac{4\pi {r_c}^2}{3}$$

$$where\ r_c = \frac{-2\sigma}{\Delta G_S}, \sigma = surface\ energy$$

Here particles $>r_c$ will continue to grow and particles smaller, will dissolve in solution. Pure homogenous nucleation requires a higher free energy in comparison to heterogonous nucleation and is therefore less common [136, 144]. The nucleation rate (J) expresses the number of nuclei formed per unit time/volume in the form of an Arrhenius reaction velocity equation outlined below [135]:

$$J = K\ exp\frac{-\Delta G_c}{\beta T}$$

$$where\ \Delta G_c = \frac{16\pi\alpha\sigma^3 v^2}{3(\beta T ln SR)^2}$$

Equation 14

The parameters are J- Nucleation rate, K- Frequency factor, β- Boltzmann constant, T- Temperature, ΔG_c- Free energy change for critical cluster size, v- crystal molecular volume, σ- interfacial energy, α- geometric factor and SR is saturation ratio.

Heterogeneous nucleation is that which occurs in the presence of foreign solution impurities or surface defects. The presence of adsorption sites lowers the free energy demand and promotes larger crystal growth [148]. This also makes the requirement for super saturation lower for nucleation to begin [135]. Here nucleation is dominated by the wetting ability (φ) of the solute phase on the target surface [116].

$$\Delta G_{hom} = \phi \Delta G_{het}$$

$$where\ \phi = \frac{1}{4}(2 + cos\theta)(1 - cos\theta)^2$$

Equation 15

Secondary nucleation involves a process where pre-existing crystals of the same material are already present [149]. Again a lower saturation is required as the parent crystal acts as a catalyst for accelerated nucleation, more so than primary nucleation [135]. Secondary nucleation, with the addition of seed crystals has the potential for very rapid and early nucleation, due to small particle sizes [150]. The two active mechanisms during this process are debated, but are generally considered as a mixture of surface breeding and mechanical breeding [151, 152].

3.2.4 Crystal Growth

Crystal growth begins after the formation of a stable nuclei on a solid surface [153, 154]. The transformation process from the nuclei to crystals is a mixture of mass transfer and surface integration outlined through 3 main theories [135, 142].

Surface Energy Theory

This crystal growth theory is based on the assumption of thermodynamic equilibrium and Gibbs free energy. A crystal will grow in a supersaturated solution so as to minimise the total surface energy across all crystal faces in that system [135]. The shape of a crystal is closely linked to the free energies of its faces, with growth rates being proportional to the facial surface energy [155], where high surface energy faces become the dominant sites for growth (Figure 35). The theory is however limited due to its lack of application on the effects of super saturation and solution movement [156].

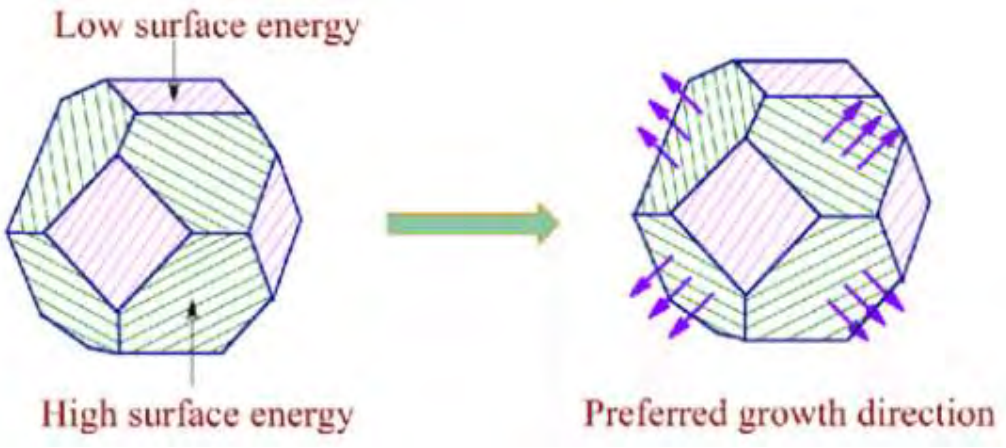

Figure 35 Influence of surface energy on crystal growth [157]

Adsorption Layer Theory

Adsorption layer theory deals with the presence of an adsorption layer (Figure 36) that permits growth without nucleation at the crystal surface [156, 158]. Growth is centred around imperfections (predominantly kinks) on the crystal surface. This theory is further subdivided into 3 growth mechanisms, which assume high local super saturation [159]:

1. Frank-Van der Merwe. Layer by layer process with dependence of further layers based on initial layer completion (2D growth).
2. Wolmer-Weber. Independent layers forming at the same time (3D growth).
3. Stranski-Krastonov. A combination of firstly 2D and then 3D growth.

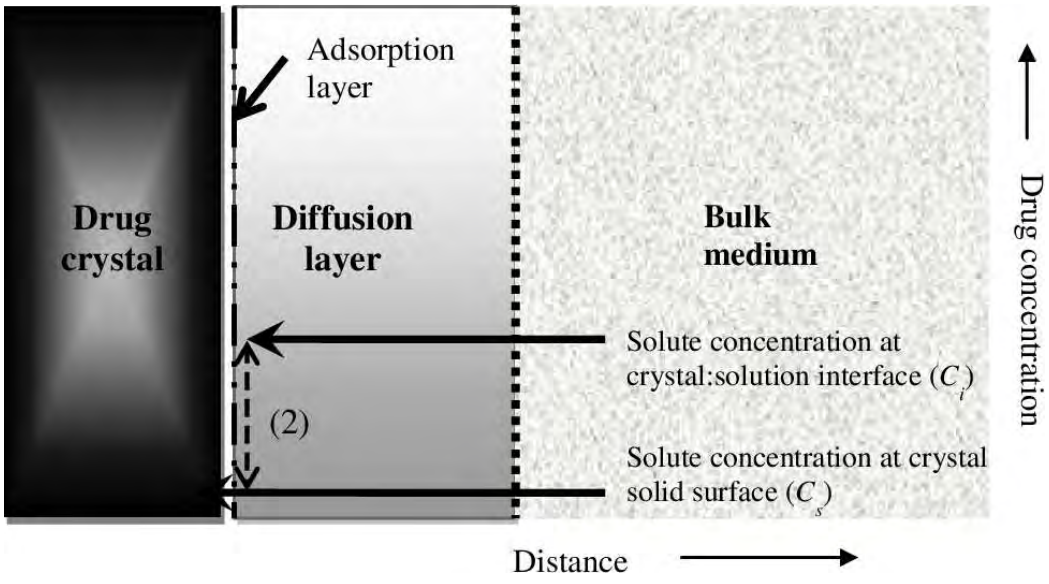

Figure 36 Adsorption layer crystal growth schematic for pharmaceutical applications [160]

Screw Dislocation Theory

Previous theories have been simulated for ideal conditions and have not taken into account systems with low super saturation [135, 161]. Screw dislocation theory is based on continuous growth as a result of crystal surface imperfections (i.e. screw dislocation points) that continue to present themselves [144] such as in Figure 37. The crystal face is constantly rotating around the dislocation point so as to resemble the thread of a screw. Theoretically no surface nucleation is necessary and this accounts for high growth rates at low super saturation.

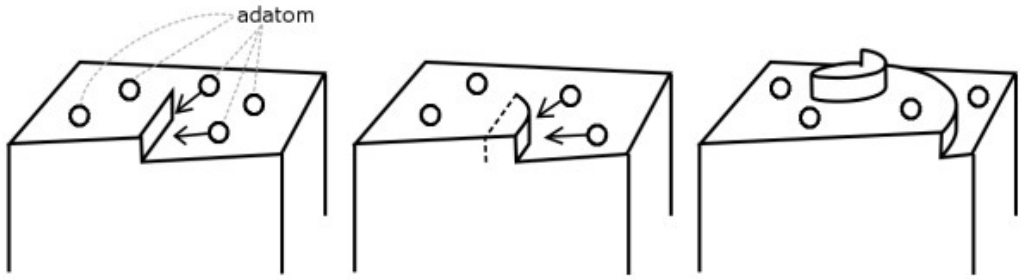

Figure 37 Schematic of crystal growth aided from screw dislocation [162]

3.2.5 Adhesion

Adhesion is not a direct step within the crystallisation process but is still an important concept concerning how particulates aggregate together and crystals attach to substrates. Adhesion is “the state in which two surfaces are held together by interfacial forces” [163]. The ability of crystals to adhere to the surface is best described by the Dejaguin, Landau, Verwey and Overbeck (DVLO) theory [164, 165]. DVLO theory accounts for adhesion as a combination of attractive Lifshitz van Der Waals forces and repulsive double layer forces. Lifshitz van der Waals forces are largely dipole-dipole, dipole induced and dispersion forces which are low strength interactions between crystals/surfaces. Double layer forces are the result of an adsorbed electric potential on the surface in solution. Further research into the complexity of the adhesion process has shown other forces are involved but this is still debated [165, 166]. Surface properties, such as surface energy and roughness have been shown to greatly influence the work of adhesion [145, 167] as will be further explored in the surface engineering section.

3.2.6 Calcium Carbonate Scale

Within the oil and gas industry, several mineral scales form with the major types summarised in Figure 38. The scale encountered is often unique to the field, being dependent on local water chemistry and downhole conditions. Based on physical properties, carbonates and sulphates tend to be the

dominant forms due to low solubility. However the influence of reservoir geology compounds the occurrence of carbonate scales due to the fact 60% of the world oil reserves lie in these types of reservoirs [168].

Name	Chemical formula	Primary variables
Calcium carbonate	$CaCO_3$	Partial pressure of CO_2, temperature, total dissolved salts, pH
Calcium sulfate		
Gypsum	$CaSO_4 \cdot 2H_2O$	Temperature, total dissolved salts, pressure
Hemihydrate	$CaSO_4 \cdot H_2O$	
Anhydrite	$CaSO_4$	
Barium sulfate	$BaSO_4$	Temperature, pressure
Strontium sulfate	$SrSO_4$	Temperature, pressure, total dissolved salts
Iron compounds		
Ferrous carbonate	$FeCO_3$	Corrosion, dissolved gases, pH
Ferrous sulfide	FeS	
Ferrous hydroxide	$Fe(OH)_2$	
Ferrous hydroxide	$Fe(OH)_3$	

Figure 38 Common oilfield scales and associated variables [169]

Calcium carbonate ($CaCO_3$) represents one of the most common scales encountered. As stated previously, this is a result of the high percentage of reservoirs in operation that are either sandstone or carbonate. For example within a sandstone reservoir, calcium carbonate makes up 33.5 wt. % of the typical scale composition [170]. This and the fact the Earth's crust contains high levels of calcite in its natural state continue to increase the probability of encountering calcium carbonate-based scales. Given its prevalence in the industry, calcium carbonate has been chosen as the mineral scale to be tested. As such the following section outlines further details on the mechanisms of calcium carbonate formation.

3.2.7 Calcium Carbonate Formation

Calcium carbonate formation occurs when a solution undergoes some form of pressure, temperature or pH change, with the driving force being supersaturation. However it is also can occur naturally through the process of bio-mineralisation, which helps link the crystallisation of $CaCO_3$ on surfaces, not just in the bulk [171]. Within the petroleum system, the formation of this

scale is governed by the following chemical reactions [172], these reactions may occur in the reservoir, tubing or on the surface:

Carbon dioxide first dissolves in water to form carbonic acid.

$$CO_{2\,(g)} + H_2O_{(l)} \rightleftharpoons H_2CO_{3\,(aq)}$$

Dissolution of carbonate components (via 2 reactions), releases hydrogen ions and increases system pH

$$H_2CO_3 \rightleftharpoons HCO_3^- + H^+$$

$$HCO_3^- \rightleftharpoons CO_3^{2-} + H^+$$

Calcium ions combine with carbonate or bicarbonate products (depending on pH) to precipitate out of solution.

$$Ca^{2+} + CO_3^{2-} \rightleftharpoons CaCO_{3\,(s)}$$

$$Ca^{2+} + 2HCO_3^- \rightleftharpoons CaCO_{3\,(s)} + CO_2 + H_2O$$

Calcium carbonate precipitates in three different anhydrous crystal structures. These are Calcite, Aragonite and Vaterite. Each form has different solubility, morphological and crystallographic properties which can be seen below in Figure 39 [136, 173, 174]. Calcite and Aragonite tend to be more thermodynamically stable than Vaterite [175], especially at low supersaturation and hence are encountered more regularly in scale deposits. Each polymorph also has a unique and easily identifiable crystal morphology which allows identification in SEM very clear [176].

	Calcite	Aragonite	Vaterite
Crystal system	Rhombohedral 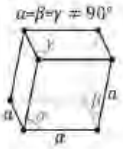	Orthorhombic 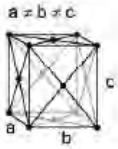	Hexagonal 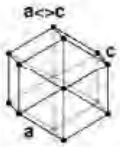
Morphology	Cubic to rhombohedral	Needle-like	Hexagonal Hemispherical Apricot kernel
Favourable condition	Instantaneous nucleation, Room temperature, Harassed by foreign ions (Mg), High oxygen concentration oxygen	Temperature above 50°C, High pH value (above 13.5)	High supersaturation, Low concentration of oxygen, Strong tendency to spread laterally
State	Excellent quality Single crystal Most stable	Excellent quality Single crystal More porous	Metastable Microcrystalline Porous

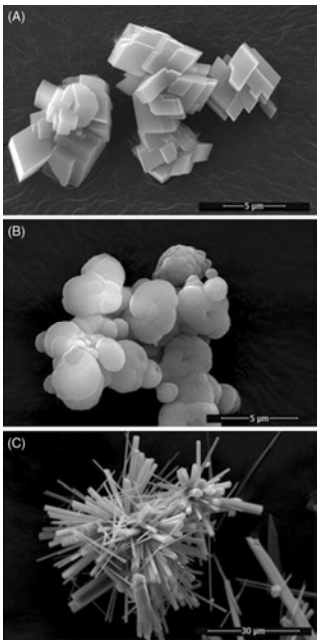

Figure 39 Calcium carbonate polymorph characteristics [52]. SEM images: A) Calcite B) Vaterite C) Aragonite

3.3 Factors Affecting Calcium Carbonate Formation

Calcium carbonate formation is influenced by a range of factors that generally fall into 2 main categories Environmental (Physical and Chemical) Conditions and Substrate Properties. These factors may impact all stages of the crystallisation process, from nucleation, growth and adhesion. Furthermore, this impact may differ from bulk precipitation compared to surface deposition. Whilst the factors listed below may, in principle, be relevant for a number of scales, they are predominantly focussed on calcium carbonate.

Temperature

Similar to the formation of iron carbonate, temperature has a strong influence on $CaCO_3$. Increases in temperature are associated with increased $CaCO_3$ scale kinetics, particularly above 60C, as solubility is reduced and super saturation is reached [177-179], particularly in oilfield formation water as shown in Figure 40. High temperatures are also associated with changes in $CaCO_3$ morphology, with higher temperatures (>50°C) favouring aragonite formation and lower temperatures (25°C to 50°C) mainly calcite and vaterite [180-182]. In oilfield applications, temperature increases have been correlated

with increased scaling tendency for carbonate brines [183]. Finally, temperature rise has also been linked with changes in crystal size, with smaller crystals found at higher temperature [184].

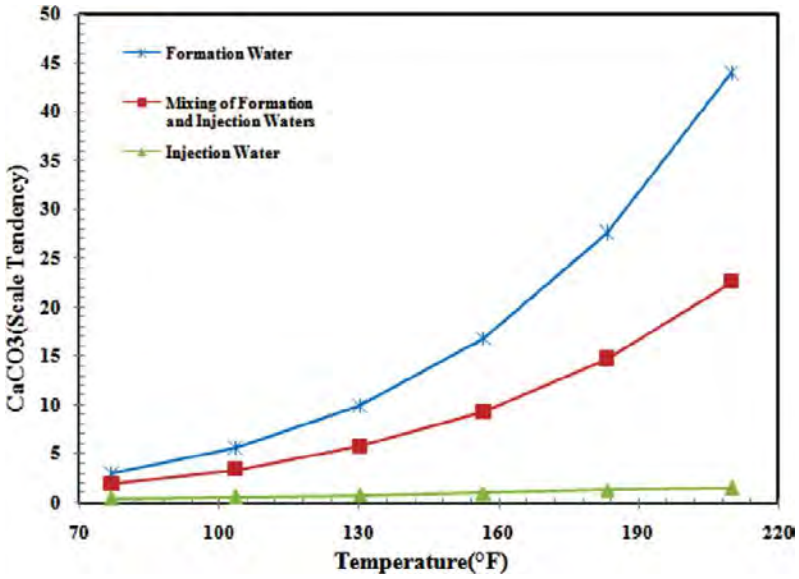

Figure 40 $CaCO_3$ scale tendency of different oilfield water sources as a function of temperature [185]

Pressure

Pressure drops have an impact by reducing the saturation limit and solubility with respect to $CaCO_3$ which increases precipitation [186] as seen in Figure 41. This impact is marginal at lower temperatures (50°C) but very significant at high temperatures (180°C) [183]. The effect of pressure on bulk precipitation has been observed contrarily for surface deposition as high pressure has been associated with lower scale surface coverage [187].

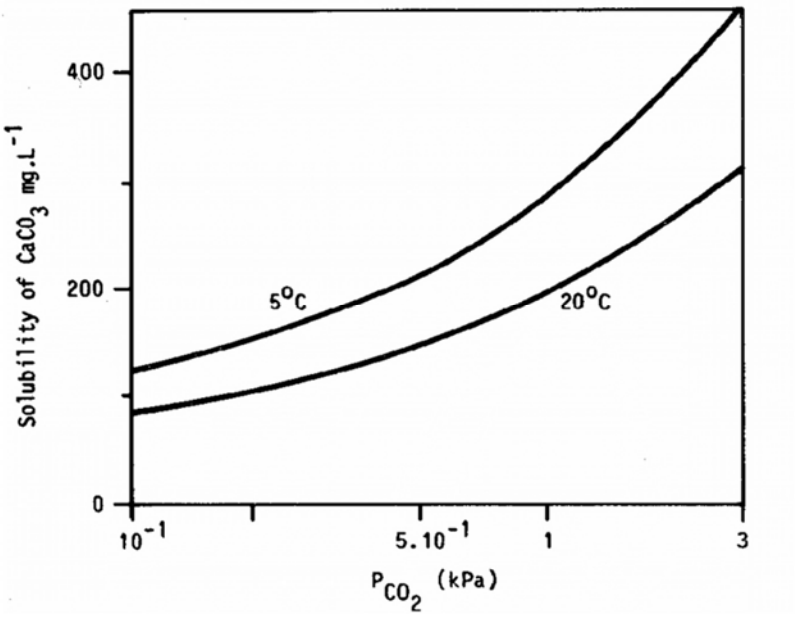

Figure 41 Effect of partial pressure on $CaCO_3$ solubility at 5°C and 20°C [188]

Hydrodynamics

The impact of flow is highly variable and usually dependant on the applied situation. Higher flow velocities are associated with increased transfer of ions and crystallisation in the bulk and surface which results in higher scale deposition (Table 3). Conversely, the same flow conditions may result in reduced surface deposition when adhesion forces are less than flow induced shear forces [189, 190]. Literature suggests there may be a sweet spot, with scaling rates rising with increased flow velocity until a stability at 0.5m/s and then decreasing after 0.7 m/s [191]. Correlations between scale deposition and Reynolds number have been shown to be linearly dependant [192]. Crystal size and morphology is influenced by flow rates, with increase in flow resulting in damaged crystal faces and smaller sizes [134, 189, 193]. Reduced induction times for calcium carbonate have also been observed with increasing flow conditions [194].

Table 3 Calcium carbonate growth rate over 4 hrs at 30, 40 50 mL/min [195]

Average growth rate of calcium carbonate scale, gr/hr		
30 mL/min	40 mL/min	50 mL/min
0.0384	0.0413	0.0463
0.0223	0.0324	0.0403
0.0156	0.0188	0.0316

pH

Changes in pH primarily effect the saturation index (SI) of a brine system and the degree of supersaturation, with high pH resulting in a higher SI and as a result increased rates of scale formation as the solubility of $CaCO_3$ reduces (Figure 42) [196, 197]. At higher pH levels this often occurs rapidly and spontaneously but this trend may have an upper limitation as pH in excess of 8 can lead to longer induction times [198]. Although high pH generally favours the formation of calcium carbonate, local pH actually decreases as the precipitation process uses up nearby carbonate ions [199]. Studies have also shown the impact of pH on crystal size and morphology, due to interruption of the nucleation process [200, 201].

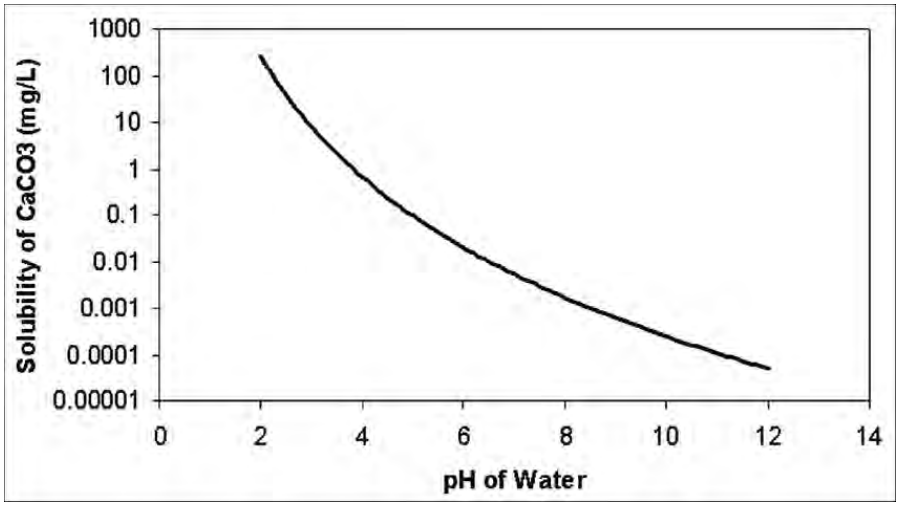

Figure 42 Solubility of limescale as a function of the pH of water [197]

Effect of Impurities

Foreign ions or impurities play a critical role in the crystallisation process. Introduced species such as Mg^{2+}, Ba^{2+}, Sr^{2+}, Mn^{2+} and $SO4^{2-}$ all impact the growth rate (inhibition due to incorporation in the crystal structure) and are commonly found in oilfield applications [202]. $SO4^{2-}$ has been shown to increase induction times [179]. Mg^{2+} in particular has a strong impact on the formation of calcium carbonate. Presence of Mg^{2+} in a system has been linked with an inhibiting effect in the bulk solution and a preference for aragonite formation over calcite (Figure 43) [203]. Tests on other trace elements have also demonstrated the same inhibiting tendency, the likely mechanism being the adsorption of these ions into the crystal structure retarding growth [204]. During the corrosion process, Fe^{2+} will also reduce scaling rates due to competition for available carbonate/bi carbonate ions [205].

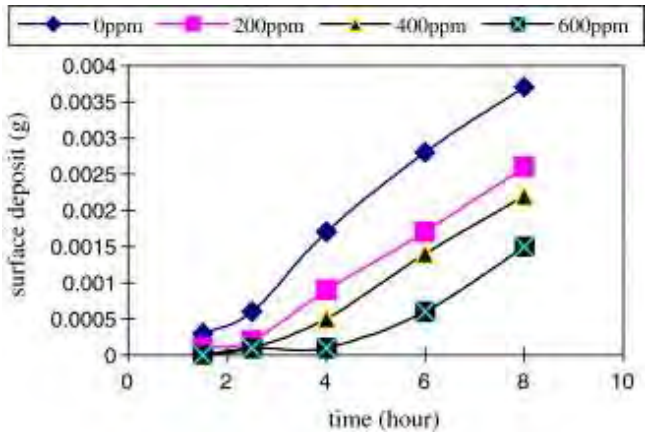

Figure 43 Influence of Mg^{2+} concentration on $CaCO_3$ deposition over time

Effect of Substrate

Physiochemical and surface properties of the substrate can have significant impact on all aspects of the scaling process, from nucleation to crystal morphology. The two primary features of substrates being surface roughness and surface energy are covered in more detail within the surface engineering section. The impacts of changes in substrate properties will be greater explored in the surface engineering section in mineral scaling prevention.

3.3.1 Control of Mineral Scaling

Due to the inherent dangers to project costs and safety, the prevention and control of mineral scaling remains a pressing concern for operators. Currently, there exists a wide array of solutions available to tackle the oilfield scale problem. Scale management and mitigation is usually separated into two main branches 1. Pre-emptive (scale prevention) and 2. Reactive (scale removal). A key strategy in the fight against scale is a strong predictive capability to forecast what scale problems may be faced in the design phase (i.e. type of scale, drive mechanism etc.). The options available to manage the scale problem can be applied individually as a standalone solution or as a combination treatment and the effectiveness depends on the scale being targeted. Often a delicate balance needs to be struck, to ensure treatment methods do not interfere with production and other pipeline integrity/oilfield chemicals. The following is a summary of well-known and commonly used solutions for both scale prevention and control available in the market [125, 170, 206, 207]:

- Reduction of scale potential. This method helps reduce the likelihood of precipitation by removing scaling ions before solutions are mixed. In the field this usually involves a sulphate reduction plant (SRP) that removes sulphate ions from seawater to produce low sulphate seawater (LSSW) for reservoir injection.
- Scale inhibitors (SI). SI are a chemical intervention that can control, delay or reduce scale from forming downhole. This method is often seen as the most economical and effective treatment, with the most common inhibitor chemicals being inorganic phosphates, organophosphorus compounds, and organic polymers. The inhibition method can vary but usually focusses on restricting one stage of the crystallisation process. For example, in the case of $CaCO_3$ scaling and the two most popular oilfield SI, PPCA prevents nucleation while DETPMP reduces crystal growth [208]. The development of more

environmentally favourable inhibitors, represent a growing research field with much potential.

- Mechanical removal. This a reactive measure, largely limited to the wellbore/tubing itself, that physically removes scale that has built up on internal surfaces. Pigging, jetting and reaming require specialised equipment that remove scale by force (either flow induced or mechanical) and can be expensive due to complications integrating into drilling operations or lost production time.
- Chemical removal. This method also assumes the scale has already deposited and is a low cost, commonly employed strategy in the Oilfield. Chemical removal, also known as stimulation, focuses on the dissolution of targeted scales within the downhole system (both in the reservoir and tubing). The two primary methods used to remove scales, including $CaCO_3$ are: 1. Acidizing, which depending on the scale, involves the use of organic or inorganic acids (i.e. HCl, being the most popular choice) to dissolve deposits. However this often needs to be balanced with risks associated with corrosion, particularly at high temperature. 2. Chelating is a method that involves the addition of agents (often aminopolycarboxylic acids) to dissociate the $CaCO_3$. Here the mechanism involves the binding of the calcium ion with the chelating agent to become water soluble. Unlike acidizing, chelation has the advantage of reducing expected corrosion rates and the need for other additives, although the agent itself may be more costly than HCL.
- Engineering. This field includes technological developments in the form of physical oilfield equipment that help prevent scale deposition. One such method is the use of smart completions in downhole scale control. Smart well technology uses real-time monitoring and automated control of inflow control valves/devices (ICV/D) to directly restrict gas and water breakthrough, preventing the mixing of incompatible brines or ingress of scale carrying formation water. Surface engineering or coatings also represent an important, alternative method of scale

prevention. This is the area of focus for this research and is explored in further detail in the next section.

3.3.2 Surface Engineering

Surface engineering is an important tool in the scale mitigation arsenal. Surface engineering, through the form of coatings, seek to interrupt the build-up of scale by interfering with the deposition and adhesion of crystals to the surface. To understand the effectiveness of surface engineering for scale it is necessary to understand two important surface parameters and their influence on scale.

Surface energy is the first property that effects the scaling process. According to classical nucleation theory, we expect that the smaller the affinity between salt nucleus and substrate, the larger the free energy barrier for heterogeneous nucleation [209]. Here we find that substrates with lower surface energy should result in lower scale mass gain or nucleation. Of the components that make-up surface energy, apolar (Lifshitz van der Waals) and polar (Lewis acid and Lewis base), it has been found that the polar component is the dominant force in controlling scale formation. In Figure 44, using self-assembled monolayers of organosilanes on glass slides it was found that moving from a substrate of surface energy 52 mJ/m2 to 10.4 mJ/m2, resulted in a 90% reduction in $CaSO_4$ mass gain [210]. Morphology is also affected by changing surface energies with lower values producing fewer but larger crystal deposits.

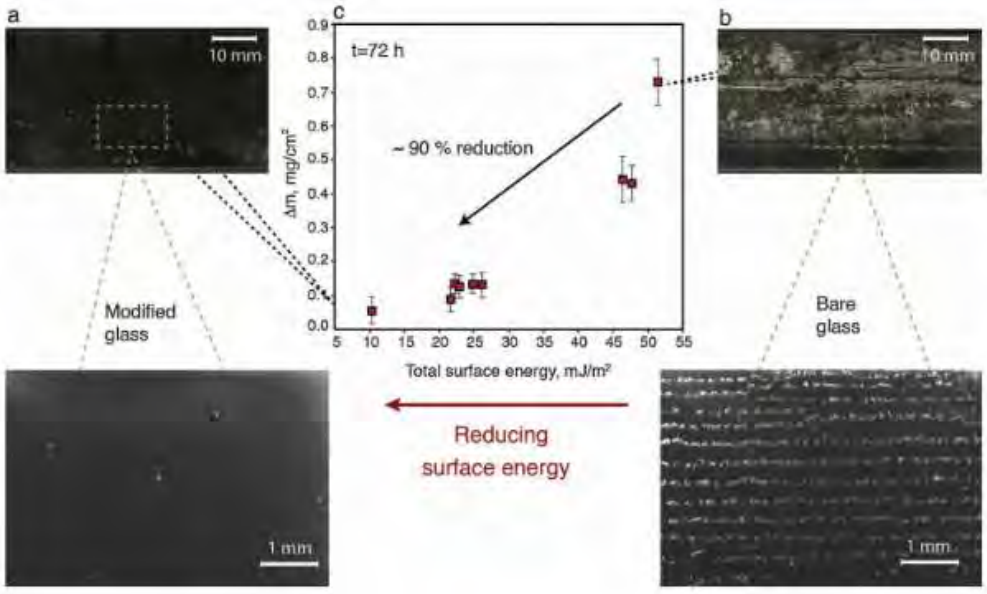

Figure 44 Effect of total surface energy on scale mass deposition [210]

The second surface parameter influencing the scale process is surface roughness. Generally speaking it has been shown that increases in surface roughness provide a larger contact area and thus a stronger adhesion force between crystal and substrate. However the impact and trend on scale deposition is not clear. It has been shown that rougher surfaces do not always correspond with higher scale deposits [79]. Furthermore the influence of roughness varies with length scales. Whilst micro roughness may have an effect by minimising the number of nucleation sites, nanoscale roughness is more important in the determination of adhesion.

Whilst previous studies have shown trends in individual surface components and their influence on scale, combining parameters under the pretence of evaluating coatings proves more difficult. *Cheong et al* [145] found that a selection of coatings under $CaCO_3$ deposition showed an unclear correlation in surface energy and scale mass gain particularly between polymer and stainless steel coatings. Whilst the correlation with roughness was the opposite of prevailing understanding that high roughness lead to increased deposition (Figure 45). Although *Wang et al* [211] confirmed the correlation

between increased coating roughness and surface energy on the adhesion strength through submerged impinging jet (SIJ) tests with calcium carbonate.

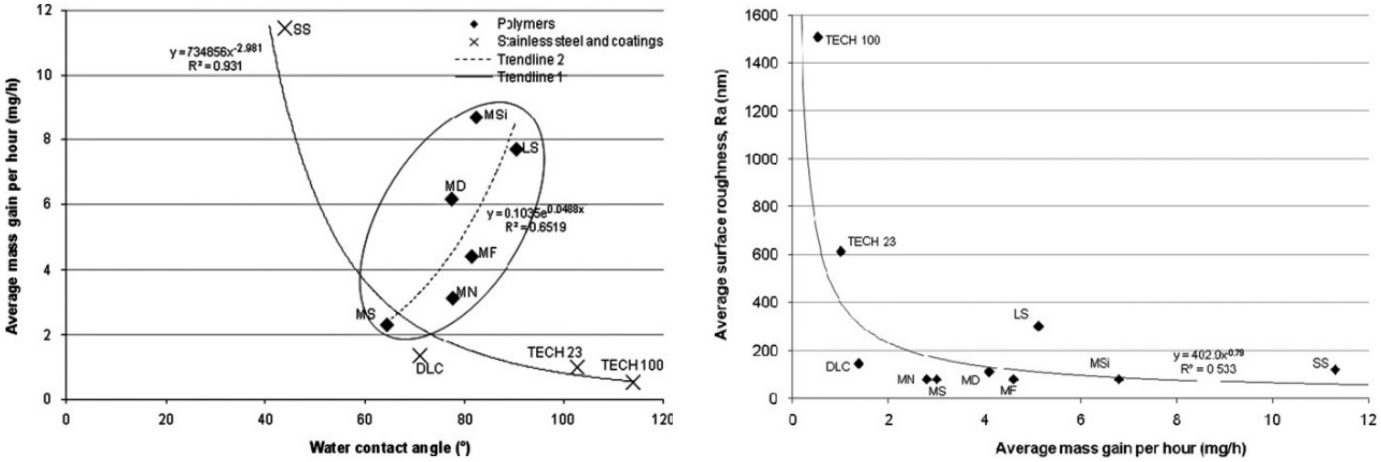

Figure 45 $CaCO_3$ mass gain vs water contact angle and $CaCO_3$ mass gain vs surface roughness for a selection of coatings

In assessing commercially available coatings for scale management, laboratory and field tests have proved inconclusive in providing a link between surface characteristics and effective anti-scale surfaces. *Vazirian et al [212]* showed that there is a clear improvement in scaling efficiency between a coating system and an uncoated pipeline through field tests (Figure 46). Surfaces ranging from epoxy paints, DLC, sol-gel ceramics and fluoropolymers were lab tested, each with different surface energy and roughness values. These tests were in both sulphate and carbonate dominated brines, as well as laminar and turbulent flow regimes failed to prove a conclusive link between surface parameters and scale defence. However it has been established, that a coating system will prevent scale to a greater level than that of an uncoated sample.

		Efficiency (%)			
No.	Coating	Mass average	SR const.	SR (lin.)	SR (non-lin)
1	Uncoated-1	-	-	-	-
2	B5891	41.31	52.35	49.63	44.21
3	3M SK 6258	16.50	32.20	24.03	12.98
4	B1341	27.87	41.43	30.18	19.76
5	IPC ME 35	13.71	29.93	10.76	0
6	B1391	22.46	37.04	13.93	5.42
7	IPC Magna	35.90	47.95	23.21	19.02
8	Uncoated-2	-	-	-	-

Figure 46 Scaling tendency efficiency of industrial coatings relative to uncoated surfaces [79]

An interesting note is the influence of flow regime on scale deposition (Figure 47), with turbulent flow having a greater rate of deposition than laminar, but also a greater overall impact compared to changes in surface properties. *Harouaka et al* [213] also supports the hypothesis that flow regime plays a more critical role compared to surface composition in the success of surface engineering options. Although this does not apply to smooth, hydrophobic surfaces in the study.

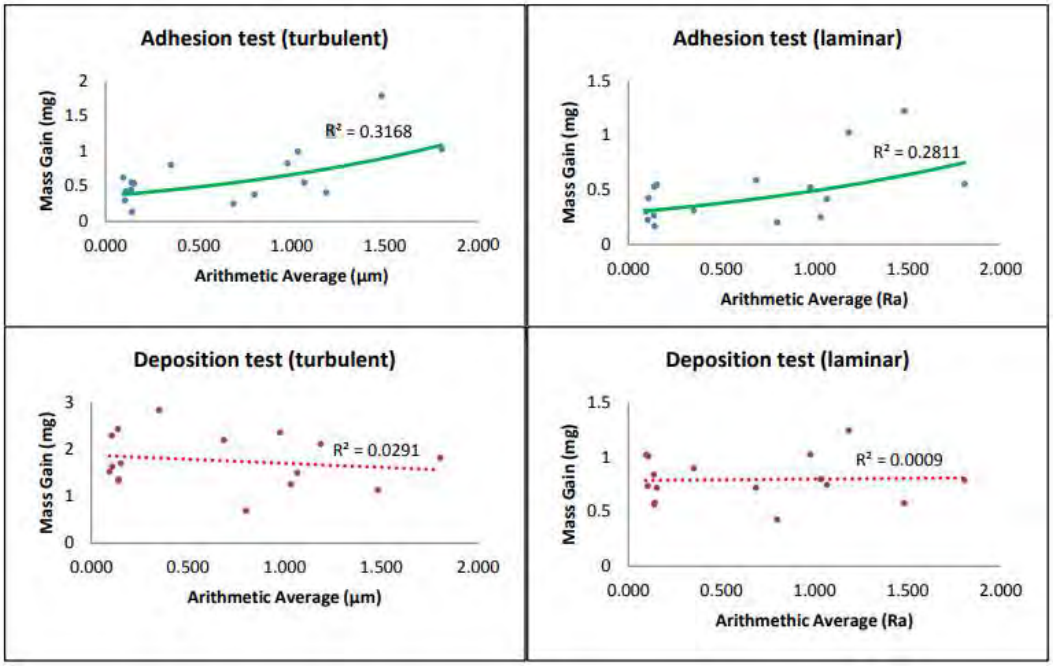

Figure 47 Effect of surface roughness on $CaCO_3$ mass gain in turbulent/laminar flow [79]

In summary, mineral scaling remains a core flow assurance issue for Oil and gas operators and is encountered in various other industries. In the field, scale deposition can lead to serious financial consequences through reduced/lost production, maintenance costs and the risks to HSSE. It remains an important research field with potential for continued innovation. In the context of this thesis, scaling is the problem that is being targeted and in particular $CaCO_3$. This has been chosen based on its dominance in the industry and the ease of precipitation replication in the laboratory. The fundamental theory covered in this chapter highlights the main thermodynamic and kinetic mechanisms that effects its formation. Many of which are similar to those that influence the corrosion process, particularly the deposition of $FeCO_3$ layers highlighted in the previous chapter.

In the prevention of $CaCO_3$ and oilfield scaling in general there exists a number of strategies and tools available. These come with historical success,

can be pre-emptive or reactive, mechanical or chemical and are heavily dependent on the scale and field in which they are employed. One such method is the use of coatings or surface engineering to reduce or inhibit both the nucleation and adhesion of scale crystals on the surface. The feasibility of coatings in reducing scale build-up has been proven and leaves the possibility of a SLIPS surface for scale mitigation open. The mechanism of prevention is largely attributed to two key properties, surface roughness and surface energy. However there remain questions regarding the synergies and relationship between both properties in the context of a single coating system and their effectiveness as indicators of predictive scaling capability in coating evaluation. A fundamental understanding of both concepts is crucial as they form the basis of a functional SLIPS system for $CaCO_3$ prevention.

Chapter 4
All things SLIPS

4. Slippery Liquid Infused Porous Surfaces

4.1 Fundamental Theories

Essential to understanding the mechanics of SLIPS and surface engineering is a comprehension of certain background theories. These provide fundamental guidance on how liquids, solids and gases interact. They allow predictive modelling of certain behaviour and form the basis for how lab equipment process information and results. In regard to surface engineering there are 3 primary areas of interest, which include: 3-phase wetting, Wetting of textured surfaces and Scale formation.

3-Phase Wetting

The foundation of wetting and capillarity action begins with Young's equation [214]. The equation states that when a liquid comes in contact with a solid, in the presence of gas, a relationship exists between the contact angle, liquid surface tension, interfacial liquid/solid tension and the free surface energy of the solid. This relation is valid in a 3-phase system at equilibrium on an ideally smooth solid (Figure 48).

$$\gamma cos\theta_e = \gamma_{SV} - \gamma_{SL}$$

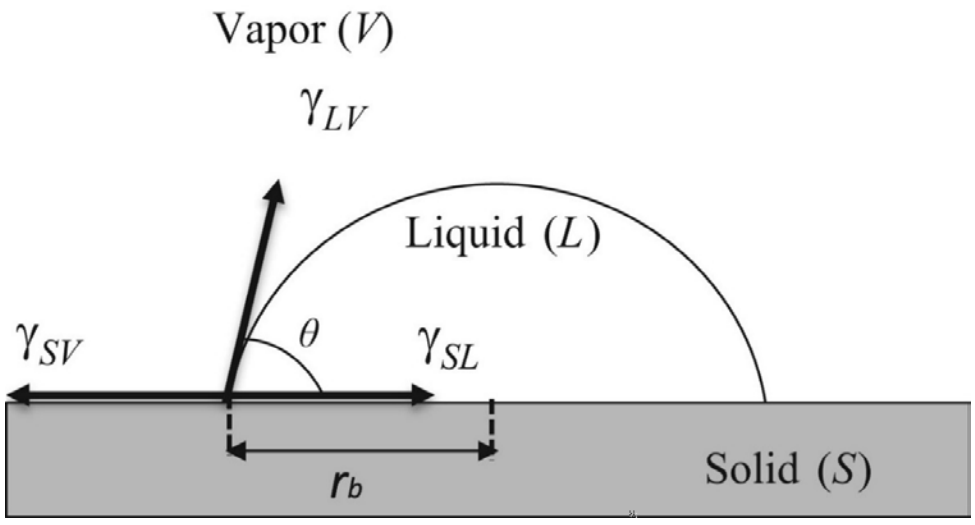

Figure 48 Depiction of 3 phase contact point [215]

The spreading coefficient is a measure of a liquids ability to spread on a surface and represents the difference between adhesive (between the two phases) and cohesive (spreading liquid) forces [216]. The relation links the surface tension of a liquid, a solid and the interfacial tension between the two. Spreading occurs when the coefficient is >0, when S<0 droplets will form.

$$S = \gamma_{SV} - (\gamma_{SL} + \gamma)$$

Young-Dupre law is a relationship between the Young's equation and the spreading coefficient. The law is restricted to cases where S<0 and partial wetting only has occurred, otherwise there are no physical solutions for θ. This is commonly employed in software used to calculate contact angle measurements.

$$S = \gamma(cos\theta_e - 1)$$

Wetting of Textured Surfaces

The previous section dealt with wetting on an ideal, homogenous solid surface however this is generally not the case found in reality. When a droplet wets a textured surface there exists two primary models that describe its behaviour, Wenzel and Cassie-Baxter (Figure 49).

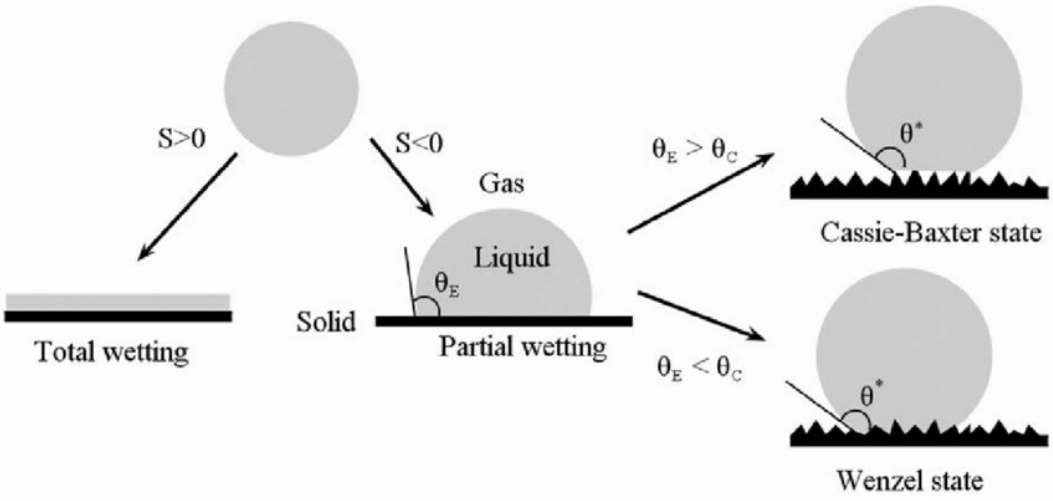

Figure 49 Pathways for wetting on a textured surface [217]

Wenzels model established in 1936 provided the initial model for a homogenously rough surface [218]. Here the droplet falls into the gaps within the roughened surface so that there is complete contact underneath the droplet. This model implies that an apparent contact angle, at equilibrium, was equal to the ideal Young contact angle multiplied by a roughness ratio. The roughness ratio being a measure of the ratio of contact area. In this state surface roughness magnifies the underlying wetting properties, so that hydrophobic surfaces become more hydrophobic and vice versa.

$$cos\theta^* = rcos\theta_e$$

In moving towards more realistic surfaces, Cassie-Baxter provided an update to Wenzel for heterogeneous solids [219]. This model best represents surfaces with multiple and random textures. Here the apparent angle is calculated using an average of the angles characteristics of each section. Visually the droplets sit on the top of pillars/high points within the textured surface and thus the droplet only comes into fractional contact with the surface. This model can also be adapted for a two-component system, for example when air pockets are trapped beneath the droplet as per the lotus leaf.

$$cos\theta_e = f_1 cos\theta_1 + f_2 cos\theta_2 + \cdots + f_n cos\theta_n$$

The transition point between these two models is also an important concept in relation to SLIPS. During this transformation of wetting state, the droplet moves from CB (sitting on the top) to Wenzel as the air pockets beneath become thermodynamically unstable [220]. Here the droplet penetrates into the texture and the liquid begins to propagate outwards from the middle of the drop. The penetration front seeks to minimise the surface energy until arriving at Wenzel state and is often referred to as the phenomena of hemi wicking [221]. This critical contact angles occurs as a function of solid/liquid contact area and solid roughness.

$$cos\theta_c = \frac{1 - \varphi_s}{R - \varphi_s}$$

Scale Formation

Scale formation is a complex process and is governed by a number of theoretical models and equations. For scale deposition, the impact of surface engineering is best seen through classical nucleation theory. The steady state nucleation rate (J) at a given temperature is a function of density of nucleation sites (N), atomic attachment rate (B*), Zeldovich factor (Z) and the activation barrier for nucleation (ΔG*) [135]. Density of nucleation sites is dependent on roughness and heterogeneity of the surface [222].

$$J = NZ\beta^* \frac{\Delta G^*}{K_g T}$$

Equation 16

The activation barrier for nucleation is also surface dependent and is a function of interfacial energy between the substrate, salt solution and salt nucleus [223].

$$\Delta G^* = \frac{\pi \sigma_{cw} r^{*2}}{3}(2 - 3m + m^3)$$

$$where\ m = \frac{\sigma_{sw} - \sigma_{cs}}{\sigma_{cw}}$$

Equation 17

4.2 SLIPS Capabilities

Introduction

The Slippery Liquid Infused Porous Surface first appeared in a Nature article by *Wong et al* in 2011 [224]. Bio-inspired by the carnivorous Nepenthes pitcher plant, the surface consists of a dual roughness structure infused with a lubricant (Figure 50). As a natural coating it provides a uniformly smooth surface with superior liquid repellence, self-healing/cleaning capabilities and pressure stability. Following on from natural surfaces such as the hydrophobic Lotus leaf, SLIPS provides a solution to many of their shortcomings. In current literature, SLIPS are also commonly referred to as lubricant impregnated or liquid infused surfaces [225]. At the moment the two research hubs are the Wyss Institute (Harvard) and the Varanasi lab (MIT). Both academic centres have spun out companies seeking to commercialise the technology in the form of Adaptive Surface Technologies and Liquiglide respectively. This section of the literature review will review some of the capabilities that make SLIPS such a breakthrough in surface engineering and coating technology and also the variety of applications and fabrication methods in which they exist.

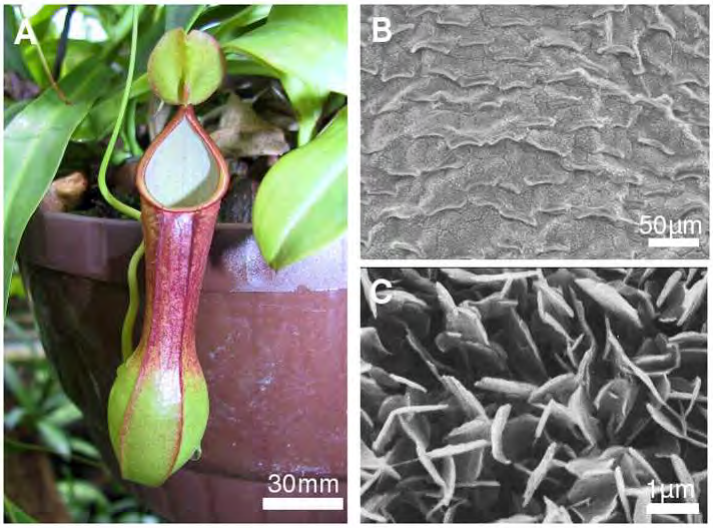

Figure 50 Nepenthes pitcher plant, exhibiting dual scale roughness [226]

Biofouling

After the initial paper, SLIPS surfaces were created for use in an anti-biofilm application in the same Harvard laboratory. *Epstein et al* [227] used a PTFE

(without modification) and silicon (fabricated by Bosch process and silanised) substrate infused with perfluorinated fluids (Krytox and FC-70). Testing under different flow regimes on Escherichia coli, Pseudomonas aeruginosa and Staphylococcus aureus found an advance of 1-2 orders of magnitude in attachment prevention compared to existing best-case scenario on PEG-functionalised surfaces. After 7D immersion tests 99.6% reduction in attachment were observed and 99.6% reduction in bio-film accumulation shows the strong impact of SLIPS in disrupting both the deposition and adhesion processes.

SLIPS surfaces have also been adapted for use in a marine environment. *Tesler et al* [228] used an electro chemical deposition method for Nano porous tungsten oxide films on a variety of steel substrates. After functionalisation with Krytox oil or perfluorodecalin, high omniphobicity and low sliding angles/CAH were observed. In the presence of green alga chlamydomonas reinhardtii, the SLIPS showed a reduction in fouling surface area by 93% compared to a SHS and control surface. Unlike the lubricant layer in SLIPS, SHS surfaces which are immersed can find that the trapped air pockets can be bypassed by microorganism and are less stable due to compressibility. Toxicity and retention of the lubricant is also a key consideration when observing the SLIPS system and its surrounding environment

Using an anodised aluminium surface with FOTS functionalisation and a PFPE lubricant, *P Wang et al* [229] tested another SLIPS system for algae settlement. Results show strong inhibition in both the deposition and adhesion process of C. Vulgaris, with less than 0.04% coverage in static and dynamic conditions. The study shows that low length scale and uniformity, act as primary factors for anti-fouling surfaces in static conditions. It is also seen that the liquid like property of SLIPS is the main contributor to its solid anti-biofouling properties.

Amini et al [230], successfully translated SLIPS lab tests into field results. The SLIPS systems consisted of a 3D polydimethylsiloxane (PDMS) network and a 2D silica nanoparticle coating both on glass substrates and infused with silicone oil. The surface was once again successful in reducing the attachment process of Asian green mussels, through disruption of the mechano-sensing

ability and decreasing the molecular work of adhesion (Figure 51). Adhesive strength tests of mussel plaque were smaller by a factor of 2-5 compared to commercially available coatings and field studies of mussel settlements showed 4-30-fold decreases in total coverage area.

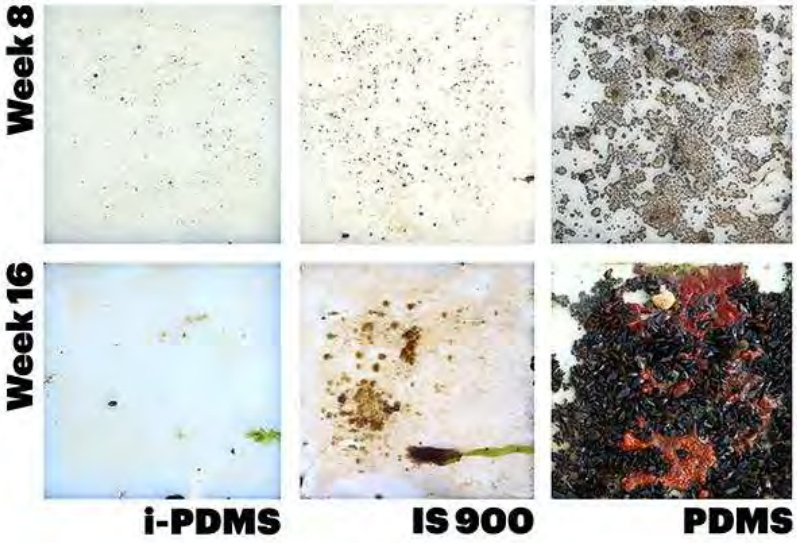

Figure 51 Anti-biofouling results from PDMS SLIPS in aquatic environment [230]

Recently Nano-wrinkled polymeric surfaces have been used by *Ware et al* [231] as SLIPS surfaces. A combinations of Teflon AF, polystyrene and poly (4-vinylpyridine) polymers on polyshrink or shrink-wrap substrates and silicone oil infusion were tested. Successful outcomes against marine and bacterial attachment were observed with a focus on lubricant retention and durability. Volume of lubricant was quantified using a novel fluorescence process, and surface durability was proven after 2 weeks of shear in seawater in lab conditions and reduced algal attachment after 7 weeks in the field.

Liquid Repellence

SLIPS surfaces have shown solid performance in repelling a range of liquids with different physical and chemical properties. Performance is usually enhanced dependent on SLIPS fabrication and lubricant choice. Initial studies provided repellence to both simple and complex liquids, including water, crude oil, blood and hydrocarbons [224]. Its superior repellence has seen the surface

used successfully in anti-condensation applications where the need to form discrete droplets is a priority [225]. Solid/ highly viscous liquids have been successfully repelled both in a commercialised setting (i.e. Liquiglide) and in an anti-icing system. In the natural world, SLIPS repellence is the primary factor that makes SLIPS such an effective anti-biofouling surface (as discussed earlier). Low sliding angles and low contact angle hysteresis are interrelated properties that are a result of liquid repellence on the SLIPS surfaces. Low contact angle hysteresis has been observed on differing surface tension liquids from alkanes, di propylene glycol, glycerol and water (Figure 52). Recent SLIPS, using an IPA infused silicon substrate has been successfully tested to repel Butane [232].

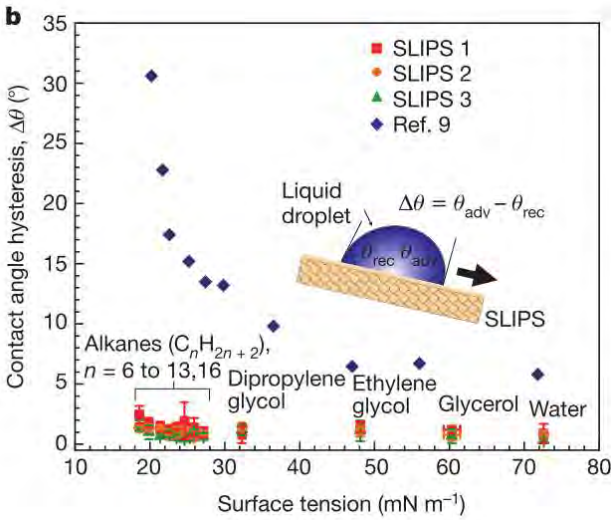

Figure 52 SLIPS contact angle results for liquids of varying surface tension [224]

Drag Reduction

Drag reduction is another established benefit of SLIPS surfaces. For an oilfield pipeline introducing a slippery surface on pipes will increase production flow rates and reduce the power required to pump it. Generally at the fluid solid interface a no-slip boundary condition exists but the lubricant layer of SLIPS creates a new slip interface. SLIPS are more stable than traditional hydrophobic due to the stability of the lubricant layer compared to air (i.e. compressibility etc.), however the viscosity of the lubricant can have a detrimental effect on drag reduction properties [233]. *Schoneker et al* [234]

used a laminar flow regime to prove a SLIPS surface with working fluid to lubricant velocity ratio of 56 can produce a 20% flow increase. However assessment of drag reduction must take into account geometric considerations of the intended surface to be used. Higher Reynolds number (between 7000-9000) were tested by *Rosenberg et al* [235]. Here a heptane impregnated surface demonstrated a 14% drag reduction in Taylor-Couette geometry. Theoretical work on models for turbulent flow have also been linked with drag reduction potential [236].

Self-cleaning and Self-healing

Durability of SLIPS surfaces are further enhanced by their ability to both self-heal and self-clean. The self-healing capability arises from the roughness/porosity acting as a reservoir for lubricant, such lubricant can self-wick through capillarity forces from the undamaged to damaged areas. *Wong et al* [224] demonstrated through high speed camera the ability of SLIPS to recover rapidly after a significant fluid displacement (Figure 53). Similarly rapid recovery of the liquid repellence was observed after larger damage with a scalpel in the presence of crude oil. *Xi Yao et al* [237] demonstrated a flexible SLIPS with Teflon PDMS and Krytox oil showing self-healing after bending, poking and fingerprints. *Xiang et al* [238] measured self-healing capability as a function of anti-corrosion performance. With a mild steel substrate, ZNC coating and Krytox oil the system was subjected to NaCl solution were anti-corrosive functionality was restored after 2hrs from scratching.

Self-cleaning on SLIPS works in a two-stage process. Firstly contaminant is unable to penetrate through the lubricant and remain on the surface. Secondly, due to the omniphobicity of the surface, foreign liquids form discrete droplets and as they roll across the surface (due to a lack of pinning) they take contaminants with them [225]. *Lafuma et al* [239] demonstrated this through video footage of water drops cleaning silica particles across a tilted SLIPS (made of an acrylate solid with silicone oil). This was also tested using the evaporation of a coffee drop, which showed reduced signs of staining/deposition due to the floating nature of the droplet. Studies using water and ethanol droplets on SLIPS surfaces have also been observed to

self-clean particles ranging from carbon dust to silicon dioxide powder [229, 240].

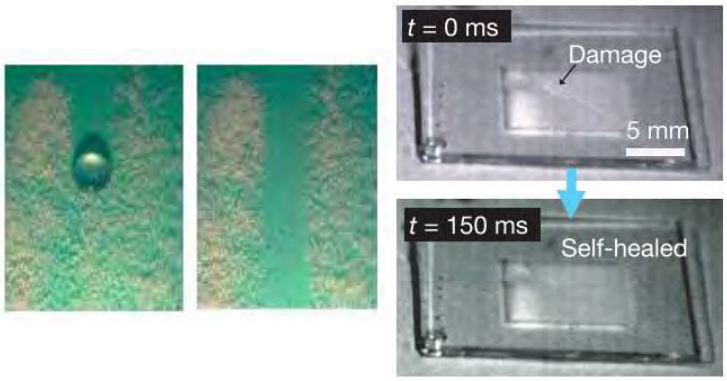

Figure 53 Visual observation of SLIPS self-healing/cleaning

High Pressure and High Temperature

The original SLIPS from Epoxy resin based nanostructures and Teflon membranes, lubricated with perfluorinated fluids was tested in a pressurised nitrogen set-up [224]. Here SLIPS were seen to repel water and liquid hydrocarbons at and while transitioning to 676 atm. Low sliding angles (~ 5°) were achieved for a droplet of decane with increasing pressure (Figure 54). However pressure stability is closely linked with the surface tension of the lubricant (i.e. lower surface tension, lower pressure stability).

Resistance to high temperatures is another beneficial property of SLIPS. This property is usually a function of the lubricant in the system, with the most promising results displayed with ionic liquids. One of the problems with maintaining omniphobic repellence at high temperatures is due to the fact surface tension reduces considerably for organic liquids when temperatures exceed 200 °C. *Daniel et al [241]* using a fluorinated, UV-cured polyurethane with Krytox oil demonstrated water repellence at 95 °C. Similarly with a Krytox infused Teflon membrane crude oil was repelled at 200 °C. Further study by *Miranda et al* [242], on dewetting and durability under thermal damage showed SLIPS stability with ionic liquids at 250 °C and after annealing at 250 °C for 12 hrs. The low volatility and high thermal stability of ionic liquids

was preferred over perfluoropolyether's due to the difference in viscosities at room temperature.

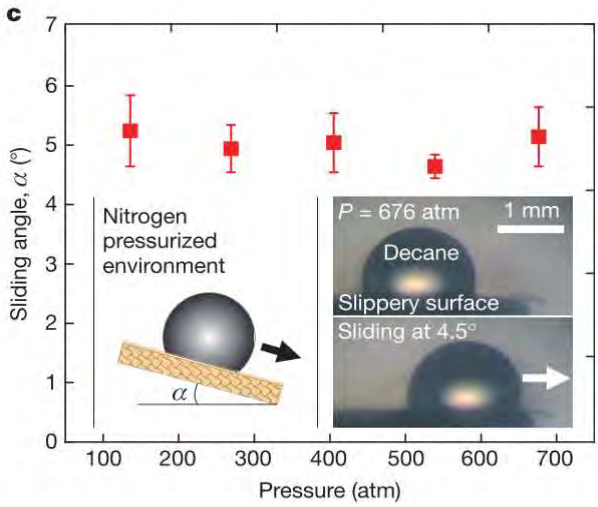

Figure 54 Sliding angle results for decane at high pressure

Scale Specific

SLIPS for application in a scaling environment were first tested by *Charpentier et al* [243] in a calcium carbonate solution. Using a layer of polypyrrole and a fluoro carbon film on stainless steel discs the chosen lubricants were FC-70 and BMIm. After 2 hr immersion times, SLIPS surfaces exhibited reductions in scale mass gain compared to stainless steel control surfaces in both precipitating (286 mg/cm2 vs 16mg/cm2) and pre-precipitating (41 mg/cm2 vs 3 mg/cm2) scaling solutions. These results show the main process of scaling at the surface is direct growth of crystals as opposed to indirect adhesion from the bulk solution. SLIPS proved to be successful in altering both adhesive forces and surface nucleation of scale.

Subramanyan et al [244] delved deeper into the design of SLIPs specifically to prevent scale formation. Using classical nucleation theory, design was optimised based on surface tension of lubricant and its spreading coefficient on the substrate. The environmental scaling conditions consisted of a gypsum supersaturated solution, with two test substrates, dry etched silicone with an OTS coating and sand blasted steel. Lubricants consisted of silicone oil and DC704. The observed results were in line with previous literature, a strong

reduction in surface coverage and mass gain specifically the longer the immersion time (80 hrs being the maximum). SLIPS Performance was stronger with the lower surface energy lubricant and once again effective in inhibiting both adhesion and deposition processes (Figure 55).

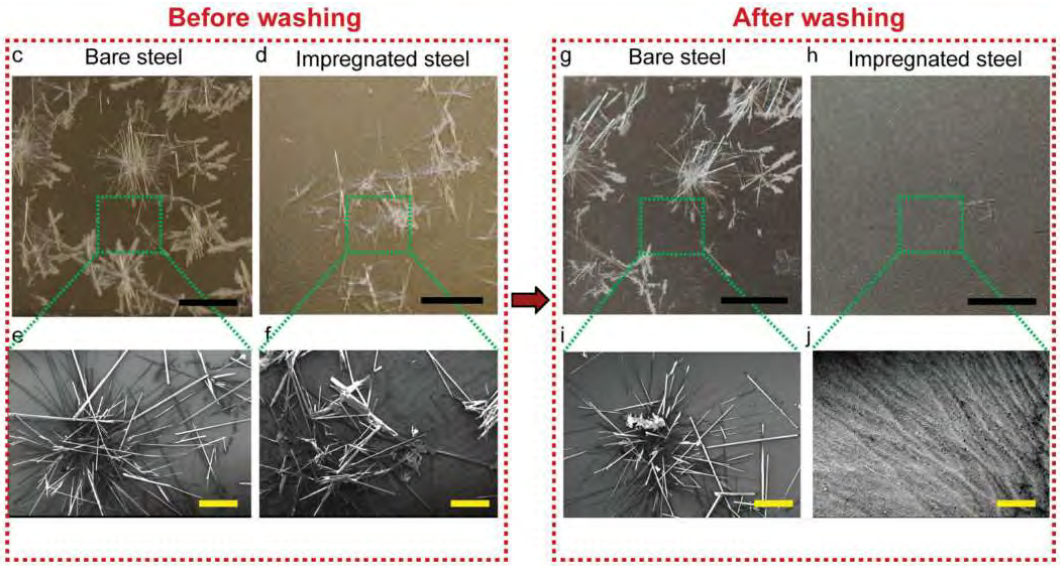

Figure 55 SEM images of gypsum scale adhesion for SLIPS based on a steel substrate [244]

4.3 SLIPS Design Criteria

The initial criteria for SLIPS detailed a design based on three criteria [224]:

- *The lubricating liquid must wick into, wet and stably adhere within the substrate*
- *The solid must be preferentially wetted by the lubricating liquid rather than by the liquid one wants to repel*
- *The lubricating and impinging test liquids must be immiscible*

To ensure the 1st rule is met a surface can be generally textured, preferably on a micro and Nano scale to aid in wettability of the lubricant onto the solid. This wettability and adhesion of the lubricating fluid can be enhanced through chemical affinity as well. The second criteria require the analysis of chemical and physical properties of combinations of substrate and lubricant. This is done by comparing energy states of a system with a substrate in the presence of an immiscible liquid and lubricating fluid. These three wetting configurations are as outlined below. In this case the following assumptions are made: The fluid layer covers the surface features, fluid layer thickness is less than capillary length, surface roughness is uniformly distributed and the two liquids are chemically inert with the solid.

Stable droplet configuration on SLIPS was further developed in *Smith et al* [245], seen in Figure 56. With ideal schematics for an interface outside and underneath the droplet. Criteria were calculated using a combination of total equivalent energy states providing a thermodynamic framework for stability. Two further layers of complexity where incorporated using both a spreading coefficient and hemi wicking criterion. Droplet cloaking is another phenomenon that had not been previously considered, this involves the spreading of a thin film of lubricating fluid across the surface of the droplet. This can have an adverse effect on lubricant retention as the droplet sheds taking some of the lubricant with it. One of the limitations of these empirical methods is the need for numerous lab tests to simulate the various wetting configurations and gather data on roughness, contact angles and interfacial tension.

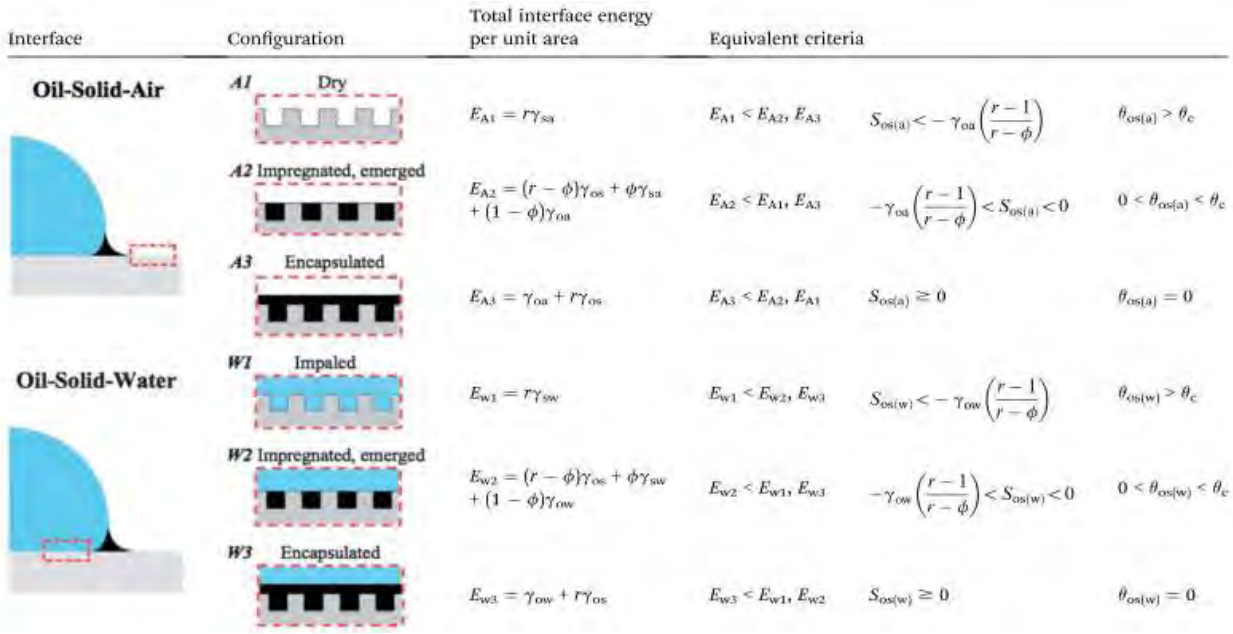

Figure 56 Wetting configurations for droplets on SLIPS surface

Predictive modelling capabilities were incorporated by *Preston et al* [232]. Using the Van Oss, Chaudry and Good (vOCG) method [246], it was proven that combination SLIPS could be theoretically investigated based on their Lifshitz van der Waals and Lewis acid-based interfacial energies. The reduction in required experiments to test SLIPS combinations was reduced by a factor of 100 times by the vOCG surface energy method. The predictive LIS model outlines 5 conditions for an ideal case (Figure 57), building on cases previously outlined in literature and incorporating surface energy values (Figure 58). The first two failure criteria deal with the spreading parameter and whether the droplet is cloaked or forms a thin film. The next criteria look at the interactions and affinity between the droplet, lubricant and surface, to see if the droplet displaces lubricant or draws it away from the substrate. The final condition is based on the miscibility between the two fluids. There are some limitations of this method, including being limited to combinations within the database, absence of metallic interactions, use of ionic liquids and difficulties assessing nonpolar impinging fluids.

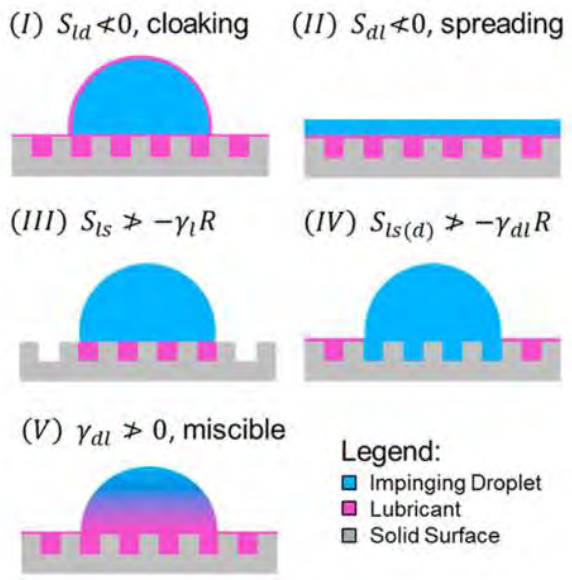

Figure 57 Schematic configuration of predictive SLIPS failure criteria [232]

Criterion (I):

$$\begin{aligned} S_{ld} &= \gamma_d - (\gamma_{dl} + \gamma_l) \\ &= \gamma_d^{LW} + 2\sqrt{\gamma_d^+\gamma_d^-} - \gamma_l^{LW} - 2\sqrt{\gamma_l^+\gamma_l^-} - \gamma_d^{LW} - \gamma_l^{LW} \\ &\quad + 2\sqrt{\gamma_d^{LW}\gamma_l^{LW}} - 2\sqrt{\gamma_d^+\gamma_d^-} - 2\sqrt{\gamma_l^+\gamma_l^-} + 2\sqrt{\gamma_d^+\gamma_l^-} \\ &\quad + 2\sqrt{\gamma_l^+\gamma_d^-} < 0 \end{aligned} \tag{8}$$

Criterion (II):

$$\begin{aligned} S_{dl} &= \gamma_l - (\gamma_{dl} + \gamma_d) \\ &= \gamma_l^{LW} + 2\sqrt{\gamma_l^+\gamma_l^-} - \gamma_d^{LW} - 2\sqrt{\gamma_d^+\gamma_d^-} - \gamma_d^{LW} - \gamma_l^{LW} \\ &\quad + 2\sqrt{\gamma_d^{LW}\gamma_l^{LW}} - 2\sqrt{\gamma_d^+\gamma_d^-} - 2\sqrt{\gamma_l^+\gamma_l^-} + 2\sqrt{\gamma_d^+\gamma_l^-} \\ &\quad + 2\sqrt{\gamma_l^+\gamma_d^-} < 0 \end{aligned} \tag{9}$$

Criterion (III):

$$\begin{aligned} S_{ls} + \gamma_l R &= \gamma_s - (\gamma_{ls} + \gamma_l) + \gamma_l R \\ &= \gamma_s^{LW} + 2\sqrt{\gamma_s^+\gamma_s^-} - \gamma_l^{LW} - \gamma_s^{LW} + 2\sqrt{\gamma_l^{LW} - \gamma_s^{LW}} \\ &\quad - 2\sqrt{\gamma_l^+\gamma_l^-} - 2\sqrt{\gamma_s^+\gamma_s^-} + 2\sqrt{\gamma_l^+\gamma_s^-} + 2\sqrt{\gamma_s^+\gamma_l^-} + \\ &\quad (R-1)(\gamma_l^{LW} + 2\sqrt{\gamma_l^+\gamma_l^-}) > 0 \end{aligned} \tag{10}$$

Criterion (IV):

$$\begin{aligned} S_{ls(d)} + \gamma_{dl} R &= \gamma_{ds} - (\gamma_{ls} + \gamma_{dl}) + \gamma_{dl} R \\ &= \gamma_d^{LW} + \gamma_s^{LW} - 2\sqrt{\gamma_d^{LW}\gamma_s^{LW}} + 2\sqrt{\gamma_d^+\gamma_d^-} + 2\sqrt{\gamma_s^+\gamma_s^-} \\ &\quad - 2\sqrt{\gamma_d^+\gamma_s^-} - 2\sqrt{\gamma_s^+\gamma_d^-} - \gamma_l^{LW} - \gamma_s^{LW} + 2\sqrt{\gamma_l^{LW}\gamma_s^{LW}} \\ &\quad - 2\sqrt{\gamma_l^+\gamma_l^-} - 2\sqrt{\gamma_s^+\gamma_s^-} + 2\sqrt{\gamma_l^+\gamma_s^-} + 2\sqrt{\gamma_s^+\gamma_l^-} \\ &\quad + (R-1)(\gamma_d^{LW} + \gamma_l^{LW} - 2\sqrt{\gamma_d^{LW}\gamma_l^{LW}} + 2\sqrt{\gamma_d^+\gamma_d^-} \\ &\quad + 2\sqrt{\gamma_l^+\gamma_l^-} - 2\sqrt{\gamma_d^+\gamma_l^-} - 2\sqrt{\gamma_l^+\gamma_d^-}) > 0 \end{aligned} \tag{11}$$

Criterion (V):

$$\begin{aligned} \gamma_{dl} &= \gamma_d^{LW} + \gamma_l^{LW} - 2\sqrt{\gamma_d^{LW}\gamma_l^{LW}} + 2\sqrt{\gamma_d^+\gamma_d^-} + 2\sqrt{\gamma_l^+\gamma_l^-} \\ &\quad - 2\sqrt{\gamma_d^+\gamma_l^-} - 2\sqrt{\gamma_l^+\gamma_d^-} > 0 \end{aligned} \tag{12}$$

Figure 58 Failure criterion mathematical formula

Chapter 5
Research Materials, Procedures and Calculations

5 Experimental Methodology

5.1 Introduction

This chapter gives a summary of the main experimental test methods and analysis techniques used during the research in this thesis (Figure 59). The chapter begins with an overview of the key materials used in the fabrication of the SLIPS samples, including the X65 carbon steel, the four tested lubricants and the scaling brine compositions. Test procedures associated with the creation of the SLIPS $FeCO_3$ base layer, SLIPS lubrication and the subsequent scaling tests for evaluating the anti-fouling performance are also summarised.

The experimental methodology includes the numerous in-situ and post experimental analysis techniques. Several electrochemical methods have been used to ascertain corrosion related data of the SLIPS samples in-situ. Post-test analysis includes the use of an array of conventional techniques employed in academia and industry for surface analysis and deposit characterisation such as SEM/ EDX/ XRD etc. Where possible techniques have been used where they complement and verify the results of another technique. Finally, theoretical considerations used in the process of conducting this research have been highlighted. These contain calculations around the surface free energy values obtained from contact angle data, the incorporation of these values in an existing SLIPS model and the use of XRD data to construct Fe/Ca mole fractions for mixed corrosion products.

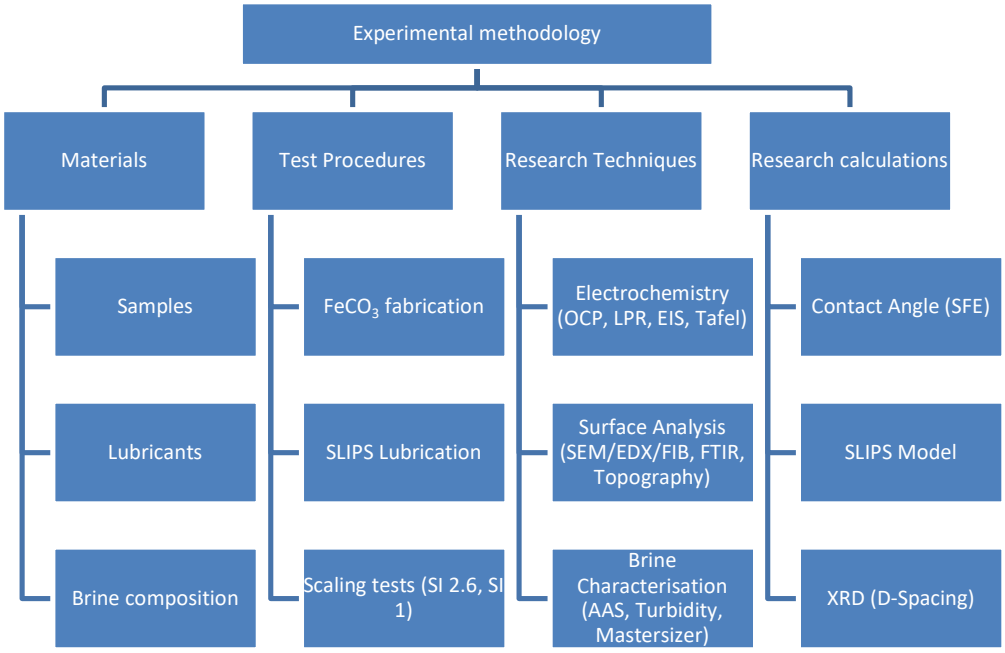

Figure 59 Breakdown of experimental methods and techniques

5.2 Materials

Metal samples

Test specimens used as the base for the SLIPS system are made from X65 Carbon Steel (CS) samples. X65 CS is a typical pipeline steel used in the Oil and Gas industry with an elemental composition provided in Table 4. X65 CS is prone to corrosion, with the formation of $FeCO_3$ deposits (both protective and unprotective) well documented in the literature [59, 247-250]. Figure 60 shows the optical microscopy of a sample after etching with 2% Nital solution. The microstructure shows a typical mixture of evenly distributed ferrite and perlite grains.

Table 4 Elemental composition of X65 carbon steel

C	Si	Mn	P	S	Cr	Mo	Ni
0.12%	0.18%	1.27%	0.01%	0.00%	0.11%	0.17%	0.07%
Cu	Sn	Al	B	Nb	Ti	V	Fe
0.12%	0.01%	0.02%	0.00%	0.05%	0.00%	0.06%	97.81%

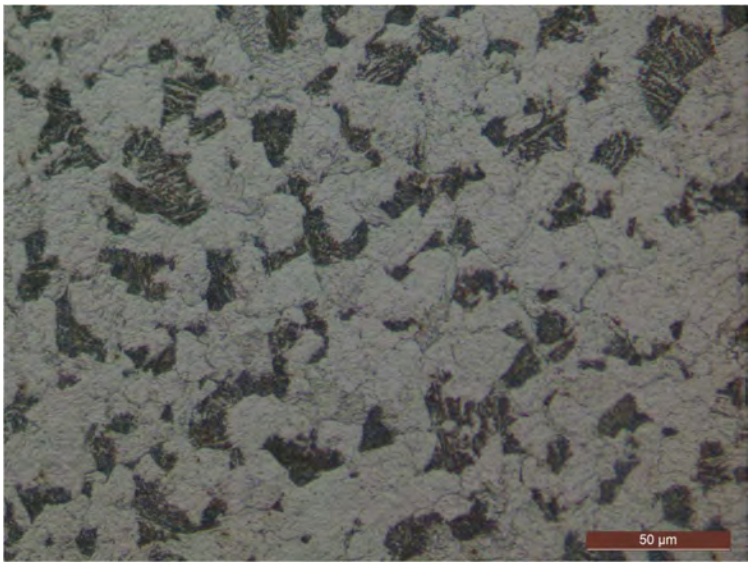

Figure 60 X65 carbon steel microstructure

Test samples were machined into discs of diameter 25 mm and a thickness of 6 mm. Samples were then soldered with an insulated 3mm copper wire on one face and set in a non-conductive resin with the unsoldered circular face exposed (Figure 61). The exposed surface area for the development of the $FeCO_3$ SLIPS layer was ~4.9cm^2. After embedding in the resin test specimens were manually wet ground successively with 120, 320, 600 silicon carbide (SiC) grit paper, followed by rinsing with distilled water. Final R_a (average arithmetic roughness) value was on average 0.1 µm.

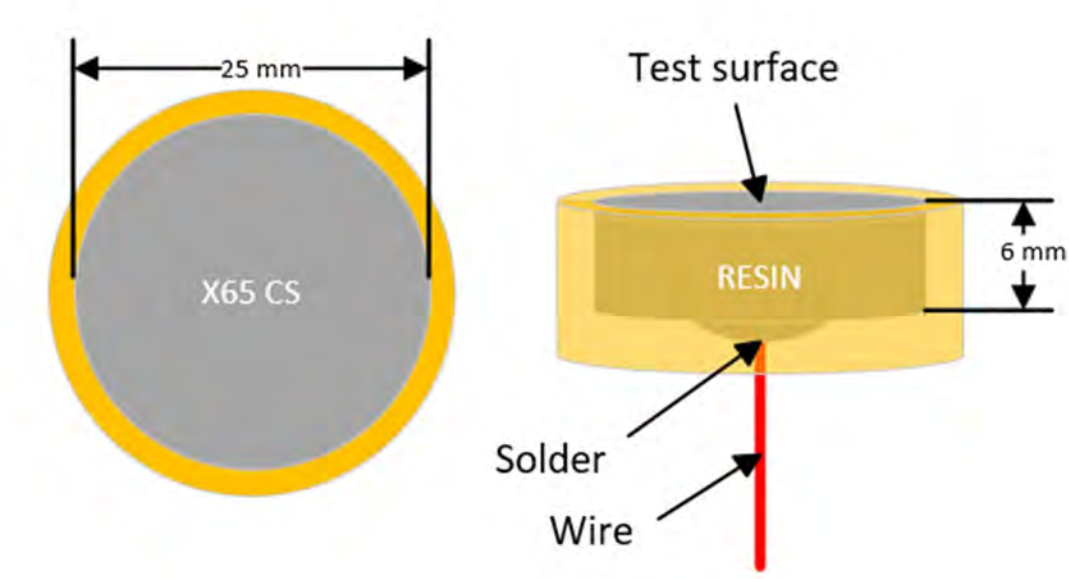

Figure 61 Schematic representation of metal samples used in testing

Lubricants

The four lubricants incorporated into the SLIPS are (with some comparable specific properties) outlined in Table 5. Initial choices of lubricants, BMIM and Krytox, are both lubricants with past success in scaling environments, producing successful results on a variety of SLIPS surfaces (including metallic ones). Lubricants are generally chosen with low surface tension (for reduced adhesion of scale and ability to spread onto the substrate), low vapor pressure (to reduce evaporation loss) and chemical inertness/compatibility with the substrate in mind. Although, this can change based on preferred properties dependent for specific applications/conditions. The crude oils have been tested due to the specific application of these SLIPS for oil and gas pipelines:

- Krytox VPF1525 (SLIPS Kr)

Krytox is a commercial perfluorinated oils/lubricants from Chemours. It is a synthetic compound commonly referred to as perfluoroalkyl ether (PFAE) or perfluoropolyether (PFPE) used in a variety of harsh applications including aerospace, automotive and chemical processing industries. It has a number of suitable properties as a lubricant including being non-reactive, thermally

stable, insoluble in water and with a low vapor pressure. The generic chemical structure is shown below.

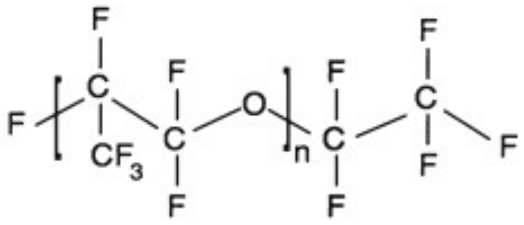

Figure 62 Typical chemical structure of a Krytox perfluorinated oil [251]

- BMIM TFSI (SLIPS BM)

BMIM is a widely studied ionic liquid or molten salt. Consisting of a cationic component of 1-Butyl-3-methylimidazolium (BMIM) and the anionic group of bis(trifluoromethylsulfonyl)imide (TFSI) as seen in Figure 63. Similarly to Krytox they have a number of properties that make them appealing for use as lubricants including being immiscible in water, non-flammable and non-volatile.

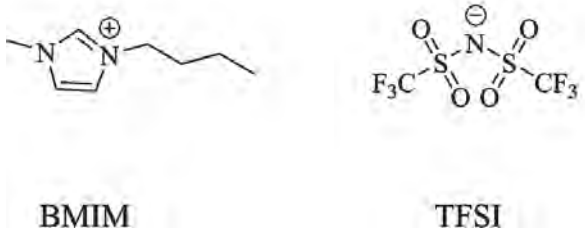

Figure 63 Chemical structure of cationic BMIM and anionic TFSI [252]

- Crude Oil Waxy (SLIPS W)

This crude oil, also known as CLOV OV-L, is a blend of crudes taken from two of Totals oilfields. The blend is considered waxy, as it contains a paraffin component consisting of hydrocarbons between nC10-nC40 of 0.55 to 3.6 wt.%. The Crude oil has an API value between 22.5- 35.6˚. The composition of some of the brines is shown below and provides a snapshot of likely chemicals to be encountered in both crude oils.

Table 5-9: O11W and OVC compositions

	Mole (%)	
	O11W	OVC
N2	0.109	0.054
CO2	0.211	5.134
C1	47.879	41.605
C2	8.380	4.217
C3	5.925	2.762
IC4	1.241	0.810
NC4	2.831	1.863
IC5	1.232	1.015
NC5	1.310	1.188
C6	2.725	2.778
C7	3.098	3.637
C8	2.883	3.415
C9	1.831	2.280
C10	1.749	2.445
CN1	7.172	6.733
CN2	11.425	12.614
CN3	0	2.837
CN4	0	2.312
CN5	0	0.000
CN6	0	1.000
CN7	0	1.301
Total	100	100
C11+	18.597	26.797

Figure 64 Fluid composition in mole (%) of two crude oils blended in CLOV OV-L (Waxy crude oil)

- Crude Oil Non-waxy (SLIPS NW)

Crude Oil Non-Waxy, also known as Begonia lima 6505, is a non-blended crude taken from one Total oilfield. It has no wax/paraffin components and has an API value of 34.7˚.

Table 5 Comparison of selected properties between the lubricants

	Krytox	BMIM	Crude Oil W	Crude Oil NW
Density (kg/m3)	1900	1430	847-919	852
Dynamic viscosity @ RT (mPa s)	496	64	22-220	5

Scaling brine Compositions

All brine reagents used (i.e. sodium chloride (NaCl), calcium chloride hexahydrate ($CaCl_2.6H_2O$) and sodium bicarbonate ($NaHCO_3$)) are in accordance with ACS requirements (Sigma Aldrich, ≥99.0%). Two brine

compositions were used to simulate different scaling systems, differentiated by saturation index. One was a high scaling system of saturation index 2.6 characterised with an excess of calcium ions and high bulk precipitation of $CaCO_3$ (Table 6). The other system (Table 7) was a more moderate scaling environment with saturation index of 1, closer in likeliness to field conditions.

Table 6 Brine composition for the SI 2.6 High scaling system

SALT	BRINE 1 (g/L)	BRINE 2 (g/L)
Sodium chloride (NaCl)	10.63	10.63
Calcium hexahydrate ($CaCl_2.6H_2O$)	31.49	-
Sodium Bicarbonate ($NaHCO_3$)	-	12.10
Saturation Index	2.6	

Table 7 Brine Composition of the SI 1 Low scaling system

SALT	BRINE 1 (g/L)	BRINE 2 (g/L)
Sodium chloride (NaCl)	5.3	5.3
Calcium hexahydrate ($CaCl_2.6H_2O$)	15.03	-
Sodium Bicarbonate ($NaHCO_3$)	-	5.9
Saturation Index	1	

5.3 Test Procedures

The following test methodologies were used for the research in this thesis (based on Figure 65). This included the fabrication of the SLIPS base layer from $FeCO_3$, the infusion of the lubricant and the final performance testing of the SLIPS created.

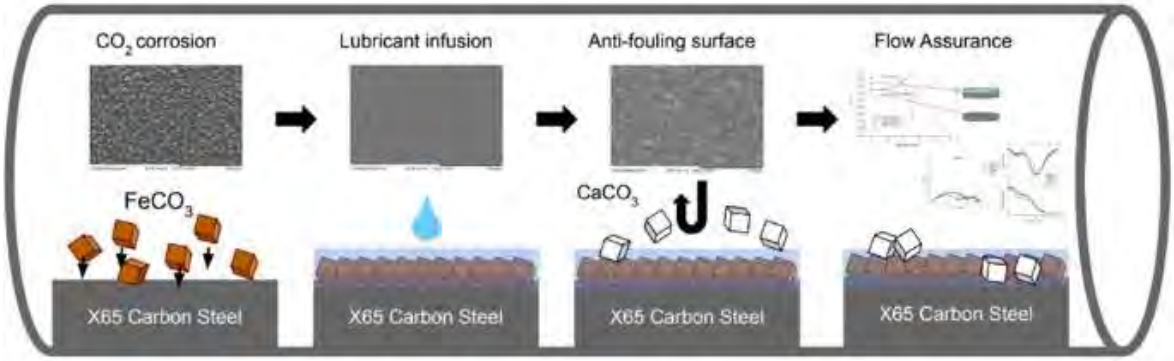

Figure 65 Schematic of the main research stages in this thesis

1. Fabrication of the SLIPS base

Conditions to develop $FeCO_3$ onto X65 steel were chosen based on prevailing literature and a series of preliminary experiments that produced a reliable and repeatable $FeCO_3$ protective film. $FeCO_3$ was generated using a standard 1L corrosion bubble cell with a Radley's hotplate/thermocouple as seen in Figure 66. Solution chemistry for the fabrication of the $FeCO_3$ base layer consisted of 16g of $NaHCO_3$ and 3.5 wt. % NaCl in a 1L beaker of distilled water. The solution was continuously bubbled with CO_2 for 12 h prior to insertion of the test specimen, with on average a pH level above 7. The test specimen was suspended in the solution via a drilled rubber bung, placed in custom made slots in the beaker lid. A magnetic stirrer, operating at 150 rpm was used to ensure uniform solution consistency throughout the experiment. Temperature was maintained at 80°C with a test duration of 72 hours. The presence of $FeCO_3$ on the steel surface was confirmed by X-ray diffraction (XRD) and Scanning electron microscopy (SEM).

Figure 66 Typical set-up for static corrosion test (also the same for scaling tests)

2. Lubrication

After fabrication of the $FeCO_3$ layer, the test specimen is removed from the solution, rinsed with distilled water and dried with a stream of nitrogen gas. Depending on the experiment the samples will be broken out of the resin (for mounting in scaling holder) or left in the resin (for electrochemistry testing). An excess of lubricant was deposited onto the exposed face of the test specimen using a pipette, left for 12 h to allow full impregnation and then blown with a stream of nitrogen to remove excess lubricant.

3. Scaling tests (SI 2.6, SI 1)

Anti-fouling capabilities were assessed through a standard bulk jar test in a $CaCO_3$ scaling scenario (this is the same set-up used in the fabrication of the $FeCO_3$ base layer). The brine compositions are not representative of a particular oil field but provide an insight into simple scaling behaviour/resistance of the SLIPS surface. The compositions are outlined previously. Brines are prepared separately in 1L beakers. Pre-test a magnetic stirrer operating at 150 rpm was used to ensure proper mixing of salts in the solution, with continuous CO_2 bubbling for 3 h at a temperature of 50°C. Temperature and CO_2 bubbling was maintained throughout the test duration.

During the test, 500 mL of each brine were mixed together, and the sample immersed in solution via suspension in the sample holder (Figure 67) for 2 h. A magnetic stirrer operating at 150 rpm was used to ensure uniform solution consistency. After testing the sample was then rinsed with DI water and dried in an oven at 35°C for 3 h before further surface analysis.

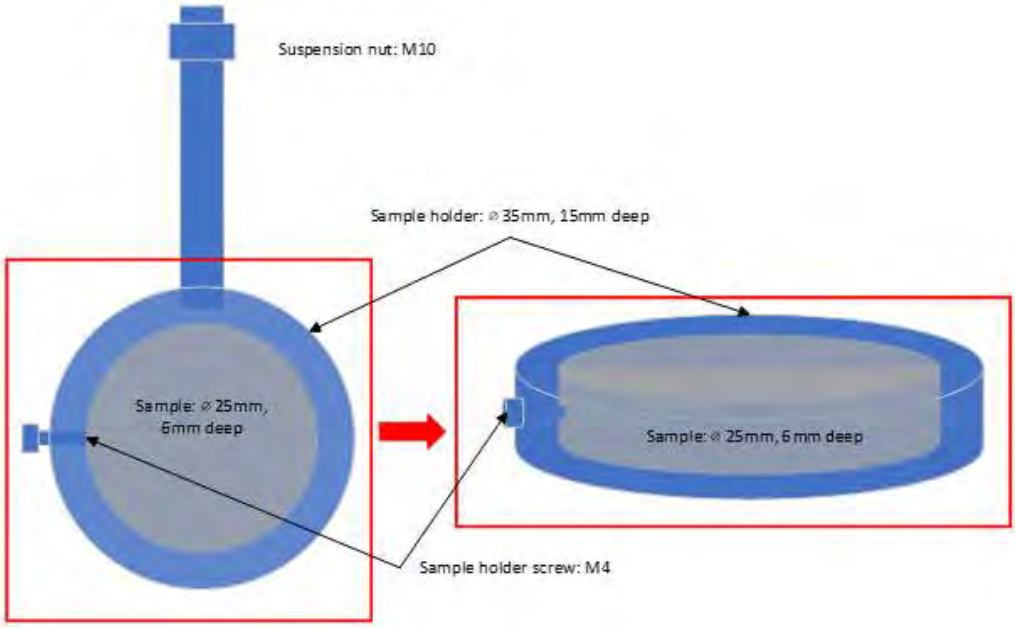

Figure 67 Schematic of sample holder for scaling tests

5.4 Research Techniques

Electrochemistry

The electrochemistry set-up used was a static 1L bubble cell test (Figure 68). This standard method used the same apparatus used in the scaling tests but with the inclusion of a potentiostat and electrodes. The three-electrode cell consisted of a working electrode (WE) that was the SLIPS sample and a Mettler Toledo InLab saturated Ag/AgCl reference redox electrode which included a platinum counter electrode. Electrodes were connected to a potentiostat that was either an IVIUM CompactStat or ACM Gill 8 and operated with the manufacturers software. The following corrosion tests were

conducted using the parameters outlined (more in-depth information on the theoretical background is discussed in the literature review):

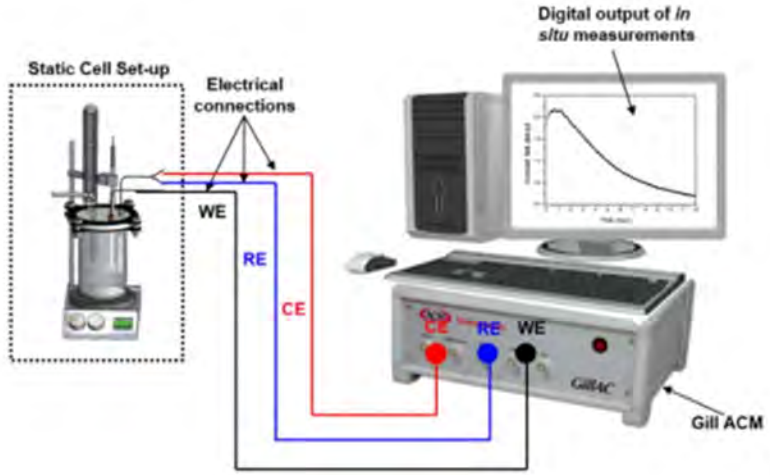

Figure 68 Typical experimental set-up for electrochemistry tests [253]

Open Circuit Potential (OCP)/ Linear Polar Resistance (LPR)

OCP measurements were monitored (per second) before tests to ensure a stable reading (generally <10 mV/ hr). These values help establish if the system is in equilibrium and the general corrosiveness of the surrounding environment. The LPR Measurements were conducted every 30 minutes by polarising the WE from -15 mV to +15 mV from OCP, at a scan rate of 0.25 mV s-1. This is standard procedure in accordance with ASTM-G102 and provides a polarisation resistance which can then be used to calculate corrosion rates. Both OCP and LPR are non-destructive in-situ corrosion measurements.

Tafel plots

Tafel plots are a form of potentiodynamic polarisation which are destructive in nature (specifically when running the anodic scan). Tafel polarisation measurements were conducted at the end of the experiment, firstly in the cathodic direction from +5 mV vs. OCP to -250 mV vs. OCP, then in the anodic direction from -5 mV to +250 mV vs. OCP. A plot of applied potential vs.

current density is plotted and can be used to estimate anodic (βa) and cathodic (βc) Tafel constants. Tafel plots provide data used in calculating the corrosion rate and the kinetics of electrochemical reactions.

Electrical Impedance Spectroscopy (EIS)

EIS was conducted on samples using a 10mV excitation AC voltage applied vs OCP between 10 mHz and 0.01 MHz, registering 60 data points. The data was saved using Scribner ZPlot and analysed using Scribner ZView to observe Nyquist and Bode plots. EIS is a common AC method used in the investigation of coating behaviour [32] and has been used here for both corrosion and scaling analysis. This method is particularly relevant to SLIPS systems, which are primarily controlled by diffusion mechanisms across two separate layers, the lubricant and EDL.

Surface Analysis

Scanning Electron Microscopy (SEM)/ Energy Dispersive X-ray (EDX)

SEM is a useful tool to observe the surface morphology of the samples, including crystal shape and size. EDX is connected to the same platform and allows for the elemental analysis of the sample surface. SEM and EDX are both ex-situ analysis methods and were conducted post experiment on either a Hitachi TM3030Plus SEM or a Carl Zeiss EVO MA15 VP SEM. Both units were installed with Oxford instruments Aztec software for EDX analysis. SEM images were taken using both secondary and backscattered imaging between 5-30kV voltage range. EDX analysis was usually undertaken as point scans or areal mapping depending on the area of focus.

Focused Ion Beam (FIB)

A FEI Nova200 dual beam FIB/SEM was used to provide SEM images with EDX line scans of SLIPS sample cross-sections. The technique provided insight into the assessment of the SLIPS samples and their conformance to the predictive framework. Samples were flash frozen in liquid nitrogen in order

to stabilise the water droplet on the lubricated surface. Next the top layer of the sample was sputtered with a platinum coating before a trench was cut in the areas of interest for SEM/EDX imaging. A voltage range of 5-30 kV was used along with a current range of 0.1-5 nA.

X-Ray Diffraction (XRD)

XRD was used to verify the formation of different crystal structures deposited on the SLIPS surface. This also included the calculation of the Ca molar fraction of mixed $Fe_xCa_yCO_3$ deposits (explained in the next section). Measurements were conducted on a Bruker D8 Xray diffractometer with a 10mm wide divergent slit and a Cu Kα source. Data was acquired over a scan range from 20-70° 2θ position. The resulting diffraction pattern was analysed using X-Pert Analysis software for the identification of crystalline material.

Fourier Transform Infrared (FTIR)

FTIR was used to identify and compare the residual lubricant traces found on the SLIPS samples, particularly for the crude oil samples. A PerkinElmer spectra 100 FTIR-ATR has been used to analyse the lubricant sample footprint. A background signal is first collected, and the sample spectrum obtained after subtraction of the background signal. Data is analysed through Spectrum software. The signal is collected within the wavenumber range of 650 to 4000 cm^{-1}. An average of 25 scans is utilised with a resolution of 2 cm^{-1}.

Topography

Topography was analysed via two different machines. Surface roughness parameters were obtained using a Form Talysurf PG1800m this is a contact stylus profilometer. Arithmetic average line scans (R_a) were measured at 0.5mm/s over 10mm lengths. Developed interfacial ratio (Sdr) is an area measurement giving the percentage of an additional surface area produced by a texture/roughness, here boxes were stitched together over a $10mm^2$ square section. Linear (R_a) surface roughness is used as a point of

comparison within SLIPS literature whilst area (Sdr) roughness is substituted as R in the SLIPS prediction model (Criteria III, IV, explained in the next section). A Bruker NPFLEX was used as a point of comparison for roughness values. The NPFLEX is a non-contact surface profiler which uses white light interferometry to generate topographical data. Two random 3*3 mm regions were targeted on a sample. A 2.5X objective was used with a working distance of approximately 3.5 mm. The results gathered were then analysed using Vision64 on a PC.

Brine Characterisation:

Brine analysis was undertaken on the scaling solution after the mixing of brines (either SI 2 or 1) to understand the bulk characteristics. A magnetic stirrer was used to ensure proper mixing and brine consistency, with temperature maintained at 50 °C and continuous CO_2 bubbling. Exposure time was 2 hours. Bulk analysis methods included:

Turbidity

Turbidity was determined using a Hach DR/890 Colorimeter/ turbidity meter and indicates precipitate matter in solution (vs time). A 20mL sample was collected from Brine 1 (containing Ca^{2+}) before mixing as initial 0 min time point (i.e. no suspended solids/precipitation). After mixing, 20mL samples were collected at the following time intervals (mins): 1, 2, 3, 4, 5, 10, 15, 30, 60, 120. With the meter giving results in FAU.

Atomic absorption spectroscopy (AAS)

AAS analysis was used to determine bulk calcium concentration (vs time) and was undertaken by an Agilent 200 series spectrophotometer A 1mL sample was collected from Brine 1 (containing Ca^{2+}) before mixing as initial 0 min time point (i.e. maximum Ca^{2+} concentration). After mixing, 1mL samples were collected at the following time intervals (mins): 1, 2, 3, 4, 5, 10, 15, 30, 60, 120. 1mL samples were immediately passed through a syringe filter (to remove formed $CaCO_3$) and mixed with 9mL of quenching solution.

Quenching solution was used to halt the precipitation reaction (of further $CaCO_3$) and was prepared using 1 g of polyvinyl sulfonate (PVS) scale inhibitor and 5.71 g of KCl in 1000 ml of distilled water.

Mastersizer

A Malvern 3000 Mastersizer with a dry dispersion unit was used to determine the size distribution of $CaCO_3$ crystals that were precipitated. This was determined at the experiment conclusion (i.e. after 2 hours exposure). The mixed solution was drained via vacuum pump through a filter to capture $CaCO_3$ precipitate. Filter paper was then dried in an oven at 37 °C for 12 hours, with the dried powder collected after for analysis in the Mastersizer.

5.5 Research Calculations

Contact Angle measurements and Surface free energy (SFE)

Apparent contact angle measurements were obtained through sessile drop analysis on a KSV Cam2000 Tensiometer (Figure 69). These contact angle (CA) experiments were conducted with 3 probe liquids. DI Water, Diiodomethane and Ethylene glycol whose known surface energy components are listed in Table 8. Probe liquids are selected based on use in the literature and differing surface energy components. Individual droplet volume was 5µl administered by pipette at atmospheric pressure and ambient temperature (≈23℃.) onto the tested surface. Images are sequentially taken at 1 frame per second (for a period of 10 seconds) after the droplet contacts the surface from which angles are measured.

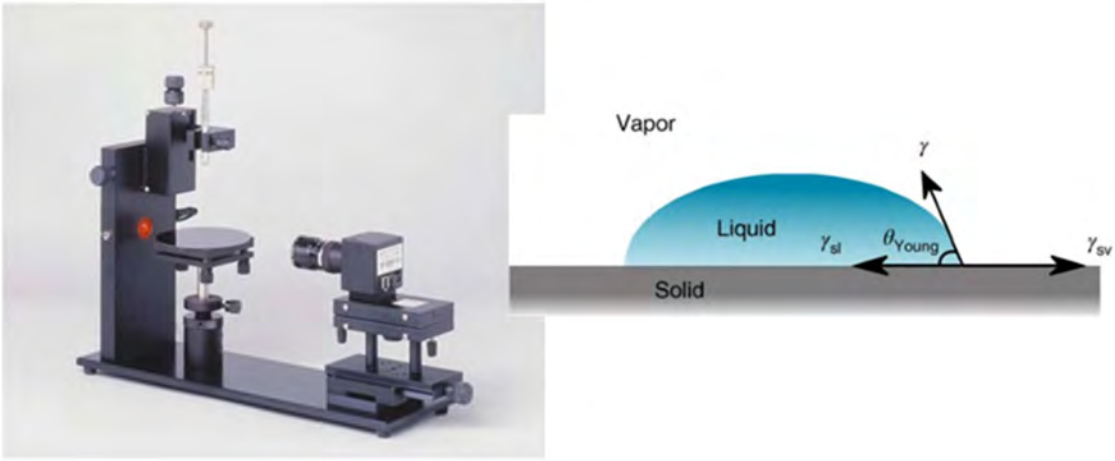

Figure 69 Contact angle tensiometer with schematic of droplet [254]

Table 8 Probe liquid surface energy components [255]

Probe Liquid	γ (mN/m)	γ^{LW} (mN/m)	γ^{+} (mN/m)	γ^{-} (mN/m)
Diiodomethane (Sigma Aldrich 99%))	50.8	50.8	0	0
Ethylene Glycol ((Sigma Aldrich 99.8%)	48	29	1.92	47
DI water	72.8	21.8	25.5	25.5

Surface free energy (SFE) was calculated based on the Van Oss, Chaudhury and Good model (vOCG) [246]. In the vOCG method surface free energy of a solid (ɣ) is considered a mixture of the different interactions occurring at the solid-liquid interface, where γ^{LW} is the polar component associated with Lifshitz van der Waals forces and γ^{+}/ γ^{-} are the Lewis acid (+) and base (-) parameters. In the vOCG method, a system of 3 linear equations was solved to calculate solid surface energy components of the tested sample. Each of the 3 equations (Equation 18-20) represent the contact angle values of each probe liquid measured from the contact angle experiments.

$$Probe\ liquid\ 1\ (l1): 0.5\gamma_s(1+\cos\theta) = \sqrt{\gamma_{l1}^{LW}\gamma_s^{LW}} + \sqrt{\gamma_{l1}^{-}\gamma_s^{+}} + \sqrt{\gamma_{l1}^{+}\gamma_s^{-}}$$

Equation 18

$$Probe\ liquid\ 2\ (l2): 0.5\gamma_s(1+cos\,\theta) = \sqrt{\gamma_{l2}^{LW}\gamma_s^{LW}} + \sqrt{\gamma_{l2}^{-}\gamma_s^{+}} + \sqrt{\gamma_{l2}^{+}\gamma_s^{-}}$$

Equation 19

$$Probe\ liquid\ 3\ (l3): 0.5\gamma_s(1+cos\,\theta) = \sqrt{\gamma_{l3}^{LW}\gamma_s^{LW}} + \sqrt{\gamma_{l3}^{-}\gamma_s^{+}} + \sqrt{\gamma_{l3}^{+}\gamma_s^{-}}$$

$$\gamma_s^T = \gamma_s^{LW} + 2\sqrt{\gamma_s^{-}\gamma_s^{+}}$$

Equation 20

SFE- SLIPS Framework

The SLIPS compatibility framework is taken from the model by Preston et al [255] and visually highlighted in Figure 70. The development of SLIPS design theory is highlighted in Section 4.3 and the relevance to the current research is further explored in the results in Section 6.7. Put simply it represents the current thinking and an ability to predict the stability of the SLIPS surface for a selected combination of impinging droplet, lubricant and solid surface. The model has five criteria for a stable SLIPS which are:

I. The lubricant does not cloak the impinging droplet.
II. The impinging fluid forms discrete droplets on the lubricant.
III. The impinging droplet does not draw the lubricant away from the surrounding substrate.
IV. The impinging droplet does not displace the lubricant on the substrate.
V. The impinging droplet and lubricant are immiscible. These equations are represented mathematically below

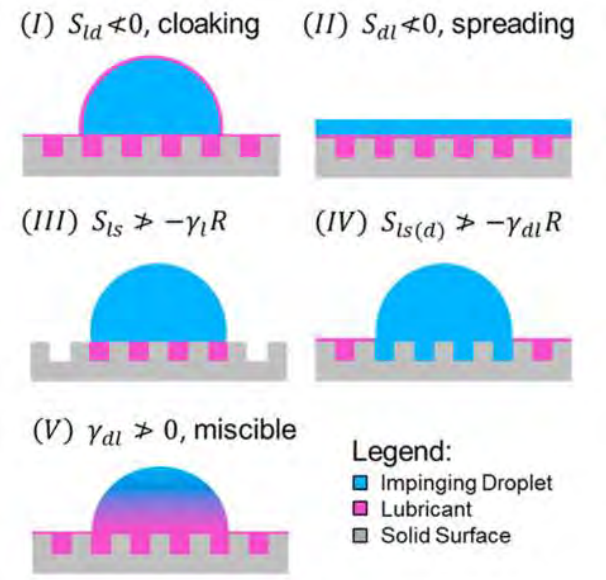

Figure 70 SLIPS compatibility model by Preston et al [232]. explained further in Section 4.3

This model is governed by interfacial relations between the 3 phases that comprise the SLIPS system (i.e impinging droplet, lubricant and solid surface) and a geometric factor (roughness). Mathematically this is represented in the Criterion equations (I)-(V) below. Here subscript l denotes lubricant (Krytox, BMIM or Crude Oil), d is impinging droplet (water, but representative of the scaling medium) and s is the solid ($FeCO_3$ grown on carbon steel). ɣ represent the SFE components of the various elements in the SLIPS system and are either known from literature or calculated previously from the contact angle measurements. This includes LW, + and – or Lifshitz van der Waals, Acid and Base parameters. The R value is a measured roughness value taken from surface analysis on the NPFLEX machine. The results for each criterion given are pass or fail.

$$\textbf{Criterion (I)}: S_{ld} = \gamma_d^{LW} + 2\sqrt{\gamma_d^+\gamma_d^-} - \gamma_l^{LW} - 2\sqrt{\gamma_l^+\gamma_l^-} - \gamma_d^{LW} - \gamma_l^{LW} + 2\sqrt{\gamma_d^{LW}\gamma_l^{LW}} - 2\sqrt{\gamma_d^+\gamma_d^-} - 2\sqrt{\gamma_l^+\gamma_l^-} + 2\sqrt{\gamma_d^+\gamma_l^-} + 2\sqrt{\gamma_l^+\gamma_d^-} < 0$$

$$\textbf{Criterion (II)}: S_{dl} = \gamma_l^{LW} + 2\sqrt{\gamma_l^+\gamma_l^-} - \gamma_d^{LW} - 2\sqrt{\gamma_d^+\gamma_d^-} - \gamma_d^{LW} - \gamma_l^{LW} + 2\sqrt{\gamma_d^{LW}\gamma_l^{LW}} - 2\sqrt{\gamma_d^+\gamma_d^-} - 2\sqrt{\gamma_l^+\gamma_l^-} + 2\sqrt{\gamma_d^+\gamma_l^-} + 2\sqrt{\gamma_l^+\gamma_d^-} < 0$$

$$\textbf{Criterion (III)}: S_{ls} + \gamma_l R = \gamma_s^{LW} + 2\sqrt{\gamma_s^+\gamma_s^-} - \gamma_l^{LW} - \gamma_s^{LW} + 2\sqrt{\gamma_l^{lw} - \gamma_s^{lw}} - 2\sqrt{\gamma_l^+\gamma_l^-} - 2\sqrt{\gamma_s^+\gamma_s^-} + 2\sqrt{\gamma_l^+\gamma_s^-} + 2\sqrt{\gamma_s^+\gamma_l^-} + (R-1)\left(\gamma_l^{LW} + 2\sqrt{\gamma_l^+\gamma_l^-}\right) > 0$$

$$\textbf{Criterion (IV)}: S_{ls(d)} + \gamma_{dl} R = \gamma_d^{LW} + \gamma_s^{LW} - 2\sqrt{\gamma_d^{LW}\gamma_s^{LW}} + 2\sqrt{\gamma_d^+\gamma_d^-} + 2\sqrt{\gamma_s^+\gamma_s^-} - 2\sqrt{\gamma_d^+\gamma_s^-} - 2\sqrt{\gamma_s^+\gamma_d^-} - \gamma_l^{LW} - \gamma_s^{LW} + 2\sqrt{\gamma_l^{lw}\gamma_s^{lw}} - 2\sqrt{\gamma_l^+\gamma_l^-} - 2\sqrt{\gamma_s^+\gamma_s^-} + 2\sqrt{\gamma_l^+\gamma_s^-} + 2\sqrt{\gamma_s^+\gamma_l^-} + (R-1)\left(\gamma_d^{LW} + \gamma_l^{LW} - 2\sqrt{\gamma_d^{LW}\gamma_l^{LW}} + 2\sqrt{\gamma_d^+\gamma_d^-} + 2\sqrt{\gamma_l^+\gamma_l^-} - 2\sqrt{\gamma_d^+\gamma_l^-} - 2\sqrt{\gamma_l^+\gamma_d^-}\right) > 0$$

$$\textbf{Criterion (V)}: \gamma_{dl} = \gamma_d^{LW} + \gamma_l^{LW} - 2\sqrt{\gamma_d^{LW}\gamma_l^{LW}} + 2\sqrt{\gamma_d^+\gamma_d^-} + 2\sqrt{\gamma_l^+\gamma_l^-} - 2\sqrt{\gamma_d^+\gamma_l^-} - 2\sqrt{\gamma_l^+\gamma_d^-} > 0$$

D-Spacing and Calcium molar fraction

The equation used to determine the molar fractions of Ca and Fe within the $Fe_xCa_yCO_3$ corrosion products is based on the interplanar spacing for a hexagonal Bravais lattice (shown in Equation 21). Where h, k and l are the Miller indices and a and c are the unit cell parameters. The original equation was modified when Davidson et al [256] developed a set of linear correlations expressing unit cell volume and unit cell parameters as a function of molar fraction (y), from experiments synthesising $Fe_xCa_yCO_3$. This new equation (Equation 22) uses the [104] d- spacing as it gives the most intense Bragg peak for both $CaCO_3$ and $FeCO_3$ and is used in the calculations for this research. Full derivations of this process and its validation can be found in the literature [257-259].

$$\frac{1}{d^2} = \frac{4}{3}\left(\frac{(h^2 + hk + k^2)}{a^2}\right) + \frac{l^2}{c^2}$$

Equation 21

$$\frac{1}{d^2} = \frac{4}{3}\left(\frac{2.924y + 26.626}{148.214y + 582.680}\right) + \frac{16}{(1.688y + 15.373)^2}$$

Equation 22

The XRD data collected and Equation 23 help link the shift in 2θ with the stoichiometry of the mixed $Fe_xCa_yCO_3$ deposit. The reason this works is that both $CaCO_3$ and $FeCO_3$ are structurally comparable R-3C rhombohedral with similar atomic positions, however they have differing D-spacing ($CaCO_3$ > $FeCO_3$). With the incorporation of the Ca into $FeCO_3$ the d-spacing increases, this is represented in the XRD diffraction patterns as a shift towards lower 2θ values. D-spacing was calculated from the XRD diffraction patterns by using the 2θ value of the [104] peak and substituting into Braggs law (Equation 6), where n is an integer and λ is 1.5406 Å (wavelength of the K α Cu source in the XRD). This value is then used in Equation 5 to solve for y (the Ca mole fraction in the tested $Fe_xCa_yCO_3$).

$$d = \frac{n\lambda}{2\sin\theta}$$

Equation 23

Chapter 6
Building SLIPS

6 Fabrication of a SLIPS System

6.1 Introduction

At a fundamental level a SLIPS system consists of three basic components: a textured surface, a lubricant and a target environment. From this scope, certain parameters are limited due to the intended application and availability of materials. In this case, the design is for a potential anti-fouling pipeline coating and therefore the target environment ($CaCO_3$ scaling) and the substrate (carbon steel) are fixed in nature. The starting point in the design of any SLIPS system is the base surface or substrate. From here a texture is generated from which a lubricant can then be infused and retained. This chapter explores the initial fabrication stages of a SLIPS system. In particular, the development of an iron carbonate SLIPS derived from pipeline carbon steel and its suitability within existing SLIPS design frameworks (Figure 71). This chapter is broken into two main parts covering the fabrication process.

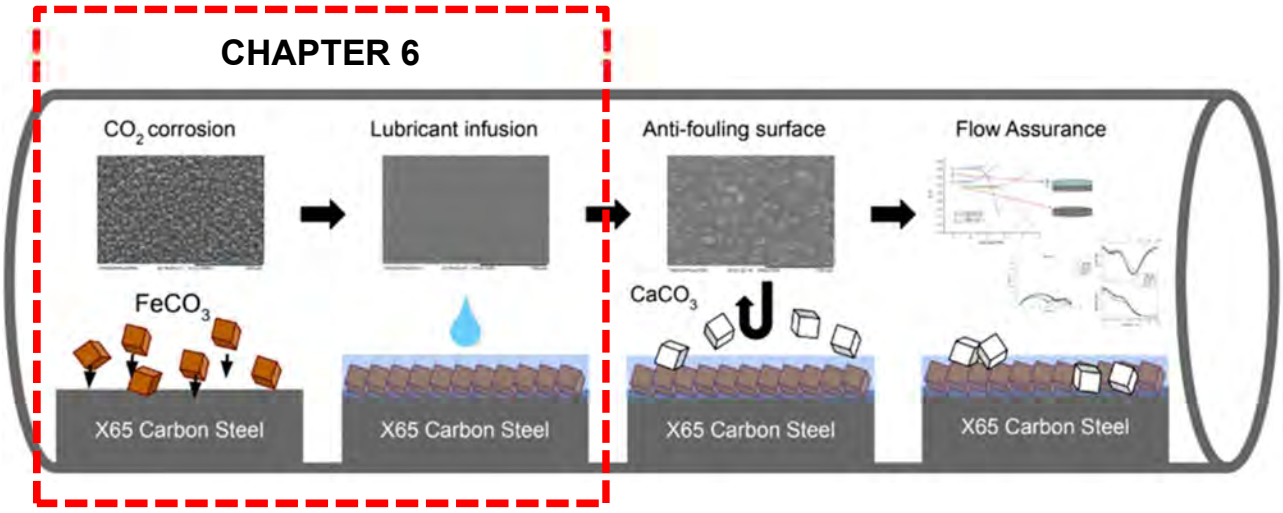

Figure 71 Thesis schematic of the main focus of Chapter 6 results

Part A is a fundamental study into the nature of $FeCO_3$ growth in pipeline systems. Here the formation of iron carbonate layers via the CO_2 corrosion process is observed through a series of static bubble cell experiments. These experiments examine the influence of two distinct environmental conditions (with regards to pH and temperature) and initial surface roughness on the production of $FeCO_3$ layers. Electrochemical techniques have been used to explore film formation, with surface analysis performed through SEM and XRD to determine $FeCO_3$ crystal size, morphology and overall surface coverage to better understand the creation of the SLIPS base layer.

Part B provides further insight into the $FeCO_3$ layer regarding certain properties relevant to SLIPS design criteria. Roughness and Surface free energy (SFE) are characterised in greater detail, with a series of contact angle (CA) experiments providing a basic SFE approximation. This provides a point of comparison for $FeCO_3$ as a functional SLIPS base layer with other systems. The selected lubricants (Krytox vacuum oil, BMIM Ionic liquid and two crude oils) are justified and the lubricant behaviour on the $FeCO_3$ layer examined. Furthermore this section provides an indicator of the theoretical stability of the different $FeCO_3$ and lubricant combinations.

6.2 Fabrication and Growth of SLIPS $FeCO_3$ Base Layer

CO_2 corrosion within carbon steel pipelines is a well-documented phenomena impacting a variety of industries. $FeCO_3$ is a particularly common by-product from this process [59]. The formation of $FeCO_3$ crystals and films can be either protective or non-protective and can have a profound influence on the corrosion rate [80, 81, 117, 259, 260]. The key to protective $FeCO_3$ precipitation resides in the super-saturation ratio. Precipitation kinetics are controlled by several parameters covering environmental, physical and interfacial properties. Temperature and pH are two environmental parameters (discussed in the Literature review section) that have a well-documented influence with $FeCO_3$ formation in laboratory corrosion tests [114, 249, 261]. With high temperatures and pH levels conducive to the formation of protective $FeCO_3$ layer. Surface roughness is a physical property that also impacts $FeCO_3$ precipitation providing crystal nucleation sites. These layers will

provide the platform for the SLIPS base layer aimed at preventing inorganic fouling. Producing a textured layer that also provides corrosion protection allows for the potential resolution of two key flow assurance problem, corrosion and scaling.

The following study seeks to observe the growth of organic $FeCO_3$ layers in two different environmental conditions. The first is an upper boundary condition (high temp, high pH) conducive to the formation of dense, protective $FeCO_3$ layers. The second represents a lower boundary condition (low temp, low pH) or an environment that does not readily facilitate the precipitation of $FeCO_3$ crystals or protective $FeCO_3$ layers. As texture roughness has a direct impact on the effectiveness of a SLIPS base layer, this property has also been varied to provide three levels of initial surface roughness to the samples. Electrochemical techniques have been used to understand the corrosion performance of the $FeCO_3$ layers being produced. Post experiment surface analysis involving SEM and XRD have been employed to understand the characteristics of the $FeCO_3$ layer with regards to crystal size and morphology, with further surface analysis providing insight into the layer composition and crystal surface coverage.

The tests are aimed at confirming prevailing research on the influence of environmental conditions (i.e. Temperature and pH) on $FeCO_3$ layers and their associated corrosive protection. The influence of initial roughness on these $FeCO_3$ layers is also examined due to the texture dependency of SLIPS base layers. This fundamental understanding of growth mechanisms allows the identification of a set of conditions to provide a consistent and repeatable $FeCO_3$ platform for further scaling tests in subsequent chapters. It also provides insight on the types of layers that may be produced from an operational standpoint and opportunities for other corrosion derived SLIPS.

6.3 Experimental Matrix for $FeCO_3$ base layer fabrication

Full experimental methodologies are included in the corresponding chapter; a brief summary is given here. Standard bubble cell experiments were conducted in 1 litre beakers at atmospheric pressure. Prior to sample immersion, solutions were purged with CO_2 for a minimum of 12 hours.

Magnetic stirrers were used throughout the experimental process to ensure solution consistency (set at 200 rpm [122]). Temperature was continuously monitored through a thermocouple integrated with the hotplate.

All carbon steel samples were soldered with insulated copper wire and set in a non-reactive resin. Samples were wet ground on a polisher to final roughness by using the following incremental process of silicon carbide (SiC) abrasive papers: **120**, 320, **600**, 800, **1200.**

For electrochemical techniques a simple 3 electrode set-up was used. Consisting of the carbon steel working electrode, Ag/Ag-Cl reference electrode and platinum counter. The system was connected to an Ivium potentiostat for LPR measurements set at ±15 mV vs. OCP, with a scan rate of 0.25 mV/s and E step of 0.25 mV.

The solution parameters for the UB and LB tests are outlined in Table 9. After tests were finished, samples were removed, rinsed with distilled water, dried and placed in a desiccator. Ex-situ analysis was undertaken post experiment using SEM, XRD and Talysurf techniques to examine $FeCO_3$ crystal and $FeCO_3$ layer characteristics on the top surface [262].

Table 9 Experimental test matrix for Iron carbonate formation at Upper and Lower boundary conditions

CONDITION	UPPER BOUNDARY	LOWER BOUNDARY
Sodium Bicarbonate ($NaHCO_3$), grams	16	6
pH	7.6	6.1
Temperature, ℃	80	50
Final roughness, SiC	120, 600, 1200	120, 600, 1200
Sodium Chloride (NaCL), grams	35	35
Carbon Dioxide (CO_2) partial pressure (bar)	0.54	0.54

Magnetic stirrer (rpm)	150	150
Time (hours)	72	72

6.4 Electrochemical Response of Boundary Conditions

Characterisation of the samples via electrochemical LPR measurement allows for in-situ real time observations of corrosion rate. The tests conducted over 3 days provide an indication of the corrosion behaviour of the carbon steel samples in the two different boundary conditions. Initial comparison of the two conditions is as expected and in line with established literature regarding temperature and pH differentials. In Figure 72a) across the 3 roughness forms in the **Upper Boundary (UB)** conditions of high pH and temperature, corrosion rates decrease over the test duration. CR drops to a level of 0.1 mmPY, considered to be a level associated with dense, compact corrosion product layers. Elevated pH and temperature provide an environment that favours homogeneous nucleation and growth of $FeCO_3$ crystals into protective layers by influencing carbonate formation and the solubility product or K_{sp} respectively. This in turn drives the supersaturation ratio leading to rapid precipitation kinetics. This is seen with the sharp drop-in corrosion rates within the first 15 hours to a level below 0.1 mmPY.

Conversely, Figure 72b) shows the **Lower Boundary (LB)** conditions exhibit higher corrosion rates for extended periods of time. This behaviour is observed across the different roughness levels. Initially corrosion rates peak above 1.6 mmPY before moving to a narrower range in the 1.4-1.6mmPY band over the first 24 hrs. After this time corrosion rates begin to drop, however this occurs at different rates and gradually. Only one sample reaches a corrosion rate below 1 mmPY and this does not occur until 54 hrs. This is expected due to the environmental conditions created by low pH and low temperature. This synergy exacerbates the corrosion process of steel by hindering the formation of protective $FeCO_3$. On average UB samples show a corrosion rate drop of 95% over 72 hrs, compared to a 60% decrease for those in the LB. It is also seen that corrosion rate is separated into 2 distinct steps in UB conditions, with a rapid, initial drop and then an extended plateau of low CR rate offered by the formation of a protective layer. In the LB this two-step

process is not always distinct and differs by having an initial, relatively flat high CR, before a gradual drop occurs. Within the 3 days tests most LB samples do not reach a stabilised rate, as CR continues to drop.

Corrosion rates can also be further examined with respect to the corrosion products that appear via SEM (Figure 73). Top view SEM images show a disparity between $FeCO_3$ surface coverage compared to corrosion rates, which is unusual. Although the presence of $FeCO_3$ crystals on the surface seems connected to lower corrosion rates at UB conditions. Surface coverage values are approximately 55% (120P), 87% (1200P) and 100% (600P). This variation does not seem to have a substantial impact on corrosion rates, with 0.1mmPY levels achieved within the 15 hrs despite the different coverage levels. It is generally expected at corrosion rates of 1 mmPY, a dense, thick

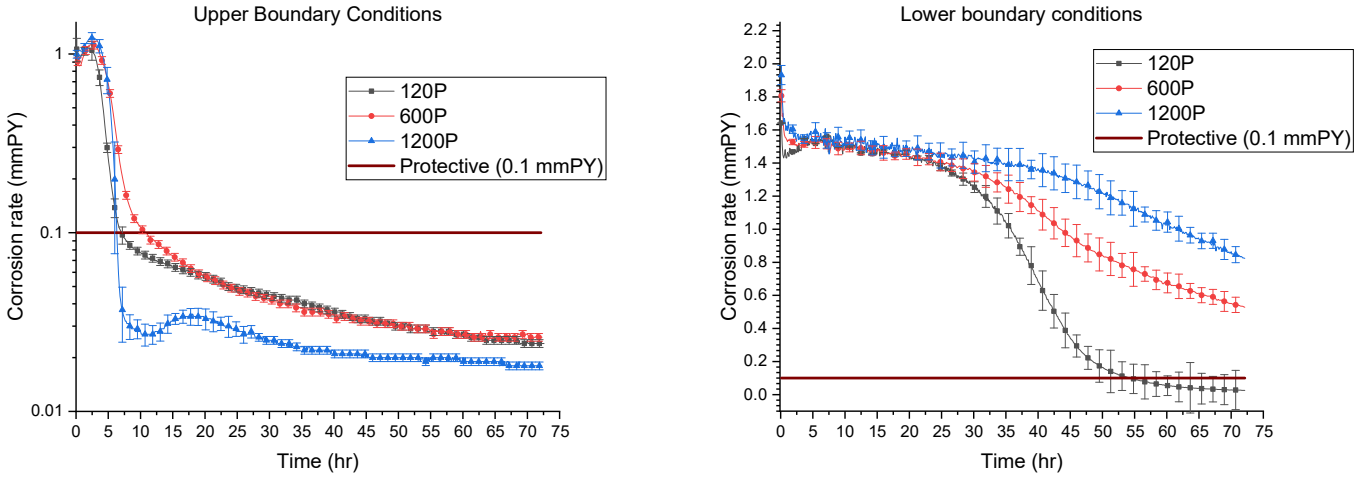

Figure 72 Corrosion rate vs Time for 72 hr test across varying roughness levels. a) Upper Boundary b) Lower Boundary

$FeCO_3$ has formed but this is not the case. 120P shows the lowest level of $FeCO_3$ crystal coverage (Figure 73d)), with concentration connected to grooves associated with the 120P grade surface finish. It is also noted that where corrosion products do not appear to be present, the surface is not particularly degraded. The UB conditions favour the creation of corrosion products with minor damage to the existing surface, as a rapidly declining CR suggest.

OCP values are in line with CR behaviour showing a sharp change with the rapidly decreasing CR before flattening out in a low range that fluctuates ±10mV. This behaviour is almost identical to the results shown in the 600P tests; however the samples are completely covered by an $FeCO_3$ film (Figure 73e)). The 1200P tests exhibit a similar response with CR although it is noted a sharp spike in OCP before settling. The sharp increases in OCP, along with rapid CR drops suggest some form of minor passivation. The range is small at ≈50 mV and is expected at elevated pH levels. Passivation protection is reinforced by SEM depicting incomplete $FeCO_3$ films with exposed steel that still result in low CR. Once the 0.1mmPY CR threshold has passed, the rate of decrease slows and the OCP stabilises or increases slightly for the remaining duration of the experiment. UB conditions clearly favour the creation of $FeCO_3$ crystals but whether they form complete layers is not necessarily the case. The impact of varying roughness is inconclusive in the impact on corrosion rates. SEM images do highlight the fact they offer nucleation sites for $FeCO_3$ crystals. These are particularly apparent in the 120P samples were the striations produced from polishing provide parallel lines of increased $FeCO_3$ crystal concentrations. These deeper grooves provide localised conditions that favour growth as well as nucleation compared to the surrounding surface.

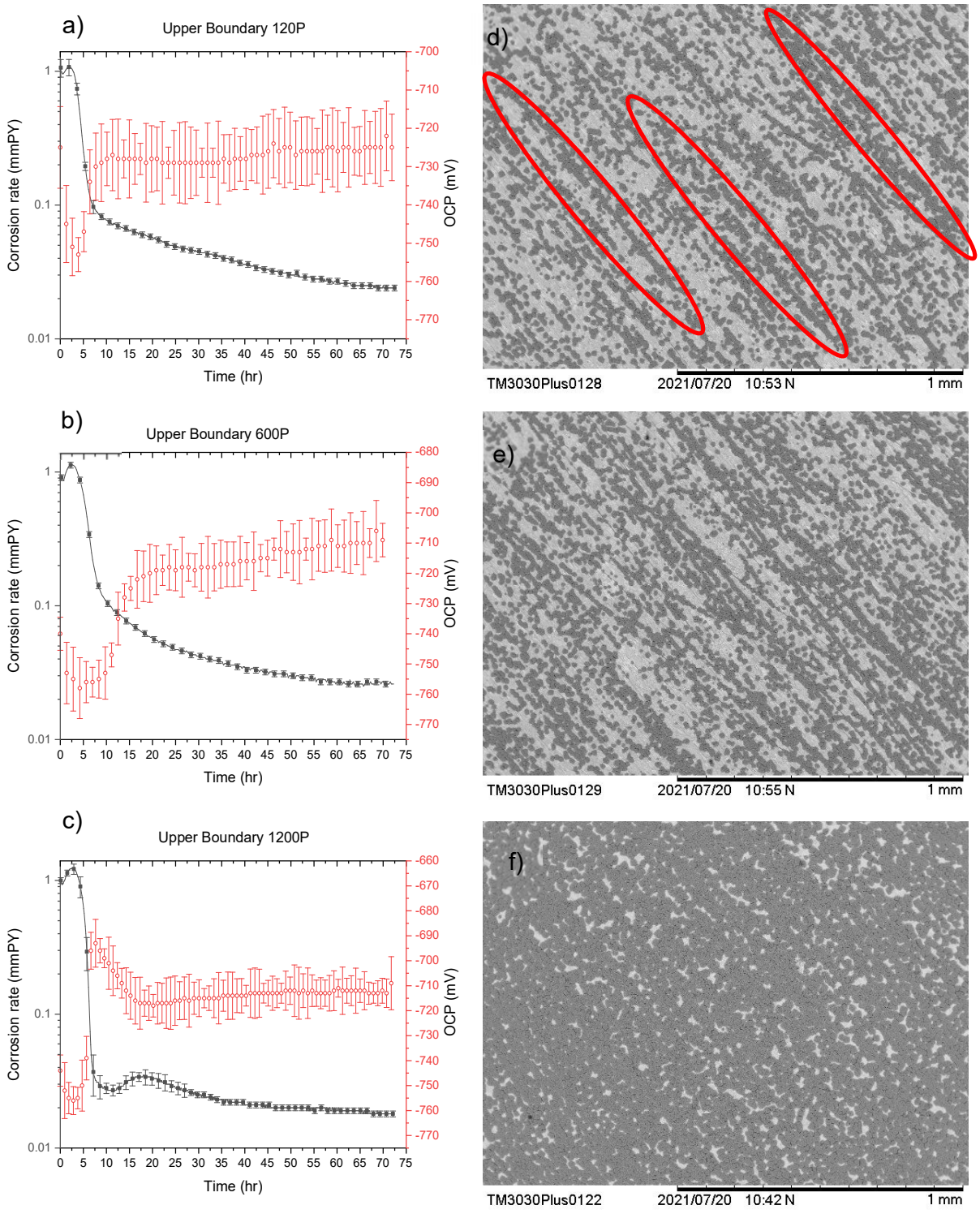

Figure 73 Corrosion rate and OCP vs time over 72 hr test in UB conditions. Roughness: a) 120P, b) 600P, c) 1200P. SEM image of surface $FeCO_3$ coverage. Roughness: d) 120P, e) 600P, f) 1200P

LB conditions produce rates of corrosion that are higher and continue for prolonged periods compared to UB samples (Figure 74). As a result substantial material damage to the surface is noted on all samples after the 3-day test duration. Although mass loss tests were not undertaken, material loss is evident with numerous pits and crevices across the surface. Both the 600P and 1200P samples show a slight two step CR, which is not clearly defined as the UB samples. Initially there is a very gradual decrease followed by a secondary, faster rate over the course of the experiment, with no clear plateau or stabilisation. OCP is reflected with no well-defined rate steps and a near constant, gradual increase over time. The rougher surface finish on the 120P samples provides a more unusual response (Figure 74a)). Although CR and OCP follows a similar early trend for the first 25 hours, there is a significant rate change as CR decreases rapidly and OCP rises. Unlike the other samples, the corrosion rate falls to a level of 0.1 mmPY (after 55 hrs) without visible indication of any $FeCO_3$ layer. Even with a final CR in this range, the damage to the steel surface is severe due to the extended exposure at elevated corrosion rates.

The corrosion products that appear are predominantly an iron carbide (Fe_3C) network/nest, although $FeCO_3$ is also apparent within this structure. In both the 600P and 1200P samples $FeCO_3$ coverage appears to be integrated within the lattice itself (Figure 74 e, f)). $FeCO_3$ coverage in these samples is roughly 29% and 34% for the 600P and 1200P respectively. Although significant voids between the $FeCO_3$ and Fe_3C network exist and due to this the corrosion film is non protective, as evidenced in the higher CR observed. As the CR has not fully stabilised, it may have the potential to form a protective layer with a longer timeframe as the $FeCO_3$ reduces the porosity within the film. It is interesting to note that in both the UB and LB conditions the 120P samples reach corrosion rates of <0.1 mmPY with incomplete films from the low magnification SEM's. However it may be the case that there exists a thin film of nano-crystalline $FeCO_3$/ Fe_3O_4 that offers some protection, which will be examined in the next section. The 120P LB surface has patches where the steel has not undergone major transformation (Figure 74d), these areas are relatively

untouched similar to those that appear in the 120P UB samples, highlighting the possibility of some form of protective film.

Reproducibility of corrosion rates in UB samples that reached a level of protection associated with 0.1 mmPY was consistent across all samples. Initial and final CR were similar, with the presence of a two-rate corrosion process made up of an early, rapid drop in CR followed by a prolonged, stabilised rate. LB results produced varying corrosion rates with some samples showing a one-step gradual corrosion reduction or limited two stage corrosion behaviour. Again similar CR results are obtained in a narrow range for the initial 24hr period, before rates diverge. The variation is likely a result of the heterogenous roughness created by a rapid transformation of the surface under elevated corrosion levels.

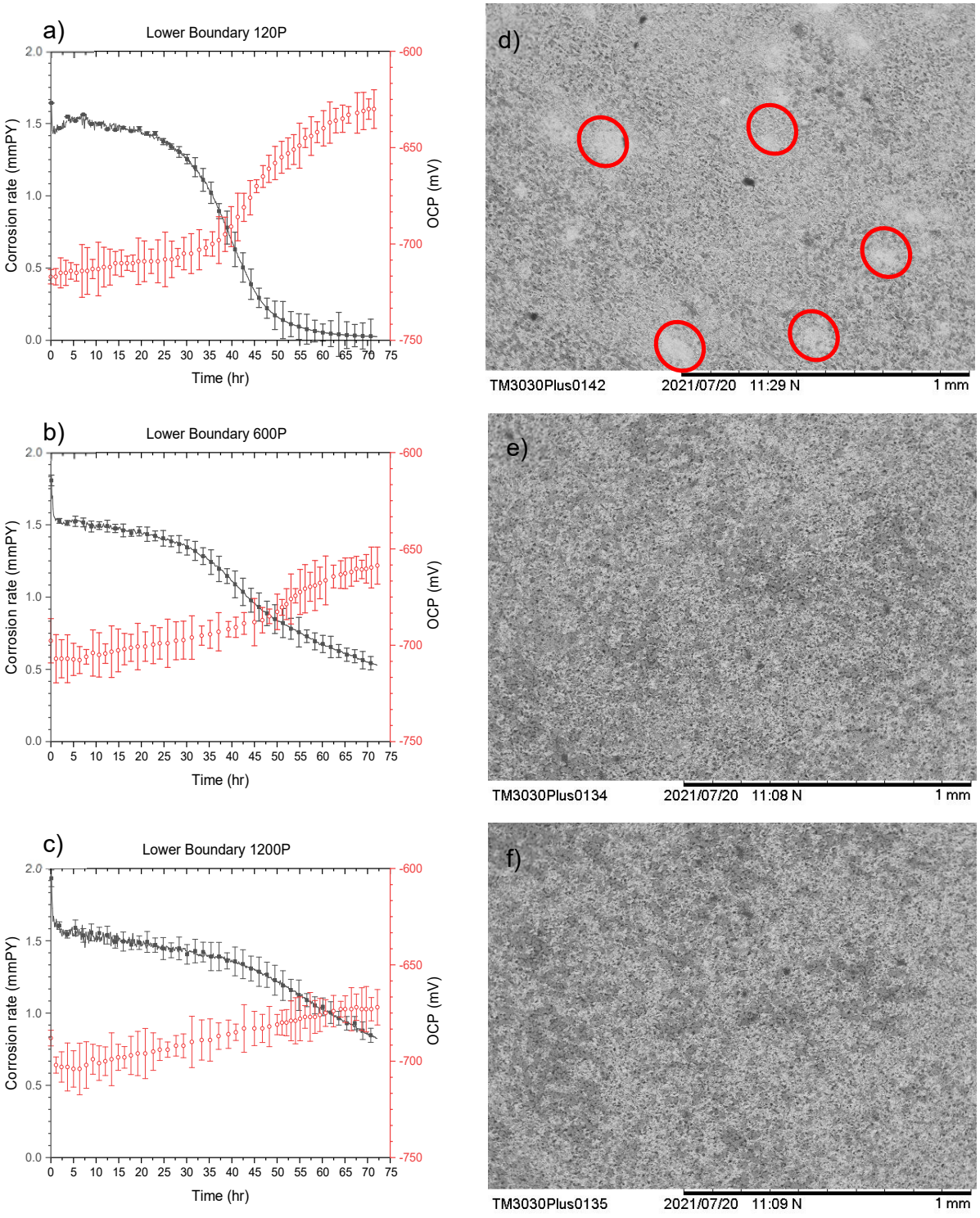

Figure 74 Corrosion rate and OCP vs time over 72 hr test in LB conditions. Roughness: a) 120P, b) 600P, c) 1200P. SEM image of surface $FeCO_3$ coverage. Roughness: d) 120P (Circles: Uncorroded patches of CS), e) 600P, f) 1200P

(1) Crystal composition and morphology

Crystal morphology, composition and size can be further verified with the use of XRD and higher magnification SEM. The mineral by-products from the sweet (CO_2) corrosion of carbon steel are well documented and appear in various forms here. XRD tests are run across the range of 10-70° 2theta, which covers the primary corrosion relevant peaks. For reference a non-corroded sample of the same carbon steel used has been tested in Figure 75. The surface shows no appearance of crystals with the primary Fe peaks of the (110) and (200) planes at roughly 45° and 65°, respectively. The main corrosion products that have been identified in the samples are combinations of iron oxides (either Fe_2O_3/hematite or Fe_3O_4/magnetite), iron carbonate ($FeCO_3$, siderite) and iron carbide (Fe_3C).

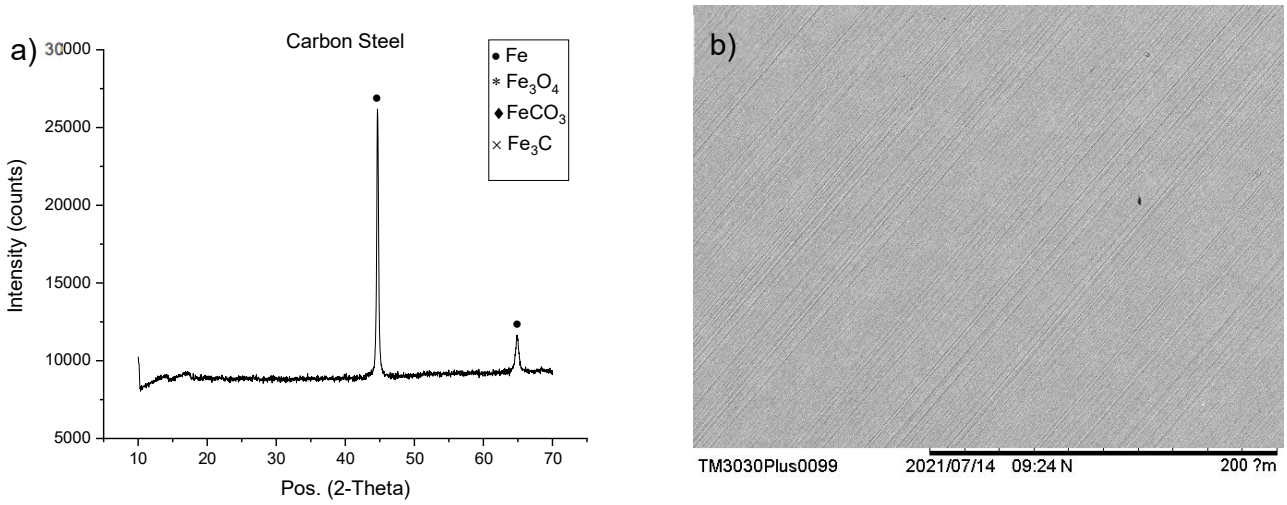

Figure 75 XRD pattern showing primary Fe peaks (a) and SEM (b) of carbon steel surface

Throughout the LB tests, conducted at lower pH (≈6) and temperature (50℃) the formation of protective corrosion products is unfavourable (Figure 76). SEM shows visible deterioration of the surface metal with widespread pitting and voids. XRD confirms that the primary response is Fe peaks, representative of the underlying carbon steel (Figure 76d) and is consistent across the three surface grades. In the smoother samples (600P and 1200P) there are moderate signals for $FeCO_3$ across several peaks (012, 110, 113,

116), although the dominant (104) plane at ≈32° remains weak (Figure 76 b,c)). The presence of $FeCO_3$ can be seen visually on SEM as the darker crystals found within the surface network. Crystal structure appears to be elongated, rhombohedral crystals, up to 20μm in length. The dominant length crystal face is curved in nature and well formed (smooth) (Figure 76e)). The corrosion process has also left a cementite skeleton particularly around grain boundaries (Figure 21). This can be seen on the right side area of Figure 76e) and extends to the whole area seen in Figure 76d. Iron carbide appears on the XRD pattern, albeit as a weaker signal and often masked by those of Fe or $FeCO_3$ in the 40-50° 2theta range. There also appears to be other forms of non-protective, amorphous iron oxide scales either micaceous sheets with cracks or lamellar/platy crystal nests evident on some samples (Figure 76f)) [263, 264]. Unusually in the 120P there are patches of the surface that have not corroded like the surrounding area. There is no visible protective film or corrosion product (at a microscopic level visible on SEM) on the surface and the electrochemical response suggests CR has stabilised at a low level.

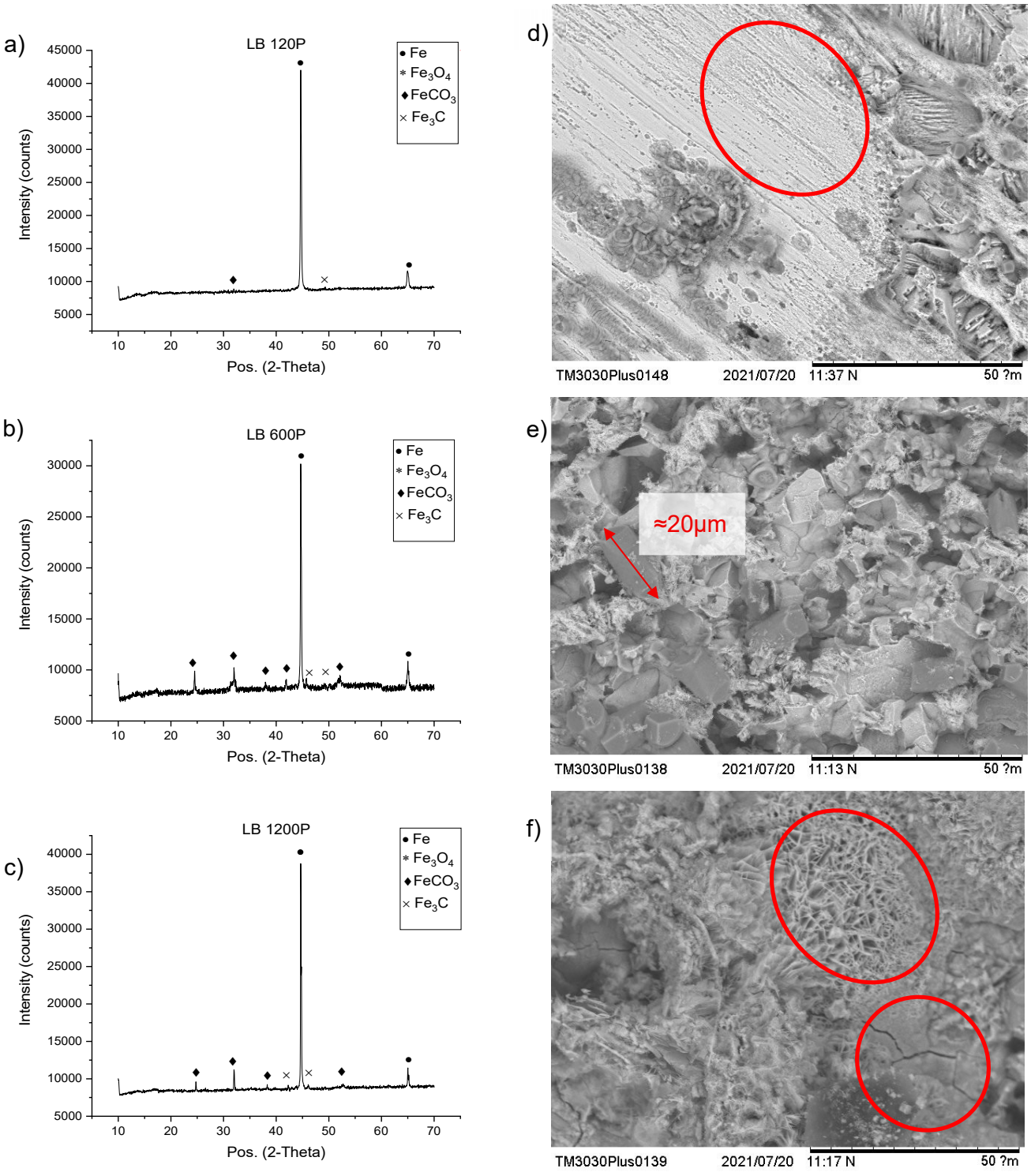

Figure 76 XRD pattern of sample in LB conditions. Roughness: a) 120P, b) 600P, c) 1200P

SEM image of surface. Roughness: d) 120P (Circled: CS surface), e) 600P, f) 1200P (Circled: Iron Oxide scales).

The higher pH and temperature found in the UB conditions allow an environment more conducive for the formation and growth of $FeCO_3$ crystals. This is seen across all samples and is the dominant corrosion product found both on XRD and SEM (Figure 77). $FeCO_3$ appears in XRD across a number of peak intensities as stated previously, the main peak being the (104) plane at 32°. The intensity is similar in nature to that of the Fe (110) peak at 45° and tends to increase with surface coverage on the SEM. Overall the intensity across all $FeCO_3$ peaks is stronger compared to those encountered in LB tests. The $FeCO_3$ crystal morphology is also very different. In the UB conditions crystals are of a more cubic/rhombohedral shape with equal planar faces compared to pellet-like hexagonal structures with a curved dominant plane in LB tests (Figure 77 d,e,f)). Again size and morphology does not appear to be substantially impacted by the level of initial roughness. Crystal size varies across the surface with smaller platy crystals (<3μm) ranging up to larger rhombohedral of 20 μm. In both conditions the largest crystals observable are roughly 20μm, suggesting an upper limit to individual $FeCO_3$ crystal size.

Nucleation sites for $FeCO_3$ in the LB tests appear random but occur generally in valleys/voids across the corroded topography of the surface. This is similar to the deposition on UB samples, where those samples with incomplete surface coverage have $FeCO_3$ crystals that are concentrated along straight vectors. These grooves are generally parallel and a result of the surface finishing technique/ SiC grit paper (Figure 73d). Both the pits and valleys provide nucleation areas, that both increase the metal surface area open to reaction and act as physical feature or anchor point for $FeCO_3$ crystals to agglomerate. The rapid drop and generally low CR measurements encountered in the UB tests suggest that a protective film has been formed. XRD shows strong intensities for Fe peaks and the SEM depicts a layer of larger $FeCO_3$ crystals that do not fully cover the surface. The likely cause of the reduced CR is the formation of a fine $FeCO_3$ bilayer, that appears as an amorphous nano-crystalline film between and possibly under the larger $FeCO_3$ crystals (Figure 77d-f)). Visibility of this underlying area decreases with increasing surface deposition of larger $FeCO_3$ crystals. This fine layer is noted

in literature as being the primary protection mechanism resulting in lower corrosion rates [265-268]. In the UB 1200p sample this fine layer can be seen surrounding/growing on the outer layer of individual $FeCO_3$ crystal faces. There are other corrosion products that can appear in these conditions including Chukanovite ($Fe_2(OH)_2CO_3$) and Magnetite (Fe_3O_4) [120] [73]. With the elevated pH levels (>7.5), Fe_3O_4 is a high possibility however the temperatures tested (80℃) are at the lower end of previously known conditions (i.e. 100℃). Fe_3O_4 is known to form passive nano-films, between the iron carbonate and metal interface that offers good protective properties [269]. XRD shows trace intensities for Fe_3O_4 around 30° and 35° 2theta. The electrochemical response shows indications of passive type behaviour with sharp drops in CR accompanied with increasing OCP; however the magnitude is not sufficient to suggest major passivation as the protective mechanism [58, 270, 271].

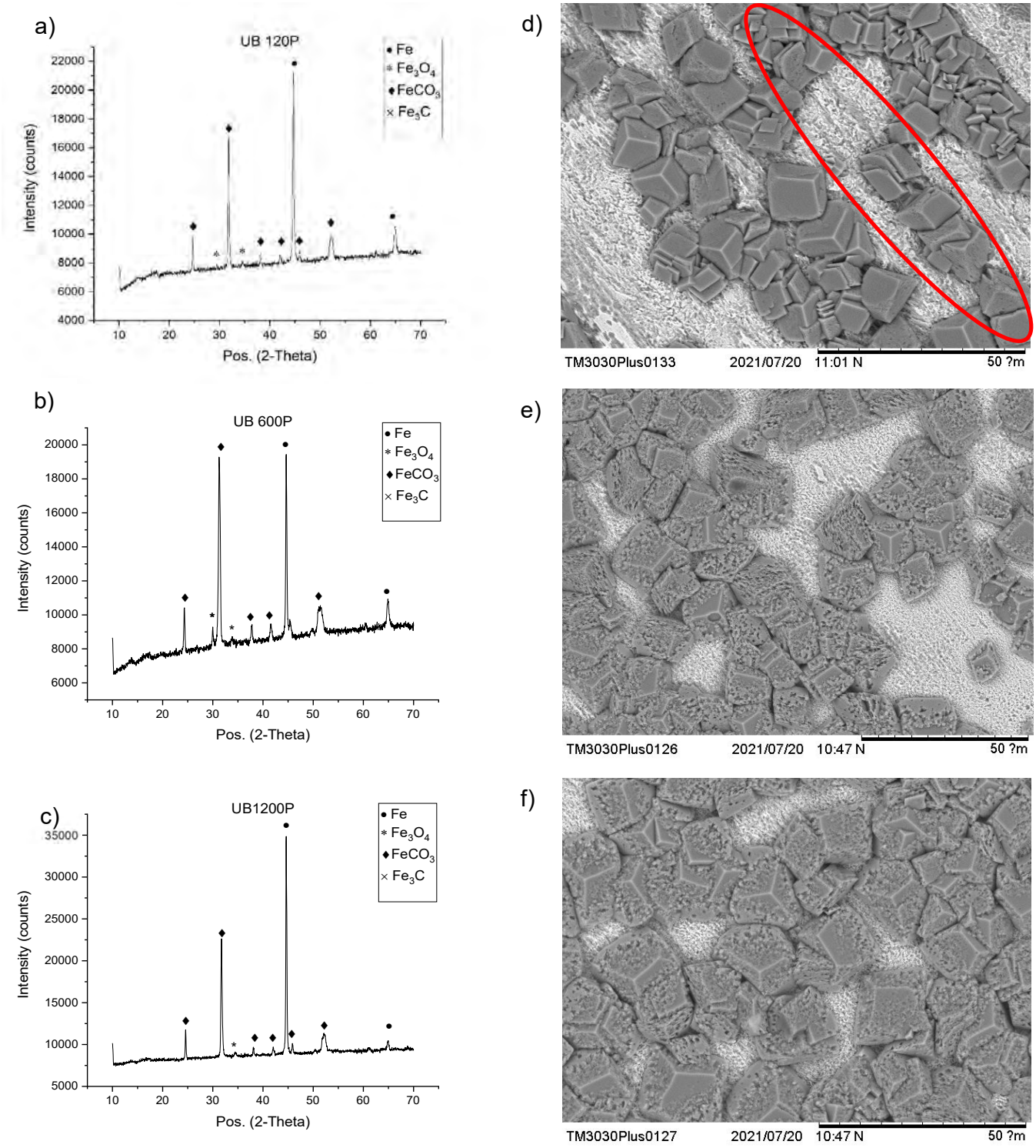

Figure 77 XRD pattern of sample in UB conditions. Roughness: a) 120P, b) 600P, c) 1200P SEM image of surface. Roughness: d) 120P (Circled: roughness vectors from polishing) , e) 600P, f) 1200P.

6.5 Influence of roughness

Roughness plays an integral role in the functionality of a SLIPS surface by providing the texture within which the lubricant resides. Two common means (Figure 78) of assessing surface roughness are arithmetic average (R_a) and skewness (R_{sk}). R_a provides the profile changes from the mean line (in μm), while R_{sk} is the difference of the profile from symmetry (dimensionless). A Talysurf profilometer was used to collect one dimensional data along 20mm line scans. These parameters provide an idea of the surface topography, allow for comparison between tests and with existing SLIPS substrate roughness.

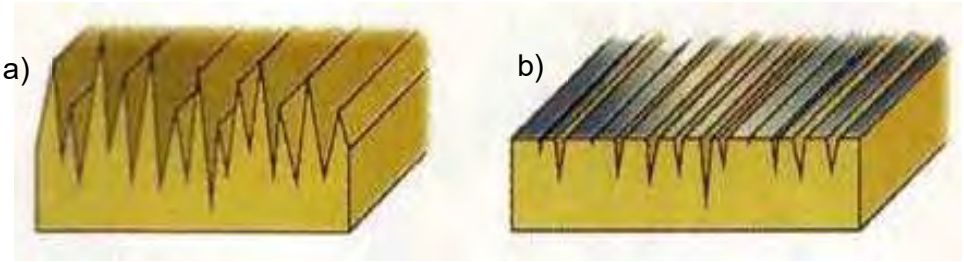

Figure 78 Example surface profiles demonstrating positive skewness (a) vs negative skewness (b)

A set of blank (uncorroded) samples were tested, to gauge the initial surface finish of the 3 roughness samples tested (Figure 79). The finishing grade of silicon carbide polishing paper for the 3 samples were 120P (roughest), 600P and 1200P (smoothest). As is expected the trend of R_a decreases with continued polishing and higher-grade grit paper. The drop is quite substantial between the initial 120P finish to the 600P; however this is expected as the step involves the use of 320P in between. SEM visuals show successive deep grooves with jagged edges and surface defects. The purpose of 120P is generally to remove surface build-ups (i.e deposits/rust) and is generally not deployed as a finishing surface grade. The coarser grains are focused on stripping as much material from the surface, hence the unevenness and jagged nature of the striations, as the larger grit bites/ tears the surface (Figure 79a). With consecutive grinding and higher-grade paper the surface eventually smoothens as is apparent in the R_a trend. Skewness for all samples is negative with surface finish being strongly anisotropic (Figure 80). This is

consistent with profiles that have undergone machining/polishing and hint towards a surface made up primarily of valleys. Skewness of the 120P samples is lowest, given the sample has only undergone rudimentary polishing.

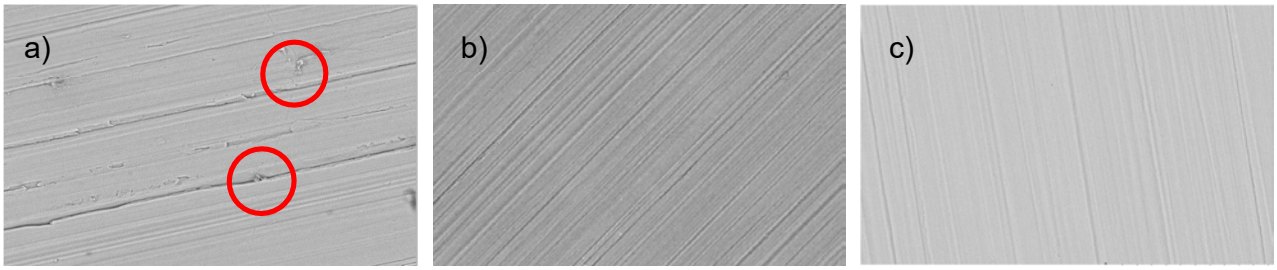

Figure 79 SEM image of initial surface finish from roughness a) 120P, b) 600P, c) 1200P. Red circles showing surface defects from polishing effect

After the corrosion process, the two conditions (UB and LB) display different roughness topographies (Figure 80). Prevailing literature suggests roughness has a strong influence on general corrosion and pit nucleation, with the trend associating lower order roughness with corrosion resistance [272-275]. The mechanism behind this is the increase in surface area exposed to the electrolyte and subsequent increase in corrosion potential. This impact is counterintuitive to the influence of roughness on the formation of $FeCO_3$ crystals. This process favours rough profiles with a high density of asperities due to classical nucleation theory that these points act as nucleation sites. In the LB conditions tested, where general corrosion is higher and $FeCO_3$ coverage low, the R_a follows the same trends as the blank samples. R_a decreases from 1.1 to 0.4 with increasing polish grade, however the values themselves are substantially higher. This occurs due to the creation of pits and the deposition of corrosion products which distorts the profile. The skewness profile shows an increase in negative skewness, suggesting a trend to deeper valleys compared to the initial finish. This is in good agreement with the higher CR experienced, which suggest the growth of these existing valleys/pits and a lack of surface deposits seen on the SEM.

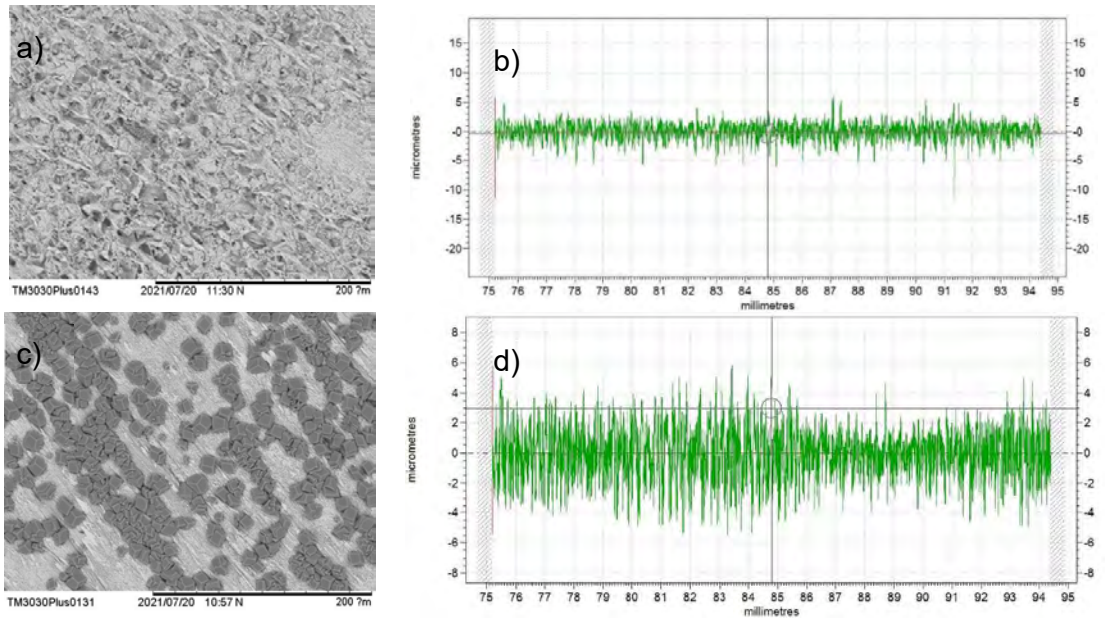

Figure 80 Comparison of UB (a,b) and LB (c,d) 120P corrosion surface profile. (a) and (c) show SEM images from the surface showing differing corrosion features. (b) and (d) show line scans using stylus profilometry measuring arithmetic roughness (R_a) in micrometres.

UB conditions produce roughness results that follow a distinctively different trend. Across the samples it is expected that R_a will increase compared to blank samples due to the corrosion process. However the mechanism that produces the additional roughness is different (Figure 81). Whereas in the LB condition material loss was the primary driver of increased topography, the UB condition results from the deposition/nucleation of $FeCO_3$ crystals. UB conditions produce a surface profile with the highest values of R_a and with no clear trend as roughness changes. Increasing polishing grit size does not lead to significantly different post-test roughness, with values within 5% of each other. This might suggest in these conditions an upper limit to the roughness that can be attained, regardless of initial surface finish. Skewness values also occur at a higher threshold than both LB and blank samples (Figure 82). This suggests that the profile returns to a more neutral or symmetrical surface shape from its original state. SEM images show that this is a result of $FeCO_3$ crystal nucleation behaviour that favours depressions in the surface as initial concentration areas (Figure 69, 73, 76). These sites dominate the early nucleation and growth of $FeCO_3$ in the UB conditions, thus reducing the

severity of the valleys/pits and increasing the skewness to a more balanced profile.

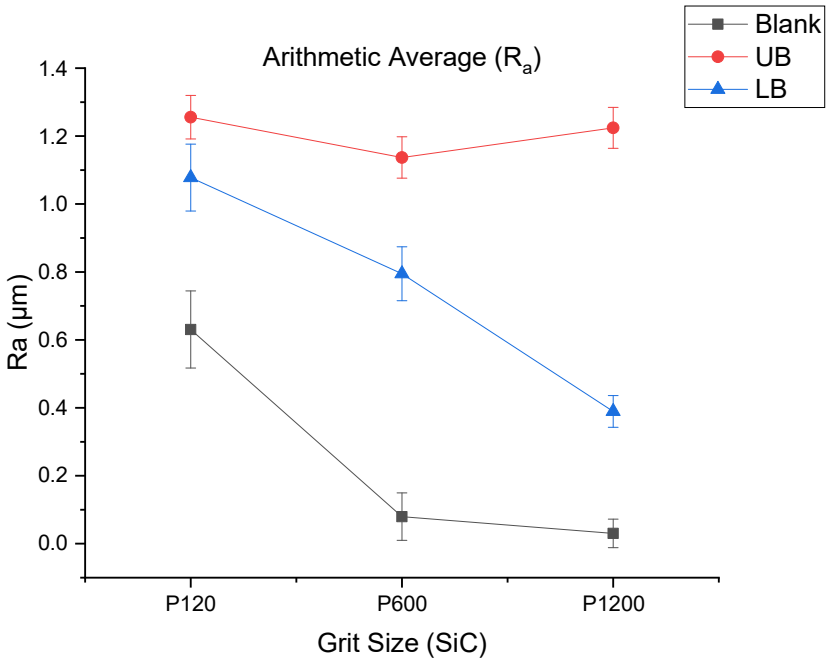

Figure 81 Roughness vs grit Size over UB and LB conditions

The UB conditions show that the roughness attributed to $FeCO_3$ deposition is higher than those created from the corrosion process associated with material loss. In comparison with roughness values tested in wider SLIPS literature, R_a values in the UB samples of around 1.2 µm are within values used by successfully tested alternatives. Indeed R_a values for SLIPS include a Polypyrrole substrate tested in similar brine conditions at 0.672 µm [243]. Other metallic SLIPS substrates have made use of Copper oxide derived textures at 0.1277 µm and even 0.03 µm Boehmite crystal layers on aluminium have been tested [276]. At the other end of the spectrum, Iron tetradeconoate textures have been tested with roughness height differences up to 70 µm [277]. The trend of samples towards negative skewness is a trait favoured in tribological surfaces for potential lubrication applications. Given the SLIPS surface will also maintain a lubricant, this is also seen as beneficial to the $FeCO_3$ intended function as a reservoir. Furthermore, positive

skewness would increase the possibility of local asperities projecting above the lubricant layer, potentially providing nucleation sites in future scaling tests and lower mechanical strength of the $FeCO_3$ peaks.

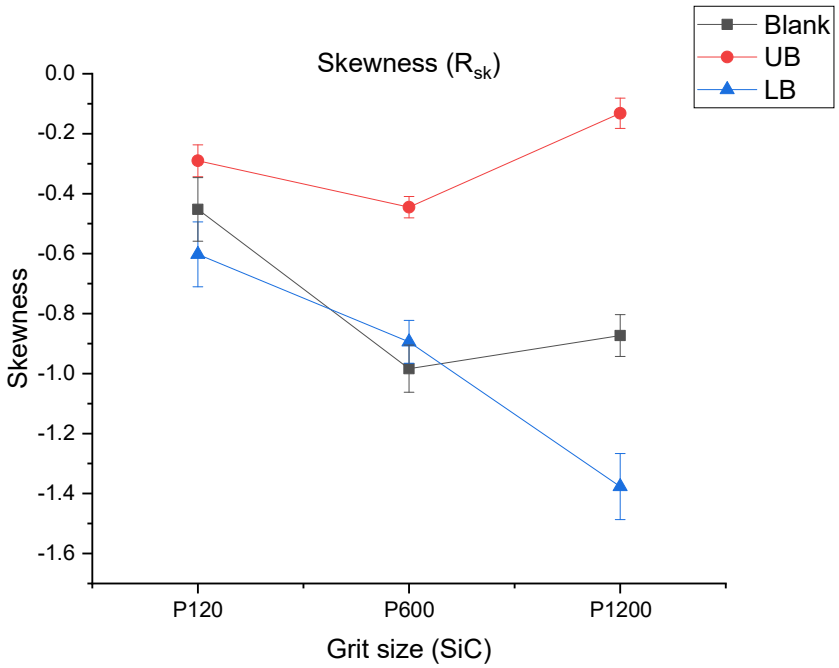

Figure 82 Skewness vs grit Size over UB and LB conditions

6.6 Summary

- Initial tests have reinforced existing trends in literature of the synergistic benefits of both higher temperature (80℃) and higher pH (7.6) in the formation of $FeCO_3$ crystals. In the conditions where $FeCO_3$ forms in abundance this often provides a protective film that reduces corrosion rates. This manifests in the corrosion rate visually via a two-stage process, an initial rapid drop in CR (with an associated OCP increase) and then a gradual/stabilising CR once protected. LB conditions have also shown the presence of quantities of $FeCO_3$ but this comes with corrosion damage due to extended periods of higher CR.
- Corrosion products generated under these conditions are predominately $FeCO_3$ verified on XRD (strongest signal at the 32° peak) and SEM (as darker contrast crystals). However there are stark differences in the type of $FeCO_3$ crystal growing in each condition. In the UB conditions there exists two types of $FeCO_3$, one of an

amorphous nano-crystalline form and also larger fully formed cubic crystals between 5-20 µm in size. The $FeCO_3$ crystals in the LB conditions tend to be a more elongated, rhombohedral morphology. XRD and SEM also highlight the presence of other corrosion products such as Fe_3O_4 and Fe_3C.

- The tests have not produced clear trends on the influence of initial roughness or surface finish on the corrosion rate of carbon steel in either condition. It has been noted that for UB conditions where $FeCO_3$ nucleation and growth is favoured, this occurs principally around grooves/valleys generated from the polishing process. Arithmetic roughness measurements show that $FeCO_3$ films form a higher order of R_a compared to initial surface finish and surfaces that have undergone material loss due to corrosion (i.e. LB conditions). Skewness values for all samples are also of a negative value, suggesting the prevalence of topographical valleys compared to peaks.
- The initial fundamental study puts a viable case for the potential use of $FeCO_3$ films as a SLIPS substrate. Firstly when formed under UB conditions, the layer formed is corrosion resistant (i.e. CR <0.1mmPY) and protective. These UB conditions, particularly at 600P, provide a steel sample with good surface coverage of $FeCO_3$ crystals for further testing. The roughness (R_a) values obtained are in line with those seen in other SLIPS tested previously and the negative skewness is a beneficial property of surfaces intended for lubrication purposes.

6.7 The $FeCO_3$ SLIPS System

Introduction

This chapter focuses on the integration of the $FeCO_3$ base layer into the SLIPS system as a whole (Figure 83). Examining the impact of different environmental conditions on $FeCO_3$ formation has provided fundamental information on how these layers form. This provides context to the operational conditions for future applications and a level of control that can be used to tailor the surface. From the previous section a set of conditions has been selected which produce the most reliable and consistent $FeCO_3$ film from

which further testing can be carried out. Indeed two separate $FeCO_3$ morphologies were observed in Upper boundary conditions. The intention is to focus on an outer $FeCO_3$ layer made up of the larger cubic crystals, as opposed to the fine bilayer that may exist beneath. These larger deposits are necessary to produce the roughness and porosity sufficient to hold the lubricant component of the SLIPS system.

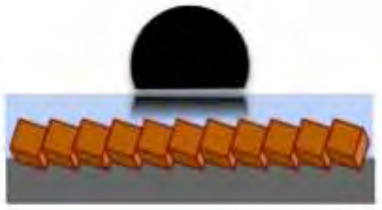

Figure 83 Schematic of SLIPS configuration. Impinging droplet (d), Lubricant (l) and solid (s)

The $FeCO_3$ layer fabricated has undergone further surface characterisation to better understand its compatibility with the lubricant component. Further topographical analysis has been undertaken along with contact angle experiments to provide an indication of the surface energy of this layer. This is an important step in incorporating the lubricant and base layer, as both roughness (Equation (1)) and surface energy (Equation (2)) are co-dependent parameters and directly related to SLIPS theoretical design. This design provides a predictive capability of the stability of the SLIPS structure.

$$\boldsymbol{Geometric\ Factor}\ (R) = 1 + \frac{S_{dr}}{100} \quad (1)$$

$$\boldsymbol{Wenzel\ Model}: \cos\emptyset_M = R\cos\emptyset_A \quad (2)$$

Prestons' model [232] provides a theoretical forecast for SLIPS combinations via five criteria and can be matched experimentally (Figure 84). These criteria represent a set of equations based on surface energy obtained from the vOCG method and geometric factors (or surface roughness). In simple terms the criteria are summarised as:

I. Lubricant cloaks droplet in thin film

$$\boldsymbol{Criterion}\ (\boldsymbol{I}): S_{ld} = \gamma_d^{LW} + 2\sqrt{\gamma_d^+\gamma_d^-} - \gamma_l^{LW} - 2\sqrt{\gamma_l^+\gamma_l^-} - \gamma_d^{LW} - \gamma_l^{LW} + 2\sqrt{\gamma_d^{LW}\gamma_l^{LW}} - 2\sqrt{\gamma_d^+\gamma_d^-} - 2\sqrt{\gamma_l^+\gamma_l^-} + 2\sqrt{\gamma_d^+\gamma_l^-} + 2\sqrt{\gamma_l^+\gamma_d^-} < 0\ \#(3)$$

II. Droplet fully wets lubricated surface

$$\boldsymbol{Criterion}\ (\boldsymbol{II}): S_{dl} = \gamma_l^{LW} + 2\sqrt{\gamma_l^+\gamma_l^-} - \gamma_d^{LW} - 2\sqrt{\gamma_d^+\gamma_d^-} - \gamma_d^{LW} - \gamma_l^{LW} + 2\sqrt{\gamma_d^{LW}\gamma_l^{LW}} - 2\sqrt{\gamma_d^+\gamma_d^-} - 2\sqrt{\gamma_l^+\gamma_l^-} + 2\sqrt{\gamma_d^+\gamma_l^-} + 2\sqrt{\gamma_l^+\gamma_d^-} < 0$$

III. Droplet draws lubricant out from surrounding substrate

$$\boldsymbol{Criterion}\ (\boldsymbol{III}): S_{ls} + \gamma_l R = \gamma_s^{LW} + 2\sqrt{\gamma_s^+\gamma_s^-} - \gamma_l^{LW} - \gamma_s^{LW} + 2\sqrt{\gamma_l^{lw} - \gamma_s^{lw}} - 2\sqrt{\gamma_l^+\gamma_l^-} - 2\sqrt{\gamma_s^+\gamma_s^-} + 2\sqrt{\gamma_l^+\gamma_s^-} + 2\sqrt{\gamma_s^+\gamma_l^-} + (R-1)\left(\gamma_l^{LW} + 2\sqrt{\gamma_l^+\gamma_l^-}\right) > 0$$

IV. Droplet displaces lubricant in surrounding substrate

$$\boldsymbol{Criterion}\ (\boldsymbol{IV}): S_{ls(d)} + \gamma_{dl} R = \gamma_d^{LW} + \gamma_s^{LW} - 2\sqrt{\gamma_d^{LW}\gamma_s^{LW}} + 2\sqrt{\gamma_d^+\gamma_d^-} + 2\sqrt{\gamma_s^+\gamma_s^-} - 2\sqrt{\gamma_d^+\gamma_s^-} - 2\sqrt{\gamma_s^+\gamma_d^-} - \gamma_l^{LW} - \gamma_s^{LW} + 2\sqrt{\gamma_l^{lw}\gamma_s^{lw}} - 2\sqrt{\gamma_l^+\gamma_l^-} - 2\sqrt{\gamma_s^+\gamma_s^-} + 2\sqrt{\gamma_l^+\gamma_s^-} + 2\sqrt{\gamma_s^+\gamma_l^-} + (R-1)\left(\gamma_d^{LW} + \gamma_l^{LW} - 2\sqrt{\gamma_d^{LW}\gamma_l^{LW}} + 2\sqrt{\gamma_d^+\gamma_d^-} + 2\sqrt{\gamma_l^+\gamma_l^-} - 2\sqrt{\gamma_d^+\gamma_l^-} - 2\sqrt{\gamma_l^+\gamma_d^-}\right) > 0$$

V. Droplet and lubricant are miscible

$$\boldsymbol{Criterion}\ (\boldsymbol{V}): \gamma_{dl} = \gamma_d^{LW} + \gamma_l^{LW} - 2\sqrt{\gamma_d^{LW}\gamma_l^{LW}} + 2\sqrt{\gamma_d^+\gamma_d^-} + 2\sqrt{\gamma_l^+\gamma_l^-} - 2\sqrt{\gamma_d^+\gamma_l^-} - 2\sqrt{\gamma_l^+\gamma_d^-} > 0$$

The lubricants chosen for infusion into the $FeCO_3$ layer are Krytox oil, BMIM and two crude oils variants. Cryo-SEM and FIB have also been used to observe stability underneath the droplet interface.

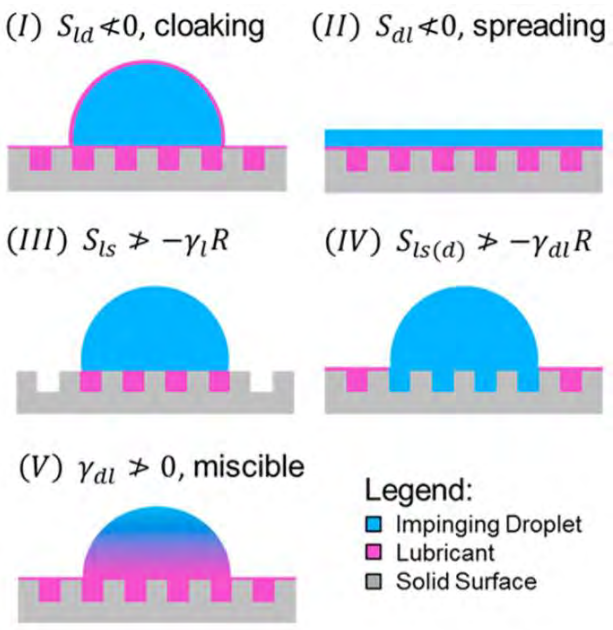

Figure 84 The 5 criteria for SLIPS design failure

6.8 Experimental matrix for characterisation of SLIPS base layer

The tests conducted previously provided a set of conditions with which to grow a consistent $FeCO_3$ film derived from the corrosion process. The environmental conditions for this film are outlined in Table 10. The fabrication method involving the standard corrosion bubble cell is identical to those used previously. All samples used for testing in subsequent chapters have been fabricated under these conditions.

Table 10 Environmental parameters/ Brine concentration for Iron carbonate fabrication.

Sodium Bicarbonate (grams)	16
pH	7.6
Temperature, (℃)	80
Final roughness (SiC)	600
Sodium Chloride (grams)	35
Carbon Dioxide partial pressure (bar)	0.54
Magnetic stirrer (rpm)	150
Time (hours)	72

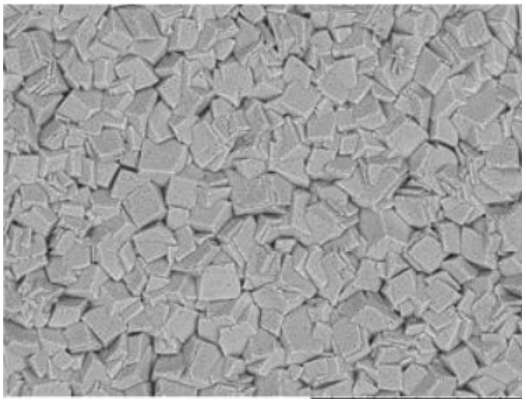

Figure 85 Representative SEM image of $FeCO_3$ layer grown under environmental conditions outlined in Table 10

After $FeCO_3$ film formation, the samples are rinsed with DI water, dried and stored in a desiccator until needed. A number of surface characterisation tests with respect to roughness and surface energy have been conducted. Surface roughness has been further developed with the use of NPFLEX white light interferometry to provide additional parameters on the $FeCO_3$ topography. Surface free energy (SFE) experiments involved collecting data obtained via contact angle measurements collected on a KSV tensiometer. These contact angle (CA) experiments were conducted with 3 probe liquids. DI Water,

Diiodomethane and Ethylene glycol whose known surface energy components are listed in Table 11. Individual droplet volume was 5µl administered by pipette at atmospheric pressure and ambient temperature (≈23℃.) onto the $FeCO_3$ surface. Images are sequentially taken at 1 frame per second (for a period of 10 seconds) after the droplet contacts the surface from which angles are measured.

Table 11 vOCG Surface energy components of contact angle probe liquids

FLUID	γ_T (mN/m)	γ_{LW} (mN/m)	γ^+ (mN/m)	γ^- (mN/m)
Water	72.8	21.8	25.5	25.5
Diiodomethane	50.8	50.8	0	0
Ethylene Glycol	48	29	1.9	47

Van Oss Chaudhury and Good (vOCG) surface free energy (SFE) is solved using a set of simultaneous equations. CA data and the known vOCG properties of the 3 probe liquids allows the construction of 3 separate equations, seen in Equation 24. Using the matrix solver function in Microsoft excel the vOCG surface energy components of iron carbonate can be determined (γ_s). Where superscript LW stands for Lifshitz van der Waals dispersive energy, + for Acid element and – base element. Total surface energy (γ_s^T) is then calculated in Equation 25

$$\text{Probe liquid 1 (l1)}: 0.5\gamma_s(1+\cos\theta) = \sqrt{\gamma_{l1}^{LW}\gamma_s^{LW}} + \sqrt{\gamma_{l1}^{-}\gamma_s^{+}} + \sqrt{\gamma_{l1}^{+}\gamma_s^{-}}$$

$$\text{Probe liquid 2 (l2)}: 0.5\gamma_s(1+\cos\theta) = \sqrt{\gamma_{l2}^{LW}\gamma_s^{LW}} + \sqrt{\gamma_{l2}^{-}\gamma_s^{+}} + \sqrt{\gamma_{l2}^{+}\gamma_s^{-}}$$

$$\text{Probe liquid 3 (l3)}: 0.5\gamma_s(1+\cos\theta) = \sqrt{\gamma_{l3}^{LW}\gamma_s^{LW}} + \sqrt{\gamma_{l3}^{-}\gamma_s^{+}} + \sqrt{\gamma_{l3}^{+}\gamma_s^{-}}$$

Equation 24

$$\gamma_s^T = \gamma_s^{LW} + 2\sqrt{\gamma_s^- \gamma_s^+}$$

Equation 25

6.9 $FeCO_3$ Layer Characterisation

$FeCO_3$ Roughness

The $FeCO_3$ layer has been initially scanned with a stylus profilometer which provides a quick and convenient method for assessing and comparing roughness between samples. The line scans provided are limited to 2D scans and resolution for areal stitching can be poor due to the anisotropic output. White light interferometry provides greater accuracy of the surface topography and provides 3D areal data and processing of hybrid roughness parameters such as developed interfacial area ratio (S_{dr}). This parameter plays a key role in defining the geometric factor that has direct implications on contact angle behaviour of the $FeCO_3$ layer (via the Wenzel model).

Topography comparison with SEM show several physical features typical of the undulating nature of a corroded surface (Figure 86c). The presence of elevated peaks (denoted in bright red) is consistent with line scans and representative of structural edges of larger single crystals (10-20 μm) (Figure 86a). Deep blue regions would signify areas of lower elevation to the mean line (or valleys) highlight areas where the iron carbonate film may be incomplete or the underlying carbon steel is exposed (as observable) (Figure 86b). Green regions and areas of reduced height differentials (i.e. low colour shift on contours) represent plateaus/ flat areas of the $FeCO_3$. Here peak changes occur in the order of single digit μm values and are consistent with SEM images that indicate areas where smaller (<5μm) $FeCO_3$ crystals are concentrated (Figure 86a).

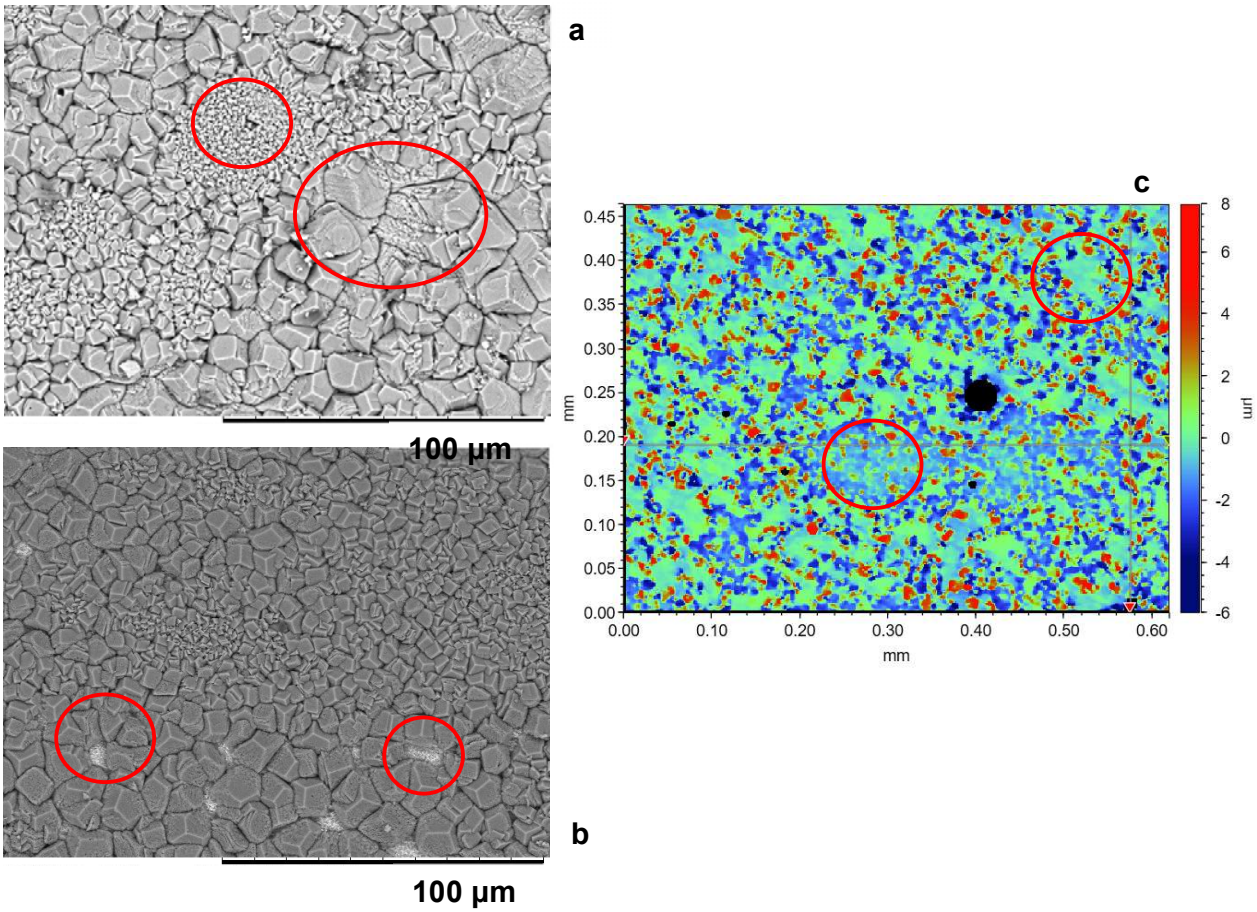

Figure 86 a) SEM image showing clustering of tiny $FeCO_3$ crystals and larger, fully formed crystals (Circles). b) SEM image showing gaps with underlying nanocrystalline $FeCO_3$ valleys (Circles). c) NPFLEX topographical height map of $FeCO_3$ surface showing topographical features seen on SEM images (Circles).

R_a roughness results are consistent across samples between the measurement methods. From the previous results chapter using stylus profilometry, R_a levels fluctuate around 1.2 ± 0.1 µm (Figure 87a). This occurs across all samples, regardless of the initial level of roughness. As stated earlier, this value appears to be an upper limit to the R_a obtainable in the UB environmental conditions used. White light interferometry results of $FeCO_3$ layers produce R_a values of samples at 1.3 ± 0.1 µm (Figure 87b). Anisotropy as observed in SEM of samples where $FeCO_3$ forms in valleys does not appear to be evident on surface roughness scans, consistent with full coverage of samples with crystals. Scan length is slightly different due to the low absorbance encountered with the dull $FeCO_3$ surface. This means a scan

of a smaller area (with close focus) has been used at 0.6mmx 0.45mm compared to the line scan of 20mm in length used with the stylus.

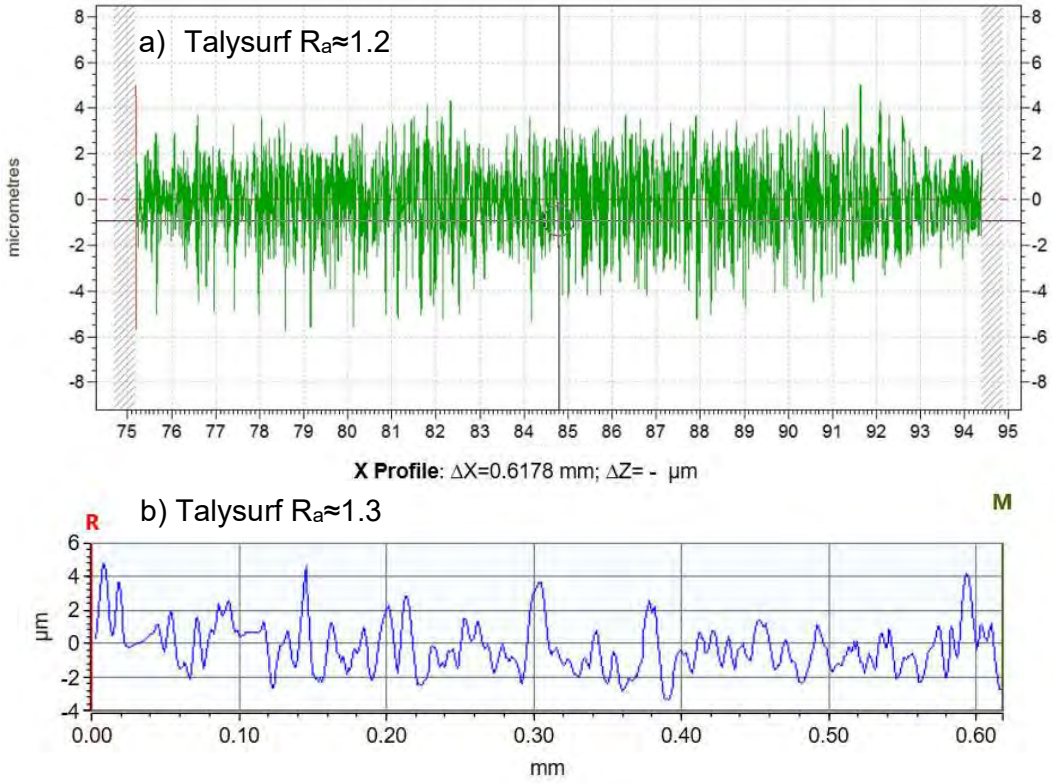

Figure 87 a) Talysurf line scan output. b) NPFLEX line scan output

The corrosion process and subsequent formation of the $FeCO_3$ film produces an S_{dr} value between 17-21% (Figure 88). On average the $FeCO_3$ layer increases the topographical surface area by a 1/5 relative to an uncorroded sample of similar area. This roughness is similar in nature to S_{dr} values of samples obtained from steel corrosion in marine environments in the range of 5-53%, but predominantly between 10-30% [272, 278, 279]. Generally roughness of pipeline surfaces is preferred to increase bonding and adhesion of protective paints/coatings. In the context of surface finish treatments, the topography and S_{dr} values lie within the range of a low grade (80 grit) polishing (19.4%) and acid etching (39.4%) [280]. These are also comparable with R_a values for the same methods taken by line scans. Substitution into the geometric factor equation provides R values between 1.17 and 1.21 which will influence the wettability of the surface.

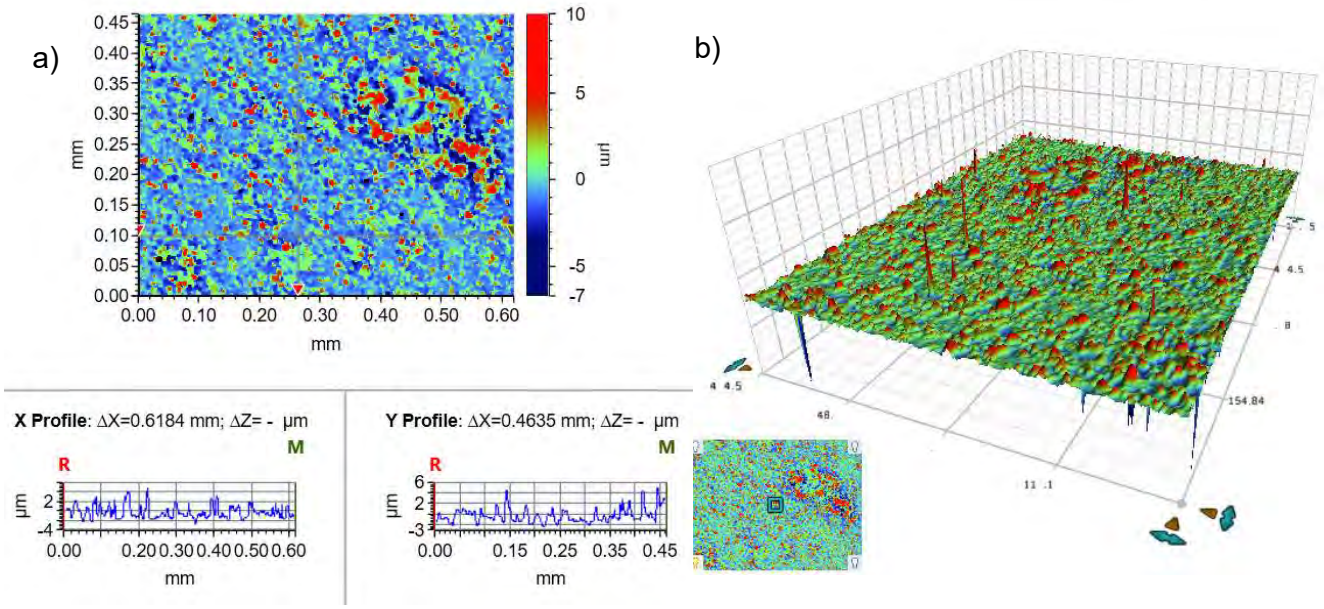

Figure 88 a) 2D Topographical map of random spot on $FeCO_3$ surface, including X and Y profile. b) 3D NPFLEX topographical map of surface with average Sdr 17-22%

Cross-sectional SEM provides information regarding the thickness of the $FeCO_3$ base layer. Thickness fluctuates across the surface with an average of 7.2±4.2 µm across the section. The thinnest observable portions of the layer are <1 µm and are likely to be exposing the underlying carbon steel or covered by a bi-layer of fine $FeCO_3$ crystals at the nano level (Figure 89a). At the other end of the spectrum higher thicknesses of 10 µm tend to appear across cleaved larger crystals. This is where porosity is less observable across the cleaved face suggesting a fully formed crystal and not several smaller crystals clustered together. It is interesting to note that top-down SEM images of the layer have shown the presence of larger crystals that have a horizontal/lateral size up to 25 µm (Figure 89a). However maximum thickness at a cross-sectional level never tends to reach an equivalent value and is on average 50% lower than the highest recorded thicknesses. This shows horizontal crystal size does not correlate with vertical crystal size from SEM and is not reflective of potential thickness. The corroded carbon steel surface underneath is not parallel with the $FeCO_3$ film above and remains uneven in nature. Localised pitting is observed in some areas, with the pits generally

occupied with $FeCO_3$ (Figure 89a). Stylus scans are in a consistent range with cross-sectional SEM profiles. Large topographical fluctuations from high peaks to low valleys of up to 10 µm height differentials are recorded with minor changes on a similar length/height scale Figure 89b/c).

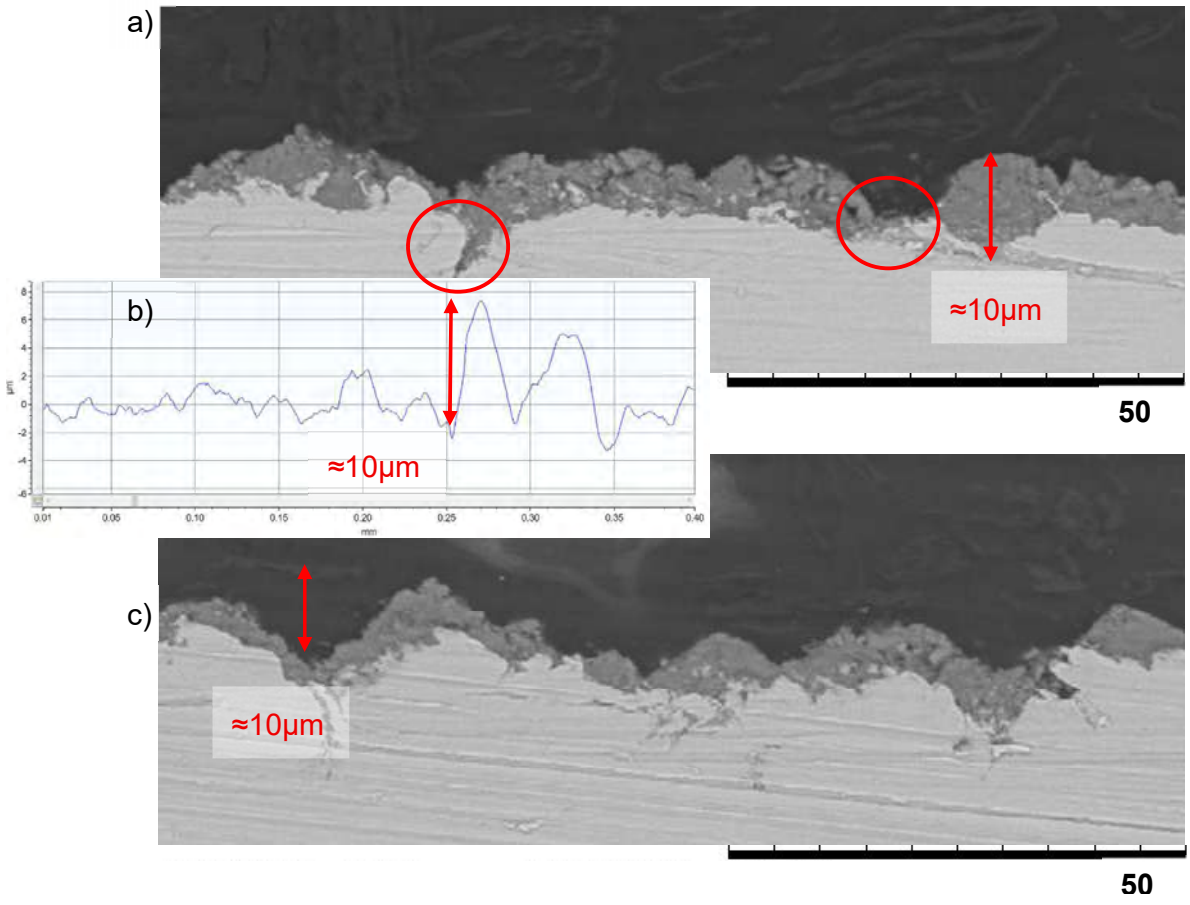

Figure 89 a) Cross section SEM of $FeCO_3$ layer. Highlighted areas show presence of pits, typical minimum thickness areas (<1 µm) and maximum thickness areas (10 µm) b) Line scan output from NPFLEX showing average max height differentials of 10 µm across surface profile. C) SEM cross section showing similar surface profile to NPFLEX outputs.

$FeCO_3$ Surface free energy

To validate the contact angle apparatus and vOCG surface energy method a preliminary test has been conducted. This test was carried out on a typical untreated glass slide with the proposed probe liquids, de ionised water, ethylene glycol and diiodomethane. The following contact angle

measurements found in Figure 90 show similar angles between ethylene glycol and water due to both compounds being polar compared to the apolar diiodomethane. Calculated surface energies for glass can be validated and are in good agreement with those in literature using vOCG [232, 281] and other methods [282]. Acid base components are also of a similar magnitude, with variations likely to be a result of probe liquid purity or ambient conditions.

a)

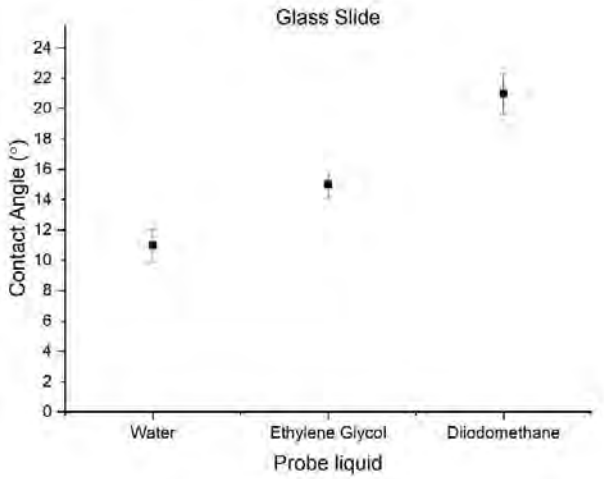

b)

	Surface Energy (mN/m)	
	Calculated	Literature [232]
γ^T	50.1	51.1
γ^{LW}	47.4	40.8
γ^-	0.03	0.49
γ^+	65.2	60.8

Figure 90 a) Contact angles results for probe liquids and b) Calculated surface energy values of glass slide

The $FeCO_3$ layer that forms the SLIPS base has been characterised next, along with a sample representing the underlying carbon steel. This provides an understanding of the hydrophobicity/hydrophilicity and SFE changes to the carbon steel induced by the $FeCO_3$ layer. DI water contact angles (WCA) give values of 68°± 1.3 for a polished X65 carbon steel sample (Figure 91). Hydrophilic surfaces are associated with WCA < 90° and this is consistent with hydrophilic results and WCA results in the literature for steel specimens [283-286]. Measured WCA for the SLIPS $FeCO_3$ layer is lower at 60°± 2.7 indicating an increase in surface hydrophilicity. The actual WCA is determined by applying a roughness correction to the measured WCA through the Wenzel model. A roughness ratio (R) is generated via equation and incorporates an average S_{dr} value of 22% (calculated previously). Accounting for the sample

roughness, actual WCA is slightly higher at 65°± 2.7 than measured roughness. Compared to the untreated carbon steel the $FeCO_3$ WCA remains lower. Wenzel model supports this theoretically as surfaces in an initial hydrophilic state become more hydrophilic with increased roughness (or R). Contact angle behaviour is also supported from existing studies that report a reduction of WCA on steel samples before and after corrosion effects to the surface[285-288]. Probe liquid contact angles for ethylene glycol and diiodomethane are also reported in Figure 91.

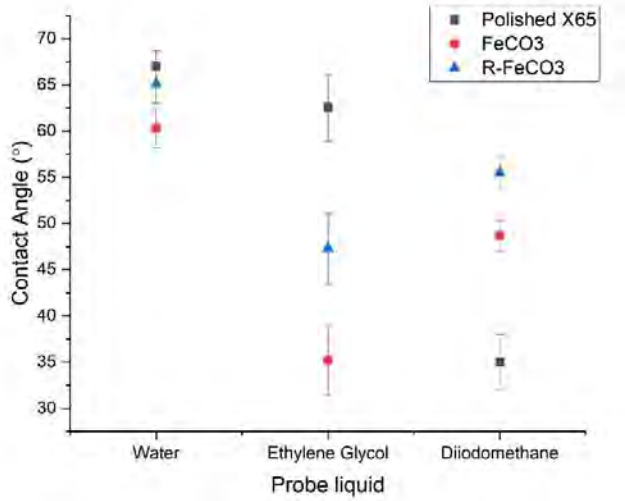

Surface Energy (mN/m)

	Polished X65	$FeCO_3$	R-$FeCO_3$
Y^T	44.4	42.1	36.4
Y^{LW}	42.0	35.4	31.0
Y^-	13.9	19.7	19.1
Y^+	0.1	0.5	0.3

Figure 91 Contact angle results and calculated surface energy values for polished X65, $FeCO_3$ and roughness corrected R- $FeCO_3$

Total surface energy (Y^T) is 44 mN/m for an uncorroded X65 carbon steel sample. This falls in line with currently reported values for various metal alloys ranging from 34 mN/m (galvanised steel) to 51 mN/m (Cold rolled steel) as per Figure 92 [289-293]. Pure metallic elements, such as chromium and aluminium tend to have higher calculated vOCG values towards the 60 mN/m mark [232]. The development of an $FeCO_3$ layer produces a total surface energy value of 36 mN/m, which represents a decrease of 8 mN/m from the untreated carbon steel surface. This value is corrected for the roughness generated by the $FeCO_3$ to the droplet via Wenzel mentioned previously. This is a reduction in Y^T of roughly 13%, from 42 mN/m to 36 mN/m (Figure 92).

The Y^T constituents of Lifshitz van der Waals (Y^{LW}) and acid (Y^+)/ base (Y^-) are similar across the 3 samples and in line with general conventions that Y^- is an order of magnitude greater than Y^+. $FeCO_3$ leads to a decrease in the Y^{LW} or dispersive component and an increase in acid-base (Y^+/Y^-) components compared to the original steel surface. This acid-base component (which considers polar interactions) is increased with the formation of surface layers (i.e. oxides/ nano-structures) [294, 295].

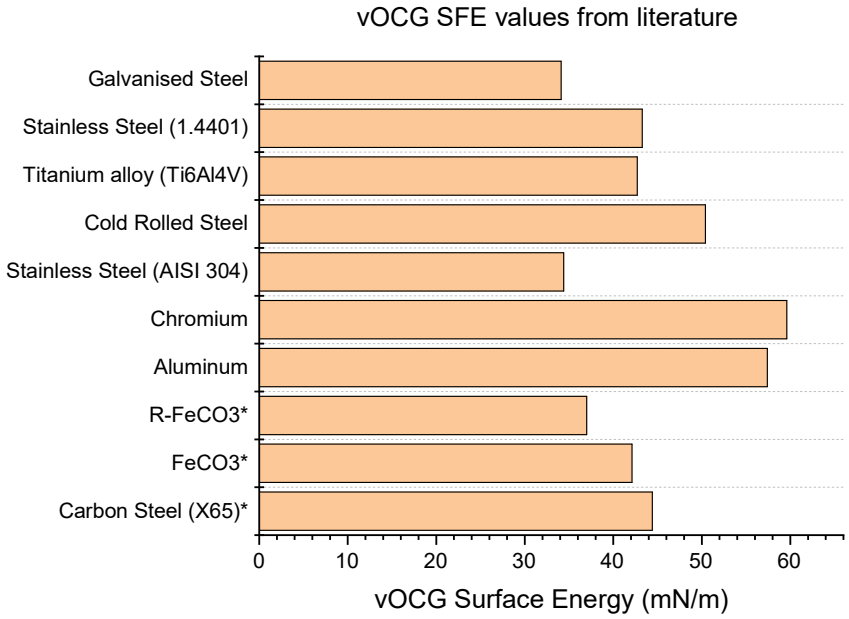

Figure 92 Comparison of calculated total surface energy values with materials taken from literature

SLIPS Compatibility

SLIPS Compatibility between the various components in the $FeCO_3$ SLIPS can be theoretically assessed via 5 criterion according to the Preston model. These criteria require the vOCG surface energy values from the solid (s), lubricant (l) and droplet (d) of the $FeCO_3$ SLIPS system (with further information provided in Section 4.3, 5.5 and 6.7). Values for the $FeCO_3$ layer have been calculated in the previous section and appear in Table 12 alongside the other elements. The lubricants tested are Krytox, BMIM and two types of crude oil. Surface energy values have been obtained from existing data in the literature. In the case of crude oil, there is not a direct vOCG value available

for the oil tested. As the primary constituents of crude oil are paraffins, aromatics and naphthene's a spectrum of hydrocarbons have been used. This includes paraffin, benzene and cyclohexane which have been substituted to represent each group respectively.

Table 12 Surface energy values for the different components of the FeCO3 SLIPS system

	Material	γ^T	γ^{LW}	γ^+	γ^-
Droplet 	Water	72.8	21.8	25.5	25.5
Lubricant	Krytox	18.8	12.7	0.03	0.02
	BMIM	34.0	25.0	1.0	13.9
	Paraffin	25.5	25.5	0	0
	Benzene	28.9	28.9	0	1.0
	Cyclohexane	25.2	25.2	0	0
Solid 	Iron Carbonate	36.4	31	19.1	0.3

For Criterion 3 and 4 a geometric factor (R) is involved, with 0 representing a flat surface and 1 a rough surface. As outlined in Equation 26, the geometric component is made up of r (surface area/projected area or S_{dr}) and Φ (the fraction of solid that contacts the base of the impinging droplet). Determination of Φ would only be possible experimentally and is difficult to obtain. S_{dr} can be used from previous data on sample roughness. Given S_{dr}, Φ can be assumed for values from 0-1, with a minimum value of R between 0.15-0.17 (@ Φ = 0, S_{dr} = 17-21%). This would be theoretically difficult and assumes the droplet would essentially float on the lubricant with 0 contact (conceptually

similar to the Lotus effect). Towards the other end of the spectrum, a maximum of R = 1 is achieved at Φ = 1.

$$R = \frac{(r - 1)}{(r - \Phi)}$$

Equation 26

Table 13 highlights the success and failure in each criterion for the 5 chosen lubricants. Criteria 2, 3 and 5 show a strong pass condition (black), for criterion 3 this is regardless of the value of the geometric component. In Criterion 1 results are mixed, with both success and failure. For BMIM and Kr, failure means a water droplet will be cloaked by the surrounding lubricant. In the case of a crude oil, the mixed results suggest a pass or fail possibility depending on the composition. A crude with higher levels of aromatics (benzenes) would lead to failure, whilst higher paraffin or cyclohexane content could provide a pass condition. Criterion 4 is highly sensitive to the geometric factor. This criterion only passes at R=1 (Φ = 1) for all lubricants except BMIM. At values where contact levels between the droplet and lubricant are Φ<1, failure occurs. Suggesting the droplet will theoretically displace the lubricant underneath.

Table 13 Predicted results for SLIPS criterion model. Red represents failure in criterion. Blue represents borderline result.

	SLIPS CRITERION THEORETICAL				
	(I) $S_{ld} \leq 0$	**(II)** $S_{dl} \leq 0$	**(III)** $S_{ls} + Y_l R \geq 0$	**(IV)** $S_{ls(d)} + Y_{dl} R \geq 0$	**(V)** $Y_{dl} \geq 0$
SLIPS-Kr	*10.93*	-109.17	27.91	0.01	49.12
SLIPS-Bm	*29.52*	-51.12	36.02	7.28	10.80
SLIPS-Pa	-3.84	-98.44	30.73	1.98	51.14

SLIPS-Be	*2.30*	-85.50	32.04	3.29	41.60
SLIPS-Cy	-3.57	-98.69	30.70	1.96	51.13

The SLIPS criteria provide a framework of design considerations for potential combinations. Failure does not automatically disqualify a SLIPS from application. For example in the instance of Criterion 2, the physical lubricant barrier to the impinging droplet is preserved, however in a condensation application this would be ineffective as it fully wets the surface. Theoretical predictions can be matched with experimental outcomes, to varying degrees of certainty. Table 14 shows the theoretical outcomes predicted in Table 13 vs experimental observations. In the experimental section, the actual lubricants for the different SLIPS were used. This included a waxy and non-waxy crude oil which has been compared to the hypothetical results of cyclohexane, benzene and paraffin.

Table 14 Experimental results compared with predicted outcomes. Tick represents match between experimental and theoretical. x is no match. Colours are carried over from previous table.

	SLIPS CRITERION EXPERIMENTAL				
	(I) $S_{ld} \leq 0$	**(II)** $S_{dl} \leq 0$	**(III)** $S_{ls}+\gamma_{l}R \geq 0$	**(IV)** $S_{ls(d)}+\gamma_{dl}R \geq 0$	**(V)** $\gamma_{dl} \geq 0$
SLIPS-Kr	✓	✓	✓	✓	✓
SLIPS-Bm	✓	✓	✓	✓	✓
SLIPS-Pa	×	✓	✓	✓	✓
SLIPS-Be	✓	✓	✓	✓	✓
SLIPS-Cy	×	✓	✓	✓	✓

In the case of Criterion 1 theoretical predictions showed a failure, or cloaking effect of the lubricant across the surface of the water droplet. This film can often be at a nano-scale thickness or monolayer and is difficult to observe. One indication of the presence of the cloaking effect is the wetting ridge. In contact angle images this appears as a concave surface at the 3-phase contact point of the impinging droplet as indicated in Figure 93b/d). The presence of this wetting ridge plays an important part in droplet shedding mechanics; however the cloaking of droplets can present challenges with regards to lubricant depletion. The extent of this cloaking impact is difficult to quantify. Using cryo-SEM/EDX lubricant presence can be detected at the apex of the droplet, however the flash freezing (liquid N_2) process often damages the film integrity (Figure 93c).

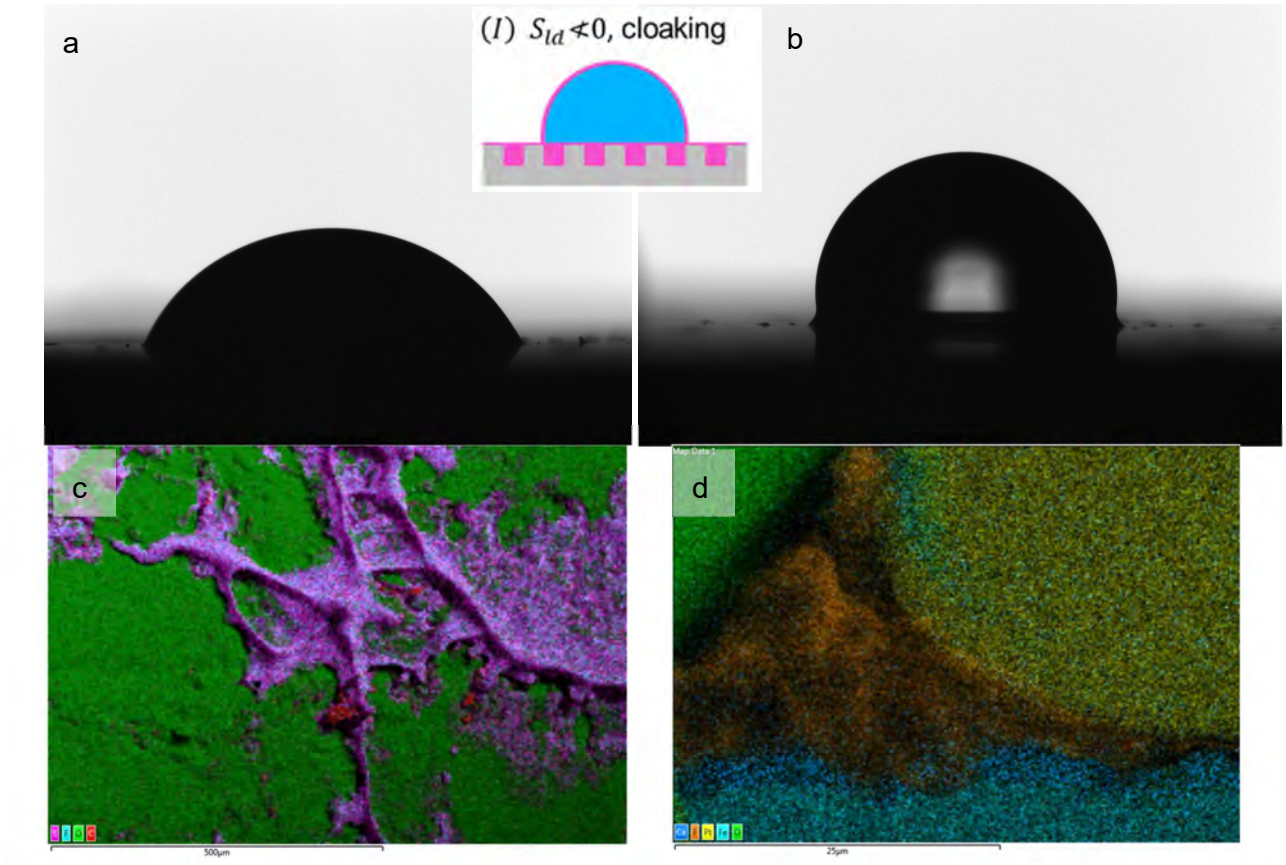

Figure 93 a) Water droplet on X65 carbon steel (non -SLIPS) b) Water droplet on SLIPS surface (note meniscus at 3 phase contact point) c) Lubricant traces (Purple) on top peak of droplet surface. d) Wetting ridge of lubricant (Orange) at 3 phase contact point

Both criteria 1 and 2 are functions of the surface energies of only the impinging droplet and lubricant. Polarity or the acid/base (γ^+/ γ^-) component is the primary driver of success and failure between lubricant and droplet, particularly when large differentials exist. Criterion 2 is easily observed via contact angle as the impinging droplet will fully wet the surface (i.e. WCA = 0°) during failure. The presence of discrete water droplets on the surface is consistent with theoretical predictions for all SLIPS types (Figure 94a). Given both crude oils and Krytox have acid/base components (γ^{AB}) that are close to 0, they present WCA that are similar in nature and also higher than that of BMIM ($\gamma^{AB} \approx$ 9 mN/m) which has some polar component that attracts the highly polar water molecule. In the case of lubricant and droplet combinations, where one fluid is polar and the other non-polar a further condition must be met. In order for criteria 1 and 2 to pass in parallel, the equality must be satisfied (Figure 94c). Given none of the SLIPS combinations pass this equality and criterion 2 experimentally shows a pass outcome, this further reinforces the presence of a cloaking film and failure in criterion 1. It is interesting to note that pure paraffin would pass in criterion 1 (given known data), however the waxy crude must not possess this in sufficient quantities as the result is a failure.

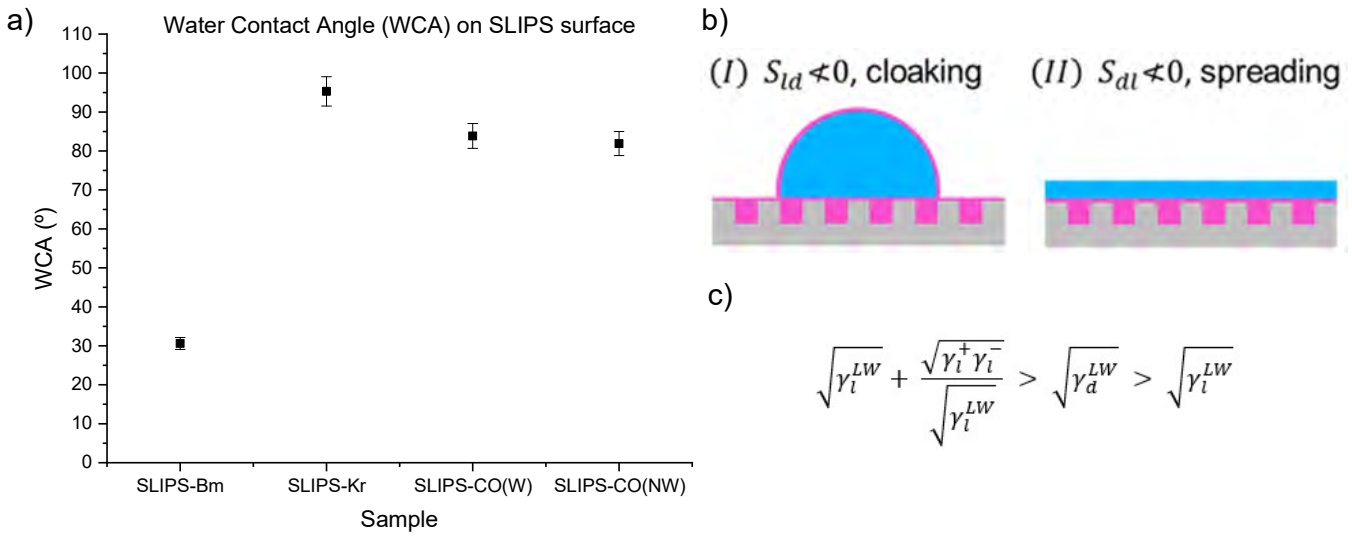

Figure 94 a) Water contact angle on SLIPS b) Schematic drawing of Criterion I, II failures. c) Inequality for successful pass state for both Criteria I and II

Criteria 3 and 4 requires the geometric factor (or roughness) of the $FeCO_3$ and features surface energy for all 3 of the SLIPS components. Static cryo-SEM/ Normal SEM images can be used to visualise that criterion 3 is matched both experimentally and theoretically from images of the droplet and surrounding texture. Lubricant coverage is maintained around the droplet as per Figure 95a, which shows the impinging droplet does not significantly draw out lubricant from the surrounding $FeCO_3$ layer. Although it is noted there exists some attraction between lubricant and droplet, given the lubricant cloaks droplets under criterion 1 and the presence of a wetting ridge drawing up the lubricant datum in the immediate region (both under/outside droplet) as per Figure 95c.

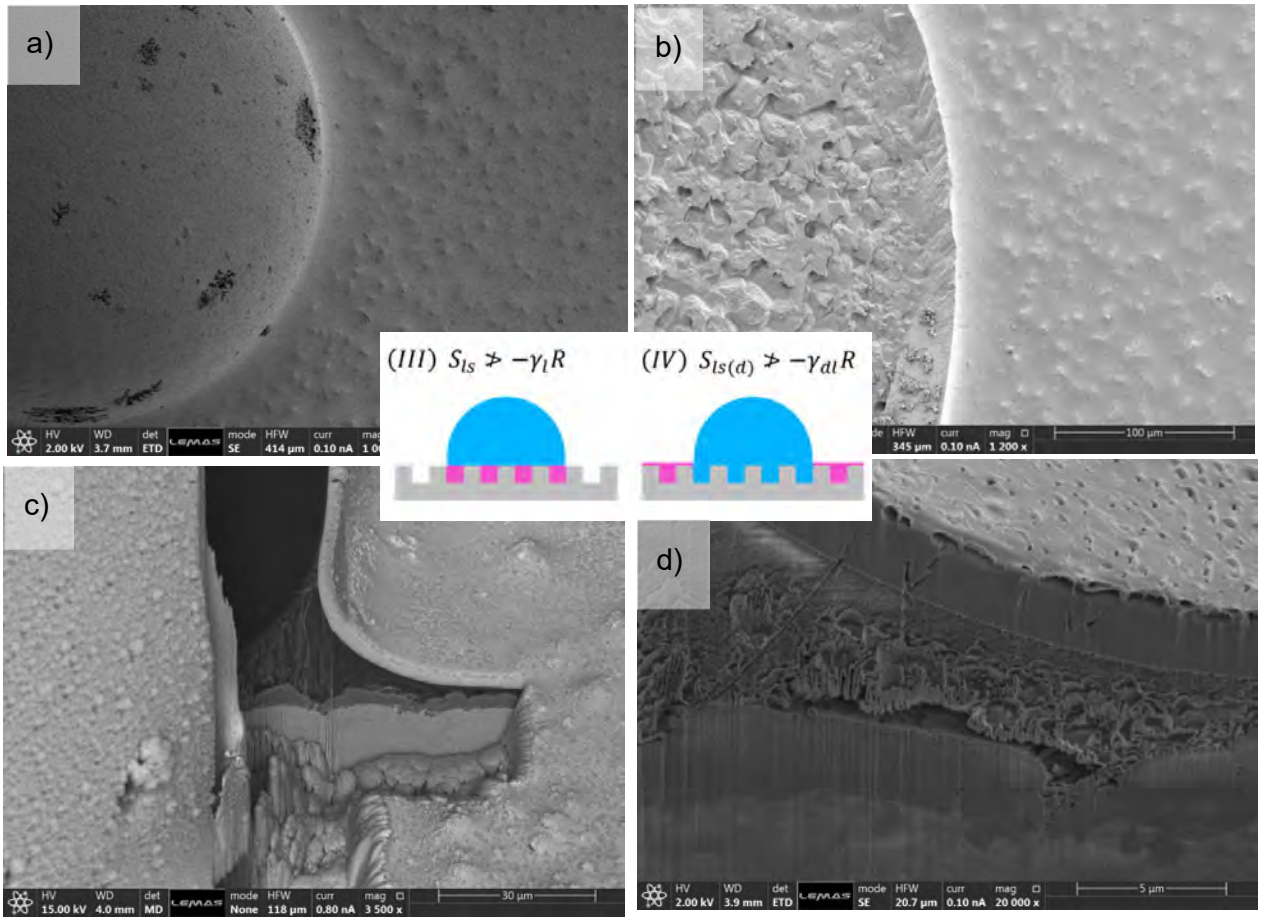

Figure 95 a) Cryo-SEM of droplet showing boundary with surrounding lubricant. b) Cryo-SEM with droplet removed showing wetting ridge and state under droplet. c) Cryo SEM FIB section showing 3 phase contact point, wetting ridge and underlying iron carbonate/steel base. d) Higher magnification of wetting ridge away from droplet.

Criterion 4 is the most sensitive of the 5 design considerations considering the borderline pass/fail state. It also remains the most difficult to verify experimentally given the behaviour underneath the droplet is hidden. Theoretically given the high polarity (γ^{AB}) of both water and the $FeCO_3$ relative to the lubricants there would be higher attraction forces between them, given the strength of like for like interactions. This would lead to the likelihood of the droplet displacing the surrounding lubricant, hence the weak calculated values. In the case of the BMIM, the higher acid/base values allow for a stronger interaction with the $FeCO_3$ layer and this is not an issue. Also these criteria only consider surface energy interactions and not physical characteristics like porosity or capillarity of the $FeCO_3$ that would improve lubricant retention.

In order to establish the state under the droplet, a novel method was attempted using Cryo-SEM. The droplet was placed on the lubricated $FeCO_3$ then frozen, after freezing it was then physically detached Figure 95b) to observe the environment underneath. Qualitatively the method verifies the presence of lubricant under the droplet as per criterion 4. However, it also shows the peaks of some $FeCO_3$ crystals, whether this has occurred from displacement of the lubricant by the droplet or shear damage from attachment to the droplet during removal is unclear. The difference between lubricant levels that straddle the wetting ridge may also be a result of mass displacement on the surface.

This static test can also be compared with dynamic results from contact angle behaviour. WCA across all SLIPS remain constant as per Figure 96a, indicating a stability of the droplet in regard to surface wetting on the lubricant. If we examine the case of a similar failure in criteria 4 as exhibited in Figure 96b using a methanol droplet on a silicon oxide structure lubricated with diiodomethane, the results are visually apparent [232]. Here the failure is severe, with the methanol fully wetting the underlying substrate within seconds and actively displacing all diiodomethane in the immediate vicinity. The interface between methanol and diiodomethane can be visually observed as it expands from the initial droplet centre to achieve full wettability (or a CA = 0°) across the surface. The stability of these droplets on the SLIPS tested suggests that failure in Criterion 4 does not result. However even though the

droplet may not be actively displacing the lubricant it may still occur on a more limited scale (i.e. only under the droplet itself).

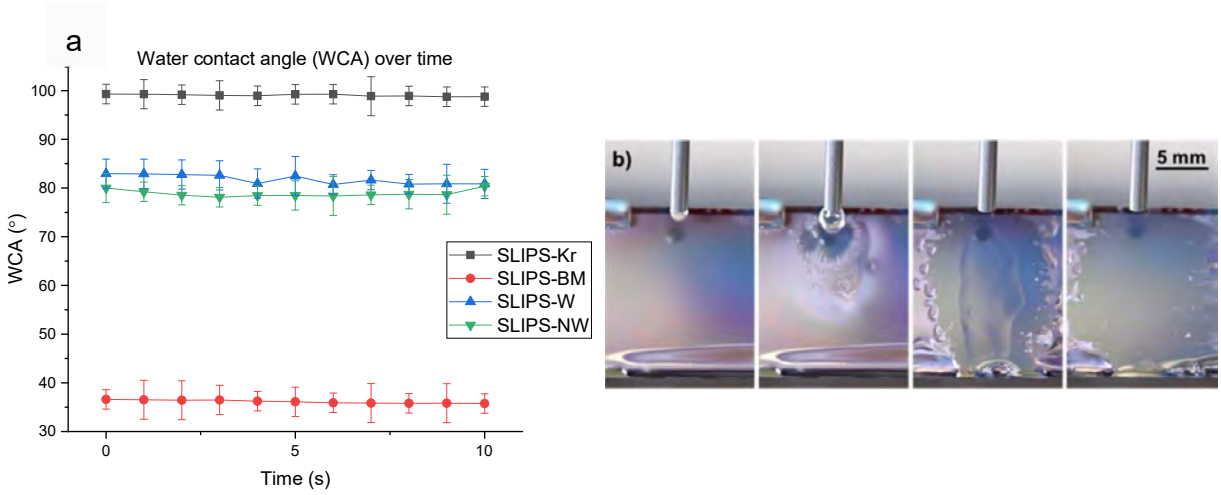

Figure 96 a) Dynamic water contact angle on SLIPS surface. b) Active displacement of SLIPS lubricant by impinging droplet (Criterion 4 failure)

Criterion 5 focuses on the miscibility of the droplet and lubricant. This case is easily seen experimentally and is in agreement with theoretically predicted results. In all cases tested, the chosen lubricants are immiscible with water as seen in Figure 97. With the crude oils used, there are parts often termed water-soluble fraction (WSF), that will leach into the water phase seen around the oil/water interface [296]. The immiscibility between lubricant and droplet is expected due to the polarity difference between the highly polar water molecules and lubricants with low/zero polarity. Here attraction tends to favour like for like interactions of the same fluid. Immiscibility for SLIPS is important to preserve the lubricant/droplet interface however it is noted as per Figure 97 that the layering of water/oil and oil/water is different for the two sets of lubricants. With higher densities both the BMIM (1.4 gm/cm^3) and Krytox Oil (1.9 gm/cm^3) are not likely to suffer from additional displacement forces (i.e. buoyancy) in the presence of water than the crude oils of lighter densities (0.84-0.88 gm/cm^3).

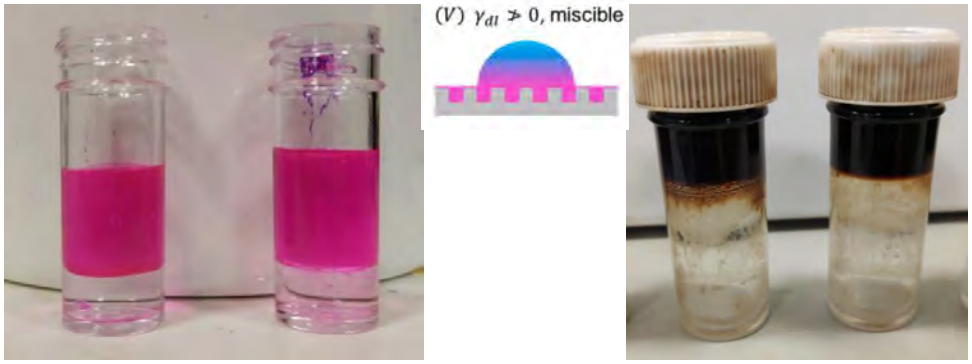

Lubricant	Kr	BM	CO (W)	CO (NW)
Density (g/cm^3)	1.9	1.4	0.88	0.84

Figure 97 Miscibility results of the four lubricants with DI water. In order: Water (Pink)/Kr (clear), Water (Pink)/ BM (clear), Crude oil W (black)/ Water (clear), Crude oil NW (black)/ Water (clear). Inset densities of lubricants.

Looking at lubricant selection on a broader level, Preston's work outlines 153 possible fluids/solids with known vOCG SFE values. Substituting the intended impinging droplet of water and the calculated values of $FeCO_3$ provide further options for potential lubricant choice. Of the 153 listed, 33 provide a stable configuration by passing all 5 of the criteria tests, 112 are unstable and 8 non-applicable. This includes possibilities such as diiodomethane, tridecane with all successful lubricants being by nature non-polar ($\gamma^+/ \gamma^- = 0$). If the selection process were relaxed so that only 4 criteria are necessary, the lubricant possibilities increases by roughly 40%. This is to accommodate the additional limitation as stated previously that either Criteria 1 or 2 will fail in the case of low polarity lubricants and high polarity impinging droplets. Of the same 153 prospects, 95 now achieve a stable design (including many -ane, -ene and aromatic hydrocarbons), 50 are unstable and again 8 non-applicable. The lubricants chosen for ongoing tests represent two with a proven track record in SLIPS literature within the application of anti-fouling either organic or inorganic. With the remaining two crude oil lubricants providing an alternative development in the lubricant space for an industrially relevant SLIPS in a petroleum application.

6.10 Summary

1. The $FeCO_3$ layer formed in Part A has been further characterised with respect to roughness and thickness. The $FeCO_3$ layer has an average R_a between 1.2-1.3 μm, consistent between both surface profilometry and white light interferometry. 3D roughness or S_{dr} is around 1.22, representing an increase in surface area of 22% generated by $FeCO_3$ crystal coverage. Thickness of the layer is on average 7.2 μm ±4.2 across crystal peaks and valleys.
2. Contact angle measurements have been used to calculate the vOCG SFE components of the $FeCO_3$ layer. Results, corrected for roughness, indicate a $\gamma^T \approx 36.4$ mN/m, $\gamma^{LW} \approx 31.0$ mN/m, $\gamma^+ \approx 19.1$ mN/m and $\gamma^- \approx 0.3$ mN/m. This represents a slight decrease in SFE from the original untreated carbon steel base. WCA suggest that the $FeCO_3$ substrate is hydrophilic (WCA<90°) and nominally more than the un-corroded carbon steel base.
3. Calculated $FeCO_3$ SFE values have been substituted into an existing stability model simulating compatibility with the 4 individual lubricants and water. Lubricants that are being tested include an ionic liquid, perfluorinated oil and two crude oil types. Theoretical failure in Criterion 1 (cloaking) is a common issue and is representative of combining highly polar water droplets with low polarity lubricants. Criterion 4 (displacement) is also highly sensitive to changes in the geometric factor and subsequently roughness.
4. Model predictions have been verified with experimental work. Through a mixture of Cryo-SEM, EDX and contact angle methods theoretical outcomes can be physically confirmed. However, there remains further work in the determination of the true state of Criterion 4. Particularly, increasing the certainty and extent of lubricant displacement directly beneath the droplet.
5. Theoretical predictions for $FeCO_3$ SLIPS provide a range of lubricant possibilities. Lubricants currently chosen for further anti-fouling testing have been done so with the following considerations. A foundation in hypothetical compatibility between SLIPS components (i.e. substrate,

droplet and lubricant), industrial relevance (i.e. Oil and Gas) and previous success in literature for anti-fouling applications.

Chapter 7
SLIPS performance evaluation

7 SLIPS scaling performance in $CaCO_3$ systems

7.1 Introduction

The previous chapter explored the construction of a stable SLIPS based on an $FeCO_3$ derived corrosion layer. This chapter focuses on the anti-fouling performance of the SLIPS with regards to inorganic scale (i.e surface crystallisation/deposition of minerals other than $FeCO_3$). The capabilities have been evaluated in a brine system where the dominant scale species that precipitates is calcium carbonate ($CaCO_3$). $CaCO_3$ is a common mineral scale encountered across many industries, including the Oil and Gas sector [297]. Its presence often appears as surface deposits that can cause flow assurance issues with severe safety and economic consequences [298]. Surface engineering is one solution and SLIPS presents a novel innovation in the field that deals with fouling build-up at the surface level (as opposed to the bulk).

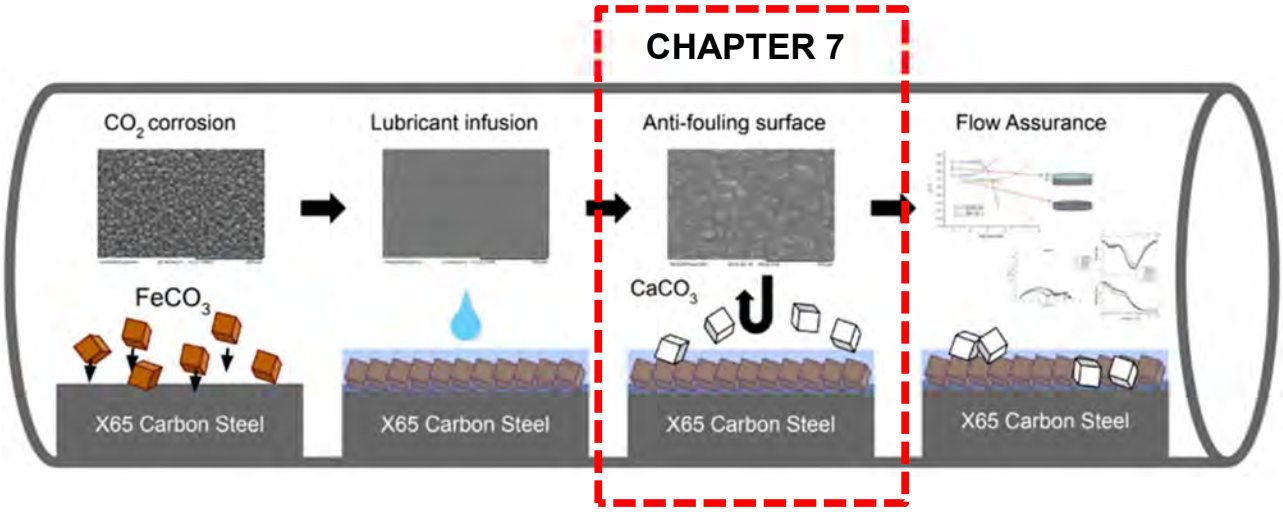

Figure 98 Thesis schematic of the main focus of Chapter 7 results

Testing conditions have been constructed to simulate both a high scaling environment with a saturation index (SI) of 2.6 and a low scaling environment of SI 1. This is not representative of any specific field but uses a commonly

encountered mineral scale found in oilfield settings. As the research is fundamental, the initial testing regime has focused on a single-phase system (aqueous) for simplicity. The performance of the SLIPS has been evaluated through analysis of surface $CaCO_3$ deposits and trace elements of the remaining lubricant outlined in the next paragraph. The four lubricants tested are perfluorinated vacuum oil (Krytox), ionic liquid (BMIM) and two crude oils. The crude oils are denoted by the presence of paraffins, either with (waxy) or without (non-waxy). The capability of the SLIPS systems in relation to fouling performance is associated with links to SLIPS compatibility, physical lubricant properties and SLIPS surface energy.

Figure 99 provides an outline of how the chapter is structured. Initially the two brine systems are characterised with regards to properties such as turbidity, crystal precipitation and ionic concentration. Next the individual SLIPS systems are characterised via contact angle (CA) measurements to determine apparent surface energy and establish the link with classical nucleation theory regarding Surface Free Energy (SFE). Scaling tests are then conducted for the different SLIPS and a control (i.e. untreated carbon steel) specimen to evaluate crystal surface deposits. Surface analysis includes SEM for crystal surface coverage and morphology. EDX has been used for Ca wt.% and to determine lubricant trace elements, this has been used in conjunction with FTIR. FTIR provides a clearer picture with respect to crude oil lubricants (detecting carbon chains in hydrocarbons). Finally XRD provides information on the crystal structure of surface deposits. In particular the iron calcium carbonate ($Fe_xCa_yCO_3$) structure is of note, with the degree of calcium incorporation into the underlying $FeCO_3$ layer providing an indication as to the effectiveness of the lubricant barrier and fouling performance.

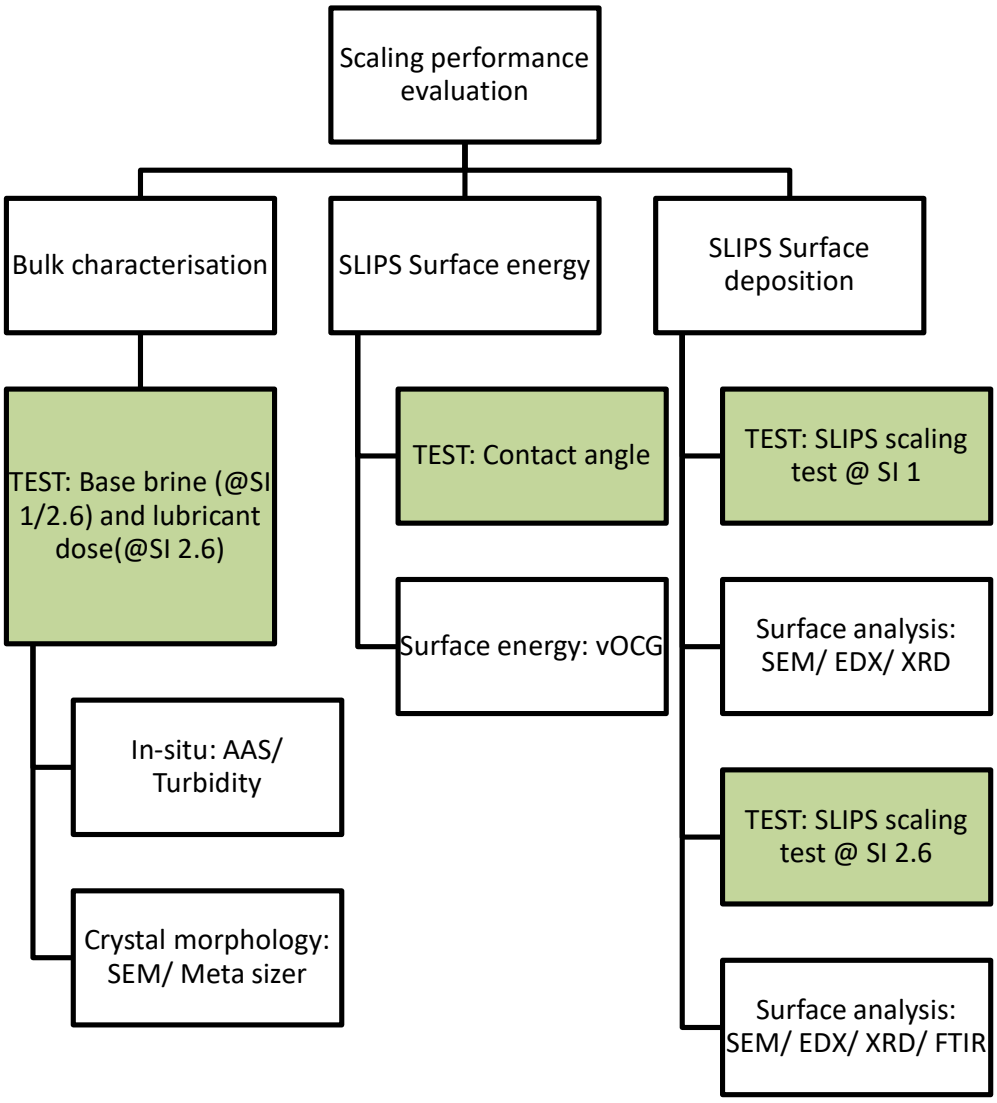

Figure 99 Test matrix for scaling performance evaluation

7.2 Bulk Characterisation of brine systems

This section provides background information on the scaling environment produced from the mixing of the two test brines. It includes crystallisation data on $CaCO_3$ formation in the bulk solution and the influence of any SLIPS lubricant on this system. Analysis of the bulk solutions, for both high (SI 2.6) and low saturation (SI 1) index systems, provides information on precipitation kinetics and allows for the separation of bulk mechanisms from surface scaling phenomena. This provides a baseline picture of how the system will work for future tests where SLIPS samples are submerged in solution. AAS and turbidity techniques have been used for in-situ monitoring of the precipitation reaction and calcium ion concentration respectively. This provides a graphical representation of various stages of the crystallisation process including induction times, nucleation and crystal growth. Post-test analysis of collected precipitates is undertaken via metasizer (for crystal size distribution), SEM (for Calcium carbonate morphology) and XRD (for polymorph type). These techniques provide complementary validation and provide fundamental knowledge on the crystals forming in the bulk vs on the surface.

In-situ characterisation of base brine systems

Initial base line tests provide a point of reference for the scaling system in its natural state and bulk phase (i.e. without the addition of SLIPS lubricants) for comparison to surface deposition tests later on. These tests also provide a level of validity towards the brine compositions and SI predictions from the Multiscale software. Both SI 1 and SI 2.6 brines show the different crystal formation mechanisms associated with a typical low and high scaling regime.

Turbidity measurements map the inorganic scaling process and allow insight into the induction times associated with each brine. After mixing of the brines, the delay between 0 FAU (or no formed crystals) and the first observable measurement is an indication of the induction time. This time is the transition from a supersaturated state without spontaneous nucleation to spontaneous nucleation of the first visible crystals. Turbidity also shows the crystal stages of nucleation and growth. Graphically, the nucleation stage is seen as the time until the turbidity values begin to plateau or the FAU rate reduces. After this,

crystals in the system are generally understood to enter the stage of crystal growth. Typically for a high saturation solution, a short induction time is expected with a sudden increase in turbidity (from rapid precipitation) until a maximum value plateau. Conversely, a lower SI brine would provide a more gradual profile on a turbidity curve.

Figure 100 shows the turbidity profiles of the SI 2.6 and SI 1 brine mixtures at 50°C over 2 hours. As expected, the two brines show distinct differences in the evolution of turbidity within each system. The high scaling system of SI 2.6 shows a rapid increase in turbidity after mixing of the two brines almost instantaneously. Within the first two minutes, the turbidity readings move from an initial starting value of 0 to 350 FAU. A maximum value of 675 FAU is reached at 30 minutes, before a relative plateau that concludes at 656 FAU after 2 hours. The SI 1 system shows a more gradual onset of precipitation, with only light precipitation (FAU <50) occurring for the first 5 minutes and a lower maximum/final value of roughly 200 FAU.

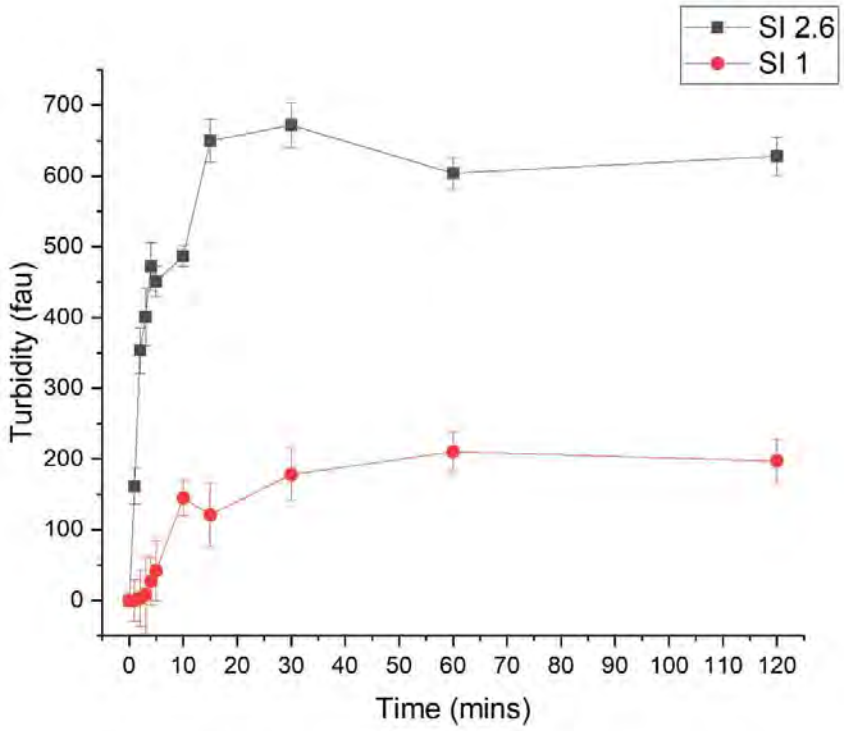

Figure 100 Turbidity values of SI 1 and SI 2.6 over time

High turbidity values in the SI 2.6 system are verified through the visual existence of a cloudy white mixture signalling extensive $CaCO_3$ precipitation. Confirmation is also given by large quantities of white crystal deposits (typically calcite) settling in the beaker. In the SI 1 system these deposits are smaller and are mostly visible in deposits adhering to the side walls of the beaker, as opposed to gravity assisted deposits forming at the bottom. In the SI 2.6 solution induction times are extremely short as crystals precipitate quickly, this is in comparison to the SI 1 solution where the appearance of crystals tends to take longer (however this is also likely due to lower observable concentrations in the system).

AAS analysis reveals the Calcium ion concentration for the duration of the experiment. The consumption of $[Ca^{2+}]$ ions is associated with the formation of $CaCO_3$ particulates in the system. Initial concentration levels are highest during the brine preparation while the $[Ca^{2+}]$ and $[CO_3^{2-}]$ species are yet to react. After mixing the rate of consumption is evident of the precipitation taking place. With the lowest $[Ca^{2+}]$ concentrations expected once the system reaches equilibrium and all $CaCO_3$ has precipitated. The impact of SI, again, will be graphically reflected in the slope of the concentration profile. The stages of nucleation and growth are also highlighted. Systems with higher SIs will react faster, with rapid consumption of $[Ca^{2+}]$ (i.e. a near vertical slope) and the early onset of a minimum concentration plateau. This graphical representation is usually an inverse profile of the curve produced for turbidity.

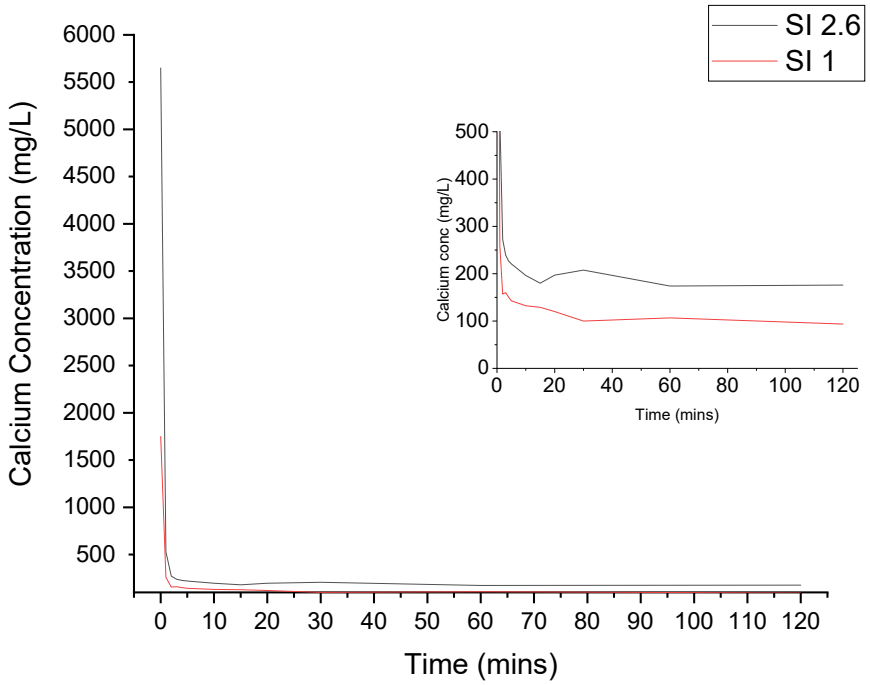

Figure 101 AAS Calcium concentration for SI 1 and SI 2.6 brine

Figure 101 shows a rapid depletion of the calcium concentration associated with the precipitation of calcium carbonate. This decline occurs over a small window of roughly 10 minutes and is observable in both the SI 1 and SI 2.6 brines. Although concentrations are different the curve is similar in nature with an almost vertical depletion followed by an extended plateau. It shows that the majority of calcium ions in these brines are used in the reaction that forms calcium carbonate. The efficiency of this reaction is likely helped using the hexahydrate ($CaCl_2.6H_2O$) form over the anhydrous salt. As the saturation index of both brines is greater than 0, this represents a super saturated solution with regards to equilibrium. As super saturation is a driving force for precipitation, the sudden decrease in calcium concentration is expected. There also appears to be a minimum threshold around 100-200 mg/l where the concentration begins to plateau.

Initial concentrations can be calculated from the amount of $CaCl_2.6H_2O$ added in the original brine composition. At 15g for SI 1 brine and 35g for SI 2.6 brine,

starting concentration before mixing is 2739mg/L and 6400mg/L respectively. There is a disparity between the theoretically calculated and experimentally measured starting concentration with AAS showing results -35% (SI 1) and -11% (SI 2.6). Suggesting there may be errors in machine resolution particularly at lower saturation indexes. Qualitatively the data fits with the expected trends of a super saturated solution and prevailing literature. Both turbidity and AAS are complementary analysis methods and help establish that both brine systems will precipitate calcium carbonate for further scaling tests. Increases in turbidity are in line with decreases in calcium concentration (and hence calcium carbonate precipitation).

Ex-situ characterisation of base brine crystals

After precipitation, calcium carbonate crystals were collected for further characterisation. Crystals were filtered via vacuum pump through Grade 42 filter paper, dried with analysis conducted on particle distribution via metasizer, crystal morphology via SEM and structure via XRD. This has been conducted only for the SI 2.6 brine. This is due to the insufficient precipitation volume created in the SI 1 brine using the same collection methods. However given the only change between the systems is concentration, there is not expected to be any change in the dominant polymorph (Calcite), which is also the most stable. Although there is previous literature that suggests there may be a correlation with saturation and crystal size [299, 300]. Size distribution results are shown in Table 15. Results show that the median Dx(50) value for calcium carbonate crystals precipitate din this system is roughly 17.4 µm. With crystals in the top and bottom 10% percentiles of 8.4 and 31.3 µm respectively.

Table 15 Statistics of distribution for SI 2.6 Calcium carbonate precipitation

	Dx (10)	**Dx (50)**	**Dx (90)**
Size (µm)	8.4	17.4	31.3

SEM images of the calcium carbonate crystals are consistent with the sizes seen in the Mastersizer distribution. Numerous, well-formed crystals are apparent in the 10-20 μm range. In Figure 98a), higher magnification SEM shows smaller crystals < 10 μm and lower magnification in Figure 98b) shows the presence of larger crystals around the 30μm mark. Morphologically, the crystals are trigonal in shape, both small and large crystals. Given the environmental conditions and based on literature, calcite is expected to be the dominant polymorph encountered [301-303]. Observed SEM trigonal structures reinforce this idea, with both vaterite (hexagonal) and aragonite (needle-like) having distinctive dissimilar shapes which are not present.

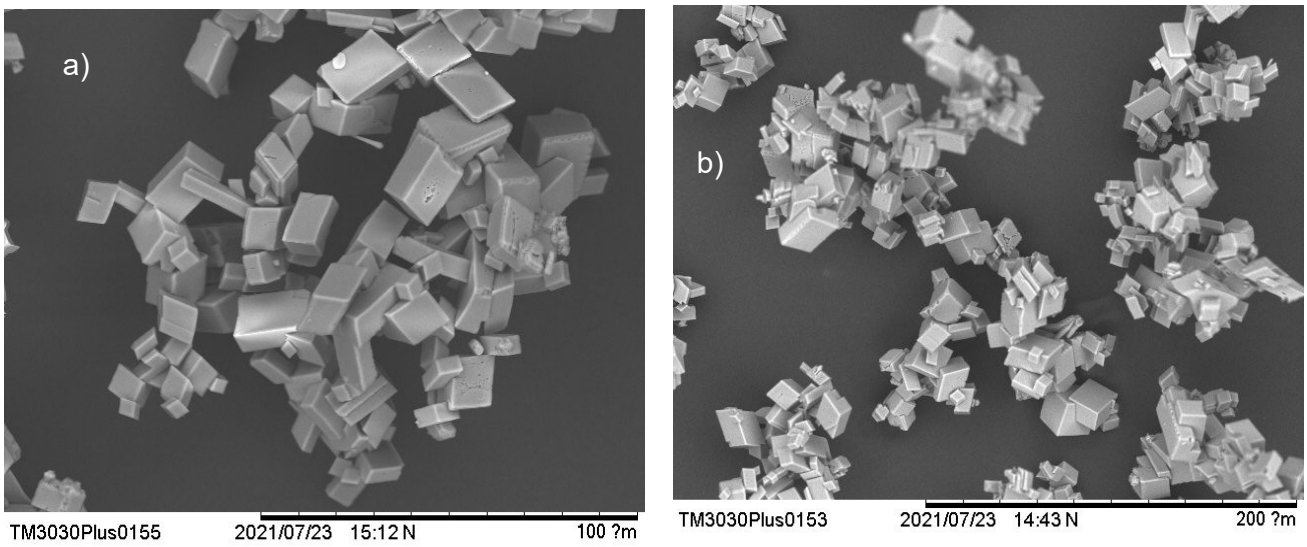

Figure 102 a)/b) SEM image of calcium carbonate precipitate from SI 2.6 brine

X-ray diffraction of the precipitated crystals are shown in Figure 103. The dominant intensity peak at around the 28-30 position is synonymous with the presence of calcite (104) [304-307]. Other smaller intensity peaks for calcite are shown in Figure 103 along the dashed red lines including at 2theta ≈ 36, 39, 43, 47, 49, all of a similar magnitude. The XRD is consistent with the results from the SEM, with the conclusion the dominant calcium carbonate precipitate in this system is calcite.

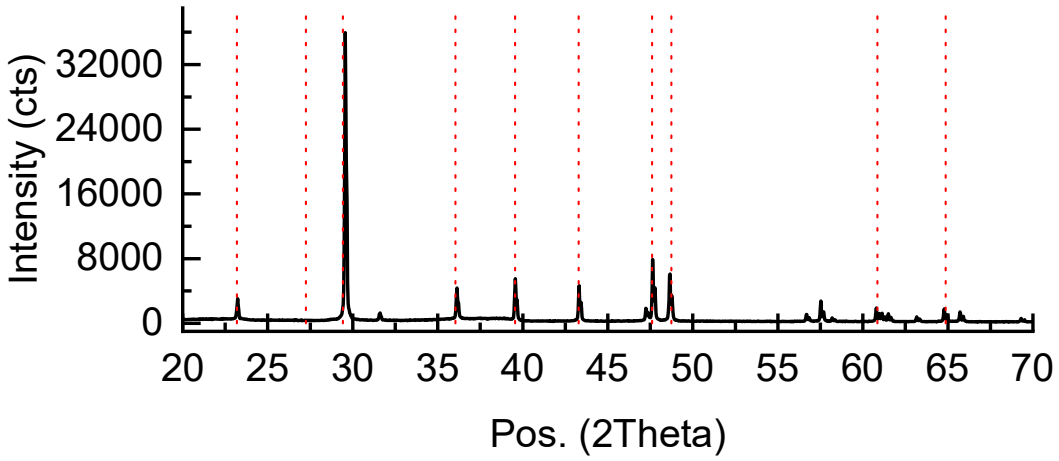

Figure 103 XRD pattern for calcium carbonate precipitate from SI 2.6 brine

Influence of lubricants on SI 2.6 brine system

The potential influence of the lubricants on the precipitation behaviour and crystal morphology occurring in the bulk phase has been studied. Although the focus of this research is surface deposition of scale, this section looks at any potential impacts occurring in the bulk solution of the tested brine for comparison. To understand this, the same test methodology have been used, with the addition of lubricant doses to examine potential interactions occurring in the bulk. However it must be noted that there are some limitations in the effectiveness of this testing. The primary protective mechanism of previous SLIPS incorporating the same lubricants has been that of a physical barrier. Thus scale inhibition has not been a primary driver of protective capability compared to hydrophobicity. Experimentally, the limitations of these lubricants lie in the incompatibility with mixing in solution. As the lubricants are insoluble, they do not mix with the water. Depending on their density they either accumulate by floating on the surface (low density- crude oil) or sinking to the bottom (high density- Kr/ BMIM).

Initially lubricant dosage was conducted at 3 different concentrations: 1, 16 and 200 ppm. The 16-ppm dosage is the rough concentration of the lubricant that would be introduced on a sample in the same test volume. This is

theoretically calculated based on mass gain of the sample (before and after lubrication), known sample surface area and density of the lubricant (assuming uniform thickness of film across sample surface). 1 ppm and 200 ppm were tested as an order of magnitude above and below the normal concentration. The 200ppm dosage simulates an environment closer in likeness to the local surface concentration where the level should be elevated (as lubricant would be infused and held in place by the iron carbonate). These tests (with variable concentration) were only conducted in SI 2.6 with BMIM and Krytox lubricants.

AAS results in Figure 104 show that the initial stages of mixing show rapid nucleation and visual precipitation, which is largely unaffected by lubricant type or concentration compared to normal (non-dosed) test. This is observed through the vertical line on the graph which shows the consumption of Calcium into $CaCO_3$ and a subsequent sudden drop in concentration within the first 5 minutes of mixing. Separation of the curves does not occur until roughly <250 mg\L when the concentration begins to stabilise and plateau. The fluctuations in concentration during the expected period of crystal growth or horizontal plateau (5-120 mins) are likely the result of variations due to calibration/machine errors. These changes of roughly ±15% occur across all tests, with results trending towards more comparable values at the end. The machine requires a calibration for the highest concentration expected (with the initial concentration at roughly 5000mg/L, resolution at the lower end may be less accurate). Increasing concentration of either lubricant does not appear to have any material impact on calcium concentration. Although Krytox at 200ppm seems to trend slightly lower it returns to a more similar range after 120 mins. This increase in bulk concentration is likely attributable to calibration/machine variations rather than dissolution of precipitated $CaCO_3$.

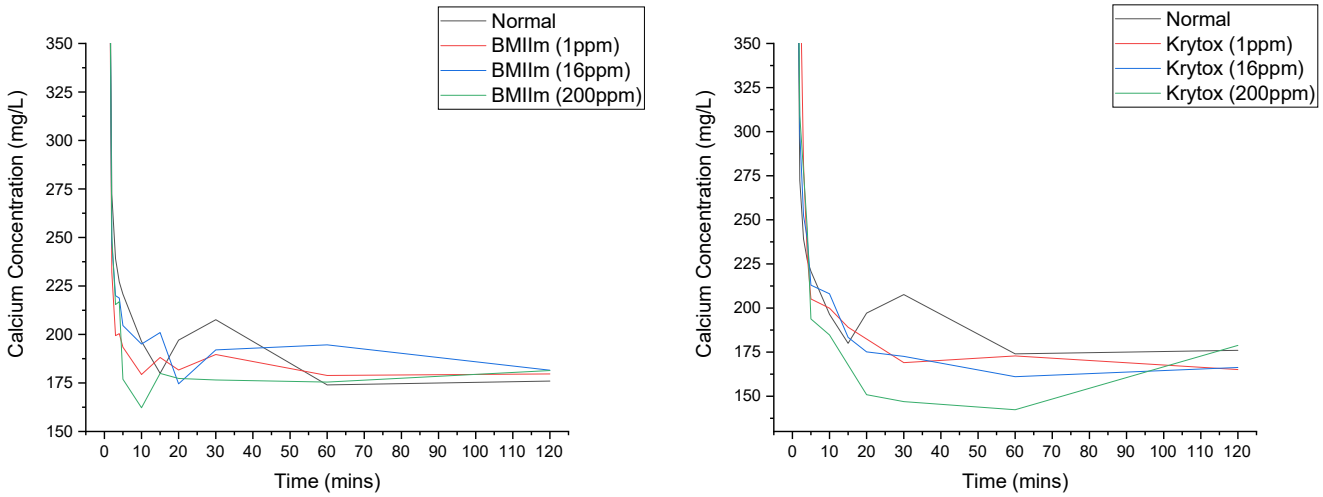

Figure 104 AAS Calcium concentration results for BMIM and Krytox at different concentrations in SI 2.6 brine

Comparison of calcium concentration for the four tested lubricants (200ppm) in SI 2.6 brine is shown in Figure 105. The general trend and calcium concentration levels for dosages across all lubricants appears very similar on the global scale. The inset portion of the graph below 300/mg//l shows a delineation between lubricants that occurs after the 5-minute mark. The lack of variation in the initial stages may be due to experimental process. The brines are mixed then the lubricant is introduced; this is the same process to be used with the infused metal samples. Here the possibility exists that any inhibition/chelating effect does not have time to interreact due to the rapid (vertical) nucleation stages. During the crystal growth or stabilised concentration regime (from 5-120 minutes) there is a minor separation between the lubricants. However the fluctuations are probably an indicator of experimental uncertainty rather than genuine interactions of the lubricant on the concentration. The main noticeable observation being that the non-waxy lubricant appears to have an average drift and final concentration higher than the other lubricants. Overall, based on calcium concentration, there does not appear to be a substantial inhibition/chelation effect of the lubricants on the SI 2.6 brine that was tested.

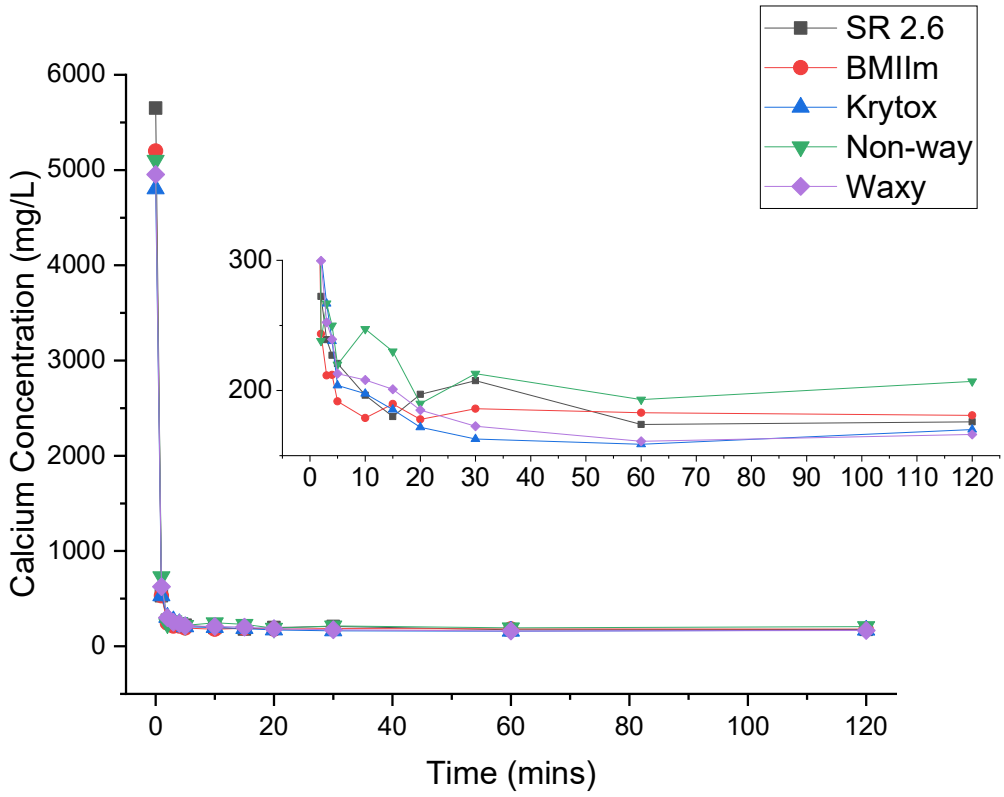

Figure 105 AAS Calcium concentration for SI 2.6 brine with lubricant addition (200ppm). Inset: Magnified scale

A Mastersizer was used to determine lubricant impact on particle size in the SI 2.6 brine. The results are shown in Table 16 and Figure 106 for the four lubricants. For both Krytox and BMIM lubricants, crystal size across all Dx percentiles (i.e. 10,50 and 90) are relatively similar (±1-2μm) to the sizes collected without any lubricant dosage. This suggests similar to the AAS results, that the impact of Krytox and BMIM on the bulk precipitation seems to be minimal. The results of crystal size and calcium concentration being similar in nature to the un-dosed brine mixture support this. The dosage of crude oil lubricants produces a substantial effect on precipitate size. Across all percentiles the crystal size is higher. The difference is more pronounced with the median to higher end of the crystal size range. With Dx(50) and Dx(90) percentiles almost double the size of those previous tests. At the lower end, the crystal sizes are much closer in nature to the base SI 2.6 and Krytox/BMIM

tests, suggesting the impact is not likely an inhibition effect from the crude oil. Inhibition of either nucleation or crystal growth stages would produce a reduction in crystal size, which is not evident. This increase in crystal size distribution may be the result of the formation of Pickering emulsions [308]. These have been encountered in water/oil emulsions with calcium carbonate and occurs as oil droplets attract the precipitate given the nature of calcite to be oil wet [309-311]. This could lead to the formation of crystal clusters/agglomerations that may result in the elevated crystal sizes, particularly towards the higher end. All samples were exposed to the same wet dispersion methods in the Mastersizer.

Table 16 Mastersizer results of crystal sizer per lubricant

Lubricant	**Size (µm)**		
	Dx (10)	**Dx (50)**	**Dx (90)**
Krytox	6.87	15.7	30.1
BMIM	8.16	16.3	28.4
Waxy crude	13.8	33.1	69.7
Non-way crude	14.5	31.6	61

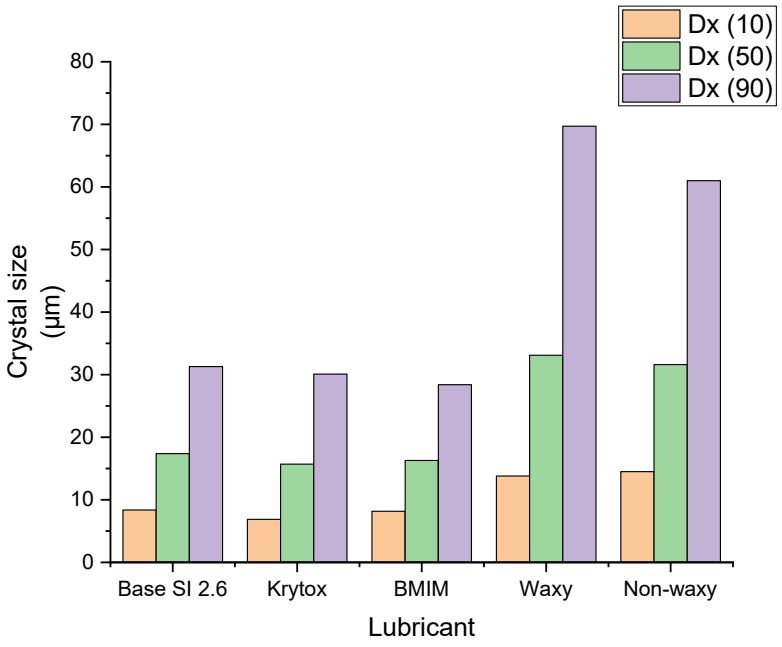

Figure 106 Comparison of crystal size per lubricant in SI 2.6 brine

SEM images of powders have been taken to examine the impact of lubricants and validate other analysis techniques. Figure 107-105 show the powder SEM images taken from BMIM, Krytox, Non-waxy and Waxy tests respectively. Across all tests, various standard crystal shapes are observed with rhombohedral, cubic and trigonal being the more commonly encountered. Generally, crystals were fully formed (not amorphous calcium carbonate-ACC) and individual, however occurrences of crystal twinning and parallel growth are scattered throughout samples irrespective of lubricant used. Based on shape alone there does not appear to be a material impact from the dosage of lubricants. Although there is variation in shapes and polymorphs, this distribution of shapes is generally in line with those encountered in the non-dosed samples (excluding the presence of aragonite). Crystals do not appear to exhibit the effects of inhibition on either nucleation or crystal growth stages. Features associated with such effects including curved crystal edges/planes, porosity and irregular/stepped crystal faces are not apparent.

Based on visual assessment, the majority of crystals appear to be calcite polymorphs, similar in nature to those crystals encountered in the un-dosed

samples. Although calcite is the dominant polymorph, thin needle-like flowers/clusters were also identified in samples where the lubricant was crude oil. These crystals are generally associated with aragonite polymorphs and were up to 40μm in length (Figure 105) [312, 313]. The reaction to precipitate $CaCO_3$ from dissolved Na_2CO_3 and $CaCl_2$ has been studied extensively, with calcite being the primary polymorph synthesized [314]. However it is not unexpected that aragonite forms due to the simultaneous mixing of the brines used experimentally and the possible presence of trace elements of magnesium in the crude oil (that favor aragonite formation) [315-318]. Polymorph type is confirmed with XRD analysis which is outlined further on.

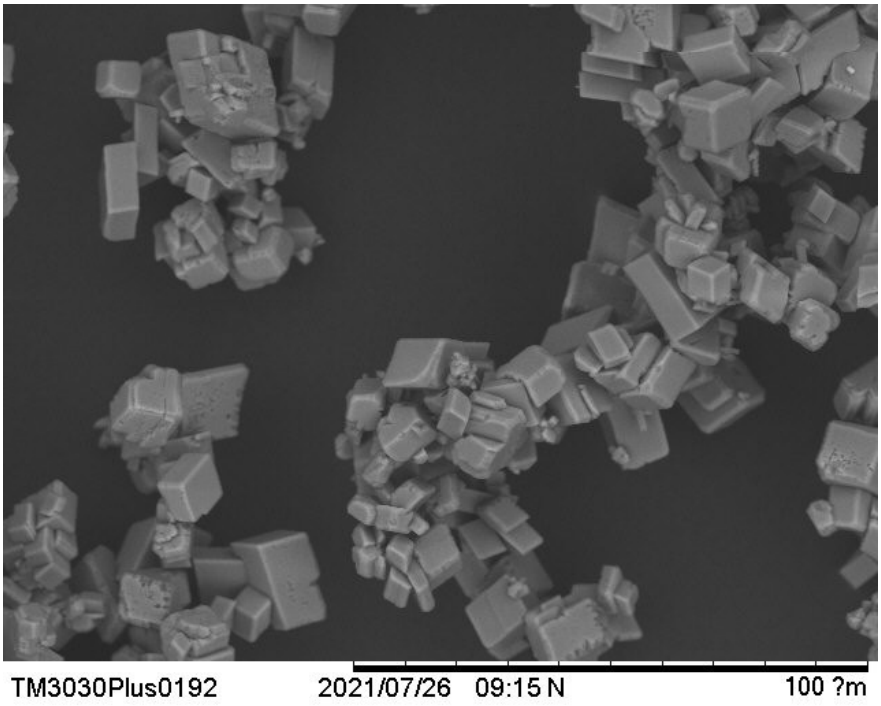

Figure 107 SEM image of crystals from BMIM dosage

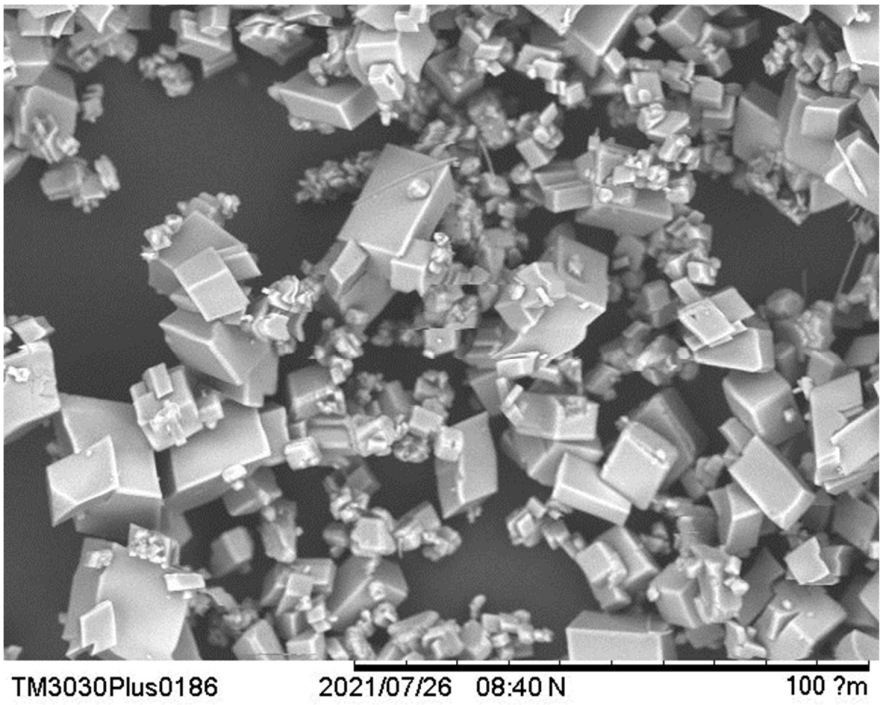

Figure 108 SEM image of crystals from Krytox dosage

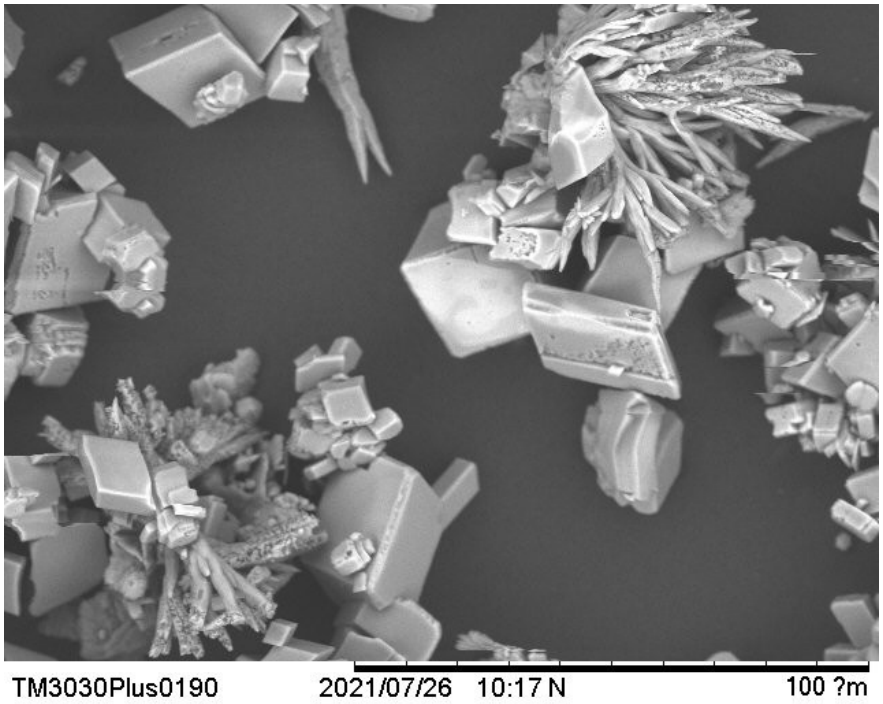

Figure 109 SEM image of crystals from Non-waxy crude dosage. Note: Aragonite flower/clusters

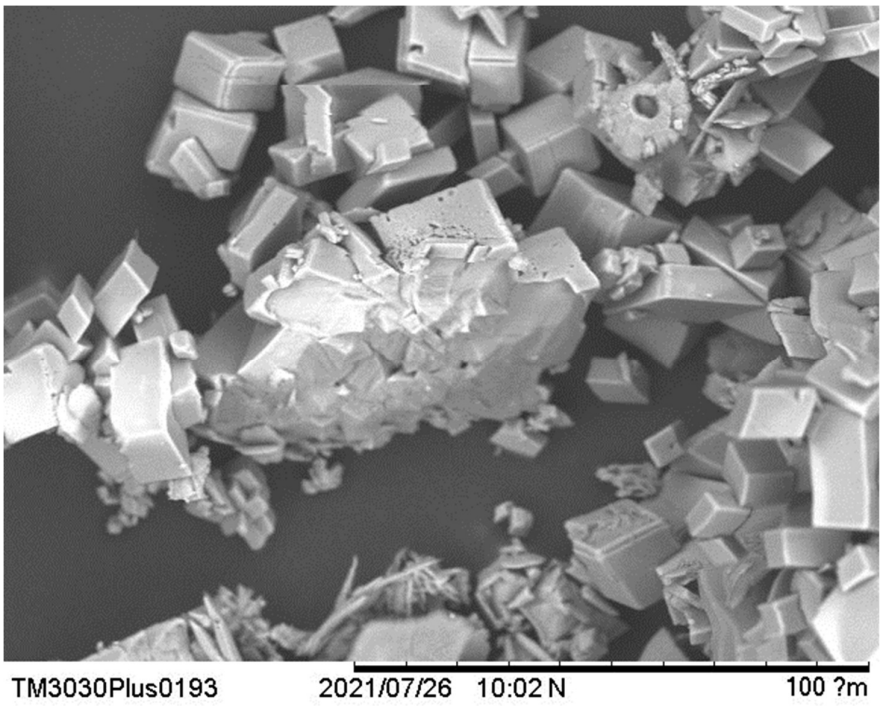

Figure 110 SEM image of crystals from Waxy crude dosage. Note: Aragonite flower/clusters

In terms of crystal size, SEM images visually support size distributions obtained from the Mastersizer (Figure 111). A wide assortment of sizes are observed from 5-40 μm, which is the primary range indicated from the distribution. Comparison between the Krytox/BMIM vs Waxy/Non-waxy crude oils show a distinct difference in average size, with a larger proportion of crystals in the 20-40 μm band. This correlates well with the increase in the Dx(50)/ median size seen when moving from non-crude oil to crude oil (CO) lubricants. The larger crystal sizes (>60 μm) which form the Dx(90) percentile are also seen in these crude oil dosed samples as seen in Figure 110. It seems these crystals are not clustered together in an agglomeration but seem to have an amorphous centre with crystalline shapes on the exterior. There also appears to be a greater distribution of smaller crystals (<5 μm) in the Krytox sample (Figure 111 b) that don't seem to have impacted the size distribution.

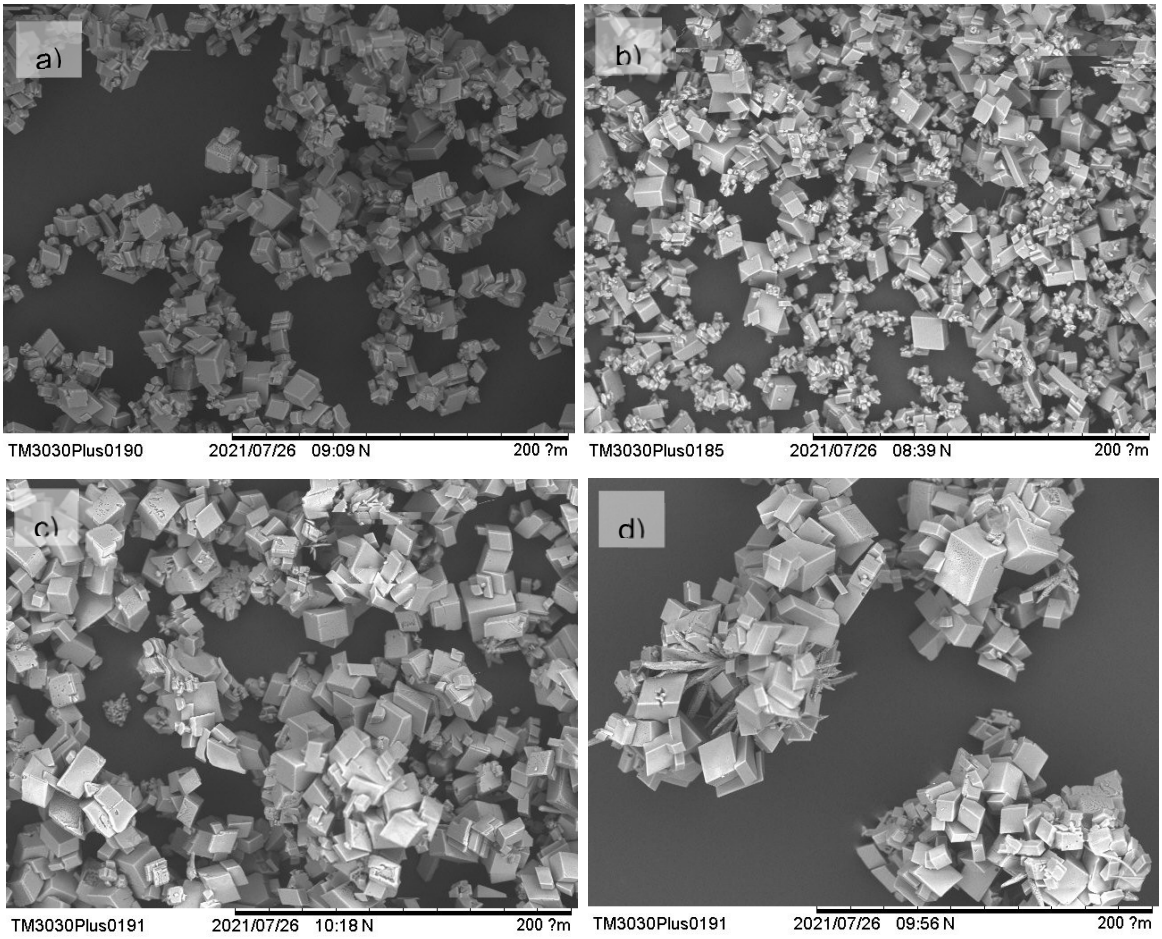

Figure 111 SEM images of crystals dosed with a) BMIM, b) Krytox, c) Non-waxy CO, d) Waxy CO

XRD data has been taken from the powders and this is shown in Figure 112. The largest intensity peak across all powders occurs in the 28-30 2theta position associated with the (104) face of calcite. Again, other intensity peaks for calcite are shown in dashed red lines. This correlates well with the SEM images, which show that the dominant crystal encountered is the calcite polymorph of $CaCO_3$. This is again expected given the most stable form of $CaCO_3$ is Calcite. In the samples dosed with CO the presence of aragonite has been visually observed and the XRD patterns are slightly different to those of BMIM/Krytox. In Figure 112 C and D, calcite peaks are smaller and there are distinct peaks around the 26.5 and 46 2Theta positions. These peaks are

commonly associated with Aragonite and the (111) and (221) faces respectively [319-321].

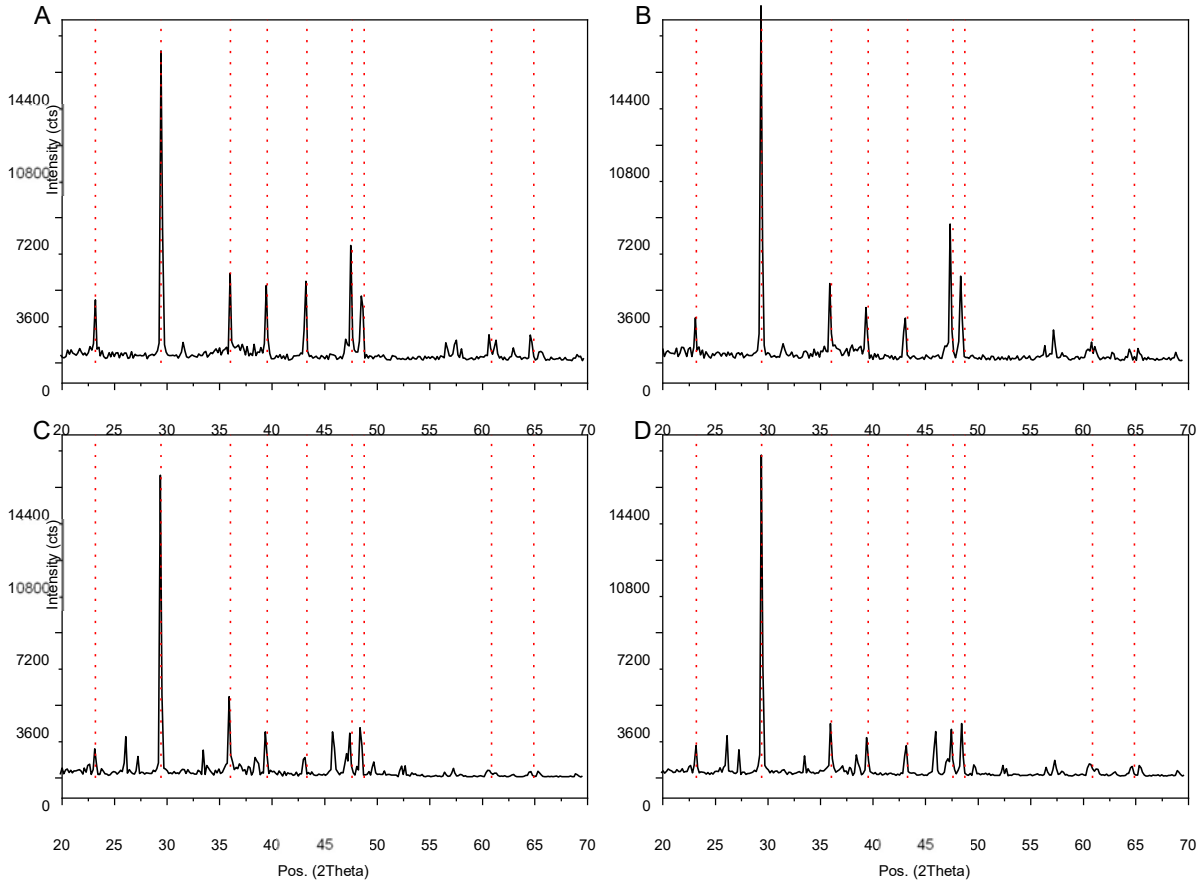

Figure 112 XRD patterns of powders: A) BMIM B) Krytox C) Non-waxy CO, D) Waxy CO

7.3 Summary

The brine system to be used in the scaling performance evaluation of SLIPS has been characterised through a number of techniques. The purpose of this is to provide information on the bulk phase through two questions:

1. What type of global/bulk scaling environment will the SLIPS samples be tested in (i.e. kinetics, crystal type, size etc)?
2. What impacts, if any, do the lubricants have on bulk scaling (i.e. kinetics, crystal type, size etc)?

Although SLIPS are primarily used as a surface mitigation method for scaling deposition, it is important to understand what occurs in the bulk phase. This insight helps to potentially predict what might be expected on the surface during the SLIPS tests and differentiate scaling mechanisms such as surface nucleation vs adhesion.

Two distinct types of scaling environments will be tested simulating a high and low saturation index of SI 2.6 and SI 1 respectively. Although the quantity of $CaCO_3$ in the system will be different across the two brines, the dominant polymorph is expected to be calcite. The influence of the lubricants on the precipitation kinetics and final crystal morphology/size in SI 2.6 has been observed. Through AAS, consumption of calcium (precipitation of $CaCO_3$) is largely unaffected by the presence of lubricant. While there is minor differences during the crystal growth (plateau) stage, behaviour is dominated by the high saturation index rather than influence of lubricant. In other analysis, Metasizer data shows that crystal size can be influenced by lubricant dosage. With both Non-waxy and waxy crude oils producing larger crystals on average, supported by SEM imaging. The main polymorph encountered with the addition of lubricants is still calcite although crude oils show the presence of aragonite also. However whether this is the result of the lubricant or mixing method is uncertain.

Overall the presence of the lubricants does not have a material impact on the formation of bulk phase crystals (excluding size). It is expected that the primary scale deposits on the tested SLIPS will be calcite, primarily in a range from 6-60 µm in size. Any inhibitive effect in the bulk is minor and therefore it would be assumed the primary driver of any SLIPS anti-scaling capacity would be that of a physical barrier, between the surface and surrounding environment. Or the possibility the concentrations tested are not sufficiently high enough to produce the effects seen at the near surface.

7.4 Surface Energy of SLIPS

In this section, the surface free energy (SFE) of the fabricated SLIPS has been calculated. As mentioned in the literature review, there are two dominant physical parameters that influence the scaling potential of a substrate, surface

energy and surface roughness. With regards to SLIPS, roughness is usually an assumed surface characteristic that imparts beneficial anti scaling properties. This assumption is based on the infused layer presenting as the anatomically smooth top film of a static body of fluid [322]. This smoothness is generally associate with improved anti scaling performance by reducing the potential contact area, especially with regards to adhesion of scale species. Although it must be noted with regards to the deposition of scale the influence of roughness is not as certain [212]. Validating this assumption and the smoothness of SLIPS can be difficult given the impracticality of measuring the roughness of liquids (especially transparent ones) and has fallen outside the scope of this study. Primarily the focus of comparison between SLIPS variants is usually performed on the basis of surface energy and hydrophobicity.

The method for calculating SFE values utilises an optical tensiometer. This is used to measure the contact angle of probe liquids (with differing but known surface energy properties) dropped on the targeted surface. In this case the targeted surface is the SLIPS being tested and the 3 probe liquids are diiodomethane, ethylene glycol and de-ionised water. From the contact angle results, the Van Oss-Good-Chaudhury (vOCG) method has been used to theoretically predict the SFE. The method is further explained in the experimental methodology section with the SFE consisting of a Lifshitz van der Waal (LW)/dispersive component and an acid-base (AB)/polar component, as per Equation 27. The values for untreated/bare carbon steel (X65) and the fabricated iron carbonate ($FeCO_3$) layer have been calculated and reviewed in the Chapter 6. The purpose of calculating the surface energy is to provide a framework for comparing SLIPS based on physical properties. This will also provide insight into what may be expected during scale testing based on prevailing literature/theory on surface features and scaling potential.

$$\gamma_{vocg} = \gamma^{LW} + \gamma^{AB}$$

Equation 27

The results of the tensiometer tests are provided in Figure 113. This includes average contact angles for each of the 3 probe liquids across all 6 samples. For the test, both DI water and Ethylene glycol are polar liquids, whilst Diiodomethane is used as an apolar probe liquid, properties are found in Table 17. Contact angles range from close to 0˚ with the highest result collected at 98˚. Across the probe liquids, DI water generates the highest contact angle in each sample, apart from SLIPS BMIM where it is the lowest. Given the high surface tension (relative to other probe liquids), the higher values are not unexpected. Ethylene glycol and Diiodomethane have similar surface tension values, although one is polar and the latter dispersive. The disparity between probe liquids is smallest on the SLIPS Kr sample and largest for the SLIPS NW sample. There does not appear to be a distinct difference between the data collected from the dry metal samples as opposed to the wetted SLIPS sample.

Table 17 Probe test liquid surface energy properties

Probe liquid	γ_T (mN/m)	γ_{LW} (mN/m)	γ_+ (mN/m)	γ_- (mN/m)
Diiodomethane	50.8	50.8	0	0
Ethylene glycol	48	29	1.92	47
DI water	72.8	21.8	25.5	25.5

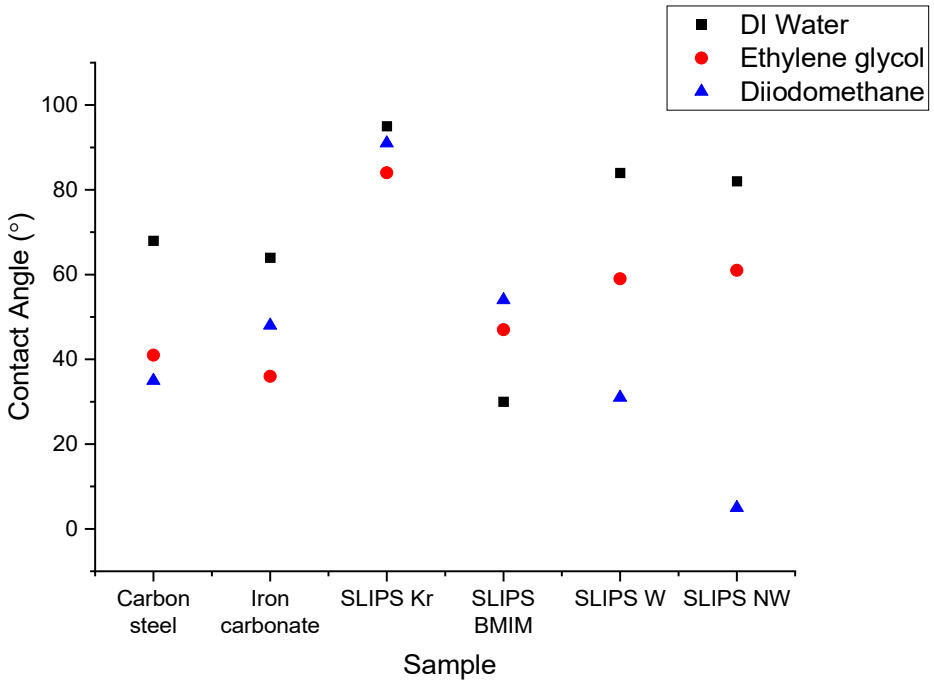

Figure 113 Contact angle of probe test liquids on samples

Figure 114 shows specifically the water contact angle (WCA) for the 6 samples. WCA is a simple indicator that can show the hydrophobicity (>90˚ WCA) or hydrophilicity (<90˚ WCA) of a surface [323]. In this case its ability to attract or repel water that may be carrying calcium carbonate ($CaCO_3$) or other scaling deposits. Hydrophobicity is defined as a WCA > 90˚ and in these tests only the SLIPS Kr (96˚) can be defined as hydrophobic. Although both SLIPS W and SLIPS NW are close at >80˚. The addition of lubricant appears to reduce hydrophilicity of the underlying surface based on comparison to the uncoated carbon steel and $FeCO_3$ samples. Given that lubricants are initially selected based on immiscibility with water, this is understandable. However the SLIPS BMIM wetting behaviour is quite different to the other samples, showing substantially higher hydrophilicity and a low WCA (30˚) compared to the other SLIPS.

Generally the WCA behaviour and results are in line with trends and data seen in the literature [324-327]. In the context of this study, the best performing lubricant from the literature (Krytox) has shown WCA up to 155˚ [328], much

greater than achieved here . This type of surface is usually classified as superhydrophobic (>145˚). Whether the addition of lubricant increases or decreases hydrophobicity or water repellence is usually dependent on the initial state of the substrate. Surfaces that originally show low WCA usually experience an increase in the WCA (or improved water repellence) with the addition of lubricant (regardless of choice) and vice versa. The addition of Krytox to a surface usually retains a hydrophobic state (>90˚), which is very different from BMIM infusion. As said before, the infusion of lubricant usually improves repellence from a low start, even in the case of BMIM. However BMIM rarely shifts the resulting surface from a hydrophilic to hydrophobic state. The result being that ionic liquid infused surfaces generally achieve WCA <90˚ [245, 329-331]. SLIPS infused with crude oil are a very rare occurrence in the literature and the data present is related to surface wettability of oil and gas pipelines. It is important to note that the experimental method to measure WCA here is different and is taken in an inverted position submerged in the crude oil/lubricant (as opposed to air) [332, 333]. However the result is similar, with the immersion of the sample into the crude oil acting to pre-wet the surface with a film before water droplet addition. The water in oil method mentioned usually produces WCA that support a hydrophilic state [334]. With the presence of higher wax content leading to potentially higher WCA compared to those crude oils with less [335].

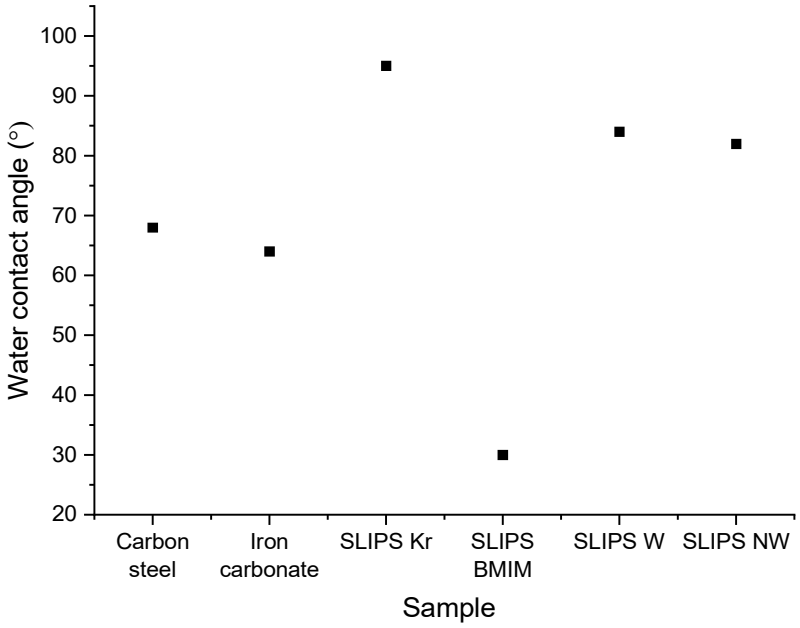

Figure 114 Water contact angle (WCA) on tested samples

Using the collected contact angle data, surface energy components have been calculated using vOCG theory. This provides a total surface energy value that is comprised of a dispersive component (DS) and an acid-base (AB) component. Figure 115 shows both SFE components and the cumulative total SFE value, noted at the top of each column, for each sample. Across all samples, surface energy is dominated by the dispersive force, which make up the majority of interactions compared to the acid-base or polar component. This ratio is highest for SLIPS W and lowest for the iron carbonate sample. Given the non-polar nature of these groups i.e. metal alloys [336, 337], Krytox compounds [338, 339], ionic liquids [340] and hydrocarbons [341-343] this behaviour is to be expected.

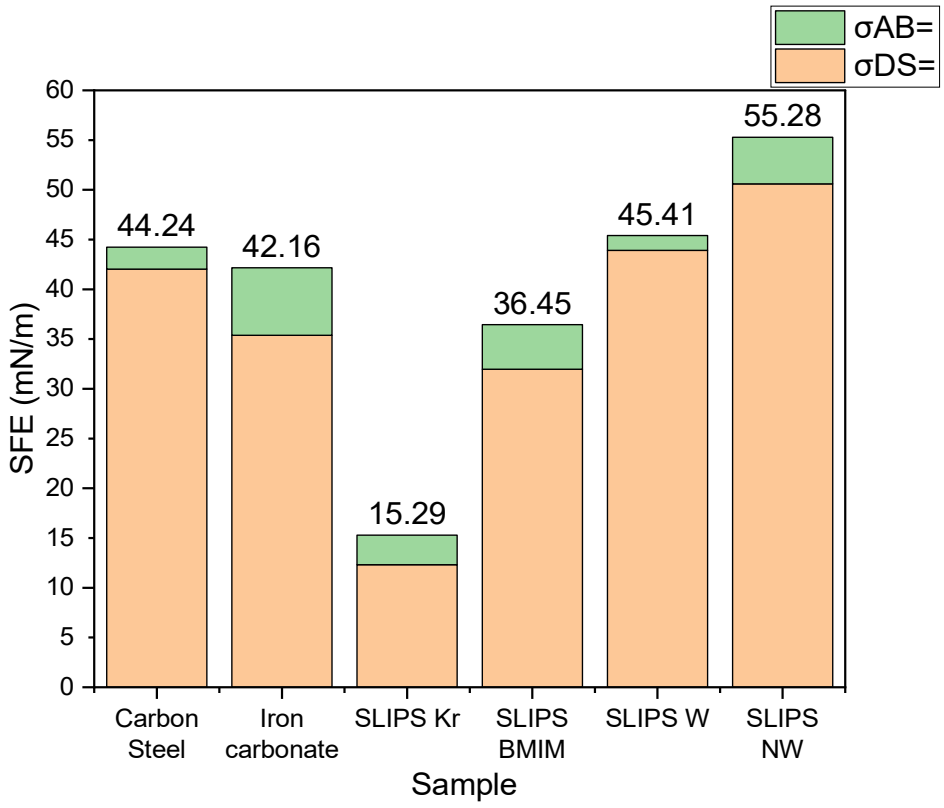

Figure 115 Calculated vOCG surface energy components of tested samples

In comparison of total SFE values, the lowest value obtained is ≈15mN/m using Krytox as a lubricant. This is a substantial change in the SFE compared to the underlying substrates of steel or $FeCO_3$ (44 mN/m and 42 mN/m, respectively). For SLIPS BMIM, the surface energy is also lower than the base $FeCO_3$. In the case of both crude oil SLIPS, surface energy values are higher with the SLIPS NW having the highest value calculated (55 mN/m). When related to WCA, lower surface energies are linked with higher contact angles (or increased hydrophobicity/ decreased hydrophilicity) as the water droplet has an affinity to itself rather than wetting the surface. For the SLIPS Kr sample we see this low SFE corresponds well to the hydrophobic state the WCA shows. Similarly, the WCA and surface SFE of the 2 metallic surfaces and crude oil SLIPS appear in a similar range as one another. SLIPS BMIM goes against this trend with a low WCA compared to the other samples, but a

SFE within the same range showing wetting behaviour is not always indicative to surface energy values.

Calculated SFE values can also be compared for validity with surface energy values of the lubricants themselves. Although it should be noted that manufacturers may not mention the method employed to generate the value or the method may be different to that used here. For both the BMIM and Krytox compounds, published values are 17 mN/m and 34 mN/m, respectively [344]. This compares well with the SFE results obtained here falling within a 10% range. In the case of the crude oil, surface energy is not a useful property collected by Oil companies and is very specific to the field etc. The values fall in a realistic range to that reported in the literature; the data given by the operators for the crude oils show a blend of different fields [345-347]. The API values of the Crude oils used for the SLIPS samples here range between 22-35˚, with 25-35 considered a medium crude, <25 heavy and >35 light. From the literature, lower API or heavier crude oils are associated with higher SFE values compared to higher API/ lighter crudes [348, 349]. The SLIPS NW is a slightly heavier crude in terms of API (as it has a component of an API 22 oil in the blend), thus its slightly higher calculated SFE value over the Waxy crude is reasonable.

Considering the results obtained in this section and established trends found in literature, inferences may be made into predicting the outcome of scaling performance of the SLIPS samples. From the perspective of hydrophobicity, the most hydrophobic surface would be assumed to produce the better results given the nature of the surface in repelling brine carrying aqueous droplets. In this case SLIPS Kr would be expected to perform well. On the other hand, the increased wetting behaviour of the SLIPS BMIM might indicate poorer scaling properties. With regards to SFE, the lowest SFE and outlier is again linked to SLIPS Kr and it would be assumed to perform better than the other samples. The rest of the samples being comparable in value would be expected to reflect this in analogous scaling performance. One final point of interest is that as SFE figures trend towards that of the lubricants themselves suggests SLIPS take on the properties of those lubricants. However given that WCA can change drastically across different underlying substrates with the same lubricant suggests there remains a texture or lubricant thickness dependence.

7.5 SLIPS scale deposition

Introduction

The previous chapter explored the construction of a stable SLIPS based on an $FeCO_3$ derived corrosion layer. This section focuses on the anti-fouling performance of the SLIPS with regards to inorganic scale (i.e crystals other than $FeCO_3$). The capabilities have been evaluated in a brine system where the dominant scale species that precipitates is calcium carbonate ($CaCO_3$). $CaCO_3$ is a common mineral scale encountered across many industries, including the Oil and Gas sector where it is prevalent. It's presence, often appearing as surface deposits, can cause flow assurance issues with sever safety and economic consequences. Surface engineering is one solution and SLIPS present a novel innovation in the field that deals with fouling build-up at the surface level (as opposed to the bulk).

Testing conditions have been constructed to simulate both a high scaling environment with a saturation index (SI) of 2.6 and a low scaling environment of SI 1. This is not representative of any field in particular and only provides results for a single-phase system (aqueous). The performance of the SLIPS has been evaluated through analysis of $CaCO_3$ deposits and surface trace elements of the remaining lubricant. The four lubricants tested are perfluorinated vacuum oil (Krytox), ionic liquid (BMIM) and two crude oils. The crude oils are denoted by the presence of paraffins, either with (waxy) or without (non-waxy). The capability of the SLIPS systems in relation to fouling performance is associated with links to SLIPS compatibility, physical lubricant properties and SLIPS surface energy.

Figure 116 provides an outline of how the chapter is structured. Scaling tests are performed for the different SLIPS and blank (i.e. carbon steel) specimens to evaluate crystal surface deposits. Surface analysis includes SEM for crystal morphology and size. EDX has been used for Ca wt.% and to determine lubricant trace elements, this has been used in conjunction with FTIR. FTIR provides a clearer picture with respect to crude oil lubricants (detecting carbon chains in hydrocarbons). Finally XRD provides information on the crystal structure of surface deposits. In particular the iron calcium carbonate ($Fe_xCa_yCO_3$) structure is of note, with the degree of calcium incorporation into

the underlying $FeCO_3$ layer reflecting the effectiveness of the lubricant barrier and fouling performance.

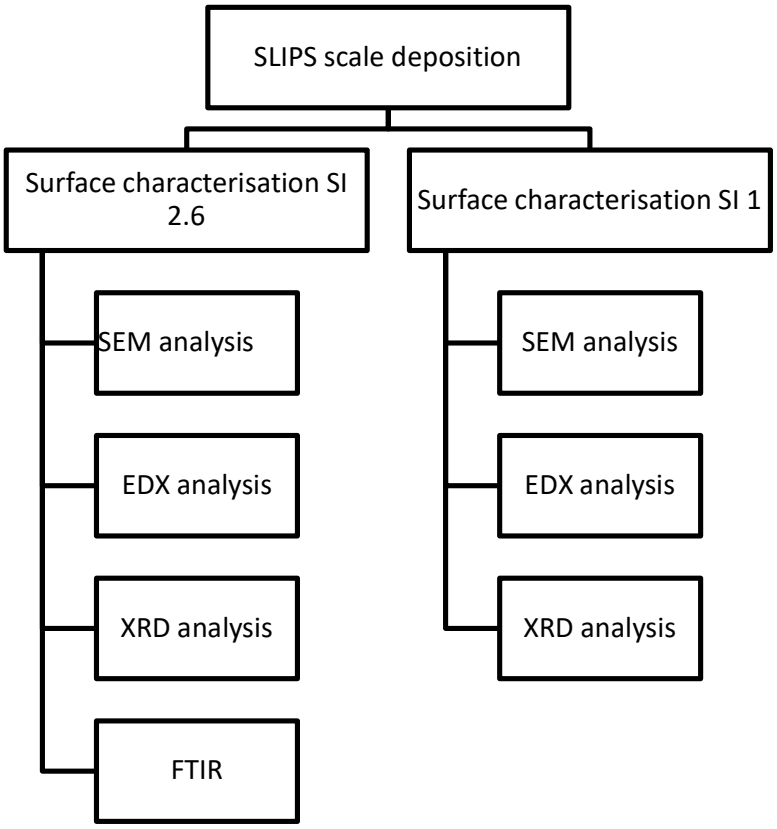

Figure 116 Experimental analysis matrix of surface scale deposits post-test

7.6 Surface Characterisation of Samples in SI 2.6 brine

The scaling tests run at Saturation Index 2.6 are the equivalent of an aggressive and extreme scaling system. In this environment the induction time is low and the concentration/mass of scale/crystals in the bulk is large.

SEM Analysis of Scale Deposits

SEM images have been taken to better examine the surface scale deposits occurring on the test samples. From here scale morphology and size can be determined, along with other physical details of the surface topography. Images have been taken from one of two machines. With the number denoting the SEM used: 1. Hitachi tabletop TM3030Plus and 2. Carl Zeiss EVO MA15.

1. X65 Carbon Steel (CS)

The CS sample was used as an experimental control to represent the untreated original substrate of the SLIPS created. This would be the equivalent of the internal surface of a typical in-service pipeline. The typical results as per SEM (Figure 117-114) show substantial build-up of scale on the sample. As per the preliminary tests in the bulk, from this brine system the expected scale deposit is calcium carbonate ($CaCO_3$) and generally of the polymorph calcite. Based on SEM, crystals generally appear as a rhombohedral/ cubic shape with large, flat crystal faces. XRD results are used to confirm polymorph (Section 7.8), but visually resemble calcite as expected. Crystal size tends to vary within the range of 1-10 µm, with denser crystal groups appearing as lines as opposed to amorphous clusters (which reinforces importance of topography). Where the underlying CS is exposed, it appears with a pockmarked pattern indicating minor corrosion of the steel with the carbide visible (Figure 117, Figure 118, Figure 119). The deposition process (with regards to distribution) tends to be similar to that of iron carbonate ($FeCO_3$) with the crystals tending to be deposited in parallel lines (Figure 118) which tend to match the valleys/peaks left from the polishing process.

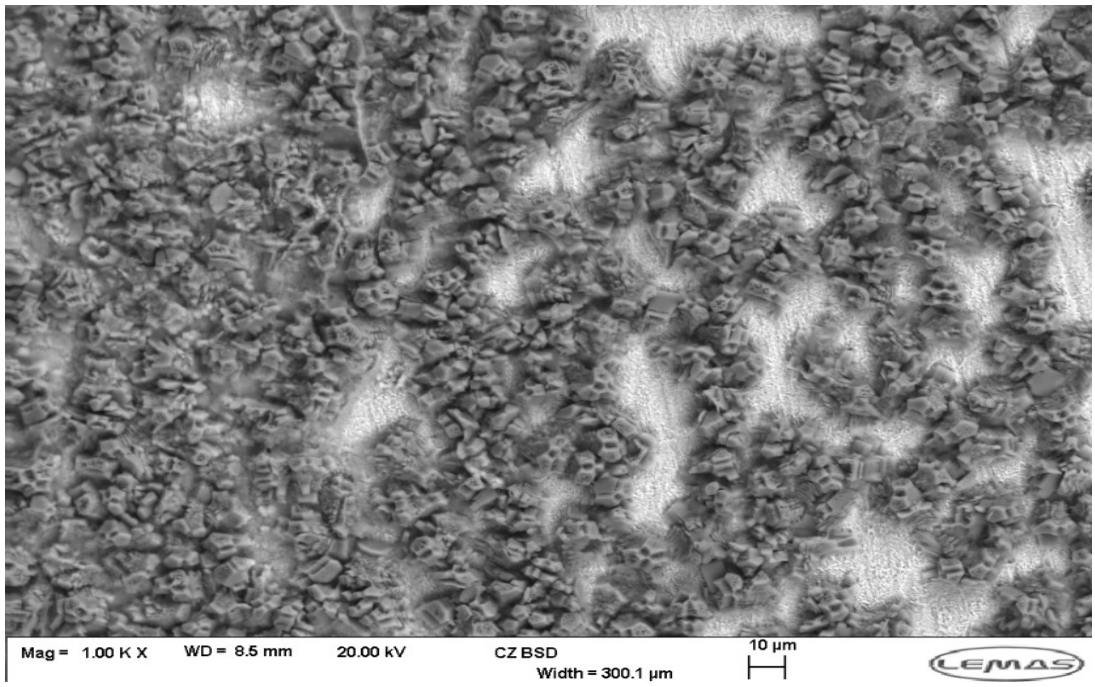

Figure 117 1000x magnification SEM (2) image X65 CS sample with $CaCO_3$ scale deposits (darker contrast)

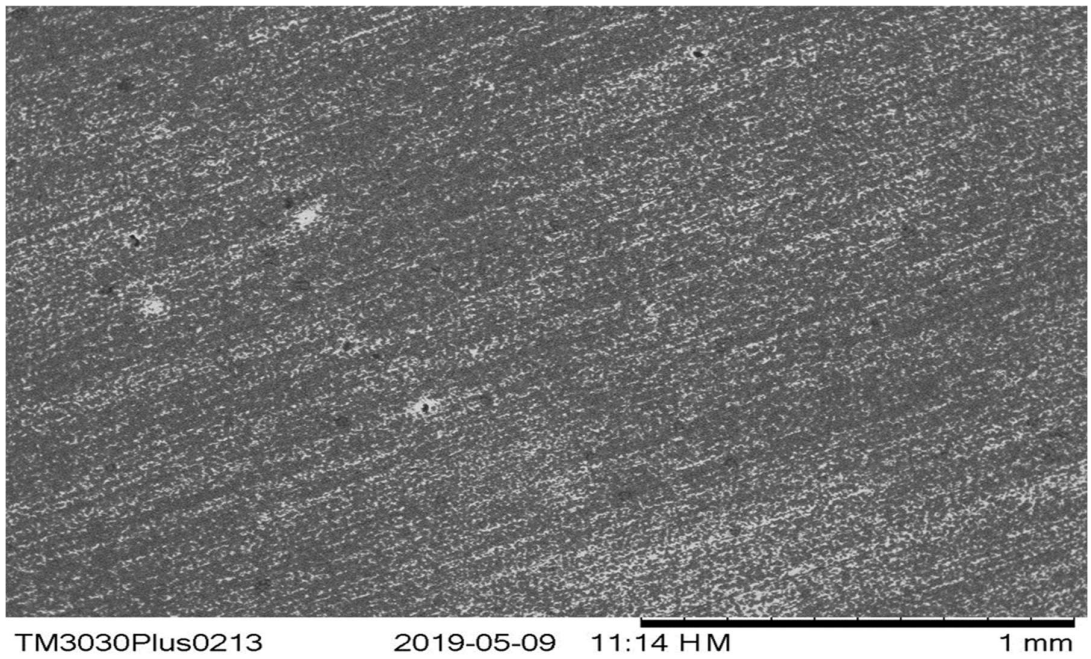

Figure 118 SEM (1) image X65 CS sample with $CaCO_3$ scale deposits showing parallel striations (darker contrast)

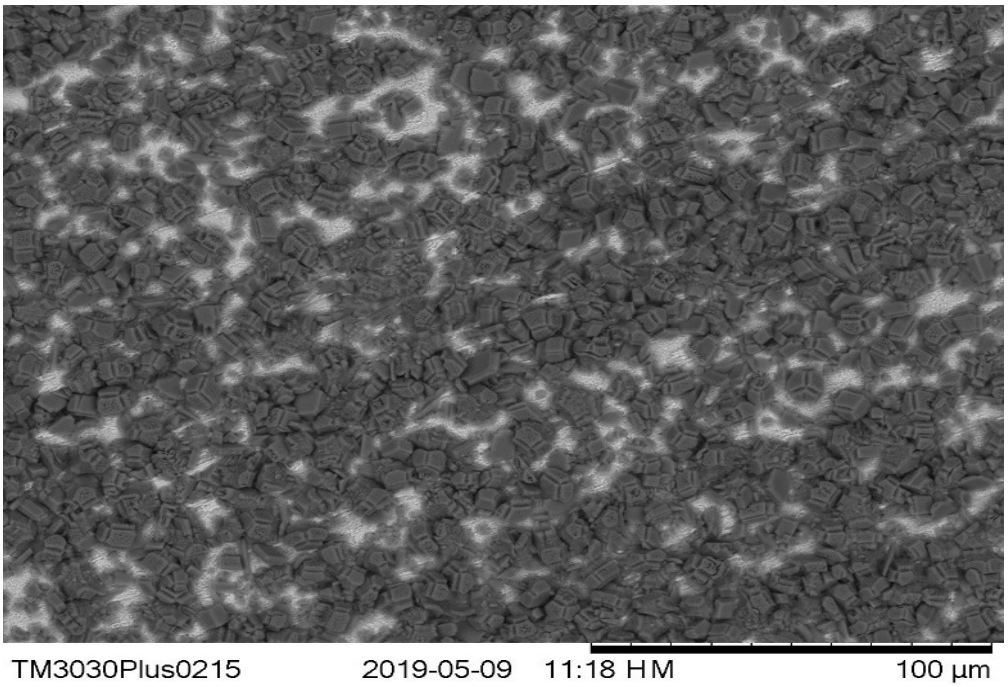

Figure 119 SEM (1) image X65 CS sample with $CaCO_3$ scale deposits (darker contrast)

2. Iron carbonate ($FeCO_3$)

The $FeCO_3$ is fabricated on the CS sample to provide a layer for the lubricant to infuse into and is the base layer of all the SLIPS combinations tested. Physically this sample would represent the inside of a pipeline that has already undergone some form of CO_2 corrosion. Typical SEM images of scale coverage on samples indicates a severe layer of scaling across the surface (Figure 120-117), with limited areas of the underlying $FeCO_3$ layer apparent. Again crystal morphology is similar to that expected from calcite crystals with cubic/ rhombohedral structures evident, although there are variations. Crystals in Figure 120 tend to have slender, plate like crystals with planar faces as opposed to Figure 121 where crystals are less cubic (more rhombohedral). Crystal size ranges from 1-10 µm, with a larger number of crystals in the 10-15 µm range compared to the X65 CS sample. Where the underlying $FeCO_3$ can be seen, the crystals tend to show as more porous than those of the $CaCO_3$ crystals (Figure 122). Given the random topographical nature of the $FeCO_3$ layer, the scale deposition does not show indications of the underlying surface like that of the X65 CS sample (i.e striations).

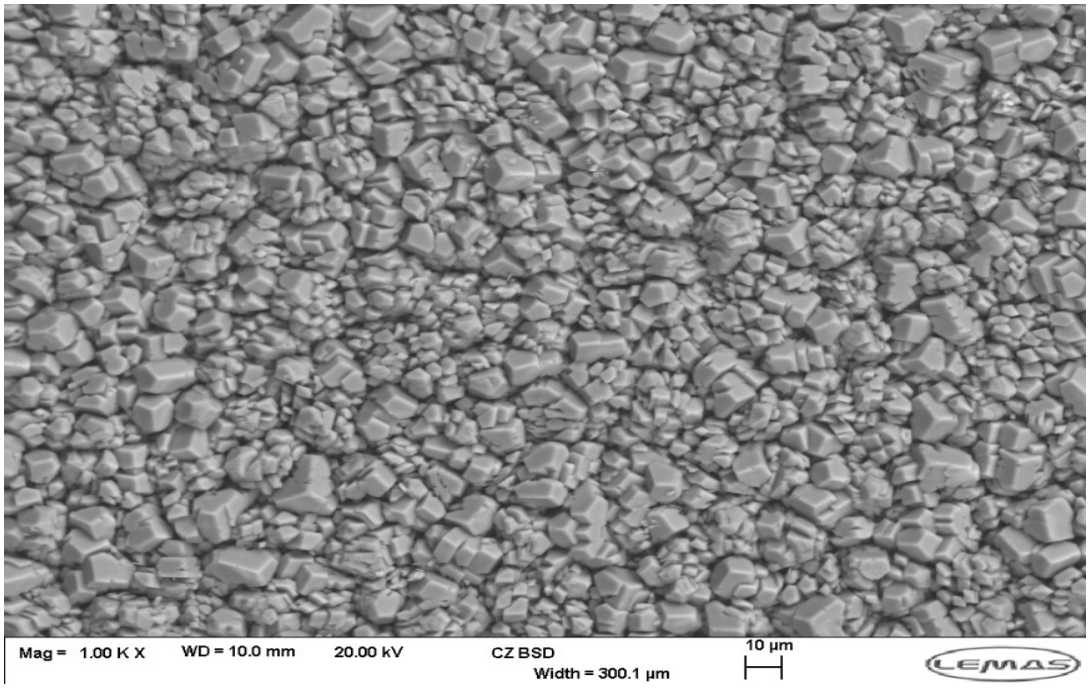

Figure 120 SEM (2) image of $FeCO_3$ sample with varied size $CaCO_3$ scale deposits (darker contrast)

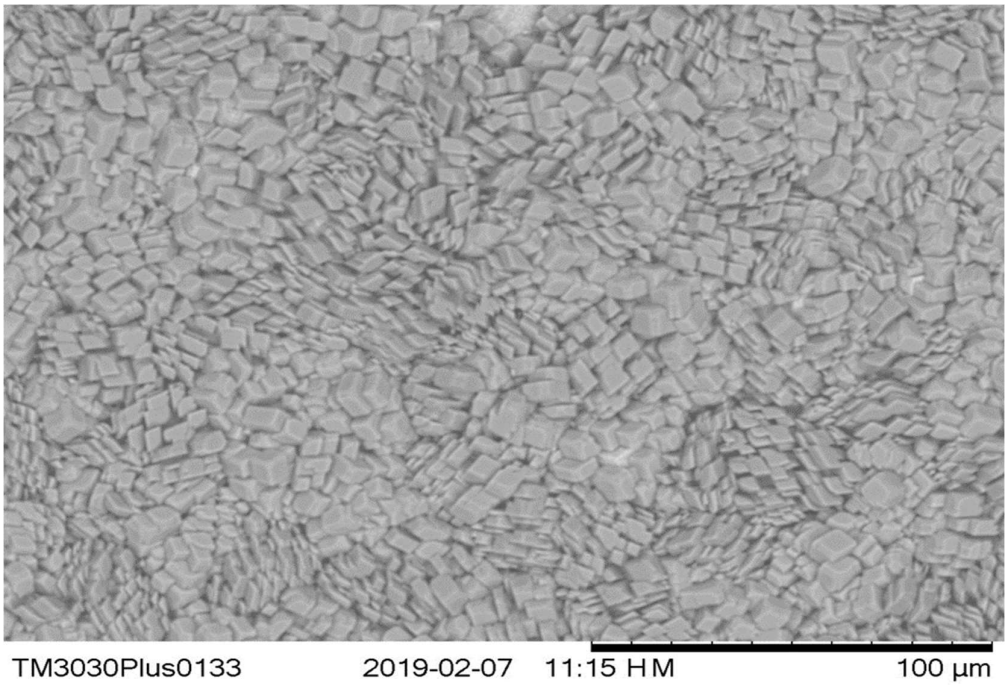

Figure 121 SEM (1) image of $FeCO_3$ sample with full surface coverage of $CaCO_3$ scale deposits (darker contrast)

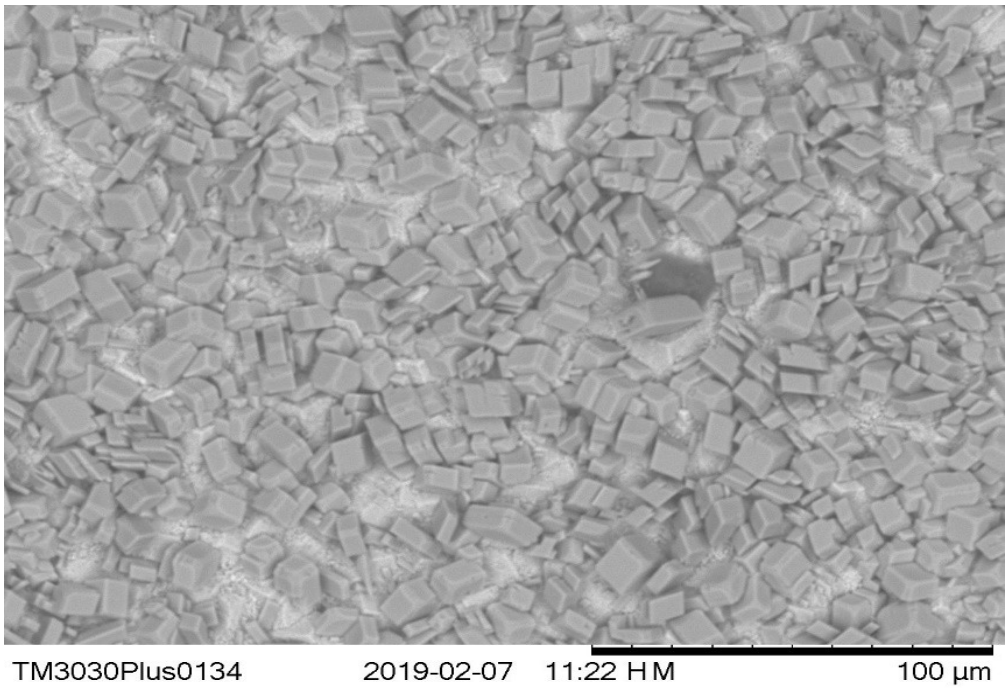

Figure 122 SEM (1) image of $FeCO_3$ sample with incomplete surface coverage of $CaCO_3$ scale deposits (darker contrast)

3. SLIPS Krytox (Kr)

The first SLIPS combination tested is the $FeCO_3$ layer infused with Krytox perfluorinated lubricant. With the addition of a 3rd component (Krytox), the darker areas of contrast are no longer scale deposits. In Figure 123-120, the darker areas are residual pools of lubricants surrounding the $FeCO_3$ layer. In this case the light areas represent mainly $FeCO_3$ but also $CaCO_3$ scale crystals. Calcite crystals appear both individually and in clusters however overall scale coverage is minimal compared to the previous samples. It is interesting to note that only SLIPS Kr showed indications of substantial remaining or retained lubricant from SEM. Under higher magnification, shape and roughness help separate $FeCO_3$ crystals from $CaCO_3$ scale crystals. Particularly in Figure 123 and Figure 125, typical calcite morphologies can be identified with smooth, planar faces on rhombohedron crystals. This is in stark contrast to the $FeCO_3$ base layer, which appears porous and without a well-defined crystal shape. The calcite appears to be floating in remaining lubricant as opposed to being anchored to exposed $FeCO_3$ peaks. Crystal size ranges from 2-20 µm and whilst calcite is the primary polymorph, needle-like aragonite flowers have also been observed (Figure 125).

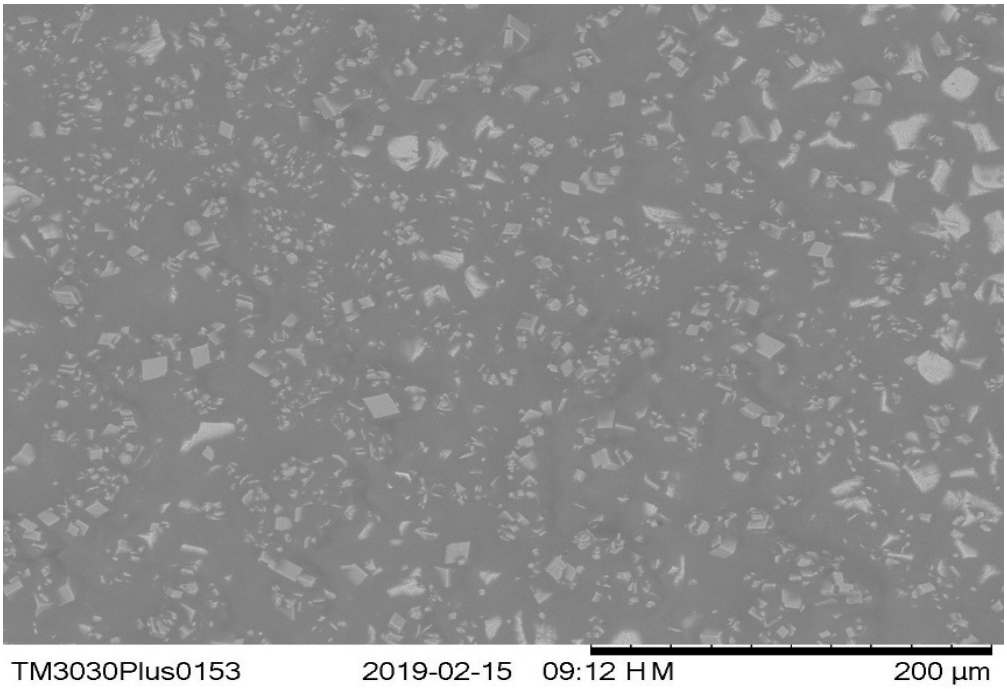

Figure 123 SEM (1) image of SLIPS Kr sample with $CaCO_3$ scale deposits and residual lubricant on the surface

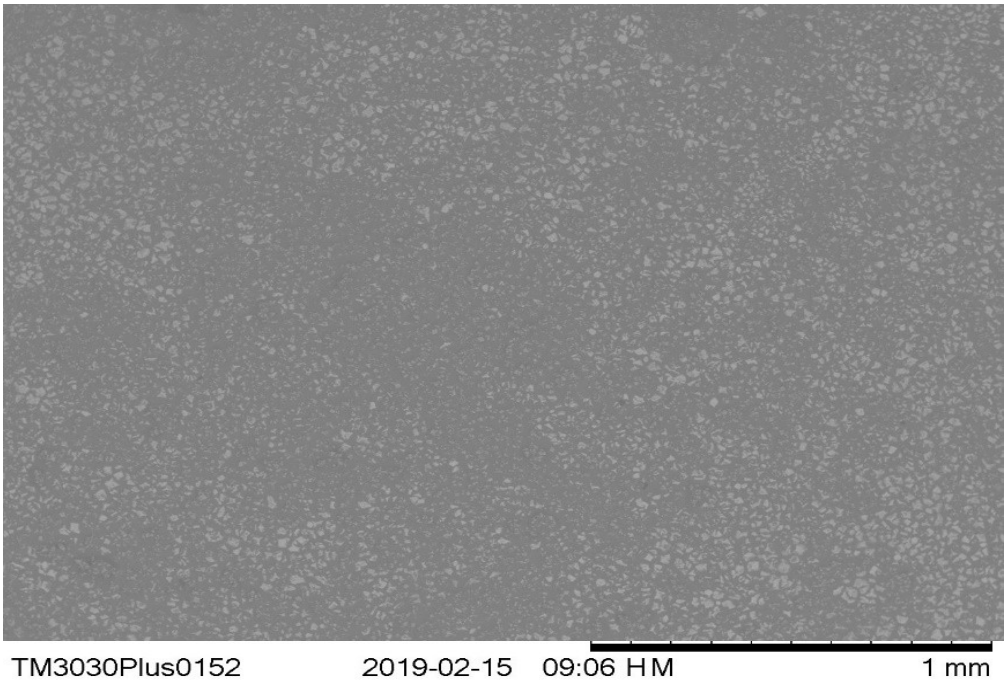

Figure 124 Lower magnification SEM (1) image of SLIPS Kr sample with $CaCO_3$ scale deposits and residual lubricant on the surface

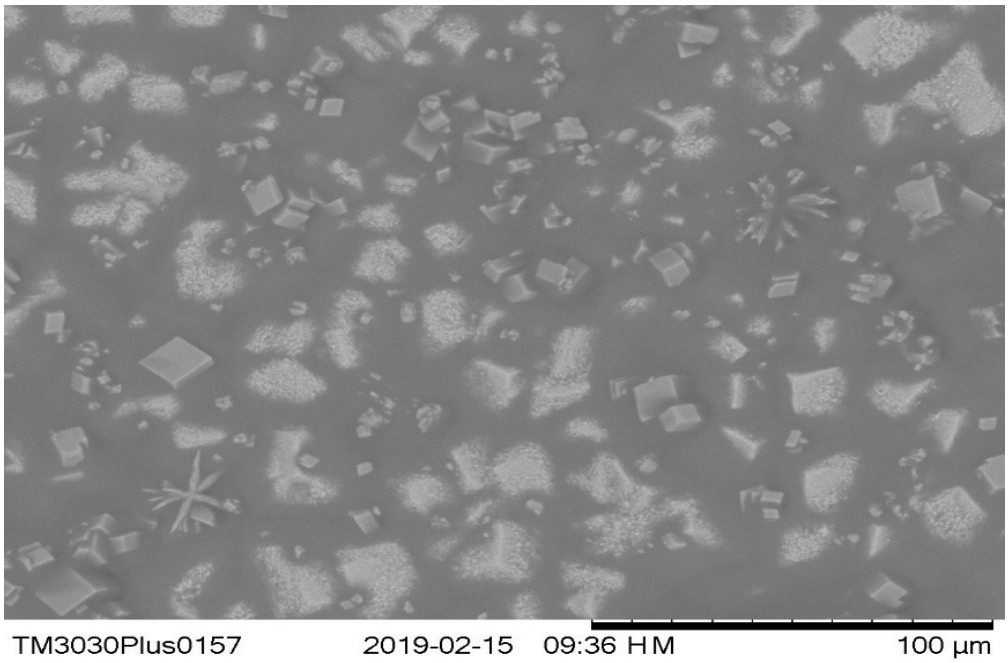

Figure 125 SEM (1) image of SLIPS Kr sample with different $CaCO_3$ scale polymorphs

4. SLIPS BMIM (BM)

SEM imaging of the SLIPS BM showed considerable scale deposits across the surface (Figure 126). Surface images do not appear to show any visible remaining lubricant like that of the SLIPS Kr. Scale deposits vary across samples, both in morphology and coverage (Figure 126-123). Figure 128 shows sporadic coverage with more conventional calcite crystals (dark contrast) as seen in previous samples. These crystals are deposited on top of the $FeCO_3$ layer (light contrast) which is observable. Average crystal size (≈10µm) is comparable with other samples. In contrast Figure 127, shows densely packed crystals of a much smaller and different morphology. Crystals are predominantly <6 µm with more rounded and irregular structure and faces. Although the use of IL's has been studied as carbonate dissolvers [350], due to the lack of porosity/roughness observable on the crystal faces it is unlikely this is the case. The use of IL's to control crystallisation or morphology tuning has also been documented in the literature hence the variations in size/shape and reproducibility of crystal morphologies [351].

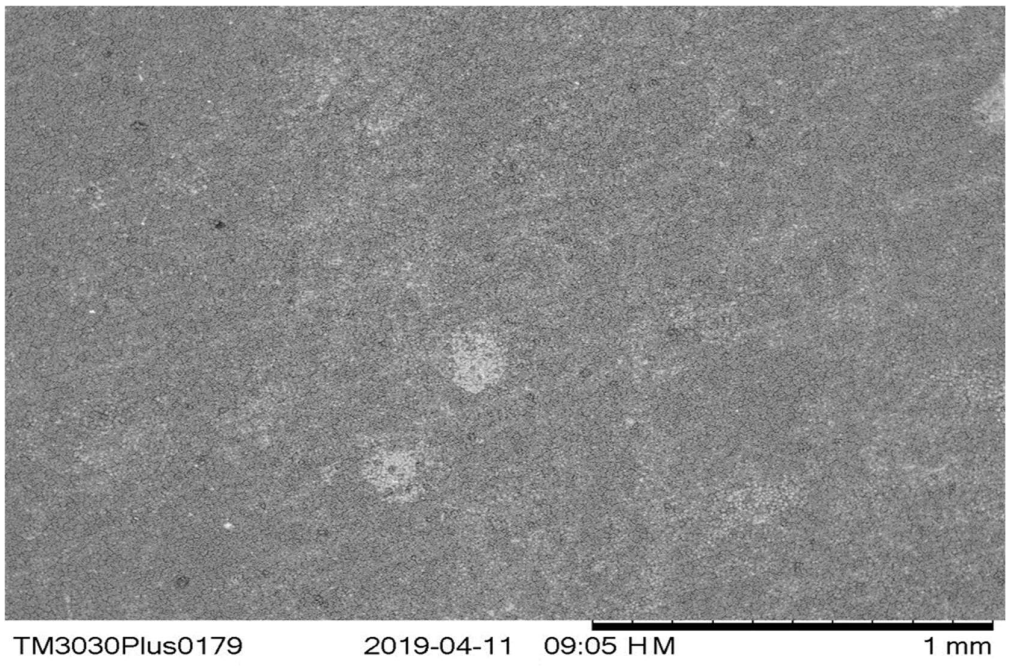

Figure 126 SEM (1) image of SLIPS BM sample with surface coverage of $CaCO_3$ scale deposits

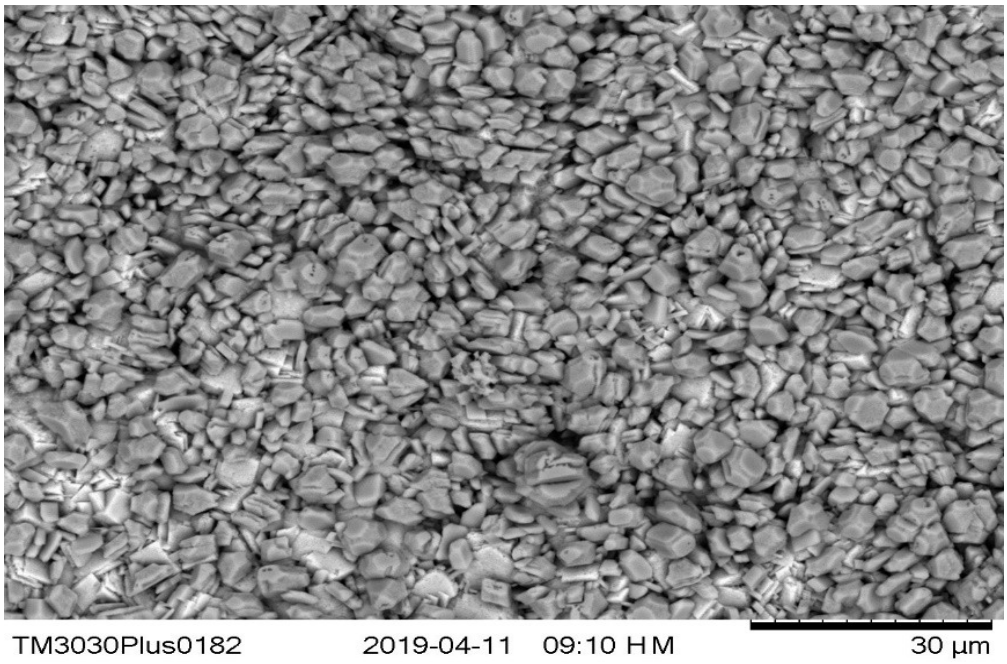

Figure 127 High magnification SEM (1) image of SLIPS BM sample with altered $CaCO_3$ scale deposits

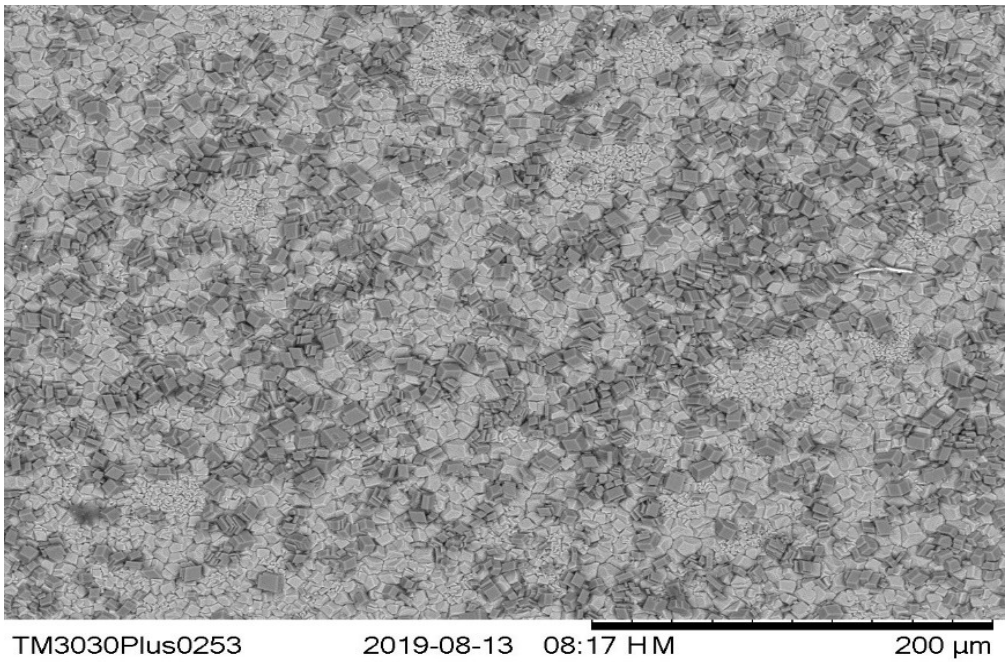

Figure 128 SEM (1) image of SLIPS BM sample with lower concentration of $CaCO_3$ scale deposits

5. SLIPS Waxy (W)

The SLIPS samples infused with crude oil containing wax/paraffin components, displayed extensive scale deposits (Figure 129 and Figure 130) with large agglomerations of $CaCO_3$ crystals across the surface. $CaCO_3$ size varies from small crystals in the 1-2 µm range to larger sizes up to 15 µm. Shape varies from the typical calcite cubic/ rhombohedral structure with sharp edges to more irregular shaped crystals with multiple rounded features and stepped edges (Figure 131). Darker areas of the SEM image may signal trace amounts of lubricant left on the surface but not to the scale seen on Krytox samples. These darker areas are apparent in the voids between $CaCO_3$ crystals with underlying $FeCO_3$ layer also visible in areas.

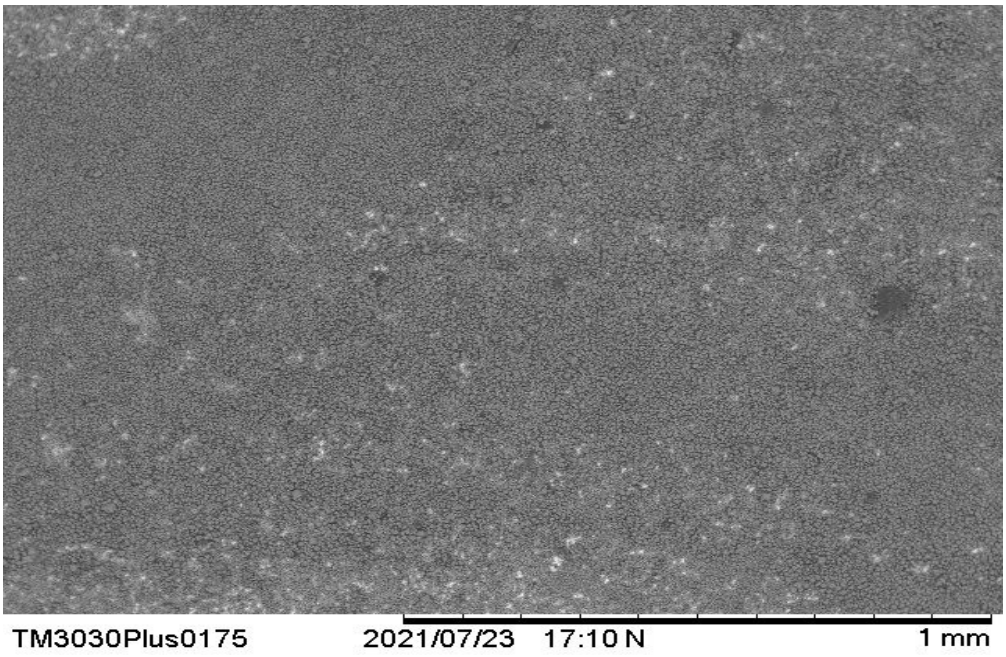

Figure 129 Low magnification SEM (1) image of SLIPS W sample with $CaCO_3$ scale deposits

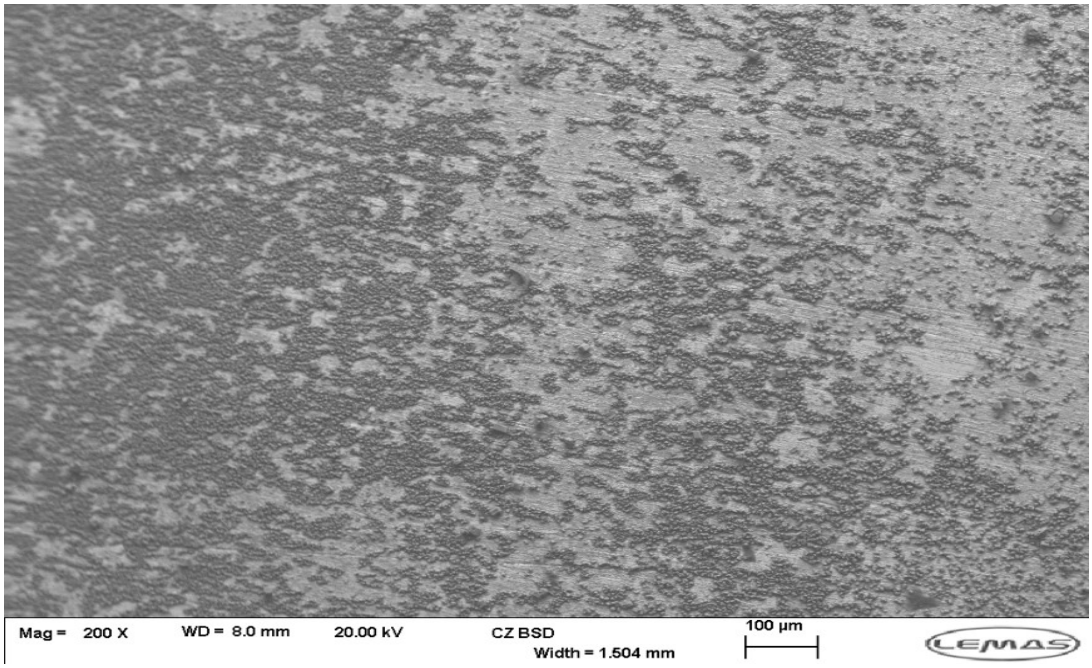

Figure 130 SEM (2) image of SLIPS W sample with $CaCO_3$ scale deposits showing incomplete surface coverage

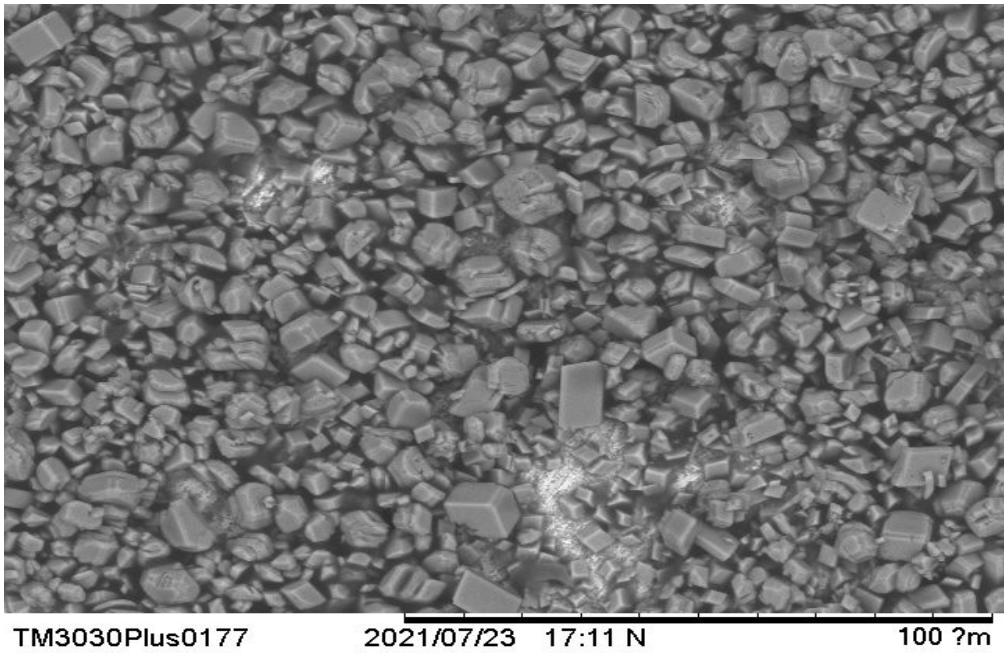

Figure 131 High magnification SEM (1) image of SLIPS W sample with differing $CaCO_3$ scale morphology and residual lubricant

6. SLIPS No-Wax (NW)

The other crude oil SLIPS, with minimal wax/paraffin compounds (no wax), shares similarities with the waxy version. Samples show large build-ups of $CaCO_3$ scale deposits across the surface (Figure 132-129). This is made up of areas of high concentration (complete coverage) and lower concentration (where underlying $FeCO_3$ is still visible). The $CaCO_3$ crystals themselves are in a similar size range to the other SLIPS samples tested, the scale running from 5-20 μm. Precipitated crystals have typical calcite morphology with cubic/rhombohedral structures. The $CaCO_3$ crystals are well formed (with little face/edge rounding) compared to the crystals found on the SLIPS infused with Waxy oil. Exposure of the underlying $FeCO_3$ layer shows the presence of regular $FeCO_3$ crystals but also patches of very fine (<1 μm) clusters.

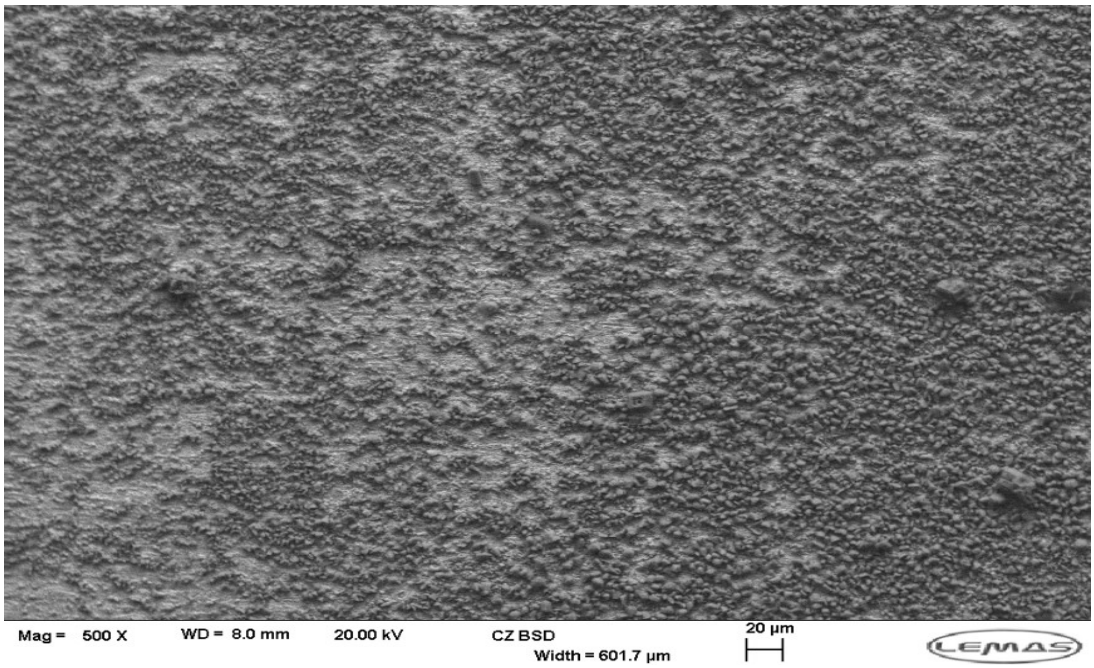

Figure 132 SEM (2) image of SLIPS NW sample with $CaCO_3$ scale deposits

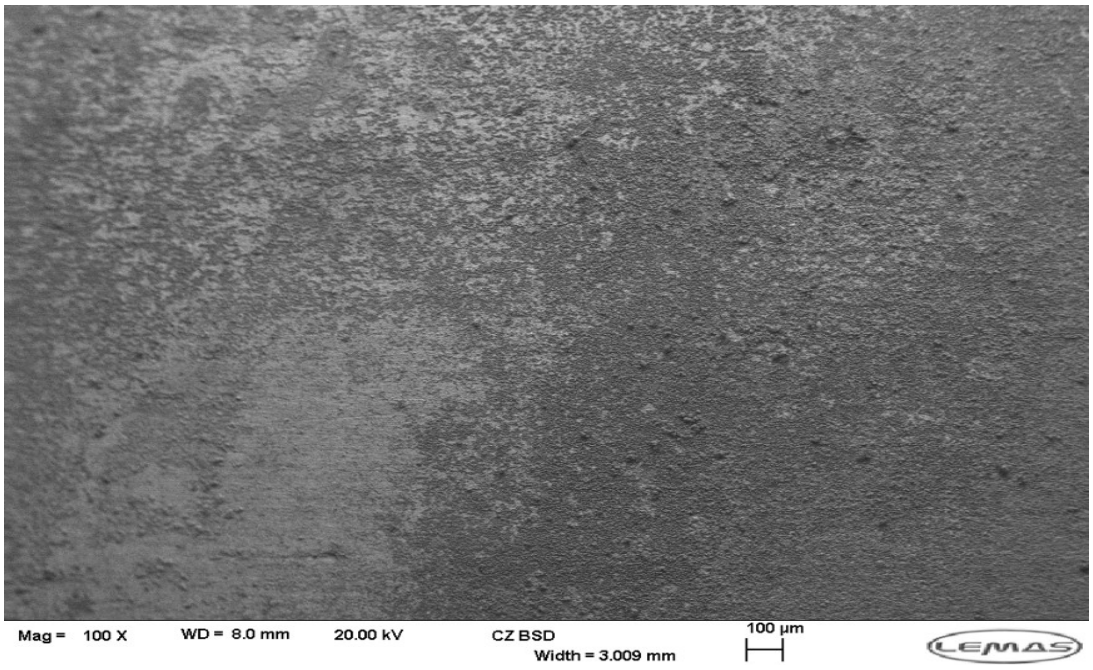

Figure 133 100x magnification SEM (2) image of SLIPS NW sample with $CaCO_3$ scale deposits

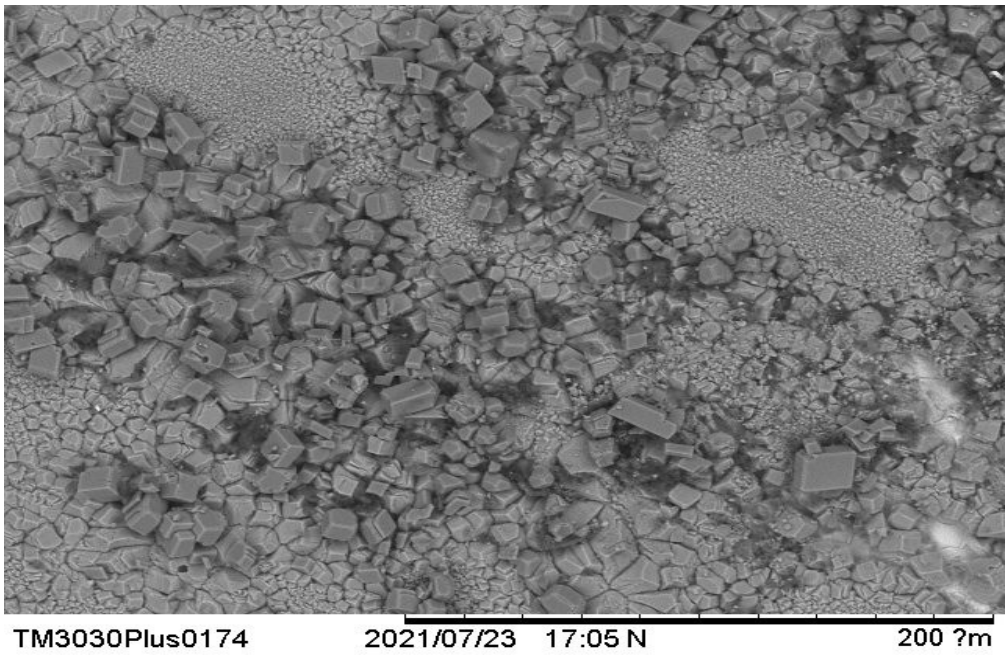

Figure 134 High magnification SEM (1) image of SLIPS NW sample with $CaCO_3$ scale deposits and differing $FeCO_3$ base scale layer

EDX Analysis of scale deposits SI 2.6

EDX analysis has been taken to examine the elemental composition of surface scale deposits. Images have been taken from one of two machines. With the number denoting the SEM used: 1. Hitachi tabletop TM3030Plus and 2. Carl Zeiss EVO MA15. EDX analysis was made using Aztec software. In this section EDX is used to show both qualitative and quantitative calcium concentration/distribution across the sample, differentiate between $CaCO_3$ and $FeCO_3$ scales (alongside SEM) and to detect trace levels of remaining lubricants. Areal values of Calcium (Ca) Wt. % have been taken from map scans of 5 mm^2 (minimum) portions of sample surface.

1. X65 Carbon Steel (CS)

EDX analysis of the X65 CS sample shows a good contrast between the main elements on the surface. The predominant $CaCO_3$ scales in higher magnification are clear against the underlying steel base (with elevated Fe). Calcium distribution on the surface is high, both in visible $CaCO_3$ deposits and Ca Wt. % detected from the EDX analysis. Post test analysis of samples showed values ranging from 17-38 % Ca Wt.% (Figure 135). With higher Ca

Wt.% evidenced by large, widespread $CaCO_3$ deposits on the surface. Ca Wt.% was also linked with Fe Wt.%, as would be expected as increasing $CaCO_3$ deposits mask the underlying steel (or Fe signal). At 17 Ca Wt.%, the Fe wt.% is 51%, while a sample with 38% Ca Wt.% has a Fe Wt.% of 6% (Figure 136).

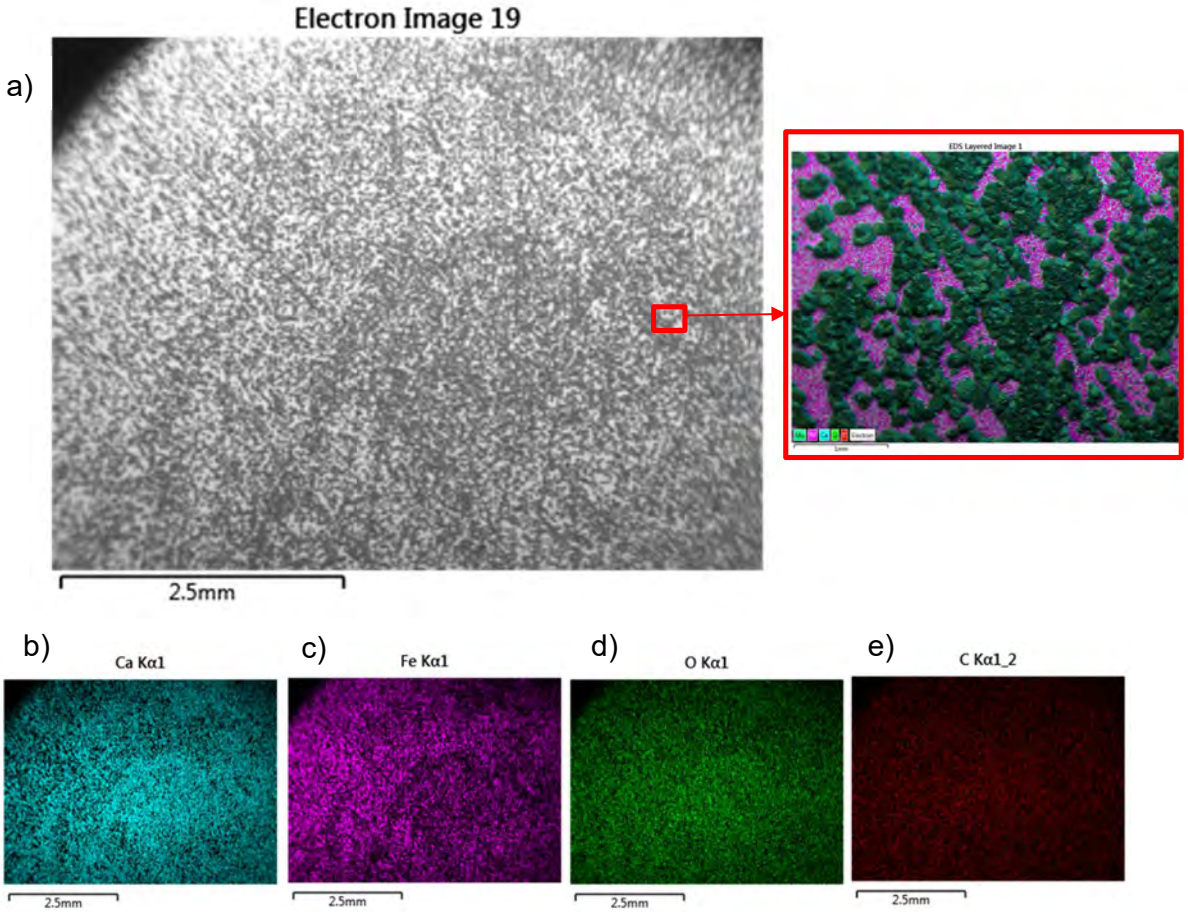

Figure 135 a) Areal SEM and magnified EDX elemental map of X65 CS sample. Inset: EDX map of $CaCO_3$ crystal on surface, b) Ca, c) Fe, d) O, e) C

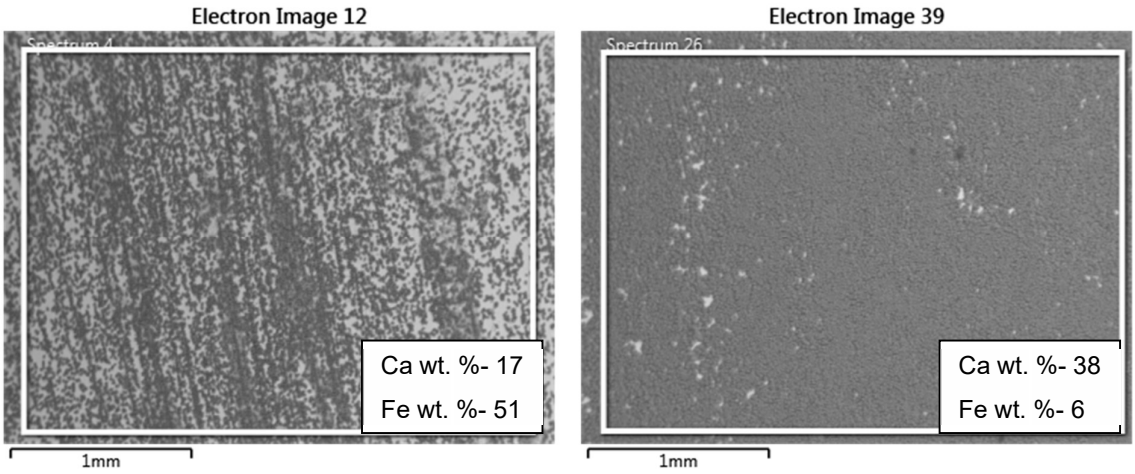

Figure 136 EDX wt. % for Ca and Fe for two separate X65 CS samples

2. Iron carbonate ($FeCO_3$)

The base $FeCO_3$ layer consistently had the highest values for Ca Wt.% for all samples, in both SI 1 and SI 2.6 environments. This may indicate some attraction with the Ca in the bulk and its interactions with the $FeCO_3$ layer, whether as $CaCO_3$ deposits or integration within the existing $FeCO_3$ layer. The range of Ca Wt.% was shown between 33 up to 51 (Figure 137), with 51 Ca Wt.% being the highest value encountered. Some iron carbonate samples showed substantial coverage with a sheet-like layer of $CaCO_3$ deposits obscuring the whole surface being analysed in the EDX (Figure 138). It was interesting to note that under higher magnification, the correlation between increasing Ca Wt. % and decreasing Fe Wt. % did not always hold true. As can be seen, even where the Ca wt.% was highest (at Ca Wt. 50%), Fe wt. % was 17, while in a sample that appears full covered on SEM the Ca wt. % is lower at 38 wt. %, whilst the Fe wt. % is 3 (Figure 139).

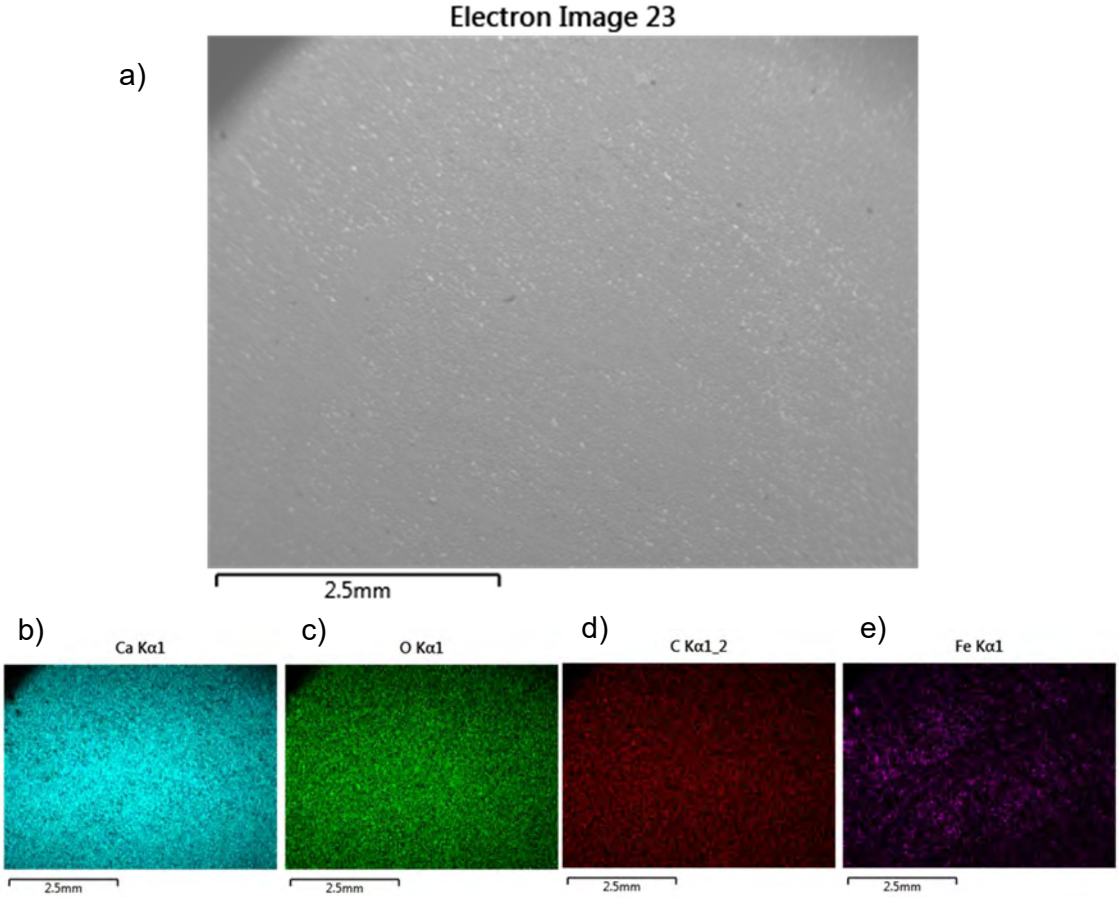

Figure 137 a) Areal SEM and EDX elemental map of b) Ca, c) O, d) C and e) Fe for $FeCO_3$ sample.

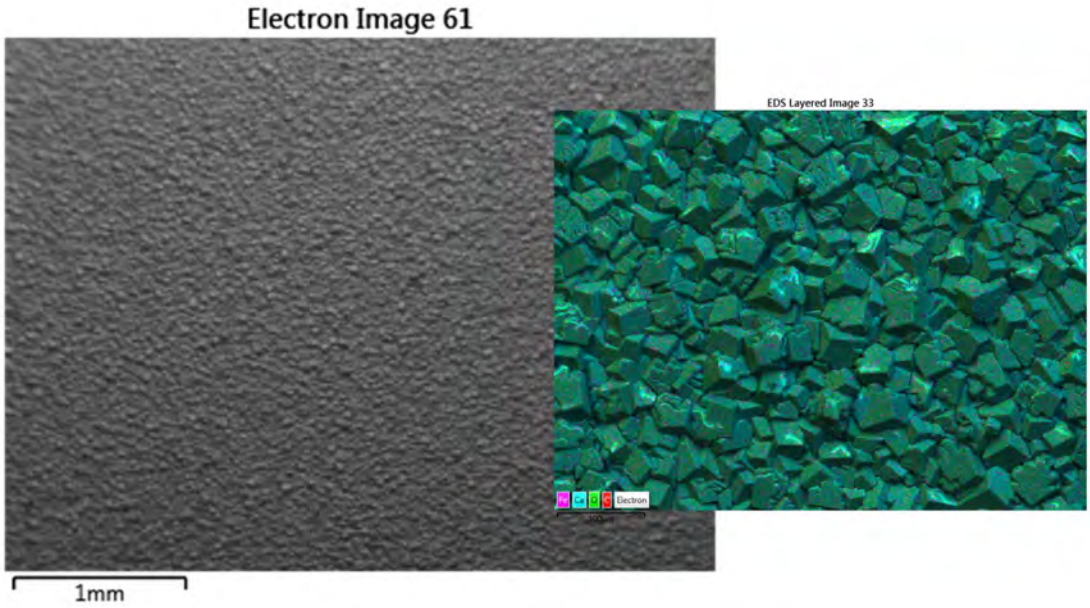

Figure 138 Areal SEM and inset: higher magnification EDX map of continuous $CaCO_3$ surface deposit on $FeCO_3$ sample

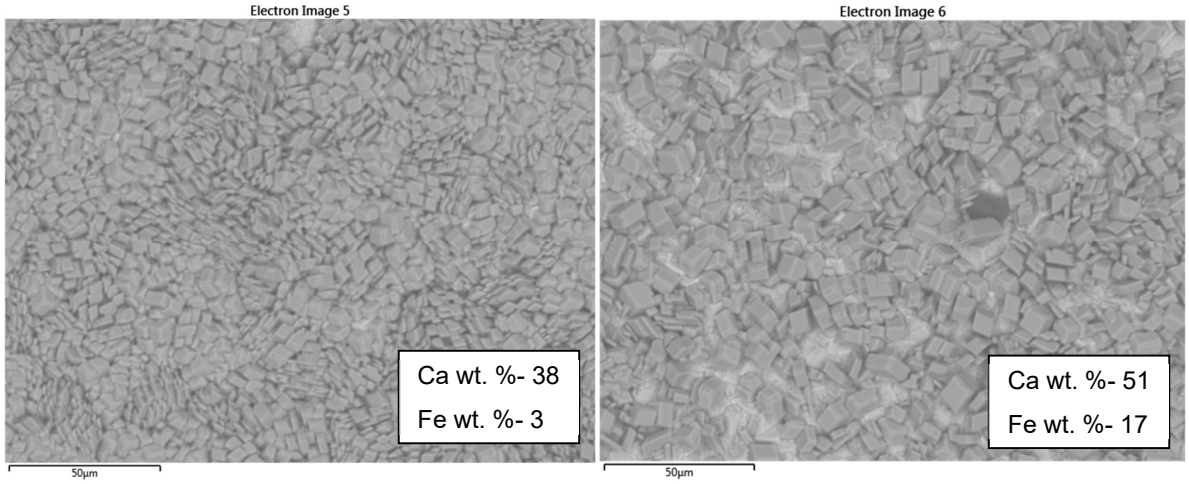

Figure 139 EDX wt. % for Ca and Fe for two separate $FeCO_3$ samples

3. SLIPS Kr

The SLIPS Kr displays the most promising scaling behaviour of the SLIPS samples tested in SI 2.6. Ca wt. % ranged from lows of 2% up to highs of 17%. The trace element for Krytox was F and when lubricant elements are present

at all (either in Krytox/BMIM) there is a correlation with improved scaling performance (or less Ca wt. %) within the same lubricant tested. However there is not always a correlation between higher concentrations of that lubricant trace element and reduced Ca wt. % (scaling performance). As Figure 141 shows this sample has a lower Ca wt.% (3) with a lower F wt. % (9) than Figure 140 which has a much higher F concentration (higher residual lubricant) and yet a poorer level of calcium on the surface. The distribution of the F across the surface is also relatively uniform, even where visibly on the SEM it looks more concentrated. Many samples show a congealed lubricant that often sits atop the $FeCO_3$ layer; however the F concentration does not reflect this. With EDX mapping showing equal F concentrations on both the exposed $FeCO_3$ layer and the amorphous congealed lubricant itself (Figure 143). This congealed layer, when visibly apparent on the surface generally appears to have higher levels of Ca wt.%.

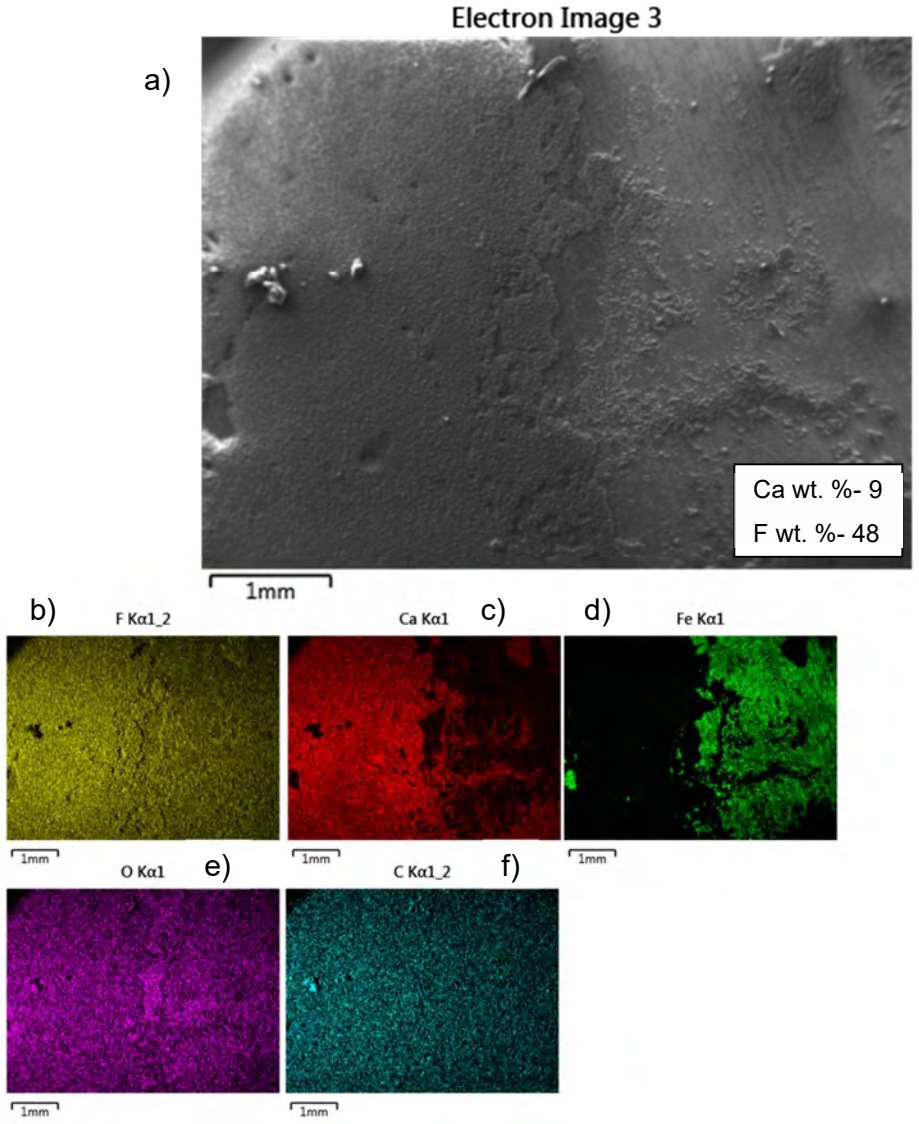

Figure 140 a) Areal SEM and EDX elemental map of b) F, c) Ca, d) Fe, e) O and f) C for SLIPS Kr sample.

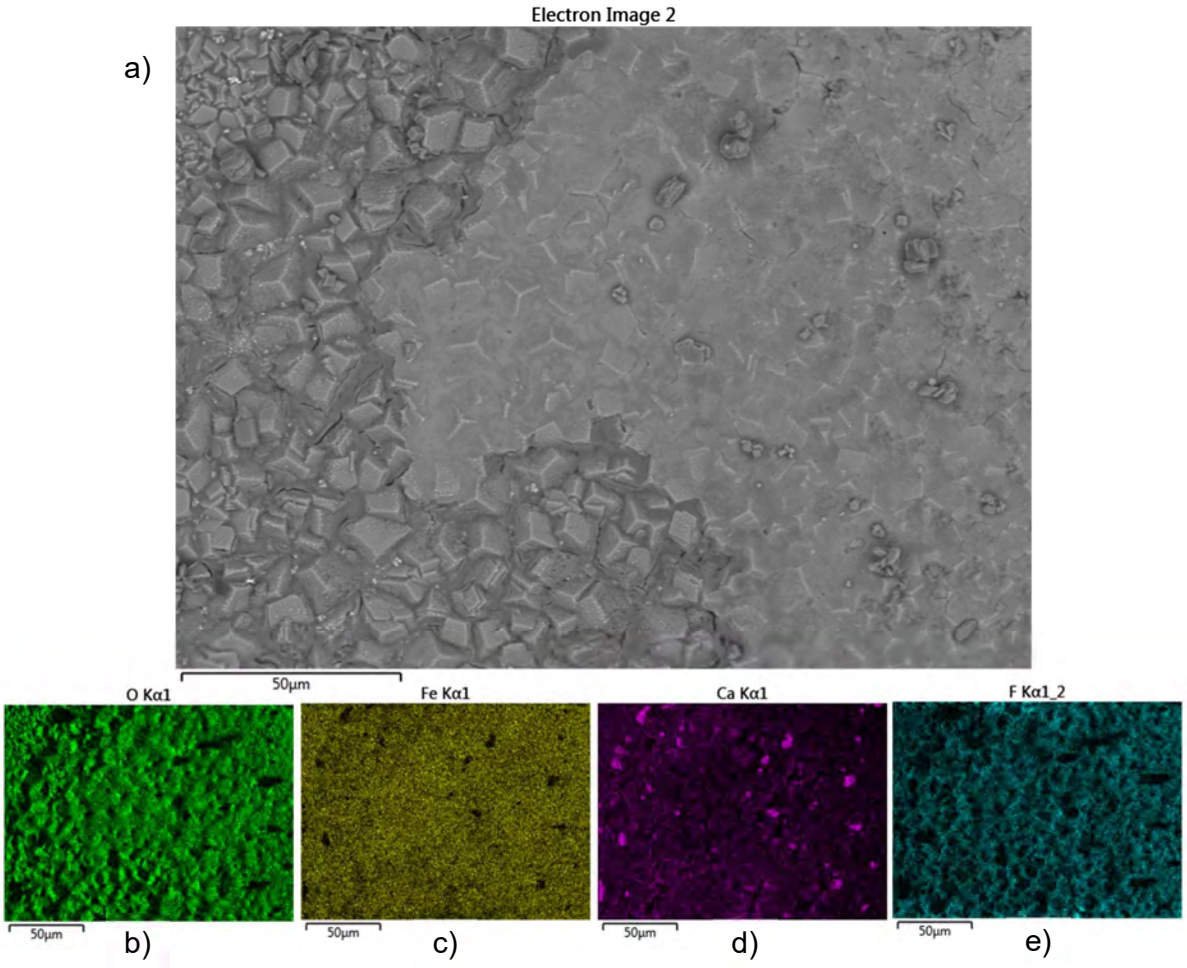

Figure 141 a) SEM and EDX mapping of b) O, c) Fe, d) Ca, e) F for SLIPS Kr showing visible congealed lubricant on the surface

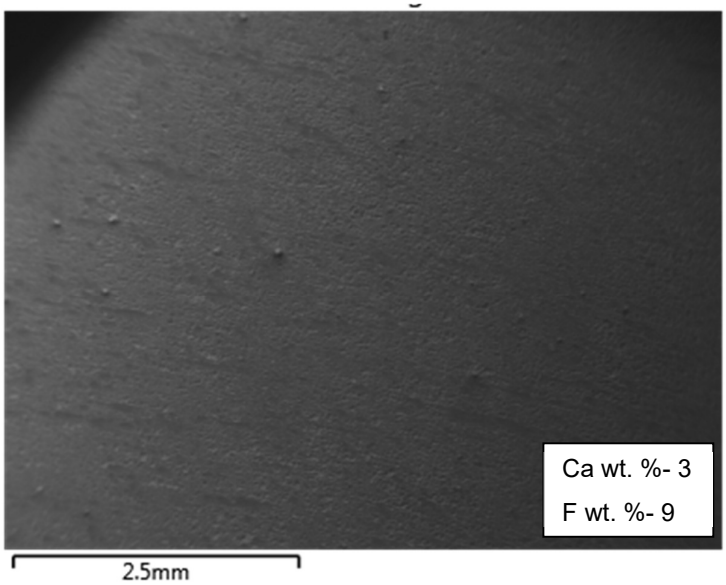

Figure 142 SEM EDX Analysis of Ca and F wt. % for SLIPS Kr sample

4. SLIPS BM

The ionic liquid SLIPS, similar to that of the $FeCO_3$ base layer displays a poor level of scaling performance based on Ca wt.%. Ca wt. % values range from lows of 21% to 44% (Figure 144). The higher values of Ca wt.% were also associated with low or zero elemental markers of the lubricant. As stated previously, BMIM has both F and S elements in measurable quantities. Only at lower Ca wt.% were they seen at detectable levels, where F was 3 wt.% and S 0.44 wt. % (Figure 145). However for other samples at lower readings, no elemental traces of the lubricant were seen. The distribution of the lubricant elements is also interesting and similar to the results seen in SI 1. The F wt. % usually displays higher concentrations in those areas where there is lower Ca wt. %. Again it is not certain whether this is due to the Ca covering the F signal or theoretically because the F has disappeared (hence the protective capability is lost and the Ca then deposits). This is similar in nature to how F is distributed in the SLIPS Krytox sample. S however appears to be dispersed more evenly across the sample, with little correlation to Ca or F concentrations.

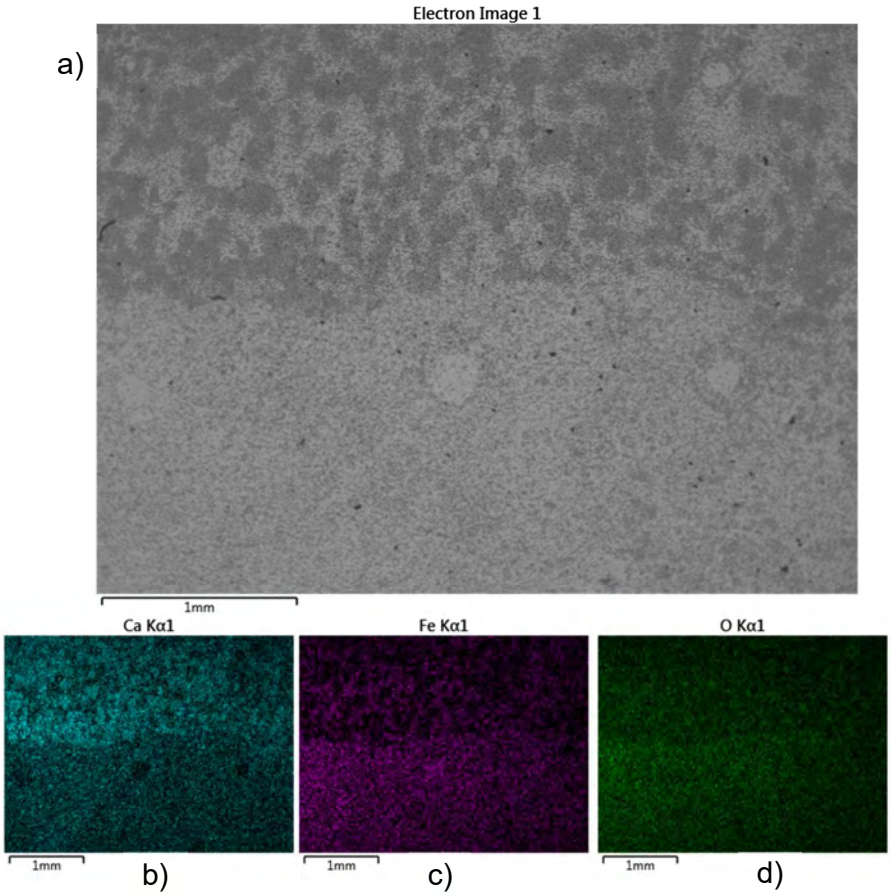

Figure 144 a) Areal SEM and EDX elemental map of b) Ca, c) Fe, d) O for SLIPS BM sample. No Lubricant markers detected

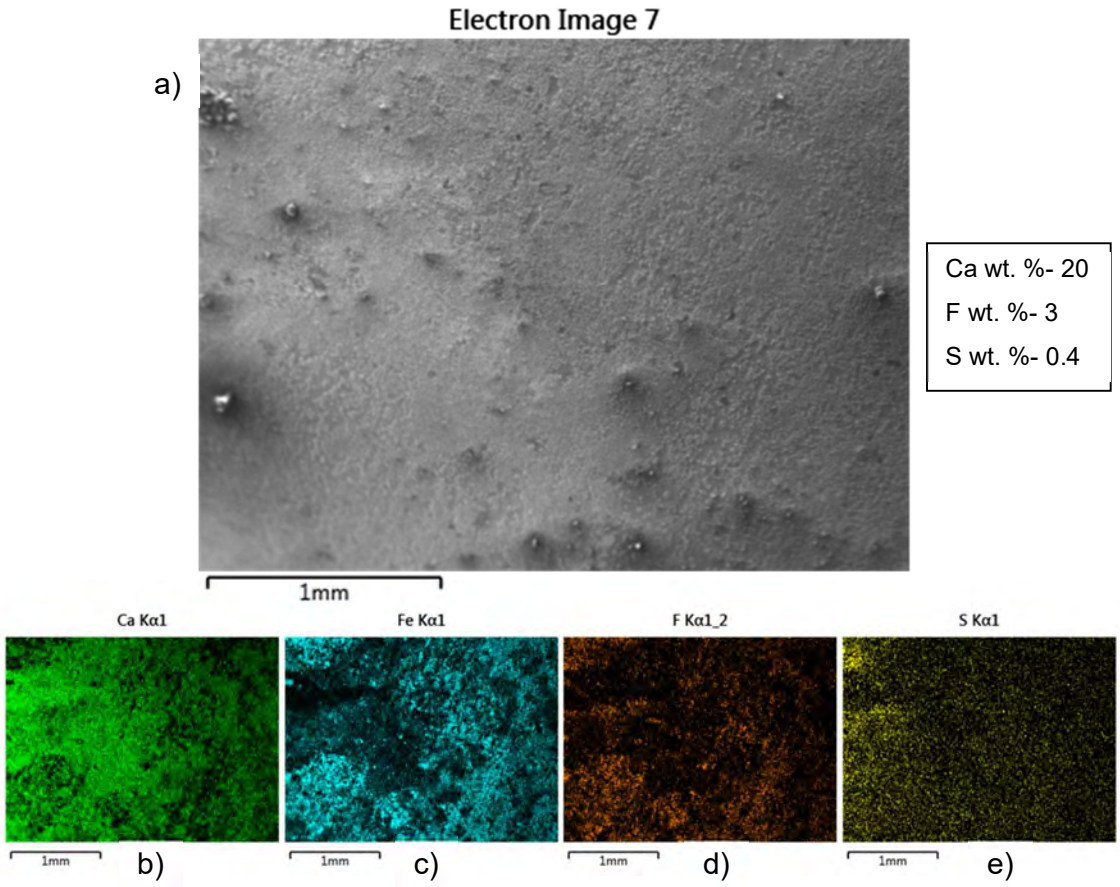

Figure 145 a) Areal SEM and EDX elemental map of b) Ca, d) Fe, d) F, and e) S for SLIPS BM sample. Lubricant markers detected (F, S)

5. SLIPS Waxy (W)

The SLIPS W performed well with regards to Ca wt. % compared to other samples. Ca wt. % was on average lower and ranged from lows of 4.6% to highs of 17.8%. The Ca wt.% was usually distributed evenly across samples on lower magnification EDX maps (Figure 146). The formation of visible $CaCO_3$ clusters was not common, even under higher magnification maps. The SLIPS W, similar to the tests conducted in SI 1 displayed a number of small residual trace elements associated with impurities. This included Mn (also found in the SLIPS NW) but also a variety of other elements including Zn, Cu, Si and S. wt. % linked with these elements were very low, usually < 1%. Even where concentrations were higher than 1%, distribution was generally uniform across the EDX map area and there was no link to where higher concentrations of Ca appeared (Figure 147).

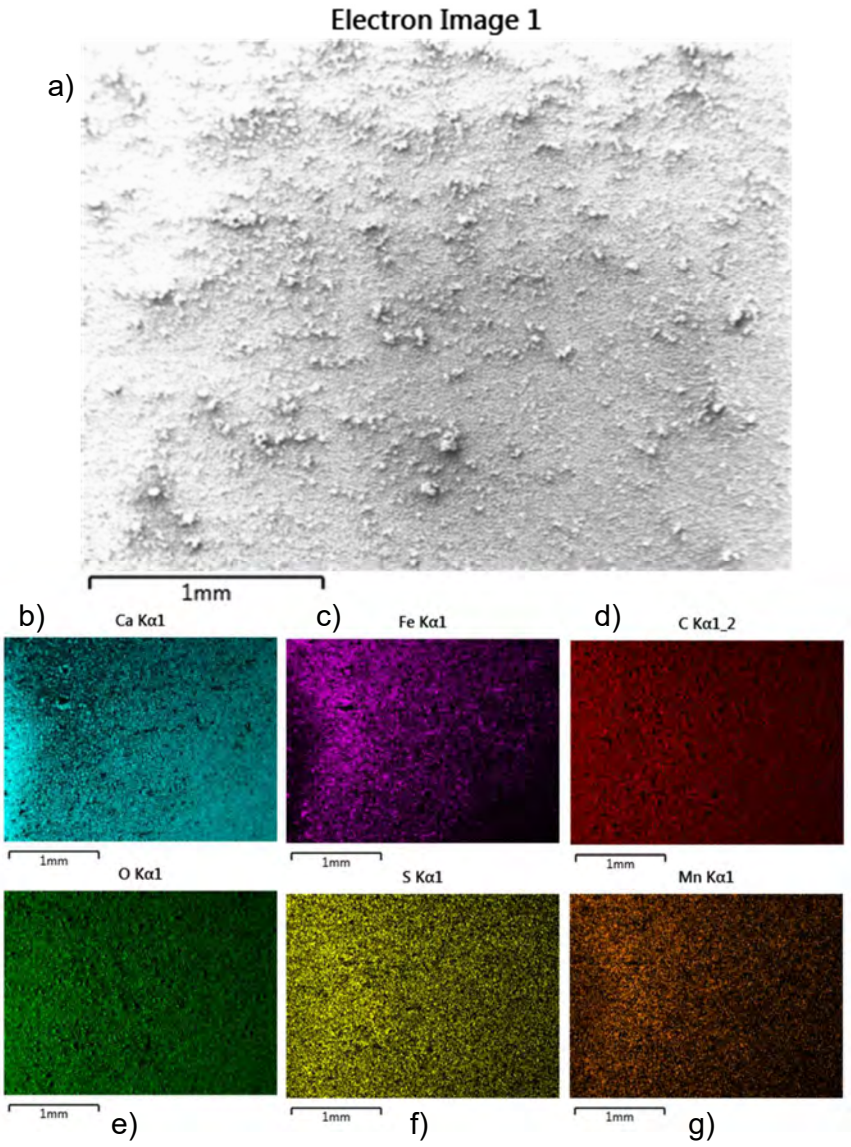

Figure 146 a) Areal SEM and EDX elemental map of b) Ca, c) Fe, d) C, e) O, f) S and g) Mn for SLIPS W sample

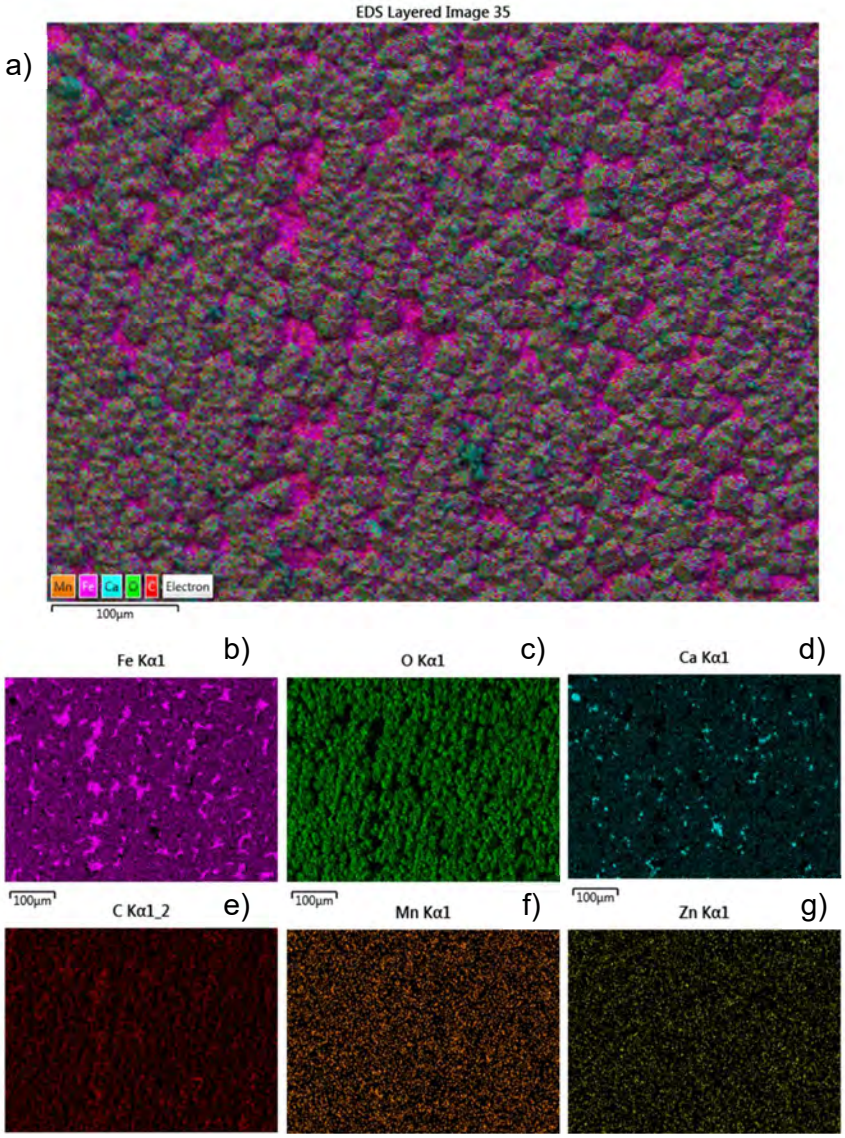

Figure 147 a) High magnification EDX elemental map of b) Fe, c) O, d) Ca, e) C, f) Mn and g) Zn for SLIPS W sample

6. SLIPS Non-Waxy (NW)

The SLIPS NW displays scaling behaviour similar to that of the waxy versions, but unlike its behaviour in the SI 1 tests. Within SI 2.6 tests, Ca wt. % was highly variable falling in a range between 4.42% and 36.22% (Figure 148). Samples towards the upper end of the range with Ca wt. % > 30, tended to be visually covered with $CaCO_3$ scales. As stated, before there are no strong trace element indicators for the crude oil SLIPS, with EDX mapping largely limited to that of the main elements of Fe, C, Ca and O. Mn was a reoccurring

element across samples, often found in crude oils as impurities, however the levels barely reach 1 wt. % at higher magnifications (Figure 149).

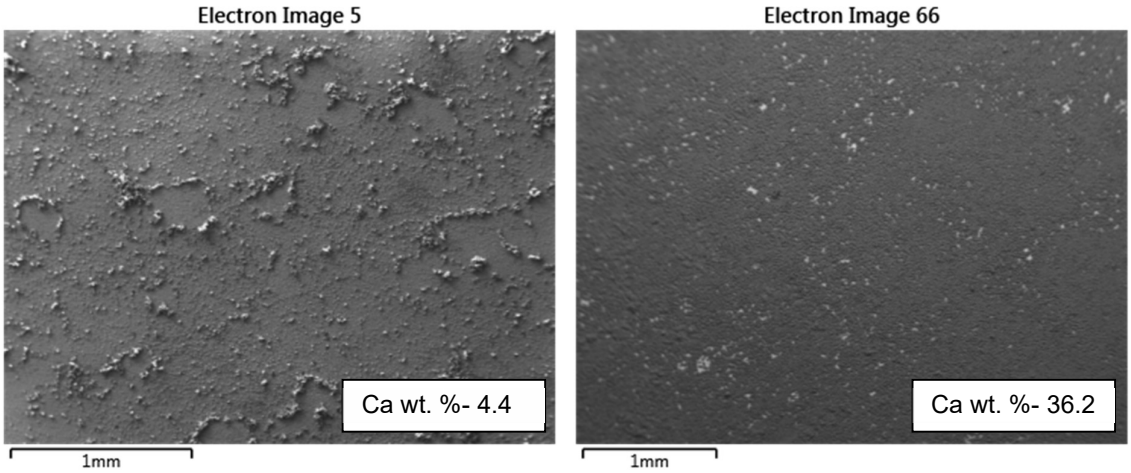

Figure 148 SEM and Ca wt. % of two separate SLIPS NW samples

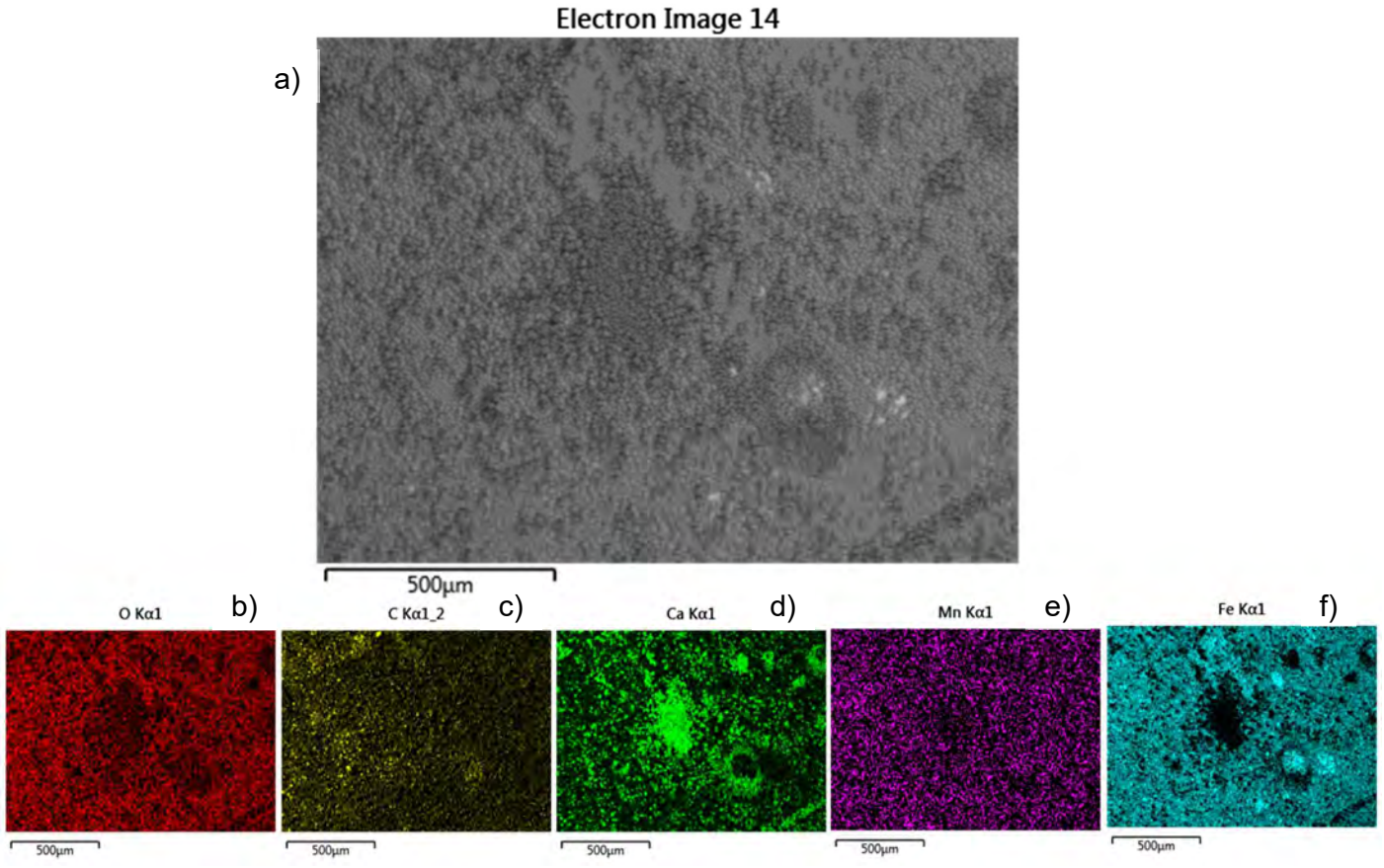

Figure 149 a) High magnification SEM and EDX elemental map b) O, c) C, d) Ca, e) Mn, f) Fe for SLIPS NW sample

7.7 Surface Characterisation of Samples in SI 1

The scaling tests conducted at Saturation Index 1 represent a more typical scaling system that might be encountered in the field. In this environment, the induction time is relatively slow (compared to that of SI 2.6) and the concentration/mass of scale/crystals in the bulk is much smaller.

SEM Analysis of scale deposits

SEM images have been taken to examine surface scale deposits. Images have been taken from one of two machines. With the number denoting the SEM used: 1. Hitachi tabletop TM3030Plus and 2. Carl Zeiss EVO MA15.

1. X65 Carbon Steel (CS)

The untreated carbon steel sample has accumulated $CaCO_3$ scale deposits in the SI 1 brine, with coverage across the majority of the exposed surface (Figure 150). Crystallisation behaviour tends to favour clusters along the lines of the striations left from polishing/grinding of the surface. $CaCO_3$ morphology in some samples appear as amorphous type clusters, not similar to the more typical morphological characteristics of the main polymorphs. Individual crystal clusters are generally larger in nature to crystals encountered in a more stable polymorph form and are usually a minimum of 10 up to 40 µm (Figure 152). These formations tend to have stepped sharp edges, in the shape of a flower/rosetta like structure. The amorphous clusters might be in the process of recrystallisation/conversion into a more stable polymorph although they do not share the typical spindle like characteristics of an aragonite crystal. Fully formed cubic calcite crystals can also be observed (Figure 151).

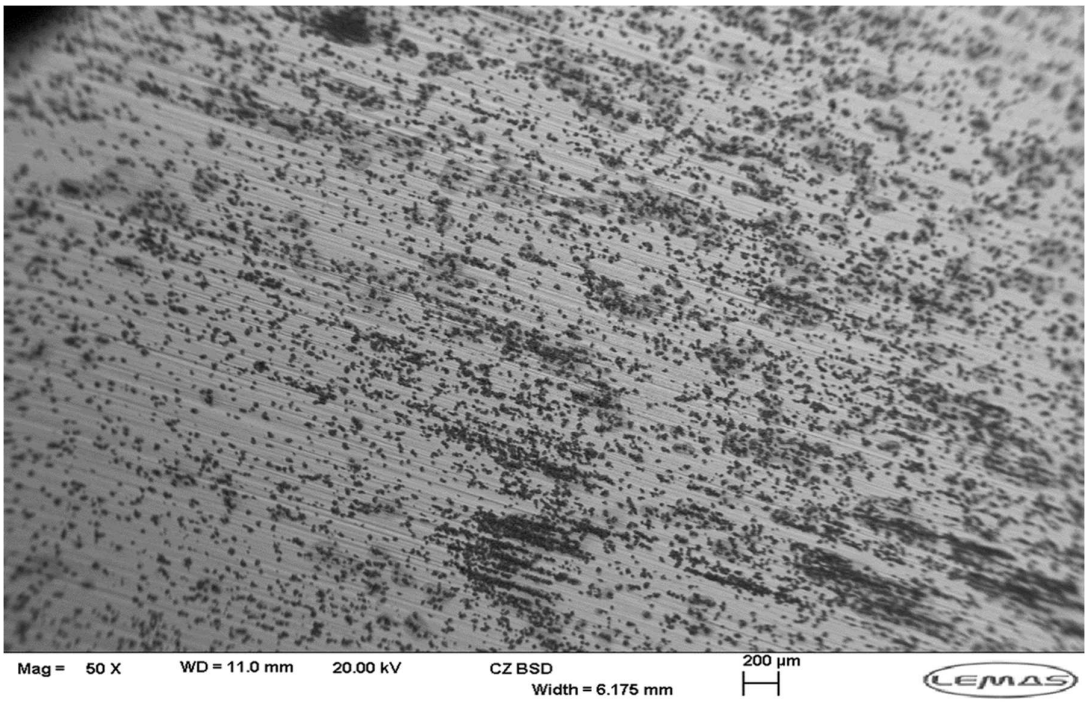

Figure 150 50x magnification SEM (2) image of X65 CS sample with $CaCO_3$ scale deposits

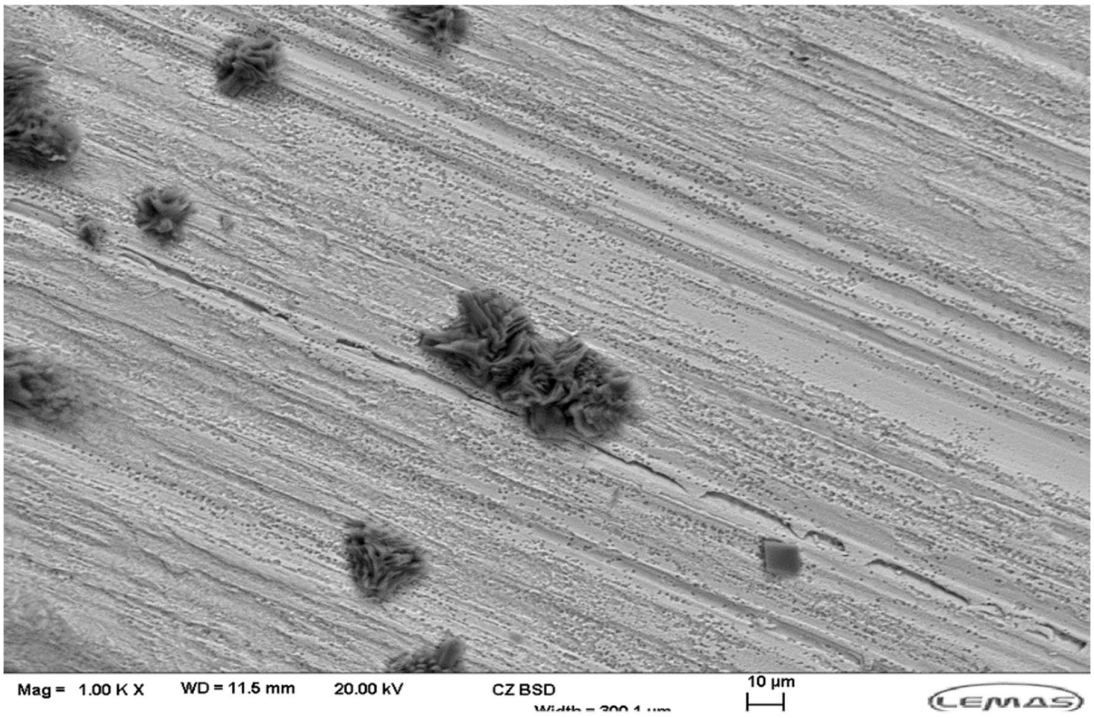

Figure 151 SEM (2) image of X65 CS sample with individual $CaCO_3$ crystals and underlying surface roughness (from abrasive polishing)

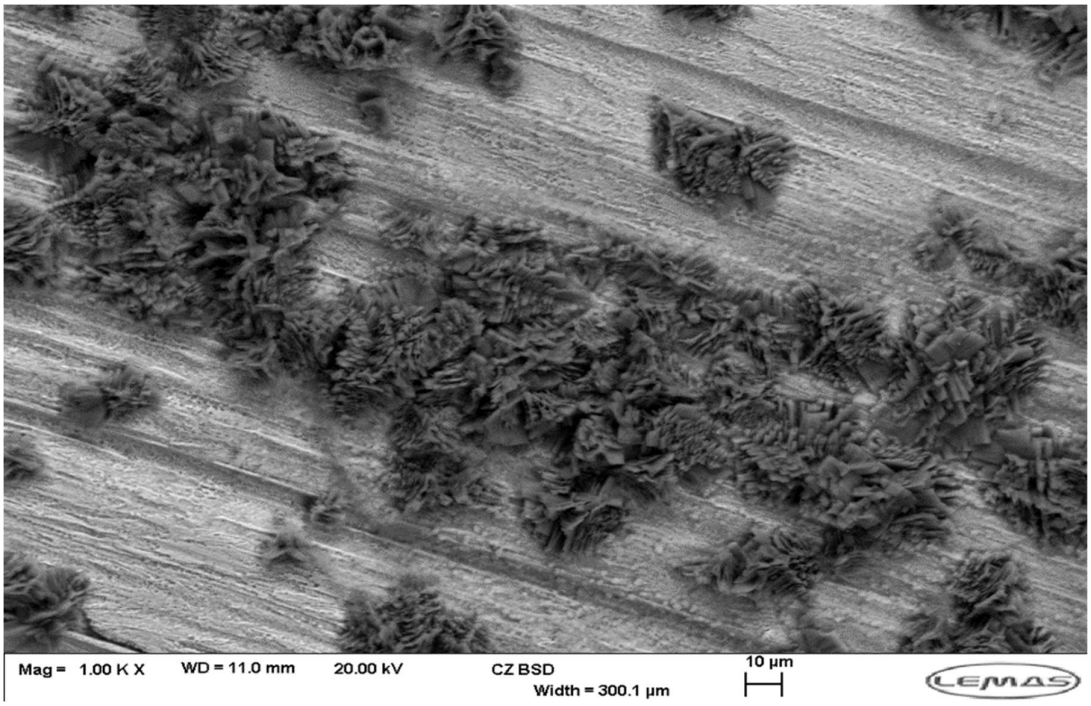

Figure 152 SEM (2) image of X65 CS sample with $CaCO_3$ scale deposits

2. Iron carbonate ($FeCO_3$)

The $FeCO_3$-covered sample shows scale deposits, again similar to the behaviour encountered in the SI 2.6 brine but with a visibly reduced quantity (Figure 153). SEM imaging show a well-defined $FeCO_3$ layer of rhombohedral crystals ranging from 5 – 15 µm. The $CaCO_3$ deposits are well formed cubic calcite clusters that are in a similar size range as the underlying $FeCO_3$ layer (5 – 15 µm). In some areas clusters are also found in parallel lines, suggesting topographical effects of underlying polishing/ grinding of the original surface (Figure 154 and Figure 155).

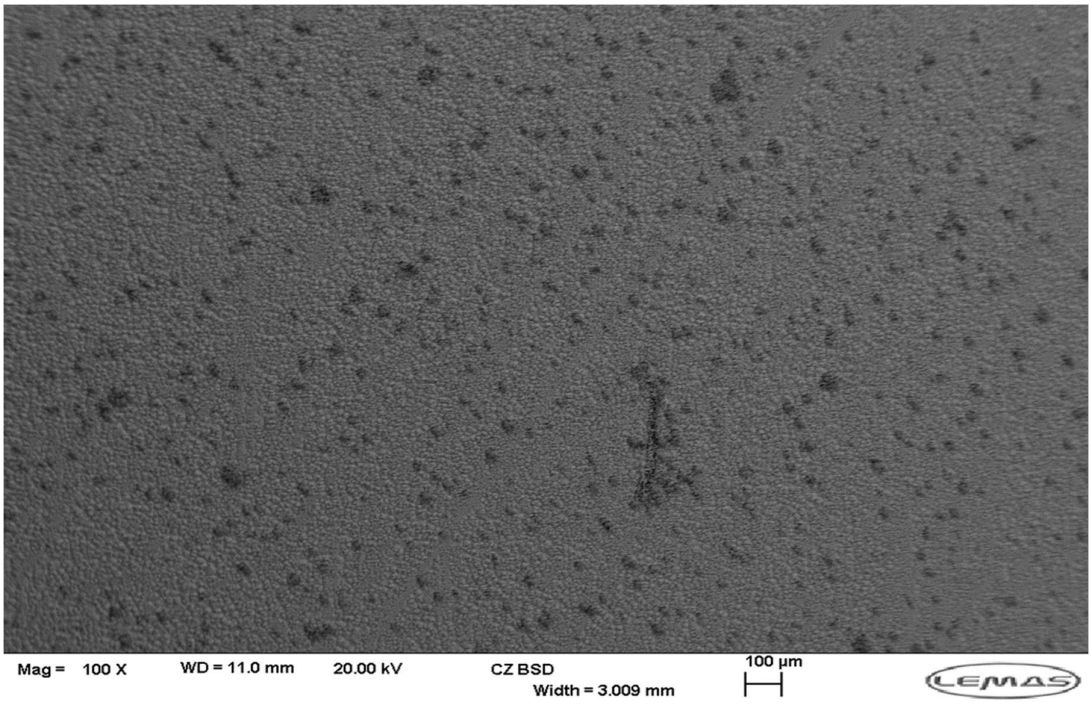

Figure 153 100x magnification SEM (2) image of $FeCO_3$ sample with $CaCO_3$ scale deposits

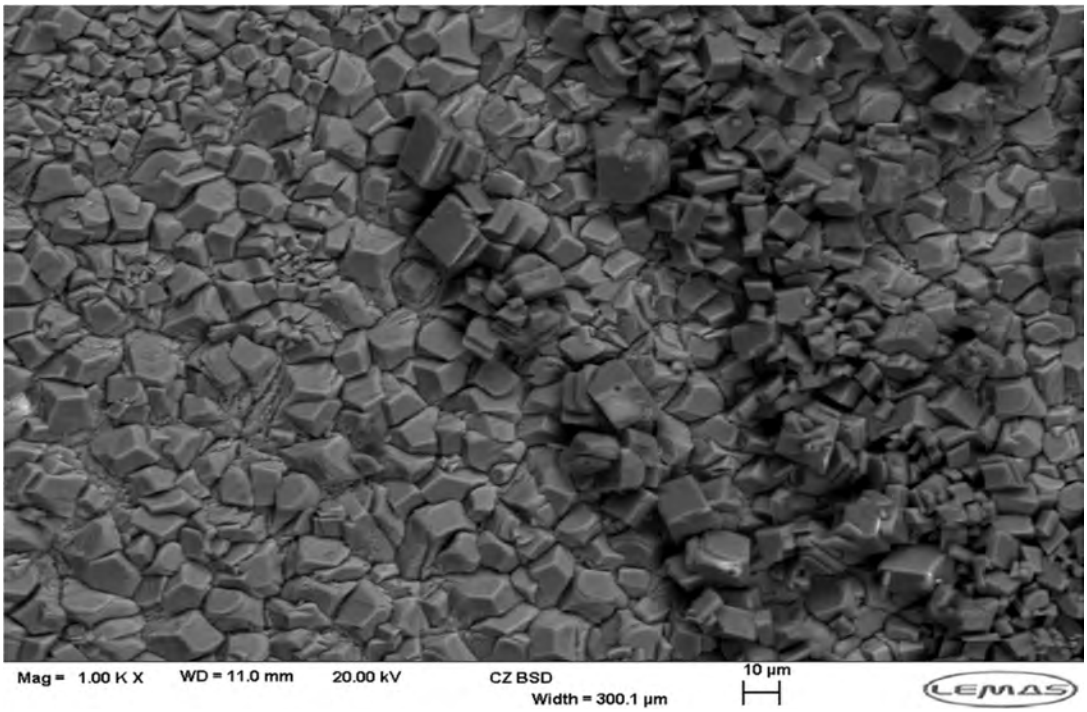

Figure 154 1000x magnification SEM (2) image of $FeCO_3$ sample with linear $CaCO_3$ scale deposits

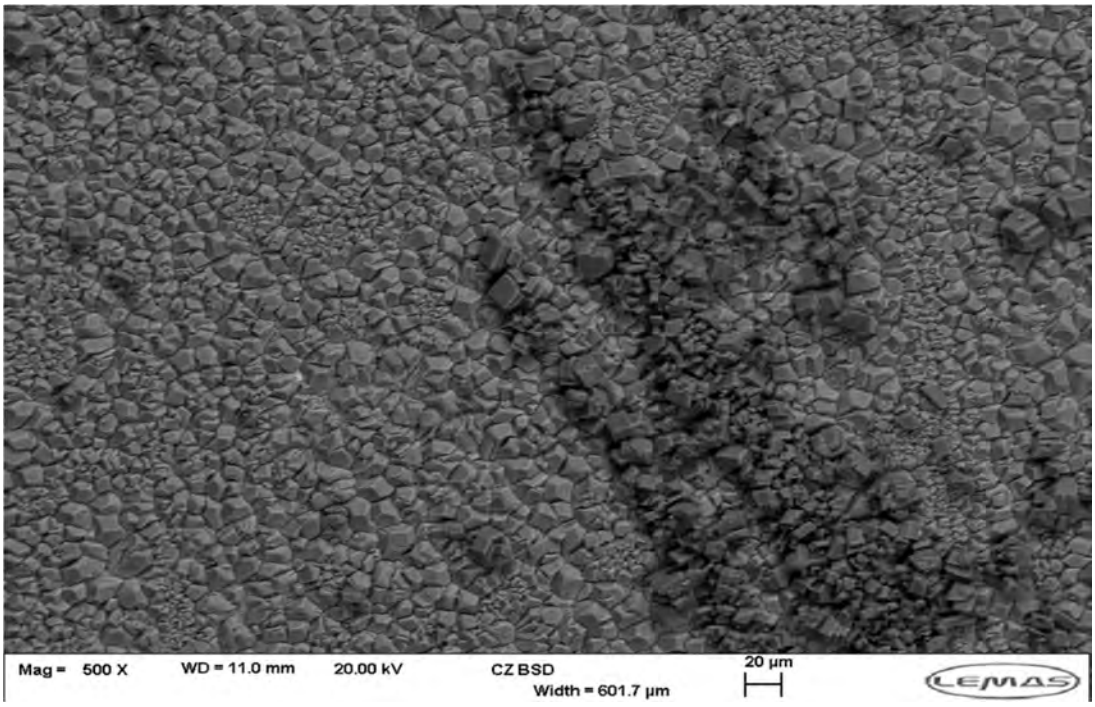

Figure 155 500x magnification SEM (2) image of $FeCO_3$ sample with $CaCO_3$ scale deposits

3. SLIPS Krytox (Kr)

SLIPS Kr shows reduced coverage of $CaCO_3$ scale deposits compared to untreated samples and similar in nature to the results obtained in SI 2.6 for the SLIPS Kr (Figure 156). Based on visual SEM results this demonstrates a type of protective effect from the deposition of $CaCO_3$. Higher magnification also shows evidence of remaining lubricant infused amongst the $FeCO_3$ layer (the darker contrast regions between crystals). The $FeCO_3$ layer also shows the existence of the 2 different morphologies encountered with flatter patches of much smaller $FeCO_3$ (< 1 µm) observed (Figure 157 and Figure 158). Here calcite crystals can be more readily observed suggesting penetration/retention of the Krytox lubricant may not be as great as that obtained in the areas with larger $FeCO_3$ crystals. Scale deposits appear as both amorphous $CaCO_3$ clusters and individual cubic calcite (5-10 µm in size).

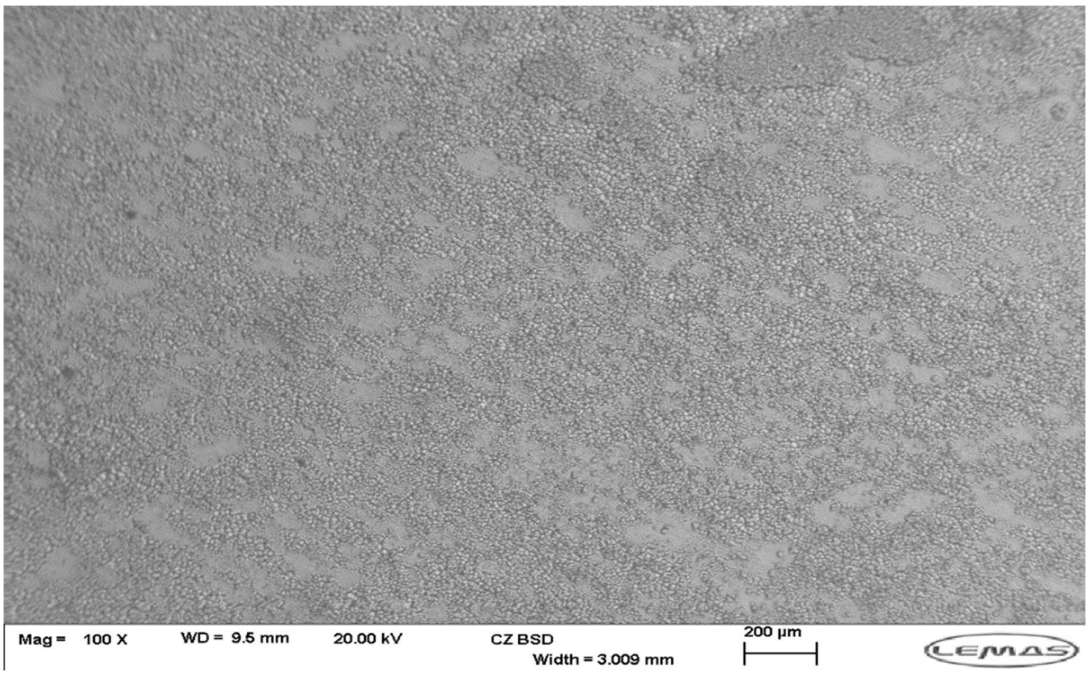

Figure 156 SEM (2) image of SLIPS Kr sample with $CaCO_3$ scale deposits

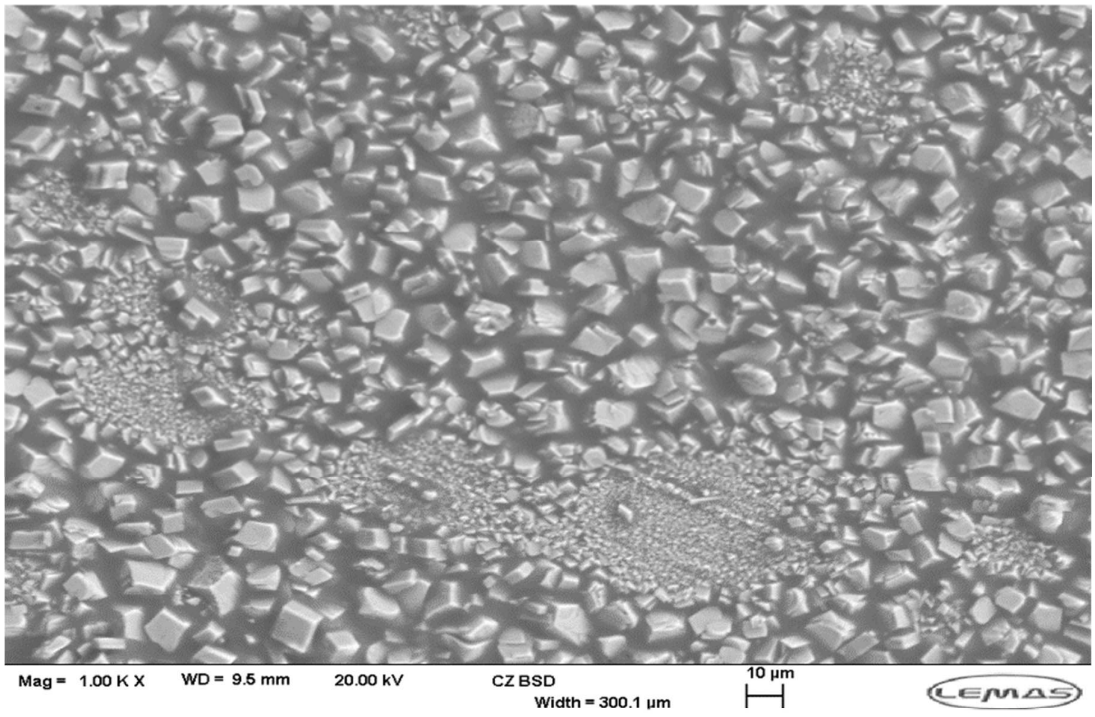

Figure 157 1000x magnification SEM (2) image of SLIPS Kr sample with $CaCO_3$ scale deposits and residual lubricant

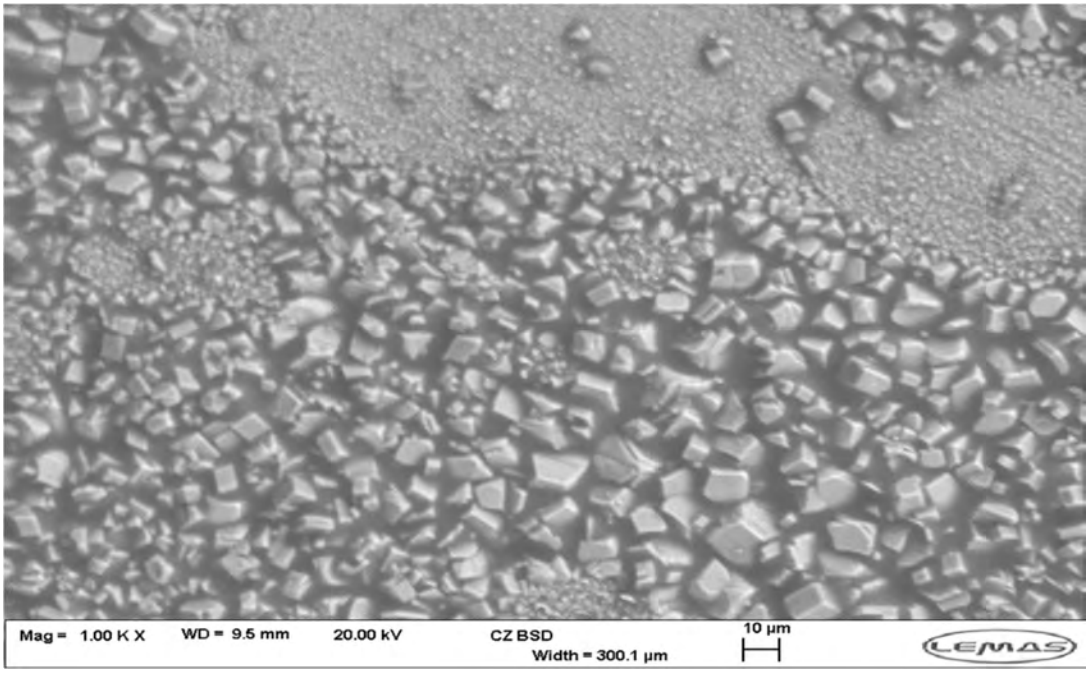

Figure 158 SEM (2) image of SLIPS Kr sample and differing $FeCO_3$ base crystal sizes.

4. SLIPS BMIM (BM)

SLIPS BM show $CaCO_3$ deposits on the surface but on a reduced scale to those encountered in the SI 2.6 brine (Figure 159). The underlying $FeCO_3$ layer is clearly visible across the sample (again showing the presence of two separate $FeCO_3$ size patches). The $FeCO_3$ layer shows little to no traces of remaining lubricant. $CaCO_3$ deposits are predominantly cubic calcite crystals, that appear in large agglomerations or clusters (Figure 160 and Figure 161). Morphologically the crystals are well formed and are markedly different compared to the orthorhombic/curved crystals precipitated in the SI 2.6 system. Crystal agglomerations are up to 200 µm in size, with individual crystals in 10-25 µm range.

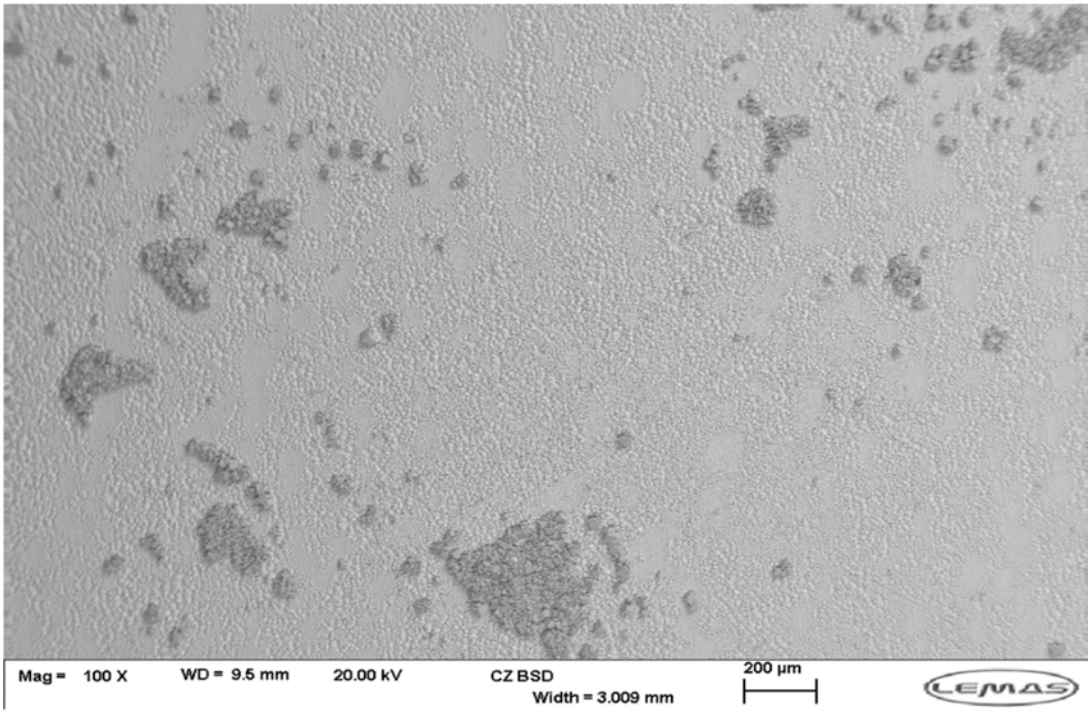

Figure 159 SEM (2) image of SLIPS BM sample showing variations in underlying $FeCO_3$ base layer and $CaCO_3$ scale clusters

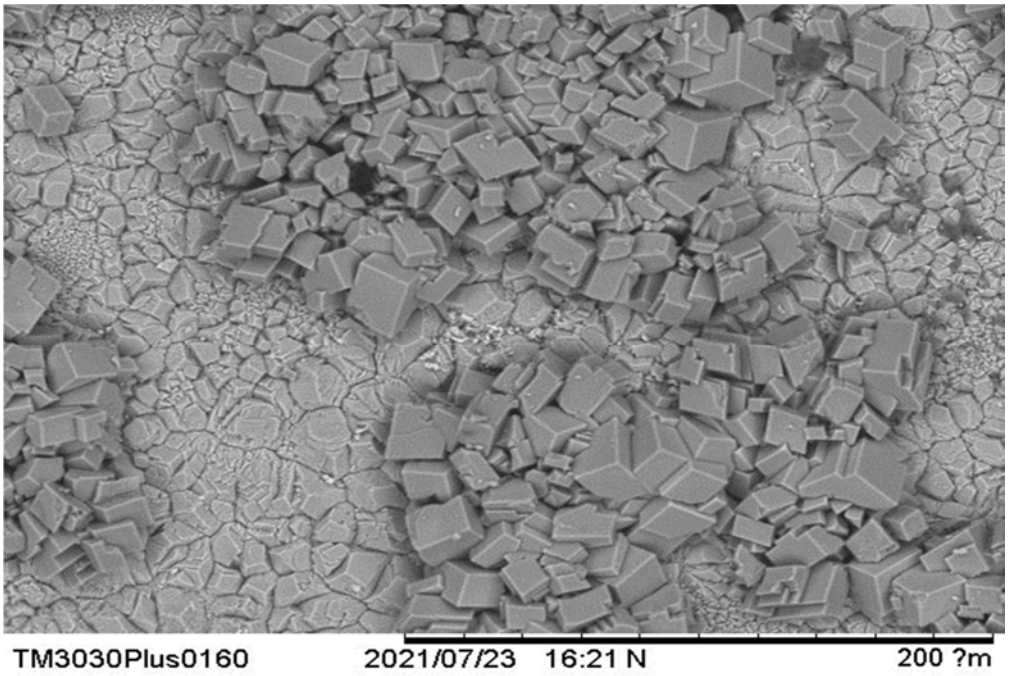

Figure 160 SEM (1) image of SLIPS BM sample with large $CaCO_3$ scale clusters on exposed underlying $FeCO_3$ layer

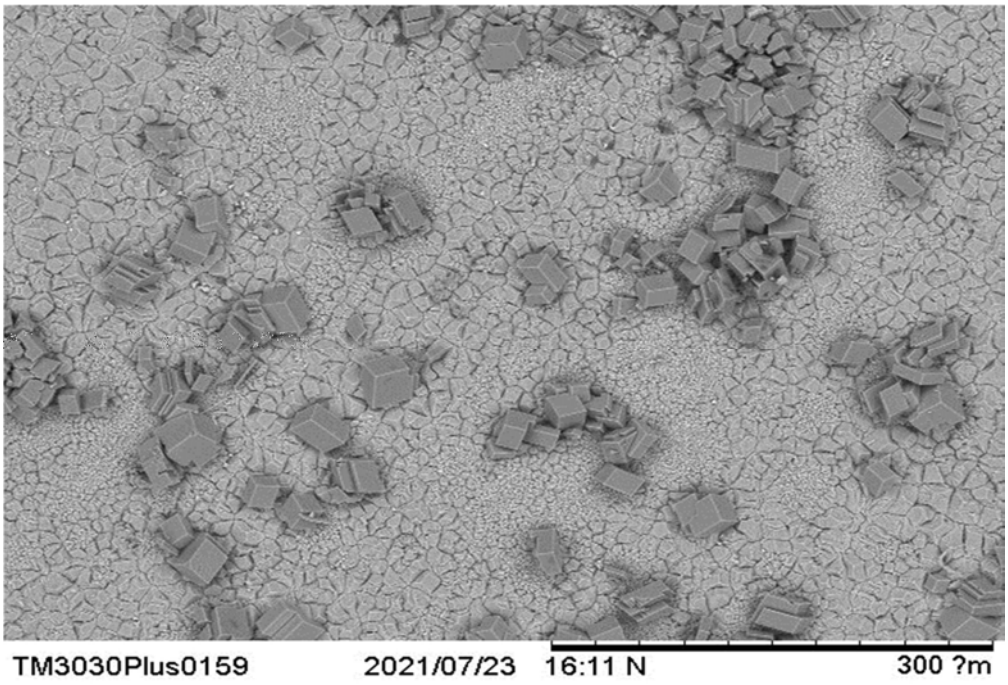

Figure 161 SEM (1) image of SLIPS BM sample with smaller $CaCO_3$ scale clusters and individual crystals

5. SLIPS Waxy (W)

The SLIPS W samples show higher coverage of $CaCO_3$ scale deposits compared to the other SLIPS and untreated samples (Figure 162-158). Both individual and larger crystal agglomerations are apparent. The underlying $FeCO_3$ layer is visible in sections, with some traces of remaining lubricant present (darker contrast). However, even where lubricants remain there appear high levels of $CaCO_3$ crystals. This suggests the lubricant may not offer the same protective capabilities as the Krytox. $CaCO_3$ crystals are typically well-defined cubic calcite crystals. Within the larger agglomerations of $CaCO_3$ crystals (sizes ranging from 5-20 μm) there are sections of tightly packed clusters of smaller crystals (<5 μm) (Figure 163). This is unlike the fairly random crystal size distribution found in crystal agglomerations from other samples. However this pattern of certain sections made up of similar sized crystals (in this case smaller crystals) is also evident in the $FeCO_3$ layer.

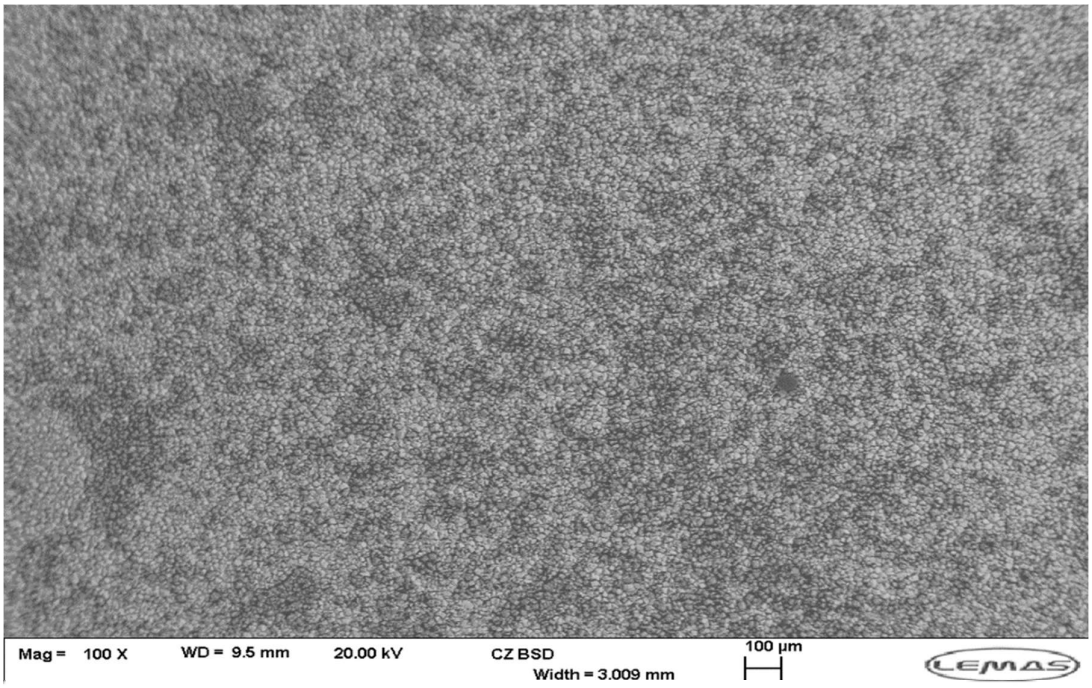

Figure 162 SEM (2) image of SLIPS W sample with $CaCO_3$ scale deposits distributed on the surface

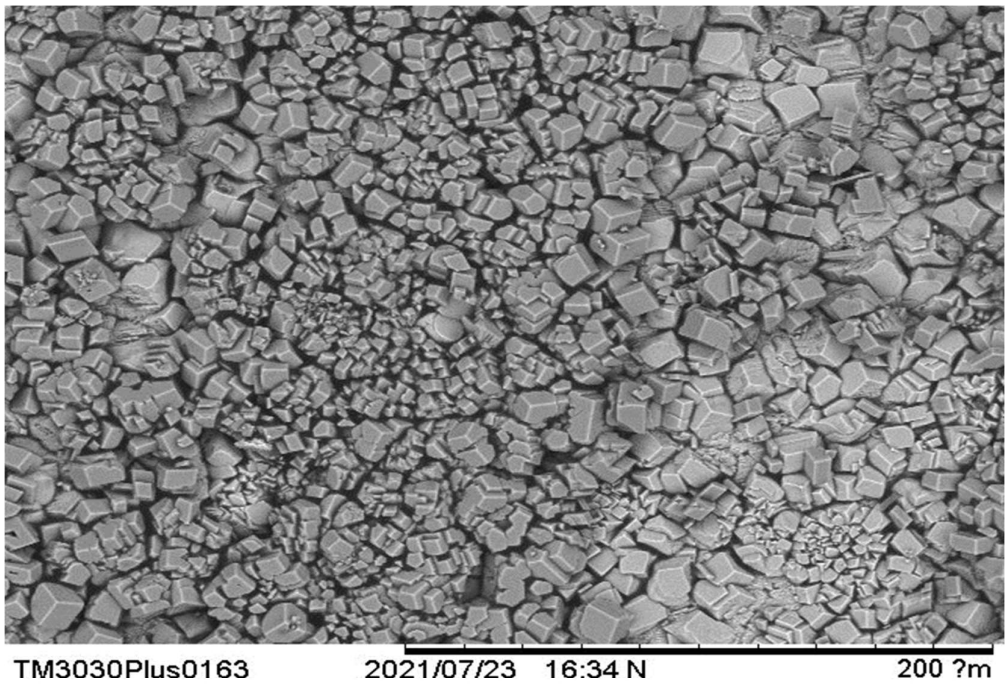

Figure 163 SEM (1) image of SLIPS W sample with varying $CaCO_3$ crystal sizes

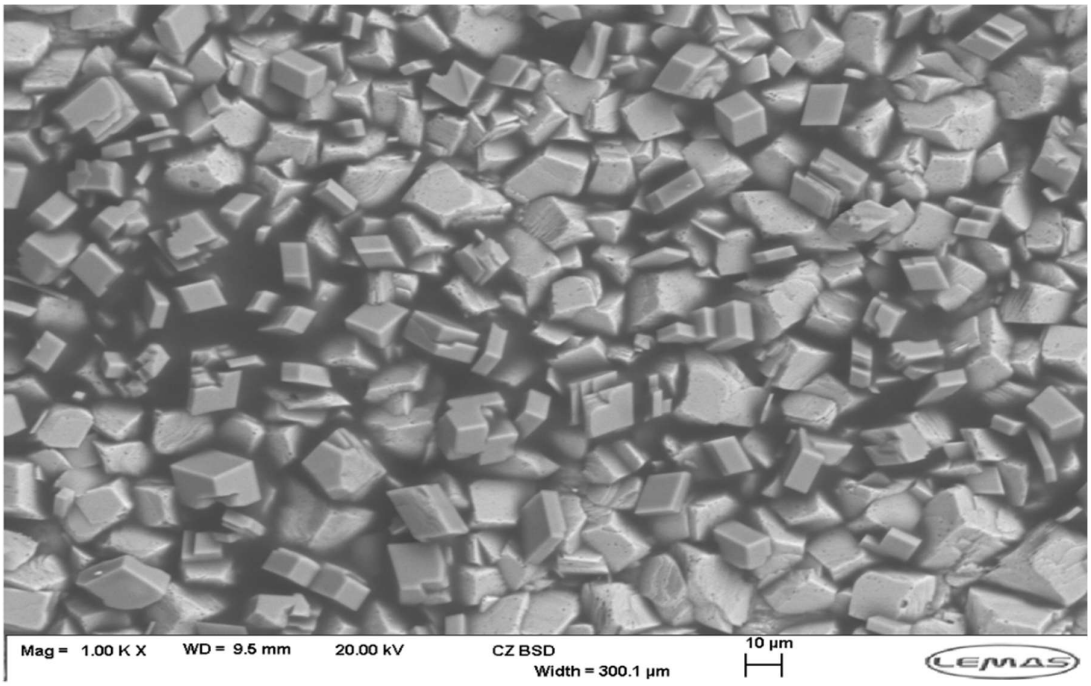

Figure 164 1000x SEM (2) image of SLIPS W sample with $CaCO_3$ scale deposits

6. SLIPS Non-Waxy (NW)

The SLIPS NW shows a similar level of $CaCO_3$ deposits across the surface compared to the SLIPS W (Figure 165). However, $CaCO_3$ crystal agglomeration are not as large and the size distribution of crystals within them are more random. The underlying $FeCO_3$ layer is also visible, again including patches of micro $FeCO_3$ crystals < 1 µm (Figure 166). Interestingly, $CaCO_3$ does not tend to adhere/ nucleate in these areas as much, likely due to the smoother topography. No residual levels of lubricant are visually present, compared to the levels observed on the SLIPS W. The primary polymorph found appears to be calcite, with both individual crystals and those in agglomeration presenting a clearly cubic form in the size range of 5 – 20 µm (Figure 167).

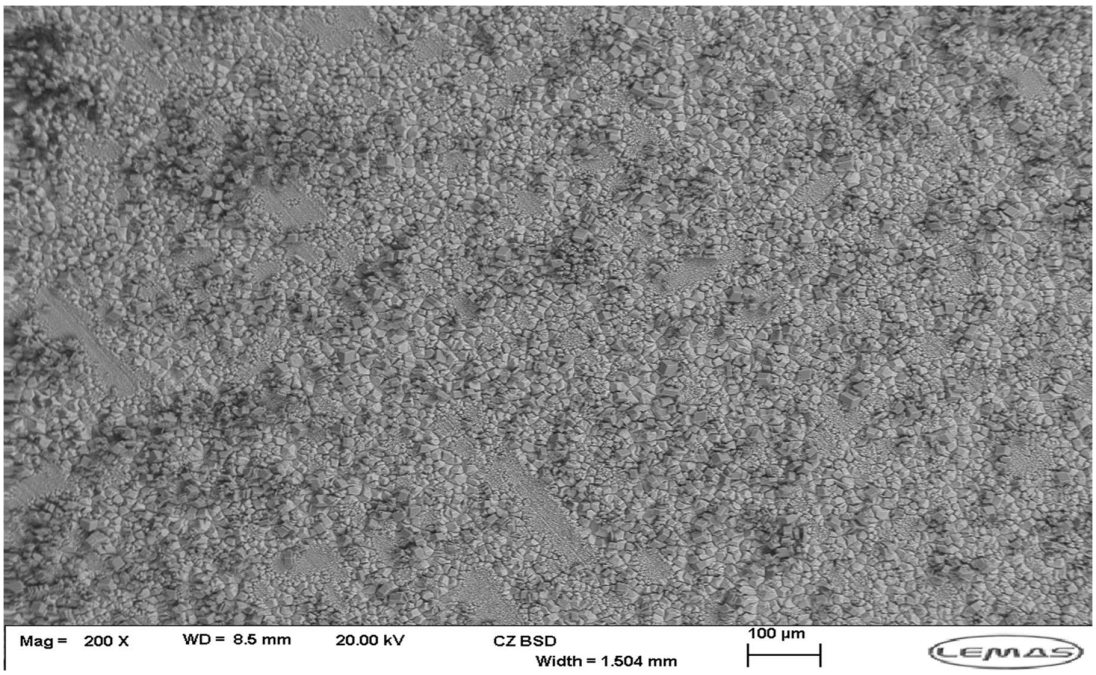

Figure 165 SEM (2) image of SLIPS NW sample showing distribution of $CaCO_3$ scale deposits and underlying $FeCO_3$ layer

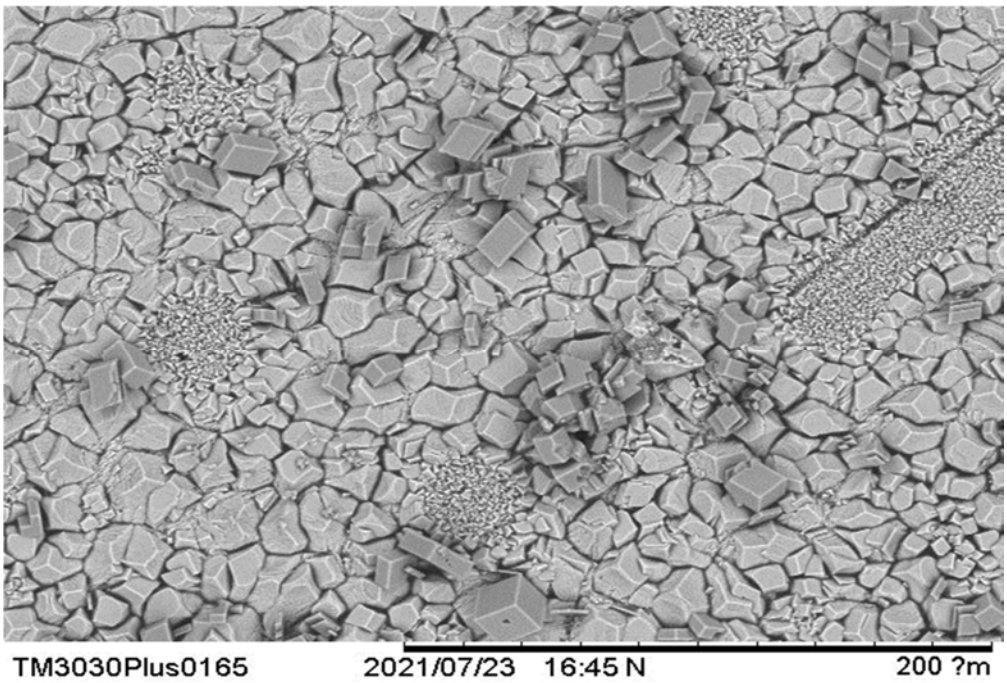

Figure 166 SEM (2) image of SLIPS NW sample with $CaCO_3$ scale deposits and nano scale $FeCO_3$ clusters

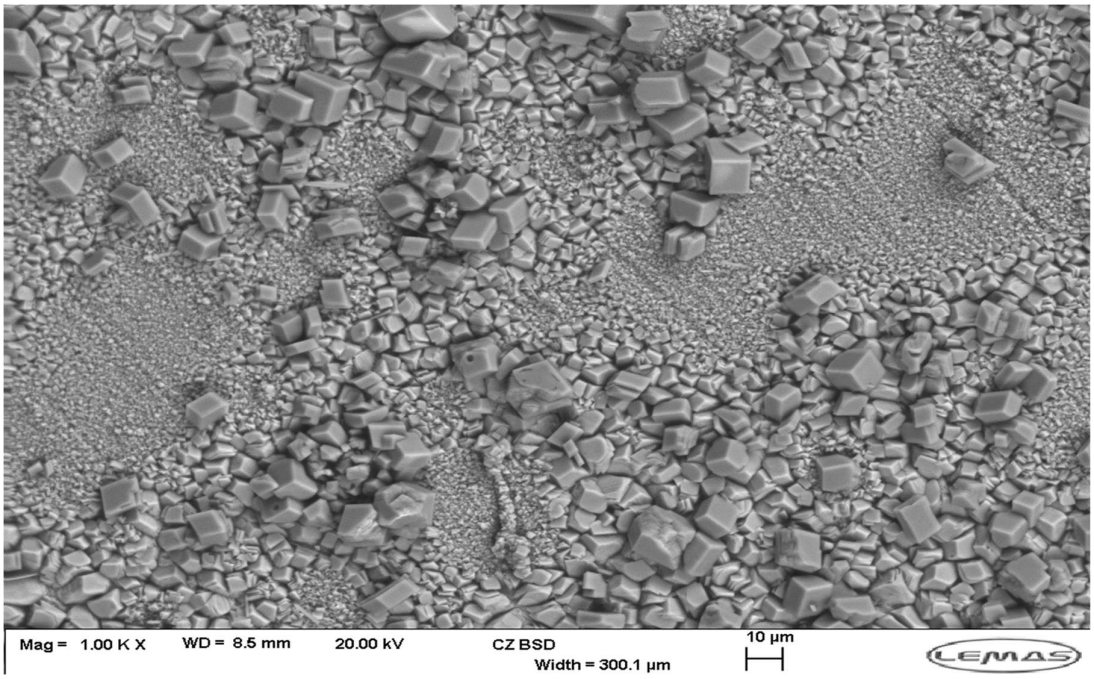

Figure 167 1000x SEM (2) image of SLIPS NW sample with $CaCO_3$ scale deposits and nano scale $FeCO_3$ patches

EDX Analysis of scale deposits Sl 1

EDX analysis has been undertaken to examine the elemental composition of surface scale deposits. Images have been taken from one of two machines, with the number denoting the SEM used: 1. Hitachi tabletop TM3030Plus and 2. Carl Zeiss EVO MA15. EDX analysis was made using Aztec software. In this section EDX is used to develop both qualitative and quantitative understanding relating to calcium concentration/distribution across the sample, differentiate between $CaCO_3$ and $FeCO_3$ scales (alongside SEM) and to detect trace levels of remaining lubricants. Areal values of Calcium (Ca) wt. % have been taken from map scans of 5 mm^2 (minimum) portions of sample surface.

1. X65 Carbon Steel (CS)

Analysis of the carbon steel samples provides clear mapping of the surface composition given the simplicity of the system (i.e no $FeCO_3$ or lubricant). Here, formed $CaCO_3$ crystals can be seen on the surface with clusters of elevated concentrations of Ca on the EDX (Figure 168). Ca is also distributed

across the rest of the surface (not always in visible deposits on the SEM) but at lower concentrations. As expected, the main element that dominates is the background iron (Fe) signature of the steel sample (usually around the 70 wt. % mark, Figure 169). Carbon is also present, with the existence of oxygen (possibly associated with both $FeCO_3$/ $CaCO_3$ nucleation) occurring around the higher concentrations of visible scale deposits and Ca. Areal concentrations of Ca range from lows of 2 wt.% to highs of 17 wt.%, with lower surface deposition associated with the lower saturation index clear.

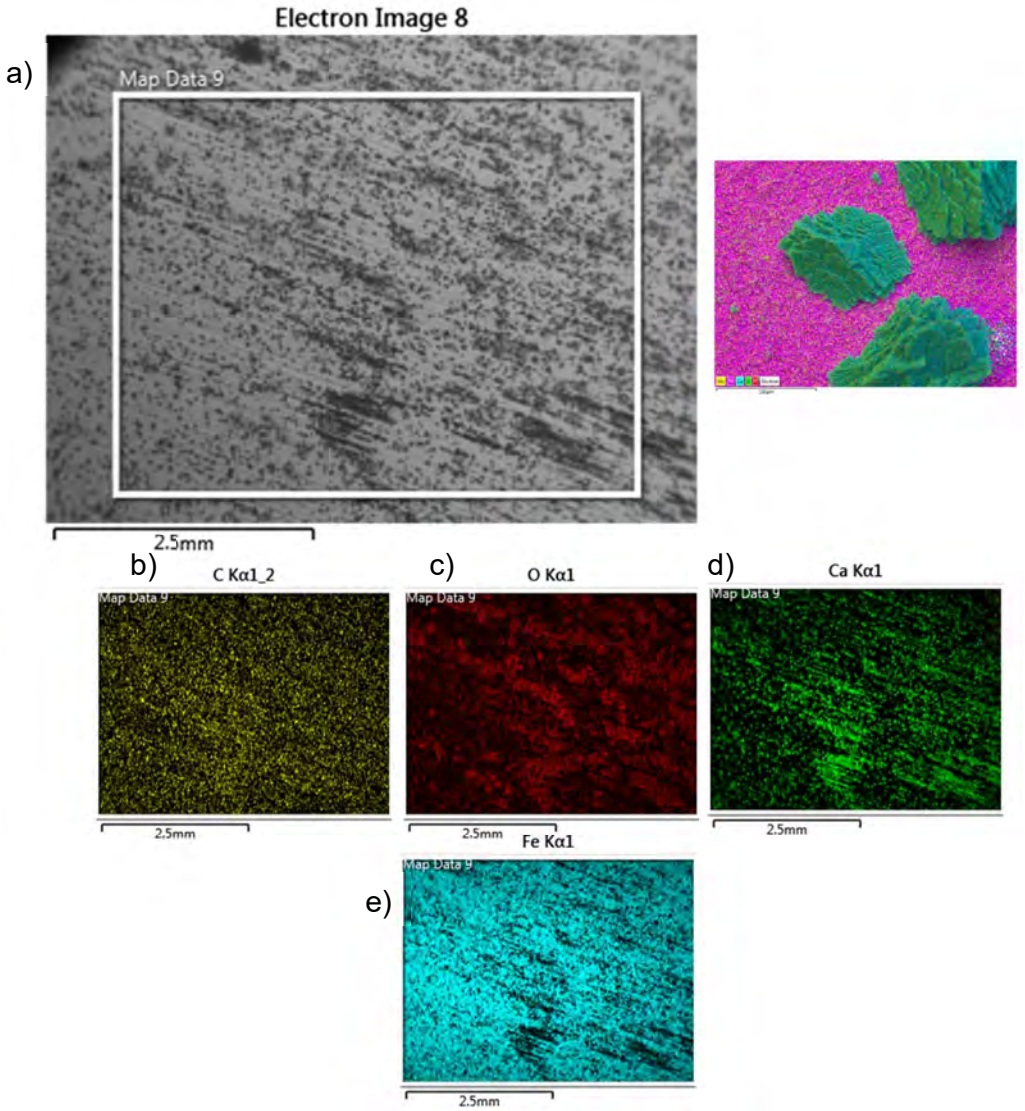

Figure 168 a) Areal SEM and Inset: EDX map of $CaCO_3$ crystal on surface. EDX elemental map of b) C, c) O, d) Ca and e) Fe for X65 CS sample.

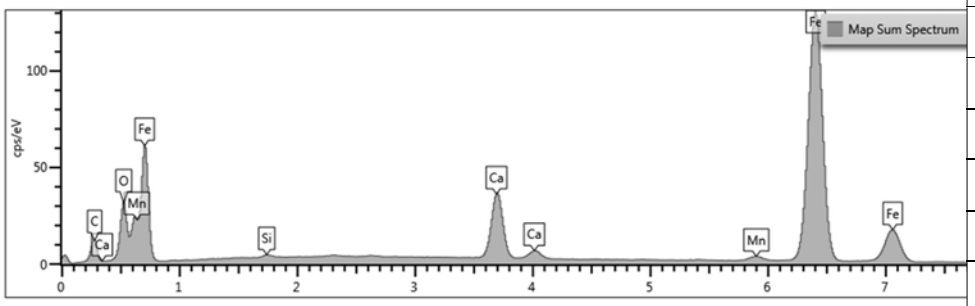

Element	wt.%
C	14.05
O	11.39
Si	0.16
Ca	5.37
Mn	1.01
Fe	68.02
Total:	100

Figure 169 Typical EDX map sum spectra and elemental composition table for X65 CS

2. Iron carbonate ($FeCO_3$)

Given that the base has now been replaced with the grown $FeCO_3$ layer, there are a number of differences in surface composition after scaling. Levels of carbon and oxygen are elevated and relatively uniform across the surface due to the presence of both the iron and calcium carbonates deposited. The Fe signature is also significantly reduced (>25 wt.%) compared to the X65 CS sample due to widespread coverage of both types of scales (Figure 170). Ca appears in highly concentrated clusters that in conjunction with original images can be identified as the $CaCO_3$ scale deposits. However Ca is also present in small concentrations across the rest of the surface, but whether this is a layer on top of the existing $FeCO_3$ or actually integrated into the structure cannot be determined. Although the Ca concentrations in areas that are not visible $CaCO_3$ deposits (on SEM) are higher on the $FeCO_3$ (5 wt. %, Figure 171b) surface than the X65 CS surface (1 wt. %, Figure 171a). One sample achieved close to 100% coverage of $CaCO_3$ with areal Ca levels peaking at 39 wt.% (Figure 171d). This value is close to that of individual $CaCO_3$ crystals which measured Ca levels at 50 wt.% (Figure 171c). Ca readings at the lower end of the range were 4 wt.% showing a considerable variation in Ca surface composition across the $FeCO_3$ samples.

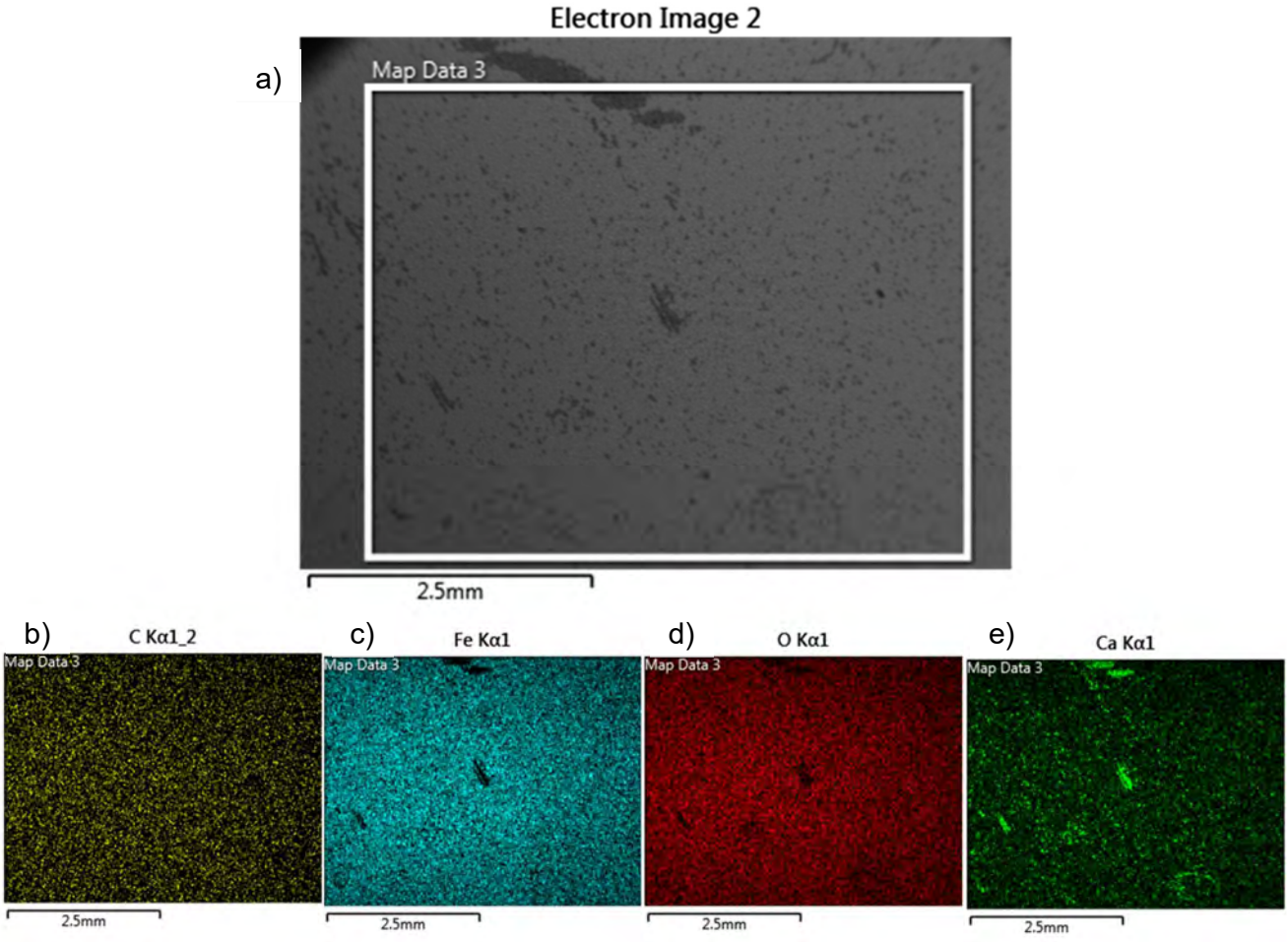

Figure 170 a) Areal SEM and EDX elemental map b) C, c) Fe, d) O, e) Ca for $FeCO_3$ sample

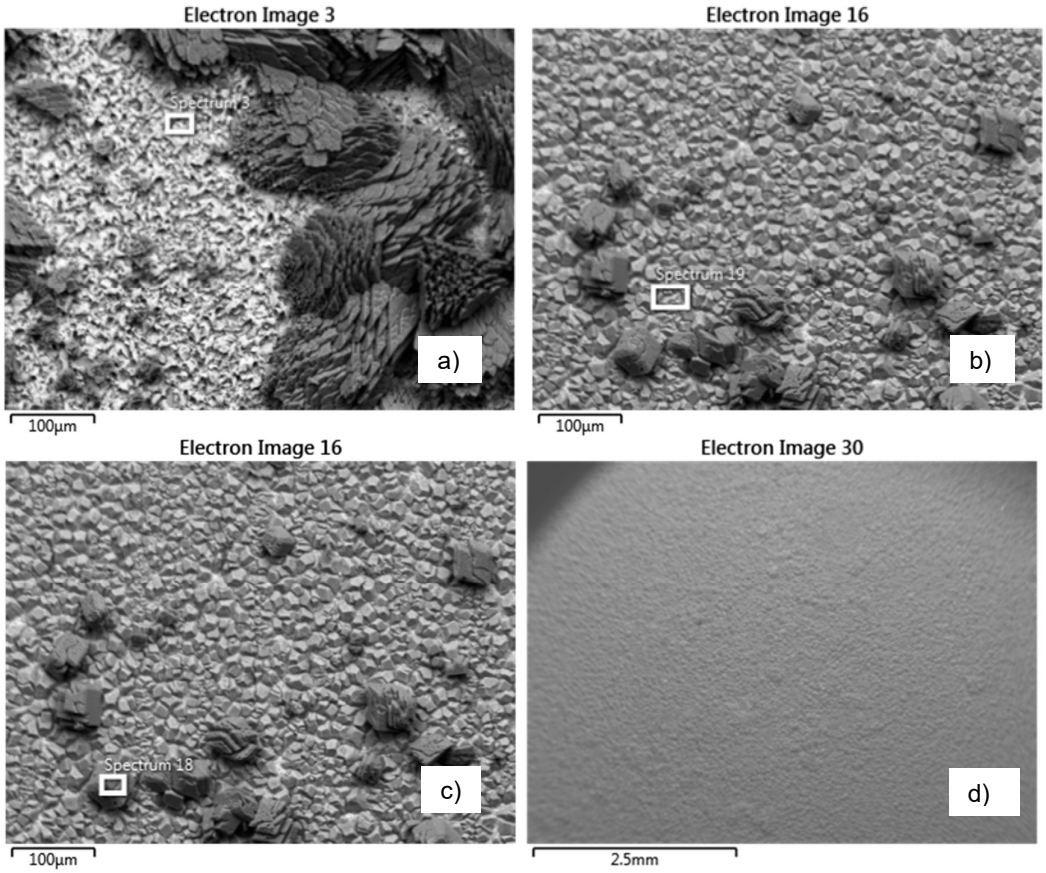

Figure 171 a) X65 CS sample b)-c) $FeCO_3$ sample with $CaCO_3$ deposits d) $FeCO_3$ sample fully covered with $CaCO_3$ deposits

3. SLIPS Kr

The SLIPS samples introduce a 3rd component into the system which is the lubricant. In this case all lubricants represent an organic compound that is being introduced to the otherwise inorganic system. In the EDX analysis the primary identifying element for the Krytox lubricant is the presence of fluorine (F) with levels before the test at roughly 70 wt.% (

Figure 172).

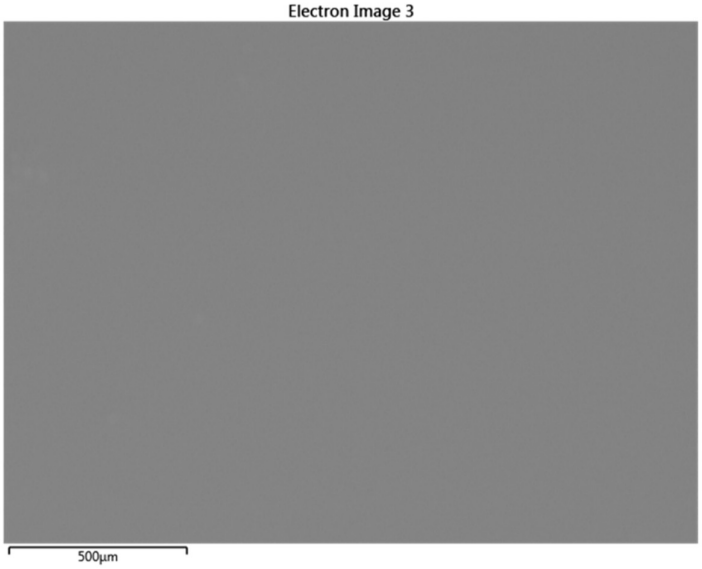

Element	wt. %
C	22.08
F	70.03
O	7.23
Fe	0.66
Total	100.00

Figure 172 SEM of Krytox lubricant used for EDX. Inset table: EDX element Wt. %

After scaling tests, SLIPS Kr samples show areal Ca levels as low as 0.16 wt.% and highs of 10 wt.%. These samples show lubricant depletion across the surface through a reduction in the areal F wt.% to levels around 15-39 wt. % (Figure 173). In the areas with $CaCO_3$ deposits or elevated Ca concentrations, F levels are almost non-existent. Whether this is a result of the deposit covering the F signature or the complete loss of the protective lubricant is difficult to verify. Ca levels in areas where there are not visible scale deposits are similar in value (≈3-5 wt. %) to those in the non-lubricated $FeCO_3$ sample. Suggesting although scaling performance is better than the non-lubricated sample (i.e lower Ca wt.%) there is some minimal uptake into the $FeCO_3$ layer of Ca.

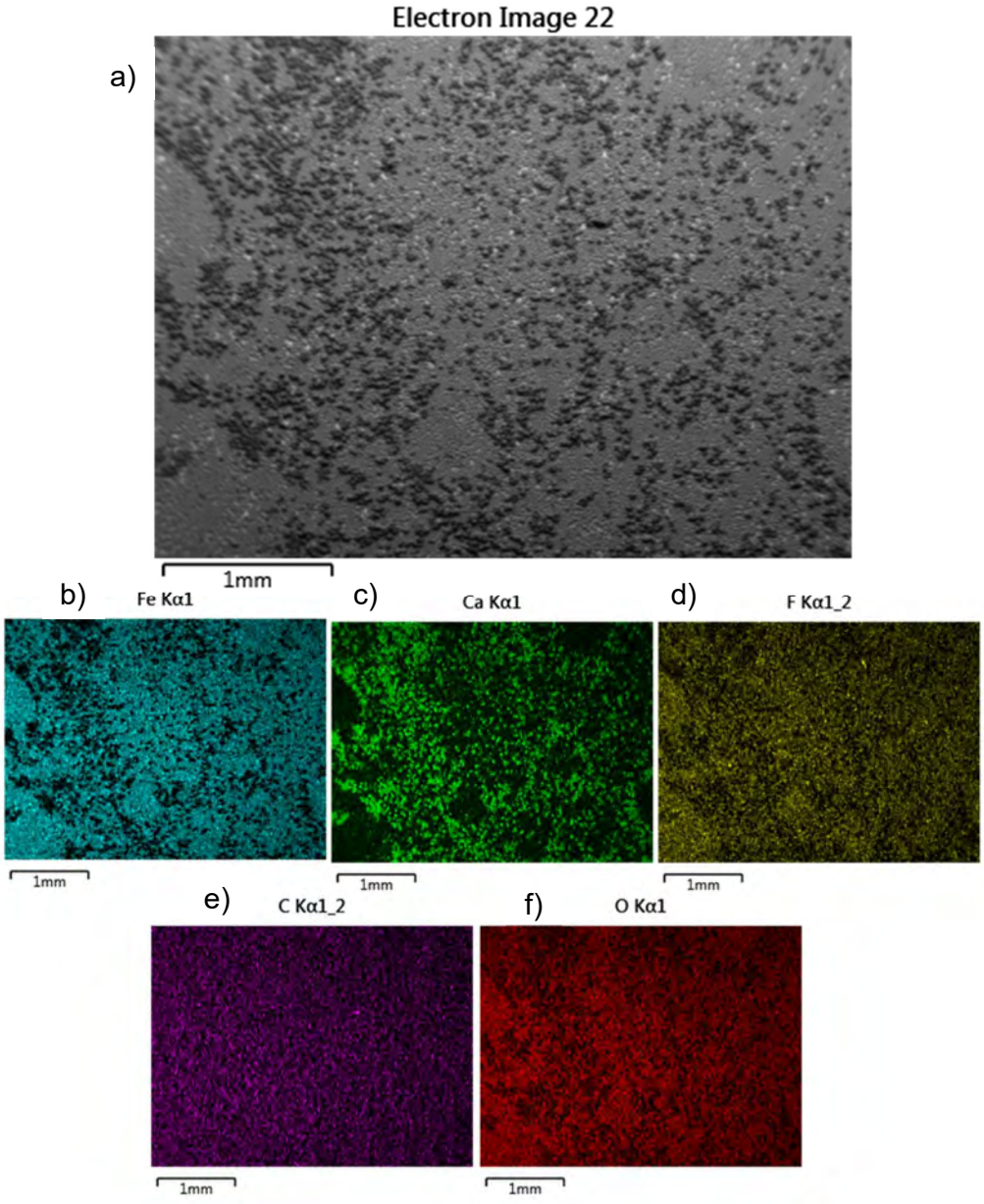

Figure 173 a) Areal SEM and EDX elemental map of b) Fe, c) Ca, d) F, e) C and f) O for SLIPS Kr sample

4. SLIPS BM

In EDX analysis, the lubricant BMIM is detected by both fluorine (F) and sulfur (S). The F level is significantly lower at 30 wt. % than that detected on the Krytox samples, with S identified around 19 wt. % (Figure 174).

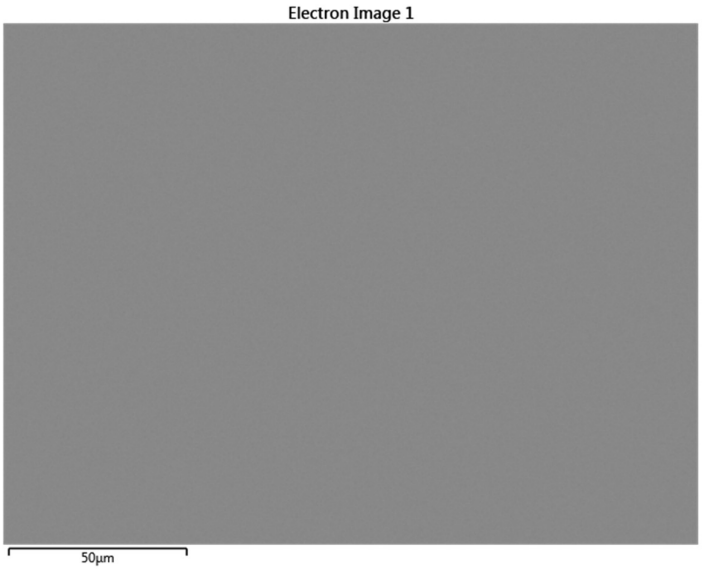

Element	wt. %
C	36.30
O	13.33
F	30.66
S	19.09
Fe	0.62
Total	100.00

Figure 174 SEM of BMIM lubricant used for EDX. Inset table: EDX element Wt. %

Post test analysis of areal Ca composition ranges from 28 wt.% to 41 wt.%. This range is at the higher end of surface scale composition. Similar to samples found with the non-lubricated $FeCO_3$ layer there were SLIPS BM samples that were fully covered in $CaCO_3$ layers, with a high (≈ 40%) Ca wt. % uniformly across the surface. Mapping of the lubricant layer via EDX was similar to that of the SLIPS Kr with areas that registered low/zero F wt. % being higher in Ca wt.% (Figure 175). In this case it is interesting to note that the other marker of the BMIM lubricant, S, was more consistently distributed across the surface. Conversely some areas rich with Ca wt. % were also in areas with higher S wt. %. This could suggest that the lubricant layer is still present even when scale deposits are above or that there is some integration with the BMIM lubricant into the $CaCO_3$. Indeed residual levels of the BMIM lubricant (F/S wt. %) occur at much lower levels (<3%) or are usually not detected in the EDX analysis.

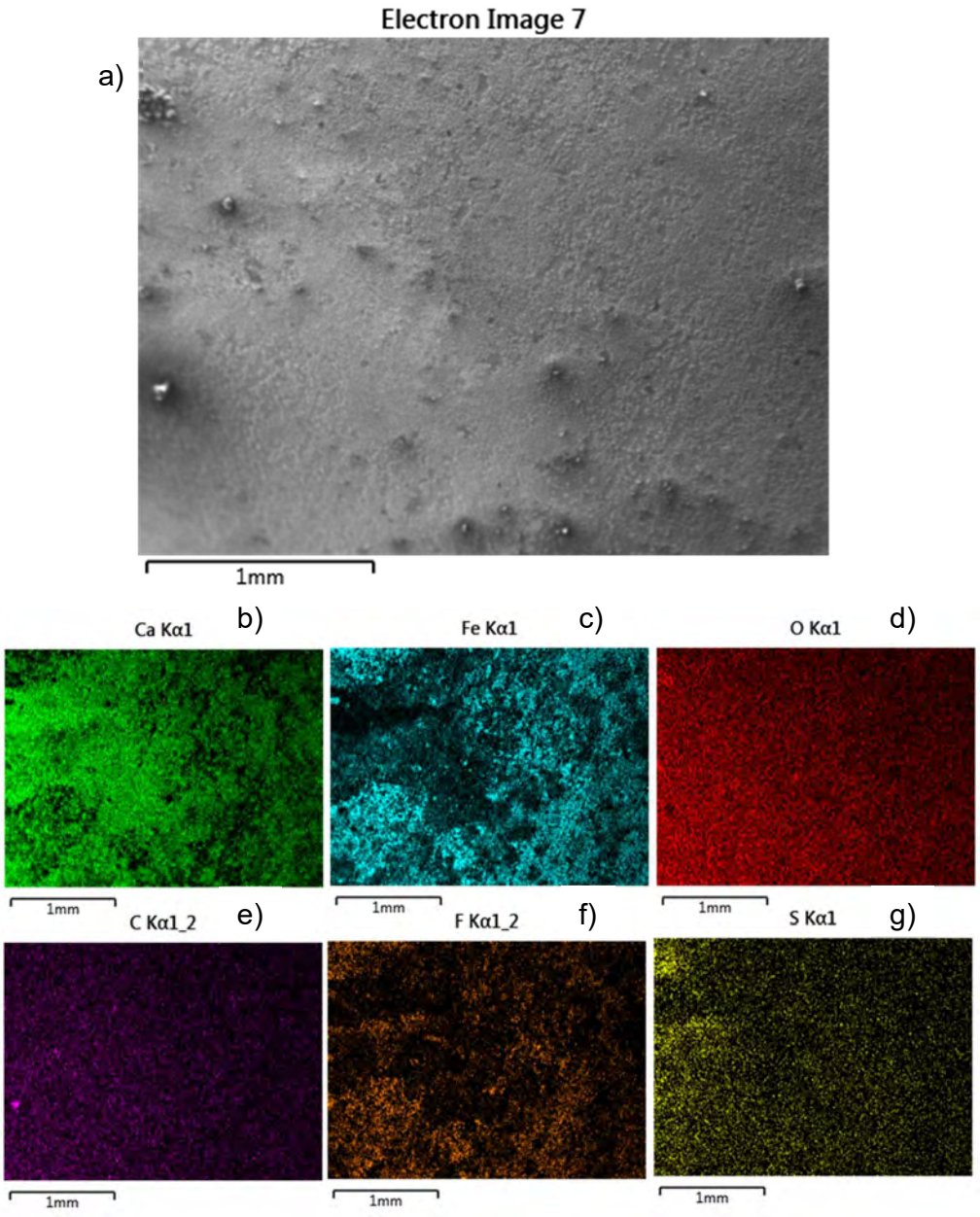

Figure 175 a) Areal SEM and EDX elemental map of b) Ca, c) Fe, d) O, e) C, f) F and g) S for SLIPS BM sample

5. SLIPS W

The Crude Oil SLIPS represent a separate category of lubricants where the use of EDX analysis for lubricant mapping/ depletion is not very effective. This is due to the fact they possess much higher vapor pressures (evaporating any residual lubricant) and a lack of identifying marker elements for EDX detection (i.e F, S etc). The range of Ca wt. % for SLIPS W samples (Figure 176) was highly variable with some samples showing levels as low as 2-4% wt. %, a

level similar to that detected on areas of the non-lubricated $FeCO_3$ layer not covered with $CaCO_3$ deposits. However there was also samples that were fully covered by $CaCO_3$ deposits with areal Ca values of (>40 wt. %). Ca wt. % was distributed equally across the EDX map area in samples that were either low or high in surface Ca wt. %. Also of note, when the sample wasn't fully covered in $CaCO_3$ deposits there were a number of trace elements (i.e Cu, Si, S Zn etc) likely associated with impurities in the crude oil scattered across the surface, usually at levels lower than 5 wt. %.

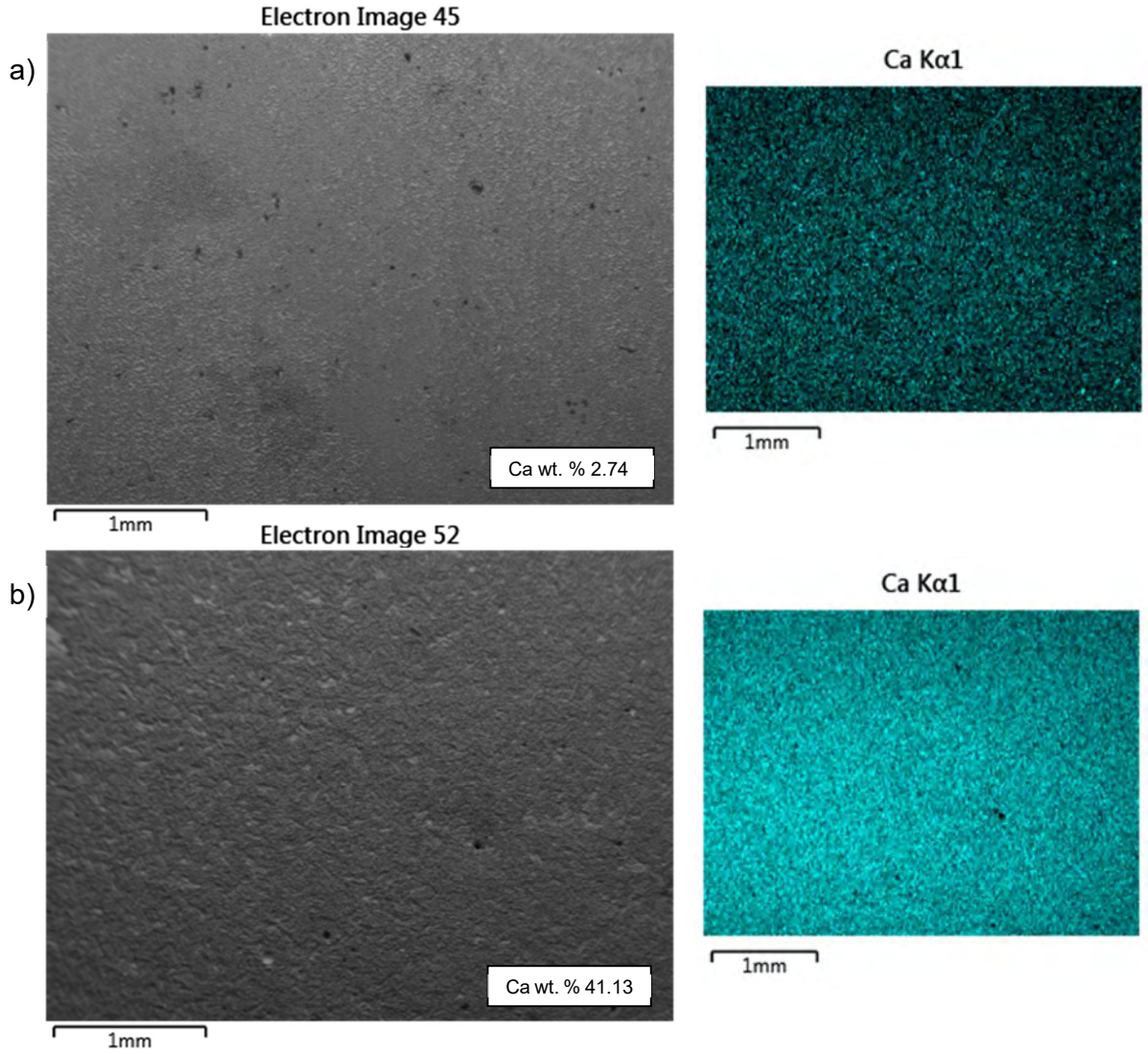

Figure 176 SEM and inset: EDX calcium map for two separate SLIPS W samples with a) Low Ca wt. % and b) High Ca wt. %

6. SLIPS NW

The SLIPS NW behaved differently to the waxy version both in terms of Ca wt.% and variability between samples (Figure 177). Ca wt.% was in a much tighter band with lower levels from 2.79 up to 8.51. Under the areal mapping Ca was not distributed as evenly as that of the SLIPS W, with areas of elevated Ca clusters clearly visible. In terms of trace elements the No Waxy crude oil lubricant also contained a number of impurities such as Cl, Mn, Zn and Cu at low levels (<5 wt. %).

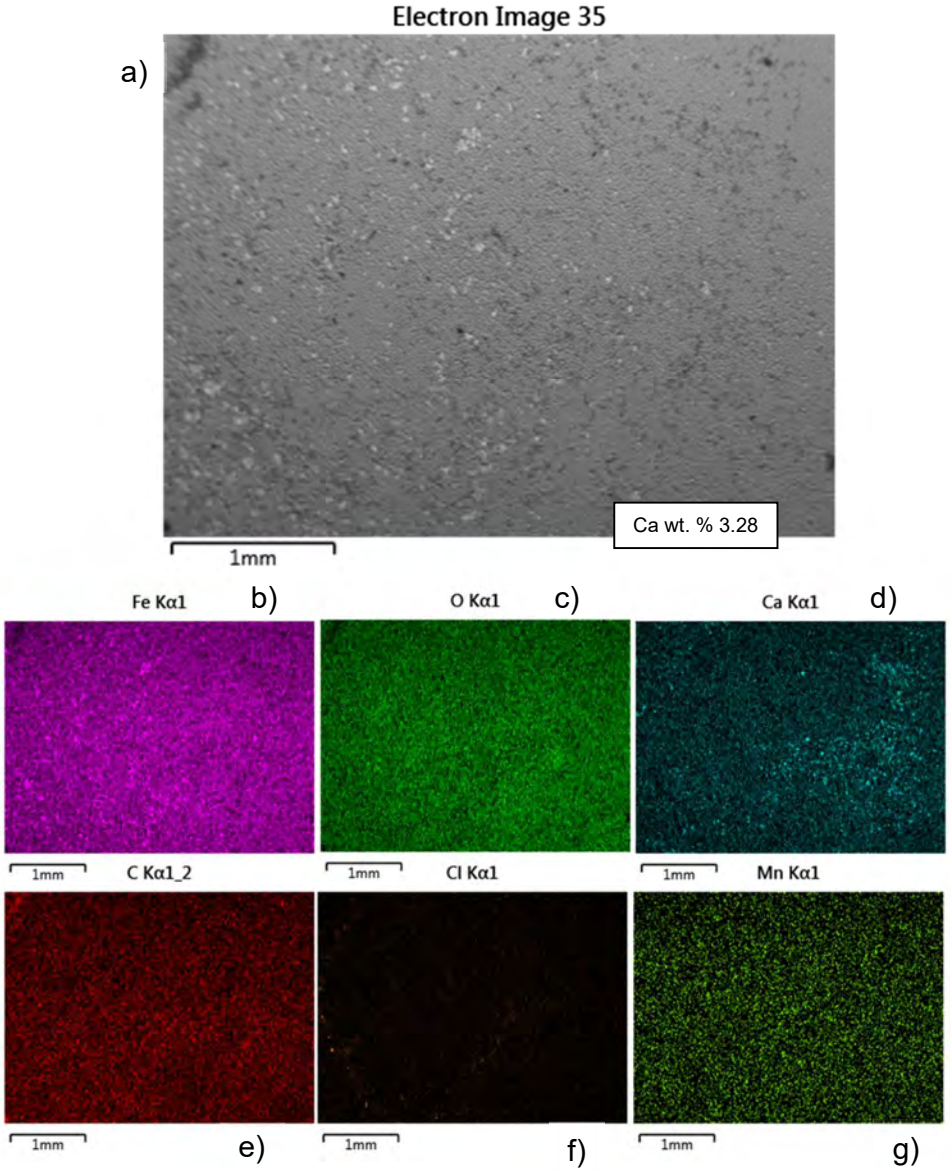

Figure 177 a) Areal SEM and EDX elemental map of b) Fe, c) O, d) Ca, e) C, f) Cl and g) Mn for SLIPS NW sample

Summary SEM and EDX

SEM and EDX analysis has been conducted on samples to observe $CaCO_3$ scale deposition in SI 1 and SI 2.6 brine. The following conclusions have been drawn:

- $CaCO_3$ scale deposits are predominantly calcite polymorph crystals from SEM observation. The polymorph type (i.e morphology and size) is similar in nature to those observed in the bulk characterisation section. This is across all samples and both brine saturations. Occasionally lone aragonite crystals are also seen.
- Ca Wt.% across samples is variable. Higher levels of Ca Wt.% are seen on samples from the SI 2.6 brine compared to SI 1. This is likely given the increased saturation index, generating a higher level of crystals in the bulk and more favourable nucleation conditions on the surface. The Ca Wt. % range for samples in the SI 1 brine is also in a tighter band compared to SI 2.6.
- With regards to performance, SLIPS Kr showed lower Ca Wt. % in both brine systems. On the other hand, SLIPS Bm consistently performed poorly when compared to the other SLIPS systems. SLIPS surfaces generally showed improved scaling performance over non-SLIPS samples such as the X65 CS and $FeCO_3$. The samples analysed via EDX are ranked below (in order of decreasing Ca Wt.%)

SI 1: SLIPS BM> SLIPS W > $FeCO_3$ > X65 CS> SLIPS NW > SLIPS Kr

SI 2.6: $FeCO_3$ > SLIPS BM > X65 CS > SLIPS NW > SLIPS Kr > SLIPS W

- The presence of lubricant can be seen post-test. Either visually via SEM, through trace element analysis on EDX or FTIR signature. This is dependent on the type of lubricant providing a mixture of qualitative and quantitative information. The stronger the trace/presence of lubricant post-test is usually associated with lower Ca Wt. % and a good indicator of improved performance. There is also the possibility of using this as a measure of compatibility between the lubricant and underlying substrate when reflecting on the initial theoretical design criteria.

- A Pearsons correlation has been conducted to see correlations of Ca Wt.% with SLIPS material properties determined earlier (i.e WCA and SFE). The results are shown below in Table 18. Correlations between the two brine systems are of a similar nature. With regards to SFE, there appears to be no correlation with Ca Wt.% (Coefficient $-0.2 < \rho < 0.2$). Indeed this is seen when comparing SLIPS Kr (lowest SFE) with either SLIPS NW or W (highest SFE). Here both samples perform equally well with lower Ca Wt.% values. There does appear to be a strong negative correlation between WCA and Ca Wt. % (Coefficient $-1 < \rho < -0.5$). This indicates higher WCA (or hydrophobicity) is linked with lower Ca Wt. %. This is in line with conventional thinking with lower contact angles associated with hydrophilicity and an attraction between the surface and scale containing brine. The lower WCA would also maximize contact area between droplets and the underlying lubricant/surface (via greater spreading).

Table 18 Pearson correlation for SFE and WCA for both brine systems

	SI 1			**SI 2.6**		
	SFE	WCA	Ca Wt. %	SFE	WCA	Ca Wt. %
SFE	1	-	-	1	-	-
WCA	-0.165	1	-	-0.177	1	-
Ca Wt. %	0.049	-0.869	1	0.104	-0.679	1

7.8 X-Ray Diffraction (XRD) Analysis of samples

XRD analysis has been performed to verify the identification of materials found through the other analysis methods such as FTIR, EDX and SEM. This includes the presence of both the underlying $FeCO_3$ layer that the SLIPS is built from, the scale deposits primarily made of $CaCO_3$ and the mixed iron-calcium carbonates ($Fe_xCa_yCO_3$) that also form. Apart from phase identification, XRD has also been used to observe the changes in the crystal structure and a means of assessing the scale resistance of SLIPS. At a crystalline level, the integration of Ca^{2+} into the $FeCO_3$ layer and the presence of mixed $Fe_xCa_yCO_3$ provides insights into the protective capabilities of the lubricants. Using d-spacing to measure the molar fraction of Ca^{2+} in the mixed carbonates allows an understanding of the effectiveness of the lubricants as physical barriers in protecting the $FeCO_3$ layer. In literature, the mole fraction is calculated using Equation 28 (derived in Methodology) and the d-spacing of the (104) crystal peak. The [104] interplanar d-spacing is used due to its position as the most intense Bragg peaks for both $FeCO_3$ and $CaCO_3$. Generally speaking the mole fraction of Ca within the mixed $Fe_xCa_yCO_3$ increases linearly with an increasing d-spacing.

$$\frac{1}{d^2} = \frac{4}{3}\left(\frac{2.924y+26.626}{148.214y+582.680}\right) + \frac{16}{(1.688y+\quad.373)^2}$$

Equation 28

XRD Analysis of base materials

Figure 178, Shows the base line readings for the three primary materials expected to be encountered. This includes the $FeCO_3$ layer used for the SLIPS base, $CaCO_3$ powder extracted from the brine system and the original X65 carbon steel (CS) sample. The CS sample shows an isolated sharp peak at roughly 45˚, which is associated with the [110] face of α-Fe. A smaller peak is also seen at 65˚ representing the [200] plane. The $CaCO_3$ powder has a large peak just before 30˚ that is synonymous with the [104] plane, the size of the intensity with relation to the other peaks also confirms (along with other

analysis methods) that the primary polymorph is calcite. Other minor peaks are also identified at 36˚, 39˚, 43˚, 47˚ and 48˚ corresponding to the following planes [110], [113], [202], [108] and [116] respectively. In the case of the $FeCO_3$ sample, the largest intensity occurs in the [104] plane at 32˚. Again a number of minor peaks are found at 24, 38, 41, 46, 52 marking the following $FeCO_3$ planes of [012], [110], [113], [202] and [116]. The minor peak of [110] α-Fe is also present. Overall, sharp and strong peaks particularly for the [104] plane confirm the products are well-crystallised and are in line with peak intensities and positions for these materials in the literature. The intensity of the [104] face in both the $FeCO_3$ and $CaCO_3$ compared to other peaks is clear and their use in Equation 28 for determining the Ca molar fraction is valid.

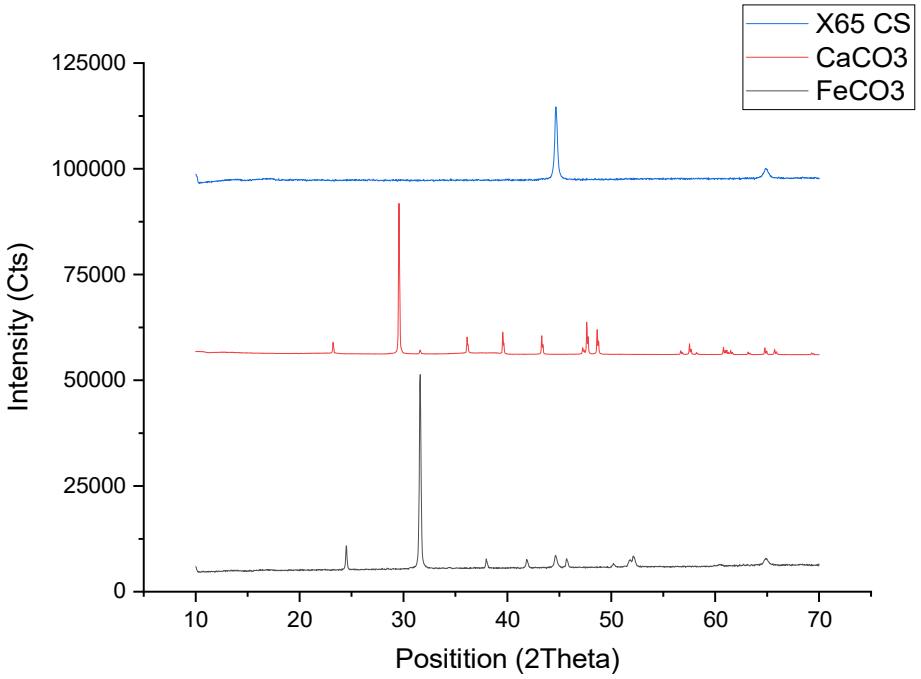

Figure 178 XRD Patterns from base X65 CS, precipitated $CaCO_3$ and grown $FeCO_3$ samples

XRD Analysis of SI 2.6 Samples

Figure 179-178 show the XRD results for the 6 samples tested in the SI 2.6 brine system. All samples share a number of similarities across relative peak

intensities and position. Peaks are primarily linked with the three base materials of $FeCO_3$, $CaCO_3$ and X65 CS, with all samples showing indications of the 3 materials. Lubricants are not easily identifiable on XRD analysis and this is not a method commonly used for this. The primary peak seen on samples is that at 29.4˚ corresponding to the [104] plane of $CaCO_3$. Intensity is expected to be high given crystals would precipitate on the top-most layer of the sample (subsequently reflecting stronger signals) and the high saturation index associated with the brine (i.e SI 2.6). The strongest signals at this position came from SLIPS BM (Figure 180) and X65 CS (Figure 184), which were also associated with higher levels of Ca wt.% in the EDX analysis. The lowest signal detected was from SLIPS Kr, with a level similar in intensity to the [104] $FeCO_3$ peak (Figure 179) on the same sample. The next strongest signal for $CaCO_3$ was seen at position 47˚ representing the [108] face. α-Fe peaks are also seen across all samples with the [110] face being the most prominent. Other secondary, smaller peaks for both $FeCO_3$ and $CaCO_3$ are visible across the spectrum. One observation is that while all $CaCO_3$ peaks are in line with expectations from literature, $FeCO_3$ peaks show a distinct shift in the spectra position. The shift in position for only one of the carbonates groups ($FeCO_3$) suggests this is the cause of incorporation of the Ca^{2+} into the $FeCO_3$ and formation of mixed $Fe_xCa_yCO_3$. Rather than a shift caused by other sources such as poor levelling of the sample in the XRD unit.

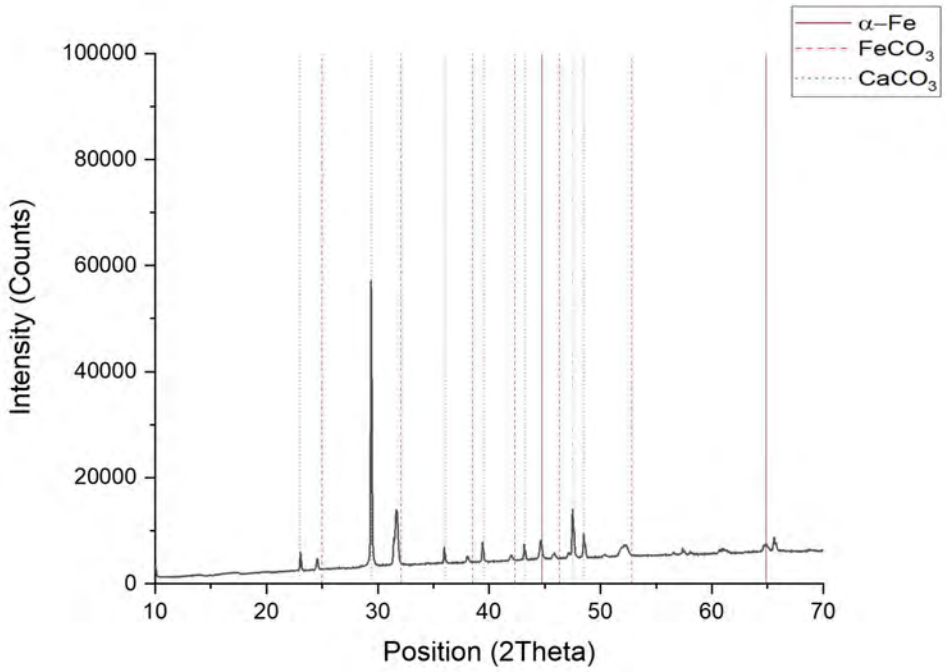

Figure 179 XRD pattern in SI 2.6 system for FeCO3

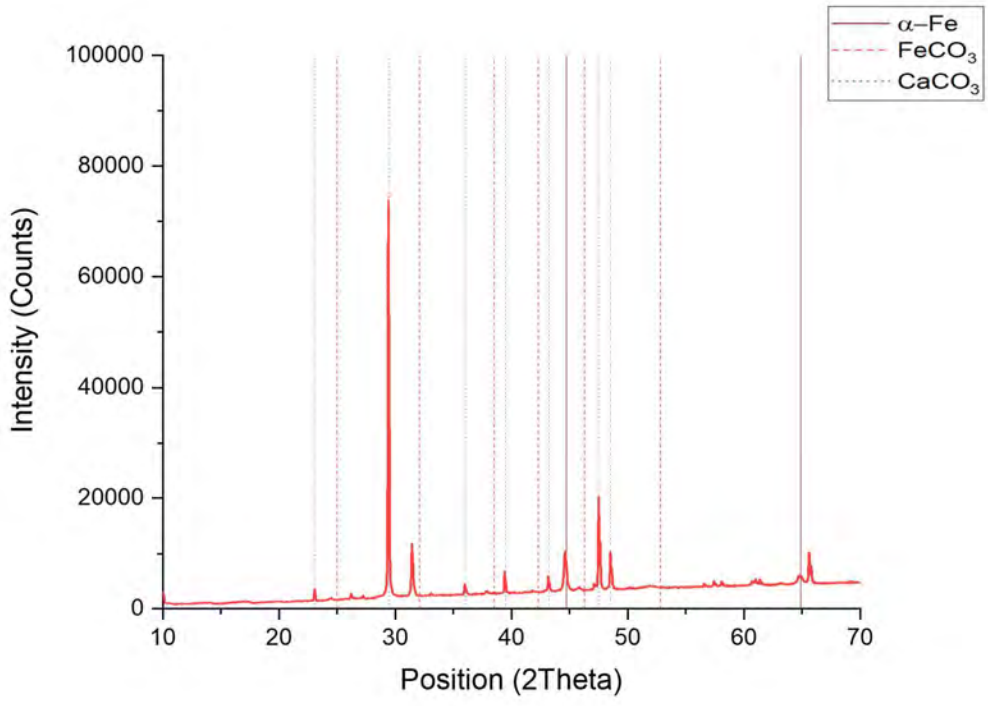

Figure 180 XRD pattern in SI 2.6 system for SLIPS BM

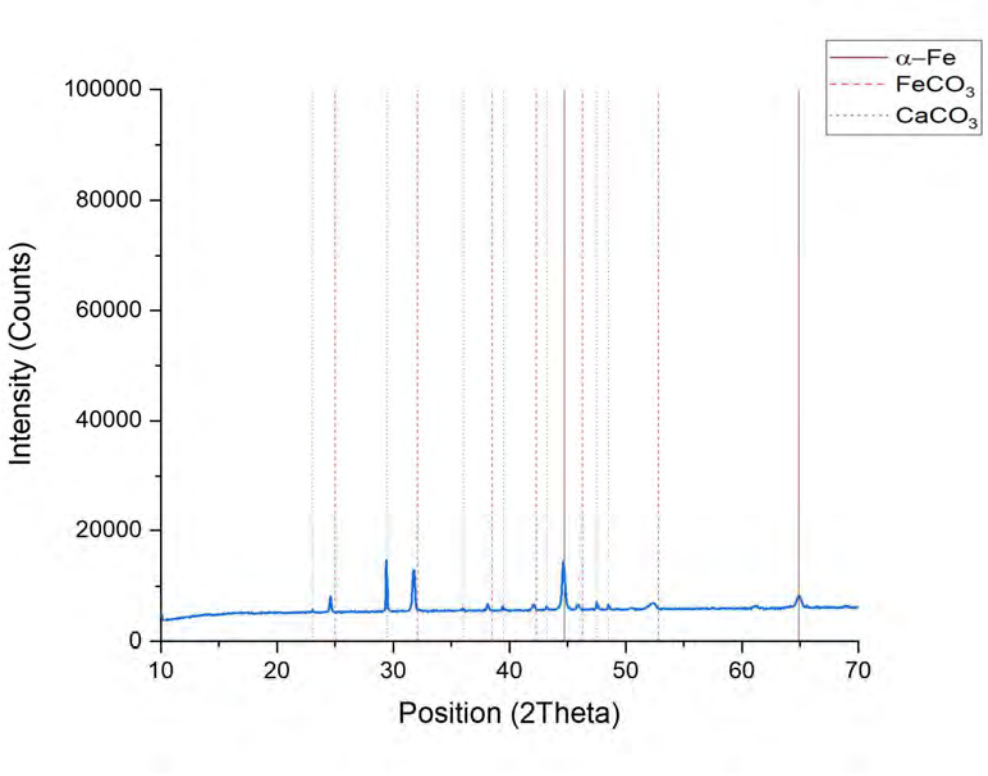

Figure 181 XRD pattern in SI 2.6 system for SLIPS KR

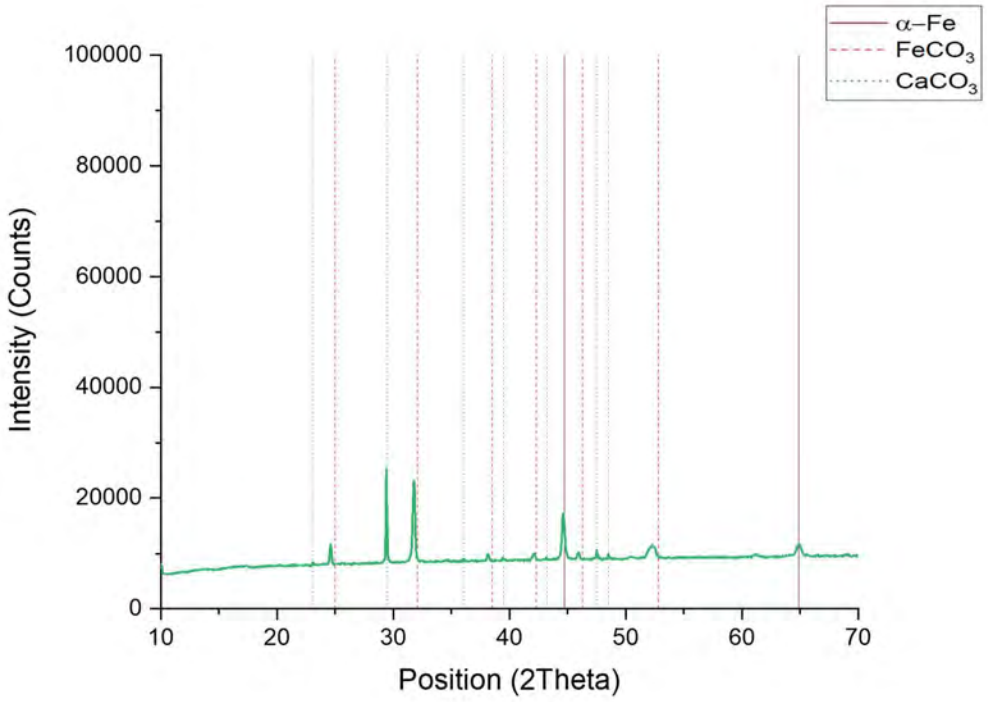

Figure 182 XRD pattern in SI 2.6 system for SLIPS NW

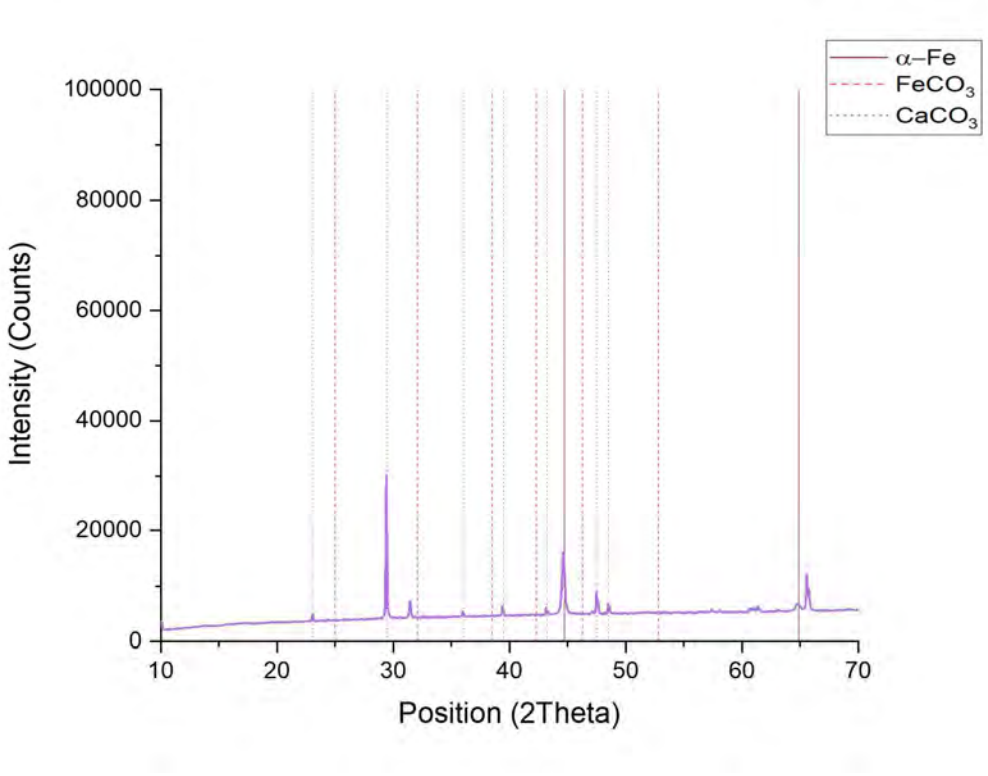

Figure 183 XRD pattern in SI 2.6 system for SLIPS W

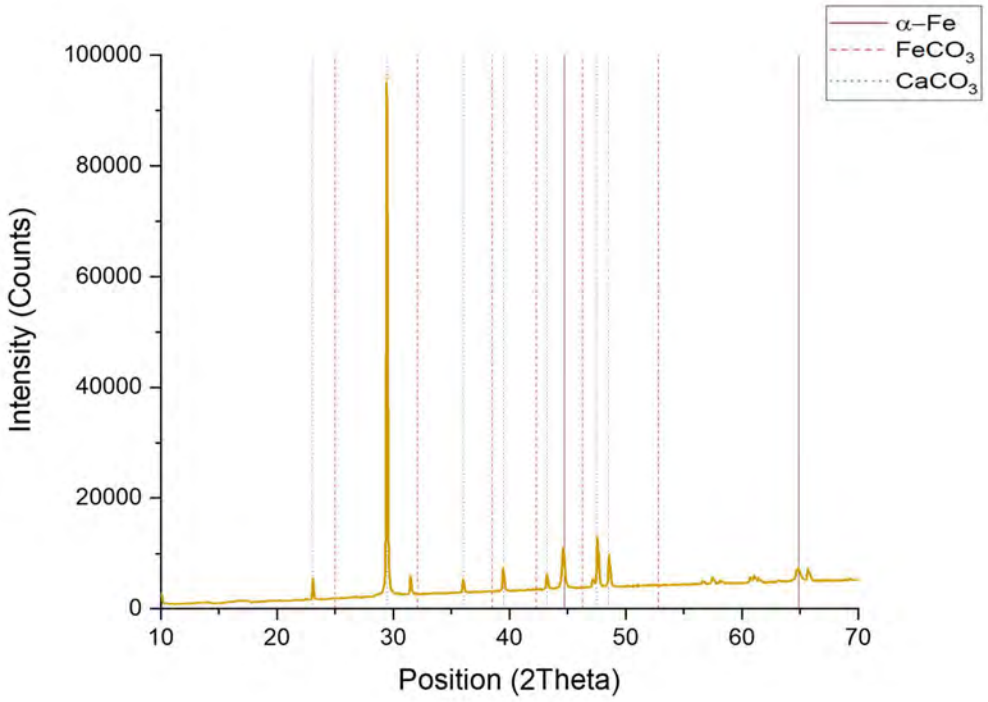

Figure 184 XRD pattern in SI 2.6 system for X65 CS

The shift to lower values of 2Theta in the dominant [104] $FeCO_3$ peak is seen more clearly in Figure 185 for all tested samples. This shift is generally considered to occur as the introduced Ca (increasing molar fraction) within the $FeCO_3$ expands the unit cell with higher d-spacing values (as seen in Table 19). The previous analysis identifies the products on the surface and has some relative qualitative purposes with regards to intensity of peaks. The calculation of the molar fraction of the $Fe_xCa_yCO_3$ gives an indirect evaluation of the barrier effect of the lubricant in separating the $FeCO_3$ layer from the surrounding $CaCO_3$ brine system. The calculated molar fractions based on the [104] $FeCO_3$ peak are given in Table 19. The highest molar fraction is seen in both SLIPS BM and SLIPS W at 21.7% each. SLIPS Kr exhibited the lowest calculated molar fraction at 9.2%. It is expected that Ca wt.% from EDX will be far higher given the majority of the calcium signal is generated from fully formed $CaCO_3$ rather than mixed carbonates. In this case there is some link between increased Ca wt.% seen in EDX and increasing molar fraction calculated from XRD in the SI 2.6 samples. Interestingly $FeCO_3$ does not follow this trend, with molar fraction of 13.7% Ca not in line with the higher Ca wt.% seen in the EDX. This may suggest at an interfacial level; some lubricants may accelerate or assist the integration/incorporation of Ca into $FeCO_3$.

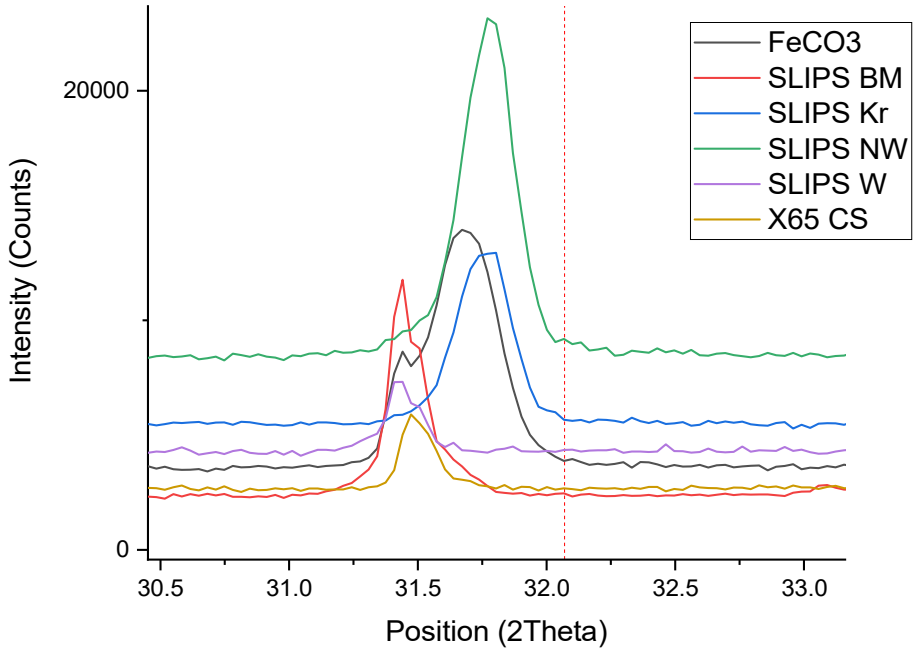

Figure 185 Peak shifts for the FeCO3 [104] peak for all samples tested in SI 2.6

Table 19 Calculated values for D-Spacing and Mole fractions for samples tested in SI 2.6

Sample	D-Spacing	Mole Fraction (yCa)
$FeCO_3$	2.823	0.137
SLIPS BM	2.843	0.217
SLIPS KR	2.812	0.092
SLIPS NW	2.814	0.102
SLIPS W	2.843	0.217
X65 CS	2.841	0.206

XRD Analysis of SI 1 Samples

Figure 186-185 show the XRD results for the 6 samples tested in the SI 2.6 brine system. Again, samples show the presence of the 3 key elements of $CaCO_3$, $FeCO_3$ and the underlying X65 CS. However there are some considerable differences when compared to the SI 2.6 samples. Firstly, intensities across all positions are generally weaker than those encountered in SI 2.6. This is especially the case of the $CaCO_3$ [104] peak. In terms of relative intensities, the key difference is that all samples show a higher intensity for the $FeCO_3$ [104] peak compared to $CaCO_3$ [104] peak (or the [110]) α-Fe in X65 CS), except for the $FeCO_3$ sample. This due to the lower average concentration of Ca and $CaCO_3$ precipitated on the top surface of the sample. The lack of surface coverage from precipitated $CaCO_3$ would also expose more of the underlying $FeCO_3$ (or X65 CS) layer as well. The strongest $CaCO_3$ [104] intensities were detected in the $FeCO_3$ and X65 CS sample. The lowest intensities were found in SLIPS Kr and SLIPS W. This is similar to those results seen in the EDX Ca wt.%. Again $CaCO_3$ peak positions showed no shift in the spectra where as $FeCO_3$ peaks showed a clear shift to lower 2theta positions.

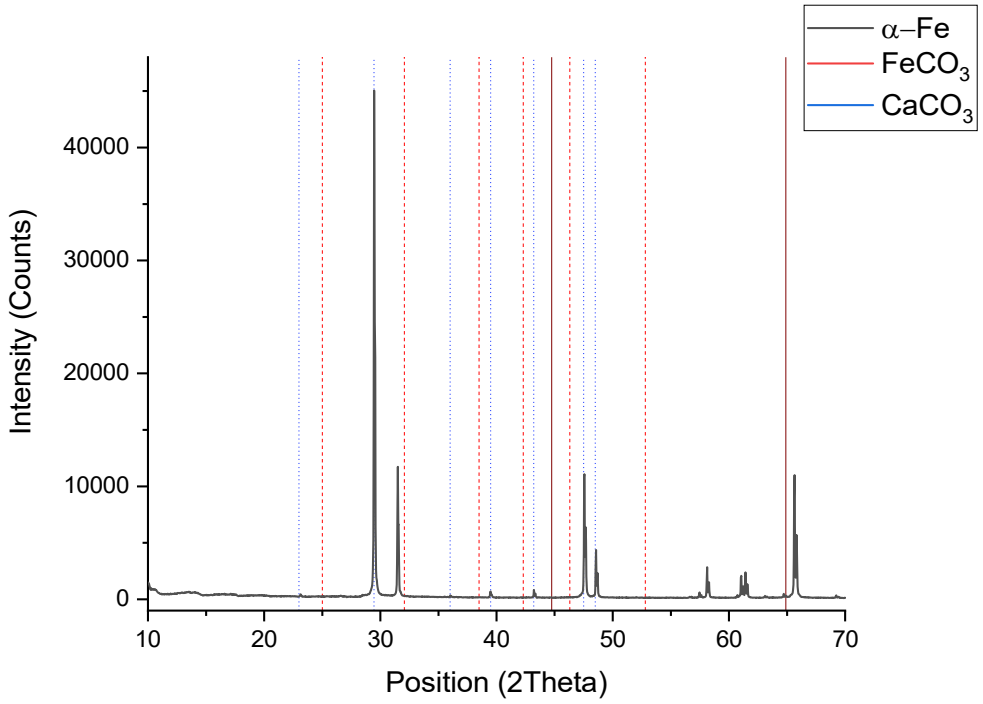

Figure 186 XRD pattern in SI 1 system for $FeCO_3$

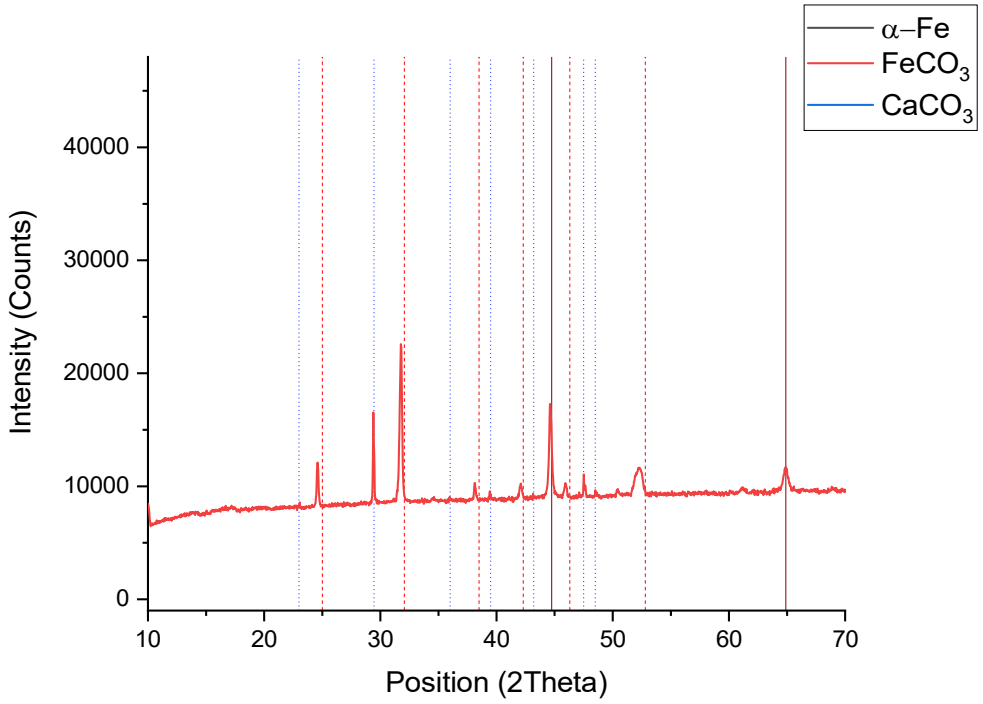

Figure 187 XRD pattern in SI 1 system for SLIPS BM

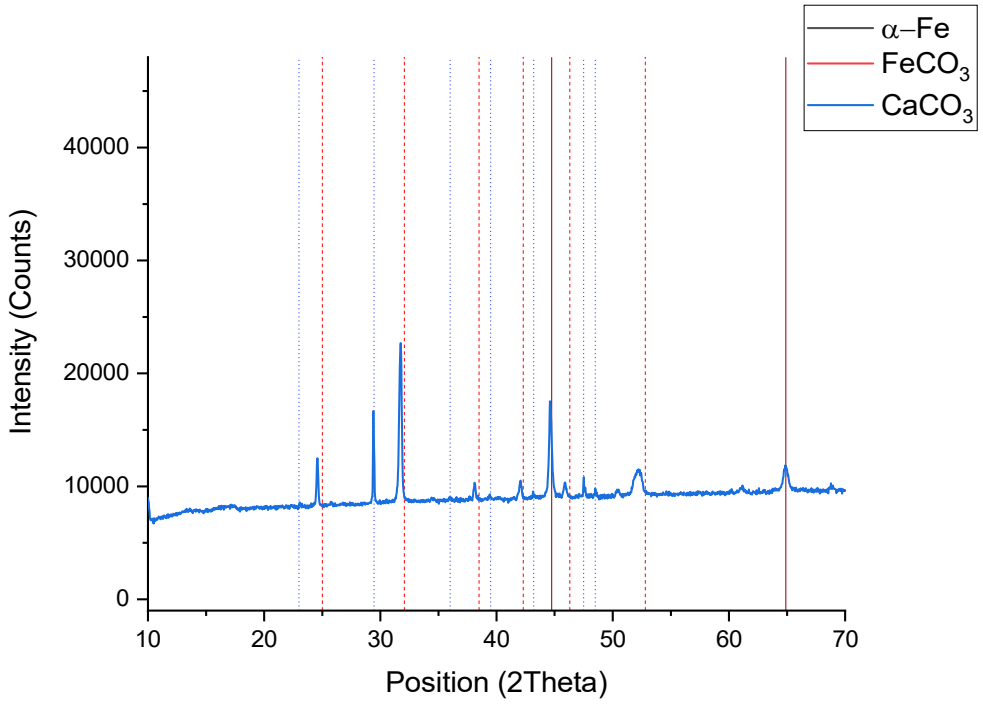

Figure 188 XRD pattern in SI 1 system for SLIPS Kr

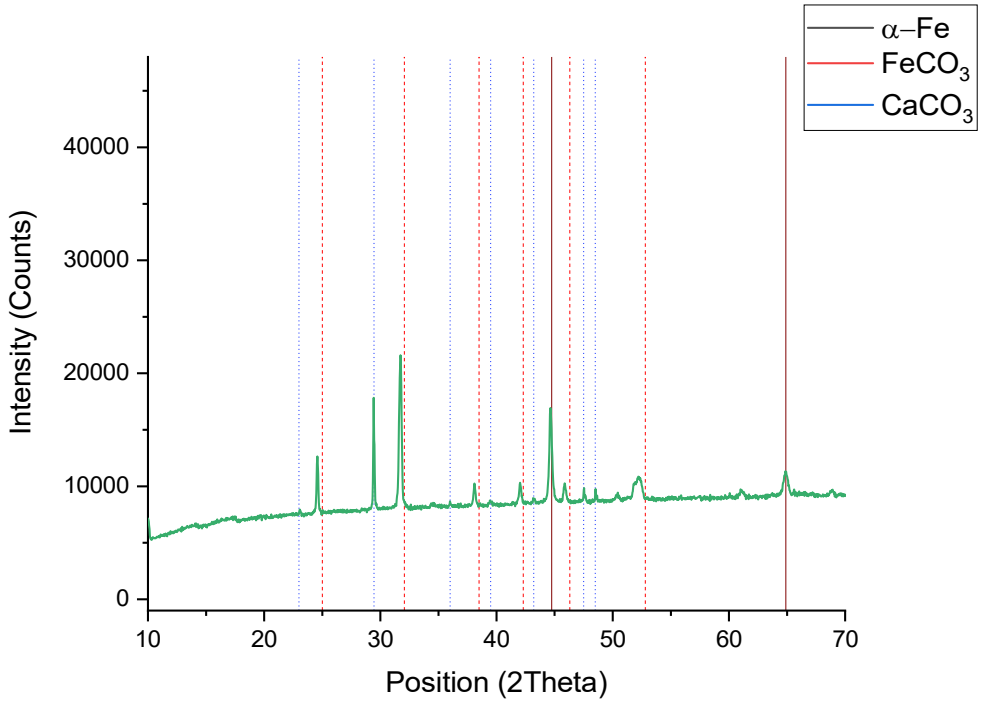

Figure 189 XRD pattern in SI 1 system for SLIPS NW

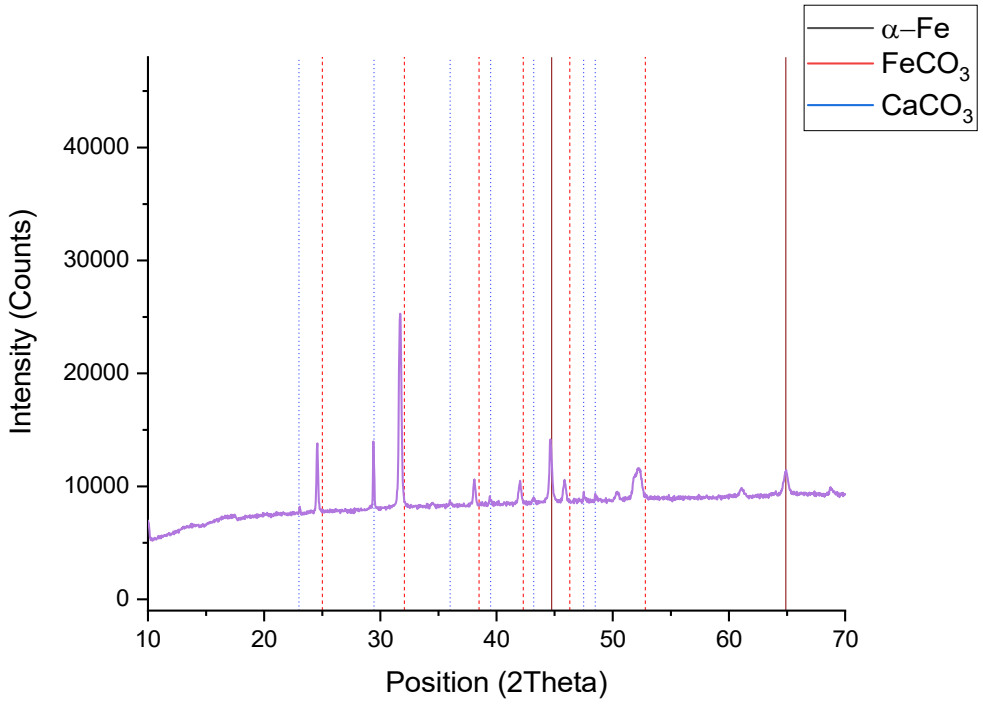

Figure 190 XRD pattern in SI 1 system for SLIPS W

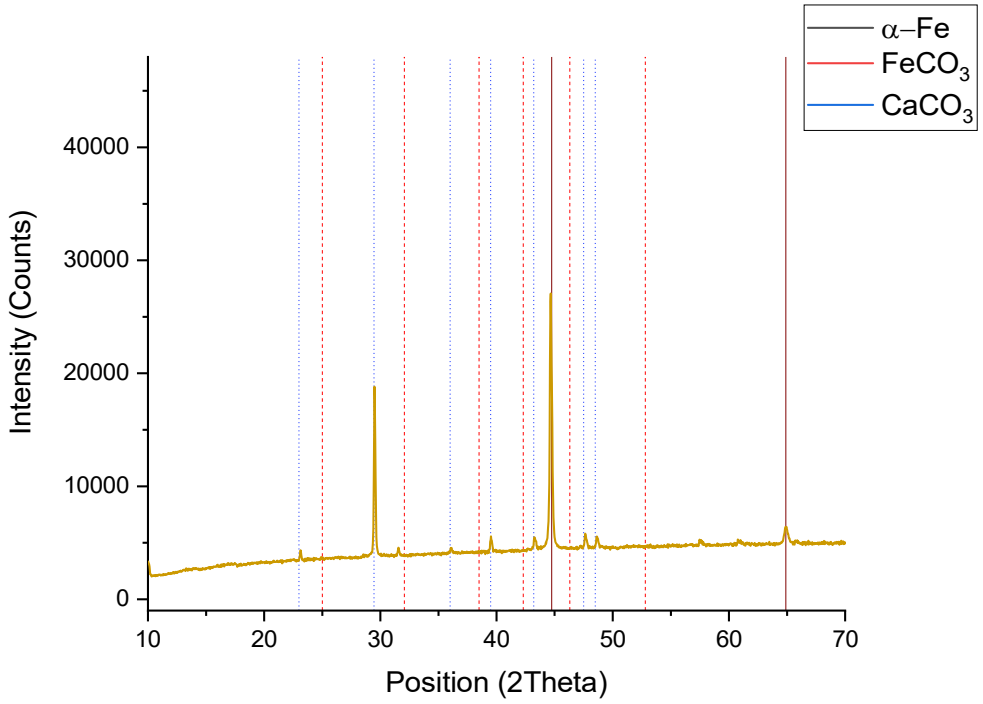

Figure 191 XRD pattern in SI 1 system for X65 CS

The shift in the $FeCO_3$ [104] peak is shown in Figure 192 for all tested samples. On average, the range of position shift is not as great as that experienced in the SI 2.6 system. With the $FeCO_3$ and X65 sample shifting furthest away from the original 32.07˚ 2Theta position. The rest of the samples are grouped in a tight position cluster around 31.75˚ 2Theta. This is also similar in nature to the EDX Ca wt.%, where the range across samples were not as pronounced as sample range in the SI 2.6 system. The XRD pattern at the 32.07 peak and the calculated mole fractions (from Table 20) show a clear delineation between samples with a lubricant (i.e SLIPS) and non-lubricated samples. The Ca molar fraction is highest at 19.3% for the $FeCO_3$ sample, followed by the X65 CS sample at 18.2%. Given the similarities in molar fraction of lubricated samples, this suggests the presence of any lubricant (regardless of type) provides a greater relative protection to the formation/incorporation of mixed carbonates than having no lubricant. The lowest Calcium molar fraction calculated was SLIPS BM at 10.2% with SLIPS Kr and SLIPS NW at 11.3% each. Again the average Ca molar fraction across all samples was lower than that of the SI 2.6 average value. This is likely a result of lower Ca concentrations in the system to begin with. Although SI 2.6 Ca molar fractions do show a larger shift at the [104] peak, relatively this is not as large as expected given the increase in Ca concentration. It is likely that this may be the result of competition from precipitated $CaCO_3$ on the surface absorbing a higher level of free Ca than the $FeCO_3$ layer below.

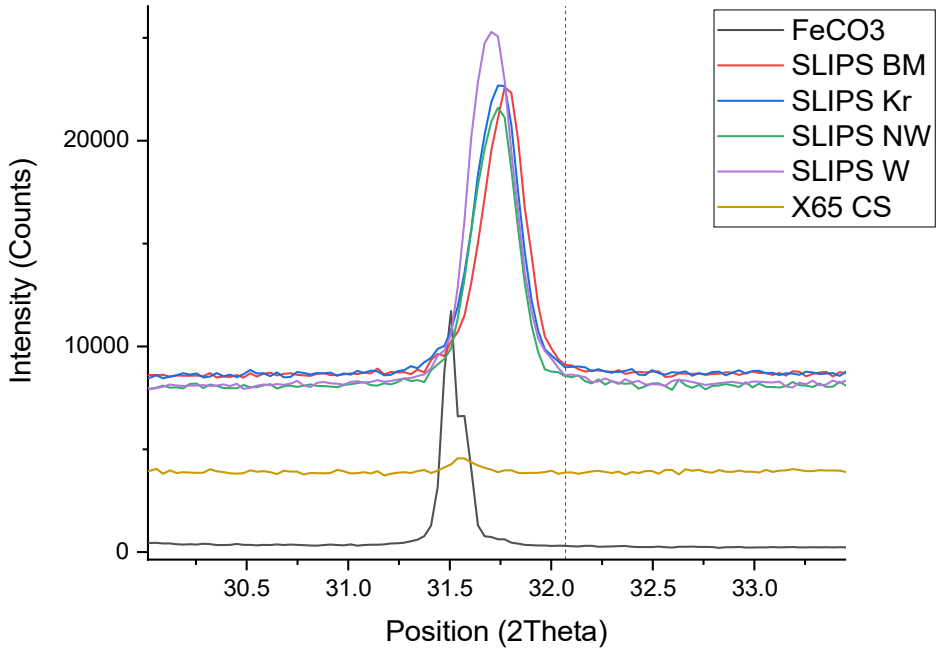

Figure 192 Peak shifts for the FeCO3 [104] peak for all samples tested in SI 1

Table 20 Calculated values for D-Spacing and Mole fractions for samples tested in SI 1

Sample	D-Spacing	Mole Fraction (yCa)
$FeCO_3$	2.837	0.193
SLIPS BM	2.814	0.102
SLIPS KR	2.817	0.113
SLIPS NW	2.817	0.113
SLIPS W	2.820	0.125
X65 CS	2.834	0.182

7.9 Fourier Transform Infra-Red Spectroscopy (FTIR) Analysis of samples

FTIR analysis has been undertaken as a complementary method to analyse surface deposits and chemistry on samples. FTIR allows the identification of chemical bonds within molecules that allows the detection of different components in the SLIPS system. This includes the presence of inorganic scales, such as iron and calcium carbonates represented by (CO_3) bonds and trace lubricant compounds specifically for the crude oil SLIPS (seen through hydrocarbon C-H chains).

For the FTIR analysis the focus has been for scaling tests at SI 2.6. The SI 2.6 has been chosen due to the possibility of stronger CO_3^{2-} signals given the known higher concentrations in the bulk system but also those higher values detected in EDX analysis. The primary reason for FTIR analysis is to provide an alternative measure of the residual lubricant (Figure 193), where this was not easily detected in the EDX (i.e particularly for the crude oil samples). Given the weak transmittance of the iron and calcium carbonates and overlap with peaks in the other lubricants (particularly around 3000 and <1500 wavenumber), remarks on scaling deposition are limited.

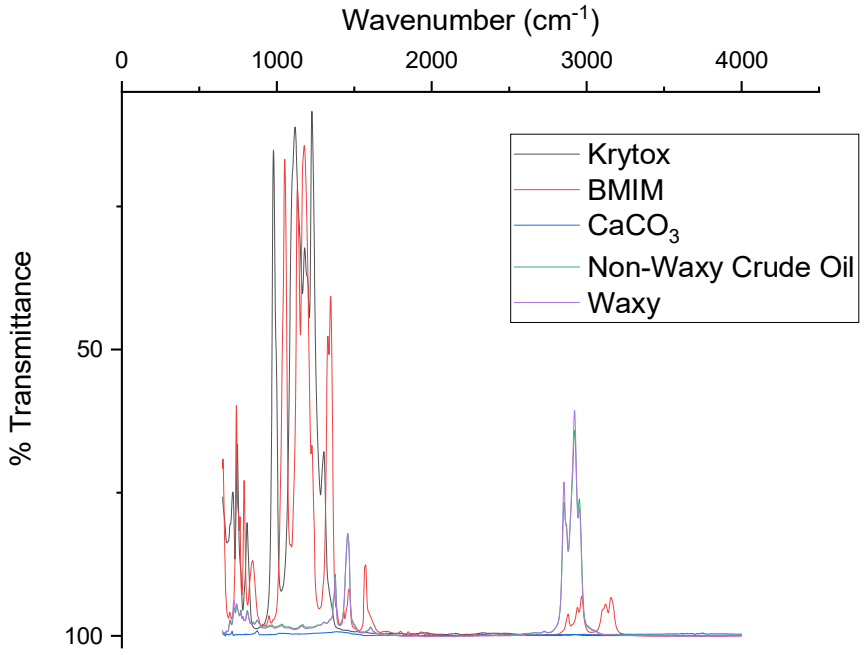

Figure 193 FTIR Spectra of SLIPS lubricant and $CaCO_3$ powder

Iron and Calcium Carbonate

The FTIR signatures of both iron and calcium carbonates are of a very similar nature and can be seen in Figure 194. Generally for inorganic salts, FTIR analysis would not be a recommended standalone method for observing $FeCO_3$ or $CaCO_3$ deposition but is useful as a complementary analysis method to EDX. Particularly in this case it would be difficult to separate whether the carbonate is associated with Ca or Fe. The primary purpose of FTIR is focused on providing additional analysis of the lubricants themselves. This is largely due to the nature of FITR being more suited for identifying functional groups in organic compounds (such as C-H bonds). Both carbonates have primary peaks representing the CO_3^{2-} bond, which is independent of whether it is Iron or Calcium. These primary peaks occur in bands around 1425, 870 and 720 cm^{-1} wavenumbers and are usually associated with the calcite polymorph [352-357]. As can be seen in the analysis of the organic lubricants later on, many of the common peaks occur around and below the 1500 cm^{-1} band. As such, there will be significant overlapping between peaks, with the intensity of the inorganic carbonates masked by the stronger signals from the organic lubricants and hydrocarbons. This area is often complex and known as the fingerprint region [358, 359].

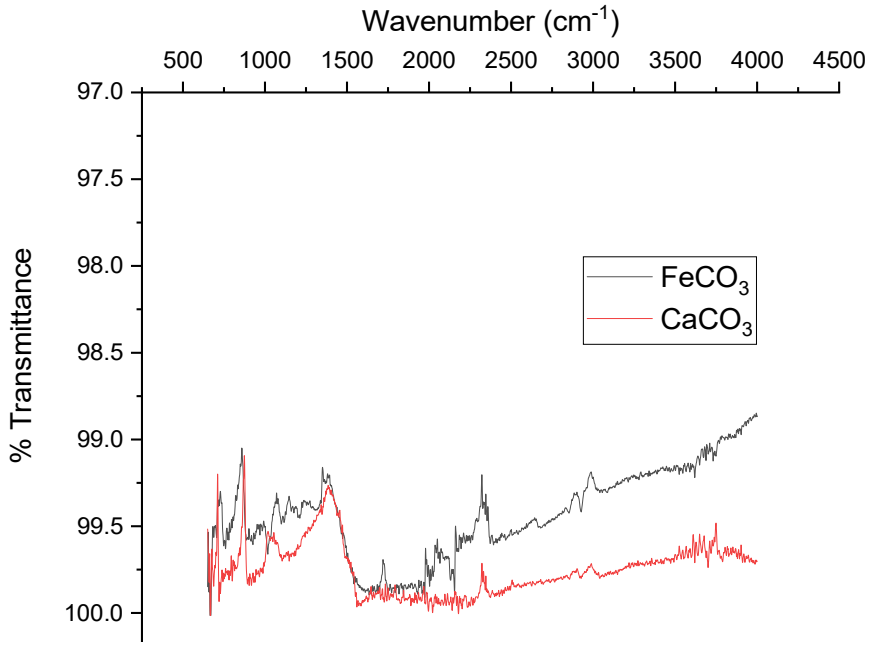

Figure 194 FTIR Spectra of $FeCO_3$ base layer and $CaCO_3$ powder

FTIR results from the scaling tests can be seen in Figure 195-Figure 196. These results are compared to the original base state pre-test. In the case of the $FeCO_3$ sample (Figure 195), we can see a strong increase in transmittance over the 3 dominant peaks associated with CO_3^{2-} after the test. The results are almost a mirror image with sharp peaks around 715 and 875 cm^{-1} but also the much broader peak seen at 1400 cm^{-1}. Although the FTIR alone does not show if this is calcium or iron carbonate, from EDX/SEM this is likely a result of the increased presence of calcium carbonates in the scale either depositing/incorporating into the existing iron carbonate layer. The post-test results of the blank X65 samples (Figure 196) show an almost identical spectrum as the $FeCO_3$ sample. Again this includes sharp peaks around 715 and 875 cm^{-1} and the thicker peak at 1400 cm^{-1}. This is in stark contrast to the base X65 sample, with the lack of surface compounds producing any strong signals hence the near flat base line. Comparing to Figure 194, it does appear that deposited calcium carbonate signals produced larger transmittance than either pure calcium carbonate powder or the base $FeCO_3$ SLIPS layer.

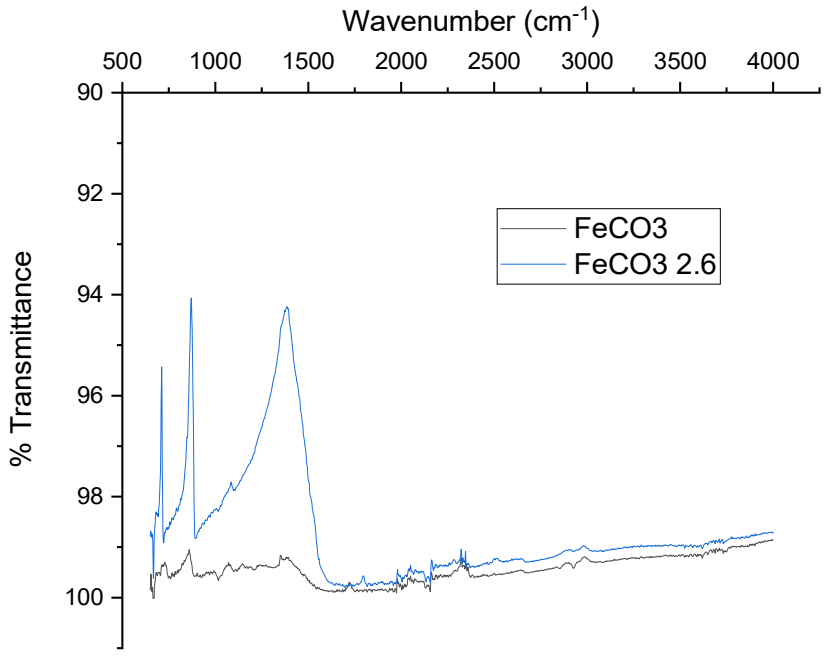

Figure 195 FTIR Spectra of $FeCO_3$ base layer (pre and post-test in SI 2.6 brine)

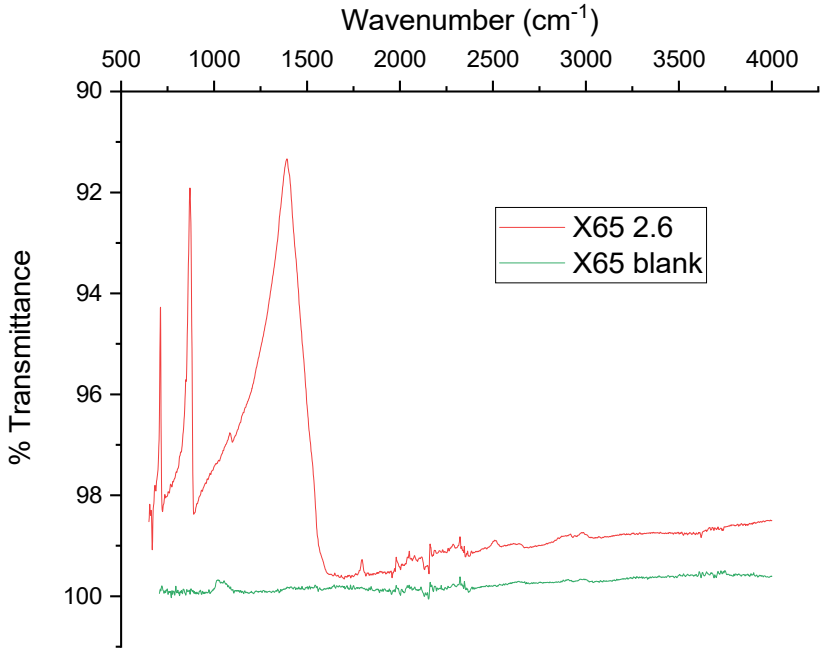

Figure 196 FTIR Spectra of X65 blank CS (pre and post-test in SI 2.6 brine)

Crude Oil SLIPS

The SLIPS that have utilised crude oil have been categorised as waxy and non-waxy. These designations have come based on commercial parameters from the supplier and have been blended from a number of oilfield sources. Commercial tests show a range of differences between the oils based on physical parameters (viscosity, pour point, density etc). Under closer examination through FTIR the differences are less distinct. FTIR results shown in Figure 197, show very similar profiles. Each crude oil has 3 prominent and comparable bands associated around 700-900 cm^{-1}, 1300-1500 cm^{-1} and 2800-2950 cm^{-1}. The first band is generally associated with aromatic rings and/or chains, 1300-1500 includes nitro-, amines and amides while 2800-2950 is linked with alkanes [360-365]. A small peak is also seen around 1600 cm^{-1} which represents alkenes. The major differences between the 2 samples are slightly higher peaks around 2925, 2850 and 725 cm^{-1} for the Waxy crude oil. The peak at 725 cm^{-1} is known as having higher intensity with the presence of wax (caused by the rocking vibration of methylene)[366].

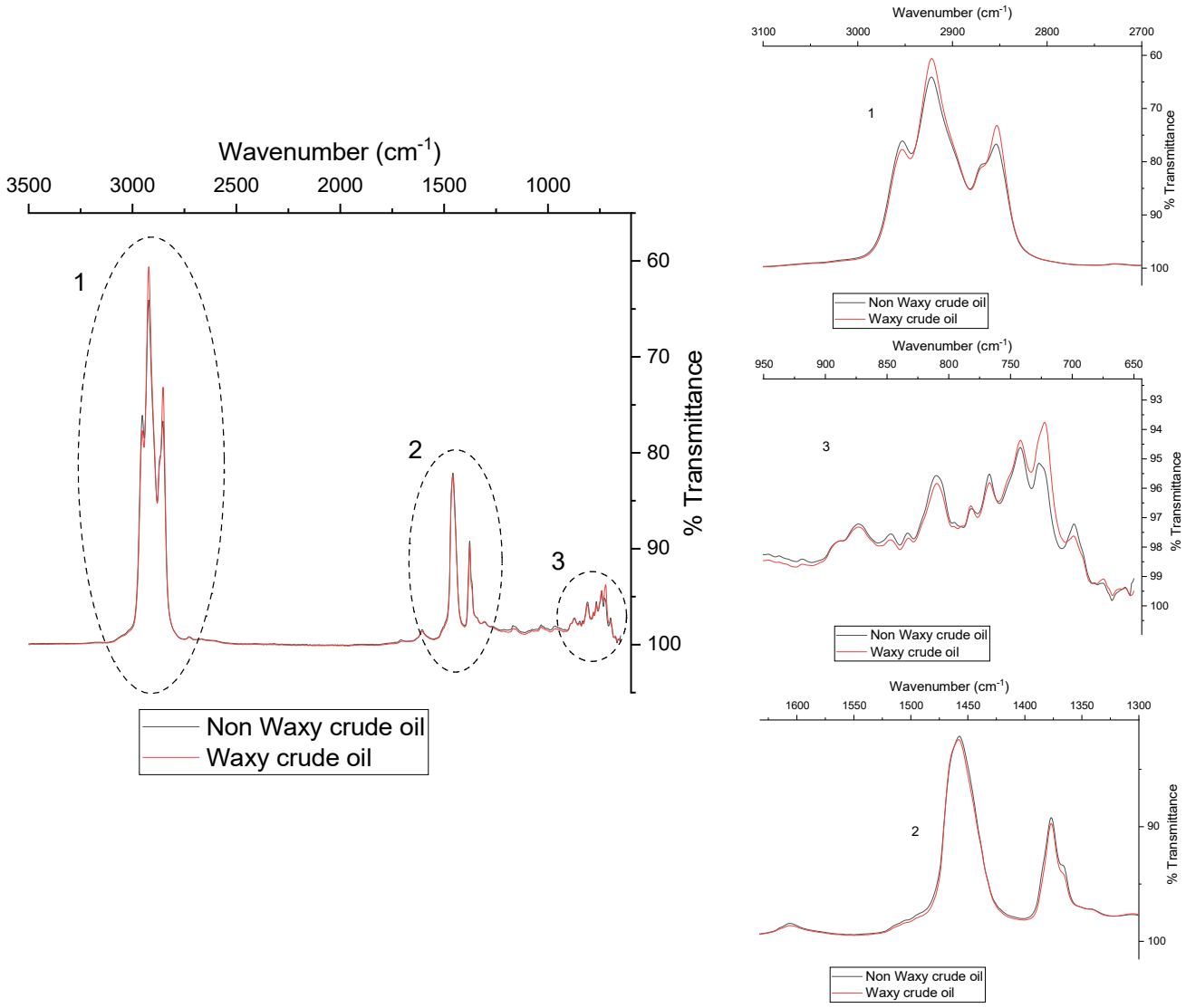

Figure 197 FTIR Spectra of Crude Oils (Inset: Zones 1-3)

Post scaling FTIR analysis show similar behaviour between the samples with the presence of both deposited calcite and residual hydrocarbon present. The peaks for deposited calcium carbonate can be clearly seen around 715, 875 cm^{-1} and the larger hump at 1400 cm^{-1}. Unlike the X65 and $FeCO_3$ samples previously, there is considerable overlap of peaks between the hydrocarbons and calcium carbonate particularly in <1500cm^{-1} area. In the Non-waxy crude oil SLIPS (Figure 198), there remains visible peaks around 715, 875 cm^{-1} both before and after the test, however the transmittance % is much higher after scaling. The larger calcite peak around 1400 cm^{-1}, does not show any traces

of the hydrocarbon peaks at 1375 or 1459 cm^{-1}. There is also the minor peak at 1800 cm^{-1} associated with calcite [367]. The region between 2750-3000 cm^{-1} is a strong indicator of residual lubricant on the surface. As seen in the pre-test FTIR this is the dominant peak both in wavenumber and transmittance. Post-test, this shape is still visible with tip peaks at 2850, 2920 and 2954 cm^{-1} showing the clear presence of remaining lubricant on the surface. The Waxy SLIPS shows post-test (Figure 199), single peaks at 875 cm^{-1} and 715 cm^{-1}, however the broader calcite peak at 1400 cm^{-1} is much broader at the tip. The crude oil peaks at 1375 or 1459 cm^{-1} can be seen to influence this signal, particularly the 1459 cm^{-1}. The minor calcite peak at 1800cm^{-1} is absent. Again post-test, residual lubricant is visible with the same structure seen between 2750-3000 cm^{-1}, with tip peaks at 2850, 2920 and 2954 cm^{-1}. Transmittance % between Non-waxy and Waxy SLIPS samples show similar levels for residual lubricant in 2750-3000 cm^{-1} at around 96 %. However peak transmittance for the calcite wavenumbers (715, 875,1400 cm^{-1}) is different, with the Non-waxy crude transmittance showing >10 % higher compared to the Waxy sample.

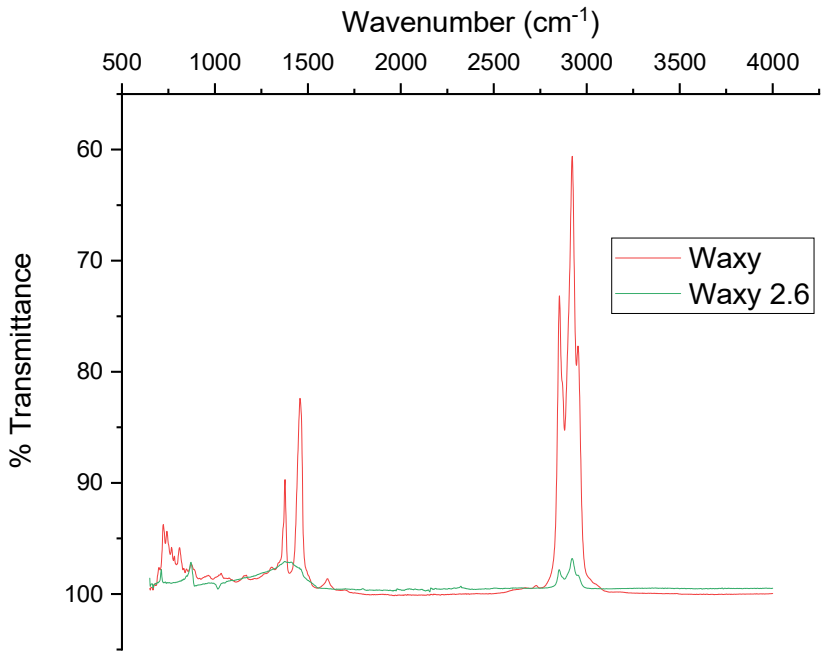

Figure 198 FTIR Spectra of SLIPS W (pre and post-test in SI 2.6 brine)

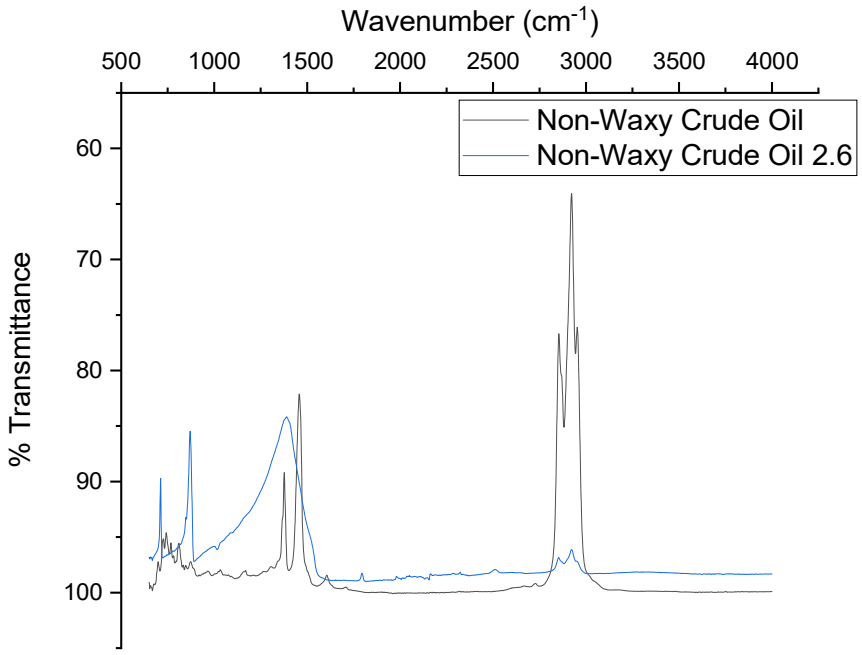

Figure 199 FTIR Spectra of Non-Waxy SLIPS (pre and post-test in SI 2.6 brine)

SLIPS Kr and SLIPS BM

Krytox and BMIM are both organic compounds with a strong signal in the band below 1500 cm^{-1} wavenumber (Figure 200). Krytox is a fluorinated oil commonly classified as perfluoropolyether (PFPE) or perfluoroalkylether (PFAE). FTIR analysis of Krytox shows a strong intensity in a broad band from 1050 to 1350 cm^{-1} and a single spike around 980 cm^{-1}. Above 1350, the signal remains almost flat with no further peaks. These results are in line with major peak analysis in the literature [368-371]. BMIM is an organic salt, with the main difference compared to the inorganic carbonate salts being the presence of C-H bonds in the chemical structure. The primary intensities occur in a strong band between 1000 to 1250 cm^{-1} and a peak at 1350 cm^{-1} [372-375]. The imidazolium rings contained in the BMIM also produce unique, weaker peaks at 1570, 2950 and 3150 cm^{-1}.

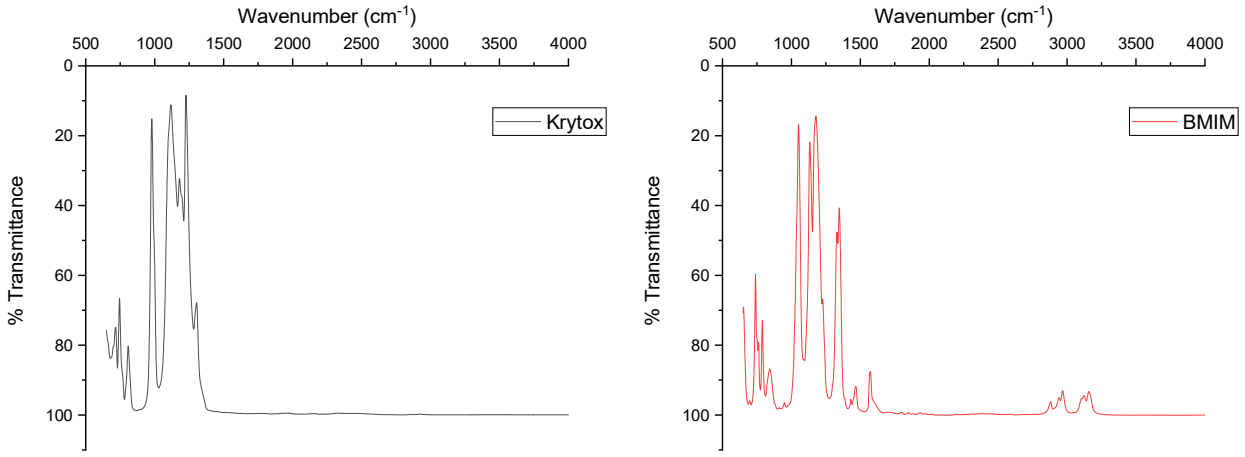

Figure 200 FTIR Spectra of Krytox and BMIM lubricants

The post-test analysis of the SLIPS Kr sample show FTIR signals almost entirely in the <1500 cm^{-1} region (Figure 201). In this case due to the overlapping peaks with $CaCO_3$, FTIR analysis is not the most suited method for this lubricant. However both residual lubricant and calcite deposits are still detectable. Transmittance levels across the spectrum are low but the single peaks associated with calcium deposits at 715 and 875 cm^{-1} are clearly detected. The peak at 875 cm^{-1} is not a peak seen in the Krytox lubricant itself. The basic broad structure associated with the lubricant is still seen, albeit at a much lower transmittance %. This broad hump between 900-1375 cm^{-1} has notable peak tips at 980, 1120, 1230 and 1305 cm^{-1}. In the post-test sample the bottom of this base extends over 1400 cm^{-1}, which is the other dominant peak of calcite, suggesting some overlap in the signal. This was the only sample where the 1400 cm^{-1} calcite peak was not the major signal. The SLIPS BM shows the familiar peaks of calcite at 715, 875 and 1400 cm^{-1} (Figure 202). Interestingly however there are no residual traces of the lubricant on the surface. None are noticeable in the <1500 cm^{-1} region or particularly in the 2800-3200 cm^{-1} area where there is no evidence of any remaining peaks. This suggests a lack of remaining lubricant on the surface after scaling.

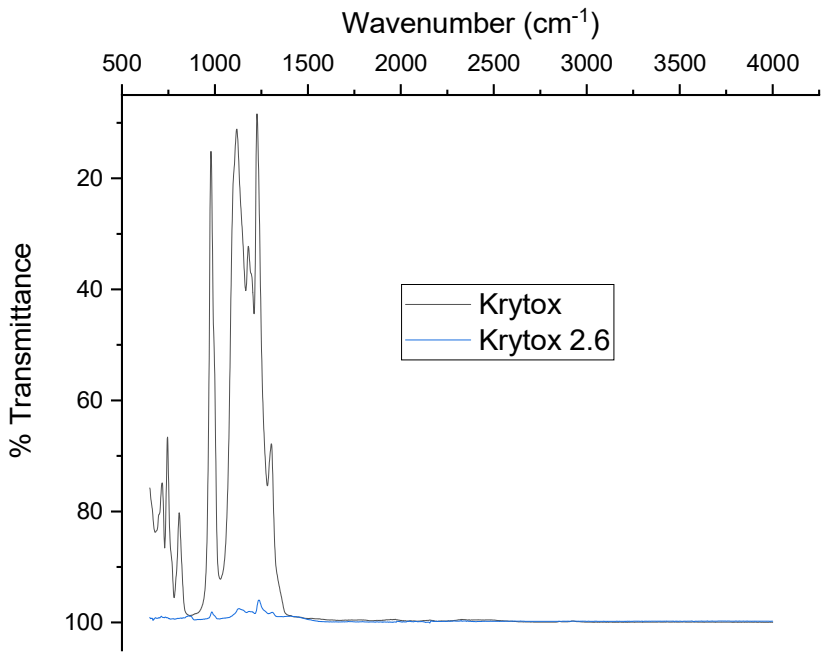

Figure 201 FTIR Spectra of Krytox SLIPS (pre and post-test in SI 2.6 brine)

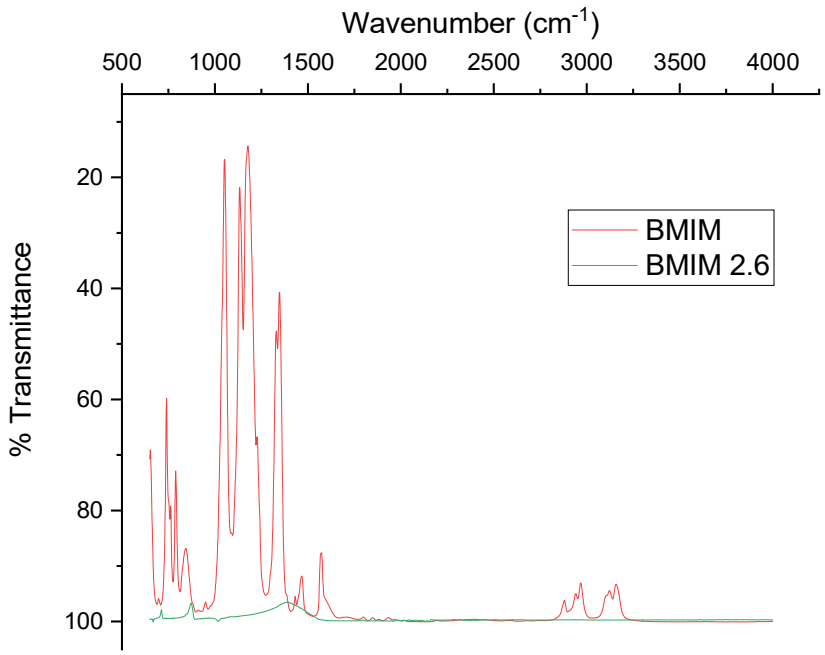

Figure 202 FTIR Spectra of BMIM SLIPS (pre and post-test in SI 2.6 brine)

Summary

FTIR analysis of samples has been undertaken in the SI 2.6 brine system shown in Figure 203, with the following observations:

- Calcium carbonate (in particular calcite) has been detected across all samples. This is based on the presence of peaks at wavenumber 715 and 875 cm^{-1} and a thicker peak at 1400 cm^{-1}. Where carbonates were present originally (i.e $FeCO_3$ base), the transmittance signal is stronger. The scale deposit signature was stronger than any residual lubricant presence.
- In decreasing order of Calcium carbonate transmittance %:

  SLIPS NW > X65 > $FeCO_3$ > SLIPS BM > SLIPS W > SLIPS Kr

  The 1400 cm^{-1} peak has been used for this, due to it being the dominant peak, peaks at 715 and 875 cm^{-1} are also in the same ratio/scale to each other and across samples.

- The presence of residual lubricant was detected in all samples, except that of the SLIPS BM. The Kr, NW and W SLIPS all showed identifying structures and peaks similar to those seen in pre-test samples, although at lower transmittance levels. This suggests a level of depletion/loss of lubricant across all SLIPS samples.

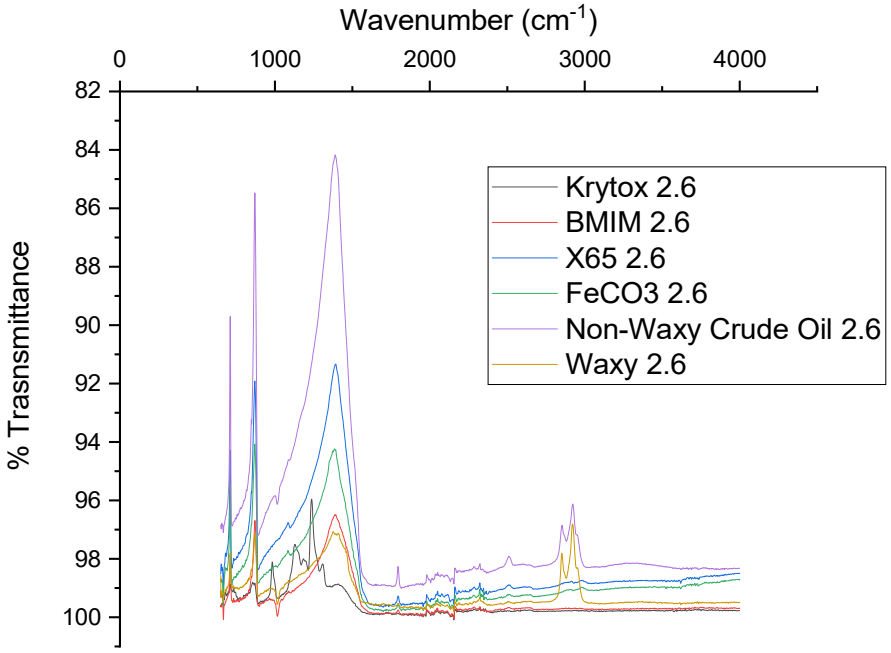

Figure 203 FTIR Spectra of all samples (Post-test in SI 2.6 brine)

Chapter 8
SLIPS and Flow Assurance

8 SLIPS Tafel and EIS Evaluation

8.1 Introduction

This chapter provides insight into electrochemical assessments of the flow assurance behaviour of the SLIPS systems (Figure 204). Within industry, flow assurance encompasses a broad field of pipeline issues that includes both corrosion AND mineral scaling. In the first chapter, the fabrication of the SLIPS ($FeCO_3$) base layer has been developed so as to be protective against corrosion (i.e CR <0.1mmpy) even before the addition of a lubricant. In the 2nd Chapter, evaluation of the mineral scaling performance with respect to $CaCO_3$ has been undertaken, post experiment, on SLIPS with various lubricants. However, the previous chapters did not observe:

1. The corrosion resistance of the $FeCO_3$ layer after lubrication (or as a complete SLIPS system).
2. In-situ insights into the behaviour of the SLIPS system during tests.

Although SLIPS showed an enhancement in reducing mineral scale compared to the original X65 or bare $FeCO_3$, it is still not demonstrated whether the material degradation due to electrochemical corrosion is affected in any way by the lubrication/ SLIPS system.

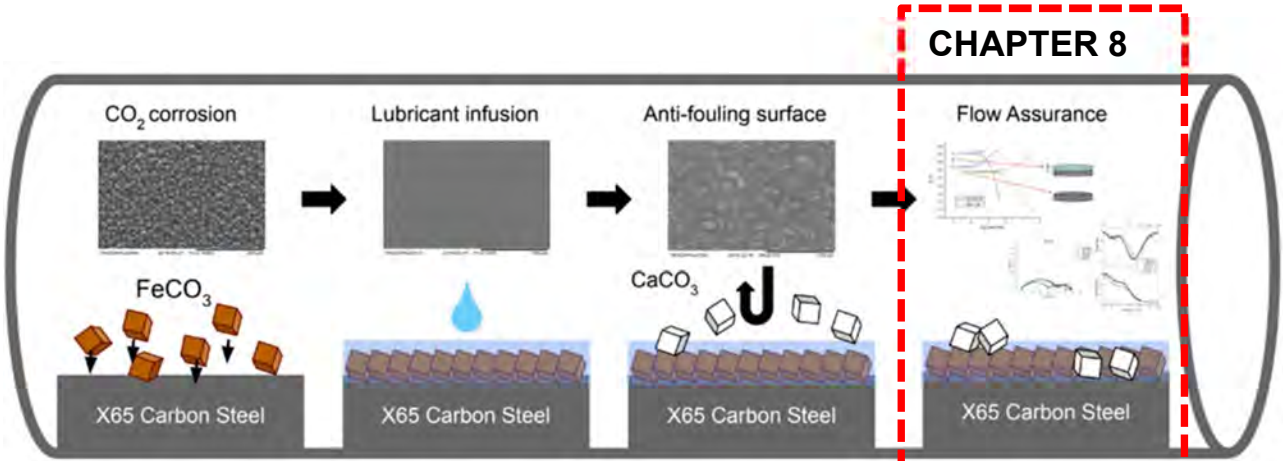

Figure 204 Thesis schematic of the main focus of Chapter 8 results

The evaluation of the SLIPS on corrosion values and comparative performance of the SLIPS systems will be investigated, as summarised in Figure 205. For this, Tafel extrapolation has been utilised to explore the relative corrosion behaviour and kinetics across the samples in the presence of, and without $CaCO_3$ scale. Electrical Impedance Spectroscopy (EIS) is a well-established method used for the evaluation of protective coatings and has been used in this research to monitor the in-situ behaviour of the SLIPS during scaling. This allows an understanding of the corrosion performance and insight into the mechanisms occurring on the SLIPS surface. Tafel and EIS tests have been conducted on all SLIPS in the same SI 1 brine for a 2 hrs duration as used in Chapter 2 for the scaling assessment. A further test in the same SI 1 brine, without the addition of $CaCl_2.6H_2O$ has been conducted to simulate conditions without the CaCO3 scale present. Post experimental analysis has been undertaken in the form of XRD, where similarly in Chapter 7, the composition of $Fe_xCa_yCO_3$ is observed to couple the performance of the lubricant barrier with the EIS analysis.

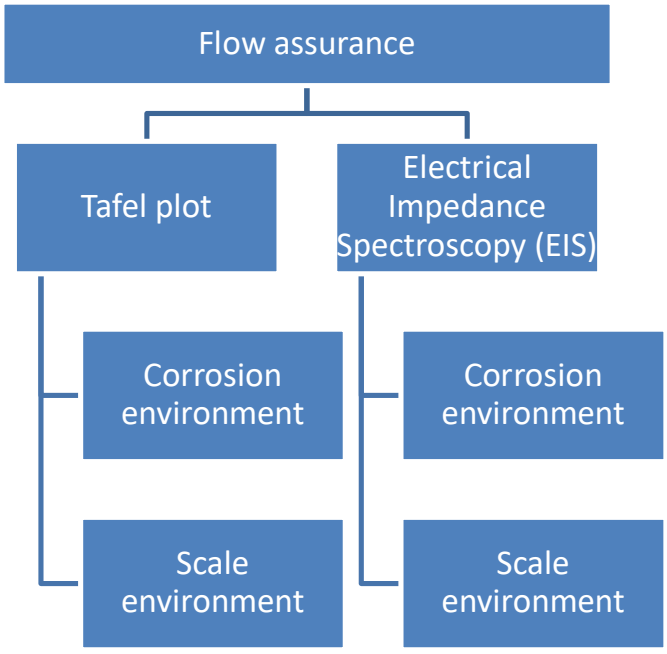

Figure 205 Breakdown of experimental methods and techniques

8.2 **Tafel Plot Results**

The foundation of the SLIPS system lies in the porous surface that becomes infused with the addition of lubricant. In this research, it is the underlying $FeCO_3$ layer produced as a corrosion product of carbon steel undergoing aqueous CO_2 corrosion. Chapter 6 of the results highlighted the fabrication process for this layer and indicated (visually and by CR) to be a generally protective layer. A protective layer being one that has a CR < 1mmpy [248, 376, 377]. The assumption is that this layer retains its protectiveness after infusion/impregnation of the lubricant. In this section Tafel polarisation tests have been undertaken on the SLIPS samples to reassess the corrosion protection of the samples after lubrication (Figure 206). The Tafel sweeps have been conducted at a fixed time for all samples. This time period was based on the stabilisation period (steady state) for the **X65 and $FeCO_3$** samples to return to the same resting OCP or E_{corr} (in this case considered as a change <5mV in 30 mins) after the cathodic sweep but before starting the anodic section.

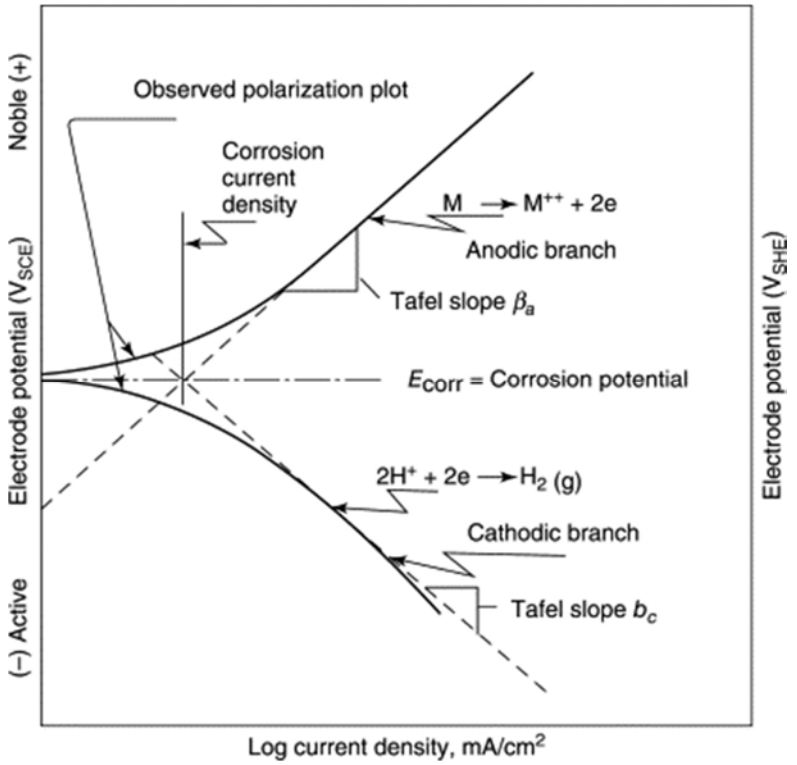

Figure 206 Hypothetical cathodic and anodic Tafel polarization showing major parameters obtained [378]

This standardised time period has been used to build a qualitative indication of the lubricant layer based on potential. The qualitative value is in the form of ΔE, which is the difference in potential between the initial E_{corr} value (at the start of the cathodic sweep) and the E_{corr} value obtained during the anodic sweep. The idea being that the higher the potential difference, the thicker the diffusion layer provided by the lubricant (as seen in Figure 207). There is the possibility that the cathodic polarisation could be causing the effects of separation between sweeps due to damage at the interface (caused by hydrogen bubbles/ local pH). However using the tail sections (±0.015 V in the opposite direction) of the individual sweeps show similar I_{corr} values which do not suggest material changes to the tested surfaces.

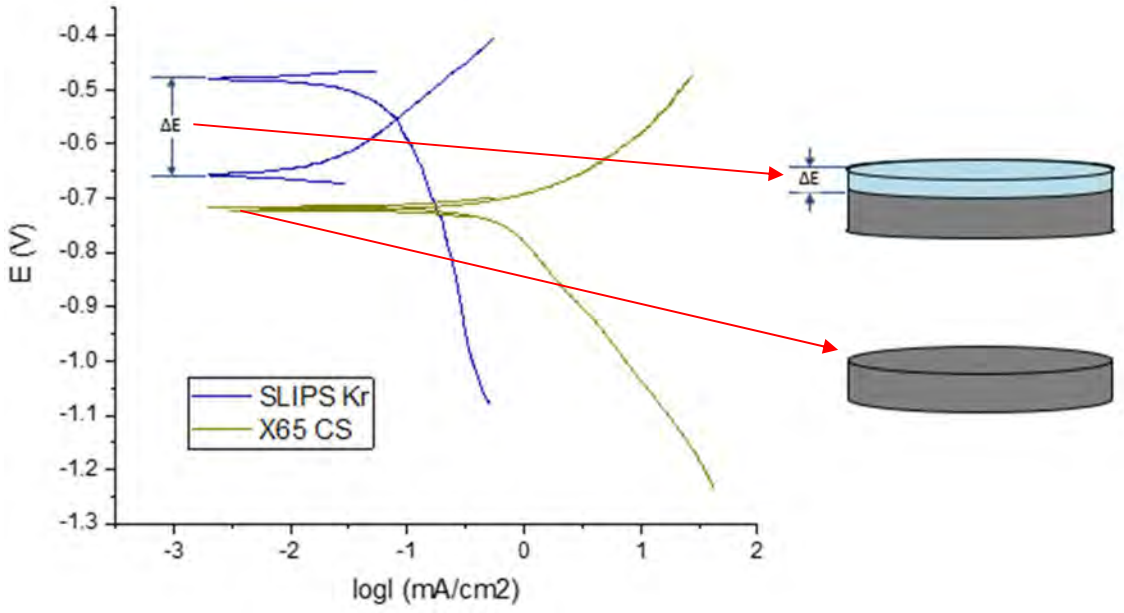

Figure 207 Physical interpretation of ΔE, lubricant thickness indicator, for potential difference between cathodic/anodic Tafel scans

All Tafel plots were conducted in the same environmental conditions which consisted of 6g of NaHCO3, 3.5% wt. NaCl at 50 C. These conditions represent those experienced in the SI 1 scaling tests but without the addition

of $CaCl_2.6H_2O$ (calcium chloride hexahydrate). A second set of test results was conducted with the addition of $CaCl_2.6H_2O$ to observe the dual effects of corrosion and scale. Tafel plots were obtained by sweeping around the OCP at a sweep rate of 0.01V/min in the following ranges:

- Cathodic sweep range was from +0.015V to -0.6V.
- Anodic sweep range was from -0.015V to 0.25V.

Corrosion rate was calculated from Equation 29.

$$CR\ (mmpy) = \frac{K\ i_{corr}\ M_{Fe}}{n\ \rho}$$

Equation 29

Where K is 3.273.27 ×1023 mm·g·s/A·cm·year (a constant derived from ASTM G102), i_{corr} is the corrosion current density obtained from the Tafel plot, M_{fe} is 55.85 g/mol (the molar mass of iron), n is 2 (the equivalent per moles) and p is 7.87 g/cm^3 (the density of iron).

Corrosion tests

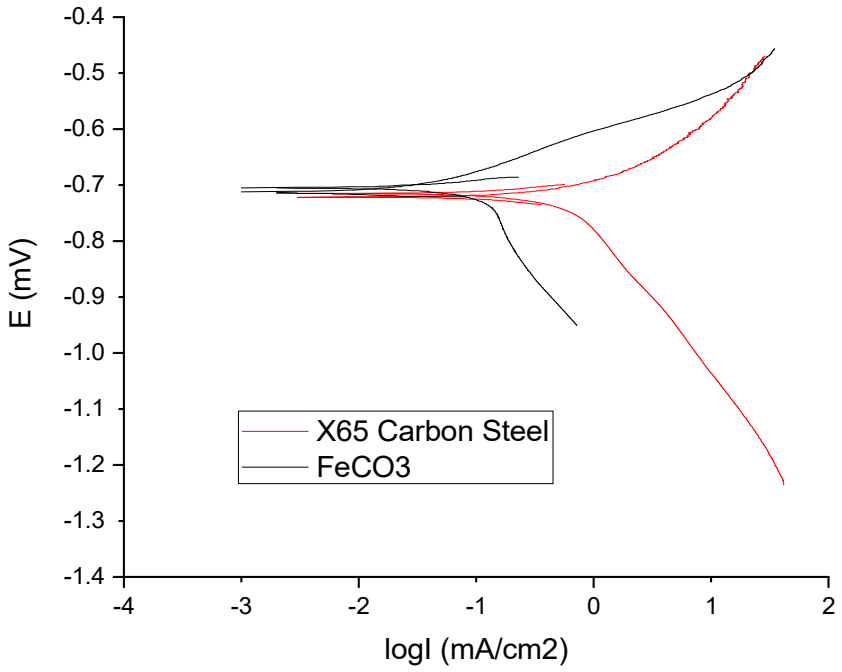

Figure 208 Anodic and Cathodic Tafel slopes of X65 Carbon Steel and $FeCO_3$

Figure 208 shows both the anodic and cathodic sweeps for an unmodified carbon steel sample and a $FeCO_3$ sample. The $FeCO_3$ sample uses the fabrication method for the standard SLIPS base layer used in previous tests. With regards to the typical corrosion potential and current parameters, measured E_{corr} for both samples is broadly in the same range of -0.705 V to -0722 V. However I_{corr} values show differences between the X65 and SLIPS $FeCO_3$ measured values. As would be theoretically expected the I_{corr} values associated with the X65 sample are higher than those of the $FeCO_3$ sample at 0.53 mA/cm^2 and 1.35mA/cm^2, respectively. As corrosion current density is proportional to the corrosion rate, comparatively the $FeCO_3$ has a lower CR than that of the X65, as expected. Both I_{corr} and E_{corr} values for X65 carbon steel samples in this solution are typical of that found in the literature [379-381]. The shape of the Tafel sweeps, particularly observing the anodic sweep, provides some insight into the electrochemical differences between the 2 samples. The flattened anodic section of the $FeCO_3$ shows a much more linear

region of oxidation compared to that of the curved blank X65 sample, where small changes in potential have a greater effect on the current response. This is representative of the protectiveness of the $FeCO_3$ barrier in slowing corrosion kinetics.

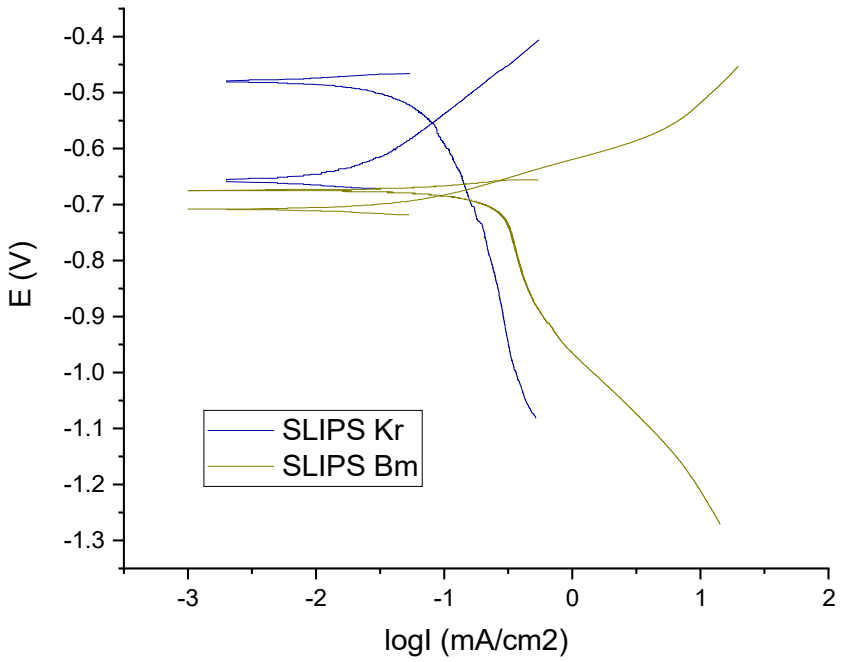

Figure 209 Anodic and Cathodic Tafel slopes of SLIPS Kr and SLIPS Bm

Tafel plots of the SLIPS systems show differences in corrosion behaviour compared to the un-lubricated X65 and $FeCO_3$ samples as seen in Figure 209. The Slips Kr sample shows a lower I_{corr} response at 1.84 mA/cm^2. The initial E_{corr} at the start of the cathodic sweep is 0.48 V which is also the highest potential (most noble) potential value obtained throughout the samples. As was stated before, the time for stabilisation was fixed for all samples as a means of providing a qualitative value of the thickness of the diffusion layer (or lubricant) across the SLIPS systems tested. The SLIPS BM sample has an E_{corr} value of 0.675 V very similar in nature to that of the X65/ $FeCO_3$. ΔE is 0.033 V which along with the initial E_{corr} value close to the untreated samples (X65/ $FeCO_3$) suggests the diffusion capabilities/thickness of the lubricant layer is weak. The I_{corr} value is 1.41 mA/cm^2, again similar to that of the

untreated $FeCO_3$ sample and is also consistent with lower concentrations of trace lubricant elements seen on samples tested post-test in the scaling chapter. Both SLIPS shows a flat anodic sweep, although the SLIPS Bm sample shows a cathodic curve with 2 distinct control regions.

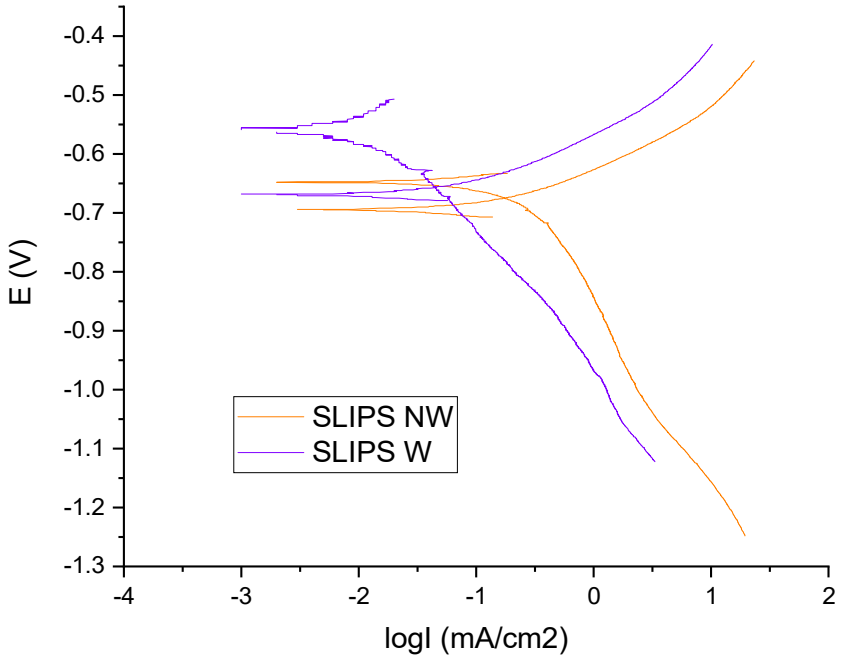

Figure 210 Anodic and Cathodic Tafel slopes of SLIPS NW and SLIPS W

The SLIPS crude oil samples exhibit similar behaviour to the other SLIPS samples (Figure 210). E_{corr} for SLIPS NW is lower than the SLIPS W, at -0.65 V compared to -0.56 V respectively. However I_{corr} values are 1.95 mA/cm^2 for SLIPS W which is almost double that of the SLIPS NW system at 1.16 mA/cm^2. Looking at the shape of the anodic sweep the curve is more similar in nature to the untreated X65 sample, suggesting that perhaps the lubricant layer is not acting in such a protective capacity (or has been displaced by a $FeCO_3$ layer). The SLIPS NW sample shows a cathodic curve with two slightly depressed regions (similar to that of the SLIPS Bm sample). Suggesting there is some interaction occurring but not in a mechanism that promotes corrosion resistance. In terms of ΔE, SLIPS W has a significantly higher value of 0.11 V compared to the SLIPS NW value of 0.046 V. Theoretically there is an

expectation that diffusion will be higher again in the SLIPS W (in likeliness to SLIPS Kr) due to the higher physical properties of density and viscosity between the two lubricants. As both density and viscosity are generally inversely proportional to diffusion.

Tafel constants have also been extracted from the plots for all samples. The baseline Tafel constants of the X65 carbon steel samples are 0.059 v/decade for the anodic (β_a) sweep and 0.066 v/decade for the cathodic (β_c). Comparing the anodic sweep across all samples, the values are similar in value to the baseline. With the exception of SLIPS Kr at 0.155 v/decade and SLIPS W at 0.031 v/decade. Both samples also have lower corresponding I_{corr} values. β_c values of all samples are higher than the X65 carbon steel sample, again with SLIPS Kr and W having higher values on average. The $FeCO_3$ base layer has the highest value at 0.195 v/decade, while the SLIPS Bm has a value similar to that of the X65 CS. The Tafel constants will be used in the calculation of corrosion rates based on the EIS output in the next section. Here they are summarised in Table 21, below.

Table 21 Electrochemical corrosion parameters extracted from corrosion Tafel plots

Sample	*E_{corr} (V)*	*I_{corr} (mA/cm2)*	*β_a/β_c (V/decade)*	*CR (mmpy)*	*ΔE (V)*
X65 CS	-0.72	0.53	0.059/ 0.066	3.42	<0.01
$FeCO_3$	-0.70	1.35	0.060/ 0.195	0.52	<0.01
SLIPS Kr	-0.48	1.84	0.155/ 0.117	0.17	0.18
SLIPS Bm	-0.68	1.41	0.058/ 0.070	0.45	0.03
SLIPS NW	-0.65	1.16	0.054/ 0.102	0.80	0.05
SLIPS W	-0.56	1.95	0.031/ 0.133	0.13	0.11

Based on the I_{corr} values obtained from the Tafel plots, corrosion rates (CR) have been determined via Equation 29. This is standard practice as described in the ASTM standard G102 for the calculation of CR from electrochemical measurements. As expected, the CR value is the highest for the untreated

X65 carbon steel sample at 3.42 mmpy. This sample does not have the protection of either the SLIPS lubricant layer or the base $FeCO_3$ layer to inhibit the corrosion process. The CR of the base $FeCO_3$ layer is 0.52 mmpy, which is higher than the 0.1 mmpy rates achieved during the fabrication process. Although difficult to compare separate methods of obtaining CR the increase may be a result of interactions with the $FeCO_3$ layer and lubricants, or initial dissolving of the $FeCO_3$ layer itself. However from all the SLIPS tested it can be seen from CR, that the SLIPS system has a corrosion resistance greater than that of the X65 CS but not always from the $FeCO_3$ base layer itself. This suggest that the addition of lubricant may not confer additional protection than that already given by the $FeCO_3$, as is the case in SLIPS NW (CR= 0.80 mmpy). The lowest CR achieved were obtained from SLIPS Kr (CR= 0.17 mmpy) and SLIPS W (CR= 0.13 mmpy). The protectiveness of these SLIPS is further supported by more positive E_{corr} values (representing a lower corrosion thermodynamical tendency) and a higher ΔE suggesting a thicker lubricant/diffusion layer.

Scale tests

In the next part, Tafel plots have been constructed for the same samples in the presence of $CaCO_3$. This simulates the same environmental conditions used previously in the scale evaluation chapter (i.e SI 1 brine). Figure 211 shows the Tafel plots for both X65 and $FeCO_3$ with E_{corr} values (-0.66 V and -0.71 V respectively), similar in nature to those seen in the corrosion Tafel experiments. Given that the SI 1 brine was more of a gradual scaling system, it is expected that the system would not have as pronounced effects from precipitating scale as testing in the SI 2.6 brine would have. Also given the induction time, the effect would be more pronounced in the anodic section of the Tafel plot as more precipitate would drop out of the bulk onto the surface. I_{corr} values were lower for both samples compared to the previous test. The change in starting OCP (or ΔE) between sweeps is negligible given both systems lack the presence of the diffusion layer associated with the lubricant.

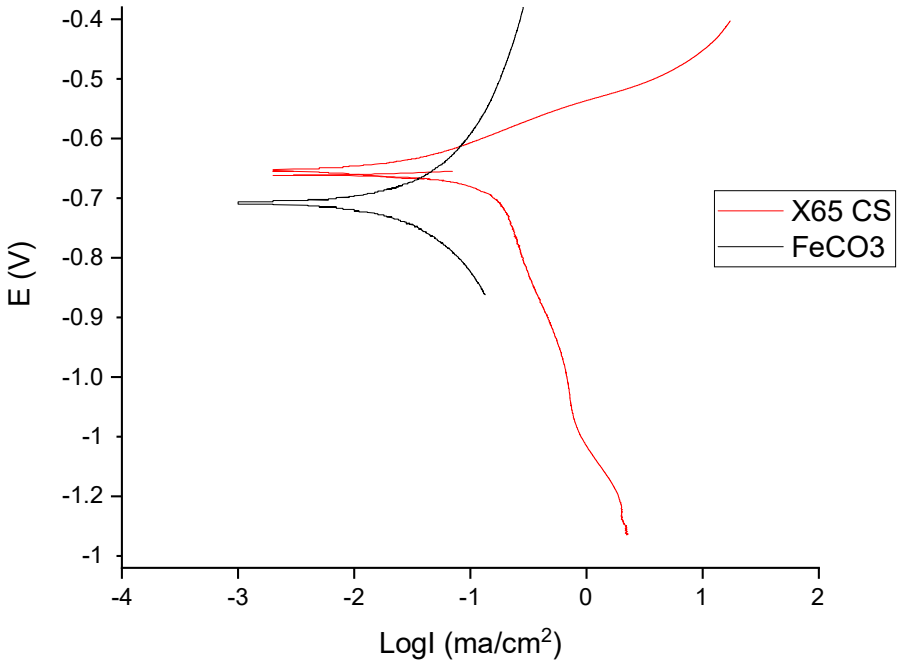

Figure 211 Anodic and Cathodic Tafel slopes of X65 Carbon Steel and $FeCO_3$ (Scale test)

Only one sample out of all tested in both systems showed signs of a separation or (ΔE) where the anodic sweep started at a higher OCP. This was the SLIPS BM sample where the ΔE was a positive value of 0.031 V. This may be the results of some breakdown in the surface as seen in the sudden kink during the cathodic sweep between -0.9 to -1.1 V. BMIM presents an interesting lubricant as in some medium (i.e. acidic) it can act as a corrosion inhibitor but when diluted with water can become a corrosive agent [382-384]. Figure 212, shows the plots for SLIPS Kr and SLIPS BM. Both SLIPS have similar E_{corr} values but dissimilar I_{corr} values. Again the ΔE value of SLIPS Kr is the largest compared to the other samples, although not as large as seen in the corrosion Tafel tests. This reinforces the idea that the Krytox lubricant provides the highest barrier to diffusion (also correlated with higher density of the lubricant itself).

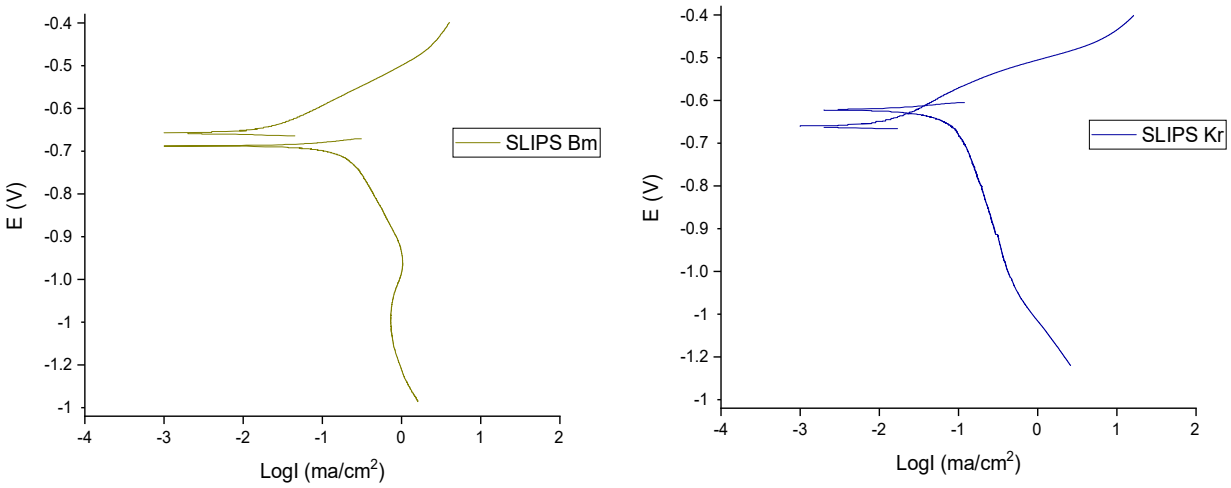

Figure 212 Anodic and Cathodic Tafel slopes of SLIPS BM and SLIPS Kr (Scale test)

The SLIPS W and NW Tafel plots are almost mirror images and are shown in Figure 213. This contrasts with the corrosion Tafel plots where both SLIPS had distinctly different shapes. $E_{corr,}$ ΔE and $I_{corr\ values}$ for both SLIPS were very similar, with the main distinguishable feature being a slight shift to right in the cathodic sweep for SLIPS W. The crude oil SLIPS also exhibit this behaviour in the corrosion Tafel plot, where the anodic plot is identical in shape. The 0.02 V ΔE value for the SLIPS W is noticeably different to that obtained in the Corrosion Tafel plots (0.1 V). This much lower value suggests a partial breakdown or loss of the lubricant layer during the scale Tafel test compared to the corrosion test. This assumption is based on the lower potential difference indicating a smaller diffusion path (or lubricant layer). However unlike the SLIPS BM this does not seem to be a complete loss of the layer (where there is no crossover of the cathodic/anodic branches) as there still exists a marginal diffusion time between the sweeps.

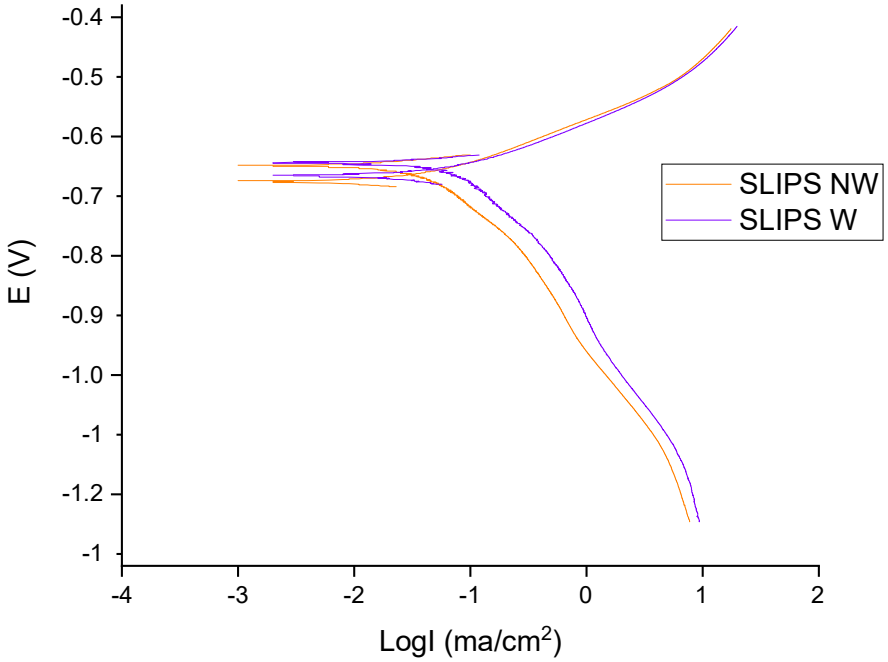

Figure 213 Anodic and Cathodic Tafel slopes of SLIPS NW and SLIPS W (Scale test)

Calculated corrosion rates and Tafel constants for the samples are shown in Table 22. Corrosion rates vary from 0.18 mmpy to 0.57mmpy and are in a much more constrained range than those obtained in the corrosion only conditions. Similarly Tafel constants are slightly higher as a whole compared to the corrosion tests. The 0.18 mmpy rate occurred in the $FeCO_3$ sample which exhibits the best corrosion performance. Conceptually this makes sense as the addition of $CaCO_3$ is known to form mixed $Fe_xCa_yCO_3$ deposits. The protectiveness of these layers is still under debate [105, 106, 108, 260], however any additional thickness (mixed or pure) of scale deposits on top of the original protective film would improve corrosion performance. The worst CR was 0.88 mmpy obtained by the SLIPS BM sample, this is also in line with poorer performance in the corrosion only tests. This seems to be the likely result of negative interactions, with the BMIM lubricant degrading the original $FeCO_3$ layer. ΔE values in both cases are low or in a positive direction for SLIPS BM suggesting a small or non-existent lubricant layer. However if the

lubricant layer has been lost, it would be expected to perform similar to the unlubricated $FeCO_3$ sample. Hence the poor corrosion performance cannot be the result of solely a loss of lubricant.

Table 22 Electrochemical corrosion parameters extracted from scale Tafel plots

Sample	E_{corr} *(V)*	I_{corr} *(mA/cm2)*	β_a/β_c *(V/decade)*	*CR (mmpy)*	*ΔE (V)*
X65 CS	-0.66	1.31	0.072/ 0.118	0.57	<0.01
$FeCO_3$	-0.71	1.80	0.092/ 0.108	0.18	<0.01
SLIPS Kr	-0.62	1.63	0.095/ 0.110	0.27	0.036
SLIPS BM	-0.68	1.12	0.090/ 0.192	0.88	0.031*
SLIPS NW	-0.65	1.44	0.045/ 0.130	0.42	0.026
SLIPS W	-0.64	1.35	0.057/ 0.133	0.52	0.02

Conversely SLIPS Kr displays lower corrosion rates and higher ΔE values. This indicates some connection of the higher ΔE differential being associated with more protective/ thicker lubricant layers. Although the potential difference obtained in the scale experiment is not as great as that in the corrosion only test, this may be a result of calcium ions (not calcium carbonate crystals) entering the lubricant layer and increasing local mass transfer. The X65 sample showed starkly different corrosion rates, although still poor relative to the sample set. This is unusual given the pH is relatively similar in both cases and would not be expected to add any substantial benefit to corrosion resistance in the short term. The crude oil SLIPS, SLIPS W and SLIPS NW, show similar corrosion performance at 0.52 and 0.42mmpy respectively. In the case of the SLIPS W sample, varying corrosion rates were seen between the two sets of tests. The 0.13 mmpy CR obtained by SLIPS W in the corrosion tests was the lowest observed, however this was not matched by the response in the scale test. Waxy crudes have been shown to have corrosion inhibitive properties however this protection can be non-uniform [385-387], with uneven

dispersion of the waxy components in the crude possibly the cause in the varied performance.

8.3 Summary

Polarisation tests have been carried out to construct Tafel plots on both base material (X65 CS, $FeCO_3$) and various SLIPS (Kr, BM, NW, W). From these plots qualitative estimates for a range of corrosion parameters (i.e current, potential etc) have been made. Two conditions were tested including mild corrosion conditions and the SI 1 scaling conditions of the previous chapter. With the following observations made:

- Ranges for the primary corrosion parameters taken in both test conditions are found in Table 23 (below).

Table 23 Value ranges for corrosion parameters

Parameter	**Range**	
	Corrosion test	**Scale test**
E_{corr} (V)	-0.48 to -0.72	-0.62 to -0.71
I_{corr} (V)	0.53 to 1.95	1.12 to 1.80
CR (mmpy)	0.13 to 3.42	0.18 to 0.88
ΔE (V)	0.03 to 0.18	-0.031 to 0.036

- Corrosion testing of the SLIPS system shows an improvement in corrosion performance compared to non-SLIPS systems (i.e. X65 CS and $FeCO_3$). However this is not replicated in the scale conditions. In both cases observed CR is not as low as final values obtained during the fabrication of the SLIPS $FeCO_3$ base layer (i.e. < 0.1 mmpy).
- In corrosion tests, SLIPS Kr and SLIPS W show the lowest CR at 0.17 and 0.13 mmpy, respectively. In the scale test, the top performers are $FeCO_3$ and SLIPS Kr at 0.18 and 0.27 mmpy.
- The presence of $CaCO_3$ scale in the system shows a marginal influence on all samples with CR grouped in a tighter, slightly lower

range between 0.18-0.88 mmpy. Likely the result of the deposition of mixed scales and/or Ca ions in the lubricant creating a greater diffusion barrier.

- ΔE values tend to be correlated with lower CR indicating a thicker diffusion layer/ protection from the lubricant is in place. Lower values may indicate the deterioration or removal of the lubricant layer entirely (such as SLIPS BM)
- It is also important to note that lubricant selection is critical, and performance may vary in differing conditions. The lowest corrosion rate in both conditions was different. However results in both tests clearly favour SLIPS Kr in consistency regarding reduced CR.

8.4 Electrochemical Impedance Spectroscopy (EIS) Results

Introduction

In this section Electrical Impedance Spectroscopy (EIS) has been used to examine the surface behaviour of the SLIPS specimens over time. Performance comparisons in separate scaling and corrosion environments have also been made across the various SLIPS. Both corrosion resistance and mineral deposition is expected to affect the impedance of the system studied, with distinct impacts on the electrical properties. Nyquist and Bode plots constructed from experimental data have been used to visualise impedance data, frequency dependent behaviour and individual time constants.

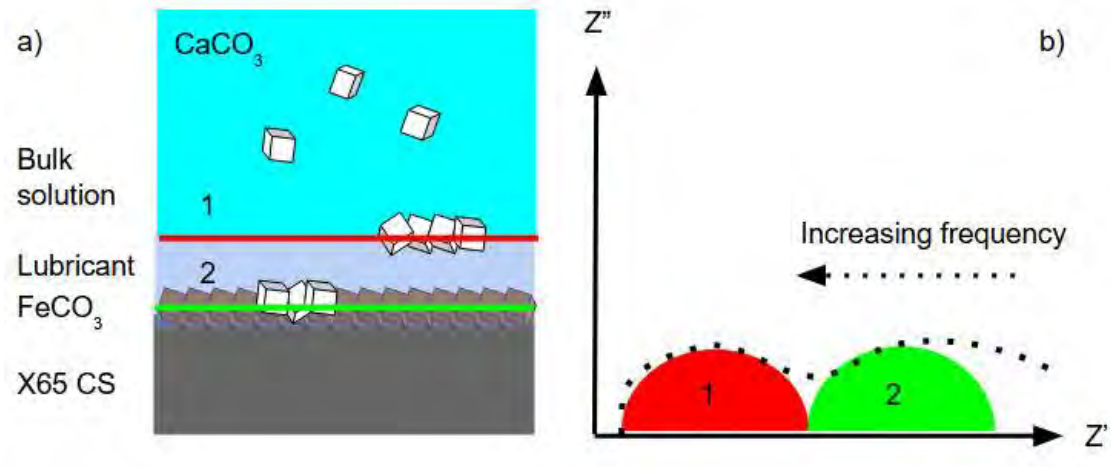

Figure 214 a) Schematic interpretation of tested interfaces b) Nyquist representation of these interfaces

Figure 214a), shows a simplified schematic of the system that is being studied in the EIS. In the corrosion tests, this system will be without the presence of $CaCO_3$ precipitation and crystals. This environment consists of the bulk solution, SLIPS (lubricant and $FeCO_3$ layer) and the underlying carbon steel (CS). Within the following analysis, generally two interfaces have been studied. The 1st interface (1) represents the bulk solution/lubricant boundary, and the 2nd interface (2) composes of the $FeCO_3$/ X65 CS area. In reality, multiple interfaces would exist in this example with concentration dilution of the lubricant into the surrounding bulk solution, porosity/thickness changes in the $FeCO_3$ layer, $FeCO_3$/lubricant edge etc. The focus here is on a simplified upper (1) and lower (2) boundary analysis. An ideal case has been represented as two individual capacitive arcs shown in the Nyquist plot (Figure 214b), based on the scenario depicted in Figure 214a). The upper boundary is represented as the first semi-circle/feature/time constant (red), whilst the lower boundary is displayed as the second feature (green). The dotted line depicts a more realistic, experimental set of data where often the resolution of these features is not as clear, open to interpretation and usually appear as constant phase elements compared to pure capacitors. Frequency generally increases from left to right on the Nyquist plot, where generally the 1 semi-circle (red) is associated with a high frequency (HF) domain and the 2 semi-circle is a low frequency (LF) region [388-390].

Corrosion tests

The EIS results for all samples in the corrosion solution (same bulk solution as Tafel experiments) have been collected in this section. Corrosion solution is used to represent the test environment that has no $CaCO_3$ present in the system. Therefore expected impacts would be increases in real and total impedance, symbolizing corrosion resistance. Each scan is typically 45 minutes long, with a total test duration of roughly 2 hours and 15 minutes, similar in nature to the scaling tests conducted previously. Solution resistivity (R_s) for all tests has been taken as the intercept with the X-axis (Real impedance) on the Nyquist plot. Values are in good agreement and within a range from ~ 2-3.5 $\Omega.cm^2$, as seen in Figure 215. All Nyquist plots showed a typical constant phase element (CPE) behaviour, with a distinct lack of symmetrical circularity as that normally found with a purely capacitive Randle's circuit [391, 392]. This shape is commonly associated with surfaces with some form of roughness and/or varying degrees of lubricant thickness [393, 394]. Both are expected given the nature of the SLIPS system, including the surface preparation of the base material and the $FeCO_3$ layer.

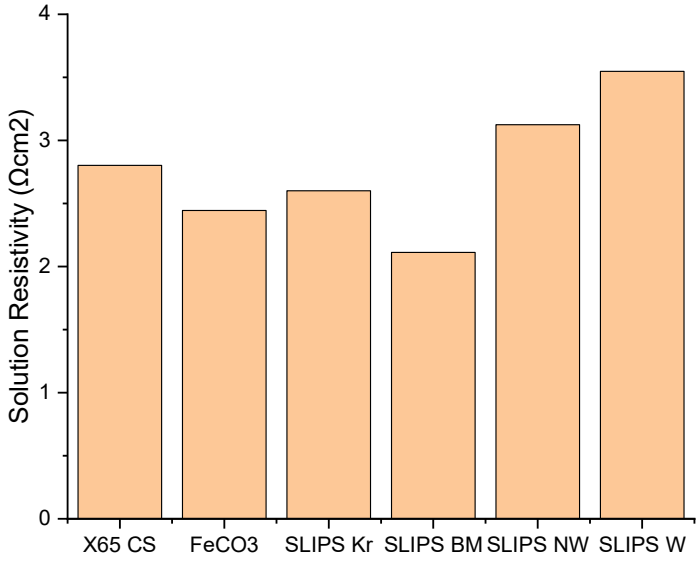

Figure 215 Solution resistance (Rs) for all samples tested in Corrosion solution

The Nyquist and Bode plot of X65 CS can be seen in Figure 216. The Nyquist shows two clear time constants or semi circles in all scans. These capacitive semi-circles are almost double the impedance in real (Z') terms compared to imaginary (Z'') suggesting the CPE behaviour mentioned previously. Time constants are also seen on the phase angle Bode plot at 0.1 hz and 30 hz, respectively. The initial 0 min scan is the smallest in both real and imaginary impedance. There is an increase in impedance to the next scan at 45min, however the surface seems to stabilise as both 90min and 135min scans are of a very similar nature. In terms of real impedance or resistivity, the X65 CS base material exhibits the lowest value at ~34 $\Omega cm^{2.}$

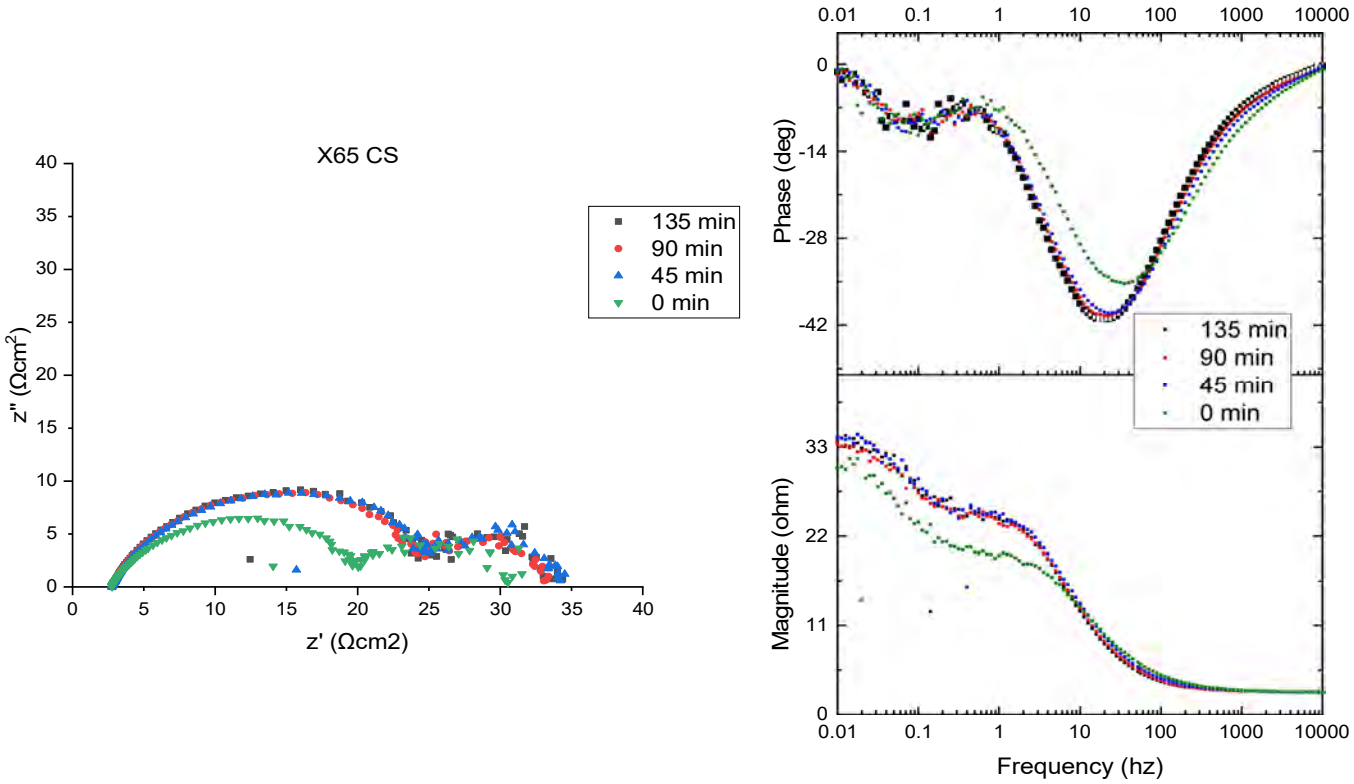

Figure 216 Nyquist plot and Bode (Phase/Magnitude) plots for X65 CS in Corrosion test

The Iron carbonate covered sample displays a more resistive nature based on the Nyquist Plot (Figure 217). This is expected given the CR rates shown during the fabrication process already provide a degree of protection. The 0 min scan has a real impedance value almost double that of the final scan

obtained for the X65 CS. As time progresses, both real and imaginary impedance increases, with a stabilisation in the imaginary component compared to the real component. With the surface becoming more resistant at the same capacitance level. This stabilisation over subsequent scans is also indicative of a more complete/ uniform coverage of the surface with a singular interface. The tail end of the Nyquist plot has a noisier and more vertical curve. This may be the lag effect of residual porosity in the existing $FeCO_3$ network becoming blocked [389, 395]. One primary time constant is observed in the Bode plot but there is a minor arc in the low frequency (around 0.1 hz). Again likely the active corrosion process on the surface associated with the remaining pockets of $FeCO_3$ porosity or non-uniformity in the layer.

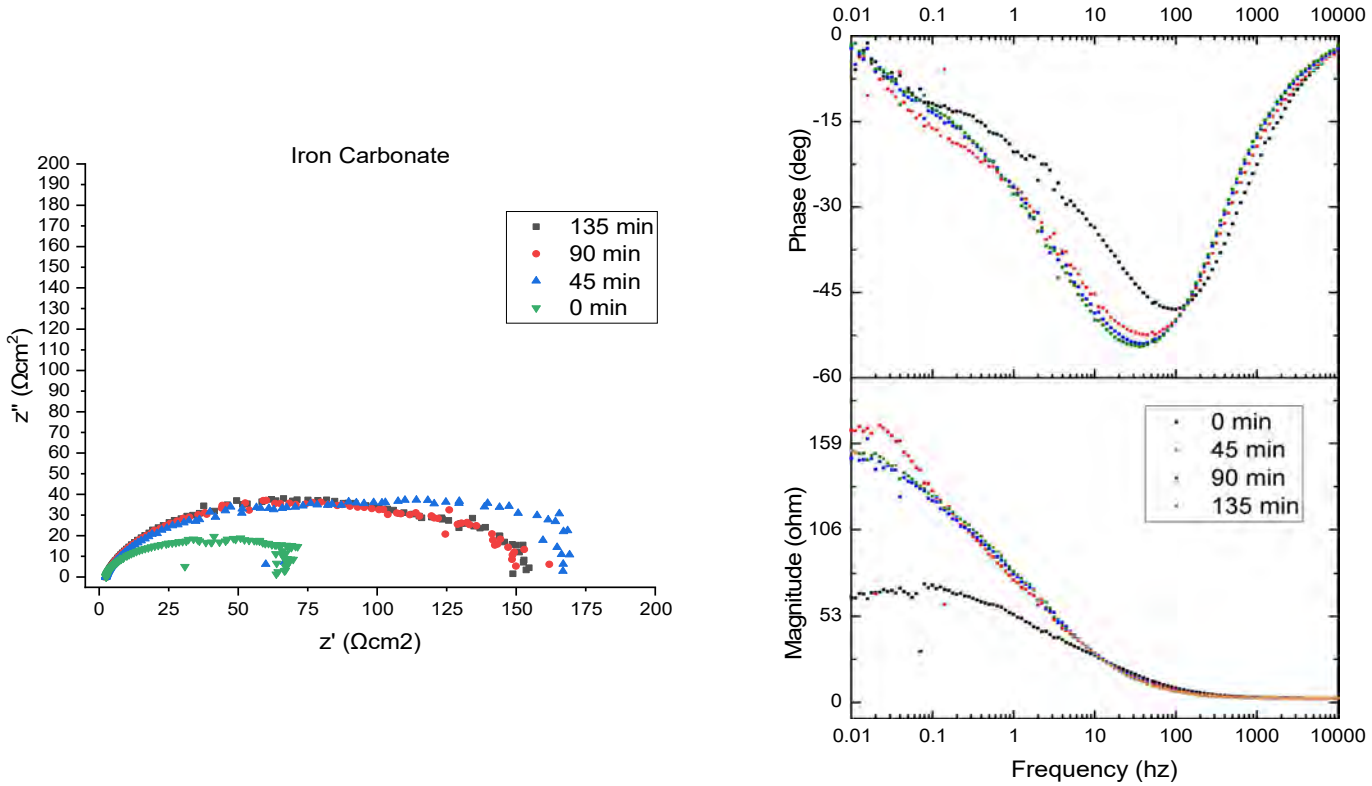

Figure 217 Nyquist plot and Bode (Phase/Magnitude) plots for Iron carbonate in Corrosion test

The SLIPS Kr sample shows increasingly protective behaviour over time, with a sharp increase in both imaginary and real terms shown in Figure 218. Immediately, the first (0 min) scan shows a higher real impedance of 200 $\Omega cm^{2,}$ higher than both the X65 CS and $FeCO_3$ final values. This initial scan,

as with the other samples, tends to have a much smaller semi-circle arc (or shape in general) compared to subsequent scans (i.e 45, 90, 135 min). Within the timeframe of the experiment the greatest change occurs between the 0 and 45min scans and this tends to be the case in all samples and conditions. This change is the smallest in the X65 sample where no extra major interface exists (compared to $FeCO_3$ or a SLIPS system). The Nyquist and Bode plot show one primary time constant in the 100 Hz range. The Nyquist plot is a uniform semi-circle, but the tail does not tend towards the real axis. The symmetrical nature of this circle and only one time constant indicate a greater degree of homogeneity of the SLIPS and integration of the lubricant in the $FeCO_3$ layer.

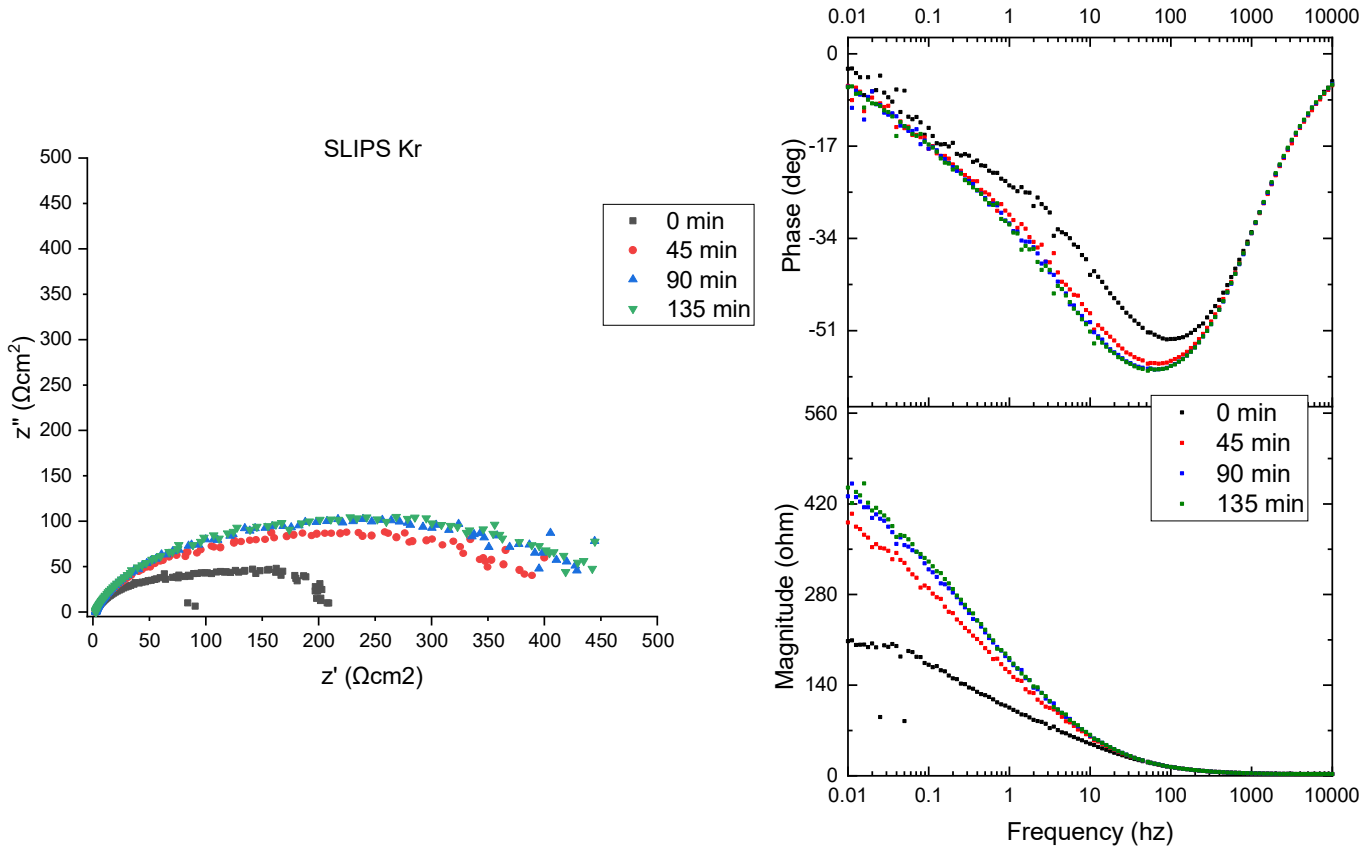

Figure 218 Nyquist plot and Bode (Phase/Magnitude) plots for SLIPS Kr in Corrosion test

The SLIPS BM sample Nyquist plot is shown in Figure 219 and shows changing behaviour over time. The initial 0 min scan shows two clear time constants, a small initial semi-circle followed by a larger one. These time

constants are also evident on the Bode plot at 110 Hz and 0.5 Hz respectively, however over time this becomes one. In the Nyquist plot this behaviour is observed as a response to a damaged coating, where the first semi-circle represents the coating layer (lubricant) with the second larger semi-circle indicative of behaviour at the metal interface or corrosion processes [389, 396]. With the progression in time, the first semi-circle grows with both an increase in real and imaginary impedance. This increase in capacitance (imaginary) impedance is associated with water uptake and likely the displacement of the lubricant by electrolyte in the $FeCO_3$ porosity/roughness [397-399]. The magnitude Bode plot still shows an increase over time (indicating greater protection); however the final value is still lower than the starting value obtained for the SLIPS Kr sample.

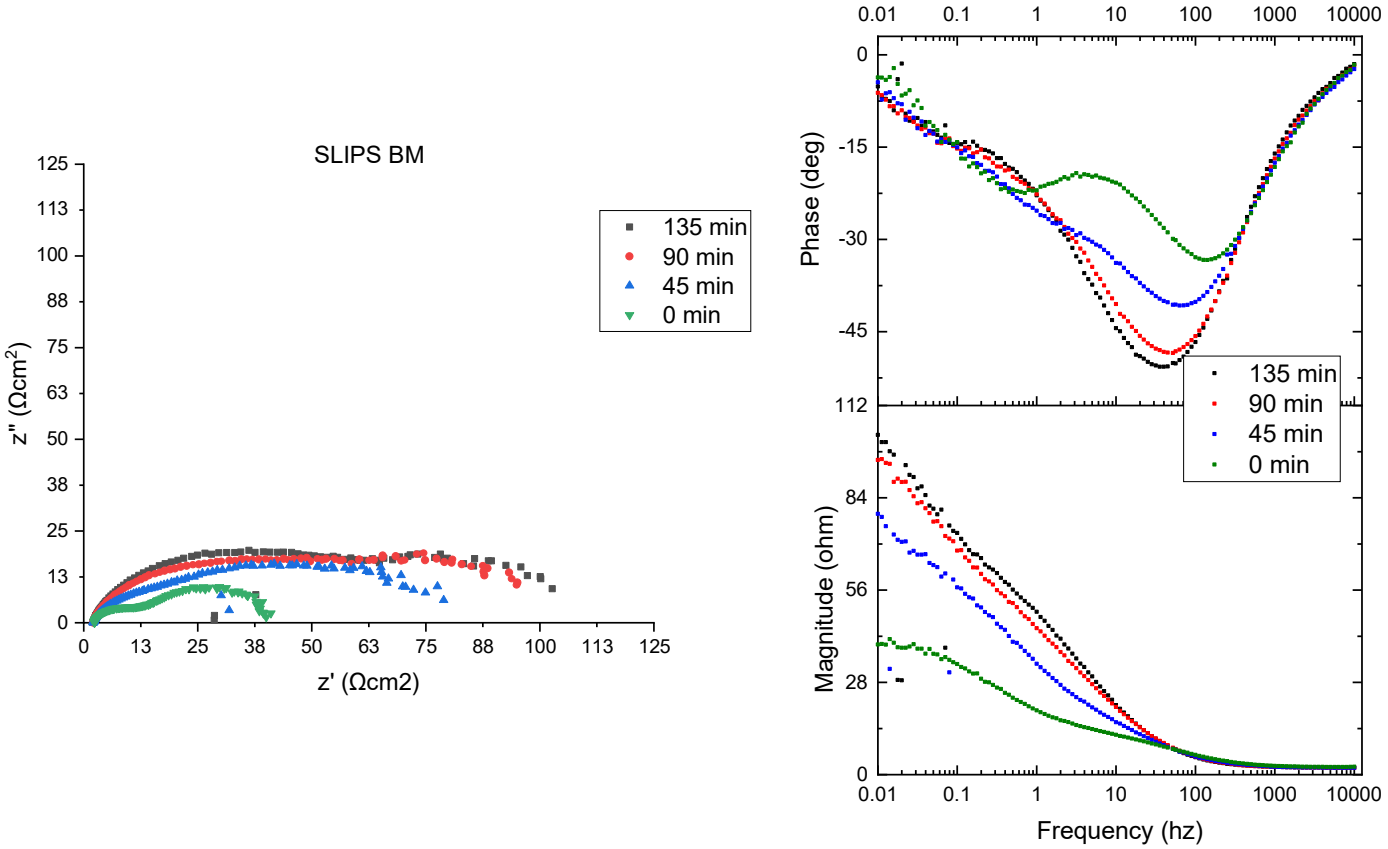

Figure 219 Nyquist plot and Bode (Phase/Magnitude) plots for SLIPS BM in Corrosion test

SLIPS NW shares some similarities in behaviour to that of SLIPS BM, as shown in Figure 220. Over time there is a distinct change in the shape of the

Nyquist plot. Initially there appears to be one primary semi-circle (or time constant) with an increase in noise towards the lower end frequencies (<1 hz). Although not quite clear in shape, this region is likely a remnant of inductive behaviour associated with the crude oil lubricant. A common response in water/oil emulsions where the inductive character at low frequencies is related to adsorption of species (asphaltenes or other crude oil polar compounds) onto the metal interface [400, 401]. In literature these surface-active species can have an inhibitive effect on corrosion (where the EIS response also mirrors behaviour associated with traditional corrosion inhibitors) [387, 402, 403]. This seems to be the case here with an increase in Bode plot magnitude as well as increasing impedance (real and imaginary) of the 2nd semi-circle (representing the metal interface) over time. The shape of the Nyquist plot (and Bode) continually shifts over time. At 45min, a secondary semi-circle is introduced (around 0.1 Hz), larger than the first and increasing in size over the remaining scans (also evident in the Bode plot).

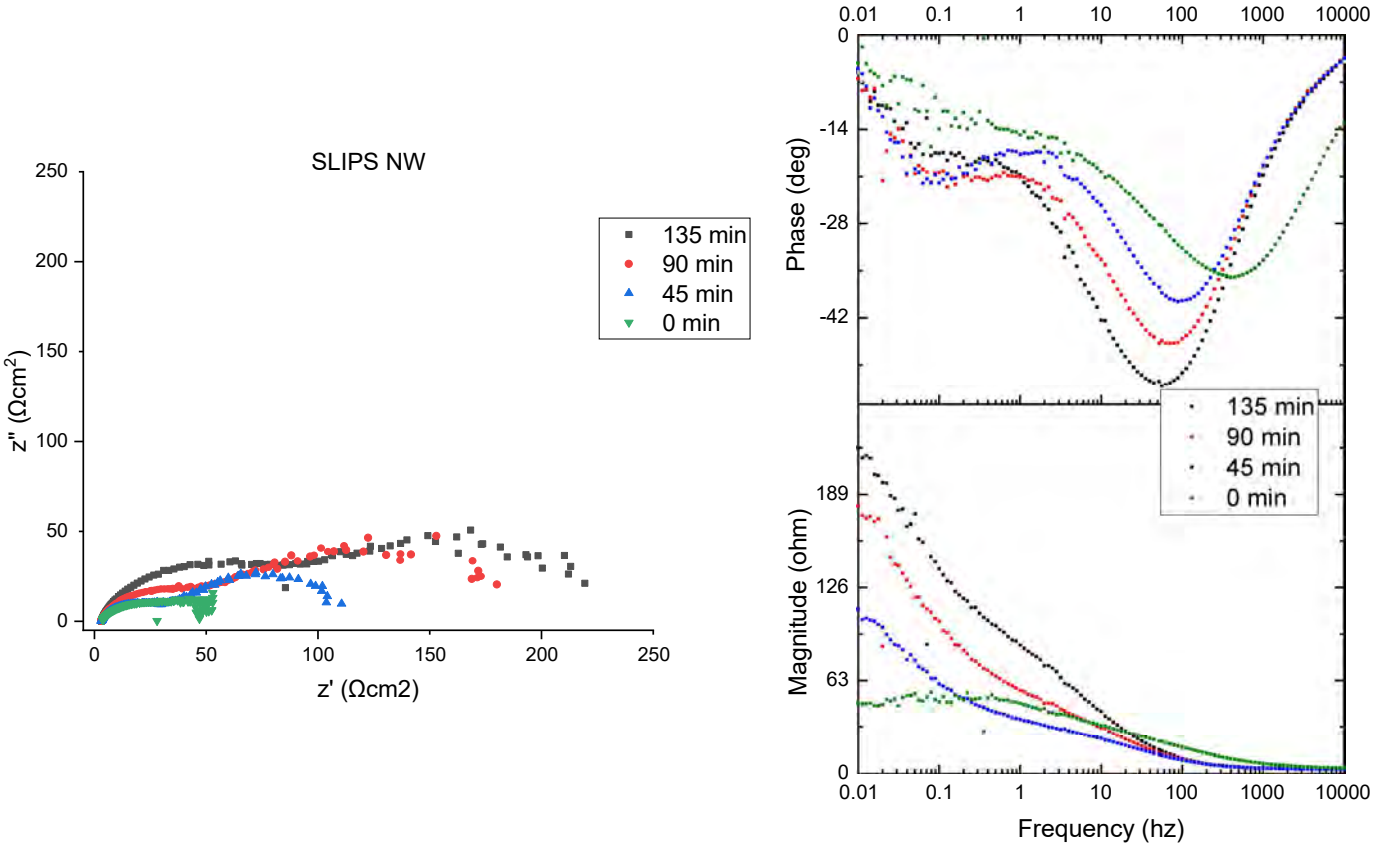

Figure 220 Nyquist plot and Bode (Phase/Magnitude) plots for SLIPS NW in Corrosion test

SLIPS W is the final SLIPS sample tested, with the Nyquist and Bode plots shown in Figure 221. This sample shows initial behaviour similar to the previous crude oil slips, with a much more pronounced inductive loop seen in the Nyquist plot during the 0 min scan. The Phase Bode plot shows a secondary kink around the 0.2 Hz mark, with the primary time constant seen around 200 Hz. After this initial scan, there is a large jump in impedance (both real and imaginary) until there is a stabilisation into a shape resembling one time constant (or semi- circle). Where the rate of increase over time slows, much in the same way that is seen for the SLIPS Kr. This stabilisation in later scans show a delineation in behaviour between those lubricants that are generally immiscible (i.e oil) and those where dilution (miscibility) with the bulk electrolyte causes fluctuations in the behaviour on the surface. This response in these tests is also associated with greater performance in terms of

impedance magnitude and resembles the response of intact coatings generally seen in literature [389, 396].

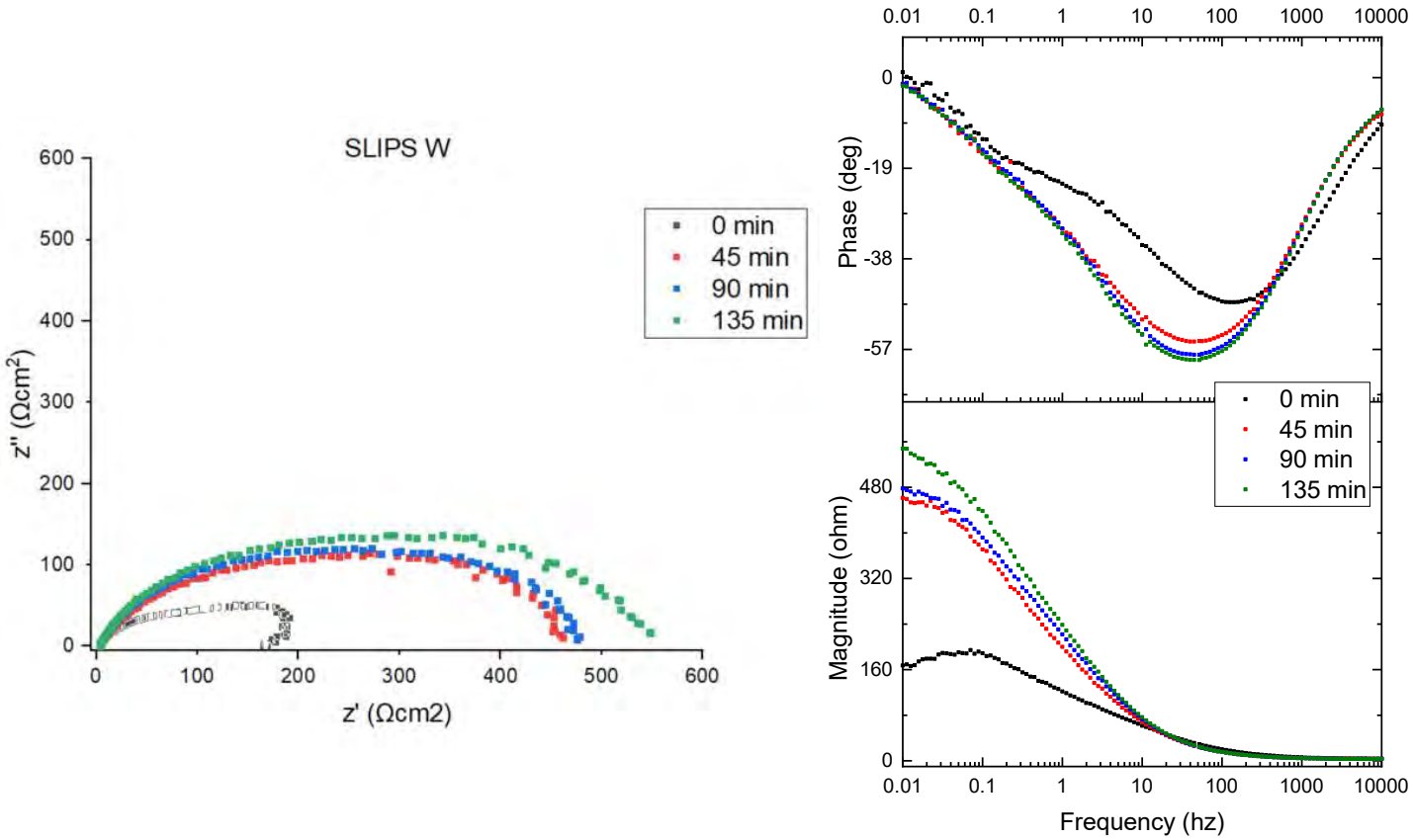

Figure 221 Nyquist plot and Bode (Phase/Magnitude) plots for SLIPS W in Corrosion test

Scaling Tests

The EIS tests conducted on the samples in a $CaCO_3$ scaling environment (the same conditions as tested in the previous chapter) are shown in this section. The differences and similarities between the SLIPS systems, alternative environmental conditions and observed EIS response are explored here. With regards to the conditions, firstly as seen in Figure 222. solution resistivity is slightly higher across all samples (except the X65 CS). This increase in resistivity is likely the cause of $CaCO_3$ precipitation in the bulk electrolyte. With the low induction time and high saturation index (SI 2.6), the electrochemical impact is rapid. Due to the loss of ionic species precipitating out of the electrolyte and the insulative properties of $CaCO_3$ [404, 405], the real

impedance or resistivity shifts to a higher level. The largest difference is seen with the crude oil samples, with the SLIPS W following the trend of higher solution resistivity compared to SLIPS NW. Again this variation is likely due to the complex nature of crudes (i.e more chemically reactive) and the potential formation of other products/ precipitates (including filter cake, calcium naphthalene's etc.) [406-408] increasing resistivity by a higher magnitude compared to the corrosion test.

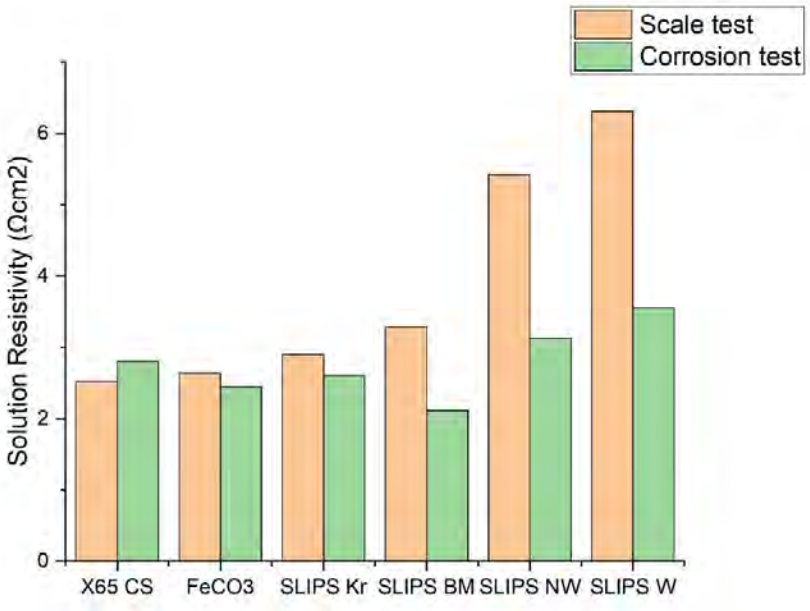

Figure 222 Comparison of solution resistivity between corrosion and scale test conditions

The EIS response for the X65 CS sample is shown in Figure 223. The Nyquist plot shows the presence of one primary semi-circle and a smaller secondary time constant in the HF area. Interestingly, this sample shows an inverse trend where a decrease in impedance magnitude over time. This decrease is very small relative to all other samples tested in both corrosion and scale conditions, in impedance magnitude it represents a change of only 1.45 Ωcm^2. The presence of two-time constants is also clearly seen in the Phase Bode plot around 10 Hz and 0.007 Hz. From the 0 min to 30 min scan there is a distinct frequency shift in the time constant. This is probably the result of the insulative/resistive effect of the $CaCO_3$ precipitation being largely connected to this initial scan, with subsequent scans stabilising in an environment where

the bulk of precipitation has concluded. The size of this first semi-circle is similar in nature to that obtained from the X65 CS in the corrosion test, with the major difference being the development of this second time constant/semi-circle which is much smaller in this test.

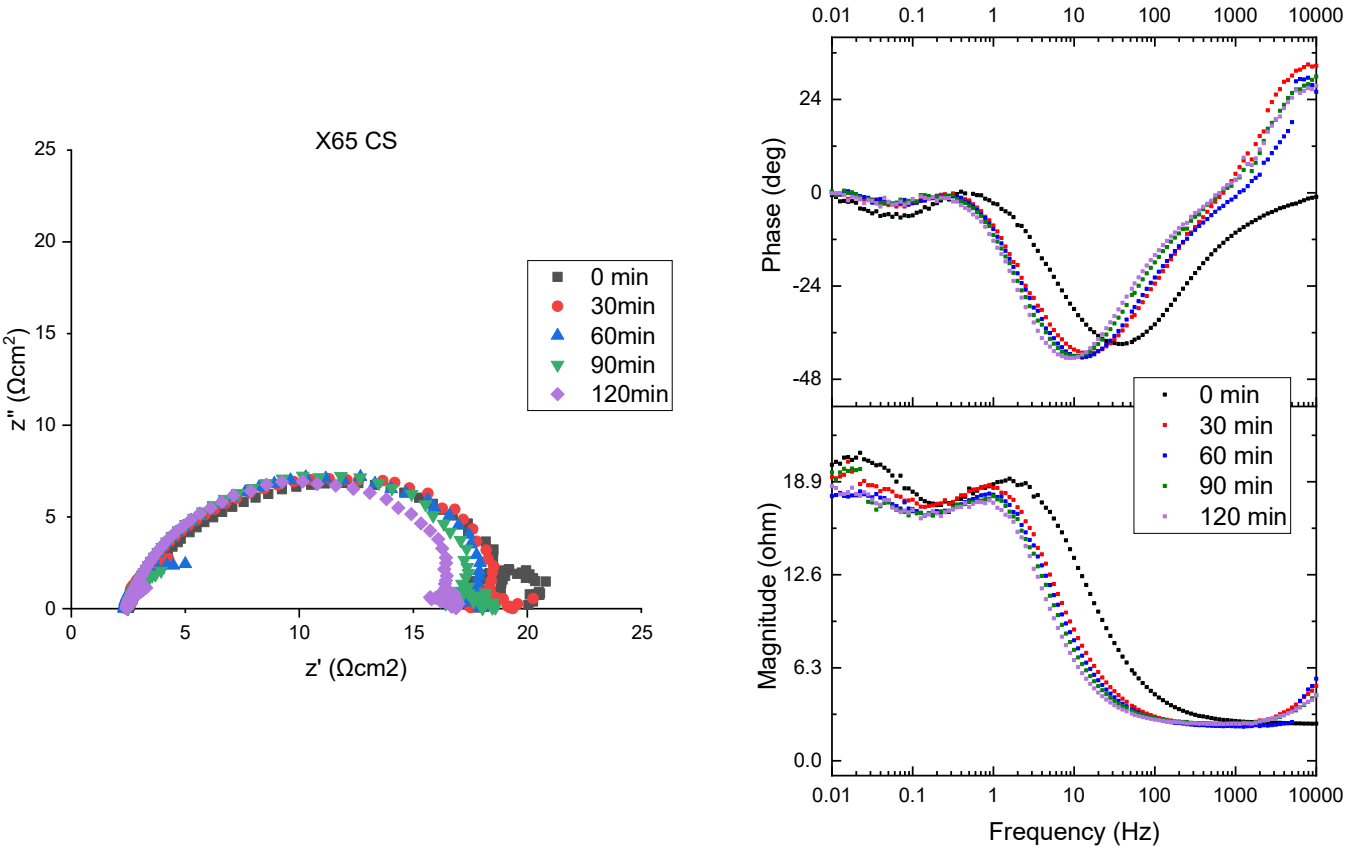

Figure 223 Nyquist plot and Bode (Phase/Magnitude) plots for X65 CS in Scale test

The iron carbonate SLIPS base exhibits one primary semi-circle as seen in Figure 224. The presence of this singular time constant is also seen in the Bode plot at 20 Hz and does not shift in frequency for the duration of the experiment. The impedance magnitude also increases over time, with the largest increase seen from the 0min to 30min scan, where the rate of increase than stabilises. In the low frequency area, primarily on the Nyquist but also in the Phase bode plot there appears another time constant. In the Nyquist plot this is the presence of a shifting tail section (<0.1 Hz), that increasingly moves towards higher values on the real (resistance) impedance axis. This suggests the incorporation of Ca^{2+} into the existing $FeCO_3$ network and $CaCO_3$

deposition are simultaneously occurring. This is based on the insulating effect of $CaCO_3$ or mixed carbonates increasing impedance/ resistance at both time constants (one at the $FeCO_3$/electrolyte interface and the other at the $FeCO_3$/steel interface) [409]. The total impedance value (~93 Ωcm^2) compared to that seen in the corrosion test (~159 Ωcm^2) is also in line with literature that shows less protective properties for mixed iron-calcium carbonate scales [105].

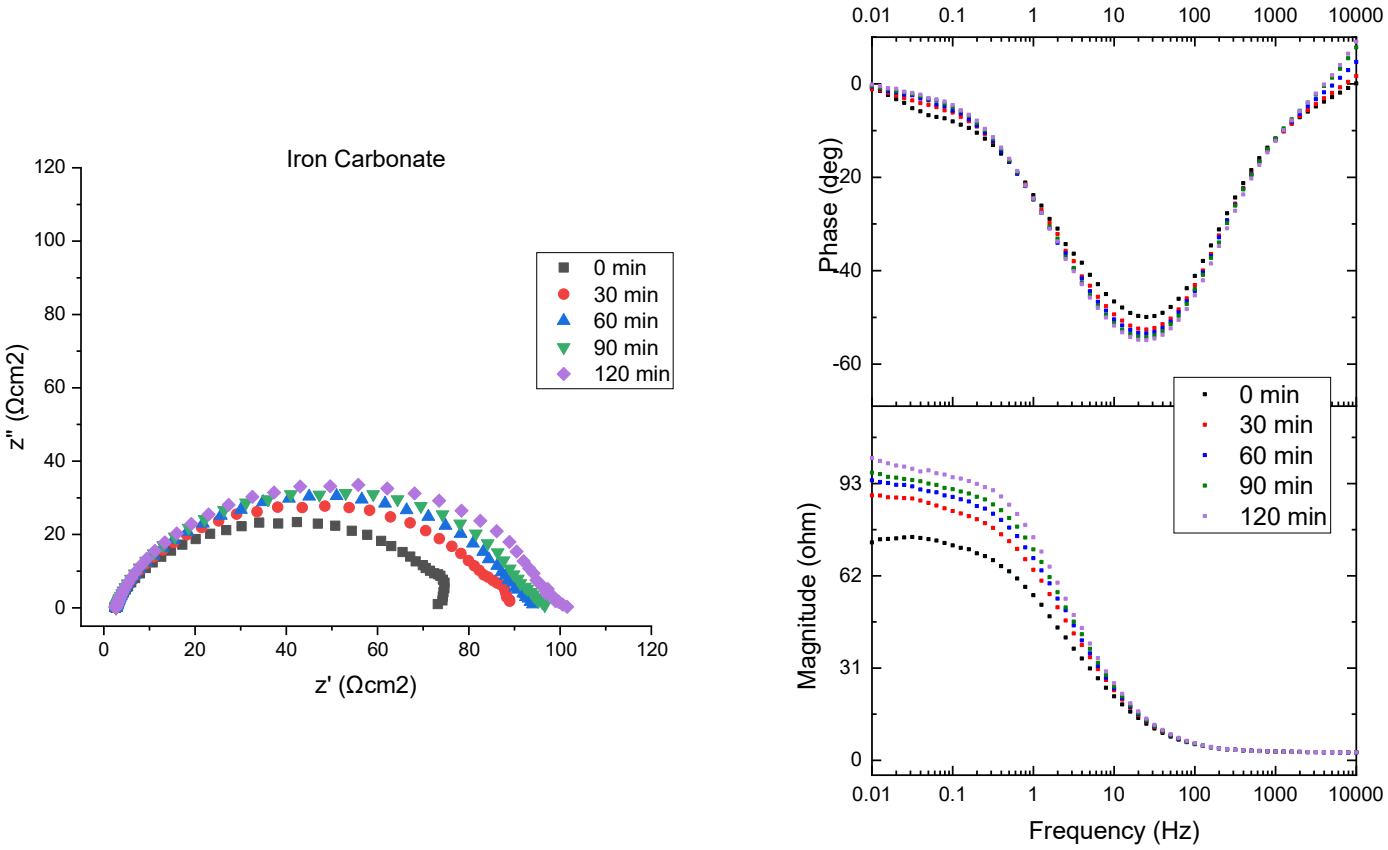

Figure 224 Nyquist plot and Bode (Phase/Magnitude) plots for Iron carbonate in Scale test

Results for the SLIPS Kr sample are shown in Figure 225. The Nyquist plot shows two clear time constants, also observed on the Phase Bode plot. The first-time constant is a typical capacitive arc around 100 Hz, increasing in impedance over time, however the time constant moves in frequency from the 0 min to 30min scan. The gradual increase of the first semi-circle is representative of increasing impedance attributed to the deposition or nucleation of CaCO3 scale at the top of the lubricant/electrolyte interface. At

0.1 Hz on the phase Bode plot we see a secondary time constant that is reflected on the Nyquist plot as a tail. This tail section in the low frequency, changes over time from an arc to a straight line and is commonly associated with diffusional impedance (although development to the 45° angle linked to Warburg diffusion is not present). In this case representative of the formation of further scales (either $CaCO_3$, $FeCO_3$ or Fe_xCa_yCO3) and higher impedance occurring at the lower $FeCO_3$/metal interface [410, 411].

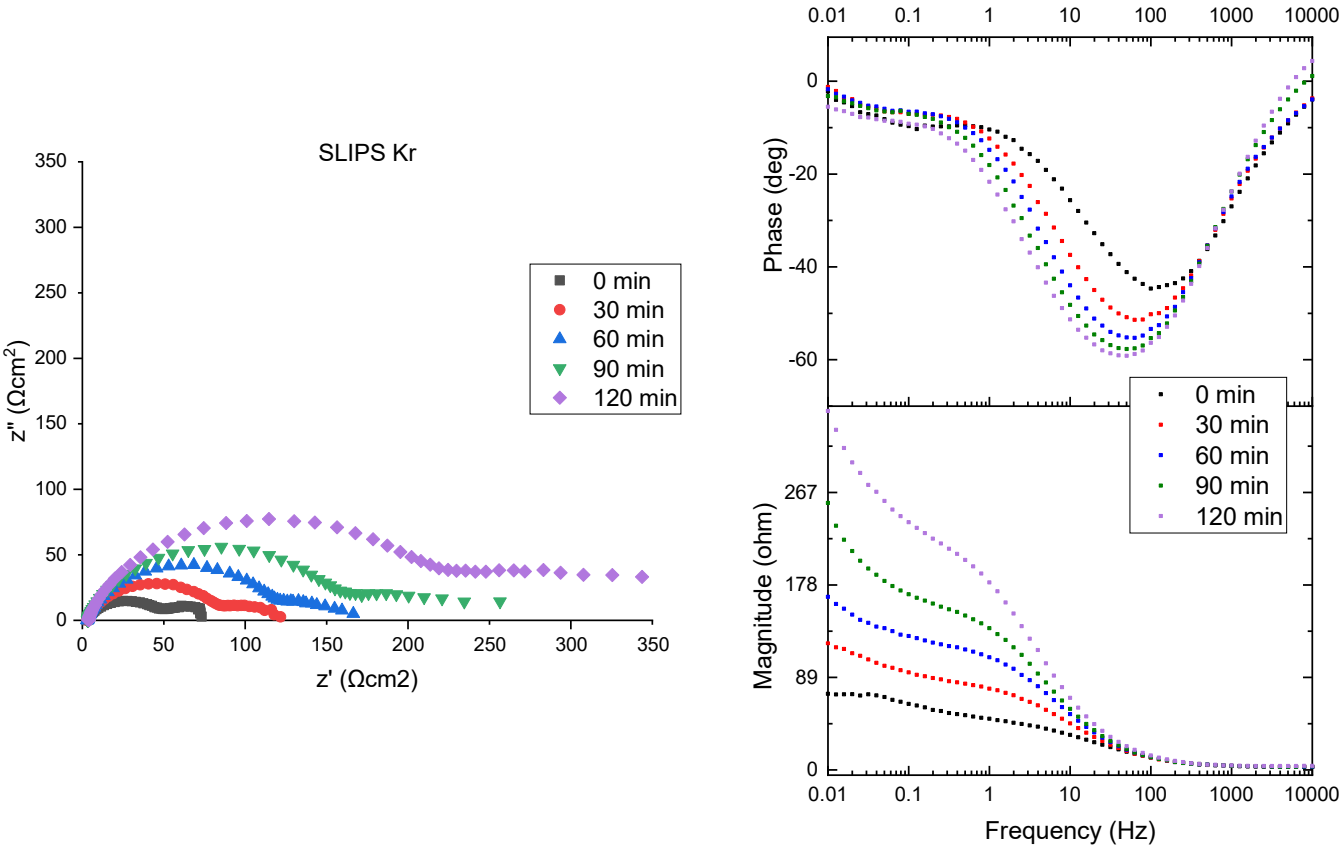

Figure 225 Nyquist plot and Bode (Phase/Magnitude) plots for SLIPS Kr in Scale test

In the SLIPS BM, the Nyquist plot shows a primary capacitive arc in the frequency range of 10Hz-100Hz (Figure 226). This first arc grows in real and imaginary impedance over time, although unusually the final (120 min) scan shows a sudden shift in the starting real impedance or solution resistance which has not been resolved. The preceding 90 min scan does seem to show a change in the system with noise and a higher phase angle in the primary time constant of the Bode plot. This shift to higher phase angles at a slightly

lower frequency occurs while impedance magnitude is still increasing. The tail section of the arc is minor at inception but continues to develop into a secondary arc commonly associated with a 45˚ Warburg diffusion element [412, 413]. The increase in this arc in proportion to the initial section indicates 2 mechanisms, increasing capacitance (imaginary impedance) would indicate water uptake or some dilutionary effect on the lubricant barrier and also increasing resistance (real impedance) and the formation of a possible Warburg finite-length diffusion element formed from increasing $CaCO_3$ deposition both occurring at the lower interface.

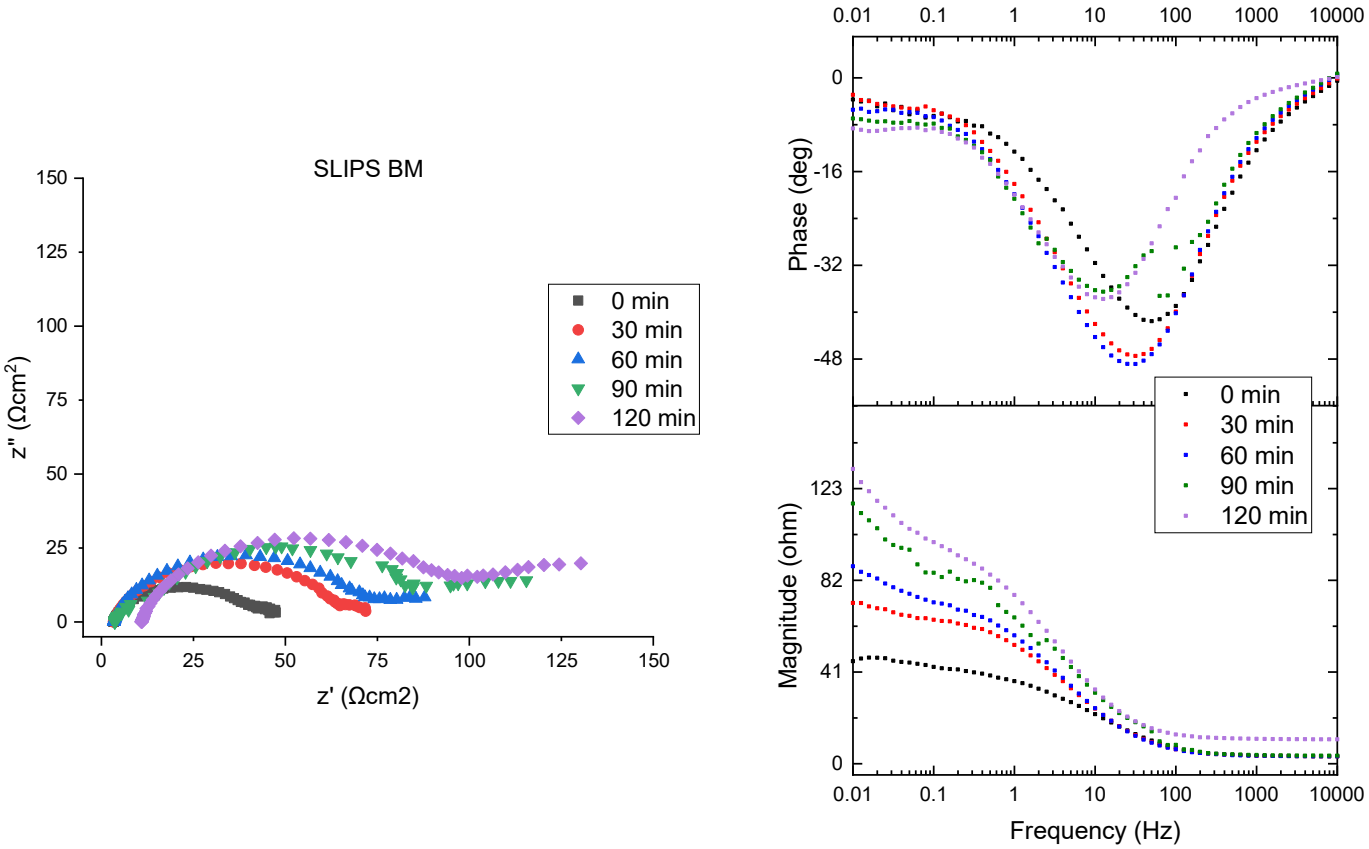

Figure 226 Nyquist plot and Bode (Phase/Magnitude) plots for SLIPS BM in Scale test

EIS results for the SLIPS NW sample are shown in Figure 227. Nyquist plot shows a primary, depressed semi-circle increasing in impedance over time, with the largest increase occurring after the 0min scan. The impedance increase for this arc occurs with a shift towards lower frequencies, 200Hz to 30Hz, on the same time constant in the Phase bode pot. Again, attached to

the primary capacitive arc is a secondary time constant/ feature in the low frequency region. In the initial scan this secondary feature is a complete inductive loop intersecting at the real impedance axis, as stated previously this is normally associated with some adsorption of active species in the crude oil to the lower metallic interface. This inductive loop is also only seen during the initial scan. Subsequent scans show the secondary feature to stabilise as an almost horizontal tail on the Nyquist plot of a similar real impedance length, this is also seen on the Phase Bode plot as a horizontal plateau below 0.2 Hz. Impedance magnitude increases at a decreasing rate over the duration of the experiment, suggesting a relatively uniform deposition of $CaCO_3$ on the surface.

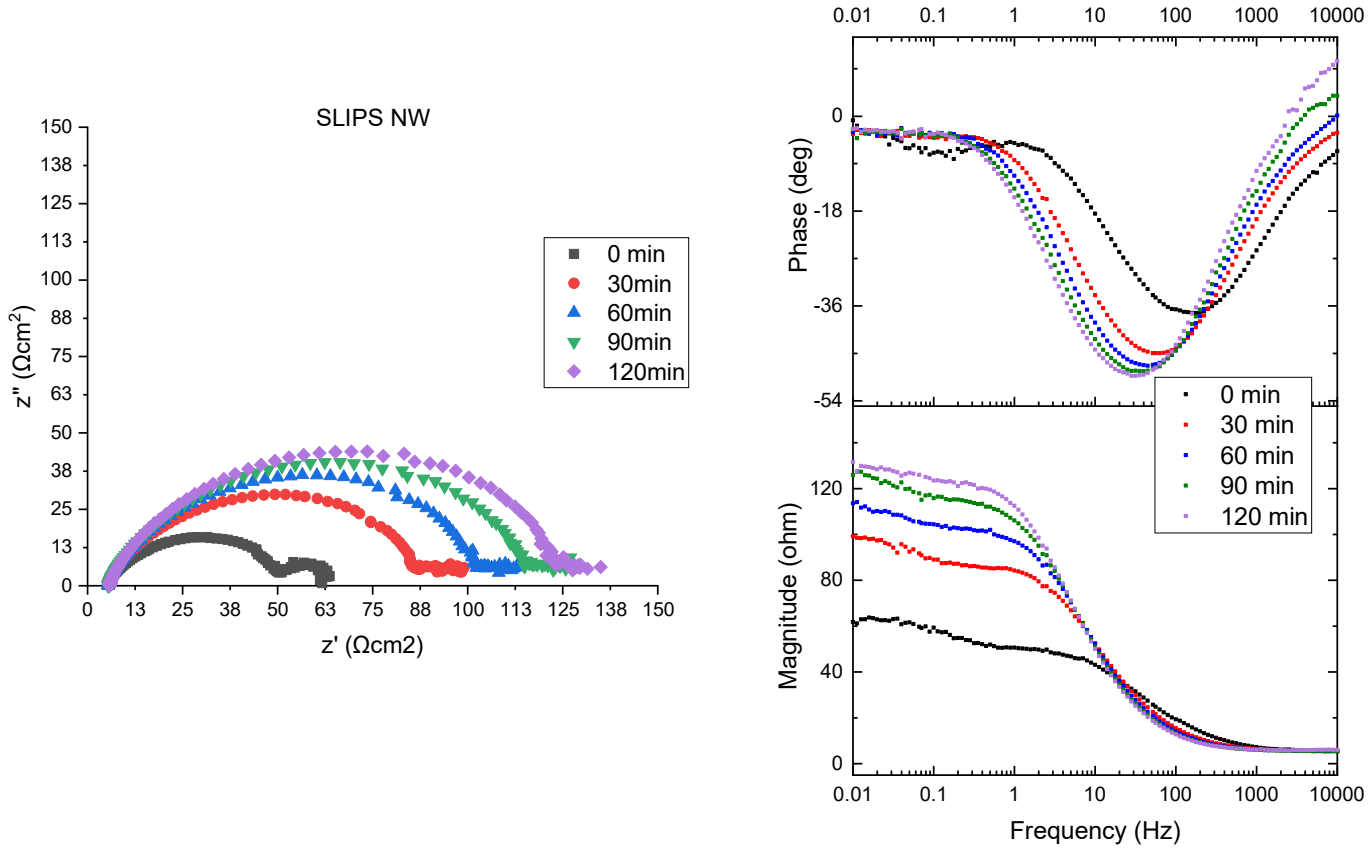

Figure 227 Nyquist plot and Bode (Phase/Magnitude) plots for SLIPS NW in Scale test

SLIPS W presents an interesting EIS response in the scale test conditions. The EIS response is shown in Figure 228 and shows the presence of only a single time constant. This single time constant is a semi-circle which includes

an inductive loop. The first scan shows a very strong inductive curve with the low frequency region returning back towards the initial real impedance axis intercept. This is also seen on the Magnitude Bode plot, albeit with some noise, where the impedance magnitude increases up to 156 Ωcm^2 but subsequently drops to <78 Ωcm^2 in the low frequency region (<0.1 Hz). This pattern is also seen in subsequent scans, where there is a reduction in magnitude. The SLIPS W sample is interesting as the trend changes as a function of time. During the 0min, 30min, 60min scan an increase in impedance magnitude and the Nyquist curve is observed. However for 90min and 120min a reversal is indicated as both parameters decrease. Traditionally, increases in Bode magnitude indicate improved corrosion resistance (i.e such as the addition of a corrosion inhibitor or formation of protective layer) [414-417]. Conversely, in the sense of scale inhibition, a reduction in impedance magnitude would be associated with the removal of insulating scale deposits on the interface, a conventional sign of a good scale inhibitor [418, 419]. However, this also comes at the cost of destruction/dissolution of the $FeCO_3$ base layer in the SLIPS system [420, 421]. Hypothetically, given that the impedance first increases and then decreases, with the final total magnitude and Nyquist semi-circle being larger than the initial scan it would point towards a reduction in scale deposition without the loss of the underlying $FeCO_3$ base.

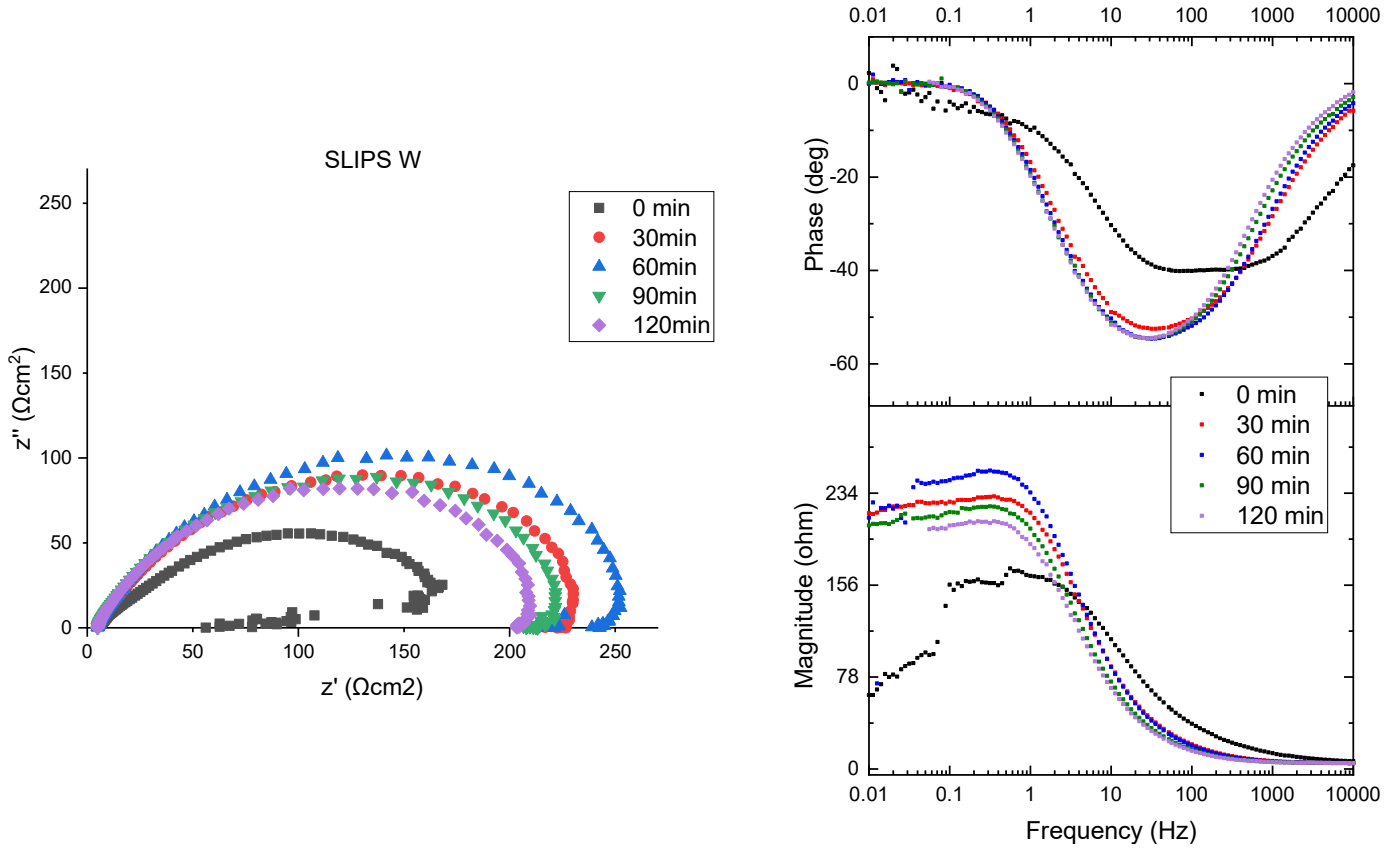

Figure 228 Nyquist plot and Bode (Phase/Magnitude) plots for SLIPS W in Scale test

8.5 Summary

Impedance magnitude values at the initial (0 min) and final (135 min) scans for all EIS corrosion tests conducted are shown in Figure 229. These values have been taken from the Low frequency region (0.01 Hz) in the Bode Phase plot where corrosion processes take place. These values have been compared with the corrosion rates obtained from the Tafel plots in the first part. Although there is no clear trend observed across all samples, it is seen that at the extremities high relative impedance is linked with depressed corrosion rates. This is supported by conventional thinking in literature [422-425] and in these tests significantly higher impedance levels are associated with the lowest corrosion rates (i.e SLIPS Kr and SLIPS W) whilst the low

impedance values obtained in the bare X65 CS sample have the highest corrosion rate. It is also seen over the duration of the experiment that impedance magnitude increases for all samples. This suggests a continuous protective barrier over this time, likely associated with the continued build-up of the protective $FeCO_3$ barrier. Where there is no existing $FeCO_3$ network, the change in protectiveness is negligible (i.e X65 CS).

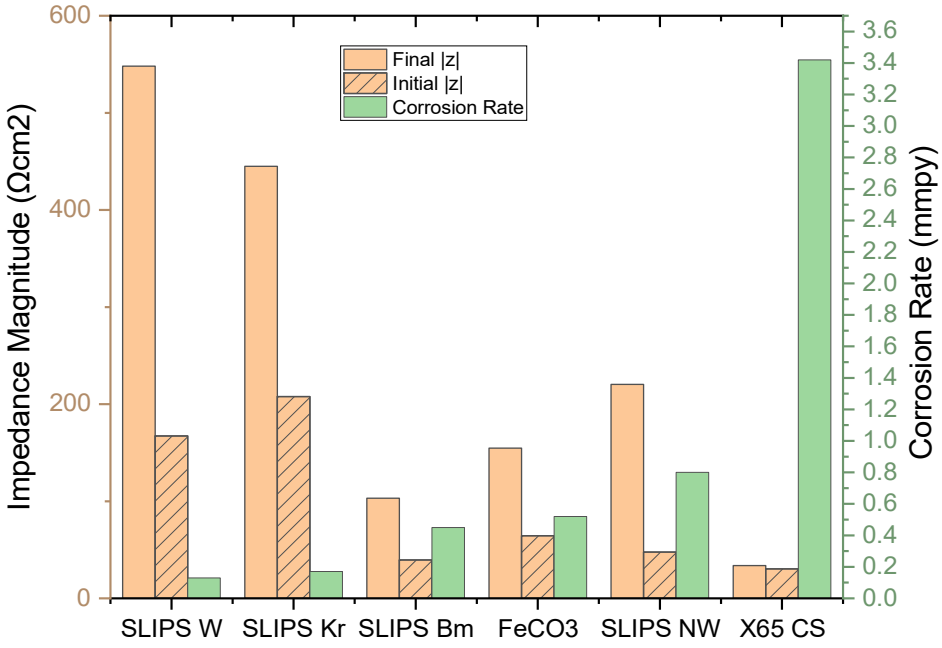

Figure 229 Final and Initial Impedance Magnitude vs Increasing Corrosion Rate for all samples in Corrosion test conditions

Figure 230 shows the same parameters as the preceding graph (Figure 229) but for the results obtained in the scale test. The addition of $CaCO_3$ into the system tends to have an impact on both corrosion rate behaviour and EIS impedance values compared to those obtained in the Corrosion test. In general impedance values are not a good indicator of corrosion performance (or CR) in the scale test conditions. Within the scale test conditions, comparatively higher impedance levels are not reflected in lower corrosion rates across the samples, although there does seem to be more consistency with this trend for Initial |z| values. For example the lowest CR obtained by the

$FeCO_3$ sample has the lowest Final |z|, whilst the SLIPS Kr sample has the highest Final |z| but also a low CR. Across the samples we see that impedance values tend to increase from initial to final scans. From a corrosion perspective it shows, even with the addition of $CaCO_3$, the SLIPS systems have a continuing corrosion resistance over the duration of the experiment. However, comparing impedance values between conditions, average values tend to be lower in the scale test. The presence of $CaCO_3$ is known in literature to produce less effective corrosion resistance when integrated with otherwise protective $FeCO_3$ layers [105, 108, 426-428].

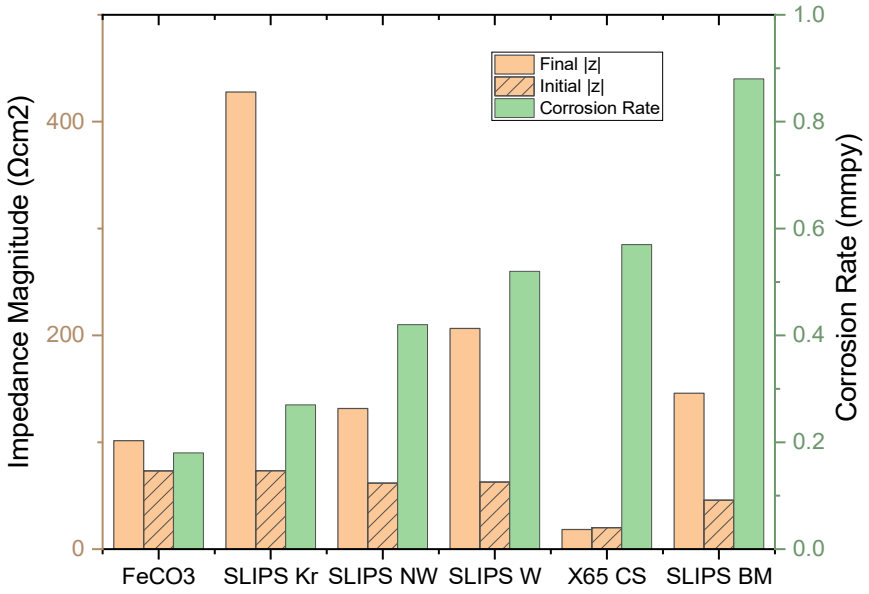

Figure 230 Final and Initial Impedance Magnitude vs Increasing Corrosion Rate for all samples in Scale test conditions

The effectiveness of SLIPS in reducing corrosion compared to an untreated X65 CS sample has been clearly demonstrated (except in the case of SLIPS BM in scale test conditions). In order to see if corrosion performance can also be linked with scale performance, impedance values have been compared to $CaCO_3$ scale markers obtained in the 2nd results chapter. The impedance values used are the Final |z| (Ωcm^2), given the scale evaluation and markers were carried out post-test (i.e after 2 hrs). The markers used are EDX Calcium Wt.% and XRD Calcium molar fractions of mixed ($Fe_xCa_yCO_3$) deposits seen

in Figure 231. Here impedance values do not seem to be indicative or correlated with scaling performance. At the highest impedance values (i.e SLIPS Kr and SLIPS W), Ca Wt. % is low however the remaining samples show mixed results (Figure 231a). Similarly with the mole fraction, no observable trends are apparent between impedance and integration of Ca into mixed scale products (Figure 231b). Looking at the Tafel scale tests, there is some connection with the ΔE value (which has been attributed to lubricant diffusion thickness) and the XRD molar fraction. With higher ΔE values (i.e SLIPS NW and SLIPS Kr) reflect lower Ca molar fractions in the mixed carbonate deposits. From both corrosion and scale metrics there seems to be a more consistent best and worst performer which are SLIPS Kr and X65 CS, respectively.

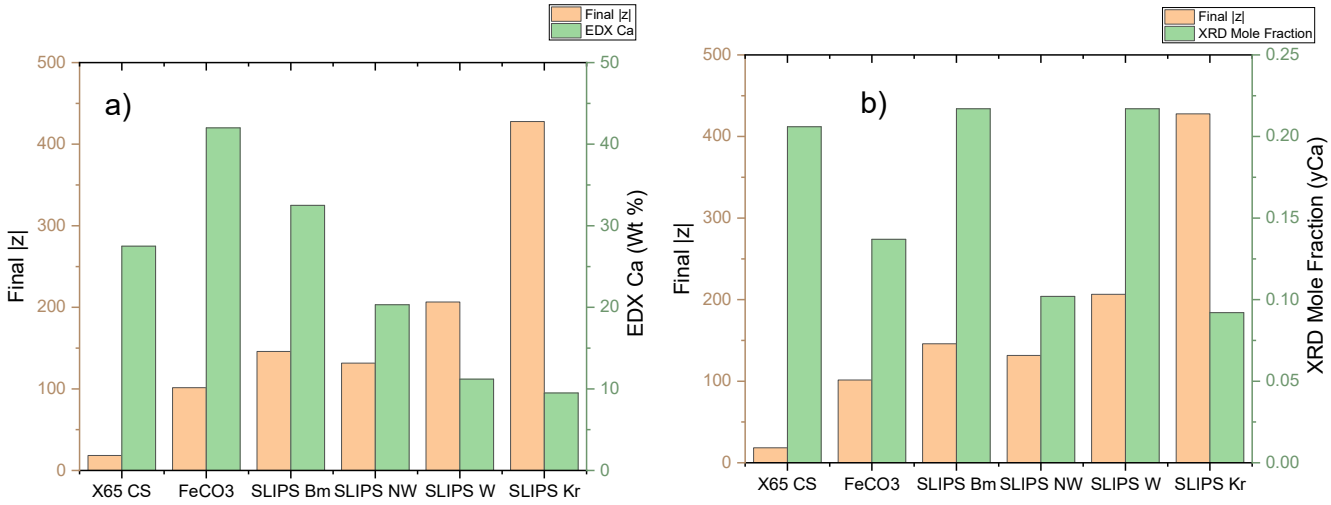

Figure 231 a) Final Impedance Magnitude vs EDX Ca wt. % and b) vs XRD Mole Fraction

With regards to observed Nyquist behaviour wise, a variety of physical cases have developed in the samples. These curves have presented behaviour more in likeness to what is seen with the addition of corrosion inhibitors compared to a traditional capacitive coating. For an intact/ undamaged coating, the Nyquist plot would look more like a straight vertical line, increasing only in imaginary impedance as the coating acts as physical barrier to the surround electrolyte [417, 429, 430]. In the case of corrosion EIS experiments,

the physical interpretation is usually one of two scenarios as shown in Figure 232 [431, 432]. In the first case, there is the presence of only one arc/time constant which shows a singular consistent interface across the sample surface, this case is normally associated with a stabilisation of the film and higher impedance values (lower corrosion rate), such as SLIPS Kr/SLIPS W. These SLIPS also tend to have better immiscibility properties. On the other hand, the 2nd case shows the development of different time constants at different rates due to the changing nature of the surface, which might include a combination of concentration gradients from dilution or uneven lubricant thickness across the surface.

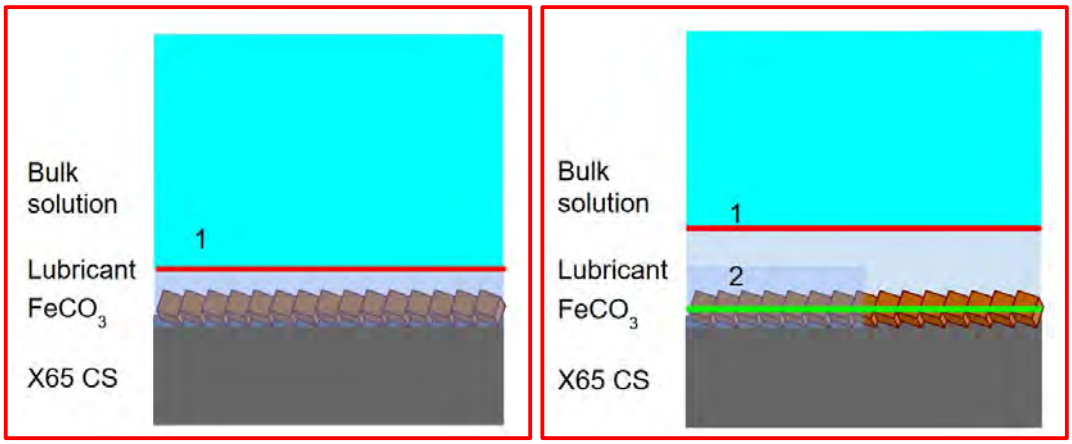

Figure 232 Physical interpretation of EIS Corrosion test results

In the more complex EIS system that develops in the scale test, the deposition of $CaCO_3$ deposits on the surface can be observed. Again this deposition can be seen across the interfaces. Figure 233-228 shows the physical interpretation of the SLIPS Kr and SLIPS BM samples. In the SLIPS Kr sample, EIS shows the primary buildup of scale to be occurring on the (1) interface (or first semi-circle), this is the outer SLIPS surface. SEM/EDX results reinforce this interpretation. As can be seen in the EDX map (Figure 233) lubricant traces (i.e. F) are evenly distributed across the surface, showing relatively uniform coverage. The Ca and Fe EDX maps show a clear delineation across the surface into two zones. On one side is an area high in Ca, this represents the (1) lubricant/brine interface. The other side shows an area with high levels of Fe representing the underlying (2) $FeCO_3$ /interface,

that has been protected from scale deposition. Whilst calcium is still present on the upper layer, when this layer separates the underlying surface is generally protected (and free from Ca). In the case of SLIPS BM, we see a different behaviour (Figure 234). Firstly, there is a lack of residual lubricant markers, but also the relatively even distribution of both Fe and Ca. This calcium is higher in concentration for $CaCO_3$ deposits in the upper half (represented by darker contrast areas on the SEM) but also indicated in general Ca levels in the bottom portion (with a stronger Fe signal) where it exists in the $FeCO_3$ matrix. This shows that the scaling phenomena is occurring at both interfaces, hence the poorer performance.

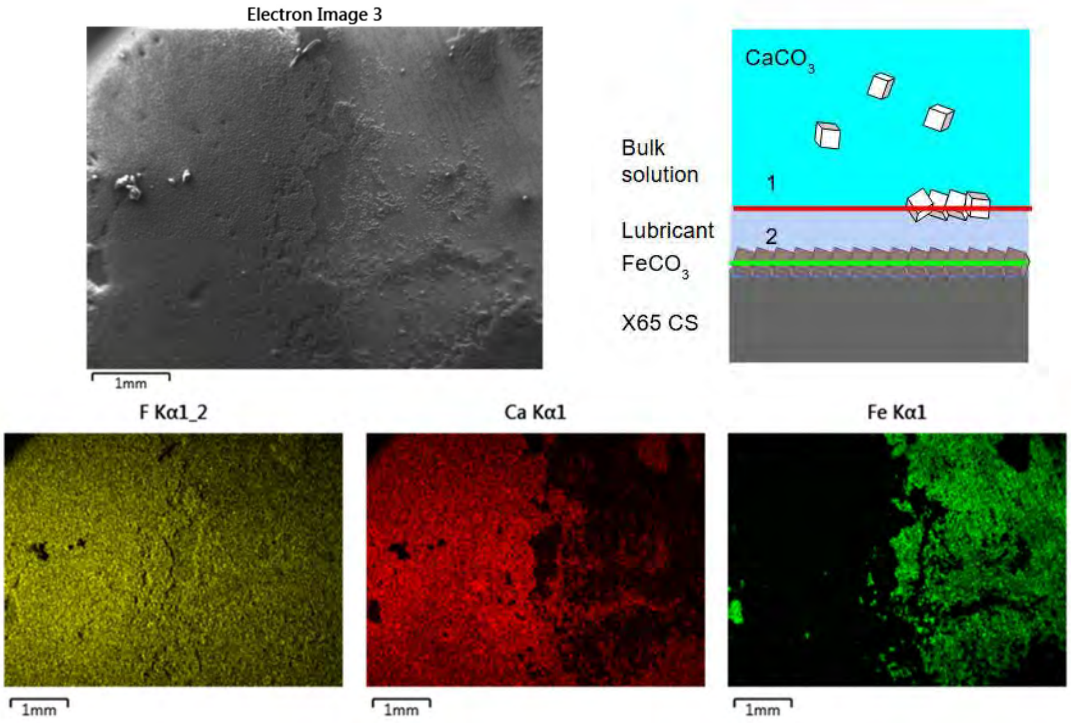

Figure 233 SEM, EDX and physical interpretation of scaling limited to one interface

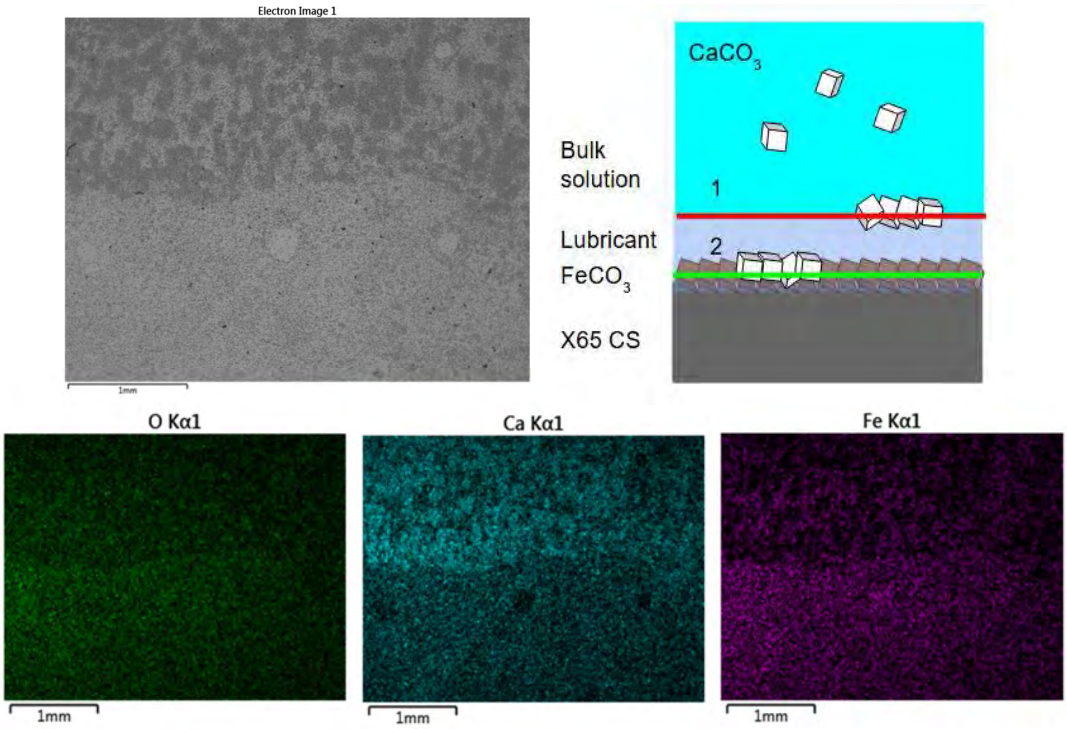

Figure 234 SEM, EDX and physical interpretation of scaling at both interfaces

Chapter 9
Discussion

9. Introduction

This thesis presents a novel and industrially relevant approach to the fabrication of SLIPS for mitigating inorganic mineral scale. The central contribution of this work is the successful demonstration of a proof-of-concept that leverages a typically detrimental process—aqueous CO_2 corrosion—as a beneficial, in-situ fabrication method for creating a functional anti-fouling surface. This strategy addresses a significant gap in the field of SLIPS technology, which has, despite its promise, been hindered by the challenge of developing durable and scalable porous substrates suitable for harsh industrial environments. By repurposing the naturally occurring corrosion by-product of X65 carbon steel, this research establishes a viable pathway toward a self-generating and potentially self-healing surface engineering solution.

The foundational work presented in Chapter 6 systematically established the optimal conditions for the formation of a stable and protective $FeCO_3$ layer. Through a series of controlled bubble cell experiments, it was determined that "Upper Boundary" (UB) conditions, characterized by a temperature of 80°C and a pH of 7.6, were conducive to the rapid formation of a dense, crystalline film. Electrochemical monitoring confirmed that under these conditions, the corrosion rate of the X65 substrate decreased rapidly to below 0.1 mmpy, a level indicative of protection associated with the formation of a highly protective barrier. Crucially, this process yielded a surface with a micro- and nano-scale topography ideal for lubricant retention. Surface characterization revealed an R_a of approximately 1.2–1.3 µm, a S_{dr} of 17–22%, and a negatively skewed profile, all of which are desirable properties for creating a robust lubricant reservoir.

Subsequent investigations detailed in Chapters 7 and 8 evaluated the performance of this novel $FeCO_3$ substrate when infused with four distinct lubricants: a perfluoropolyether (Krytox, SLIPS-Kr), an ionic liquid (BMIM, SLIPS-BM), a waxy crude oil (SLIPS-W), and a non-waxy crude oil (SLIPS-NW). The comprehensive evaluation against $CaCO_3$ scaling and electrochemical corrosion demonstrated that the SLIPS systems, particularly SLIPS-Kr and SLIPS-W, offered a substantial improvement in performance compared to both the uncoated X65 steel and the bare $FeCO_3$ substrates. As

detailed in Table 25 and Table 26, these systems exhibited significantly reduced scale deposition and lower corrosion rates, thereby validating the core hypothesis of the thesis. This initial synthesis of the principal findings confirms the success of the overarching concept and provides the necessary foundation for the detailed mechanistic analysis and critical evaluation that constitute the remainder of this discussion.

9.1 The Role of Lubricant Properties in Surface Interactions

The performance of the fabricated SLIPS is not a monolithic property but rather a complex and nuanced outcome dictated by the specific physicochemical properties of the infused lubricant. The data presented across Chapters 7 and 8 reveal a clear hierarchy of performance that can be directly attributed to the interplay between the lubricant's chemical composition, its physical properties such as viscosity and density, its stability within the scaling environment and texture surface. The discussion that follows deconstructs the performance of each SLIPS variant by linking these fundamental lubricant properties to the observed mechanisms of scale and corrosion inhibition. This approach moves beyond a simple ranking of effectiveness to a deeper understanding of why each system succeeds or fails, highlighting that the lubricant's role extends from being a simple physical barrier to being an active participant in interfacial chemistry.

The Inert Barrier: Krytox

The consistently superior performance of the SLIPS-Kr system across nearly all performance metrics can be ascribed to the unique combination of physical and chemical properties inherent to its perfluoropolyether composition. The primary mechanism of action for SLIPS-Kr is the creation of a robust, stable, and chemically inert barrier that is thermodynamically unfavorable for interaction with the aqueous brine. The non-polar, perfluorinated chemical structure of Krytox results in a very low SFE of approximately 15.3 mN/m. This low SFE creates a highly hydrophobic interface, as evidenced by the high WCA of approximately 105° observed in Chapter 7. According to classical wetting theory, this high contact angle signifies poor wettability of the surface by the aqueous brine, which in turn establishes a significant energetic barrier to the nucleation of $CaCO_3$ crystals at the interface. By minimizing the affinity between the scale-forming solution and the surface, the lubricant layer effectively suppresses the initial stages of heterogeneous nucleation.

Beyond this thermodynamic repellency, the physical properties of the Krytox lubricant contribute significantly to its stability and barrier function. As noted in

Table 5, Krytox VPF1525 possesses a high density (1900 kg/m^3) and a relatively high dynamic viscosity (496 mPa·s at room temperature). The high viscosity is particularly critical, as it enhances the lubricant's resistance to displacement by the impinging brine and, more importantly, would confer greater resistance to depletion under the shear stresses that are prevalent in dynamic flow environments. This physical robustness ensures the integrity of the lubricant layer, maintaining the physical separation between the corrosive, scaling brine and the underlying reactive $FeCO_3$ substrate. This combination of an inert chemical nature, which prevents detrimental interactions with brine constituents, and robust physical properties, which ensure layer stability, explains the top-tier performance of SLIPS-Kr. It exhibited low total scale deposition as measured by EDX, was the most effective at preventing ionic ingress as measured by XRD and demonstrated superior corrosion resistance in both corrosion-only and scaling environments via electrochemical tests.

The Unstable Interface BMIM

In stark contrast to the success of SLIPS-Kr, the consistently poor performance of the SLIPS-BM system serves as a compelling case study in lubricant failure. The mechanism behind this failure is not an indictment of the SLIPS concept or the $FeCO_3$ substrate, but rather a direct consequence of the inherent instability of the BMIM ionic liquid within the aqueous test environment. The chemical nature of BMIM is fundamentally different from that of Krytox. As an ionic liquid, it possesses significant polarity [433], which is reflected in its relatively high surface free energy of approximately 36.5 mN/m. This polarity leads to a strong chemical affinity for the highly polar water molecules in the brine, resulting in a hydrophilic surface with a low WCA of approximately 60°. This hydrophilic nature means there is no significant thermodynamic barrier to wetting by the aqueous solution, rendering the surface susceptible to interaction with scale-forming ions.

However, the primary failure mechanism appears to be more severe than simply poor repellency. The evidence strongly suggests a near-complete depletion of the lubricant layer during the 2-hour scaling tests. Post-test surface analysis presented in Chapter 7 revealed a stark absence of the lubricant's elemental markers (Fluorine and Sulfur) in EDX maps of the scaled surfaces. This was further corroborated by FTIR analysis, which showed a post-test spectrum almost identical to that of the uncoated, scaled $FeCO_3$ surface, with no discernible peaks corresponding to the BMIM lubricant. This lubricant loss is likely exacerbated by the low viscosity of BMIM (64 mPa·s), which would offer little resistance to displacement or dissolution into the

surrounding brine. Once the lubricant is depleted, the underlying $FeCO_3$ substrate is left directly exposed to the aggressive scaling and corrosive environment. Consequently, the SLIPS-BM system performed on par with, or in some cases worse than, the uncoated control surfaces, exhibiting high levels of scale deposition and poor corrosion resistance. This outcome underscores a critical design principle for SLIPS: the lubricant must not only be immiscible with the working fluid but also exhibit long-term stability and retention at the interface to maintain its function.

The Chemically Active Barrier: Crude Oils (Waxy and Non-Waxy)

The performance of the crude oil-infused SLIPS (SLIPS-W and SLIPS-NW) cannot be explained by a simple physical barrier model alone. Their complex and, at times, seemingly contradictory behavior points to a dual mechanism of action, whereby the crude oil functions as both a physical, hydrophobic barrier and a chemically active fluid. This chemical activity stems from the complex composition of crude oil, which, in addition to its bulk non-polar hydrocarbon content, contains a significant fraction of surface-active polar species, including asphaltenes, resins, and various naphthenic acids.

The physical barrier effect is derived from the bulk hydrocarbon nature of the oils, which, like Krytox, are immiscible with water and create a hydrophobic interface. This is reflected in their intermediate WCA values (around 90-95°) and SFE values (45-55 mN/m), which place them between the highly repellent SLIPS-Kr and the hydrophilic SLIPS-BM. This barrier alone provides a degree of scale and corrosion resistance.

However, the more significant contribution comes from the chemical activity of the polar components. A key piece of evidence for this is presented in the bulk characterization experiments in Chapter 7. These experiments indicated that certain compounds within the crude oils are acting as crystal growth modifiers (via morphology or size), directly interfering with the crystallization process. Furthermore, it is well-established in corrosion science that polar species in crude oil, particularly asphaltenes and long-chain carboxylic acids, can adsorb onto steel surfaces and act as effective natural corrosion inhibitors. This chemical inhibition mechanism likely explains the exceptionally low corrosion rate of 0.13 mmpy observed for SLIPS-W in the corrosion-only Tafel tests, a rate comparable to the best-performing SLIPS-Kr. This dual physical-chemical mechanism helps to rationalize the variable performance of the crude oil systems. For instance, the superior performance of SLIPS-W in resisting total calcium deposition (as measured by EDX) under high-scaling conditions may be attributed to its higher wax content, which could form a

more robust, semi-solid physical barrier at the test temperature, enhancing its anti-adhesion properties.

9.2 An Analysis of Scaling Using Multiple Methods

With regards to developing a framework for measuring scaling performance, the data presented in Chapter 7 reveals significant inconsistencies in the rankings of the SLIPS systems when evaluated by different analytical techniques. As summarized in Table 25, the "best" performing surface changes depending on whether the metric is total surface calcium (EDX), ionic incorporation into the substrate (XRD), or adhered crystalline mass (FTIR). These discrepancies are not indicative of methodological flaws but serve as diagnostic tools, allowing for the deconvolution of distinct and nuanced failure mechanisms for each SLIPS variant. By understanding what each technique uniquely measures, a more sophisticated picture of performance emerges. This moves beyond a simple pass/fail assessment based on theoretical considerations and allows an elucidation of how and why each surface succeeds or fails.

The apparent contradictions arise because each analytical method probes a different aspect of the complex scaling process:

- **EDX:** This technique provides an average elemental composition over a selected surface area. The reported Ca wt.% is therefore a measure of the *total calcium accumulation* on and within the near-surface region. It represents the sum of two distinct phenomena: (1) the mass of discrete $CaCO_3$ crystals that have nucleated and adhered to the lubricant surface, and (2) the quantity of calcium ions that have successfully permeated the lubricant barrier to become incorporated into the crystal lattice of the underlying $FeCO_3$ substrate. As such, EDX serves as a measure of the overall failure of the SLIPS to prevent any form of calcium ingress or deposition.
- **XRD:** The novel analytical approach of using the d-spacing shift of the $FeCO_3$ peak as a measure of lubricant protection is a highly specific and powerful probe. This method exclusively quantifies the formation of a mixed $Fe_xCa_yCO_3$ layers which occurs via 2 pathways. For this reaction to occur, calcium ions must diffuse through the lubricant layer to reach the reactive substrate and/or the lubricant layer has to be depleted or displaced. Therefore, the calculated mole fraction of incorporated calcium is a direct and quantitative measure of the lubricant's effectiveness. It provides no information about macroscopic

scale crystals adhered to the top surface but offers a unique window into the integrity and stability of the lubricant as an ionic barrier.

- **FTIR:** This technique is sensitive to the characteristic vibrational modes of the carbonate functional group within a crystalline lattice, specifically calcite in this case. The intensity of the characteristic calcite peaks (e.g., at 875cm^{-1} and 1400cm^{-1}) correlates with the mass of well-formed, adhered $CaCO_3$ crystals on the surface. FTIR is also a complementary technique to provide insight on lubricant retention specifically for the organic SLIPS (i.e C-H chains in crude oils) where conventional EDX markers are not readily available.

By integrating the results from these three distinct probes, a comprehensive mechanistic diagnosis can be constructed for each SLIPS system. This multi-modal analysis transforms the seemingly contradictory data into a coherent narrative of specific failure modes. For example, SLIPS-Kr demonstrates its superiority by performing well across all three metrics, indicating it is both a robust ionic barrier and an effective anti-adhesion surface. Conversely, the crude oil systems reveal more specialized behaviors: SLIPS-W is highly effective at preventing macroscopic adhesion (good EDX and FTIR) but is surprisingly permeable to ions (poor XRD), while SLIPS-NW shows the opposite trend.

9.3 The Lubricant as a barrier to ion transport

The XRD analysis presented in Chapter 7 provides a unique insight into the processes occurring at the buried solid-lubricant interface, revealing that the SLIPS system is not merely a passive coated surface but a dynamic system involving a reactive substrate. The key finding is the formation of a mixed $Fe_xCa_yCO_3$ layer, a phenomenon that serves as an indirect quantitative metric for the lubricant's protection. The data clearly demonstrates a consistent shift in the position of the $FeCO_3$ diffraction peak to lower 2θ angles after the samples were exposed to the $CaCO_3$ scaling brine. This observation can be understood within the framework of solid-state chemistry and the thermodynamics of crystal formation. Siderite and calcite are isostructural minerals, both belonging to the rhombohedral carbonate group, which allows for the substitution of cations within the crystal lattice. The central argument derived from this phenomenon is that for this reaction to occur, Ca^{2+} ions from the bulk solution must first traverse the lubricant layer to reach the reactive $FeCO_3$ substrate. The lubricant, therefore, acts as a transport medium, and the extent of the reaction—quantified by the calculated mole fraction of

incorporated calcium—becomes a direct and sensitive measure of the lubricant's failure to act as a perfect ionic barrier.

Re-interpreting the XRD results through this lens provides a deeper mechanistic understanding. The SLIPS-Kr system, which exhibited the smallest peak shift and the lowest calculated Ca mole fraction (y=0.092 in the SI=2.6 condition), is confirmed as the most effective ionic barrier among the tested systems. Its dense, non-polar structure effectively hinders the transport of charged ions. In stark contrast, the SLIPS-W and SLIPS-BM systems showed the largest peak shifts and highest Ca mole fractions (y=0.217 for both). This indicates that their respective lubricant layers are highly permeable to Ca^{2+} ions. For SLIPS-BM, this permeability is almost certainly a result of the complete loss of the lubricant layer, as previously discussed. For SLIPS-W, it suggests that while the waxy crude oil is effective at preventing the adhesion of macroscopic crystals, its molecular structure allows for the relatively easy diffusion of dissolved ions. It must be noted however that this has not been fully resolved as a function of lubricant layer thickness. That is, diffusion may be higher as a result of lower physical properties (correlated with diffusion i.e density) but also thinner layers that have been depleted or displaced.

9.4 Methodological Limitations and assumptions

While this thesis successfully demonstrates a novel proof-of-concept, its experimental design and theoretical frameworks contain certain limitations and omissions that warrant a transparent and thorough discussion. This section proactively addresses the key critiques identified during the examination process, providing justifications for the methodological decisions made within the scope of a foundational study, while simultaneously acknowledging their implications and outlining the unaddressed scientific questions that arise from them.

The most significant methodological limitation of this work is the reliance on static bulk jar tests for the evaluation of anti-scaling performance [434]. This approach, while common for initial materials screening [435], fails to replicate the dynamic hydrodynamic conditions of an operational oilfield pipeline, which are characterized by high fluid velocities and significant wall shear stresses. The use of static test conditions was a deliberate and necessary choice for this foundational, proof-of-concept investigation. The primary objective was to isolate and understand the fundamental surface chemistry and thermodynamic interactions governing scale formation on the novel SLIPS. Static tests allow for the deconvolution of complex phenomena by removing

the confounding variable of hydrodynamics, enabling a focused mechanistic study of heterogeneous nucleation, crystal adhesion, and ion transport through the lubricant layer, the very analyses that form the core of Chapter 7. This controlled environment was essential to establish a baseline understanding of how lubricant properties influence these fundamental interfacial processes.

However, this methodological choice omits the dominant physics that govern the durability and long-term performance of SLIPS in their intended application. The primary failure mechanism for SLIPS in real-world flow environments is the physical depletion of the lubricant layer due to the shear stress exerted by the flowing fluid. The gentle conditions of the jar test do not challenge the lubricant's retention within the porous $FeCO_3$ substrate apart from buoyancy, and therefore, the reported performance data provides no insight into the durability of these surfaces under operational conditions. It is highly probable that the performance rankings observed in these static tests would be altered under dynamic flow. Lubricant retention, governed largely by properties like viscosity and the capillary forces within the substrate, would become the dominant factor determining long-term efficacy. In this scenario, the higher viscosity of Krytox and the waxy crude oil might confer superior shear resistance and longevity, whereas the lower-viscosity BMIM and non-waxy crude oil could be depleted far more rapidly, leading to premature failure.

Simplification of Crude Oil Surface Free Energy

The application of the Preston predictive model to the crude oil SLIPS in Chapter 6 relied on using the SFE values of simple, non-polar hydrocarbons (paraffin, benzene) as proxies for the crude oils. This was acknowledged as a significant simplification, necessitated by the absence of established vOCG component data for such chemically complex fluids. The profound implication of this choice is that the theoretical stability predictions for SLIPS-W and SLIPS-NW are likely invalid. The Preston model's accuracy is entirely dependent on the input SFE component values, particularly the Lewis acid (γ^+) and Lewis base (γ^-) terms, which govern polar interactions. Crude oil is not a simple non-polar fluid; it is a colloidal dispersion containing highly surface-active polar species like asphaltenes and resins, which dominate its interfacial behavior. By using proxies with negligible acid-base components, the model completely fails to capture the critical polar interactions between the crude oil, the highly polar water droplet, and the moderately polar $FeCO_3$ substrate. Consequently, the claim of theoretical validation for these systems

cannot be robustly made, and their performance should be interpreted primarily through the lens of empirical data.

Omission of Equivalent Electrical Circuit (EEC) Modeling

The analysis of the EIS data in Chapter 8 was presented qualitatively, focusing on the interpretation of trends in impedance magnitude and the changing shapes of the Nyquist and Bode plots. This approach was sufficient for the primary thesis objective of a comparative proof-of-concept, as it allowed for a clear ranking of performance and the identification of distinct behavioral patterns (e.g., the emergence of one versus two-time constants, or the presence of inductive loops).

However, the omission of quantitative EEC modeling is a limitation of the analysis. EEC modeling involves fitting the experimental EIS data to a physical model composed of electrical elements (resistors, capacitors, constant phase elements) that represent the different electrochemical processes occurring at the interfaces. A full EEC analysis would have provided quantitative values for key physical parameters. For example, a common model for a coated system includes elements for the solution resistance (R_s), the coating capacitance (CPE_{coat}), and the charge-transfer resistance (R_{ct}) at the substrate-electrolyte interface. By tracking the evolution of these parameters over time, it would have been possible to better quantify the degradation of the SLIPS. An increase in CPE_{coat} could be used to model water uptake into the lubricant layer, while a decrease in R_{ct} would provide a direct quantitative measure of the acceleration of the corrosion reaction at the buried interface. While the qualitative analysis was sufficient for the comparative goals of this thesis, the application of EEC modeling represents a clear and valuable direction for future research to gain deeper quantitative insight into the degradation mechanisms of these complex surfaces.

9.5 Understanding the link between corrosion and mineral fouling

The electrochemical analysis presented in Chapter 8 revealed a significant and counter-intuitive finding: for three of the four SLIPS systems (SLIPS-BM, SLIPS-NW, and SLIPS-W), the corrosion rate was higher in the scaling environment than in the corrosion-only brine. This observation, detailed in Table 26, contradicts the expected behavior where the deposition of an insulating scale layer should reduce corrosion. It points towards a synergistic degradation mechanism, where the interplay between the lubricant and the scaling brine actively compromises the system's protective capabilities.

Several physicochemical mechanisms could account for this unexpected acceleration of corrosion.

- **Lubricant Destabilization by Calcium Ions:** The aqueous brine is rich in divalent cations, specifically Ca^{2+}. It is plausible that these ions interact directly with the lubricant at a molecular level, disrupting its structure and compromising its integrity from an electrochemical perspective. Drawing parallels from bio-tribology, calcium ions are known to destabilize the hydration layers of biological lubricants like hyaluronic acid, thereby reducing their effectiveness [436]. A similar mechanism could be at play here, where Ca^{2+} ions disrupt the lubricant's molecular arrangement, increasing its permeability to corrosive species like Cl^- ions present in the brine.
- **Formation of Localized Under-Deposit Corrosion Cells:** Once the lubricant layer is breached, even partially, by precipitating $CaCO_3$ crystals, these deposits can create occluded microenvironments at the substrate surface. This is a classic mechanism for localized corrosion, where the area under the deposit becomes chemically isolated from the bulk solution. The lubricant, now acting as a partial seal around the deposit, could exacerbate this effect by trapping corrosive species (e.g. H^+, Cl^-) at the interface, preventing their diffusion away and leading to aggressive localized attack on the underlying $FeCO_3$ and steel substrate. In this scenario, the lubricant is transformed from a protective barrier into a liability that promotes localized corrosion.
- **Disruption of Natural Inhibitors in Crude Oil:** For the crude oil SLIPS, a specific mechanism involving their natural inhibitive properties is likely. As discussed previously, polar compounds like asphaltenes and naphthenic acids in crude oil can absorb onto the steel surface and provide corrosion protection. It is conceivable that the abundant Ca^{2+} ions in the scaling brine compete with these polar organic molecules for adsorption sites on the substrate surface. This competitive adsorption could lead to the displacement of the natural inhibitors, leaving the surface more vulnerable to attack and explaining the marked increase in corrosion rate.

The fact that SLIPS-Kr, lubricated with a chemically inert PFPE, was the only system that did not show a dramatic increase in corrosion rate lends strong support to these chemically driven degradation hypotheses. Its lack of polar functional groups makes it less susceptible to interactions with Ca^{2+} ions or

displacement from the surface, allowing it to maintain its barrier function more effectively.

Chapter 10
Conclusion and Future Work

10.1 Conclusions

This chapter presents the major findings associated with the scientific work carried out in this thesis. The first section outlines the conclusions found from the 3 individual results chapters (Chapter 6,7,8). The overall focus of this research has been the creation and testing of a SLIPS system that includes an $FeCO_3$ layer on X65 Carbon Steel which is then infused with lubricants (Krytox, BMIM, Waxy crude oil and Non Waxy crude oil) as shown in Figure 235.The second part provides some future considerations and work that have been highlighted as a result of this research but also relevant practical implications for industry.

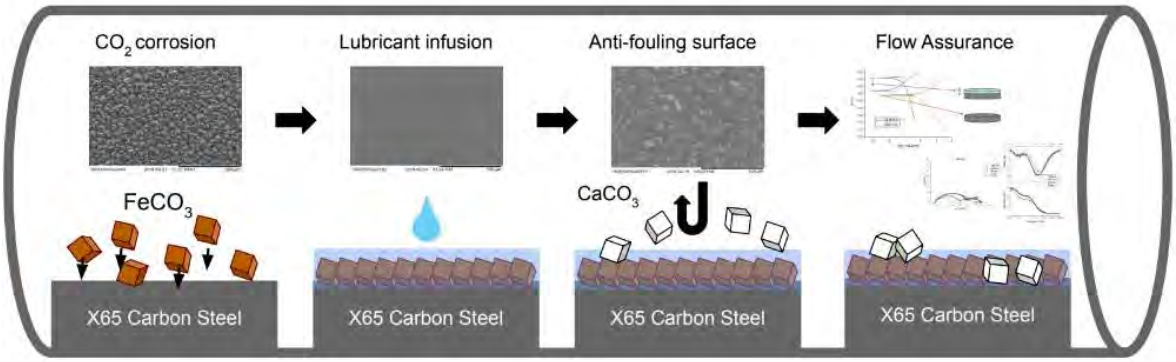

Figure 235 Thesis structure and primary research themes.

Chapter 6 focused on the fabrication of a new SLIPS system. This included a fundamental study aimed at understanding factors governing $FeCO_3$ formation on carbon steel, characterising this layer and validating combinations for use with the selected lubricant choices. The main findings are:

- The formation of $FeCO_3$ crystals and layers benefits from the synergistic effects of higher temperature and higher pH. In these conditions $FeCO_3$ layer provides a protective film that lowers

corrosion rates. This coincides with existing trends and behaviour seen in the literature review.

- A set of fabrication conditions to form a SLIPS base layer have been set with the following parameters: Temperature 80C, Duration 3 days, pH 7.6, Initial roughness 600P. Surface characterisation has been undertaken on this layer indicating a surface roughness (R_a) between 1.2-1.3 µm, 3D roughness or S_{dr} of 1.22 and thickness on average 7.2 µm ±4.2 across crystal peaks and valleys. vOCG SFE components of the hydrophilic $FeCO_3$ layer have been calculated as $\gamma T \approx 36.4$ mN/m, $\gamma LW \approx 31.0$ mN/m, $\gamma+ \approx 19.1$ mN/m and $\gamma- \approx 0.3$ mN/m.
- SLIPS design modelling has been used to predict combination suitability with the $FeCO_3$ layer and four lubricants. These lubricants are Krytox oil, ionic liquid BMIM and crude oil (divided into a waxy and non-waxy version). Common failure concerns that have been identified are droplet cloaking (Criterion 1) and lubricant displacement. (Criterion 4).

Chapter 7 involved the scale evaluation of created SLIPS samples in a $CaCO_3$ brine system. The initial parts of the chapter involved characterisation of the bulk brine system and surface energy assessment of the SLIPS system. Samples were then tested in a high and low saturation index of SI 2.6 and SI 1 respectively, before post-test analysis. The following conclusions are drawn:

- Bulk characterisation tests indicate that consumption of calcium (precipitation of $CaCO_3$) is largely unaffected by the presence of lubricant (at the concentration levels presented on the SLIPS). Scaling behaviour is dominated by the brine saturation index rather than influence of lubricant. Crude oil lubricants tend to produce larger crystals with the main $CaCO_3$ scale polymorph encountered being Calcite.
- Hydrophobicity and surface energy have been determined for the SLIPS samples, as an important parameter that can impact scaling

tendencies. Table 24 shows the ranking of samples based on increasing hydrophobicity (or WCA) and decreasing surface energy (vOCG) respectively.

Table 24 Hydrophobicity and Surface Energy ranking of tested samples

	Rank (Theoretical scaling performance improves left to right)
Hydrophobicity	SLIPS BM > $FeCO_3$ > X65 CS > SLIPS NW > SLIPS W > SLIPS KR
Surface Energy	SLIPS NW > SLIPS W > X65 CS > $FeCO_3$ > SLIPS BM > SLIPS KR

- Scaling performance for the different conditions and analytical methods are ranked in Table 25. EDX has been used to determine the presence of surface calcium wt.%, XRD shows integration of calcium within mixed carbonate layers and FTIR as a potential alternative evaluation method (for residual lubricant).

Table 25 Scaling performance of tested samples per analytical techniques and saturation index

	Scaling Performance (Decreasing calcium content)
EDX SI 1	SLIPS BM> SLIPS W > FeCO3 > X65 CS> SLIPS NW > SLIPS Kr
EDX SI 2.6	FeCO3 > SLIPS BM > X65 CS > SLIPS NW > SLIPS Kr > SLIPS W
XRD SI 1	FeCO3 > X65 CS > SLIPS W > SLIPS NW/ SLIPS KR > SLIPS BM
XRD SI 2.6	SLIPS BM/ SLIPS W > X65 CS > FeCO3 > SLIPS NW > SLIPS KR

FTIR 2.6	**SI**	SLIPS NW > X65 > FeCO3 > SLIPS BM > SLIPS W > SLIPS KR

- Scaling evaluation across analytical techniques is mixed, with differing saturation index in the brine conditions also impacting results. SI 1 conditions results tend to show smaller relative differences between samples and tighter ranges in values. Scaling performance shows samples that are better performers than others. In particular SLIPS KR followed by SLIPS W show greater potential than SLIPS BM and a non-lubricated $FeCO_3$ layer. When comparing calcium presence to parameters linked with scaling performance (such as hydrophobicity and surface energy). A stronger link is associated with the hydrophobicity (or WCA) of a surface and lower calcium presence compared to calculated surface energy.
- Key to the theoretical functionality of the SLIPS system is the presence of lubricant. Table 25 indicates whether the presence of residual lubricant was found on the surface post-test (green/positive and red/negative). In the case of scaling, lubricant choice is crucial. The mere presence of lubricant is not necessarily associated with improved scaling performance. The loss of functionality due to dilution/displacement of lubricant can be seen through residual trace elements on EDX or FTIR. Greater differences in pre/post-test lubricant markers/ residual elements are linked to poorer scaling performance.

Chapter 8 covered the performance of SLIPS from an electrochemical perspective. This involved the investigation of corrosion performance and the delineation of scaling and corrosion responses for the SLIPS system. This was conducted in a mild corrosion environment and a scaling environment. It also provided insight into the in-situ SLIPS behaviour during testing. The following findings were drawn from this chapter:

- The SLIPS system shows improved corrosion performance compared to a standard X65 CS sample across both conditions. However this

would not be considered fully protective (based on the CR achieved during the fabrication of the initial underlying $FeCO_3$ layer in Chapter 6. CR is also impacted by the presence of Ca, although the response is mixed. Generally the presence of $CaCO_3$, saw an increase in CR for SLIPS systems but a decrease for non-lubricated surfaces (Table 26).

Table 26 Corrosion rates obtained from Tafel experiments in Corrosion and Scale conditions

	X65 CS	FeCO3	SLIPS BM	SLIPS NW	SLIPS W	SLIPS KR
Corrosion CR (mmpy)	3.42	0.52	0.45	0.8	0.13	0.17
Scale CR (mmpy)	0.57	0.18	0.88	0.42	0.52	0.27

- The impact of the lubricant was also seen through the comparison of ΔE. ΔE represents the thickness of a diffusion layer based on potential differences between sweeps. With the greatest ΔE, SLIPS KR, linked with improved corrosion performance. Interestingly, CR in corrosion conditions better reflects scaling performance from Chapter 7 than CR in scale conditions. This indicates the difficulty in assessing a SLIPS system for combined flow assurance issues. Similarly in scaling performance, there is a clear better performer in corrosion resistance with SLIPS KR.
- EIS tests were conducted on all samples, with Nyquist and Bode plots constructed. All Nyquist plots showed increasing impedance over time (except one). It was also noted in all samples that the largest jump in impedance occurs between the first two scans. Nyquist curve behaviour is distinctly different in corrosion conditions compared to scale ones.

- In a corrosion setting, the better performing SLIPS (with regards to CR) tended to have a singular depressed semi-circle with only one primary time constant (i.e SLIPS KR/ Iron carbonate) that tended to stabilise after one scan. On the other hand, samples with higher corrosion rates had multiple time constants (usually 2) that were constantly changing as a function of time. These changes indicate different processes occurring on the surface, either corrosion related or lubricant diffusion/displacement. Higher impedance/modulus (|Z|) values were also associated with improved corrosion performance.
- Scale conditions showed differing behaviour to that seen in the corrosion environment. Samples tended to show two distinct time constants. One in the HF which has been interpreted as processes occurring on the top of the lubricant boundary (fluid/fluid interface) and one in the LF, processes occurring at the bottom (i.e fluid/solid interface). On average, impedance values were higher in corrosion conditions vs scale conditions and are also reflected in slightly lower relative CR obtained from the Tafel experiments. Physical interpretation of EIS results can also be directly observed from SEM/EDX analysis.
- Final impedance modulus (|z|) values show connection to EDX Ca wt.% results. With higher scale impedance values associated with lower Ca wt.%. This is the case with SLIPS Kr and SLIPS W and inversely for X65 CS and $FeCO_3$. However this is not the case for XRD mole fraction comparisons, which share no connection with increasing/decreasing impedance. Impedance values would imply an association with lubricant thickness, which is the case with increasing ΔE values (Tafel) directly linked to increased impedance (EIS) in the corrosion conditions.

10.2 Future Work

This thesis has shown the potential of a corrosion derived Slippery Liquid infused porous surface for mineral scaling mitigation. The research has

provided a framework for SLIPS assessment, and the concept has been validated. However, as with many research topics, there remains room for improvement and further academic considerations. This section covers a brief discussion on both practical considerations and future work associated with the three results chapters.

Chapter 6 covered the fabrication and characterisation of a $FeCO_3$ base layer for the SLIPS systems. This $FeCO_3$ base layer was constructed on a flat disc specimen, one consideration would be the adaptability of this SLIPS for other geometries. It is already known that dense, protective layers are formed on curved pipeline surfaces. However, these would still need to be characterised for surface properties (i.e to use SLIPS design modelling). Figure 236 shows SEM images of surface preparation for a standard disc and rotating cylinder electrode (RCE) sample in the laboratory. Clear differences can be seen in the abrasion pattern created during the initial polishing. Although the end result is still uniform coverage of $FeCO_3$ there are clear visual differences that would need to be accounted for in further studies.

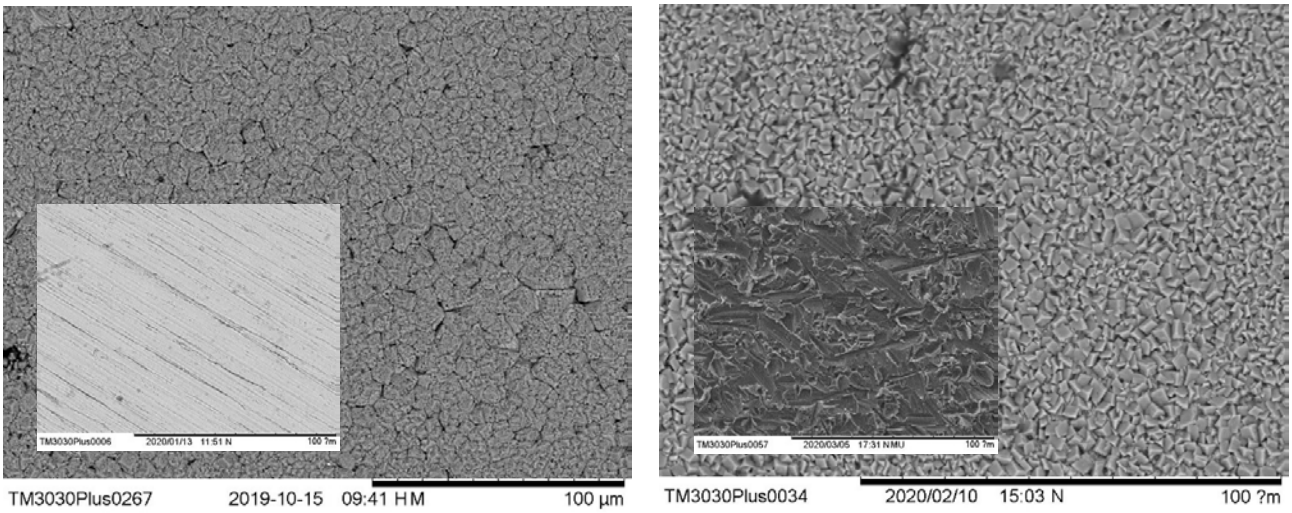

Figure 236 SEM images of surface preparation patterns and generated iron carbonate layer for X65 carbon steel samples with 600P grit

Another consideration is the level of surface characterisation for these $FeCO_3$ layers. Although electrochemistry and SEM have been used, there remain other analytical techniques that could provide further insight into this layer.

One important property that needs to be explored is porosity. Figure 237 shows images of the $FeCO_3$ layer formed in the same fabrication conditions via Micro Computed Tomography. (CT). Porosity is an important concept that has not been clearly defined in the literature and is linked with lubricant retention and overall functionality of SLIPS surfaces. Quantification of the porosity is likely connected to improvements in performance and/or durability in longer test durations, with Micro CT being a promising, non-destructive

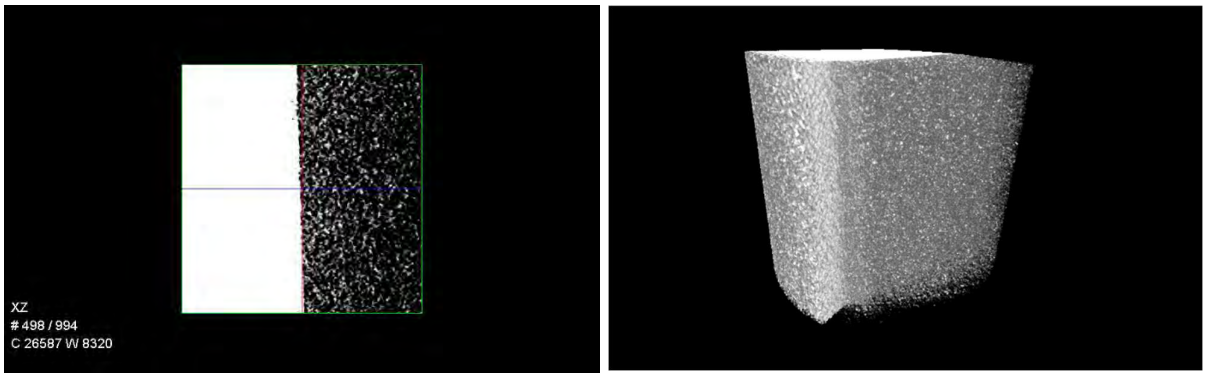

Figure 237 Micro CT image of Iron Carbonate sample formed from fabrication conditions in Chapter 6

technique to understand it [267]. Characterisation of the lubricant layer is also important with a number of analytical techniques available to measure the thickness/ loss of lubricant as a function of time or relative to other lubricants a useful path. It is expected that optical techniques (such as reflectometry/ ellipsometry) would be more beneficial over contact methods given the fluid nature of the lubricant.

The use of $FeCO_3$ as the base layer also presents a number of opportunities to modify or customize this layer for specific SLIPS purposes. Doping of the $FeCO_3$ through the addition of a range of additives can enhance the physical properties and corrosion resistance of these layers [437, 438]. Doping could also accelerate the development of these layers to make deployment in the field a more realistic solution. With respect to calcium ions, there is the potential for integration into the $FeCO_3$ network, which is known to have an impact on porosity (Figure 238). This increase in porosity would allow for improved lubricant reservoir capabilities, however the trade off in this case is potential diffusion paths and a loss of corrosion protection. In other SLIPS, the

use of silanisation on the textured surface is also used to improve adhesion and bonding between the surface and chosen lubricant.

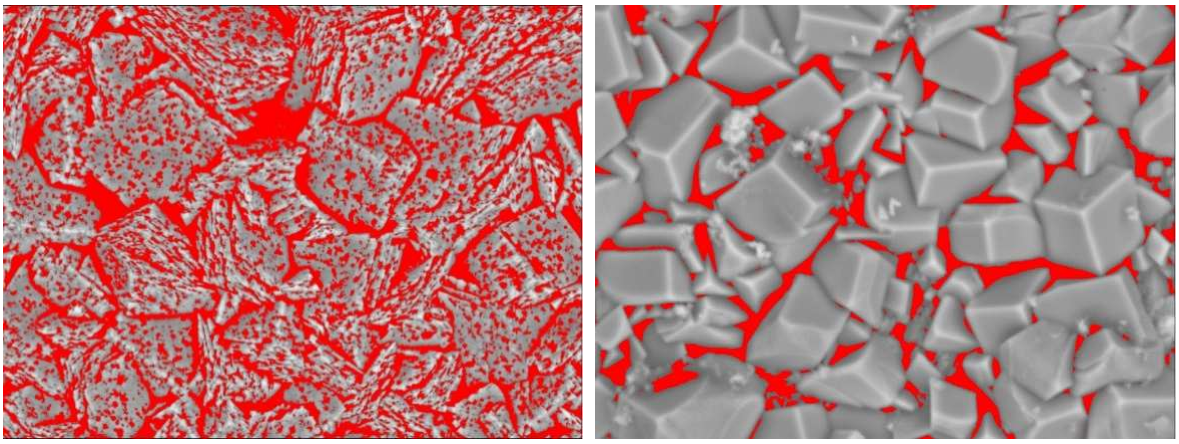

Figure 238 SEM image of iron carbonate crystals with a) addition of Calcium ions b) No calcium ions

The integration of AI/ML to research has seen massive growth in modern times, especially with regards to medicinal chemistry in drug discovery and recently corrosion inhibitors [439-441]. There remains the possibility of using these capacities within the field of SLIPS. In particular the capabilities of AI/ML could be used for designing via two methods. Firstly large datasets could be sorted/filtered for suitability between lubricant, solid textures and fluid environments either based on surface energy, chemistry or other metrics. Predicting combinations via these methods would expedite discoveries of new systems and substantially lower the number of experimental works needed. Secondly AI tools could be used to model different complex behaviours observed in SLIPS such as lubricant depletion and other surface interactions.

Chapter 7 deals with scaling evaluation of the SLIPS systems. In this work, post test analysis has focused on direct surface evaluation and electrochemistry. A number of other options exist that could prove complementary. Mass gain is an option, however given the presence of $FeCO_3$, gains/losses cannot be decoupled from each other. Dissolving scale deposits and analysis via ICP/AAS would provide Calcium concentrations of surface deposits. Providing in-situ analysis of the SLIPS system whilst

undergoing mineral scaling continues to represent an interesting topic. Options that should be considered for future work could include the use of Quartz Crystal Microbalance (QCM) using a custom-made $FeCO_3$ sensor for measurements. This method may also shed light on adsorption/infusion of the lubricant into the $FeCO_3$ layer. Another option for in-situ evaluation would be the use of visualization rigs for real-time surface image analysis (Figure 239) [442, 443]. This would provide quantitative information on surface coverage, induction times and nucleation/ crystallization behaviour.

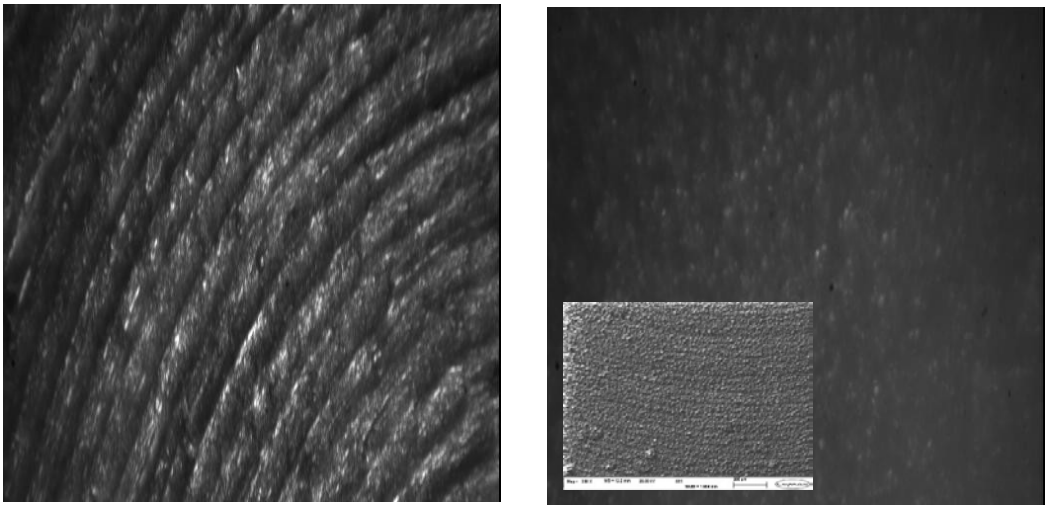

Figure 239 represents a X65 CS surface that has undergone $CaCO_3$ deposition in the same conditions (SI 2.6) used in this work

In Chapter 8, a series of EIS tests were undertaken to compare and understand the behaviour of SLIPS in both corrosion and scaling environments. As an in-situ, real-time monitoring technique the analysis was only qualitative based on the Nyquist and Bode curves constructed. Further quantitative information could be extracted by using Equivalent Electrical Circuit (EEC) models and curve fitting. However further study needs to be done on the best EEC model to use to ensure accurate results. At the moment there is no general consensus on the models to use, generally most use at least 2 elements (based on the Randles circuits). This two-element system is based on prevailing literature for conventional paint/coating systems. However EEC for SLIPS systems have also been represented as 2 elements

in series, 3 elements in parallel and sometimes with the inclusion of Warburg elements [444-446]. Hence the potential for further discoveries in the electrochemical behaviour of SLIPS.

One last consideration is based on the corrosion resistance of the fabricated layer. Originally, the SLIPS system assumed a protectiveness based on the $FeCO_3$ film via LPR and calculated CR predicted in the first results chapter. Here the CR rates show a rate lower than 0.1 MMPY for the conditions studied. However Tafel plot results show higher calculated CR, which is expected given the different conditions. However this raises the interesting point of how protective these layers are when re-used (assuming no dissolution from external sources, such as the lubricant) [447]? If a protective film is formed, then removed from a solution and dried does it retain its protectiveness and if not, by what mechanism does it lose this functionality?

References

1. IEA (2024), O., IEA, Paris https://www.iea.org/reports/oil-2024, Licence: CC BY 4.0.
2. Kleinberg, R.L., *6 - Oil and natural gas, present, and in the future*, in *Energy and Climate Change*, T.M. Letcher and V.M. Fthenakis, Editors. 2025, Academic Press. p. 123-151.
3. Mason, C.F., L.A. Muehlenbachs, and S.M.J.A.R.R.E. Olmstead, *The economics of shale gas development.* 2015. **7**(1): p. 269-289.
4. Ekrem, A., A. Yaser, and E. Muhammed Said, *Innovation in Exploration and Production: How Technology Is Changing the Oil and Gas Landscape.* Journal of Energy and Natural Resources, 2023. **12**(3): p. 25-29.
5. Guo, X., et al., *Theoretical Progress and Key Technologies of Onshore Ultra-Deep Oil/Gas Exploration.* Engineering, 2019. **5**(3): p. 458-470.
6. Caineng, Z., et al., *Theory and Technology of Unconventional Oil and Gas Exploration and Development Helps China Increase Oil and Gas Reserves and Production.* 2021. **40**(3): p. 72-79.
7. Eshiet, K.I.-I.I., *Production from Unconventional Petroleum Reservoirs: Précis of Stimulation Techniques and Fluid Systems*, in *Emerging Technologies in Hydraulic Fracturing and Gas Flow Modelling*, K.I.-I.I. Eshiet and R. G.Moghanloo, Editors. 2022, IntechOpen: Rijeka.
8. Adenuga, O.D., et al., *Maintenance in marginal oilfield production facilities: a review.* 2022. **10**(4): p. 691-713.
9. Crabtree, M., et al., *Fighting scale—removal and prevention.* Oilfield review, 1999. **11**(3): p. 30-45.
10. Kumar, A., *Perspectives of Flow Assurance Problems in Oil and Gas Production: A Mini-review.* Energy & Fuels, 2023. **37**(12): p. 8142-8159.
11. Heffron, R.J., S.F. Ashley, and W.J. Nuttall, *The global nuclear liability regime post Fukushima Daiichi.* Progress in Nuclear Energy, 2016. **90**: p. 1-10.
12. Barthwal, S., S. Uniyal, and S. Barthwal, *Nature-Inspired Superhydrophobic Coating Materials: Drawing Inspiration from Nature for Enhanced Functionality.* 2024. **15**(3): p. 391.
13. v. Baeckmann, W., *1 - The History of Corrosion Protection*, in *Handbook of Cathodic Corrosion Protection (Third Edition)*, W. von Baeckmann, et al., Editors. 1997, Gulf Professional Publishing: Burlington. p. 1-26.
14. Revie, R.W., *Corrosion and Corrosion Control: An Introduction to Corrosion Science and Engineering*. 2008: Wiley.
15. Kermani, M.B. and D. Harrop, *The Impact of Corrosion on Oil and Gas Industry.* SPE Production & Facilities, 1996. **11**(03): p. 186-190.
16. Stansbury, E.E. and R.A. Buchanan, *Fundamentals of electrochemical corrosion*. 2000: ASM international.
17. Goss, D.J. and R.H. Petrucci, *General Chemistry Principles & Modern Applications, Petrucci, Harwood, Herring, Madura: Study Guide*. 2007: Pearson/Prentice Hall.
18. Brondel, D., et al., *Corrosion in the Oil Industry.* Journal of Petroleum Technology, 1987. **39**: p. 756-762.

19. Fontana, M.G., *Corrosion engineering*. 2005: Tata McGraw-Hill Education.
20. Pourbaix, M.J.C.S., *Thermodynamics and corrosion.* 1990. **30**(10): p. 963-988.
21. McCafferty, E., *Thermodynamics of corrosion: Pourbaix diagrams*, in *Introduction to corrosion science*. 2010, Springer. p. 95-117.
22. Perry, S., et al., *Pourbaix Diagrams as a Simple Route to First Principles Corrosion Simulation.* Journal of The Electrochemical Society, 2019. **166**: p. C3186-C3192.
23. McCafferty, E., *Introduction to corrosion science*. 2010: Springer Science & Business Media.
24. Stansbury, E.E. and R.A. Buchanan, *Electrochemical Thermodynamics: The Gibbs Function, Electrochemical Reactions, and Equilibrium Potentials*, in *Fundamentals of Electrochemical Corrosion*. 2000, ASM International. p. 0.
25. Revie, R. and H.H. Uhlig, *Thermodynamics: corrosion tendancy and electrode potentials.* Corrosion and corrosion control, 2000. **1**: p. 22-66.
26. Feiner, A.-S. and A.J.J.o.c.e. McEvoy, *The nernst equation.* 1994. **71**(6): p. 493.
27. Archer, M.D., *Genesis of the Nernst equation*. 1989, ACS Publications.
28. Frankel, G.S., *Fundamentals of Corrosion Kinetics*, in *Active Protective Coatings: New-Generation Coatings for Metals*, A.E. Hughes, et al., Editors. 2016, Springer Netherlands: Dordrecht. p. 17-32.
29. Schmickler, W., *Electrochemical Theory: Double Layer*, in *Reference Module in Chemistry, Molecular Sciences and Chemical Engineering*. 2014, Elsevier.
30. Jr., F.H.S. and J.G. Kirkwood, *Theory of the Diffuse Double Layer.* 1960. **33**(5): p. 1282-1290.
31. Lillard, R.S. and B.A. Pint, *4.01 - Principles of Corrosion in Nuclear Systems: Theory and Analytical Methods ☆*, in *Comprehensive Nuclear Materials (Second Edition)*, R.J.M. Konings and R.E. Stoller, Editors. 2020, Elsevier: Oxford. p. 1-32.
32. Bindra, P. and J. Roldan, *Mechanisms of electroless metal plating. III. Mixed potential theory and the interdependence of partial reactions.* Journal of Applied Electrochemistry, 1987. **17**(6): p. 1254-1266.
33. Power, G. and I.J.E.A. Ritchie, *Mixed potential measurements in the elucidation of corrosion mechanisms—1. Introductory theory.* 1981. **26**(8): p. 1073-1078.
34. Popov, B.N. and S.P. Kumaraguru, *25 - Cathodic Protection of Pipelines*, in *Handbook of Environmental Degradation of Materials (Second Edition)*, M. Kutz, Editor. 2012, William Andrew Publishing: Oxford. p. 771-798.
35. Bohari, N.A., et al., *Optimization and Analytical Behavior of Electrochemical Sensors Based on the Modification of Indium Tin Oxide (ITO) Using PANI/MWCNTs/AuNPs for Mercury Detection.* 2020. **20**(22): p. 6502.
36. Hiromoto, S., *4 - Corrosion of metallic biomaterials*, in *Metals for Biomedical Devices*, M. Niinomi, Editor. 2010, Woodhead Publishing. p. 99-121.

37. Mohammed, A. and T. Salman, *Amino Acids as Corrosion Inhibitors for Carbon Steel in Saline Solution*. 2017.
38. Choi, W., et al., *Modeling and Applications of Electrochemical Impedance Spectroscopy (EIS) for Lithium-ion Batteries.* J. Electrochem. Sci. Technol, 2020. **11**(1): p. 1-13.
39. Harris, A.R., et al., *Correlation of the impedance and effective electrode area of doped PEDOT modified electrodes for brain–machine interfaces.* Analyst, 2015. **140**(9): p. 3164-3174.
40. Kermani, B., *Materials Optimization for Oil and Gas Sour Production*, in *CORROSION 2000*. 2000, NACE International: Orlando, Florida. p. 14.
41. Dugstad, A. *Fundamental aspects of CO2 metal loss corrosion-part 1: mechanism*. in *CORROSION 2006*. 2006. NACE International.
42. Nešić, S., et al., *An open source mechanistic model for CO2/H2S corrosion of carbon steel.* CORROSION 2009, 2009.
43. Nesic, S. *A Critical Review of CO2 Corrosion Modelling in the Oil and GAS Industry*. in *10th Middle East Corrosion Conference*. 2004.
44. Nesic, S., J. Postlethwaite, and S. Olsen, *An electrochemical model for prediction of corrosion of mild steel in aqueous carbon dioxide solutions.* Corrosion, 1996. **52**(4): p. 280-294.
45. Garsany, Y., D. Pletcher, and W. Hedges, *The Role of Acetate in CO2 Corrosion of Carbon Steel: Studies Related to Oilfield Conditions.* 2003.
46. WAARD, C.D. and D.E. MILLIAMS, *Carbonic Acid Corrosion of Steel.* CORROSION, 1975. **31**(5): p. 177-181.
47. Kermani, B. and L.M. Smith, *A Working Party Report on CO2 Corrosion Control in Oil and Gas Production: Design Considerations*. Vol. 688. 1997: Maney Pub.
48. Linter, B. and G. Burstein, *Reactions of pipeline steels in carbon dioxide solutions.* Corrosion science, 1999. **41**(1): p. 117-139.
49. Kermani, M. and A. Morshed, *Carbon dioxide corrosion in oil and gas production—a compendium.* Corrosion, 2003. **59**(8): p. 659-683.
50. Nordsveen, M., et al., *A mechanistic model for carbon dioxide corrosion of mild steel in the presence of protective iron carbonate films—part 1: theory and verification.* Corrosion, 2003. **59**(5): p. 443-456.
51. Yaro, A.S., K.R. Abdul-Khalik, and A.A. Khadom, *Effect of CO2 corrosion behavior of mild steel in oilfield produced water.* Journal of Loss Prevention in the Process Industries, 2015. **38**: p. 24-38.
52. Sun, W. and S. Nešic, *Kinetics of corrosion layer formation: part 1—iron carbonate layers in carbon dioxide corrosion.* Corrosion, 2008. **64**(4): p. 334-346.
53. Ogundele, G. and W. White, *Observations on the influences of dissolved hydrocarbon gases and variable water chemistries on corrosion of an API-L80 steel.* Corrosion, 1987. **43**(11): p. 665-673.
54. Wang, S., *Effect of oxygen on CO2 corrosion of mild steel*. 2009, Ohio University.
55. JO'M, B., D. Drazic, and A. Despic, *The electrode kinetics of the deposition and dissolution of iron.* Electrochimica Acta, 1961. **4**(2-4): p. 325-361.

56. Nešić, S., *Key issues related to modelling of internal corrosion of oil and gas pipelines–A review.* Corrosion science, 2007. **49**(12): p. 4308-4338.
57. Nesic, S., et al., *Electrochemical properties of iron dissolution in the presence of CO {sub 2}--Basics revisited*. 1996, NACE International, Houston, TX (United States).
58. Tanupabrungsun, T., et al. *Construction and verification of pourbaix diagrams for CO2 corrosion of mild steel valid up to 250 C*. in *CORROSION 2012*. 2012. NACE International.
59. Barker, R., et al., *A review of iron carbonate (FeCO3) formation in the oil and gas industry.* Corrosion Science, 2018. **142**: p. 312-341.
60. Schmitt, G. and M. Horstemeier. *Fundamental aspects of CO2 metal loss corrosion-Part II: Influence of different parameters on CO2 corrosion mechanisms*. in *CORROSION 2006*. 2006. NACE International.
61. Alsaiari, H.A., et al. *Iron Calcium Carbonate: Precipitation Interaction*. in *SPE International Oilfield Scale Conference*. 2008. Society of Petroleum Engineers.
62. Pessu, F., R. Barker, and A. Neville, *The influence of pH on localized corrosion behavior of X65 carbon steel in CO2-saturated brines.* Corrosion, 2015. **71**(12): p. 1452-1466.
63. Nešic, S. and K.-L. Lee, *A mechanistic model for carbon dioxide corrosion of mild steel in the presence of protective iron carbonate films—part 3: film growth model.* Corrosion, 2003. **59**(7): p. 616-628.
64. Ikeda, A., M. Ueda, and S. Muka, *CO2 behaviour of carbon and Cr steels in Hausler RH Giddard HP.* Corrosion, 1983. **39**: p. 131-137.
65. Tomson, M. and M. Johnson. *How ferrous carbonate kinetics impacts oilfield corrosion*. in *SPE International Symposium on Oilfield Chemistry*. 1991. Society of Petroleum Engineers.
66. Berntsen, T., M. Seiersten, and T. Hemmingsen, *Effect of FeCO3 supersaturation and carbide exposure on the CO2 corrosion rate of carbon steel.* Corrosion, 2013. **69**(6): p. 601-613.
67. Obanijesu, E., *Modeling the H2S Contribution to Internal Corrosion Rate of Natural Gas Pipeline.* Energy Sources, 2009. **Part A**: p. 348-363.
68. Dugstad, A., L. Lunde, and K. Videm, *Parametric study of CO {sub 2} corrosion of carbon steel*. 1994, NACE International, Houston, TX (United States).
69. Han, J., et al., *Roles of passivation and galvanic effects in localized CO2 corrosion of mild steel.* CORROSION/2008, paper, 2008. **8332**.
70. Gao, K., et al., *Mechanical properties of CO2 corrosion product scales and their relationship to corrosion rates.* Corrosion Science, 2008. **50**(10): p. 2796-2803.
71. Song, F.M., *A comprehensive model for predicting CO2 corrosion rate in oil and gas production and transportation systems.* Electrochimica Acta, 2010. **55**(3): p. 689-700.
72. Nesic, S., J. Lee, and V. Ruzic, *A Mechanistic Model of Iron Carbonate Film Growth and the Effect on CO2 Corrosion of Mild Steel*, in *CORROSION 2002*. 2002, NACE International: Denver, Colorado.
73. Tanupabrungsun, T., *Thermodynamics and kinetics of carbon dioxide corrosion of mild steel at elevated temperatures*. 2012, Ohio University.

74. Ning, J., B. Brown, and S. Nesic. *Verification of Pourbaix Diagrams for the H2S-H2O-Fe System at 25 oC*. in *ICMT Ohio University Advisory Board Meeting,(March, 2012)*. 2012.
75. Xu, Y., et al., *Flow accelerated corrosion and erosion−corrosion behavior of marine carbon steel in natural seawater.* npj Materials Degradation, 2021. **5**(1): p. 56.
76. Davis, J.R., *Corrosion: Understanding the basics*. 2000: ASM International.
77. Dugstad, A., H. Hemmer, and M. Seiersten, *Effect of steel microstructure on corrosion rate and protective iron carbonate film formation.* Corrosion, 2001. **57**(4): p. 369-378.
78. Ueda, M. and H. Takabe. *Effect of environmental factor and microstructure on morphology of corrosion products in CO2 environments*. in *CORROSION 99*. 1999. NACE International.
79. De Waard, C., U. Lotz, and D. Milliams, *Predictive model for CO2 corrosion engineering in wet natural gas pipelines.* Corrosion, 1991. **47**(12): p. 976-985.
80. Nesic, S., M. Nordsveen, and A. Stangel, *A Mechanistic Model for C02 Corrosion with Protective Iron Carbonate Films.* 2001.
81. Crolet, J., N. Thevenot, and S. Nesic, *Role of conductive corrosion products in the protectiveness of corrosion layers.* Corrosion, 1998. **54**(3): p. 194-203.
82. Palacios, C. and J. Shadley, *Characteristics of corrosion scales on steels in a CO2-saturated NaCl brine.* Corrosion, 1991. **47**(2): p. 122-127.
83. Asma, B., Y. Asmara, and C. Mokhtar, *Study on the Effect of Surface Finish on Corrosion of Carbon Steel in CO2 Environment.* Journal of Applied Sciences, 2011. **11**.
84. Roberge, P.R., *Corrosion engineering: principles and practice*. Vol. 2. 2008: McGraw-Hill New York.
85. Fang, H., B. Brown, and S. Nešić, *Sodium chloride concentration effects on general CO2 corrosion mechanisms.* Corrosion, 2013. **69**(3): p. 297-302.
86. Liu, Q., L. Mao, and S. Zhou, *Effects of chloride content on CO2 corrosion of carbon steel in simulated oil and gas well environments.* Corrosion Science, 2014. **84**: p. 165-171.
87. das Chagas Almeida, T., et al., *New insights on the role of CO2 in the mechanism of carbon steel corrosion.* Corrosion Science, 2017. **120**: p. 239-250.
88. Shannon, D., *Role of chemical components in geothermal brine on corrosion.* CORROSION/78, paper, 1978(57).
89. Ingham, B., et al., *In situ synchrotron X-ray diffraction study of scale formation during CO2 corrosion of carbon steel in sodium and magnesium chloride solutions.* Corrosion Science, 2012. **56**: p. 96-104.
90. Alsaiari, H.A., A. Kan, and M. Tomson, *Effect of Calcium and Iron (II) Ions on the Precipitation of Calcium Carbonate and Ferrous Carbonate.* SPE Journal, 2010. **15**(02): p. 294-300.
91. Alsaiari, H.A., M.B. Tomson, and A. Kan. *Constant Composition Study of Crystal Growth of Mixed Calcium-Ferrous Carbonate salt*. in *CORROSION 2010*. 2010. NACE International.

92. Navabzadeh Esmaeely, S., et al., *Effect of calcium on the formation and protectiveness of iron carbonate layer in CO2 corrosion.* Corrosion, 2013. **69**(9): p. 912-920.
93. Farelas, F., et al., *Evolution of dissolution processes at the interface of carbon steel corroding in a CO2 environment studied by EIS.* Corrosion Science, 2010. **52**(2): p. 509-517.
94. Farelas, F., B. Brown, and S. Nesic, *Iron carbide and its influence on the formation of protective iron carbonate in CO2 corrosion of mild steel.* CORROSION/2013, paper, 2013. **2291**.
95. Al-Hassan, S., et al., *Effect of microstructure on corrosion of steels in aqueous solutions containing carbon dioxide.* Corrosion, 1998. **54**(6): p. 480-491.
96. Zhang, C., et al., *Corrosion-resistant carbide-reinforced martensitic steel by Cu modification.* npj Materials Degradation, 2019. **3**(1): p. 30.
97. Blesa, M.A., et al., *Mechanism of dissolution of magnetite by oxalic acid-ferrous ion solutions.* Inorganic Chemistry, 1987. **26**(22): p. 3713-3717.
98. Chan, E.W.L., *Magnetite and its galvanic effect on the corrosion of carbon steel under carbon dioxide environments*. 2011, Curtin University.
99. Refait, P., et al., *Electrochemical formation of carbonated corrosion products on carbon steel in deaerated solutions.* Electrochimica Acta, 2012. **79**: p. 210-217.
100. Saheb, M., et al., *Multisecular corrosion behaviour of low carbon steel in anoxic soils: characterisation of corrosion system on archaeological artefacts.* Materials and corrosion, 2009. **60**(2): p. 99-105.
101. Han, J., et al., *Chemistry and structure of the passive film on mild steel in CO2 corrosion environments.* Industrial & Engineering Chemistry Research, 2009. **48**(13): p. 6296-6302.
102. Daneshvar-Fatah, F., et al., *Caustic corrosion in a boiler waterside tube: Root cause and mechanism.* Engineering Failure Analysis, 2013. **28**: p. 69-77.
103. Pandarinathan, V., K. Lepková, and W. van Bronswijk, *Chukanovite (Fe2(OH)2CO3) identified as a corrosion product at sand-deposited carbon steel in CO2-saturated brine.* Corrosion Science, 2014. **85**: p. 26-32.
104. Azoulay, I., C. Rémazeilles, and P. Refait, *Corrosion of steel in carbonated media: The oxidation processes of chukanovite (Fe2(OH)2CO3).* Corrosion Science, 2014. **85**: p. 101-108.
105. Matamoros-Veloza, A., et al., *Iron Calcium Carbonate Instability: Structural Modification of Siderite Corrosion Films.* ACS Applied Materials & Interfaces, 2020. **12**(43): p. 49237-49244.
106. Esmaeely, S.N., et al., *Effect of Calcium on the Formation and Protectiveness of Iron Carbonate Layer in CO2 Corrosion.* CORROSION, 2013. **69**(9): p. 912-920.
107. Tavares, L.M., et al., *Effect of calcium carbonate on low carbon steel corrosion behavior in saline CO2 high pressure environments.* Applied Surface Science, 2015. **359**: p. 143-152.
108. Esmaeely, S.N., et al., *Effect of Incorporation of Calcium into Iron Carbonate Protective Layers in CO2 Corrosion of Mild Steel.* Corrosion, 2016. **73**(3): p. 238-246.

109. Shamsa, A., et al., *The role of Ca2+ ions on Ca/Fe carbonate products on X65 carbon steel in CO2 corrosion environments at 80 and 150°C.* Corrosion Science, 2019.
110. Ramachandran, S., V. Jovancicevic, and M.B. Ward. *Understanding interactions between corrosion inhibitors and iron carbonate films using molecular modeling*. in *CORROSION 99*. 1999. NACE International.
111. Joshi, G.R., *Elucidating Sweet Corrosion Scales.* 2015.
112. Arumugam, S., N. Tajallipour, and P.J. Teevens. *Modeling the Influence of Iron Carbonate Scale Morphology in Sweet Corrosion Prediction*. in *CORROSION 2014*. 2014. NACE International.
113. Davey, R. and J. Garside, *From molecules to crystallizers*. 2000: Oxford University Press.
114. Sun, W., S. Nešić, and R.C. Woollam, *The effect of temperature and ionic strength on iron carbonate (FeCO3) solubility limit.* Corrosion Science, 2009. **51**(6): p. 1273-1276.
115. Marion, G.M., D.C. Catling, and J.S. Kargel, *Modeling aqueous ferrous iron chemistry at low temperatures with application to Mars.* Geochimica et cosmochimica Acta, 2003. **67**(22): p. 4251-4266.
116. !!! INVALID CITATION !!! {}.
117. Dugstad, A., *Mechanism of protective film formation during CO {sub 2} corrosion of carbon steel*. 1998, NACE International, Houston, TX (United States).
118. Kahyarian, A., M. Achour, and S. Nesic, *7 - CO2 corrosion of mild steel*, in *Trends in Oil and Gas Corrosion Research and Technologies*, A.M. El-Sherik, Editor. 2017, Woodhead Publishing: Boston. p. 149-190.
119. Kakooei, S., et al., *Formation of Nano-Scale FeCO3 Protective Corrosion Product in Carbon Dioxide-Saturated 3% Sodium Chloride Solution.* Key Engineering Materials, 2017. **740**: p. 3-8.
120. Ahmad, E.A., et al., *Corrosion Protection through Naturally Occurring Films: New Insights from Iron Carbonate.* ACS Applied Materials & Interfaces, 2019. **11**(36): p. 33435-33441.
121. Barker, R., Y. Hua, and A. Neville, *Internal corrosion of carbon steel pipelines for dense-phase CO2 transport in carbon capture and storage (CCS) – a review.* International Materials Reviews, 2017. **62**(1): p. 1-31.
122. Ruzic, V., M. Veidt, and S. Nešić, *Protective Iron Carbonate Films—Part 1: Mechanical Removal in Single-Phase Aqueous Flow.* Corrosion, 2006. **62**(5): p. 419-432.
123. Ruzic, V., M. Veidt, and S. Nešsić, *Protective Iron Carbonate Films—Part 2: Chemical Removal by Dissolution in Single-Phase Aqueous Flow.* Corrosion, 2006. **62**(7): p. 598-611.
124. Ruzic, V., M. Veidt, and S. Nešić, *Protective Iron Carbonate Films—Part 3: Simultaneous Chemo-Mechanical Removal in Single-Phase Aqueous Flow.* Corrosion, 2007. **63**(8): p. 758-769.
125. Zhang, P., A.T. Kan, and M.B. Tomson, *Chapter 24 - Oil Field Mineral Scale Control*, in *Mineral Scales and Deposits*, Z. Amjad and K.D. Demadis, Editors. 2015, Elsevier: Amsterdam. p. 603-617.
126. Hedgpeth, J.W., *Marine Fouling and Its Prevention. Prepared for the Bureau of Ships, Navy Department, by the Woods Hole Oceanographic Institution. Annapolis, Md: U. S. Naval Institute, 1952. 388 pp. Illus. $10.00.* 1953. **118**(3061): p. 257-257.

127. Fane, A.G., C.Y. Tang, and R. Wang, *4.11 - Membrane Technology for Water: Microfiltration, Ultrafiltration, Nanofiltration, and Reverse Osmosis*, in *Treatise on Water Science*, P. Wilderer, Editor. 2011, Elsevier: Oxford. p. 301-335.
128. Time, R. *Flow Assurance and Multiphase Flow (Part II). The university of Stavanger, Department of Petroleum Engineering*. in *Seminar Presented at Aker Solutions, Stavanger*. 2011.
129. Somerscales, E.F.C., *Fouling of Heat Transfer Surfaces: An Historical Review.* Heat Transfer Engineering, 1990. **11**(1): p. 19-36.
130. Dickinson, W., L. Sanders, and C. Lowen. *Development and performance of biodegradable antiscalants for oilfield applications*. in *Offshore Technology Conference*. 2011. Offshore Technology Conference.
131. Mackay, E.J. *Scale Inhibitor Application in Injection Wells to Protect Against Damage to Production Wells: When does it Work?* in *SPE European formation damage conference*. 2005. Society of Petroleum Engineers.
132. Jordan, M.M. and E.J. Mackay. *Intergated Field Development for Effective Scale Control throughout the Water Cycle in Deep Water Subsea Fields (SPE94052)*. in *67th EAGE Conference & Exhibition*. 2005.
133. Sandengen, K. *Prediction of mineral scale formation in wet gas condensate pipelines and in meg (mono ethylene glycol) regeneration plants*. 2006.
134. Moghadasi, J., et al. *Scale formation in oil reservoir and production equipment during water injection (Kinetics of CaSO4 and CaCO3 crystal growth and effect on formation damage)*. in *SPE European Formation Damage Conference*. 2003. Society of Petroleum Engineers.
135. Mullin, J.W., *Crystallization*. 2001: Elsevier.
136. Chen, T., A. Neville, and M. Yuan, *Calcium carbonate scale formation—assessing the initial stages of precipitation and deposition.* Journal of Petroleum Science and Engineering, 2005. **46**(3): p. 185-194.
137. Walton, A.G., et al., *The formation and properties of precipitates*. Vol. 23. 1967: Interscience Publishers New York.
138. Antony, A., et al., *Scale formation and control in high pressure membrane water treatment systems: a review.* Journal of membrane science, 2011. **383**(1-2): p. 1-16.
139. Luft, J.R. and G.T. DeTitta, *A method to produce microseed stock for use in the crystallization of biological macromolecules.* Acta Crystallographica Section D, 1999. **55**(5): p. 988-993.
140. Jones, A.G., *Crystallization process systems*. 2002: Elsevier.
141. Mullin, J. and O. Söhnel, *Expressions of supersaturation in crystallization studies.* Chemical Engineering Science, 1977. **32**(7): p. 683-686.
142. Stamatakis, E., et al., *An improved predictive correlation for the induction time of CaCO3 scale formation during flow in porous media.* Journal of colloid and interface science, 2005. **286**(1): p. 7-13.
143. Söhnel, O. and J. Mullin, *A method for the determination of precipitation induction periods.* Journal of Crystal Growth, 1978. **44**(4): p. 377-382.

144. Söhnel, O. and J. Garside, *Precipitation: basic principles and industrial applications*. 1992: Butterworth-Heinemann.
145. Cheong, W.C., P.H. Gaskell, and A. Neville, *Substrate effect on surface adhesion/crystallisation of calcium carbonate.* Journal of Crystal Growth, 2013. **363**: p. 7-21.
146. Prasad, M.R., et al., *Chapter 3 - Basics of Crystallization Process Applied in Drug Exploration*, in *Dosage Form Design Parameters*, R.K. Tekade, Editor. 2018, Academic Press. p. 67-103.
147. Ghizellaoui, S., et al., *Inhibition of scaling in the presence of copper and zinc by various chemical processes.* Desalination, 2007. **206**(1-3): p. 185-197.
148. Chen, T., et al., *Influence of PPCA inhibitor on CaCO3 scale surface deposition and bulk precipitation at elevated temperature.* Progress in Natural Science, 2005. **15**(S1): p. 35-41.
149. Garside, J. and M. Larson, *Direct observation of secondary nuclei production.* Journal of Crystal Growth, 1978. **43**(6): p. 694-704.
150. Judat, B. and M. Kind, *Morphology and internal structure of barium sulfate—derivation of a new growth mechanism.* Journal of Colloid and Interface Science, 2004. **269**(2): p. 341-353.
151. Daudey, P., G. Van Rosmalen, and E. De Jong, *Secondary nucleation kinetcs of ammonium sulfate in a CMSMPR crystallizer.* Journal of Crystal growth, 1990. **99**(1-4): p. 1076-1081.
152. Verdurand, E., et al., *Secondary nucleation and growth of organic crystals in industrial crystallization.* Journal of Crystal growth, 2005. **275**(1-2): p. e1363-e1367.
153. Myerson, A., *Handbook of industrial crystallization*. 2002: Butterworth-Heinemann.
154. Liu, X., *Effect of foreign particles: a comprehensive understanding of 3D heterogeneous nucleation.* Journal of crystal growth, 2002. **237**: p. 1806-1812.
155. Li, R., et al., *Gibbs–Curie–Wulff Theorem in Organic Materials: A Case Study on the Relationship between Surface Energy and Crystal Growth.* Advanced Materials, 2016. **28**(8): p. 1697-1702.
156. Goodman, C., *Crystal Growth*. 1974: Springer.
157. Du, J., et al., *Correlation between crystallographic anisotropy and dendritic orientation selection of binary magnesium alloys.* Scientific Reports, 2017. **7**.
158. Nancollas, G. and N. Purdie, *The kinetics of crystal growth.* Quarterly Reviews, Chemical Society, 1964. **18**(1): p. 1-20.
159. Levi, A.C. and M. Kotrla, *Theory and simulation of crystal growth.* Journal of Physics: Condensed Matter, 1997. **9**(2): p. 299.
160. Patel, D.D. *KINETICS AND MECHANISMS OF CRYSTAL GROWTH INHIBITION OF INDOMETHACIN BY MODEL PRECIPITATION INHIBITORS*. 2015.
161. Vere, A.W., *Crystal growth: principles and progress*. 2013: Springer Science & Business Media.
162. Ohtsuka, T., R. Tsai, and Y. Giga, *Growth Rate of Crystal Surfaces with Several Dislocation Centers.* Crystal Growth & Design, 2016. **18**.
163. ASTM, D., *907-05. Standard Terminology of Adhesives.* Annu. Book ASTM Stand, 2005.

164. Verwey, E.J.W., J.T.G. Overbeek, and J.T.G. Overbeek, *Theory of the stability of lyophobic colloids*. 1999: Courier Corporation.
165. Oliveira, R., *Understanding adhesion: a means for preventing fouling.* Experimental Thermal and Fluid Science, 1997. **14**(4): p. 316-322.
166. Ninham, B.W., *On progress in forces since the DLVO theory.* Advances in colloid and interface science, 1999. **83**(1-3): p. 1-17.
167. Collins, I. *A new model for mineral scale adhesion*. in *International Symposium on Oilfield Scale*. 2002. Society of Petroleum Engineers.
168. Akbar, M., et al., *A snapshot of carbonate reservoir evaluation.* 2000. **12**(4): p. 20-21.
169. Binmerdhah, A., A. Yassin, and M. Muherei, *Laboratory and prediction of barium sulfate scaling at high-barium formation water.* Journal of Petroleum Science and Engineering - J PET SCI ENGINEERING, 2010. **70**: p. 79-88.
170. Kamal, M.S., et al., *Oilfield scale formation and chemical removal: A review.* Journal of Petroleum Science and Engineering, 2018. **171**: p. 127-139.
171. Meldrum, F.C., *Calcium carbonate in biomineralisation and biomimetic chemistry.* International Materials Reviews, 2003. **48**(3): p. 187-224.
172. Plummer, L.N. and E. Busenberg, *The solubilities of calcite, aragonite and vaterite in CO2-H2O solutions between 0 and 90 C, and an evaluation of the aqueous model for the system CaCO3-CO2-H2O.* Geochimica et cosmochimica acta, 1982. **46**(6): p. 1011-1040.
173. Eroini, V., *Kinetic study of calcium carbonate formation and inhibition by using an in-situ flow cell*. 2011, University of Leeds.
174. Wang, Z., *Mineral scale formation-aspects of surface energy and adhesion*. 2006, University of Leeds.
175. Brečević, L. and D. Kralj, *On calcium carbonates: from fundamental research to application.* Croatica Chemica Acta, 2007. **80**(3-4): p. 467-484.
176. Wickramasinghe, M., G. Dias, and P. Premadasa K M Gamage, *A novel classification of bone graft materials.* Journal of Biomedical Materials Research Part B: Applied Biomaterials, 2022. **110**.
177. MacAdam, J. and S.A. Parsons, *Calcium carbonate scale formation and control.* Re/Views in Environmental Science & Bio/Technology, 2004. **3**(2): p. 159-169.
178. Helalizadeh, A., H. Müller-Steinhagen, and M. Jamialahmadi, *Mixed salt crystallisation fouling.* Chemical Engineering and Processing: Process Intensification, 2000. **39**(1): p. 29-43.
179. Østvold, T. and P. Randhol. *Kinetics of CaCO3 scale formation. The influence of temperature, supersaturation and ionic composition*. in *International Symposium on Oilfield Scale*. 2001. Society of Petroleum Engineers.
180. Kitamura, M., *Controlling factor of polymorphism in crystallization process.* Journal of Crystal Growth, 2002. **237**: p. 2205-2214.
181. Hu, Z. and Y. Deng, *Synthesis of needle-like aragonite from calcium chloride and sparingly soluble magnesium carbonate.* Powder technology, 2004. **140**(1-2): p. 10-16.
182. Han, Y.S., et al., *Factors affecting the phase and morphology of CaCO3 prepared by a bubbling method.* Journal of the European Ceramic Society, 2006. **26**(4-5): p. 843-847.

183. Dyer, S. and G. Graham, *The effect of temperature and pressure on oilfield scale formation.* Journal of Petroleum Science and Engineering, 2002. **35**(1-2): p. 95-107.
184. Yu, J., et al., *Facile preparation of calcium carbonate particles with unusual morphologies by precipitation reaction.* Journal of Crystal Growth, 2004. **261**(4): p. 566-570.
185. Amiri, M. and J. Moghadasi, *The Effect of Temperature on Calcium Carbonate Scale Formation in Iranian Oil Reservoirs Using OLI ScaleChem Software.* Petroleum Science and Technology, 2012. **30**(5): p. 453-466.
186. Cowan, J.C. and D.J. Weintritt, *Water-formed scale deposits*. 1976: Gulf Publishing Company, Book Division.
187. Peyvandi, K., A. Haghtalab, and M.R. Omidkhah, *Using an electrochemical technique to study the effective variables on morphology and deposition of CaCO3 and BaSO4 at the metal surface.* Journal of Crystal Growth, 2012. **354**(1): p. 109-118.
188. *Soil Chemical Processes*, in *Soil Formation*, N. van Breemen and P. Buurman, Editors. 2002, Springer Netherlands: Dordrecht. p. 41-81.
189. Andritsos, N., A. Karabelas, and P. Koutsoukos, *Morphology and structure of CaCO3 scale layers formed under isothermal flow conditions.* Langmuir, 1997. **13**(10): p. 2873-2879.
190. Walker, P. and R. Sheikholeslami, *Assessment of the effect of velocity and residence time in CaSO4 precipitating flow reaction.* Chemical Engineering Science, 2003. **58**(16): p. 3807-3816.
191. Zhang, Y. and R. Farquhar. *Laboratory determination of calcium carbonate scaling rates for oilfield wellbore environments*. in *International Symposium on Oilfield Scale*. 2001. Society of Petroleum Engineers.
192. Andritsos, N. and A. Karabelas, *Crystallization and deposit formation of lead sulfide from aqueous solutions: I. Deposition rates.* Journal of colloid and interface science, 1991. **145**(1): p. 158-169.
193. Trippa, G. and R. Jachuck, *Process intensification: precipitation of calcium carbonate using narrow channel reactors.* Chemical Engineering Research and Design, 2003. **81**(7): p. 766-772.
194. Yang, Q., et al., *Investigation of induction period and morphology of CaCO3 fouling on heated surface.* Chemical Engineering Science, 2002. **57**(6): p. 921-931.
195. Muryanto, S., et al., *Calcium Carbonate Scale Formation in Pipes: Effect of Flow Rates, Temperature, and Malic Acid as Additives on the Mass and Morphology of the Scale.* Procedia Chemistry, 2014. **9**: p. 69-76.
196. Gomez-Morales, J., J. Torrent-Burgues, and R. Rodriguez-Clemente, *Nucleation of calcium carbonate at different initial pH conditions.* Journal of crystal growth, 1996. **169**(2): p. 331-338.
197. Hart, P., G. Colson, and J. Burris, *Application of Carbon Dioxide to reduce water side lime scale in heat exchanges.* J. of Science and Technology for Forest Products and Processes, 2012. **1**: p. 67-70.
198. Andritsos, N. and A. Karabelas, *Calcium carbonate scaling in a plate heat exchanger in the presence of particles.* International Journal of Heat and Mass Transfer, 2003. **46**(24): p. 4613-4627.

199. Baraka-Lokmane, S. and K. Sorbie, *Effect of pH and scale inhibitor concentration on phosphonate–carbonate interaction.* Journal of Petroleum Science and Engineering, 2010. **70**(1-2): p. 10-27.
200. Feng, B., A.K. Yong, and H. An, *Effect of various factors on the particle size of calcium carbonate formed in a precipitation process.* Materials Science and Engineering: A, 2007. **445**: p. 170-179.
201. Cölfen, H. and L. Qi, *A systematic examination of the morphogenesis of calcium carbonate in the presence of a double‐hydrophilic block copolymer.* Chemistry–A European Journal, 2001. **7**(1): p. 106-116.
202. Wada, N., K. Yamashita, and T. Umegaki, *Effects of divalent cations upon nucleation, growth and transformation of calcium carbonate polymorphs under conditions of double diffusion.* Journal of Crystal Growth, 1995. **148**(3): p. 297-304.
203. Chen, T., A. Neville, and M. Yuan, *Assessing the effect of Mg2+ on CaCO3 scale formation–bulk precipitation and surface deposition.* Journal of Crystal Growth, 2005. **275**(1-2): p. e1341-e1347.
204. Zeppenfeld, K., *Prevention of CaCO3 scale formation by trace amounts of copper (II) in comparison to zinc (II).* Desalination, 2010. **252**(1-3): p. 60-65.
205. Stalker, R., G.M. Graham, and C. Simpson. *The Impact of Inorganic Scale Deposits and Their Removal on General CO2 Corrosion Rates and Corrosion Inhibitor Performance*. in *SPE International Symposium on Oilfield Corrosion*. 2004. Society of Petroleum Engineers.
206. Olajire, A.A., *A review of oilfield scale management technology for oil and gas production.* Journal of Petroleum Science and Engineering, 2015. **135**: p. 723-737.
207. Heath, S., et al. *Non-Chemical Methods for Downhole Control of Carbonate and Sulphate Scales-An Alternative Approach to Scale Management?* in *SPE International Oilfield Scale Conference and Exhibition*. 2018. OnePetro.
208. Chen, T., A. Neville, and M. Yuan. *Effect of PPCA and DETPMP inhibitor blends on CaCO3 scale formation*. in *SPE International Symposium on Oilfield Scale*. 2004. OnePetro.
209. Dirksen, J.A. and T.A. Ring, *Fundamentals of crystallization: Kinetic effects on particle size distributions and morphology.* Chemical Engineering Science, 1991. **46**(10): p. 2389-2427.
210. Azimi, G., et al., *Scale-resistant surfaces: Fundamental studies of the effect of surface energy on reducing scale formation.* Applied Surface Science, 2014. **313**: p. 591-599.
211. Wang, Z., A. Neville, and A. Meredith. *How and Why does Scale Stick-Can the Surface be Engineered to Decrease Scale Formation and Adhesion?* in *SPE International Symposium on Oilfield Scale*. 2005. Society of Petroleum Engineers.
212. Vazirian, M.M., et al., *Surface inorganic scale formation in oil and gas industry: As adhesion and deposition processes.* Journal of Petroleum Science and Engineering, 2016. **137**: p. 22-32.
213. Harouaka, K., et al. *The Effect of Surface Material on the Mechanics of Calcium Carbonate Scale Deposition*. in *SPE International Oilfield Scale Conference and Exhibition*. 2018. Society of Petroleum Engineers.

214. Makkonen, L., *Young's equation revisited.* Journal of Physics: Condensed Matter, 2016. **28**(13): p. 135001.
215. Erbil, H.Y., *The debate on the dependence of apparent contact angles on drop contact area or three-phase contact line: A review.* Surface Science Reports, 2014. **69**(4): p. 325-365.
216. de Gennes, P.G., F. Brochard-Wyart, and D. Quere, *Capillarity and Wetting Phenomena: Drops, Bubbles, Pearls, Waves*. 2003: Springer New York.
217. Attinger, D., et al., *Surface engineering for phase change heat transfer: A review.* MRS Energy & Sustainability, 2014. **1**.
218. Wenzel, R.N., *Resistance of solid surfaces to wetting by water.* Industrial & Engineering Chemistry, 1936. **28**(8): p. 988-994.
219. Cassie, A. and S. Baxter, *Wettability of porous surfaces.* Transactions of the Faraday society, 1944. **40**: p. 546-551.
220. Ishino, C. and K. Okumura, *Wetting transitions on textured hydrophilic surfaces.* The European Physical Journal E, 2008. **25**(4): p. 415-424.
221. Bico, J., U. Thiele, and D. Quéré, *Wetting of textured surfaces.* Colloids and Surfaces A: Physicochemical and Engineering Aspects, 2002. **206**(1-3): p. 41-46.
222. Page, A.J. and R.P. Sear, *Crystallization controlled by the geometry of a surface.* Journal of the American Chemical Society, 2009. **131**(48): p. 17550-17551.
223. Fletcher, N., *Size effect in heterogeneous nucleation.* The Journal of chemical physics, 1958. **29**(3): p. 572-576.
224. Wong, T.S., et al., *Bioinspired self-repairing slippery surfaces with pressure-stable omniphobicity.* Nature, 2011. **477**(7365): p. 443-7.
225. Solomon, B.R., et al., *CHAPTER 10 Lubricant-Impregnated Surfaces*, in *Non-wettable Surfaces: Theory, Preparation and Applications*. 2017, The Royal Society of Chemistry. p. 285-318.
226. Scholz, I., et al., *Slippery surfaces of pitcher plants: Nepenthes wax crystals minimize insect attachment via microscopic surface roughness.* The Journal of Experimental Biology, 2010. **213**(7): p. 1115-1125.
227. Epstein, A.K., et al., *Liquid-infused structured surfaces with exceptional anti-biofouling performance.* Proc Natl Acad Sci U S A, 2012. **109**(33): p. 13182-7.
228. Tesler, A.B., et al., *Extremely durable biofouling-resistant metallic surfaces based on electrodeposited nanoporous tungstite films on steel.* Nat Commun, 2015. **6**: p. 8649.
229. Wang, P., D. Zhang, and Z. Lu, *Slippery liquid-infused porous surface bio-inspired by pitcher plant for marine anti-biofouling application.* Colloids Surf B Biointerfaces, 2015. **136**: p. 240-7.
230. Amini, S., et al., *Preventing mussel adhesion using lubricant-infused materials.* Science, 2017. **357**(6352): p. 668-673.
231. Ware, C.S., et al., *Marine Antifouling Behavior of Lubricant-Infused Nanowrinkled Polymeric Surfaces.* ACS Applied Materials & Interfaces, 2018. **10**(4): p. 4173-4182.
232. Preston, D.J., et al., *Design of Lubricant Infused Surfaces.* ACS Appl Mater Interfaces, 2017. **9**(48): p. 42383-42392.

233. Solomon, B.R., K.S. Khalil, and K.K. Varanasi, *Drag reduction using lubricant-impregnated surfaces in viscous laminar flow.* Langmuir, 2014. **30**(36): p. 10970-6.
234. Schönecker, C., T. Baier, and S. Hardt, *Influence of the enclosed fluid on the flow over a microstructured surface in the Cassie state.* Journal of Fluid Mechanics, 2014. **740**: p. 168-195.
235. Rosenberg, B.J., et al., *Turbulent drag reduction over air-and liquid-impregnated surfaces.* Physics of Fluids, 2016. **28**(1): p. 015103.
236. Fu, M.K. and M. Hultmark. *A Model for Turbulent Drag Reduction Over Liquid Infused Micro-textured Surfaces*. 2015. Tech. rep., European Drag Reduction and Flow Control Meeting.
237. Yao, X., et al., *Adaptive fluid-infused porous films with tunable transparency and wettability.* Nature materials, 2013. **12**(6): p. 529.
238. Xiang, T., et al., *Slippery liquid-infused porous surface for corrosion protection with self-healing property.* Chemical Engineering Journal, 2018. **345**: p. 147-155.
239. Lafuma, A. and D. Quéré, *Slippery pre-suffused surfaces.* EPL (Europhysics Letters), 2011. **96**(5): p. 56001.
240. Cao, M., et al., *Water-repellent properties of superhydrophobic and lubricant-infused "slippery" surfaces: A brief study on the functions and applications.* ACS applied materials & interfaces, 2015. **8**(6): p. 3615-3623.
241. Daniel, D., et al., *Lubricant-infused micro/nano-structured surfaces with tunable dynamic omniphobicity at high temperatures.* Applied Physics Letters, 2013. **102**(23): p. 231603.
242. Miranda, D.F., et al., *Physically and chemically stable ionic liquid-infused textured surfaces showing excellent dynamic omniphobicity.* Apl Materials, 2014. **2**(5): p. 056108.
243. Charpentier, T.V., et al., *Liquid infused porous surfaces for mineral fouling mitigation.* J Colloid Interface Sci, 2015. **444**: p. 81-6.
244. Subramanyam, S.B., G. Azimi, and K.K. Varanasi, *Designing Lubricant-Impregnated Textured Surfaces to Resist Scale Formation.* Advanced Materials Interfaces, 2014. **1**(2): p. 1300068.
245. Smith, J.D., et al., *Droplet mobility on lubricant-impregnated surfaces.* Soft Matter, 2013. **9**(6): p. 1772-1780.
246. Van Oss, C.J., M.K. Chaudhury, and R.J. Good, *Interfacial Lifshitz-van der Waals and polar interactions in macroscopic systems.* Chemical Reviews, 1988. **88**(6): p. 927-941.
247. Sadeek, S.A., et al., *Protectiveness and stability of iron carbonate films on carbon steel in mildly alkaline aqueous alkanolamine CO2 environments.* Corrosion Science, 2024. **227**: p. 111773.
248. Nesic, S., et al. *Mechanistic modeling for CO2 corrosion with protective iron carbonate films*. in *NACE CORROSION*. 2001. NACE.
249. Neerup, R., I.A. Løge, and P.L. Fosbøl, *FeCO3 Synthesis Pathways: The Influence of Temperature, Duration, and Pressure.* ACS Omega, 2023. **8**(3): p. 3404-3414.
250. Jacklin, R., et al., *An electrochemical study of iron carbonate layers formed on carbon steel during corrosion in elevated pressure CO2 environments.* Corrosion Science, 2024. **235**: p. 112202.
251. Baled, H.O., et al., *Exploratory Characterization of a Perfluoropolyether Oil as a Possible Viscosity Standard at Deepwater Production*

Conditions of 533 K and 241 MPa. International Journal of Thermophysics, 2013. **34**(10): p. 1845-1864.
252. Simonis, E.D. and G.J. Blanchard, *The length-scale dependence of diffusion in a room temperature ionic liquid: insight into the effect of spatial heterogeneity.* Journal of Solid State Electrochemistry, 2025. **29**(6): p. 2189-2194.
253. De Motte, R.A., et al., *The early stages of FeCO3 scale formation kinetics in CO2 corrosion.* Materials Chemistry and Physics, 2018. **216**: p. 102-111.
254. Huhtamäki, T., et al., *Surface-wetting characterization using contact-angle measurements.* Nature Protocols, 2018. **13**(7): p. 1521-1538.
255. Preston, D.J., et al., *Design of lubricant infused surfaces.* ACS applied materials & interfaces, 2017. **9**(48): p. 42383-42392.
256. Davidson, P.M., et al., *SYNTHESIS OF THE NEW COMPOUND CAFE(CO3)2 AND EXPERIMENTAL CONSTRAINTS ON THE (CA,FE)CO3 JOIN.* Geochimica et Cosmochimica Acta, 1993. **57**: p. 5105-5109.
257. Navabzadeh Esmaeely, S., et al., *Effect of Incorporation of Calcium into Iron Carbonate Protective Layers in CO2 Corrosion of Mild Steel*. 2016.
258. Shamsa, A., et al., *The role of Ca2+ ions on Ca/Fe carbonate products on X65 carbon steel in CO2 corrosion environments at 80 and 150 °C.* Corrosion Science, 2019. **156**: p. 58-70.
259. Hua, Y., et al., *Protectiveness, morphology and composition of corrosion products formed on carbon steel in the presence of Cl−, Ca2+ and Mg2+ in high pressure CO2 environments.* Applied Surface Science, 2018. **455**: p. 667-682.
260. de Sá, J.S., et al., *Formation and Protectiveness of Fe/Ca Carbonate Layer on X80 Steel in High-Pressure CO2 Corrosion Environments.* Corrosion, 2023. **79**(7): p. 782-789.
261. Barker, R., et al., *Iron carbonate formation kinetics onto corroding and pre-filmed carbon steel surfaces in carbon dioxide corrosion environments.* Applied Surface Science, 2019. **469**: p. 135-145.
262. Dwivedi, D., K. Lepková, and T. Becker, *Carbon steel corrosion: a review of key surface properties and characterization methods.* RSC Advances, 2017. **7**(8): p. 4580-4610.
263. Shams, D.F., et al., *Characteristics of pipe corrosion scales in untreated water distribution system and effect on water quality in Peshawar, Pakistan.* Environmental Science and Pollution Research, 2019. **26**(6): p. 5794-5803.
264. Fonna, S., et al., *Investigation of corrosion products formed on the surface of carbon steel exposed in Banda Aceh's atmosphere.* Heliyon, 2021. **7**(4): p. e06608.
265. Li, W., et al., *Investigation of Pseudo-Passivation of Mild Steel in CO2 Corrosion.* Corrosion, 2013. **70**(3): p. 294-302.
266. Owen, J., et al., *In situ SR-XRD analysis of corrosion product formation during 'pseudo-passivation' of carbon steel in CO2-containing aqueous environments.* Corrosion Science, 2023. **225**: p. 111598.
267. Wang, C., et al., *Determination of thickness and air-void distribution within the iron carbonate layers using X-ray computed tomography.* Corrosion Science, 2021. **179**: p. 109153.

268. Burkle, D.P., *Understanding the formation of protective FeCO3 on to carbon steel pipelines during CO2 corrosion*. 2017, University of Leeds.
269. Hua, Y., et al., *The formation of FeCO3 and Fe3O4 on carbon steel and their protective capabilities against CO2 corrosion at elevated temperature and pressure.* Corrosion Science, 2019. **157**: p. 392-405.
270. Gulbrandsen, E. and J.H. Morard. *Study of the Possible Mechanisms of Steel Passivation in CO2 Corrosion*. in *CORROSION 99*. 1999.
271. Han, J., et al., *Spontaneous passivation observations during scale formation on mild steel in CO2 brines.* Electrochimica Acta, 2011. **56**(15): p. 5396-5404.
272. Gathimba, N., et al., *Surface roughness characteristics of corroded steel pipe piles exposed to marine environment.* Construction and Building Materials, 2019. **203**: p. 267-281.
273. Ghosh, G., A. Sidpara, and P.P. Bandyopadhyay, *Understanding the role of surface roughness on the tribological performance and corrosion resistance of WC-Co coating.* Surface and Coatings Technology, 2019. **378**: p. 125080.
274. Hilbert, L.R., et al., *Influence of surface roughness of stainless steel on microbial adhesion and corrosion resistance.* International Biodeterioration & Biodegradation, 2003. **52**(3): p. 175-185.
275. Pradhan, D., et al., *Effect of surface roughness on corrosion behavior of the superalloy IN718 in simulated marine environment.* Journal of Alloys and Compounds, 2018. **740**: p. 250-263.
276. Kim, P., et al., *Hierarchical or Not? Effect of the Length Scale and Hierarchy of the Surface Roughness on Omniphobicity of Lubricant-Infused Substrates.* Nano Letters, 2013. **13**(4): p. 1793-1799.
277. Yang, S., et al., *Slippery liquid-infused porous surface based on perfluorinated lubricant/iron tetradecanoate: Preparation and corrosion protection application.* Applied Surface Science, 2015. **328**: p. 491-500.
278. Xu, S., et al., *Influence of corrosion on the bond behavior in CFRP-steel single lap joints.* Construction and Building Materials, 2020. **236**: p. 117607.
279. Li, A., et al., *Bond behaviour between CFRP plates and corroded steel plates.* Composite Structures, 2019. **220**: p. 221-235.
280. van Dam, J.P.B., et al., *Effect of surface roughness and chemistry on the adhesion and durability of a steel-epoxy adhesive interface.* International Journal of Adhesion and Adhesives, 2020. **96**: p. 102450.
281. Smith, J.D., et al., *Hydrate-phobic surfaces: fundamental studies in clathrate hydrate adhesion reduction.* Physical Chemistry Chemical Physics, 2012. **14**(17): p. 6013-6020.
282. Chibowski, E., et al., *Surface free energy components of glass from ellipsometry and zeta potential measurements.* Journal of Colloid and Interface Science, 1989. **132**(1): p. 54-61.
283. Hedberg, Y., et al., *Correlation between surface physicochemical properties and the release of iron from stainless steel AISI 304 in biological media.* Colloids and Surfaces B: Biointerfaces, 2014. **122**: p. 216-222.
284. Sajid, H.U. and R. Kiran, *Influence of corrosion and surface roughness on wettability of ASTM A36 steels.* Journal of Constructional Steel Research, 2018. **144**: p. 310-326.

285. Behera, S.K., et al., *Effect of Microstructure on Contact Angle and Corrosion of Ductile Iron: Iron–Graphite Composite.* Langmuir, 2019. **35**(49): p. 16120-16129.
286. Knauer, S., et al., *Contact angle and corrosion of a Water – CO2 system on X70 and S41500 at 278 K and pressures up to 20 MPa.* International Journal of Greenhouse Gas Control, 2019. **89**: p. 33-39.
287. Jia, X., *Wettability of Rough Polymer, Metal and Oxide Surfaces as Well as of Composite Surfaces.* Journal of Adhesion Science and Technology, 2008. **22**(15): p. 1893-1905.
288. Tang, X., S. Richter, and S. Nesic, *Study of wettability of different mild steel surfaces.* 17th International Corrosion Congress 2008: Corrosion Control in the Service of Society, 2008. **2**.
289. Starostina, I.A., et al., *Adhesion of polymers: New approaches to determination of surface properties of metals.* Polymer Science Series D, 2013. **6**(1): p. 1-4.
290. Saul, A., et al., *Corrosion derived lubricant infused surfaces on X65 carbon steel for improved inorganic scaling performance.* Journal of Adhesion Science and Technology, 2021. **36**: p. 1-22.
291. Mantel, M. and J.P. Wightman, *Influence of the surface chemistry on the wettability of stainless steel.* 1994. **21**(9): p. 595-605.
292. Bechikh, A., et al., *Sandblasting parameter variation effect on galvanized steel surface chemical composition, roughness and free energy.* International Journal of Adhesion and Adhesives, 2020. **102**: p. 102653.
293. Kuznetsov, G.V., et al., *Influence of roughness on polar and dispersed components of surface free energy and wettability properties of copper and steel surfaces.* Surface and Coatings Technology, 2021. **422**: p. 127518.
294. McCafferty, E., *Acid-base effects in polymer adhesion at metal surfaces.* Journal of Adhesion Science and Technology, 2002. **16**(3): p. 239-255.
295. Goniakowski, J., F. Finocchi, and C. Noguera, *Polarity of oxide surfaces and nanostructures.* Reports on Progress in Physics, 2008. **71**(1): p. 016501.
296. Murray, D.A.J., W.L. Lockhart, and G.R.B. Webster, *Analysis of the water-soluble fraction of crude oils and petroleum products by gas chromatography.* Oil and Petrochemical Pollution, 1984. **2**(1): p. 39-46.
297. Vetter, O.J. and W.A. Farone. *Calcium Carbonate Scale in Oilfield Operations*. in *SPE Annual Technical Conference and Exhibition*. 1987.
298. Graham, G.M. and D.M. Frigo, *Chapter 5 - Inorganic mineral scale mitigation*, in *Flow Assurance*, Q. Wang, Editor. 2022, Gulf Professional Publishing. p. 287-442.
299. Sand, K.K., et al., *Calcite Growth Kinetics: Dependence on Saturation Index, Ca2+:CO32– Activity Ratio, and Surface Atomic Structure.* Crystal Growth & Design, 2016. **16**(7): p. 3602-3612.
300. van der Weijden, C.H. and R.D. van der Weijden, *Calcite growth: Rate dependence on saturation, on ratios of dissolved calcium and (bi)carbonate and on their complexes.* Journal of Crystal Growth, 2014. **394**: p. 137-144.

301. Chang, R., et al., *Calcium carbonate precipitation for CO2 storage and utilization: a review of the carbonate crystallization and polymorphism.* 2017. **5**: p. 17.
302. Oral, Ç.M. and B.J.P.t. Ercan, *Influence of pH on morphology, size and polymorph of room temperature synthesized calcium carbonate particles.* 2018. **339**: p. 781-788.
303. Zeller, E.J. and J.L.J.A.B. Wray, *Factors influencing precipitation of calcium carbonate.* 1956. **40**(1): p. 140-152.
304. Al-Jaroudi, S., et al., *Use of X-ray powder diffraction for quantitative analysis of carbonate rock reservoir samples.* Powder Technology - POWDER TECHNOL, 2007. **175**: p. 115-121.
305. Kontoyannis, C.G. and N.V. Vagenas, *Calcium carbonate phase analysis using XRD and FT-Raman spectroscopy.* Analyst, 2000. **125**(2): p. 251-255.
306. Smyth, J.R. and T.J. Ahrens, *The crystal structure of calcite III.* Geophysical Research Letters, 1997. **24**(13): p. 1595-1598.
307. Park, R.J. and F.C. Meldrum, *Synthesis of single crystals of calcite with complex morphologies.* Advanced Materials, 2002. **14**(16): p. 1167-1169.
308. Keogh, W., et al., *Deposition of Inorganic Carbonate, Sulfate, and Sulfide Scales on Antifouling Surfaces in Multiphase Flow.* Energy & Fuels, 2017. **31**(11): p. 11838-11851.
309. Brady, P.V., *Why oil sticks to limestone*. 2011: United States. p. Medium: ED; Size: 11 p.
310. Liu, X., et al., *Release of Crude Oil from Silica and Calcium Carbonate Surfaces: On the Alternation of Surface and Molecular Forces by High- and Low-Salinity Aqueous Salt Solutions.* Energy & Fuels, 2016. **30**(5): p. 3986-3993.
311. Yeh, S.-L., R. Koshani, and A. Sheikhi, *Colloidal aspects of calcium carbonate scaling in water-in-oil emulsions: A fundamental study using droplet-based microfluidics.* Journal of Colloid and Interface Science, 2023. **633**: p. 536-545.
312. Zhou, G.-T., et al., *Sonochemical synthesis of aragonite-type calcium carbonate with different morphologies.* New Journal of Chemistry, 2004. **28**(8): p. 1027-1031.
313. Zhu, D.-Z., D.-M. Sun, and Q.-S. Wu, *Assembly of nano-superstructural aragonite CaCO3 by living bio-membrane.* Journal of Experimental Nanoscience, 2011. **6**(6): p. 622-630.
314. Liendo, F., et al., *Factors controlling and influencing polymorphism, morphology and size of calcium carbonate synthesized through the carbonation route: A review.* Powder Technology, 2022. **398**: p. 117050.
315. Davis, K.J., P.M. Dove, and J.J. De Yoreo, *The Role of Mg²⁺ as an Impurity in Calcite Growth.* Science, 2000. **290**(5494): p. 1134-1137.
316. Seeger, T.S., et al., *Magnesium and calcium determination in desalted crude oil by direct sampling graphite furnace atomic absorption spectrometry.* Fuel, 2019. **236**: p. 1483-1488.
317. Ayirala, S.C., et al., *Coalescence of Crude Oil Droplets in Brine Systems: Effect of Individual Electrolytes.* Energy & Fuels, 2018. **32**(5): p. 5763-5771.

318. Rayhani, M., M. Simjoo, and M. Chahardowli, *Effect of water chemistry on the stability of water-in-crude oil emulsion: Role of aqueous ions and underlying mechanisms.* Journal of Petroleum Science and Engineering, 2022. **211**: p. 110123.
319. Chakrabarty, D. and S. Mahapatra, *Aragonite crystals with unconventional morphologies.* Journal of Materials Chemistry, 1999. **9**(11): p. 2953-2957.
320. Ryu, M., et al., *Comparison of Dissolution and Surface Reactions Between Calcite and Aragonite in L-Glutamic and L-Aspartic Acid Solutions.* Molecules (Basel, Switzerland), 2010. **15**: p. 258-69.
321. Zhou, G.-T., et al., *Formation of Aragonite Mesocrystals and Implication for Biomineralization.* American Mineralogist - AMER MINERAL, 2009. **94**: p. 293-302.
322. Wong, T.-S., et al., *Bioinspired self-repairing slippery surfaces with pressure-stable omniphobicity.* Nature, 2011. **477**(7365): p. 443-447.
323. Law, K.-Y., *Definitions for Hydrophilicity, Hydrophobicity, and Superhydrophobicity: Getting the Basics Right.* The Journal of Physical Chemistry Letters, 2014. **5**(4): p. 686-688.
324. Zhang, M., et al., *Lubricant-infused coating by double-layer ZnO on aluminium and its anti-corrosion performance.* Journal of Alloys and Compounds, 2018. **764**: p. 730-737.
325. Peethan, A., et al., *Wettability tailored superhydrophobic and oil-infused slippery aluminium surface for improved anti-corrosion performance.* Materials Chemistry and Physics, 2022. **290**: p. 126517.
326. Zhang, D., et al., *PDMS-Infused Poly(High Internal Phase Emulsion) Templates for the Construction of Slippery Liquid-Infused Porous Surfaces with Self-cleaning and Self-repairing Properties.* Langmuir, 2019. **35**(25): p. 8276-8284.
327. Boveri, G., et al., *Different Approaches to Low-Wettable Materials for Freezing Environments: Design, Performance and Durability.* Coatings, 2021. **11**(1): p. 77.
328. Hajeesaeh, S., et al., *Durable slippery lubricant-infused multiscale-textured surfaces for repelling highly adhesive liquids.* Materials Research Express, 2020. **7**(10): p. 106409.
329. Bittner, R.W., K. Bica, and H. Hoffmann, *Fluorine-free, liquid-repellent surfaces made from ionic liquid-infused nanostructured silicon.* Monatshefte für Chemie - Chemical Monthly, 2017. **148**(1): p. 167-177.
330. Wylie, M.P., et al., *Phosphonium Ionic Liquid-Infused Poly(vinyl chloride) Surfaces Possessing Potent Antifouling Properties.* ACS Omega, 2020. **5**(14): p. 7771-7781.
331. Wang, X.Q., et al., *Ionic liquids-infused slippery surfaces for condensation and hot water repellency.* Chemical Engineering Journal, 2018. **343**: p. 561-571.
332. Tang, X., S. Richter, and S. Nesic. *Study of wettability of different mild steel surfaces*. in *17th International Corrosion Congress*. 2008.
333. Askvik, K.M., et al., *Calculation of wetting angles in crude oil/water/quartz systems.* Journal of Colloid and Interface Science, 2005. **287**(2): p. 657-663.
334. Ajmera, P., et al., *The Role of Asphaltenes In Inhibiting Corrosion And Altering the Wettability of the Steel Surface.* Corrosion, 2011. **67**.

335. Aspenes, G., et al., *Petroleum hydrate deposition mechanisms: The influence of pipeline wettability.* 2008.
336. Zhou, W.X. and A. Ariando, *Review on ferroelectric/polar metals.* Japanese Journal of Applied Physics, 2020. **59**(SI): p. SI0802.
337. Bhowal, S. and N.A. Spaldin, *Polar Metals: Principles and Prospects.* Annual Review of Materials Research, 2023. **53**(1): p. 53-79.
338. Rudnick, L.R., *Lubricant Additives: Chemistry and Applications, Second Edition*. 2009: CRC Press.
339. Kajdas, C. and B. Bhushan. *Mechanism of interaction and degradation of perfluoropolyethers with DLC coating in thin film magnetic rigid disks—A critical review*. in *J. Info. Storage Proc. Syst*. 1999.
340. Ge, Q., et al., *Condensation of Satellite Droplets on Lubricant-Cloaked Droplets.* ACS Applied Materials & Interfaces, 2020. **12**(19): p. 22246-22255.
341. McAlpine, K. and C. Smyth, *Polarity in Certain Hydrocarbon Vapors.* Journal of the American Chemical Society, 1933. **55**(2): p. 453-462.
342. Bennett, B., et al., *Wettability alteration in petroleum systems: the role of polar non-hydrocarbons.* Petroleum Geoscience, 2004. **10**(3): p. 271-277.
343. Schrader, W., et al., *Characterization of non-polar aromatic hydrocarbons in crude oil using atmospheric pressure laser ionization and Fourier transform ion cyclotron resonance mass spectrometry (APLI FT-ICR MS).* Analyst, 2008. **133**(7): p. 867-869.
344. Sett, S., et al., *Lubricant-Infused Surfaces for Low-Surface-Tension Fluids: Promise versus Reality.* ACS Applied Materials & Interfaces, 2017. **9**(41): p. 36400-36408.
345. Harvey, E.H., *The Surface Tension of Crude Oils.* Industrial & Engineering Chemistry, 1925. **17**(1): p. 85-85.
346. Khan, M.B. and S. Anwar, *Surface tension and wettability analysis during the interaction of alkali-nano silica and its effect on acidic crude oil.* Safety in Extreme Environments, 2021. **3**(1): p. 51-61.
347. Ramírez-González, P.V., M.M. Zavala Arriaga, and V.A. Escobar-Barrios, *A rapid method for interfacial tension calculation between rock plug and crude oil based on contact angles, application for EOR.* Petroleum Science and Technology, 2018. **36**(16): p. 1242-1249.
348. Lam-Maldonado, M., et al., *Extra heavy crude oil viscosity and surface tension behavior using a flow enhancer and water at different temperatures conditions.* Heliyon, 2023. **9**(2): p. e12120.
349. Lam-Maldonado, M., et al., *Statistical Analysis of Surface Tension and Viscosity of Heavy Oil Crude by Mixing Rule.* 2022.
350. Man, M.S., H. Abdul Aziz, and S.B. Abdullah, *Application of ILs as carbonate scales dissolver.* Current Research in Green and Sustainable Chemistry, 2022. **5**: p. 100277.
351. Fernandes, M., F.A. Almeida Paz, and V. de Zea Bermudez, *Ionic-Liquid-Assisted Morphology Tuning of Calcium Carbonate in Ethanolic Solution.* European Journal of Inorganic Chemistry, 2012. **2012**(13): p. 2183-2192.
352. Matei, C., et al., *Calcium carbonate as silver carrier in composite materials obtained in green seaweed extract with topical applications.* Journal of Sol-Gel Science and Technology, 2020. **93**.

353. Rodriguez-Blanco, J., S. Shaw, and L. Benning, *The Kinetics and Mechanisms of Amorphous Calcium Carbonate (ACC) Crystallization to Calcite, Via Vaterite.* Nanoscale, 2010. **3**: p. 265-71.
354. Santos, V.H.J.M.d., et al., *Application of Fourier Transform infrared spectroscopy (FTIR) coupled with multivariate regression for calcium carbonate (CaCO3) quantification in cement.* Construction and Building Materials, 2021. **313**: p. 125413.
355. Veerasingam, S. and R. Venkatachalapathy, *Estimation of carbonate concentration and characterization of marine sediments by Fourier Transform Infrared Spectroscopy.* Infrared Physics & Technology, 2014. **66**: p. 136-140.
356. Rémazeilles, C. and P. Refait, *Fe(II) hydroxycarbonate Fe2(OH)2CO3 (chukanovite) as iron corrosion product: Synthesis and study by Fourier Transform Infrared Spectroscopy.* Polyhedron, 2009. **28**(4): p. 749-756.
357. Marius, C., *FeCO 3 Microparticle Synthesis by Fe-EDTA Hydrothermal Decomposition.* Crystal Growth & Design, 2011.
358. Schmitt, J. and H.-C. Flemming, *FTIR-spectroscopy in microbial and material analysis.* International Biodeterioration & Biodegradation, 1998. **41**(1): p. 1-11.
359. Mohamed, M.A., et al., *Fourier transform infrared (FTIR) spectroscopy*, in *Membrane characterization*. 2017, Elsevier. p. 3-29.
360. Pathak, M., et al., *Production of a non-cytotoxic bioflocculant by a bacterium utilizing a petroleum hydrocarbon source and its application in heavy metal removal.* RSC Advances, 2015. **5**(81): p. 66037-66046.
361. Permanyer, A., et al., *FTIR and SUVF spectroscopy applied to reservoir compartmentalization: a comparative study with gas chromatography fingerprints results.* Fuel, 2002. **81**(7): p. 861-866.
362. Kumar, S., et al., *Design of novel chemical solvent for treatment of waxy crude.* Int. J. Oil, Gas and Coal Technology, 2017. **15**: p. 363–379.
363. Samanta, A., K. Ojha, and A. Mandal, *Interactions between Acidic Crude Oil and Alkali and Their Effects on Enhanced Oil Recovery.* Energy Fuels, 2011. **25**: p. 1642–1649.
364. Clinch, D., J. Luzardo, and F. Fornasier, *Selecting Appropriate Lubricants for the Reservoir Section: A Customized Solution for Peregrino Field - Offshore Brazil.* 2013.
365. Nandiyanto, A., et al., *How to Read and Interpret FTIR Spectroscope of Organic Material.* Indonesian Journal of Science and Technology, 2019. **4**: p. 97-118.
366. Mashhadi Meighani, H., et al., *A new investigation of wax precipitation in Iranian crude oils: Experimental method based on FTIR spectroscopy and theoretical predictions using PC-SAFT model.* Journal of Molecular Liquids, 2018. **249**: p. 970-979.
367. Hajji, S., et al., *Study of cadmium adsorption onto calcite using full factorial experiment design.* Desalination and Water Treatment, 2017. **83**: p. 222-233.
368. Gleirscher, M., et al., *Accelerated Thermo-Catalytic Degradation of Perfluoropolyether (PFPE) Lubricants for Space Applications.* Lubricants, 2023. **11**(2): p. 81.

369. Street Jr, K.W., *Liquid space lubricants examined by vibrational microspectroscopy.* Analytical letters, 2008. **41**(3): p. 351-376.
370. Lee, M., et al., *Synchronized reinjection and coalescence of droplets in microfluidics.* Lab on a Chip, 2014. **14**(3): p. 509-513.
371. Fischer, T., et al., *A facile method for grafting functional hydrogel films on PTFE, PVDF, and TPX polymers.* Soft Matter, 2022. **18**(22): p. 4315-4324.
372. Im, J., et al., *Anomalous thermal transition and crystallization of ionic liquids confined in graphene multilayers.* Chemical Communications, 2012. **48**(14): p. 2015-2017.
373. Wen, X., et al., *A new solid-state electrolyte based on polymeric ionic liquid for high-performance supercapacitor.* Ionics, 2019. **25**(1): p. 241-251.
374. Govardhana Rao, S., et al., *Thermophysical properties of 1-butyl-3-methylimidazolium tetrafluoroborate and N-methyl-2-pyrrolidinone as a function of temperature.* Journal of Molecular Liquids, 2015. **211**: p. 1009-1017.
375. Kiefer, J., J. Fries, and A. Leipertz, *Experimental Vibrational Study of Imidazolium-Based Ionic Liquids: Raman and Infrared Spectra of 1-Ethyl-3-methylimidazolium Bis(Trifluoromethylsulfonyl)imide and 1-Ethyl-3-methylimidazolium Ethylsulfate.* Applied Spectroscopy, 2007. **61**(12): p. 1306-1311.
376. Nafday, O. and S. Nesic. *Iron carbonate scale formation and CO2 corrosion in the presence of acetic acid*. in *NACE CORROSION*. 2005. NACE.
377. Dugstad, A., *The importance of FeCO 3 supersaturation on the CO 2 corrosion of carbon steels.* A. Dugstad, Paper, 1992(14).
378. Papavinasam, S., *3 - Electrochemical polarization techniques for corrosion monitoring*, in *Techniques for Corrosion Monitoring*, L. Yang, Editor. 2008, Woodhead Publishing. p. 49-85.
379. Onyeji, L., G. Kale, and M. Kermani, *Comparative Studies of the Effects of Microstructures on the Corrosion Behavior of Micro-Alloyed Steels in Unbuffered 3.5 Wt% NaCl Saturated with CO2.* International Journal of Chemical, Molecular, Nuclear, Materials and Metallurgical Engineering, 2017. **11**: p. 131-138.
380. Ikhmal, W., et al., *Corrosion inhibition of mild steel in seawater through green approach using Leucaena leucocephala leaves extract.* International Journal of Corrosion and Scale Inhibition, 2019. **8**: p. 628-643.
381. Shamsa, A., et al., *Impact of corrosion products on performance of imidazoline corrosion inhibitor on X65 carbon steel in CO2 environments.* Corrosion Science, 2021. **185**: p. 109423.
382. Uerdingen, M., et al., *Corrosion behaviour of ionic liquids.* Green Chemistry, 2005. **7**(5): p. 321-325.
383. Zhou, X., H. Yang, and F. Wang, *[BMIM]BF4 ionic liquids as effective inhibitor for carbon steel in alkaline chloride solution.* Electrochimica Acta, 2011. **56**(11): p. 4268-4275.
384. Gurjar, S., et al., *Performance of imidazolium based ionic liquids as corrosion inhibitors in acidic medium: A review.* Applied Surface Science Advances, 2021. **6**: p. 100170.

385. Mendez, C., et al. *On the Mechanism of Corrosion Inhibition by Crude Oils*. in *CORROSION 2001*. 2001.
386. Ramirez, M., et al. *Effect of Crude Oil Contaminants on the Internal Corrosion in Gas Pipelines*. in *CORROSION 2000*. 2000.
387. Ayello, F., et al. *Crude Oil Chemistry Effects On Inhibition Of Corrosion And Phase Wetting*. in *CORROSION 2011*. 2011.
388. Lazanas, A.C. and M.I. Prodromidis, *Electrochemical Impedance Spectroscopy—A Tutorial.* ACS Measurement Science Au, 2023. **3**(3): p. 162-193.
389. Morales-Hernandez, J., et al., *Electrochemical Impedance Spectroscopy (EIS): A Review Study of Basic Aspects of the Corrosion Mechanism Applied to Steels*, in *Electrochemical Impedance Spectroscopy*, M. El-Azazy, M. Min, and P. Annus, Editors. 2020, IntechOpen: Rijeka.
390. Mei, B.-A., et al., *Physical Interpretations of Nyquist Plots for EDLC Electrodes and Devices.* The Journal of Physical Chemistry C, 2018. **122**(1): p. 194-206.
391. Van Haeverbeke, M., M. Stock, and B. De Baets, *Equivalent Electrical Circuits and Their Use Across Electrochemical Impedance Spectroscopy Application Domains.* IEEE Access, 2022. **10**: p. 1-1.
392. Loveday, D., P. Peterson, and B. Rodgers, *Evaluation of organic coatings with electrochemical impedance spectroscopy.* JCT coatings tech, 2004. **8**: p. 46-52.
393. Lasia, A., *The Origin of the Constant Phase Element.* The Journal of Physical Chemistry Letters, 2022. **13**(2): p. 580-589.
394. Kim, J., K.-T. Park, and T.H. Kwon, *Influencing Factors of Steel States in Concrete Based on Electrochemical Impedance Spectroscopic Measurements.* Applied Sciences, 2022. **12**(24): p. 12611.
395. Srinivasan, R. and R. Punathil Meethal, *EIS Technique for Corrosion Study and Analysis*, in *A Treatise on Corrosion Science, Engineering and Technology*, U. Kamachi Mudali, et al., Editors. 2022, Springer Nature Singapore: Singapore. p. 3-20.
396. Loveday, D., P. Peterspm, and B. Rodgers, *Evaluation of organic coatings with electrochemical impedance spectroscopy - Part 2: Application of EIS to coatings.* JCT CoatingsTech, 2004. **1**: p. 88-93.
397. Policastro, S.A., et al., *Experimental and Numerical Investigation into the Effect of Water Uptake on the Capacitance of an Organic Coating.* Materials, 2023. **16**(10): p. 3623.
398. Li, S., et al., *Non-destructive evaluations of water uptake in epoxy coating.* Journal of Applied Polymer Science, 2024. **141**(2): p. e54777.
399. Liu, S., et al., *Corrosion Resistance of Graphene-Reinforced Waterborne Epoxy Coatings.* Journal of Materials Science & Technology, 2016. **32**: p. 425-431.
400. Perini, N., et al., *Electrochemical impedance spectroscopy for in situ petroleum analysis and water-in-oil emulsion characterization.* Fuel, 2012. **91**(1): p. 224-228.
401. Usman, B.J., et al., *Eco-friendly 2-Thiobarbituric acid as a corrosion inhibitor for API 5L X60 steel in simulated sweet oilfield environment: Electrochemical and surface analysis studies.* Scientific Reports, 2019. **9**(1): p. 830.

402. Farooq, U., et al., *Adsorption of Crude Oil Components on Mineral Surfaces Followed by Quartz Crystal Microbalance and Contact Angle Measurements: The Effect of Oil Composition, Simulated Weathering and Dispersants.* Energy & Fuels, 2019. **33**(3): p. 2359-2365.
403. Alberto da Silva, C., et al., *Analysis of crude oil effect for CO2 corrosion of carbon steel - A rotating cylinder electrode approach.* Geoenergy Science and Engineering, 2023. **229**: p. 212085.
404. Zhang, X., et al. *Variations in Silicone Rubber Content and Mechanism Analysis During Aging Process of Insulator Coatings with Different Calcium Carbonate Content*. in *The Proceedings of the 11th Frontier Academic Forum of Electrical Engineering (FAFEE2024)*. 2025. Singapore: Springer Nature Singapore.
405. Poh, C.L., et al., *Tensile, dielectric, and thermal properties of epoxy composites filled with silica, mica, and calcium carbonate.* Journal of Materials Science: Materials in Electronics, 2014. **25**(5): p. 2111-2119.
406. Siddig, O., A.A. Mahmoud, and S. Elkatatny, *A review of the various treatments of oil-based drilling fluids filter cakes.* Journal of Petroleum Exploration and Production Technology, 2022. **12**(2): p. 365-381.
407. Havre, T., *Formation of Calcium Naphthenate in Water/Oil Systems, Naphthenic Acid Chemistry and Emulsion Stability.* 2002.
408. Huo, D., et al., *Calcium in crude oil: a review.* Petroleum Science and Technology, 2022. **40**(23): p. 2861-2876.
409. Bertin, F., et al., *Electrochemical impedance response of a thick and porous calcium carbonate layer deposited by thermal growth on a carbon steel electrode.* Corrosion Science, 2024. **227**: p. 111778.
410. Abdel-Gaber, A.M., et al., *A natural extract as scale and corrosion inhibitor for steel surface in brine solution.* Desalination, 2011. **278**(1): p. 337-342.
411. Gabrielli, C., et al., *Study of calcium carbonate scales by electrochemical impedance spectroscopy.* Electrochimica Acta, 1997. **42**(8): p. 1207-1218.
412. Skale, S., V. Doleček, and M. Slemnik, *Substitution of the constant phase element by Warburg impedance for protective coatings.* Corrosion Science, 2007. **49**(3): p. 1045-1055.
413. Taylor, S.R. and E. Gileadi, *Physical Interpretation of the Warburg Impedance.* Corrosion, 1995. **51**(9): p. 664-671.
414. De Motte, R., et al., *A study by electrochemical impedance spectroscopy and surface analysis of corrosion product layers formed during CO2 corrosion of low alloy steel.* Corrosion Science, 2020. **172**: p. 108666.
415. Garcia, S., et al., *Unravelling the corrosion inhibition mechanisms of bi-functional inhibitors by EIS and SEM–EDS.* 2013. **69**: p. 346-358.
416. Hong, T., Y. Sun, and W.J.C.s. Jepson, *Study on corrosion inhibitor in large pipelines under multiphase flow using EIS.* 2002. **44**(1): p. 101-112.
417. Tan, Y., S. Bailey, and B.J.C.s. Kinsella, *An investigation of the formation and destruction of corrosion inhibitor films using electrochemical impedance spectroscopy (EIS).* 1996. **38**(9): p. 1545-1561.

418. Marín-Cruz, J., et al., *EIS characterization of the evolution of calcium carbonate scaling in cooling systems in presence of inhibitors.* 2007. **11**: p. 1245-1252.
419. Touir, R., et al., *Corrosion and scale processes and their inhibition in simulated cooling water systems by monosaccharides derivatives: Part I: EIS study.* 2009. **249**(3): p. 922-928.
420. Lakshmi, D.S., et al., *Application of ionic liquid polymeric microsphere in oil field scale control process.* Journal of Petroleum Science and Engineering, 2013. **112**: p. 69-77.
421. Chen, H., X. Wang, and J. Shen, *Revealing the Deterioration Effect of Scale Inhibitor on the Performance of Corrosion Inhibitor under Dynamic Conditions.* Journal of Materials Engineering and Performance, 2025. **34**(3): p. 2145-2155.
422. Lopez, D.A., S.N. Simison, and S.J.E.A. De Sanchez, *The influence of steel microstructure on CO2 corrosion. EIS studies on the inhibition efficiency of benzimidazole.* 2003. **48**(7): p. 845-854.
423. Bastos, A., M. Ferreira, and A.J.C.S. Simões, *Corrosion inhibition by chromate and phosphate extracts for iron substrates studied by EIS and SVET.* 2006. **48**(6): p. 1500-1512.
424. Chen, Y. and W.J.E.a. Jepson, *EIS measurement for corrosion monitoring under multiphase flow conditions.* 1999. **44**(24): p. 4453-4464.
425. Desimone, M., et al., *Amphiphilic amido-amine as an effective corrosion inhibitor for mild steel exposed to CO2 saturated solution: Polarization, EIS and PM-IRRAS studies.* 2011. **56**(8): p. 2990-2998.
426. Osorio-Celestino, G.R., et al., *Influence of Calcium Scaling on Corrosion Behavior of Steel and Aluminum Alloys.* ACS Omega, 2020. **5**(28): p. 17304-17313.
427. Shamsa, A., et al., *The role of Ca2+ ions on Ca/Fe carbonate products on X65 carbon steel in CO2 corrosion environments at 80 and 150 C.* 2019. **156**: p. 58-70.
428. Tavares, L.M., et al., *Effect of calcium carbonate on low carbon steel corrosion behavior in saline CO2 high pressure environments.* 2015. **359**: p. 143-152.
429. Thompson, I. and D. Campbell, *Interpreting Nyquist responses from defective coatings on steel substrates.* Corrosion Science, 1994. **36**(1): p. 187-198.
430. Walter, G.W., *A review of impedance plot methods used for corrosion performance analysis of painted metals.* Corrosion Science, 1986. **26**(9): p. 681-703.
431. Hinderliter, B.R., et al., *Interpretation of EIS data from accelerated exposure of coated metals based on modeling of coating physical properties.* Electrochimica Acta, 2006. **51**(21): p. 4505-4515.
432. Wang, L., et al., *Revealing physical interpretation of time constants in electrochemical impedance spectra of Mg via Tribo-EIS measurements.* Electrochimica Acta, 2022. **404**: p. 139582.
433. Wang, X., et al., *The polarity of ionic liquids: relationship between relative permittivity and spectroscopic parameters of probe.* Industrial & Engineering Chemistry Research, 2019. **58**(17): p. 7352-7361.
434. Fawell, P.D., A.D. Costine, and A.F. Grabsch, *Why small-scale testing of reagents goes wrong*, in *Paste 2015: Proceedings of the 18th*

International Seminar on Paste and Thickened Tailings, R. Jewell and A.B. Fourie, Editors. 2015, Australian Centre for Geomechanics: Perth. p. 153-165.

435. Sanders, L., et al., *Assessment of combined scale/corrosion inhibitors – A combined jar test/bubble cell.* Journal of Petroleum Science and Engineering, 2014. **118**: p. 126-139.
436. Han, M., et al., *Calcium ions have a detrimental impact on the boundary lubrication property of hyaluronic acid and lubricin (PRG-4) both alone and in combination.* Colloids and Surfaces B: Biointerfaces, 2024. **234**: p. 113741.
437. Shaikhah, D., et al., *Augmentation of Polymer-FeCO3 Microlayers on Carbon Steel for Enhanced Corrosion Protection in Hydrodynamic CO2 Corrosion Environments.* ACS Omega, 2024. **9**(29): p. 31745-31753.
438. Taleb, W., et al., *Siderite micro-modification for enhanced corrosion protection.* npj Materials Degradation, 2017. **1**(1): p. 13.
439. Smith, J.S., A.E. Roitberg, and O. Isayev, *Transforming computational drug discovery with machine learning and AI*. 2018, ACS Publications. p. 1065-1069.
440. Quadri, T.W., et al., *State-of-the-art progress on artificial intelligence and machine learning in accessing molecular coordination and adsorption of corrosion inhibitors.* Applied Physics Reviews, 2025. **12**(1).
441. Akrom, M., S. Rustad, and H.K. Dipojono, *Machine learning investigation to predict corrosion inhibition capacity of new amino acid compounds as corrosion inhibitors.* Results in Chemistry, 2023. **6**: p. 101126.
442. Sanni, O., et al., *Study of surface deposition and bulk scaling kinetics in oilfield conditions using an in-situ flow rig*. Vol. 2015. 2015.
443. Al-Gailani, A., et al., *Inorganic fouling of heat transfer surface from potable water during convective heat transfer.* Applied Thermal Engineering, 2021. **184**: p. 116271.
444. Zhang, M., et al., *Long‐Term Stability of a Liquid‐Infused Coating with Anti‐Corrosion and Anti‐Icing Potentials on Al Alloy.* ChemElectroChem, 2019. **6**.
445. Ouyang, Y., et al., *Liquid infused surface based on hierarchical dendritic iron wire array: An exceptional barrier to prohibit biofouling and biocorrosion.* Progress in Organic Coatings, 2019. **136**: p. 105216.
446. Wang, P., T. Li, and D. Zhang, *Fabrication of non-wetting surfaces on zinc surface as corrosion barrier.* Corrosion Science, 2017. **128**: p. 110-119.
447. Kindi, M.A., et al., *Substrate Protection with Corrosion Scales: Can We Depend on Iron Carbonate?* ACS Applied Materials & Interfaces, 2021. **13**(48): p. 58193-58200.